Ignacio Rojas · Olga Valenzuela ·
Fernando Rojas · Luis Javier Herrera ·
Francisco Ortuño (Eds.)

LNBI 13346

Bioinformatics and Biomedical Engineering

**9th International Work-Conference, IWBBIO 2022
Maspalomas, Gran Canaria, Spain, June 27–30, 2022
Proceedings, Part I**

Part I

Springer

MOREMEDIA

Lecture Notes in Bioinformatics 13346

Subseries of Lecture Notes in Computer Science

More information about this subseries at

Ignacio Rojas · Olga Valenzuela ·
Fernando Rojas · Luis Javier Herrera ·
Francisco Ortuño (Eds.)

Bioinformatics and Biomedical Engineering

9th International Work-Conference, IWBBIO 2022
Maspalomas, Gran Canaria, Spain, June 27–30, 2022
Proceedings, Part I

 Springer

Editors
Ignacio Rojas (ID)
University of Granada
Granada, Spain

Fernando Rojas (ID)
ETSIIT. CITIC-UGR
University of Granada
Granada, Spain

Francisco Ortuño
University of Granada
Granada, Spain

Olga Valenzuela (ID)
Faculty of Sciences
University of Granada
Granada, Spain

Luis Javier Herrera (ID)
ETSIIT
University of Granada
Granada, Spain

Preface

We are proud to present the final set of accepted full papers for the 9th International Work-Conference on Bioinformatics and Biomedical Engineering (IWBBIO 2022) held in Gran Canaria, Spain, during June 27–30, 2022.

IWBBIO seeks to provide a discussion forum for scientists, engineers, educators, and students about the latest ideas and realizations in the foundations, theory, models, and applications for interdisciplinary and multidisciplinary research encompassing disciplines of computer science, mathematics, statistics, biology, bioinformatics, and biomedicine.

The aim of IWBBIO 2022 was to create a friendly environment that could lead to the establishment or strengthening of scientific collaborations and exchanges among attendees, and therefore IWBBIO 2022 solicited high-quality original research papers (including significant work in progress) on any aspect of bioinformatics, biomedicine, and biomedical engineering.

Submissions relating to new computational techniques and methods in machine learning; data mining; text analysis; pattern recognition; data integration; genomics and evolution; next generation sequencing data; protein and RNA structure; protein function and proteomics; medical informatics and translational bioinformatics; computational systems biology; modeling and simulation; and their application in the life science domain, biomedicine, and biomedical engineering were especially encouraged. The list of topics in the call for papers has also evolved, resulting in the following list for the present edition:

1. **Computational proteomics**. Analysis of protein-protein interactions. Protein structure modeling. Analysis of protein functionality. Quantitative proteomics and PTMs. Clinical proteomics. Protein annotation. Data mining in proteomics.
2. **Next generation sequencing and sequence analysis**. De novo sequencing, re-sequencing, and assembly. Expression estimation. Alternative splicing discovery. Pathway analysis. Chip-seq and RNA-Seq analysis. Metagenomics. SNPs prediction.
3. **High performance in bioinformatics**. Parallelization for biomedical analysis. Biomedical and biological databases. Data mining and biological text processing. Large scale biomedical data integration. Biological and medical ontologies. Novel architecture and technologies (GPU, P2P, Grid, etc) for bioinformatics.
4. **Biomedicine**. Biomedical computing. Personalized medicine. Nanomedicine. Medical education. Collaborative medicine. Biomedical signal analysis. Biomedicine in industry and society. Electrotherapy and radiotherapy.
5. **Biomedical engineering**. E-computer-assisted surgery. Therapeutic engineering. Interactive 3D modelling. Clinical engineering. Telemedicine. Biosensors and data acquisition. Intelligent instrumentation. Patient monitoring. Biomedical robotics. Bio-nanotechnology. Genetic engineering.
6. **Computational systems for modelling biological processes**. Inference of biological networks. Machine learning in bioinformatics. Classification for

biomedical data. Microarray data analysis. Simulation and visualization of biological systems. Molecular evolution and phylogenetic modeling.

7. **Healthcare and diseases**. Computational support for clinical decisions. Image visualization and signal analysis. Disease control and diagnosis. Genome-phenome analysis. Biomarker identification. Drug design. Computational immunology.

8. **E-health**. E-health technology and devices. E-health information processing. Telemedicine/E-health application and services. Medical image processing. Video techniques for medical images. Integration of classical medicine and E-health.

9. **COVID-19**. A special session analyzing different aspects, fields of application, and technologies that have been applied against COVID-19.

After a careful peer review and evaluation process (each submission was reviewed by at least 2, and on average 3.1, Program Committee members or additional reviewers), 75 papers were accepted, according to the recommendations of reviewers and the authors' preferences, to be included in the LNBI proceedings.

IWBBIO 2022 featured several Special Sessions, which are a very useful tool in order to complement the regular program with new and emerging topics of particular interest for the participating community. Special Sessions that emphasized multidisciplinary and transversal aspects, as well as cutting-edge topics were especially encouraged and welcomed, and in this edition of IWBBIO 2022 the following were received:

– **SS1. High-throughput Genomics: Bioinformatic Tools and Medical Applications.**
  Genomics is concerned with the sequencing and analysis of an organism's genome. It is involved in the understanding of how every single gene can affect the entire genome. This goal is mainly afforded using the current, cost-effective, high-throughput sequencing technologies. These technologies produce a huge amount of data that usually require high-performance computing solutions and open new ways for the study of genomics, as well as transcriptomics, gene expression, and systems biology, among others. The continuous improvements and broader applications of sequencing technologies are producing a continuous new demand for improved high-throughput bioinformatics tools.

  In this context, the generation, integration, and interpretation of genetic and genomic data is driving a new era of healthcare and patient management. Medical genomics (or genomic medicine) is an emerging discipline that involves the use of genomic information about a patient as part of the clinical care with diagnostic or therapeutic purposes to improve the health outcomes. Moreover, it can be considered a subset of precision medicine that has an impact in the fields of oncology, pharmacology, rare and undiagnosed diseases, and infectious diseases. The aim of this Special Session was to bring together researchers in medicine, genomics, and bioinformatics to translate medical genomics research into new diagnostic, therapeutic, and preventive medical approaches. Therefore, we invited authors to submit original research, new tools or pipelines, and update and review articles on relevant topics, such as (but not limited to):

- Tools for data pre-processing (quality control and filtering)
- Tools for sequence mapping
- Tools for the comparison of two read libraries without an external reference
- Tools for genomic variants (such as variant calling or variant annotation)
- Tools for functional annotation: identification of domains, orthologues, genetic markers, and controlled vocabulary (GO, KEGG, InterPro, etc.)
- Tools for gene expression studies and tools for Chip-Seq data
- Integrative workflows and pipelines

Organizers: M. Gonzalo Claros, Department of Molecular Biology and Biochemistry, University of Málaga, Spain; Javier Pérez Florido, Bioinformatics Research Area, Fundación Progreso y Salud, Seville, Spain; and Francisco M. Ortuño, Department of Computer Architecture and Technology, University of Granada, Spain.

– **SS2. Feature Selection, Extraction, and Data Mining in Bioinformatics: Approaches, Methods, and Adaptations.**
Various applications of bioinformatics, system biology, and biophysics measurement data mining require proper, accurate, and precise preprocessing or data transformation before the analysis itself. Here, the most important issues are covered by the feature selection and extraction techniques to translate the raw data into the inputs for the machine learning and multivariate statistic algorithms. Even if this is a complex task, it reduces the problem dimensionality, by removing redundant or irrelevant data, without affecting significantly the principal information. The methods and approaches are often conditioned by the physical properties of the measurement process, mathematically congruent description and parameterization, and biological aspects of specific tasks. With the increasing adoption of artificial intelligence methods to solve bioinformatics problems, it is necessary to understand the conditionality of such algorithms, to choose and use the correct approach and avoid misinterpretations, artefacts, and aliasing effects. The adoption often uses existing knowledge from different fields, and direct application might underestimate the required conditions and corrupt the analysis results. This Special Session provided a forum to dicuss the multidisciplinary overlaps, development, implementation, and adoption of feature and selection methods for datasets with a biological origin in order to setup the pipeline from measurement design through signal processing to obtaining the results. The topic should cover theoretical questions, practical examples, and results verifications.

Organizer: Jan Urban, Laboratory of Signal and Image Processing, Institute of Complex Systems, South Bohemian Research Center of Aquaculture and Biodiversity of Hydrocenoses, Faculty of Fisheries and Protection of Waters, University of South Bohemia, Czech Republic.

– **SS3. Smart Healthcare Solutions for Handling COVID-19.**
Smart healthcare plays an important role towards providing robust solutions, especially for COVID-19 related problems, both locally and globally. Collection and interpretation of data worldwide and systematic research helps in identifying the potential solutions as well as predicting the future issues. This Special Session was

organized to emphasize the potential problems and the related solutions, focusing on the following topics:

- Smart wearable healthcare
- Microbiological analysis
- Minimal invasive sensors
- Biomedical waste management
- Drug-induced therapy
- Early prediction and diagnosis
- Biostatistical driven solution
- Explainable AI and deep learning driven solutions

Organizer: N. Sriraam, Department of Medical Electronics, M.S. Ramaiah Institute of Technology, India.

– **SS4. Computational Systems for Modeling of Medical Micro Sensors.**
Medical sensors are micro devices containing several parts mainly including micro-tubes, micro-valves, biological/body fluids (blood, plasma, saliva, etc.), and chemical materials (reagents and other materials). Microfluidics is an interdisciplinary field that involves the science and technology of fluid flow through systems with micro scales. Computational systems and engineering simulation are essential from the start to the end of the medical sensor design and development process. The main advantages of computational systems (AI, CFD, etc.) in medical sensors design and development are as follows:

- Improvement and optimization of design
- Acceleration in medical device innovation
- Reduction of cost and failure risk
- Reduction of production times and regulatory approval processes

The main objectives of this Special Session were as follows:

- To determine the role of computational systems (AI, CFD, etc.) in medical sensors design and development
- To determine the role of simulation in optiming the analysis process and design of medical micro-sensors
- To discuss the use of computational fluid dynamics (CFD) in analyzing medical micro sensors
- To discuss the use of computational systems to combine engineering, biology, chemical, and other criteria

Organizers: Patrizia Piro and Behrouz Pirouz, Department of Civil Engineering, University of Calabria, Italy.

It is important to note that for the sake of consistency and readability the accepted papers are organizaed into 15 chapters over two volumes, essentially following the topics

list included in the call for papers. The first volume (LNBI 13346), entitled "Bioinformatics and Biomedical Engineering. Part I" is divided into eight main parts and includes the contributions on

1. Biomedical Computing
2. Biomedical Engineering
3. Biomedical Signal Analysis
4. Biomedicine. New Advances and Applications
5. Biosensors and Data Acquisition
6. Image Visualization and Signal Analysis in Biomedical Applications
7. Computational Support for Clinical Decisions
8. COVID-19. Bioinformatics and Biomedicine

The second volume (LNBI 13347), entitled "Bioinformatics and Biomedical Engineering. Part II" is divided into seven main parts and includes the contributions on:

1. Chip-seq and RNA-Seq Analysis
2. Bioinformatics and Biomarker Identication
3. Computational Proteomics
4. Computational Systems for Modelling Biological Processes
5. Feature Selection, Extraction, and Data Mining in Bioinformatics: Approaches, Methods, and Adaptations
6. Machine Learning in Bioinformatics
7. Next Generation Sequencing and Sequence Analysis

This 9th edition of IWBBIO was organized by the University of Granada. We wish to thank our main sponsor as well as the Department of Computer Architecture and Computer Technology at the University of Granada (CITIC-UGR) and International Society for Computational Biology (ISCB) for their support and grants. We also wish to thank the editors in charge of different international journals for their interest in publishing special issues of a selection of the best papers of IWBBIO 2022. In this edition of IWBBIO there were two awards (best contribution award and best contribution from student participant) sponsored by the Editorial Office of Genes, a MDPI journal.

We would also like to express our gratitude to the members of the different committees for their support, collaboration, and good work. We especially thank the Program Committee, the reviewers, and the Special Session organizers. We also want to express our gratitude to the EasyChair platform. Finally, we wish to thank Springer for their continuous support and cooperation.

April 2022

Ignacio Rojas
Olga Valenzuela
Fernando Rojas
Luis Javier Herrera
Francisco Ortuño

Organization

Conference Chairs

Ignacio Rojas	University of Granada, Spain
Olga Valenzuela	University of Granada, Spain
Fernando Rojas	University of Granada, Spain
Luis Javier Herrera	University of Granada, Spain
Francisco Ortuño	University of Granada, Spain

Steering Committee

Miguel A. Andrade	University of Mainz, Germany
Hesham H. Ali	University of Nebraska, USA
Oresti Baños	University of Granada, Spain
Alfredo Benso	Politecnico di Torino, Italy
Larbi Boubchir	LIASD, University of Paris 8, France
Giorgio Buttazzo	Superior School Sant'Anna, Italy
Gabriel Caffarena	University San Pablo CEU, Spain
Mario Cannataro	Magna Graecia University of Catanzaro, Italy
Jose María Carazo	Spanish National Center for Biotechnology (CNB), Spain
Jose M. Cecilia	Universidad Católica San Antonio de Murcia (UCAM), Spain
M. Gonzalo Claros	University of Malaga, Spain
Joaquin Dopazo	Fundacion Progreso y Salud, Spain
Werner Dubitzky	University of Ulster, UK
Afshin Fassihi	Universidad Católica San Antonio de Murcia (UCAM), Spain
Jean-Fred Fontaine	University of Mainz, Germany
Humberto Gonzalez	University of Basque Country (UPV/EHU), Spain
Concettina Guerra	Georgia Tech, USA
Roderic Guigo	Pompeu Fabra University, Spain
Andy Jenkinson	Karolinska Institute, Sweden
Craig E. Kapfer	Reutlingen University, Germany
Narsis Aftab Kiani	European Bioinformatics Institute (EBI), UK
Natividad Martinez	Reutlingen University, Germany
Marco Masseroli	Politechnical University of Milan, Italy
Federico Moran	Complutense University of Madrid, Spain

Cristian R. Munteanu	University of A Coruña, Spain
Jorge A. Naranjo	NYU Abu Dhabi, Abu Dhabi
Michael Ng	Hong Kong Baptist University, China
Jose L. Oliver	University of Granada, Spain
Juan Antonio Ortega	University of Seville, Spain
Fernando Rojas	University of Granada, Spain
Alejandro Pazos	University of A Coruña, Spain
Javier Perez Florido	Genomics and Bioinformatics Platform of Andalusia, Spain
Violeta I. Pérez Nueno	Inria Nancy-Grand Est and Loria, France
Horacio Pérez-Sánchez	Universidad Católica San Antonio de Murcia (UCAM), Spain
Alberto Policriti	Università di Udine, Italy
Omer F. Rana	Cardiff University, UK
M. Francesca Romano	Superior School Sant'Anna, Italy
Yvan Saeys	Ghent University, Belgium
Vicky Schneider	The Genome Analysis Centre (TGAC), UK
Ralf Seepold	HTWG Konstanz, Germany
Mohammad Soruri	University of Birjand, Iran
Yoshiyuki Suzuki	Tokyo Metropolitan Institute of Medical Science, Japan
Oswaldo Trelles	University of Malaga, Spain
Shusaku Tsumoto	Shimane University, Japan
Renato Umeton	Dana-Farber Cancer Institute and Massachusetts Institute of Technology, USA
Jan Urban	University of South Bohemia, Czech Republic
Alfredo Vellido	Polytechnic University of Catalonia, Spain
Wolfgang Wurst	GSF National Research Center of Environment and Health, Germany

Program Committee and Additional Reviewers

Magda Abdellattif	Taif University, Saudi Arabia
Fares Al-Shargie	American University of Sharjah, United Arab Emirates
Jesus Alcala-Fdez	University of Granada, Spain
Hesham Ali	University of Nebraska Omaha, USA
Georgios Anagnostopoulos	Florida Institute of Technology, USA
Patrizio Arrigo	SCITEC, Italy
Gajendra Kumar Azad	Patna University, India
Hazem Bahig	Ain Shams University, Egypt
Ugo Bastolla	Centro de Biologia Molecular Severo Ochoa, Spain

Payam Behzadi	Islamic Azad University, Iran
Alfredo Benso	Politecnico di Torino, Italy
Anna Bernasconi	Politecnico di Milano, Italy
Mahua Bhattacharya	Indian Institute of Information Technology and Management, Gwalior, India
Paola Bonizzoni	Università di Milano-Bicocca, Italy
Larbi Boubchir	University of Paris 8, France
Hacene Boukari	Delaware State University, USA
Gabriel Caffarena	Universidad CEU San Pablo, Spain
Mario Cannataro	Magna Graecia University of Catanzaro, Italy
Jose Maria Carazo	National Center for Biotechnology (CNB-CSIC), Spain
Rita Casadio	University of Bologna, Italy
Daniel Castillo-Secilla	University of Granada, Spain
Claudia Cava	IBFM-CNR, Italy
Francisco Cavas-Martínez	Technical University of Cartagena, Spain
Chinmay Chakraborty	Birla Institute of Technology, India
Ting-Fung Chan	The Chinese University of Hong Kong, Hong Kong
Satyendra Chandra Tripathi	AIIMS Nagpur, India
Kun-Mao Chao	National Taiwan University, Taiwan
Bolin Chen	Northwestern Polytechnical University, China
Brian Chen	Lehigh University, USA
Chuming Chen	University of Delaware, USA
Jeonghyeon Choi	Georgia Regents University, USA
Javier Cifuentes Faura	University of Murcia, Spain
M. Gonzalo Claros	Universidad de Málaga, Spain
Zhu Daming	Shandong University, China
Bhaskar Dasgupta	University of Illinois at Chicago, USA
Alexandre G. De Brevern	INSERM UMR-S, Université Paris Cité, France
Javier De Las Rivas	Cancer Research Center (CiC-IBMCC, CSIC/USAL/IBSAL), Spain
Ricardo de Matos Simoes	Harvard University, USA
Marie-Dominique Devignes	Loria, France
Paolo Di Giamberardino	Sapienza University of Rome, Italy
Maria Natalia Dias Soeiro Cordeiro	University of Porto, Portugal
Marko Djordjevic	University of Belgrade, Serbia
Joaquin Dopazo	Fundacion Progreso y Salud, Spain
Mohammed Elmogy	Mansoura University, Egypt
Gionata Fragomeni	Magna Graecia University of Catanzaro, Italy
Hassan Ghazal	Mohammed I University, Morocco

Razvan Ghinea	University of Granada, Spain
Christophe Guyeux	University of Franche-Comté, France
Pietro Hiram Guzzi	Magna Graecia University of Catanzaro, Italy
Michael Hackenberg	University of Granada, Spain
Nurit Haspel	University of Massachusetts Boston, USA
Morihiro Hayashida	National Institute of Technology, Matsue College, Japan
Luis Herrera	University of Granada, Spain
Ralf Hofestaedt	Bielefeld University, Germany
Jingshan Huang	University of South Alabama, USA
Cosimo Ieracitano	University Mediterranea of Reggio Calabria, Italy
Chang-Hwan Im	Hanyang University, South Korea
Hamed Khodadadi	Islamic Azad University, Iran
Narsis Kiani	Karolinska Institute, Sweden
Tomas Koutny	University of West Bohemia, Czech Republic
Konstantin Krutovsky	Georg-August-University of Göttingen, Germany
Chen Li	Monash University, Australia
Shuai Cheng Li	City University of Hong Kong, Hong Kong
Li Liao	University of Delaware, USA
Hongfei Lin	Dalian University of Technology, China
Javier Martin	IPBLN-CSIC, Spain
Francisco Martínez-Álvarez	Universidad Pablo de Olavide, Spain
Roderick Melnik	Wilfrid Laurier University, Canada
Francesco Carlo Morabito	University of Reggio Calabria, Italy
Enrique Muro	Johannes Gutenberg University, Germany
Kenta Nakai	University of Tokyo, Japan
Isabel Nepomuceno	University of Seville, Spain
Dang Ngoc Hoang Thanh	University of Economics Ho Chi Minh City, Vietnam
José Luis Oliveira	University of Aveiro, Portugal
Yuriy Orlov	Institute of Cytology and Genetics, Russia
Juan Antonio Ortega	University of Seville, Spain
Andres Ortiz	University of Malaga, Spain
Francisco Manuel Ortuño	University of Granada, Spain
Motonori Ota	Nagoya University, Japan
Mehmet Akif Ozdemir	Izmir Katip Celebi University, Turkey
Joel P. Arrais	University of Coimbra, Portugal
Paolo Paradisi	ISTI-CNR, Italy
Taesung Park	Seoul National University, South Korea
Antonio Pinti	I3MTO Orléans, France
Yuri Pirola	Università degli Studi di Milano-Bicocca, Italy
Joanna Polanska	The Silesian University of Technology, Poland

Alberto Policriti	University of Udine, Italy
Hector Pomares	University of Granada, Spain
María M. Pérez	University of Granada, Spain
Hossein Rabbani	Isfahan University of Medical Sciences, Iran
Amgad Rabie	Ain Shams University, Egypt
Jiulietta Rau	Istituto di Struttura della Materia, Italy
Khalid Raza	Jamia Millia Islamia, India
Jairo Rocha	University of the Balearic Islands, Spain
Maria Rodriguez Martinez	IBM Zurich Research Laboratory, Switzerland
Fernando Rojas	University of Granada, Spain
Ignacio Rojas	University of Granada, Spain
Gregorio Rubio	Universitat Politècnica de València, Spain
Irena Rusu	LINA, University of Nantes, France
Michael Sadovsky	Institute of Computational Modelling of SB RAS, Russia
Beata Sarecka-Hujar	Medical University of Silesia in Katowice, Poland
Jean-Marc Schwartz	University of Manchester, UK
Russell Schwartz	Carnegie Mellon University, USA
Preeti Singh	UIET, India
Surinder Singh	Panjab University, India
Sónia Sobral	Universidade Portucalense, Portugal
Jiangning Song	Monash University, Australia
Joe Song	New Mexico State University, USA
Natarajan Sriraam	M.S. Ramaiah Institute of Technology, India
Jiangtao Sun	Beihang University, China
Wing-Kin Sung	National University of Singapore, Singapore
Prashanth Suravajhala	Amrita University Kerala, India
Martin Swain	Aberystwyth University, UK
Sing-Hoi Sze	Texas A&M University, USA
Alessandro Tonacci	IFC-CNR, Italy
Carolina Torres	University of Granada, Spain
Marcos Roberto Tovani Palone	University of São Paulo, Brazil
Shusaku Tsumoto	Shimane University, Japan
Renato Umeton	Massachusetts Institute of Technology, USA
Jan Urban	Institute of Complex Systems, FFPW USB, Czech Republic
Olga Valenzuela	University of Granada, Spain
Alfredo Vellido	Universitat Politècnica de Catalunya, Spain
Jianxin Wang	Central South University, China
Jiayin Wang	Xi'an Jiaotong University, China
Junbai Wang	Radium Hospital, Norway
Lusheng Wang	City University of Hong Kong, Hong Kong

Ka-Chun Wong	City University of Hong Kong, Hong Kong
Phil Yang	George Mason University, USA
Jin Zhang	Washington University in St. Louis, USA
Yudong Zhang	University of Leicester, UK
Zhongming Zhao	University of Texas Health Science Center at Houston, USA
Huiru Zheng	University of Ulster, UK
Shanfeng Zhu	Fudan University, China

Contents – Part I

Biomedical Signal Analysis

Biomedicine. New Advances and Applications

Biosensors and Data Acquisition

Image Visualization and Signal Analysis in Biomedical Applications

Computational Support for Clinical Decisions

COVID-19. Bioinformatics and Biomedicine

Contents – Part II

Computational Proteomics

Computational Systems for Modelling Biological Processes

**Feature Selection, Extraction, and Data Mining in Bioinformatics:
Approaches, Methods and Adaptations**

Machine Learning in Bioinformatics

Next Generation Sequencing and Sequence Analysis

Biomedical Computing

Calculation of DNA Strand Breaks by Types of Electron Interaction with Monte Carlo Simulation

Youssef Lamghari[1], Huizhong Lu[2], and M'hamed Bentourkia[1]([✉])

[1] Department of Nuclear Medicine and Radiobiology, University of Sherbrooke, 12th Avenue North, Sherbrooke, QC J15N4, Canada
Mhamed.Bentourkia@USherbrooke.ca

[2] Support Service for Research, Innovation and Creation, 500, boul. de l'Université, Sherbrooke, QC J1K 2R1, Canada

Abstract. In cancer treatment with radiation, the objective is to kill tumor cells by damaging their DNA. However, the DNA strand breaks are not yet understood by which types and energy of electron interactions they are caused. Most of Monte Carlo simulations reported in the literature consider an energy deposition in water-equivalent to cause DNA strand breaks. In recent years, DNA atomistic models were introduced but still the simulations consider energy deposition in volumes of DNA material. In the present work, we report advances in the understanding of DNA single and double strand breaks by low energy electrons, and the results of the simulations were compared to experimental data. We simulated a model of atomistic B-DNA, forming 1122 base pairs twisted and forming a length of 30 nm. Each atom has been represented by a sphere whose radius is equal to the radius of van der Waals. We repeatedly simulated 10 million electrons for each of the energies from 4 eV to 500 eV and counted each interaction type with its position x,y,z in the volume of DNA. Based on the number and types of interactions at the atomic level, the number of DNA single and double strand breaks were calculated. In addition, with our simulation, it is straightforward to discriminate the strand and base breaks as a function of radiation interaction type and energy. In conclusion, the knowledge of DNA damage at the atomic level helps, for example, to design internal therapeutic agents of cancer treatment.

Keywords: Monte Carlo simulation · Cancer · Radiation · DNA · Radiotherapy

1 Introduction

In radiotherapy, both by internal or external irradiation in the patient, the objective is to kill the cancer cells of a solid tumor by damaging their DNA. This goal is attempted by adjusting the radiation energy fluence in repeated treatment sessions. For example, in brain cancers, the dose can be of 2 Gy per day, 5 days a week and for 7 weeks. With the split dose over time, the normal tissue cells have the potential to repair their damaged DNA. If untreated at the beginning, the tumor cells can migrate and provoke a metastasis which become difficult to treat with external radiation beam.

The most dominant effects of radiation interaction with DNA are by means of low energy secondary electrons set in motion by the primary beam of photons or other particles. However, the DNA strand breaks are not yet understood by which types of electron interactions and by which level of energies they are caused. Most of Monte Carlo simulations reported in the literature consider an energy deposition in water to cause DNA strand breaks based on energy levels deduced from experimental measurements [1], others, more sophisticated, used appropriate density of DNA [2]. In recent years, DNA atomistic models were introduced but still the simulations consider energy deposition in volumes of DNA material [3–5].

The Monte Carlo simulations use different platforms and algorithms to simulate radiation damage to DNA, however, the physics of radiation interaction with DNA remains mainly the same depending on the low energy threshold and types of interactions included in the simulations [6–8]. Apart from the direct interaction of the incident radiation beam and the secondary electrons set in motion in the medium, there are also the water products especially the water radicals which damage DNA [9–11]. Other simulations concentrated on Auger emissions impacting DNA [12, 13]. Even the DNA repair has been taken into account in the simulations [14, 15].

Despite the great progress in the simulation of the atomistic DNA and radiation damage to DNA either directly or indirectly, there remains hot topics still under investigation, among them the physics of low energy electrons below 5 eV, the types of interactions provoking DNA strands or bases breaks, simultaneous effects of incident radiation and secondary electrons, environment of DNA, etc. Once pairing simulations with experiments to retrieve the global experimental results, it could be an avenue to isolate individual radiation effects from the simulations. In other words, the simulations allow to decompose the experimental results in their sub-effects including the possible extraction of the cross sections.

Among the great advantages of GEANT4-DNA is the choice of the DNA breakage mechanism according to the types of interactions and the energy deposited. In this context, several studies have been carried out experimentally to measure the dose necessary to induce a DNA single strand break (SSB) and double strand break (DSB). Other studies reported simulations performed using these experimental data to quantify the DNA SSB and DSB. In addition, some algorithms have been designed to convert the energy deposited into numbers of DNA breaks such as GEANT4-DNA (PDB4DNA) [3].

In order to develop a simulation tool for internal dosimetry estimation, and in a second step for both internal dosimetry and imaging with positron emission tomography (PET) (theranostic), we wanted by the present work to reproduce with Monte Carlo simulation the yield of SSB and DSB produced by low energy electrons in an experimental setup [16, 17], and to assess the impact of each type of electron interaction on DNA breaks. For this purpose, we simulated a model of atomistic DNA, B-DNA, where each monomer was a nucleotide composed of a nucleic base (adenine, cytosine, guanine, and thymine) coupled to a deoxyribose molecule, which in turn is linked to a phosphate group, thus forming 1122 base pairs twisted and forming a length of 30 nm [11]. We used several electron energies and compared our results with the experimental results from [16, 17].

2 Materials and Methods

The geometry of DNA was created using the PDB files from The Protein Data Bank (PDB), which provides a variety of data for many molecular models (https://www.rcsb.org/) [3, 5]. These data describe the macromolecule atomic localization, i.e., the Cartesian coordinates of the atoms in a three-dimensional coordinate system. Furthermore, the PDB dataset provides a simple notation for building the DNA molecules in space, as well as many additional atomic details.

The DNA geometry chosen for this work was the B-DNA, which was formed of two anti-parallel strands wrapped around one other to form a double helix. Each strand is a polymer known as a polynucleotide. Each monomer is a nucleotide, which is composed of a nucleic base (adenine, cytosine, guanine, or thymine) coupled to a deoxyribose molecule, which in turn is linked to a phosphate group.

During the geometry simulation, a partially condensed DNA structure was chosen to represent the cells in vivo. For such needs, the atomic positions have been extracted one by one from a PDB file, giving the atomic description of a DNA molecule containing 1122 base pairs twisted with a final length of 30 nm. Each atom has been represented by a sphere whose radius is equal to the radius of van der Waals [18], and the molecules were constructed using G4UNIONSOLID class integrated into GEANT4 (https://indico.cern.ch/event/647154/contributions/2714212/attachments/1529029/2397032/BookForApplicationDevelopers.pdf). This routine allows to properly combine two solids of different shapes to create a new shape. Using this method, we have placed the molecules one by one by placing the spheres representing their atoms, each molecule was represented by a set of spheres that have been well united. The phosphate group, for example, was represented by a union of 5 spheres, 1 atom of phosphorus and 4 atoms of oxygen. The spheres were filled with materials that have the same density as the DNA molecules to which they belong. This technology not only makes geometry simulation easier, but also makes it faster to precisely identify atoms and molecules interactions with the incident and secondary particles.

We simultaneously simulated six DNA targets consisting each of a twisted DNA molecule with a length of 30 nm, all were placed in a vacuum cube with an edge of 400 nm, and an isotropic source was set at a distance of 40 nm from the six DNA targets. The primary particles were mono-energetic electrons produced according to a solid angle in order to cover all the six molecules of the DNA. The energies used were 4 eV, 6 eV, 10 eV, 15 eV, 20 eV, 30 eV, 50 eV, 100 eV, 200 eV and 500 eV. In each simulation, the DNA targets were irradiated with 10^7 electrons of the same energy, and each simulation was repeated 10 times in order to calculate the mean value and the standard deviation for uncertainty calculation. The energy deposit was counted for each interaction type and at each position x,y,z in the volume of DNA thus localizing the atoms where the interactions occurred. Based on the number and types of interactions at the atomic level, and by comparison with experimental measurements [19–22], the number of DNA single strand and double strand breaks were calculated.

The Monte Carlo code used in this work was GEANT4 which is provided in the form of a toolkit containing the elements necessary to simulate the particle transport and interactions (https://indico.cern.ch/event/647154/contributions/2714212/attachments/1529029/2397032/BookForApplicationDevelopers.pdf). In summary, GEANT4

is an open toolkit developed at the European Organization for Nuclear Research (CERN) for the simulation of particle interactions in matter and open for contributions worldwide. GEANT4 is used in several domains including high energy and nuclear physics, space and medicine. In the present work, low energy electrons are considered as they are provoked by energetic photons in radiotherapy treatment. The free path of electrons before interaction and any type of their interactions depending on energy are regulated by probabilities based on theory and experimentation. At the end, the electrons energy transfer to any molecule in the medium is registered and converted to molecular breaks, ionizations and vibrations.

In the present study, the use of new material in GEANT4-DNA necessitated the incorporation of new cross-sections during the computation of the mean free path and interactions of the particles. We used the physical processes in GEANT4-DNA to simulate all possible interactions between electrons and DNA, i.e. ionization, elastic interaction, vibrational excitation, and dissociative electron attachment (DEA).

For the two types of ionization interactions and elastic interactions, we used the two models G4DNAPTBElasticModel and G4DNAPTBIonizationModel which were introduced in GEANT4-DNA by Bug et al. [23]. A simplified model of the Auger effect has been presented as well. Any ionization of a carbon or oxygen atom results in the release of an Auger electron, whereas ionization of a nitrogen atom results in the emission of two electrons.

The interaction of vibrational excitation was also defined by introducing a new cross-section for the 6 DNA molecules: the 4 bases plus deoxyribose and phosphate group. When we had a vibrational interaction, we made a random pick of vibration mode to calculate the deposited energy. The excitation interaction is less likely to induce SSB and DSB, but it has an important role in the dose distribution.

As previously stated, electrons with energies lower than the vibrational excitation energy can induce the DNA strand breaks through DEA. For that purpose, a new cross section has been introduced in order to properly identify the effects of these electrons with energies between 0 eV and 10 eV.

The previous experimental works from which we extracted the cross-sections were those of Abdoul-Carime et al. (2005), Denifl et al. (2004), Ptasińska et al. (2004), and Pan and Sanche (2006) [19–22]. The first two works gave a detailed study on the DEA for adenine, cytosine, guanine and thymine isolated in the gas phase. Using these works, we were able to directly extract the cross-sections of the four bases. On the other hand, we extracted the cross-sections of the deoxyribose sugar fraction and the phosphate group from measurements performed by Ptasińska et al. (2004) and Pan and Sanche (2006) [21, 22].

In this work, we considered the DEA as a competitive interaction with the electronic excitation according to the cross sections discussed above. When we had a dissociative electronic attachment, we assumed a break of the molecule. As a result, the electron is no more tracked.

In present study, we used a new approach to count SSB and DSB at the DNA level. We assumed that the breakage threshold strongly depends on the type of interaction. For this purpose, we took into consideration the three main types of interactions (ionization, excitation, and dissociative electronic attachment), each interaction type has a way of inducing a DNA breakage according to the cross sections described above. First, given that the ionization is a key factor in DNA damage and is the most likely DNA damaging, we assumed that an SSB is formed at the DNA level by an ionization if the interaction occurs accompanied by a local energy deposition beyond the ionization threshold of 10 eV [24]. On the other hand, we considered that the vibrational excitation as an important role in the dose deposition, but it does not represent a dissociative pathway of DNA. Following that, we assumed that the DEA interaction is a direct DNA dissociation pathway, and that if we have a DEA interaction, it directly leads to a single break at the DNA level.

Strand breaks are most typically seen in the DNA backbone (phosphate and 2-deoxyribose) and are caused by the phosphate-deoxyribose bond or, less commonly, the base-deoxyribose bond. The breaks at the DNA bases level can also cause strand break under the effect of low energy electrons by a charge transfer from the DNA bases to the strand molecules, however in this work; we just considered the direct effects on DNA strands. For that purpose, we assumed that an SSB is defined as a break under the energy deposition as discussed above, and a DSB is defined as two SSBs located on two opposite strands with a distance less than 10 nucleotide pairs.

The first parameter calculated was the dose deposited by all interactions (in Gy) for each given energy beam. The second parameter calculated is the DNA strand break yield per incident electron, by dividing the total number of breaks by the total number of incident electrons. The yield of single strand breaks (YSSB) and double strand breaks (YDSB) were also calculated in the units of strand breaks per Gray per Dalton to make a relation between the geometry of the DNA, the deposited dose, and the DNA weight [25, 26].

$$Y_{SSB \; or \; DSB} = \frac{Number \; of \; SSB \; (DSB)}{Dose(Gy) \times DNA \; weight \; (Dalton)}$$

Finally, the number of strand breaks was determined under the effect of the incident electron energy, and at the end we made a comparison between the three electron interactions, to find out the dominant breaking mechanism for every given energy.

Because we compared our results with those in the experiments in [16, 17], we briefly describe those experimental setups. The study was conducted with an electron accelerator. The authors used a DNA with 3197 base pairs. The DNA was set on a tantalum support inside an upper high vacuum chamber and irradiated with an electron beam of energy varying between 5 eV and 1 keV. The detailed description of the experimental setup can be found in [27]. Figure 1 depicts the results from such experiments showing the yields of SSB and DSB, and also the fitting of these results in an attempt to identify the partial contribution from different electron interactions.
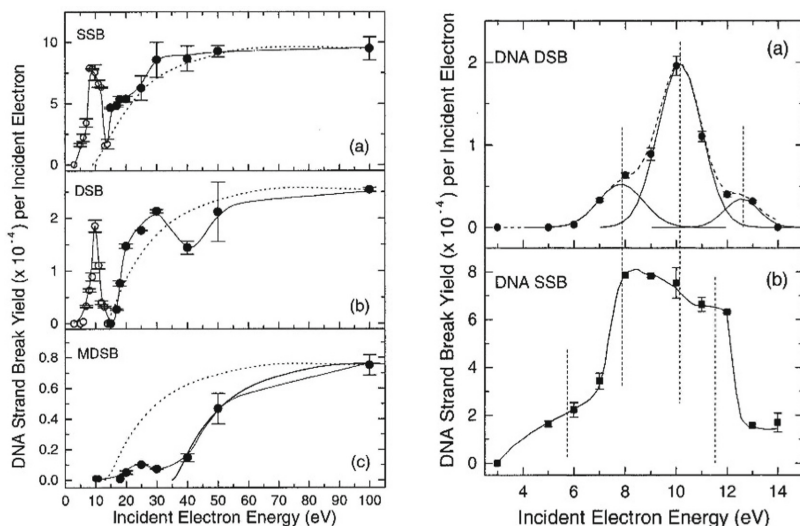
Fig. 1. Left: DNA SSB and DSB as a function of electron energy. Right: SSB and DSB fitted with gaussians to isolate electron interaction effects on DNA. Reprinted with permission from [17]. Copyright 2022 from Journal of the American Chemical Society.

3   Results

The deduced cross sections of adenine, cytosine, guanine and thymine from [19, 20], and those of the deoxyribose sugar and the phosphate group from [21, 22] are shown in Fig. 2. The cross sections of the other electron interactions are described in [23]. According to these figures (Fig. 2), the electrons can interact with the DNA bases in the energy range below 4 eV. Meanwhile, the DEA is favored in the phosphate group in DNA strand molecules, as seen in Fig. 2, which shows a high peak in the electronic energy range between 4 and 10 eV. However, the deoxyribose can be dissociated by electrons with lower energy between 0 and 2 eV.

Figure 3 shows the deposited dose in DNA increasing with the electron energy till a maximum dose of $5.7 \cdot 10^5$ Gy for 100 eV, then progressively decreasing at higher electron energies. Each data point in this curve is the result of the simulation at the corresponding energies. We notice a small peak at 10 eV, which corresponds to the high dissociative electron attachment cross section. The deposited dose for each beam depicts the amount of energy deposited through the three interaction types for every simulated energy. The deposited dose contains all doses deposited by the primary and secondary electrons.
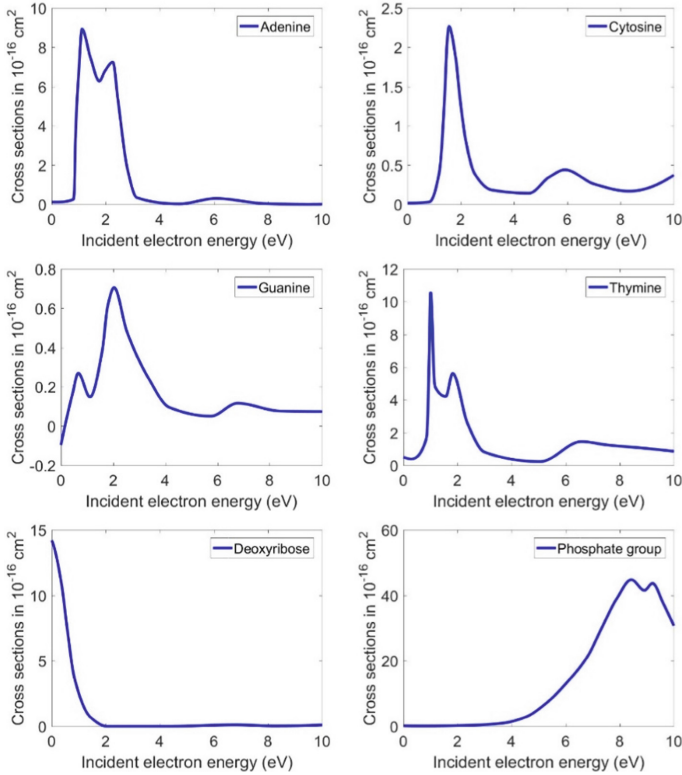
Fig. 2. Deduced cross sections from experimental studies [19–22]. These cross sections were used in our simulations.

Figure 4 shows the yields of SSB and DSB per incident electron under the effect of each energy beam between 4 eV and 300 eV. The error bars correspond to the standard deviation for each given energy deduced from simulations repeated 10 times in the same configuration. From these figures we can clearly distinguish the properties of each energy. In general, the two curves have the same features and shape, with the quantity of DSB being nearly third of that of SSB.

The creation of SSB and DSB starts at the lowest simulated energy of 4 eV. The amount of SSB and DSB rapidly increase to reach a local maximum of $5.7 \cdot 10^{-4}$ SSB per electron and $1.9 \cdot 10^{-4}$ DSB per electron at 10 eV due to the cross section of DEA which dominates in this energy range. Subsequently, the quantities of breaks decrease to make a minimum between 13 eV and 18 eV due to the disappearance of the DEA. They thereafter increase to arrive at the highest maximum of $10 \cdot 10^{-4}$ SSB per electron and $3.5 \cdot 10^{-4}$ DSB per electron for the electrons of 100 eV. We also noticed that the induced breaks by electrons of 100 eV and 200 eV do not differ significantly.
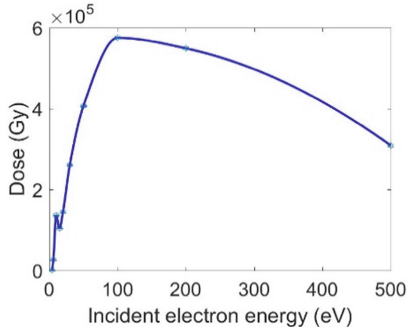
Fig. 3. Deposited dose in DNA as function of the simulated electron energies. For the energies simulated, the 100 eV electrons produced the highest dose deposited in DNA. A small peak appears at 10 eV corresponding to the dissociative electron attachment cross section.
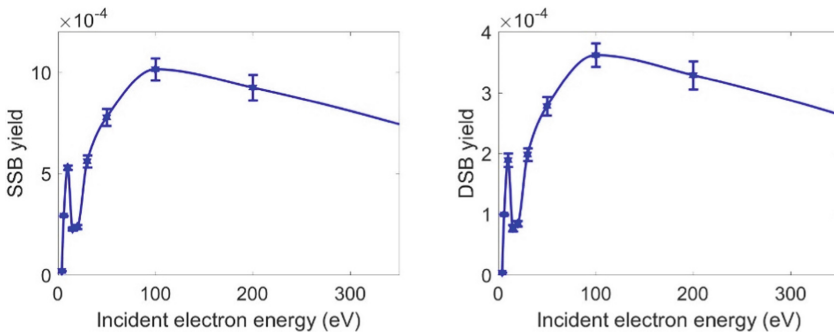
Fig. 4. DNA strand breaks for SSB and DSB per incident electrons as a function of electron energy. The energy is shown from 4 eV to 300 eV to expand the peak at 10 eV.
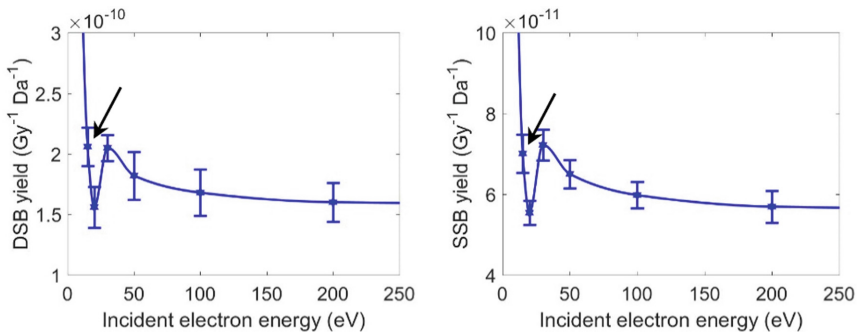
Fig. 5. Yields of SSB and DSB per Gy and per Dalton for the indicated electron energies. The arrow indicates the 15 eV data point.

Figure 5 shows the yields calculated for single-strand breaks (Y_{SSB}) and double-strand breaks (Y_{DSB}) in units of breaks by Gy and by Dalton for each simulated energy

source. Due to the small amount of the deposited dose by the electrons with the lowest energy, the high yield appears for energies less than 15 eV (black arrow in Fig. 5). This energy corresponds to DNA sensitivity to low energy electrons, which implies that even if the deposited dose is too small, the low energy electrons can cause SSB and DSB. Thereafter, at 20 eV the SSB and DSB yields increase to a maximum near 30 eV, after that the yields start to gradually decrease to make a plateau after 150 eV.
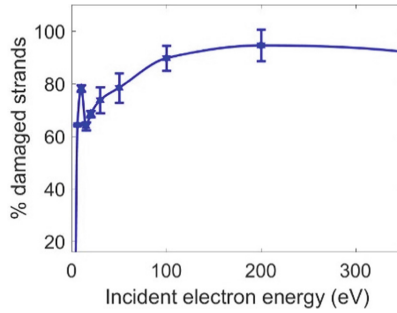
Fig. 6. The percentage of the number of strands breaks as a function of electron energy.

Figure 6 shows the percentage of the number of strand breaks under the effect of each electron energy beam. In this figure, we can distinguish two phases, in the first phase between 0 eV and 30 eV, we see that the number of strand breaks started from around 0% in the case of energy less than 4 eV, noting that 4 eV was the lowest electron energy simulated, then the energy of the electrons increased, the breaking yield also increased and showed a peak near 10 eV, then it decreased to reach a minimum of almost 63% of strand breaks for the electrons having an energy of 20 eV. The second phase depicting the number of broken strands increases with energy to reach a maximum value of around 88% near the energies of 100 eV, and it remains almost constant to show a plateau for higher energies above 100 eV. This means that electrons with energy greater than 100 eV are the most damaging to DNA, which is as expected since when using an electron beam of 100 eV for example, these electrons create secondary electrons that have low energies between 0 eV and 50 eV.

Figure 7 shows the quantity of each type of interaction for each electron energy simulated. For the simulation with 4 eV, we notice that the 10 million electrons made around 300 DEA events, whereas the 6 eV electron beam generated almost 4200 DEA events and a small quantity of vibrational excitation events. This reflects the fact that DEA is the dominant interaction in the energy range between 0 and 10 eV.

The electrons of 10 eV performed both types of interaction, vibrational excitation and DEA. However, above 10 eV, we noticed that ionization began to occur.

For the 15 eV beam, the vibrational excitation presented the major interaction, while for the 20 eV, ionization showed the major interaction indicating that the ionization cross-section was greater than those of the other interactions.

We can observe that for beams with energies greater than 20 eV, the dominant interaction remains the ionization, which reaches a maximum for beams with energies greater than 100 eV.
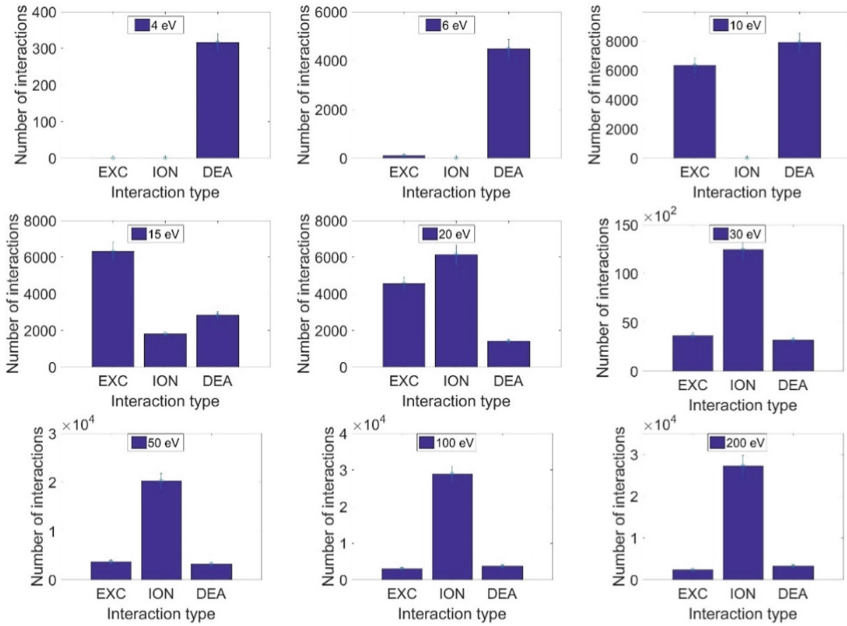
Fig. 7. The number of each type of interaction for each simulated electron energy beam. EXC is for vibrational excitation and ION for ionization.

Furthermore, when the energy exceeds 30 eV, the primary electrons can only perform the ionization events and the other types of interaction came from the secondary electrons which were released as a result of DNA ionization.

Apart from the comparison with the experimental results in Fig. 1 where our results display a great similarity, we have also compared our results with the simulations of Charlton et al. and Nikjoo et al. in Table 1 [25, 28]. Although the configuration of these simulations and the energy threshold on secondary electron tracking was not exactly similar to those in our work, the simulations mainly targeted SSB and DSB as in our work, and their results are comparable to our simulation. We compared the yields calculated for single strand breaks (Y_{SSB}) and double strand breaks (Y_{DSB}) per Gy per Dalton for electron beams of 100 eV and 300 eV, and the results are presented in Table 1. It can be seen that the calculated values for Y_{SSB} are not very dissimilar, with our value at 300 eV located between those of the other two works. However, the values of Y_{DSB} appear biased in comparison to the other works, which might depend on the definition of the occurrence of DSBs whether it was caused by the same electron and at which distance from the SSB.

4   Discussion

In internal radiation therapy (brachytherapy) of solid tumors, a capsule is placed inside or near a tumor which can be accessed with local and simple surgery. Several cancer sites can be implemented with such local treatment like cancers in the prostate and head

and neck. The capsule can remain in the body for a predefined time in minutes or days. The capsule contains radioemitter isotopes with preselected radiation types and energy [29]. The beta and gamma emitters are the most used isotopes in such treatments.

Table 1. Comparison of yields of SSB and DSB between the present work and works from Nikjoo et al. and Charlton et al. [25, 28].

E (eV)	Y_{SSB} (Gy^{-1}Da^{-1} × 10^{-10})			Y_{DSB}(Gy^{-1}Da^{-1} × 10^{-11})			Total SSB/Total DSB	
	Our work	Nikjoo et al.	Charlton et al.	Our work	Nikjoo et al.	Charlton et al.	Our work	Nikjoo et al.
100	1.55	2.5	–	5.8	1.5	–	3.4	–
300	1.6	2.5	1.36	5.7	2.3	2.64	2.8	3.4

In order to use internal radiation therapy, imaging of the patient is first conducted to locate the tumor, its density, its volume and its surrounding normal tissues. Although the tumor is macroscopic and the interaction of DNA is sub-microscopic, the dose-equivalent to SSB and DSB can be extracted from GEANT4-DNA and normalized in such a way to discriminate the dose to DNA from other doses in the tissues [30]. To date, it is very demanding in space and time to develop the geometry even at the level of a single tumor cell in order to locate its DNA. The experimentation and the simulation of isolated DNA until now have been conducted in several environment configurations, such as in water or in the presence of gases.

The knowledge of the types of interactions with DNA are of great importance in order to select the appropriate isotopes or external beams. Validating a simulation by comparison to an experimental measurement allows, in turn, to estimate the impacts of the individual types of interactions as a function of energy, which cannot be done by experimentation. Therefore, in the present work, we compared our results to the works conducted experimentally in [17] in addition to the extraction of the cross sections from the experiments on DNA [19–22], and we provided the types of interactions individually as a function of energy induced by primary beams (Fig. 7).

5   Conclusion

We reported in this paper the rates of the interaction types in DNA as a function of electron energies: ionization, vibrational excitation, and dissociative electron attachment. The single strand and double strand breaks of DNA were found comparable to those obtained with experimental setups. The dissociative electron attachment was found to be the only present at energies below 10 eV of electron energy. The excitation appears around 10 eV, while the ionization becomes dominant at around 30 eV and above.

References

1. Bernal, M.A., et al.: Track structure modeling in liquid water: a review of the Geant4-DNA very low energy extension of the Geant4 Monte Carlo simulation toolkit. Physica Med. **31**(8), 861–874 (2015). https://doi.org/10.1016/j.ejmp.2015.10.087

2. Śmiałek, M.A., Jones, N.C., Hoffmann, S.V., Mason, N.J.: Measuring the density of DNA films using ultraviolet-visible interferometry. Phys. Rev. E. **87**, 060701 (2013). https://doi.org/10.1103/PhysRevE.87.060701

3. Delage, E., et al.: PDB4DNA: implementation of DNA geometry from the Protein Data Bank (PDB) description for Geant4-DNA Monte-Carlo simulations. Comput. Phys. Commun. **192**, 282–288 (2015). https://doi.org/10.1016/j.cpc.2015.02.026

4. Bernal, M.A., et al.: An atomistic geometrical model of the B-DNA configuration for DNA–radiation interaction simulations. Comput. Phys. Commun. **184**(12), 2840–2847 (2013). https://doi.org/10.1016/j.cpc.2013.07.015

5. Lu, X.J., Olson, W.K.: 3DNA: a versatile, integrated software system for the analysis, rebuilding and visualization of three-dimensional nucleic-acid structures. Nat. Protoc. **3**(7), 1213–1227 (2008). https://doi.org/10.1038/nprot.2008.104

6. Pham, Q.T., et al.: Coupling of Geant4-DNA physics models into the GATE Monte Carlo platform: evaluation of radiation-induced damage for clinical and preclinical radiation therapy beams. Nucl. Instr. Meth. Phys. Res. Sect. B Beam Interact. Mater. Atoms **353**, 46–55 (2015). https://doi.org/10.1016/j.nimb.2015.04.024

7. Friedland, W., Dingfelder, M., Kundrát, P., Jacob, P.: Track structures, DNA targets and radiation effects in the biophysical Monte Carlo simulation code PARTRAC (2011). https://doi.org/10.1016/j.mrfmmm.2011.01.003

8. Champion, C., et al.: Dose point kernels in liquid water: an intra-comparison between GEANT4-DNA and a variety of Monte Carlo codes. Appl. Radiat. Isot. **83**, 137–141 (2014). https://doi.org/10.1016/j.apradiso.2013.01.037

9. Friedland, W., Jacob, P., Paretzke, H.G., Merzagora, M., Ottolenghi, A.: Simulation of DNA fragment distributions after irradiation with photons. Radiat. Environ. Biophys. **38**(1), 39–47 (1999). https://doi.org/10.1007/s004110050136

10. Dizdaroglu, M., Jaruga, P.: Mechanisms of free radical-induced damage to DNA (2012). https://doi.org/10.3109/10715762.2011.653969

11. Meylan, S., et al.: Simulation of early DNA damage after the irradiation of a fibroblast cell nucleus using Geant4-DNA. Sci. Rep. **7**(1), 11923 (2017). https://doi.org/10.1038/s41598-017-11851-4

12. Ftáčniková, S., Böhm, R.: Monte Carlo calculations of energy deposition in DNA for Auger emitters. Radiat. Prot. Dosimetry **92**(4), 269–278 (2000). https://doi.org/10.1093/oxfordjournals.rpd.a033292

13. Di Maria, S., et al.: Dosimetry assessment of DNA damage by Auger-emitting radionuclides: experimental and Monte Carlo studies. Radiat. Phys. Chem. **140**, 278–282 (2017). https://doi.org/10.1016/j.radphyschem.2017.01.028

14. Carlson, D.J., Stewart, R.D., Semenenko, V.A., Sandison, G.A.: Combined use of Monte Carlo DNA damage simulations and deterministic repair models to examine putative mechanisms of cell killing. Radiat. Res. **169**(4), 447–459 (2008). https://doi.org/10.1667/RR1046.1

15. Pouget, J.P., Lozza, C., Deshayes, E., Boudousq, V., Navarro-Teulon, I.: Introduction to radiobiology of targeted radionuclide therapy (2015). https://doi.org/10.3389/fmed.2015.00012

16. Boudaïffa, B., Cloutier, P., Hunting, D., Huels, M.A., Sanche, L.: Resonant formation of DNA strand breaks by low-energy (3 to 20 eV) electrons. Science **287**, 1658–1660 (2000). https://doi.org/10.1126/science.287.5458.1658

17. Huels, M.A., Boudaïffa, B., Cloutier, P., Hunting, D., Sanche, L.: Single, double, and multiple double strand breaks induced in DNA by 3−100 eV electrons. J. Am. Chem. Soc. **125**(15), 4467–4477 (2003). https://doi.org/10.1021/ja029527x

18. Aydogan, B., et al.: Site-specific OH attack to the sugar moiety of DNA: a comparison of experimental data and computational simulation. Radiat. Res. **157** (2002). https://doi.org/10.1667/0033-7587(2002)157[0038:SSOATT]2.0.CO;2

19. Abdoul-Carime, H., Langer, J., Huels, M.A., Illenberger, E.: Decomposition of purine nucleobases by very low energy electrons. Eur. Phys. J. D **35**(2), 399–404 (2005). https://doi.org/10.1140/epjd/e2005-00194-5

20. Denifl, S., Ptasińska, S., Probst, M., Hrušák, J., Scheier, P., Märk, T.D.: Electron attachment to the gas-phase DNA bases cytosine and thymine. J. Phys. Chem. A **108**(31), 6562–6569 (2004). https://doi.org/10.1021/jp049394x

21. Ptasińska, S., Denifl, S., Scheier, P., Märk, T.D.: Inelastic electron interaction (attachment/ionization) with deoxyribose. J. Chem. Phys. **120**(18), 8505–8511 (2004). https://doi.org/10.1063/1.1690231

22. Pan, X., Sanche, L.: Dissociative electron attachment to DNA basic constituents: the phosphate group. Chem. Phys. Lett. **421**(4–6), 404–408 (2006). https://doi.org/10.1016/j.cplett.2006.01.099

23. Bug, M.U., Baek, W.Y., Rabus, H., Villagrasa, C., Meylan, S., Rosenfeld, A.B.: An electron-impact cross section data set (10 eV–1 keV) of DNA constituents based on consistent experimental data: a requisite for Monte Carlo simulations. Radiat. Phys. Chem. **130**, 459–479 (2017). https://doi.org/10.1016/j.radphyschem.2016.09.027

24. Chatzipapas, K.P., et al.: Quantification of DNA double-strand breaks using Geant4-DNA. Med. Phys. **46**(1), 405–413 (2019). https://doi.org/10.1002/mp.13290

25. Nikjoo, H., O'Neill, P., Goodhead, D.T., Terrissol, M.:Computational modelling of low-energy electron-induced DNA damage by early physical and chemical events. Int. J. Radiat. Biol. **71**(5), 467–483 (1997). https://doi.org/10.1080/095530097143798

26. Ahmadi Ganjeh, Z., Eslami-Kalantari, M., Ebrahimi Loushab, M., Mowlavi, A.A.: Investigation of the direct DNA damages irradiated by protons of different energies using geant4-DNA toolkit. Int. J. Radiat. Res. **18** (2020). https://doi.org/10.18869/acadpub.ijrr.18.4.809

27. Rezaee, M., Cloutier, P., Bass, A.D., Michaud, M., Hunting, D.J., Sanche, L.: Absolute cross section for low-energy-electron damage to condensed macromolecules: a case study of DNA. Phys. Rev. E **86**(3), 031913 (2012). https://doi.org/10.1103/PhysRevE.86.031913

28. Charlton, D.E., Nikjoo, H., Humm, J.L.: Calculation of initial yields of single- and double-Strand breaks in cell nuclei from electrons, protons and alpha particles. Int. J. Radiat. Biol. **56**(1), 1–19 (1989). https://doi.org/10.1080/09553008914551141

29. Strohmaier, S., Zwierzchowski, G.: Comparison of 60 Co and 192 Ir sources in HDR brachytherapy. J. Contemp. Brachyther. **3**, 199–208 (2011). https://doi.org/10.5114/jcb.2011.26471

30. Famulari, G., Pater, P., Enger, S.A.: Microdosimetric evaluation of current and alternative brachytherapy sources—a Geant4-DNA simulation study. Int. J. Radiat. Oncol. Biol. Phys. **100**(1), 270–277 (2018). https://doi.org/10.1016/j.ijrobp.2017.09.040

Linear Predictive Modeling for Immune Metabolites Related to Other Metabolites

Jana Schwarzerova[1,2(✉)] , Iro Pierides[2], Karel Sedlar[1,3] ,
and Wolfram Weckwerth[2,4]

[1] Department of Biomedical Engineering, Faculty of Electrical Engineering and
Communication, Brno University of Technology, Brno, Czech Republic
`Jana.Schwarzerova@vut.cz`
[2] Molecular Systems Biology (MOSYS), Department of Functional and Evolutionary Ecology,
University of Vienna, Vienna, Austria
[3] Department of Informatics, Ludwig-Maximilians-Universität München, Munich, Germany
[4] Vienna Metabolomics Center (VIME), University of Vienna, Vienna, Austria

Abstract. Metabolite analysis reveals new challenges in human health care. This human health care connects to the immune system and presents opportunities for the prevention and detection of early hidden disease symptoms. Predicting the concentration of immune metabolites and confirming relationships between concentrations of individual metabolites have the potential to create breakthroughs in diagnostic techniques. This early detection of serious diseases plays a major role in overall recovery. Moreover, metabolite analysis linked to biomedical applications could provide an ideal tool for preventive healthcare and the pharmaceutical industry.

This study presents the linear prediction of selected metabolites involved in the immune system. The evaluation relied on accurate linear prediction modeling and subsequent comparison. This is the first step toward determining the relationship of metabolites and immune system using computational biomedical analysis.

Keywords: Linear regression · Immunology · Computational biomedical analysis · Metabolomic prediction

1 Introduction

Current research and experimental evidence provide a new perspective on several metabolism-influencing factors which play an important role in regulating immune response. These recent findings have led to further investigations which have pushed analysis of the interface between metabolic and immune systems to the fore [1–3]. Correct identification of the roles of immune metabolites in relation to early disease detection and prevention plays a major role in the choice of treatment options [4, 5].

The immune system plays an active part in metabolism regulation [3]. For example, lymphocyte activation initiates cell differentiation, proliferation, and cell growth, which in turn increase metabolic demand, reflected in changes in metabolite concentrations.

A study by Namrata and Rajat [1] describes how signaling through the immune system integrates with metabolic functions to drive the immune response and vice versa.

The immune system is studied not only as a defence against tumors and infectious agents attacking the host; it is also critical in the maintenance of homeostasis or for the protection against forms of immune dysregulation, such as allergies [1, 6]. Thus, the study [1] calls immune metabolism an emerging field of investigation which is at the interface between the distinct disciplines of immunology and metabolism.

In addition, the immune system also participates in the control of the resident colonizing microflora, which are essential for immunologic and metabolic health [1]. This highlights on the role of glucose in the immune system, as these regulatory processes are very energy intensive. Specifically, the pathways of glucose utilization, such as the pentose phosphate pathway are functional in lymphocyte stimulation, as they show limited resting lymphocyte metabolic activity, depending on the availability of trophic signals and nutrients such as glucose [1, 7]. However, when T-cells start proliferating, they begin moving from a quiescent to a highly secretory state after being activated, leading to processes which increase glucose consumption and hence induce activation of glycolysis [8]. Consequently, we can expect a relationship between changes in the immune system and concentrations of various metabolites, such as fumarate [9], isoleucine [10], glutamine [11], lysine [12], tryptophan [13–16], arginine [16, 17], and histidine [16].

Fumarate has interesting potential in innate immune memory and the induction of trained immunity. It is mediated by the activation of immune and metabolic pathways, which results in epigenetic regulation of cellular functional programs [9]. A study by Arts et al. [9] identified glycolysis, glutaminolysis, and the cholesterol synthesis pathway as essential for the induction of trained immunity by β-glucan in monocytes, followed by fumarate accumulation using glutamine supplementation, integrating the TCA cycle into the immune response. Moreover, fumarate alone elicits an epigenetic program [9]. Another interesting metabolite is isoleucine. Isoleucine [10], one of the branched chain amino acids, is critical in physiological functions such as immunity, protein metabolism, glucose transportation, and fatty acid metabolism. A study by Gu et al. [10] describes isoleucine as a metabolite component with potential to improve the immune system, including immune organs, cells, and reactive substances. Additionally, recent studies have shown that isoleucine can induce the expression of host defence peptides, which can lead to regulation of host innate and adaptive immunity [10]. Another key immune metabolite is glutamine [11], which is the most abundant metabolite in the body. The rate of glutamine consumption by immune cells is similar to or even greater than glucose [11]. Glutamine has interesting connections with organs, such as the gut and skeletal muscles, while other metabolites, such as lysine, have a connection with specific diseases such as obesity, type II diabetes, and cardiovascular diseases. Lysine [12] has an important role in immunological and metabolomic pathways. It connects to lysine acetylation which is vitally important in these pathways and regulates the balance between energy storage and expenditure [12].

Overall, research on immunological metabolites has huge potential in opening up new methods for cancer treatment. In particular, tryptophan, arginine, and histidine are touted as a new hope for cancer immunotherapy [16]. Tryptophan catabolism is implicated in the kynurenine pathway (KP) as one of many mechanisms involved, and the

enzymes that break down tryptophan are found in immune system cells [13, 18]. Recent studies reveal that tryptophan breakdown is necessary for maintaining aspects of immune tolerance [13]. Moreover, the balance between the production of two types of metabolites is controlled by key rate-limiting enzymes and, in turn, molecular signals such as interferon-γ (IFN-γ) [18]. These signals activate the KP metabolism of tryptophan via the enzyme, as opposed to alternative pathways for serotonin and melatonin production [18]. Thus, tryptophan catabolism produces important substances such as N-acetyl serotonin and melatonin [16]. Early work showed that tryptophan deficiency due to IFN-γ treatment was related to the anti-proliferative effect of this cytokine on intracellular parasites and tumors [16, 19].

Arginine and citrulline are closely linked biological pathways. L-arginine can be synthesized from L-citrulline inside the body [16, 17]. The main role of arginine in the enhancement of the immune system is connected to the production of insulin, prolactin, growth hormone, and insulin-like growth factor-I [16, 20]. Many studies have reported the importance of arginine in nitric oxide (NO) synthase activation for NO synthesis [16]. NO is one of the most important contributors to both innate and acquired immunity [21].

Finally, among the group of metabolites that serve as a new hope for cancer immunotherapy is histidine [16]. Histidine is abundant in plasma glycoproteins and has many biological functions, such as cell adhesion, migration, supplement activation, immune complex rescue and apoptotic cell phagocytosis [16]. A study by Tantawy et al. [16] notes that few studies have reported the role of dietary histidine in the immune system of animals, but a deficiency of dietary histidine leads to a reduction of protein levels in the plasma [22]. The present study used linear prediction algorithms for mathematical verification of the inferred relationship among metabolites. Based on these findings, we were motivated to enhance and encourage the use of prediction tools in the elucidation of relationships between metabolites implicated in immune responses.

2   Materials and Methods

This study analysed a metabolomics dataset from a study by Chu et al. [23], aiming to present a combination of the most rigorously studied branches today. The immune system and its connection to metabolic analysis were explored through the use of machine learning approaches for prediction of metabolite concentrations and the relationship to each other.

2.1   Dataset

The study by Chu et al. [23] showed insight into the differences in metabolite levels, immune responses, and immune disease risk. Chu et al. [23] published the dataset for genetic, metabolomic, and phenotype data. Our study worked only with the metabolomic datasets, which are available in Additional File 23 from Chu et al.'s study [23] or at https://500fg-hfgp.bbmri.nl. Metabolite abundance levels were acquired from General Metabolomics (GM).

2.2 Methods

Our methodology was based on regression algorithms. The dataset represented a matrix which included columns representing individual metabolite concentrations and rows representing measured subjects. Seven metabolites were selected as immune metabolites based on previous assumptions and the literature [8–18]. The pipeline of our methodology is shown in Fig. 1.
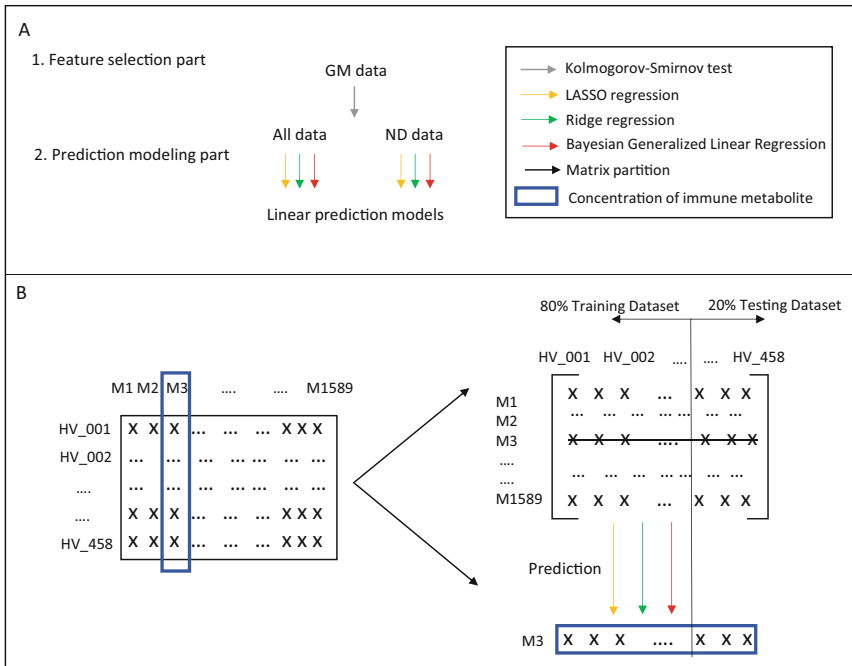
Fig. 1. Schema of whole methodology; (A) represents overview of used pipeline. *GM data* is metabolite abundance levels acquired from General Metabolomics, *All data* includes whole GM dataset, *ND data* represents metabolite data which meet the normal distribution; (B) is core of prediction methodology where the log-normalized dataset as matrix where HV_001, HV_002 etc. represent measured subjects; M1, M2, etc. represent metabolites and M3 in blue frame is representative of immune metabolites.

Firstly, the Kolmogorov-Smirnov test [24] was used to check the normal distribution of the metabolite dataset. Only 147 metabolites fulfilled the condition of a p-value greater than 0.05 after the Kolmogorov-Smirnov test from a total number of 458 metabolites. Thus, the first step in our methodology included a pre-processing step of log-transformation to fulfil the condition of a normal distribution for most metabolites. Thus, the dataset was divided into All data, which included all metabolites from the GM dataset, and ND data, which included only metabolites fulfilling the condition of a normal distribution.

The next steps were part of the predictive analysis. The pipeline of our predictive methodology is shown in Fig. 1, Section B. The core of the prediction modeling was the transposed matrix, metabolite abundance, from which immune metabolites were removed and used as validation samples for training and testing based on the remaining metabolites. Applied predictive analysis was based on regression methods, such as Least Absolute Shrinkage and Selection Operator (LASSO) regression [25], Ridge Regression (RR) [26, 27], and Bayes Generalized Linear Regression (BGLR) [29]. The whole analysis was implemented in the programing language R using the packages R/gbm [28], R/glmnet [30, 31], R/MLmetrics [32], and R/BGLR [29, 33].

LASSO Regression

LASSO regression aims to identify the variables and corresponding regression coefficients which minimize prediction error [25]. The main principles of LASSO regression rely on the model parameters which modify the regression coefficients towards zero; i.e., the sum of the absolute values of the regression coefficients is modified to be less than a fixed value (λ) [25]. The choice of λ was made by using an automated k-fold cross-validation approach using R/glmnet [30].

Ranstam [25] states that LASSO regression is a method which has been shown to outperform standard methods in some settings. However, this method is often affected by overfitting and optimism bias, which lead to the need to validate a model in an external dataset. Moreover, the LASSO methods exchange potential bias in estimating individual parameters for better expected prediction values [25].

Ridge Regression

RR is the most popular parameter estimation method for dealing with the collinearity problem in multiple linear regression [26]. RR is an extension of linear regression similar to LASSO. However, RR includes a loss function which is modified to minimize the complexity of the model. This includes a penalty parameter represented by the square of the magnitude of the coefficients.

A study by Marquardt and Snee [27] showed that if the predictor variables are highly correlated, RR produces coefficients which predict and extrapolate better than least squares and thus is a safer procedure for selecting variables. As a result, RR can sometimes appear to be more advantageous than linear regression or LASSO.

Bayesian Generalized Linear Regression

BGLR [29] is an approach which fits various types of parametric Bayesian regressions. BGLR allows integration of various parametric shrinkage and variable selection procedures in a unified and consistent manner [33].

The R/BGLR package [29] is based on a Gibbs sampler with scalar updates such as scaled-t (called as BayesA), scaled-t mixture (called as BayesB), or Gaussian mixture (called as BayesC). Our study used all of these scaled approaches for prediction analysis and compared the results.

3   Results

The modeling dataset was divided into training and testing data at a ratio of 80% (training) to 20% (testing). In total, we had 1,588 observations representing metabolites and 459 variables representing human experimental subjects.

Poisson and Gaussian were chosen for the family argument in the LASSO and RR models. However, after a subsequent comparison, a model with more advantageous parameters included Poisson family argument was selected. In the BGLR approaches, the prediction models were created using different scaled methods and also subsequently compared to each other.

3.1   Metabolomic Prediction Using LASSO Regression

The evaluation of performance prediction represents two error values: mean square error (MSE) and mean absolute error (MEA). The best model keeps errors as low as possible. The best family argument for metabolomic prediction was Poisson.

Table 1 includes the evaluation parameters of metabolomic prediction for each selected immune metabolite based on All data and ND data. The best modeling parameters were for fumarate prediction, while (iso)leucine and glutamine showed the largest MSE and MEA.

Table 1. The evaluation parameters of created metabolomic prediction based on LASSO regression. All data means prediction models based on all dataset, ND data represents models created by metabolites only with normal distribution. PV represents Poisson deviance connects to Poisson family arguments rely on Poisson distribution.

	All data			ND data		
	PV	MSE	MEA	PV	MSE	MEA
Fumarate	24.43	67.23	8.20	24.31	66.84	8.17
(Iso)leucine	46.69	164.47	12.82	46.90	164.19	12.81
Glutamine	32.42	98.66	9.93	45.69	158.25	12.58
Lysine	45.04	155.19	12.46	45.13	155.60	12.47
Tryptophan	43.22	146.50	12.10	43.12	146.48	12.10
Arginine	40.90	135.75	11.65	41.19	137.19	11.71
Histidine	45.50	157.37	12.54	45.47	157.23	12.54

3.2   Metabolomic Prediction Using Ridge Regression

The evaluated parameters of RR modeling are shown in Table 2. The parameters were very similar to those from the LASSO regression models. Slight changes here were obscured by rounding. Noticeable changes were only connected to lysine. These results matched the conclusions from the LASSO regression. Thus, there was no significant difference between the use of LASSO and RR in metabolomic prediction in the search for relationships.

Table 2. The evaluation parameters of created metabolomic prediction based on ridge regression. All data means prediction models based on all dataset, ND data represents models created by metabolites only with normal distribution. PV represents Poisson deviance connects to Poisson family arguments rely on Poisson distribution.

	All data			ND data		
	PV	MSE	MEA	PV	MSE	MEA
Fumarate	24.43	67.23	8.20	24.32	66.84	8.17
(Iso)leucine	46.69	164.47	12.82	46.90	164.19	12.81
Glutamine	32.42	98.66	9.93	45.69	158.28	12.58
Lysine	45.05	155.19	12.46	45.13	155.60	12.47
Tryptophan	43.22	146.50	12.10	43.21	146.48	12.10
Arginine	40.90	135.75	11.65	41.19	137.19	11.71
Histidine	45.50	157.37	12.54	45.47	157.23	12.54

3.3   Metabolomic Prediction Using BGLR

The evaluation of performance prediction included two error values: MSE and Pearson correlation coefficient (r_{cc}). Table 3 and Table 4 show the results of the metabolomic prediction using BGLR approaches. Contrary to previous results, the best model using BGLR was created for the lysine metabolite, where the correlation coefficient was approximately 99%. The lowest correlation coefficients, higher than 89%, were calculated for fumarate and histidine prediction. However, these values are still high.

The MSE parameter was also the best for lysine and the worst for fumarate prediction. The means of the Pearson corelation coefficient for models relying on All data, using BayesA, BayesB and BayesC, were 0.953, 0.952, and 0.950, respectively. The means of the Pearson corelation coefficient for models relying on ND data, using BayesA, BayesB, and BayesC, were 0.947, 0.950, and 0.949. Therefore, the highest Pearson correlation coefficients were included in the BayesB scaling.

Table 3. The evaluation parameters of created metabolomic prediction based on BGLR using different scaling. The evaluation parameters were calculated for all data and chosen as r_{cc} represent Pearson correlation coefficient and MSE as mean square error.

	BayesA		BayesB		BayesC	
	r_{cc}	MSE	r_{cc}	MSE	r_{cc}	MSE
Fumarate	0.864	0.010	0.864	0.010	0.856	0.011
(Iso)leucine	0.979	0.003	0.979	0.003	0.976	0.003
Glutamine	0.988	0.003	0.988	0.003	0.988	0.003
Lysine	0.993	0.001	0.993	0.001	0.992	0.001
Tryptophan	0.973	0.002	0.973	0.002	0.970	0.002
Arginine	0.986	0.002	0.984	0.002	0.984	0.002
Histidine	0.888	0.007	0.884	0.007	0.882	0.007

Table 4. The evaluation parameters of created metabolomic prediction based on BGLR using different scaling. The evaluation parameters were calculated for ND data and chosen as r_{cc} represent Pearson correlation coefficient and MSE as mean square error.

	BayesA		BayesB		BayesC	
	r_{cc}	MSE	r_{cc}	MSE	r_{cc}	MSE
Fumarate	0.871	0.009	0.870	0.009	0.870	0.009
(Iso)leucine	0.964	0.003	0.968	0.003	0.966	0.003
Glutamine	0.986	0.004	0.987	0.004	0.987	0.004
Lysine	0.990	0.001	0.990	0.001	0.989	0.001
Tryptophan	0.964	0.002	0.966	0.002	0.963	0.002
Arginine	0.980	0.003	0.983	0.002	0.983	0.002
Histidine	0.876	0.007	0.884	0.006	0.885	0.006

4   Discussion

In this study, we have presented a new approach for determining relationships resulting from biological wet experiments connected to immune metabolites. Due to the growing quality of metabolomic protocols, research has shifted to the post-genomic era, where its main purpose is to understand the relationships among the individual molecular components. Our study has focused on immune metabolites, particularly fumarate, (iso)leucine, glutamine, lysine, tryptophan, arginine, and histidine. Their relationships with other metabolites and their abundance were confirmed due to high predictions of each other. In the future, we could predict and detect early symptoms of individual immune diseases based on metabolic concentration after confirmation by mathematical

algorithms, such as those evaluated in this study. This could provide a powerful predictive capacity, where model evaluation is integral in faster diagnosis and disease prevention.

At the beginning of this study, the distribution of the data was checked through individual metabolite distributions. This was a necessary step, because the prediction methods based on the linear approach are not familiar with outlier values [34, 35]. We found that 67% of the dataset did not satisfy the condition of normalization using the Kolmogorov-Smirnov test. The dataset was then normalized using log-transformation [36]. Before prediction, we also performed overall centralization using the scale function [37–39]. Based on further verification of normalization distribution, the datasets were divided into All data and ND data which had been used to input data into the modeling. Thus, we performed prediction modeling relying on all metabolites and metabolites which have normal distribution. The expectation was that the models would have better performance parameters using ND data, because this study focused on linear prediction modeling.

The main goal of the study was achieved using linear prediction modeling, which mathematically confirmed the relationships between the concentrations of immune metabolites and other metabolites. We used the LASSO regression, RR, and BGLR modeling approaches. First, the study resolved the correct setting of input family arguments for the LASSO and RR modeling approaches. The Poisson family [30] was far more effective than the Gaussian family argument. Some studies [40] report the classical Poisson family as inappropriate for modeling. However, it proved more useful than Gaussian in our study. Using zero-Inflated Poisson regression as a modeled family could be an interesting next step, in improving linear predictions.

The resulting performance of the models themselves is expressed by their evaluated parameters. LASSO and RR modeling are described by Poisson deviance to detect outliers [41], MSE, and MAE [42, 43]. MSE is one of the most evaluated parameters for created models. However, MSE usually exhibits a misleading average error indicator; therefore, MAE may be a better metric for that evaluation in some cases [42]. Due to these inconsistencies, both errors are listed in this study. Table 1 and Table 2 include Poisson deviances, MSEs, and MAEs for the LASSO and RR models. The prediction performances were very similar for the two-model approach. Some slight changes here were obscured by rounding. One visible change was included in the lysine prediction modelsů however, this difference was very small. The results provide two perspectives connected to the choice of the right model. One of the perspectives involves selecting an appropriate prediction method from the LASSO and RR models. We can say that both methods are as suitable as they are inappropriate. However, this agreement confirms the same relationship of immune metabolites in dependence on other metabolites. Using MAE in the LASSO and RR models, (iso)leucine showed an assumed relationship with other selected metabolites. However, this predictive power is still high.

The comparisons between modeling approaches relied on All data and reduced input data using normal distribution, as ND data showed that not at all cases were better using metabolites with normal distribution. Despite that, normal distribution is a mandatory condition for linear modeling. Therefore, we would expect an improvement in the predictive value. However, this is influenced by the hidden causality between metabolites.

As a result, we did not see improvement in all linear predictions, such as the model prediction for glutamine.

We also achieved significantly better predictions with BGLR approaches. All Pearson correlation coefficients exceeded 88%. This illustrates the effectiveness of mathematical prediction methods in confirming relationships between immune metabolites and other metabolites. The best prediction was for lysine. When the metabolite was reduced based on checking a normal distribution, the prediction decreased. It can be presumed that there is hidden causality between metabolites. This opens new pathways for research focused on other possible and more sophisticated methods of feature selection including biology precursors of information. We also observed that, on average, the BayesB scale in BGLR seemed best way to scale.

Finally, using only *in-silico* models, the study has confirmed the assumption that immune metabolites have a relationship with other metabolites. These confirmations may, in future, lead to the creation of models for early detection of symptoms in diseases such as diabetes type II, and cancer. With early detection, a patient has increased chances of recovery. With many naturally occurring biological and technical variations in biomedical analyses, it is important to consider metabolomic prediction models for the prevention and early detection of diseases.

5   Conclusion

Immune metabolites are one of the most studied areas in the field. However, most studies deal purely with wet experiments. Predictive modeling is rarely used in current studies. Despite this, there is an enormous range of new possibilities in computational techniques. This study has presented prediction models which show a relationship between immune metabolites and other metabolites. The created prediction models rely on linear regression methods such as LASSO, RR, and more sophisticated approaches such as BGLR.

In total, we created 70 prediction models: 14 prediction models using LASSO regression, 14 using RR and 42 prediction models using BGLR. All approaches were modeled for seven selected immune metabolites using the current literature. The best approach for linear prediction modeling based on this metabolite dataset was BGLR. Therefore, this study successfully determined the relationship between immune metabolites and other metabolites by relying only on computational approaches.

References

1. Tomar, N., De, R.K.: Cross talk between the metabolic and immune systems. In: De, R.K., Tomar, N. (eds.) Immunoinformatics. MMB, vol. 1184, pp. 13–21. Springer, New York (2014). https://doi.org/10.1007/978-1-4939-1115-8_2

2. Perl, A.: Metabolic control of immune system activation in rheumatic diseases. Arthritis Rheumatol. **69**(12), 2259–2270 (2017)

3. Zmora, N., Bashiardes, S., Levy, M., Elinav, E.: The role of the immune system in metabolic health and disease. Cell Metab. **25**(3), 506–521 (2017)

4. Subramaniam, D., Thombre, R., Dhar, A., Anant, S.: DNA methyltransferases: a novel target for prevention and therapy. Front. Oncol. **4**, 80 (2014)

5. Kim, I., He, Y.-Y.: Targeting the AMP-activated protein kinase for cancer prevention and therapy. Front. Oncol. **3**, 175 (2013)

6. Akdis, M.: Immune tolerance in allergy. Curr. Opin. Immunol. **21**(6), 700–707 (2009)

7. Buttgereit, F., Burmester, G.-R., Brand, M.D.: Bioenergetics of immune functions: fundamental and therapeutic aspects. Immunol. Today **21**(4), 194–199 (2000)

8. Hume, D.A., Radik, J.L., Ferber, E., Weidemann, M.J.: Aerobic glycolysis and lymphocyte transformation. Biochem. J. **174**(3), 703–709 (1978)

9. Arts, R.J.W., et al.: Glutaminolysis and fumarate accumulation integrate immunometabolic and epigenetic programs in trained immunity. Cell Metab. **24**(6), 807–819 (2016)

10. Gu, C., et al.: Isoleucine plays an important role for maintaining immune function. Curr. Protein Pept. Sci. **20**(7), 644–651 (2019)

11. Cruzat, V., Rogero, M.M., Keane, K.N., Curi, R., Newsholme, P.: Glutamine: metabolism and immune function, supplementation and clinical translation. Nutrients **10**(11), 1564 (2018)

12. Iyer, A., Fairlie, D.P., Brown, L.: Lysine acetylation in obesity, diabetes and metabolic disease. Immunol. Cell Biol. **90**(1), 39–46 (2012)

13. Moffett, J.R., Namboodiri, M.A.A.: Tryptophan and the immune response. Immunol. Cell Biol. **81**(4), 247–265 (2003)

14. Nowak, E.C., et al.: Tryptophan hydroxylase-1 regulates immune tolerance and inflammation. J. Exp. Med. **209**(11), 2127–2135 (2012)

15. Opitz, C.A., Wick, W., Steinman, L., Platten, M.: Tryptophan degradation in autoimmune diseases. Cell. Mol. Life Sci. **64**(19–20), 2542–2563 (2007)

16. Tantawy, A.A., Naguib, D.M.: Arginine, histidine and tryptophan: a new hope for cancer immunotherapy. PharmaNutrition **8**, 100149 (2019)

17. Bronte, V., Zanovello, P.: Regulation of immune responses by L-arginine metabolism. Nat. Rev. Immunol. **5**(8), 641–654 (2005)

18. Lovelace, M.D., et al.: Recent evidence for an expanded role of the kynurenine pathway of tryptophan metabolism in neurological diseases. Neuropharmacology **112**, 373–388 (2017)

19. Saha, S.B., Prasanna, J., Chandrasekar, B., Nandi, D.: Gene modulation and immunoregulatory roles of Interferonγ. Cytokine **50**(1), 1–14 (2010)

20. Maechler, P., Li, N., Casimir, M., Vetterli, L., Frigerio, F., Brun, T.: Role of mitochondria in β-cell function and dysfunction. In: Shahidul Islam, Md. (ed.) The Islets of Langerhans, pp. 193–216. Springer, Dordrecht (2010). https://doi.org/10.1007/978-90-481-3271-3_9

21. Bogdan, C.: Regulation of lymphocytes by nitric oxide. In: Cuturi, M.C., Anegon, I. (eds.) Suppression and Regulation of Immune Responses: Methods and Protocols, pp. 375–393. Humana Press, Totowa, NJ (2011). https://doi.org/10.1007/978-1-60761-869-0_24

22. Poon, I.K.H., Patel, K.K., Davis, D.S., Parish, C.R., Hulett, M.D.: Histidine-rich glycoprotein: the Swiss Army knife of mammalian plasma. Blood **117**(7), 2093–2101 (2011)

23. Chu, X., et al.: Integration of metabolomics, genomics, and immune phenotypes reveals the causal roles of metabolites in disease. Genome Biol. **22**(1), 1–22 (2021)

24. Hanusz, Z., Tarasińska, J.: Normalization of the Kolmogorov–Smirnov and Shapiro–Wilk tests of normality. Biometrical Lett. **52**(2), 85–93 (2015)

25. Ranstam, J., Cook, J.A.: LASSO regression. J. Br. Surg. **105**(10), 1348 (2018)

26. McDonald, G.C.: Ridge regression. Wiley Interdisc. Rev. Comput. Stat. **1**(1), 93–100 (2009)

27. Marquardt, D.W., Snee, R.D.: Ridge regression in practice. Am. Stat. **29**(1), 3–20 (1975)

28. Ridgeway, G.: Generalized Boosted Models: A guide to the gbm package. Update, 2007, 1 January 2007
29. de los Campos, G., Pataki, A., Pérez, P.: The BGLR (Bayesian Generalized Linear Regression) R-Package (2015)
30. Hastie, T., Qian, J., Tay, K.: An Introduction to glmnet (2016)
31. Engebretsen, S., Bohlin, J.: Statistical predictions with glmnet. Clin. Epigenetics **11**(1), 1–3 (2019)
32. Yachen, Y.: MLmetrics: Machine Learning Evaluation Metrics. R package version 1.1.1 (2016)
33. Pérez, P., de los Campos, G.: Genome-wide regression and prediction with the BGLR statistical package. Genetics **198**(2), 483–495 (2014)
34. Deutelmoser, H., et al.: Robust Huber-LASSO for improved prediction of protein, metabolite and gene expression levels relying on individual genotype data. Brief. Bioinform. **22**(4), bbaa230 (2021)
35. Öllerer, V., Croux, C., Alfons, A.: The influence function of penalized regression estimators. Statistics **49**(4), 741–765 (2015)
36. Beaver, W.L., Wasserman, K., Whipp, B.J.: Improved detection of lactate threshold during exercise using a log-log transformation. J. Appl. Physiol. **59**(6), 1936–1940 (1985)
37. Becker, R.A., Chambers, J.M., Wilks, A.R.: The New S Language. Wadsworth & Brooks/Cole (1988)
38. Grueneberg, A., de los Campos, G.: BGData - a suite of R packages for genomic analysis with big data. G3 Genes Genomes Genet. **9**(5), 1377–1383 (2019)
39. van den Berg, R.A., Hoefsloot, H.C.J., Westerhuis, J.A., Smilde, A.K., van der Werf, M.J.: Centering, scaling, and transformations: improving the biological information content of metabolomics data. BMC Genomics **7**(1), 1–15 (2006)
40. Banerjee, P., Garai, B., Mallick, H., Chowdhury, S., Chatterjee, S.: A note on the adaptive LASSO for zero-inflated Poisson regression. J. Probab. Stat. **2018**, 1–9 (2018)
41. Algamal, Z.Y.: Diagnostic in poisson regression models. Electron. J. Appl. Stat. Anal. **5**(2), 178–186 (2012)
42. Chai, T., Draxler, R.R.: Root mean square error (RMSE) or mean absolute error (MAE). Geosci. Model Dev. Discuss. **7**(1), 1525–1534 (2014)
43. Chicco, D., Warrens, M.J., Jurman, G.: The coefficient of determination R-squared is more informative than SMAPE, MAE, MAPE, MSE and RMSE in regression analysis evaluation. PeerJ Comput. Sci. **7**, e623 (2021)

Modelling of Arbitrary Shaped Channels and Obstacles by Distance Function

Kristína Kovalčíková Ďuračíková[1,2] , Alžbeta Bugáňová[1],
and Ivan Cimrák[1,2(✉)]

[1] Cell-In-Fluid Biomedical Modelling and Computations Group,
Faculty of Management Science and Informatics, University of Žilina,
010 26 Žilina, Slovakia
{cellinfluid,ivan.cimrak}@fri.uniza.sk
[2] Research Centre, University of Žilina, 010 26 Žilina, Slovakia

Abstract. Numerical simulation is a tool used in multiple scientific domains. There is a wide range of simulations where we model a flow of fluid in a specific geometry, for example in simulations of blood flow in microfluidic channels. In such cases, a complex shape of channels has to be defined by describing its boundaries and rigid obstacles. The purpose of this study is develop a method of defining boundaries and obstacle objects with complex and non-trivial shapes in such numerical simulations. The obstacle or a boundary needs to be described only by a cloud of points defining its surface. Based on this point cloud a distance function determining the position and the shape of the obstacle is defined in the whole simulation domain. This general method is presented on a concrete examples involving several simulations performed within a simulation package ESPResSo. The new method of obstacle creation gives excellent results in terms of the accuracy and simulation time consumption.

Keywords: Numerical simulation geometry · Distance function · Generic obstacle · Cloud of points · Flow modelling

1 Introduction

Computational fluid dynamics (CFD) finds its application in various domains across all scales, from microfluidic devices, through a water valve, to an engineering structures on urban scale as a dam or skyscrapers. In all cases, it replaces expensive and long-lasting experiments by a cheaper and faster numerical models. In case of microfluidics, the manufacturing of such devices requires specific fabrication facilities. The creation of a specific device requires a lot of time, and a specially equipped laboratory is required for an experiment with living blood cells. A numerical CFD simulation can help in many cases, where the computational modelling is faster and cheaper than an original experiment.

Complex geometries have been used e.g. in [1] where authors used a non-trivial geometry to study a fluid wave propagation. Examples of numerical studies of fluid flow in proximity of an obstacle in larger scale can be found in [2,3], which are studies of ground or underground based structure. Another option is a study of flow around a general obstacle or in a general cavity [4]. The mentioned structures can have all ranges of complexity, nevertheless, more accurate the shape of the examined object is modelled, more precise the results describing the behavior of the fluid flow surrounding this object.

There are several discretization approaches in CFD that can be used to create and perform computer simulations. A fluid modelled with the lattice-Boltzmann (LB) method was used in [5–7]. In [2], authors used a finite element analysis software called Ansys for numerical simulation. Another finite-element analysis of fluid-structure interaction was performed in [8], where the authors examined a valve dynamics.

The complicated geometries are a subject that concerns all types of discretization approaches in numerical models, such as channels with shape of an irregular blood vessel in biological domain.

In this work, we will present a method of creation of a general obstacle and channel shape, with simulations run with ESPResSo [9], an open-source simulation package designed to perform molecular dynamics simulations. This tool uses also the LB method combined with the immersed boundary method for simulation of elastic objects. Detailed description of the underlying models are available in [10–14]. The biological application of this method is modeling of complicated microfluidic channels, e.g. shape of a narrowed blood vessel or a microfluidic device containing several different channels.

Although we present the results on a concrete implementation of fluid solver, the considerations are general and can be applied to any solver that implements obstacle definition similarly as ESPResSo does.

2 Numerical Concept of a Boundary

A general numerical model in CFD has to take into account several aspects of a simulated process. For example, it has to consider a presence of fluid flowing through the simulated geometry. After that it has to consider boundaries - obstacles in
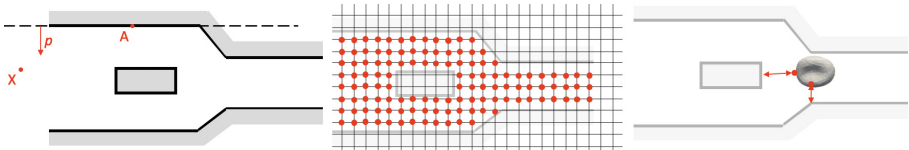
Fig. 1. Left: Example of a geometry depicting a narrowing channel with a rectangular obstacle. Middle: Fixed grid discretization of the fluid requires to identify the lattice points that are located inside the channel (in red). Right: Triangular discretization of an object requires to know the distance of its mesh points from nearest boundary (red arrows), for example to apply repelling force from the boundary. (Color figure online)

simulation box - the walls of the microfluidic device or any kind of obstacle present in the device. Last but not least, there may be solid or elastic particles or immersed objects that are flowing in the fluid and interacting with each other, see Fig. 1.

Definition of an obstacle or a boundary can be given easily for simple geometrical objects. A plane in Fig. 1 on the left, can be e.g. defined by its normal vector p and one point A on the plane. Then, using this information one can compute the distance of any point X in space from the plane using a simple expression. For complicated irregular shapes one can e.g. define a triangulation of its surface, which may be tedious or, the shape may be first described by point cloud and the triangulation may be generated from this point cloud [15].

We present a method that takes the point cloud and defines the boundary or obstacle by the distance function without necessity to define triangulation of the boundary. Such approach may be used for a coupled fluid solver and elastic object solver (e.g. the LB method and Immersed boundary method) that employ the distance function that returns the distance of any spatial point from the nearest obstacle.

As a demonstration, in ESPResSo the fluid is discretized by a fixed grid (LB method), where we need to know for each grid point whether it is inside or outside of an obstacle, Fig. 1 middle. Immersed objects (e.g. red blood cells) are modeled separately as sets of interconnected mesh points that can move freely in 3D space independently of the lattice grid. Throughout the simulation, we need to know the nearest distance between any of these mesh points and the obstacles, Fig. 1 right.

To evaluate the flow of fluid with respect to the boundaries, the discretization points in computational domain are flagged at the beginning of the simulation either as a fluid point or an obstacle/wall point. The fluid is approximated at fluid points only. The boundary is implemented e.g. by a bounce-back rule. The no-slip condition assuming a zero velocity of fluid at a solid boundary assures the correct evolution of the fluid velocity field in the whole calculated domain.

2.1   Interaction Between Boundaries and Immersed Particles

To model the trajectory and deformation of an immersed elastic object defined by mesh points on its boundary, one must ensure such object do not interfere with the boundary. Many solvers tackle this issue by introducing a force potential between the mesh points of the object and the boundary that exerts a repelling force to the mesh points that does not allow for points to reach the boundary.

Such interaction is relevant only in case when the object is close enough to the obstacle or wall and the direction of repellent force must by out-of-boundary. Therefore, we need to be able to evaluate the distance between the immersed object's mesh points and the closest obstacle for any position of the mesh points and moreover, we need to know the out-of-wall direction.

The output from a distance function will thus be twofold: A scalar value of the distance and a unit vector. Scalar distance is used to check the distance from the closest boundary, in order to verify whether the interaction between the immersed object and the boundary should be considered or not. The interaction forces are evaluated only in case when the immersed object and the obstacle

are close enough - this distance is defined as one of interaction parameters. The second output of the distance function is a distance vector. If the object and the obstacle are close enough, the interaction between the obstacle and the immersed object will result in forces acting to the object, and these forces need to have a correct vectorial orientation.

3   Algorithm for Boundary Definition

To demonstrate the methods, we create two types of boundaries, and we will explain the concept on both of them. The first boundary has a specific shape - a helix. Helix is roughly speaking a spiral tube. Its geometry is fully defined by its global axis (around which the helix is wrapped), the curvature radius, the radius of the tube, and the pitch, see Fig. 2, on the right. As local axis we call a curve that lies in the middle of the tube.

The second boundary is of general shape - a generic boundary. This one is defined only by cloud of points located on its surface.

3.1   Helix as Boundary

To calculate the distance function for any point in space in case of a helix, we use a fact that a) the cross-section of the helix in direction perpendicular to the local axis is a circle b) the vector coming from any point in simulation domain to its closest boundary point on helix is always perpendicular to the local axis and it intersects this local axis. Therefore, it is sufficient to calculate the distance from the point in the simulation domain to the closest point lying on the local axis of the helix, and reduce this distance by the radius of the helix tube.

This approach can be used to compute both vectorial and scalar distance function. In case the final distance is negative, the examined point in simulation domain is inside of the helix tube and if it is positive, the point is lying outside of the helix tube.

In case of a helix, the closest distance can not be found by an explicit formula. The reason is that the most important part in definition of the helix geometry is position of its local axis which can be defined as a set of points with coordinates $[R_c \cdot sin(t), R_c \cdot cos(t), \frac{pitch}{2\pi}t]$, where t is a parameter running along the global axis of the helix, in this case z-axis.

If we want to evaluate the closest distance between a spatial point and the helix, we would arrive to a parametric equation of type $A \cdot sin(t) + B \cdot cos(t) + C \cdot t + D = 0$ for t as an unknown variable and A, B, C, D as parameters dependent on geometry of the helix. This equation does not have closed expression for the solution for general parameters A, B, C, D, but it can be solved numerically for a given values of these parameters.

Therefore, we need to use an iterative approach to identify the closest boundary to a spatial point and to evaluate the distance to it. For this we can use a fact that for any point in the simulation domain, the helix point with minimal distance from this space point is within interval $(t-\pi, t+\pi)$ in z-coordinate (Fig. 2).

The distance between the examined spatial point with coordinates $[x_p, y_p, z_p]$ and a point on local axis with coordinates $[R_c \cdot sin(t), R_c \cdot cos(t), \frac{pitch}{2\pi}t]$ is expressed as

$$D_{ax} = \sqrt{(x_p - R_c \cdot sin(t))^2 + (y_p - R_c \cdot cos(t))^2 + (z_p - \frac{pitch}{2\pi}t)^2}$$

The distance between the spatial point and the closest boundary is then, for r as the tube radius of the helix $D_b = D_{ax} - r$.

We want to find a minimal distance between the spatial point and a boundary point, so we need to calculate the value of D_b for a sufficient number of points on helical axis within the considered loop. This number h is evaluated from the length of the helical loop and the spatial discretization of the simulation domain as $h = 1.5\sqrt{(2\pi R_c)^2 + pitch^2}/d$, where R_c is the curvature radius of the helix, $pitch$ is a distance between two adjacent loops, and d is the discretization distance in the simulation domain.
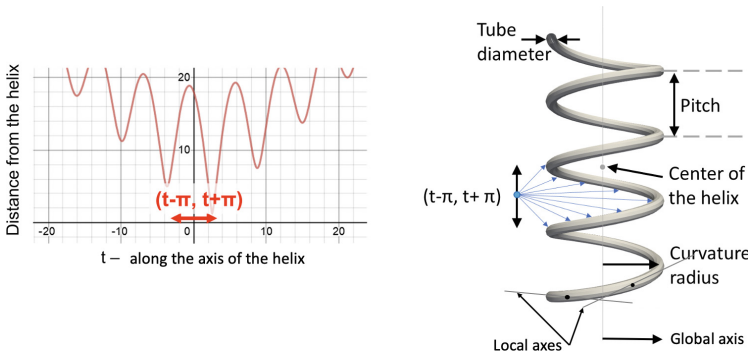
Fig. 2. The helix boundary point with minimal distance from the space point is within interval $(t-\pi, t+\pi)$. The helix is defined by its center (any point situated at the global axis of helix), its tube radius, pitch and curvature radius.

The computational complexity of simulation steps linked to a helical obstacle can be expressed as a function of the discretization box dimension n (expressed as a number of discretization points on an edge of the simulation domain) and a number of fictive particles discretizing one helical loop with the similar disctretization as the simulation domain has, h.

The initial definition of the distance function, which have to be done once at the beginning of the simulation, has a complexity $n^3 \cdot h$. During the simulation, the use of this distance function (for calculation of interactions between immersed objects and the obstacles, for example) has a complexity of $h \cdot m$, where m is a number of immersed object mesh points in simulation.

3.2   Generic Boundary

Generic boundary in this work will be defined by a cloud of its surface points. In case of a helix or other available obstacles in ESPResSo, the spatial function is calculated at the beginning of each simulation from the parameters defining the position and the shape of the obstacle. In case of the generic boundary, we need to calculate the spatial function for all fluid discretization points by a routine before running the microfluidic simulation. The input for the routine is the cloud of the obstacle's surface points, and output of this routine is a spatial function. The spatial function is stocked into a pair of .vtk files - one file for the scalar spatial function, the other one for vectorial spatial function. These two files serve than as an input parameters in definition of the generic boundary in simulation script. At the beginning of the simulation, the spatial function is defined in every discretization point of simulation domain - the values are not calculated, but they are taken from the input .vtk files.

The spatial function need to be definable not only in discretization points, but also in any point where a particle of immersed object can be found during the simulation. Therefore, the distance function in other than discretization points is calculated as a trilinear interpolation of distances in 8 closest discretization points. The calculation of the spatial function is made with an algorithm Vector distance transform (VDT) described in [16].

This algorithm does consider the distance as a vector, but it does not directly distinguish between obstacle's "inside" and "outside". To distinguish these two options, we can use an approach where we create two sets of obstacle clouds. One set would define the obstacle's shape as we explained in previous paragraphs. This one would be considered as the real description of the obstacle. The second cloud would be very similar to the first one, but it would be slightly "inflated", it would describe an obstacle that is slightly more spacious. The number of points in two clouds will be the same, and each point in the first cloud need to have an associate point in the other cloud. Each couple of points thus define an outward vector (not necessarily perpendicular to the obstacle's surface), directed from a point in first cloud to its associate point in second cloud. When the scalar spatial function will be defined, the distance to an obstacle point will be defined directly with the VDT algorithm. The sign + or - defining whether the distretization spatial point is inside or outside of the obstacle, will be obtained by comparing the direction of the outward vector (taken from the two sets of cloud points) and the direction of the vector obtained with VDT algorithm. The examined discretization fluid point will be inside or outside of obstacle, in function of the angle between the two vectors - we need to check whether this angle is sharp or obtuse.

The complexity of this algorithm can be expressed as a function of the disctretization box dimension n and number of points in simulation cloud p. The initialisation before the VDT algorithm has a complexity $n^3 + p$. The VDT algorithm calculating the distance function has a complexity n^3. Once the distance function is defined, its application into the simulation process has a complexity n^3 at the beginning of the simulation. During the simulation, the use of this

distance function has a complexity of $1 \cdot m$, where m is a number of immersed object mesh points in simulation.

3.3   ESPResSo Specific Files to Create or to Modify

From technical point of view specific to ESPResSo, six files need to be created or modified to create a new obstacle.

Files that have to be created:

- src/core/shapes/NewObstacle.hpp - defining parameters that specify the obstacle dimensions and position
- src/core/shapes/NewObstacle.cpp - defining distance function: calculating distance from a general point in simulation domain to the closest obstacle boundary, result is a scalar and also a vector
- src/script_interface/shapes/NewObstacle.cpp - defining keywords for interface between the cpp code and python scripting

Files that have to be modified: - src/python/espressomd/shapes.py - defining the text for script interface helper

- src/core/shapes/CMakeLists.txt - adding the new obstacle on the list of existing obstacles
- src/script_interface/shapes/inicialize.cpp - adding the new obstacle on the list of existing obstacles

These files, also with an example of cloud points and distance-function calculators are provided in supplementary materials.

4   Verification of the Proposed Solution

To verify the correctness of the proposed solutions for helical and generic obstacle, we prepared two sets of experiments, run on GPU [17].

The geometry of both experiments is illustrated in Fig. 3 and Fig. 4. First one served to compare a simulation with an existing basic obstacle, and an obstacle
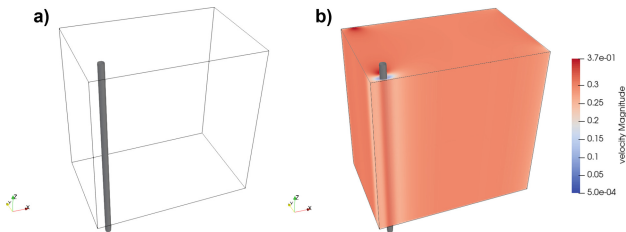
Fig. 3. Cylindrical obstacle in simulation box. **a)** Geometry of the numerical simulation **b)** Verification of the correctness of the fluid flow without particles

created with generic approach described in previous sections. This experiment contained a cylindrical obstacle. We created this obstacle by two different ways - we used an existing cylindrical obstacle which was already present among the existing basic obstacles in ESPResSo, or the cylindrical shape was created by a generic boundary approach. The dimensions of simulation box were $280 \times 180 \times 280$ µm, with discretization of 1 µm. The total number of fluid discretization points was 14 112 000.

Second experiment served to compare a simulation with a helical obstacle, once it was created with an implemented routine to create helical shapes (Sect. 3.1), and after that it was created by generic approach (Sect. 3.2). The dimensions of simulation box were $60 \times 210 \times 210$ µm, with discretization of 1 µm. The total number of fluid discretization points was 2 646 000.

In both experiments, we introduced the fluid flow, several non-dimensional particles carried by the flow and interacting with the obstacles, and we compared several simulation outputs. We compared the outputs linked to the physical processes described in simulation on one hand, and the simulation time needed to run the simulation on the other hand.

First of all, we run a simulation without particles, and we compared the vector field for fluid velocity. For this simulation we compared also the simulation time. The second simulation was run with four non-dimensional particles, and we compared their trajectories. The third simulation contained 10 000 particles, and in this case, we did not compared the particle trajectories, but only the simulation time needed.
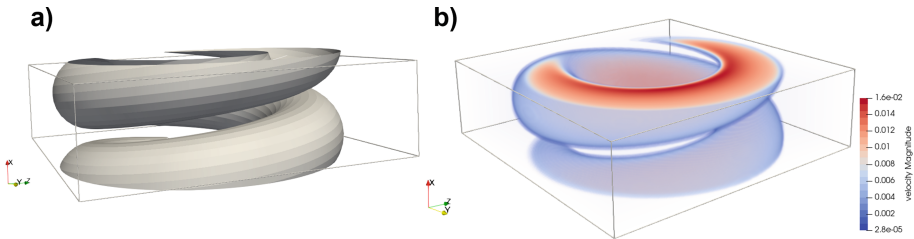
Fig. 4. Helical channel in simulation box. **a)**Geometry of the numerical simulation **b)**Verification of the correctness of the fluid flow without particles

4.1   Comparison of Fluid Flow

To compare the flow of fluid, we run a set of simulations without particles. The fluid was flowing around the cylindrical obstacle for the first set of simulations, and inside of the helical obstacle for the second set of simulations. During the simulation, the .vtk files with fluid velocity were recorded. These files contain an information about fluid velocity in each fluid discretization point. Therefore, it is possible to compare these files in order to evaluate the difference in flow between the two ways of obstacle definition.

For the simulation with cylindrical obstacle, there was no difference in the two compared flows, the difference in the fluid flow in each discretization point was literally 0 for all valid decimal places. For the simulation with helical obstacles, there was an observable difference, notably on the border of the helical obstacle. This could be possible caused by a different representation of the helical obstacle in two approaches of its creation. Evaluation of the outside and inside discretization points happens in different ways - in both cases, there is an algorithm with several iterations, and so with limited precision. The algorithms are different, therefore there could be several border points, that are defined as inner in one approach, and outer in the other approach. We can see the position of these points on Fig. 5 left. This different assignment of discretization points has also an impact to the total flow field. The difference in velocities inside of the microfluidic channel is less than 0.5%, therefore we consider the two approaches as alike.
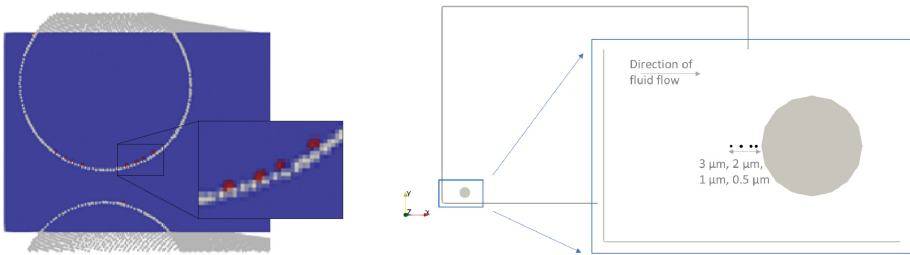
Fig. 5. Left: Cut through the simulation box with helical microfluidic channel. Red points are border points, that were flagged differently in the two examined approaches. Right: Position of the four 1D particles in flow with cylindrical obstacle. (Color figure online)

4.2 Comparison of Trajectories

In this section we will discuss the correctness of object-obstacle interactions. The aim of such interactions is to omit the overlapping of obstacles and immersed objects. Therefore, if an object approaches an obstacle, a force between the obstacle and the immersed object appears and repels the object away from the obstacle. There are several types of interaction in ESPResSo. The interaction that we used is an interaction defined with soft sphere potential:

$$V(r) = a(r - r_{offset})^{-n} \text{ for } r < r_{cutoff}, \text{ and } V(r) = 0 \text{ otherwise.}$$

In these equations, the r is a distance between the immersed object mesh point and the closest boundary. The other parameters should be defined by user in a simulation script.

To evaluate the correctness of the interactions between immersed objects and the obstacles, we introduced four non-dimensional particles into the simulation. The parameters of the soft-sphere interactions between the particles and

the boundaries are identical for both helix and cylinder except for the cut-off distance. For cylinder we used 2 µm and for helix we used 26 µm .

For the case of cylindrical obstacle, their initial position in y- and z-direction was the same, in x-direction they were seeded in different distances from the cylindrical obstacle -0.5 µm, 1 µm, 2 µm and 3 µm (Fig. 5 right). The direction of the fluid flow was set to be in x-direction as well and the particles were directed against the obstacle. The interaction between those particles and the obstacle is active when the distance between the obstacle and the particle is less than 2 µm. In Fig. 6, we can see evolution of the x-position of the four particles in time.

In case of cylindrical obstacle, the y- and z- position of the particles did not changed considerably in time. The evolution of the particle trajectories can be seen in Fig. 6. After approximately 300 µs, all of the four particles reached stabilized position. The stabilized positions, as well as trajectories of particles, differed by 0.025 µm for conventionally created cylinder and for cylinder created with generic approach.
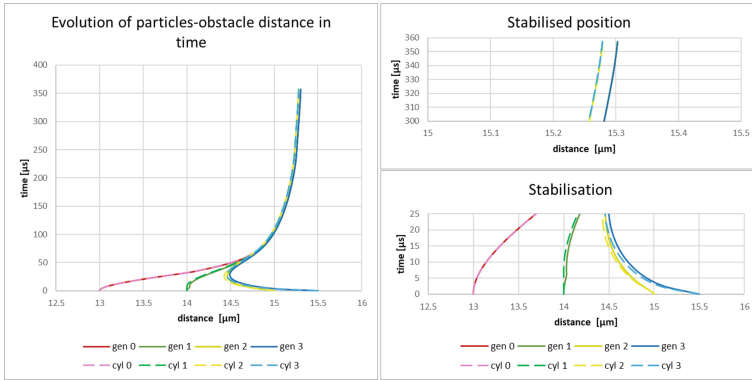
Fig. 6. Evolution of particles-obstacle distance in time. Comparison of cylindrical and generic obstacles. The border of the obstacle is at position 16 µm

For the case of helical obstacle, we introduces as well four particles into the fluid flow (Fig. 8 on the left). The interaction between those particles and the boundary is active all the time, as the distance between a particle and the closest wall is always less than cutoff-value 26 µm (the radius of the tube is 25 µm).

We studied the shape of particles trajectory (example of these graphs for one of the four particles is on Fig. 7), and the particles trajectory projected to the perpendicular cross-section of the tube (Fig. 8 on the right).

We do not show here graphs for evolution of the particles position in time, as in previous section, because the velocity of the flow was not the same in the two compared cases. To eliminate the time dependency from the comparison, we compared only the shape of the trajectory, not its time evolution.

Therefore we compared the dependence of z-coordinate and y-coordinate on x-coordinate of particles. The difference in trajectories is negligible (0,15 μm).
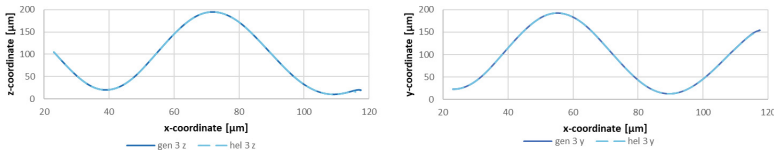
Fig. 7. Shape of particles trajectory. Comparison of helical and generic obstacles, for particle n.3
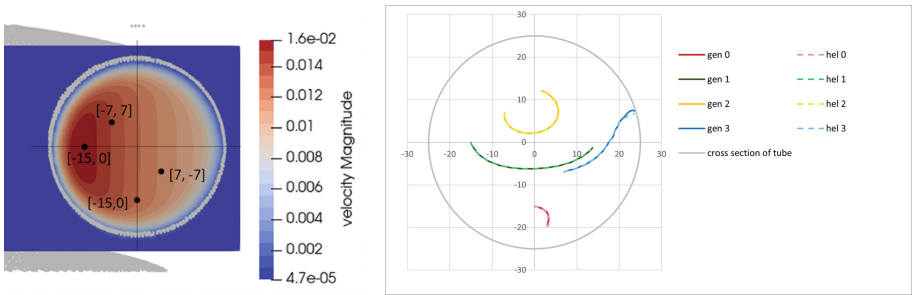
Fig. 8. Left: Position of the four 1D particles in flow with helical obstacle. Right: Trajectories of particles in the helical microchannel, projected to the cross-section of the helical tube. The initial position of each particle is marked by a black dot. (Color figure online)

The last graph shows us projection of trajectories to a plane which is perpendicular to the local axis of the helical tube. We can confirm that the trajectories of the particles are comparable.

4.3   Comparison of Computation Time

At the beginning of the simulation, an initialization of the fluid field need to be done - the flagging of the fluid discretization points. This procedure takes some time. This initiating time was one of elements that we compared.

After that, we compared the time needed to make a series of 1 000 steps, with a calculation of a particle-obstacle interaction. We included into this comparison also a calculation without particles, in order to understand what fraction of time is needed to calculate the fluid flow, and what part is needed to handle with interacting particles. We considered 10 000 particles that were placed in a cloud in front of the cylindrical obstacle, or inside of the helical channel, so they interacted with the boundaries during whole simulation.

For the cylindrical/helical obstacle, the following simulations were performed, each one with 4 000 steps:

– cylindrical/helical obstacle - only fluid
– generic cylindrical/helical obstacle - only fluid
– cylindrical/helical obstacle - 10 000 particles
– generic cylindrical/helical obstacle - 10 000 particles

Each of these simulation was run twice, in order to assure the reproducibility of the experiments. Therefore, 8 simulations were run simultaneously for cylindrical obstacle, and after that, 8 simulations were run simultaneously for helical obstacle. For each simulation setting, we obtained several values of time needed to perform 1 000 simulation steps, that were averaged in the end.

For the case of cylindrical obstacle, the real time needed to perform the 1 000 steps of simulation is very similar - around 3500 s. The difference between simulations with and without particles is of order of 1% - the majority of the time was spend to calculate and output the fluid flow.

The average time needed to perform the interactions between particles and boundary is rather comparable for both cases. For the case with cylinder created as a standard ESPResSo obstacle, we obtain 6 s, and for the case where the cylindrical obstacle was created by new generic approach, we obtain 32 s. It might seem than the average value for generic cylinder shape is five times bigger than the value for ordinary cylinder, but both values are only a fraction of time needed to perform the whole calculation. Therefore we can conclude that we did not observe a significant difference in needed simulation time, for the two examined approaches of obstacle creation.

For the case of helical microchannel, we can observe certain difference. In this case, the computational time needed to calculate the particle-less simulation was very similar for both cases (605 s), but the difference was noticeable when we focus on simulations with particles. While in case of generic obstacle, the time needed to calculate the particle interactions was 12 s, in the other case, the time needed to handle with particles was 175 s. It is approximately 15 times bigger than the equivalent time in case of helix created by generic approach.

The time required for initialisation of the fluid is variable. The shortest time is required for the case with cylinder created as a standard ESPResSo obstacle, only few seconds. Initialisation of fluid for generic cylinder is noticeably bigger as for the case of ordinary cylinder. The initialisation for helical obstacle and generic obstacle takes a comparably long time. However, this process is done only once at the beginning of the simulation, so its time duration is not so important.

The times needed for the calculation of fluid, for calculation of particle interactions and the fluid initialisation are summed up in Tables 1 2 and 3.

Table 1. Summary of calculation time for examined cases -time needed to calculate 1 000 simulation steps.

	Time for 1 000 steps
Cylinder only fluid	3 470 s
Gen. cylinder only fluid	3 451 s
Cylinder 10 000 particles	3 476 s
Gen. cylinder 10 000 particles	3 483 s
Helix only fluid	601 s
Gen. helix only fluid	599 s
Helix 10 000 particles	776 s
Gen. helix 10 000 particles	611 s

Table 2. Summary of calculation time for examined cases - time needed to calculate particles trajectories, where time needed for fluid calculation is subtracted.

	Time for 1 000 steps
Cylinder 10 000 particles no fluid	6 s
Gen. cylinder 10 000 particles no fluid	32 s
Helix 10 000 particles no fluid	175 s
Gen. helix 10 000 particles no fluid	12 s

Table 3. Summary of calculation time for examined cases - initialization of fluid.

	Time for fluid init		Time for fluid init
Cylinder	3,5 s	Helix	44 s
Generic cylinder	177 s	Generic helix	33 s

5   Conclusion

In this work, we proposed and verified a numerical concept of a generic obstacle. The concept was presented and verified within the simulation package ESPResSo, but it can be used in a wider spectrum of numerical simulations with obstacles. For example in simulations of water passing through a porous medium, or in simulations modeling the flow of air around a surface objects such as skyscrapers or towers. In biological domain, the method can be used to model complicated shapes as blood vessels or multi-channel microfluidic devices.

To define the shape of a generic obstacle, we need to define a cloud of points that describe the surface of the object. The shape of the generic obstacle is thus limited only by our ability to create such cloud of points. After that, we use a VDT algorithm to find a distance function - a function that define for each simulation point a vector and a value that correspond to the distance to the closest boundary.

There is also an important applicability of this approach in recent simulations leaded within our research group. It will be used in further simulations of helical devices with non-circular cross-section, in order to sort the cells that flow through it, in a function of their size or elasticity.
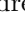
References

1. Zou, Ch., Yin, Y.: Simulation of fluid and complex obstacle coupling based on narrow band FLIP method. Water **10**, 811 (2018)
2. Velísková, Y., Chára, Z., Schügerl, R., Dulovičová, R.: CFD simulation of flow behind overflooded obstacle. J. Hydrol. Hydromech. **66**, 448–456 (2018)
3. Magdalena, I., Hariz, A.A.A., Farid, M., Kusuma, M.S.B.: Numerical studies using staggered finite volume for dam break flow with an obstacle through different geometries. Results Appl. Math. **12**, 100193 (2021)
4. Pipp, P., Hočevar, M., Dular, M.: Challenges of numerical simulations of cavitation reactors for water treatment - an example of flow simulation inside a cavitating microchannel. Ultrason. Sonochem. **77**, 105663 (2021)
5. Luo, L.-S., Krafczyk, M., Shyy, W.: Encyclopedia of Aerospace Engineering: Lattice Boltzmann Method for Computational Fluid Dynamics. In: Blockley, R., Shyy, W., (eds.) (2010)
6. Zeiser, T., Lammers, P., Klemm, E., Li, Y.W., Bernsdorf, J., Brenner, G.: CFD-calculation of flow, dispersion and reaction in a catalyst filled tube by the lattice Boltzmann method. Chem. Eng. Sci. **56**, 1697–1704 (2001)
7. Obrecht, C., Kuznik, F., Merlier, L., Roux, J.-J., Tourancheau, B.: Towards aeraulic simulations at urban scale using the lattice Boltzmann method. Environ. Fluid Mech. **15**(4), 753–770 (2014). https://doi.org/10.1007/s10652-014-9381-0
8. Yakhlef, O., Murea, C.M.: Numerical simulation of dynamic fluid-structure interaction with elastic structure-rigid obstacle contact. Fluids. **6**, 51 (2021)
9. Arnold, A., et al.: ESPResSo 3.1 - molecular dynamics software for coarse-grained models. Lecture Notes in Computational Science and Engineering, vol. 89, pp. 1–23 (2013). https://doi.org/10.1007/978-3-642-32979-1_1
10. Jančigová, I., Kovalčíková, K., Weeber, R., Cimrák, I.: PyOIF: computational tool for modelling of multi-cell flows in complex geometries. PLoS Comput. Biol. **16**(10), e1008249 (2020)
11. Jančigová, I., Kovalčíková, K., Bohiniková, A., Cimrák, I.: Spring-network model of red blood cell: from membrane mechanics to validation. Int. J. Numer. Meth. Fluids **92**, 1368–1393 (2020)
12. Tóthová, R., Jančigová I., Bušík, M.: Calibration of elastic coefficients for spring-network model of red blood cell. In: 2015 International Conference on Information and Digital Technologies, pp. 376–380 (2015). https://doi.org/10.1109/DT.2015.7223000
13. Jančigová, I., Tóthová, R.: Scalability of forces in mesh-based models of elastic objects, In: 2014 ELEKTRO, pp. 562–566 (2014). https://doi.org/10.1109/ELEKTRO.2014.6848960
14. Bachratý, H., Bachratá, K., Chovanec, M., Kajánek, F., Smiešková, M., Slavík, M.: Simulation of blood flow in microfluidic devices for analysing of video from real experiments. In: Rojas, I., Ortuño, F. (eds.) IWBBIO 2018. LNCS, vol. 10813, pp. 279–289. Springer, Cham (2018). https://doi.org/10.1007/978-3-319-78723-7_24
15. Bouchiba, H., et al. Computational fluid dynamics on 3D point set surfaces. J. Comput. Phys. **7**, 100069 (2020)
16. Kosa, B., Mikula, K.: Direct simple computation of middle surface between 3D point clouds and/or discrete surfaces by tracking sources in distance function calculation algorithms (2021), arXiv:2112.09808
17. Roehm, D., Arnold, A.: Lattice Boltzmann simulations on GPUs with ESPResSo. Eur. Phys. J. Special Topics. **210**, 89–100 (2012)

Gene Expression Profiles of Visceral and Subcutaneous Adipose Tissues in Children with Overweight or Obesity: The KIDADIPOSEQ Project

Mireia Bustos-Aibar[1,2], Augusto Anguita-Ruiz[1,2,3,4,5(✉)],
Álvaro Torres-Martos[1,2], Jesús Alcalá-Fdez[6],
Francisco Javier Ruiz-Ojeda[1,2,3,4], Marjorie Reyes-Farias[4,7,8],
Andrea Soria-Gondek[10], Laura Herrero[4,7], David Sánchez-Infantes[4,8,9],
and Concepción María Aguilera[1,2,3,4,5]

[1] Department of Biochemistry and Molecular Biology II, School of Pharmacy,
University of Granada, 18071 Granada, Spain
{mireiabustos,alvarotorres}@correo.ugr.es, caguiler@ugr.es
[2] Institute of Nutrition and Food Technology "José Mataix",
Center of Biomedical Research, University of Granada, Avda. del Conocimiento s/n.,
18016 Granada, Spain
[3] Instituto de Investigación Biosanitaria IBS. Granada, Complejo Hospitalario
Universitario de Granada, 18014 Granada, Spain
[4] CIBEROBN (CIBER Physiopathology of Obesity and Nutrition),
Instituto de Salud Carlos III, 28029 Madrid, Spain
dsanchez@igtp.cat
[5] Barcelona Institute for Global Health (ISGlobal), Doctor Aiguader 88,
08003 Barcelona, Spain
augusto.anguita@isglobal.org
[6] Department of Computer Science and Artificial Intelligence, Andalusian Research
Institute in Data Science and Computational Intelligence (DaSCI),
University of Granada, 18071 Granada, Spain
jalcala@decsai.ugr.es
[7] Department of Biochemistry and Physiology, School of Pharmacy and Food
Sciences, Institute of Biomedicine of the University of Barcelona (IBUB), University
of Barcelona, 08028 Barcelona, Spain
{marjorie.reyesfarias,lherrero}@ub.edu
[8] Department of Endocrinology and Nutrition, Germans Trias i Pujol Research
Institute, 08916 Badalona, Spain
[9] Department of Health Sciences, Campus Alcorcón, University Rey Juan Carlos
(URJC), 28922 Madrid, Spain
[10] Pediatric Surgery Department, Hospital Universitari Germans Trias i Pujol,
08916 Badalona, Spain

Abstract. Childhood obesity is a multifactorial disease influencing the
development of a range of metabolic disorders, where adipose tissue has
been proved to be fundamental. The adipose tissue can be distributed
throughout the body as visceral adipose tissue (VAT) and subcutaneous

adipose tissue (SAT), and there are considerable anatomical differences between both adipose tissues in the body. Importantly, VAT is associated with low-grade systemic inflammation and insulin resistance, which are key factors underlying metabolic alterations associated with childhood obesity [1]. This study aimed to identify the molecular signatures underlying obesity and overweight in children, differentiating between shared and individual signatures in VAT and SAT. Both tissue samples were collected from 18 children (11 girls) aged 0.54 to 16.63 years and hospitalized for abdominal surgery, of which 6 children (2 girls) had overweight or obesity. RNAseq analysis was performed to identify gene expression patterns associated with obesity and overweight in each tissue. The software tools used in the RNAseq data analysis were FastQC, to perform sequencing quality checks; HISAT, to map reads to the human genome; featureCounts to quantify raw counts; and DESeq2 to differential gene expression analysis. In VAT there were 759 genes showing statistically significant differential expression between groups (nominal p-value < 0.05), from which 48 passed an FDR threshold of 0.05. VAT's differential expression results may be observed in Fig. 1–2. In SAT there were 945 genes showing statistically significant differential expression, from which 28 passed the FDR threshold. SAT's differential expression results are shown in Fig. 3–4. We were specially interested in the identification of shared genes associated with overweight and obesity in both tissues, for which we performed a gene ontology analysis of all differently expressed genes, using Gene Ontology and Kyoto Encyclopedia of Genes and Genomes databases. Among significantly associated genes, there were 126 common genes, as it is shown in Fig. 5. The reliability of our results was assessed by matching our list of significant genes with a list of genes whose influence on obesity has been previously described in the literature (e.g., *LEP* and *TNMD*) [2,3]. Additionally, our research identified new molecular targets, highlighting the results of VAT (i.e., *XIST, PRKY* and *TTTY10*). In conclusion, our approach identified independent and shared gene expression patterns in VAT and SAT associated with overweight and obesity in children. Understanding the molecular architecture of obesity with approaches like these is crucial for the identification of powerful molecular targets and developing of effective precision medicine therapies.
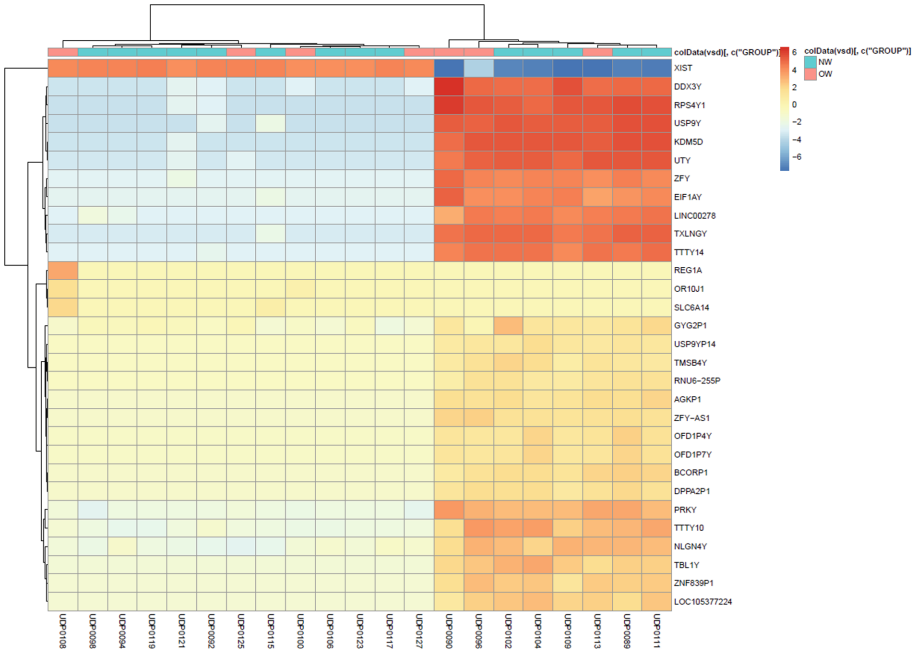
Fig. 1. Heatmap showing the 30 most significant genes in Y axis and samples (individuals) in X axis from VAT approach adjusted by sex. Genes and samples clustering was performed using k-means method.
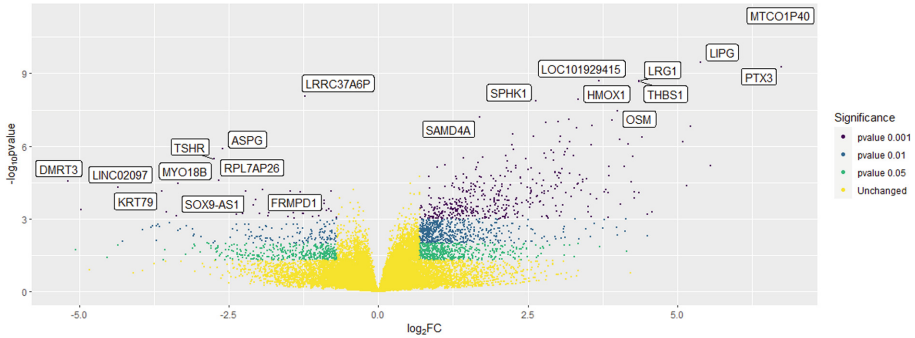
Fig. 2. Identification of the most significant and robust gene expression changes among experimental groups from VAT approach adjusted by sex. It is plotted significance level versus fold-change of each gene on the Y and X axes, respectively. Interesting genes that display both large magnitude for fold-changes (log_2FC) and high statistical significance ($-log_{10}pvalue$) (non-adjusted) are detailed. Color represents different p-value levels.
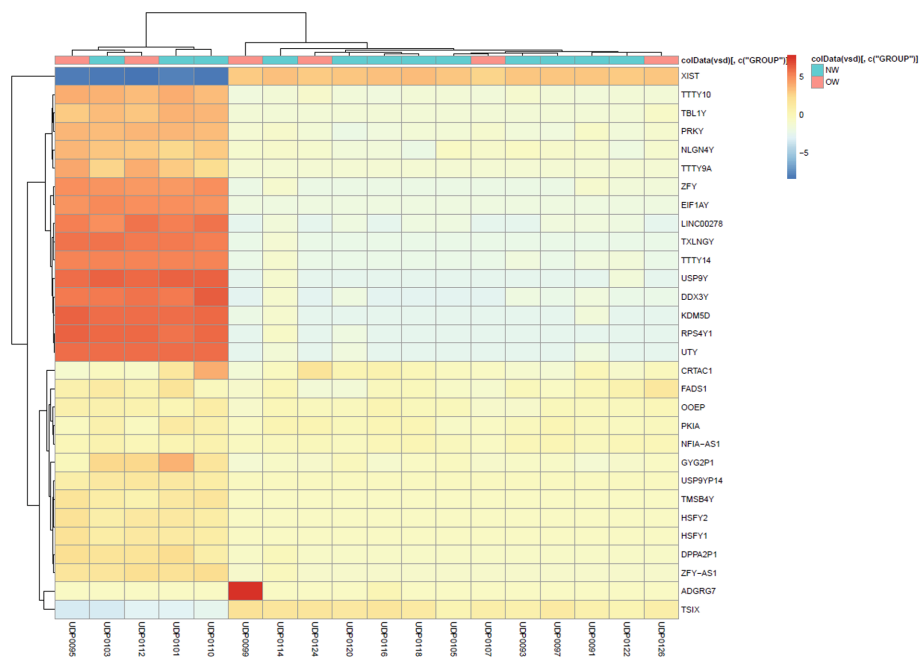
Fig. 3. Heatmap showing the 30 most significant genes in Y axis and samples (individuals) in X axis from SAT approach. Genes and samples clustering was performed using k-means method.
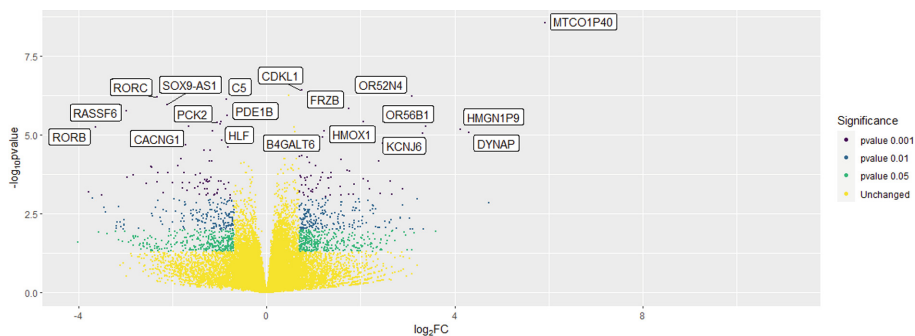
Fig. 4. Identification of the most significant and robust gene expression changes among experimental groups from SAT approach adjusted by sex. It is plotted significance level versus fold-change of each gene on the Y and X axes, respectively. Interesting genes that display both large magnitude for fold-changes (log_2FC) and high statistical significance ($-log_{10}pvalue$) (non-adjusted) are detailed. Color represents different p-value levels.
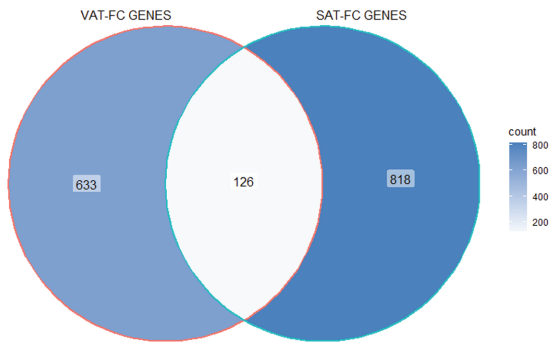
Fig. 5. Venn diagram comparing lists of differently expressed genes obtained from each tissue type adjusted by sex. Genes considered were only those showing a nominal p-value < 0.05. The number of shared genes (significant at both approaches) can be observed at the intersection of the two circles.

References

1. Gil, A., Olza, J., Gil-Campos, M., Gomez-Llorente, C., Aguilera, C.M.: Is adipose tissue metabolically different at different sites? Int. J. Pediatr. Obes. **6**(1), 13–20 (2011). https://doi.org/10.3109/17477166.2011.604326
2. Landecho, M.F., Tuero, C., Valentí, V., Bilbao, I., de la Higuera, M., Frühbeck, G.: Relevance of leptin and other Adipokines in obesity-associated cardiovascular risk. Nutrients **5**(11), 2664 (2019). https://doi.org/10.3390/nu11112664
3. Ruiz-Ojeda, F.J., Anguita-Ruiz, A., Rupérez, A.I., et al.: Effects of X-chromosome tenomodulin genetic variants on obesity in a children's cohort and implications of the gene in adipocyte metabolism. Sci. Rep. **9**, 3979 (2019). https://doi.org/10.1038/s41598-019-40482-0

The Role of Astrocytes in Alzheimer's Disease Progression

Swadesh Pal[1] and Roderick Melnik[1,2]([⊠])

[1] M3AI Laboratory, MS2Discovery Interdisciplinary Research Institute,
Wilfrid Laurier University, Waterloo, ON N2L 3C5, Canada
`rmelnik@wlu.ca`
[2] BCAM - Basque Center for Applied Mathematics, 48009 Bilbao, Spain
`http://m3ai.wlu.ca`

Abstract. Astrocytes are a particular type of glial cells observed throughout the gray matter in the brain. In a healthy brain, they help to defend evolutionarily conserved astrogliosis programs and maintain neuronal metabolism. On the other hand, in the Alzheimer's disease (AD) affected brain, they release neurotoxins because of the adopting behaviours of different functions depending on the disease progression. Along with astrocytes, amyloid-beta ($A\beta$) and tau proteins (τP) play a prominent role in AD. In this paper, we have developed a model and have studied the dual action of astrocytes with $A\beta$, τP, and their toxic forms in the brain connectome. Initial conditions-dependent solutions of the model demonstrate that the treatment depends on AD's status at the first diagnosis time. With an increase in the clearance rate of toxic $A\beta$ by the astrocytes, the model predicts a cure possibility from AD. Furthermore, the network model with non-uniform parameter values in different regions, developed here, provides a better insight into the distributions of the concentrations in the brain connectome.

Keywords: Alzheimer's disease · Brain connectome · Data-driven models · Cell interactions · Bistability and bifurcation · Amyloid-beta · Tau protein · Astrocytes · Network models

1 Introduction

Alzheimer's disease (AD) is one of the leading neurodegenerative diseases nowadays. AD causes neuronal death in the brain and disables different functional abilities. According to the Alzheimer's Association, more than 50 million people worldwide have this dementia, and it is expected to reach over 150 million in three decades [1]. AD develops very slowly in the brain at the early stage, and it is hard to identify such changes. That is one of the main reasons for the AD progression to be detected and analyzed. Numerous studies have been carried out to determine the mechanism behind AD progression, but still, it is not fully clear. As of today, only four drugs are approved by the Food and Drug Administration

(FDA) for AD treatments. Moreover, the approved drugs do not prevent the neuronal loss, although they do help in symptoms management [2]. Therefore, disease-modifying therapies play an important role in controlling the brain's AD progression.

It is well accepted that the amyloid-beta (Aβ) and tau protein (τP) are the two main ingredients in developing the AD [3,4]. Aβ is accumulated in the extracellular space and deposited in the form of insoluble plaques. On the other hand, τP forms neurofibrillary tangles (NFT) inside the brain cells. Significant production of plaques and NFTs disrupt the normal activities of the brain cell and move towards AD.

Astrocytes perform various functions in the brain, and their abnormality causes multiple neurodegenerative diseases, e.g., AD, Parkinson's disease [5,6]. They release gliotransmitters in different brain regions and help in the modulation of memory and learning processes [7–9]. Earlier research suggested that the astrocytes clear the plaques from the brain cells and keep them healthy. But, a significant production of plaque interrupts the astrocyte's functions; as a result, AD develops in the brain [10]. Glutamate NMDA in astrocytes is the most popular receptor in the physiopathology of AD, and it interferes in neuronal-glial signaling [11,12]. The difference between neuronal and glial NMDA receptor signals in astrocytes provides a better understanding of the therapy's development in AD prevention and control.

In this work, we introduce the astrocyte's interaction with Aβ and τP and their toxic forms. We use the heterodimer model in the reaction kinetics to describe the interaction between amyloid-beta and tau proteins [13,14]. In the modified model, we introduce the clearance of toxic Aβ by the astrocytes, and the astrocytes follow the Allee type dynamics. Moreover, we formulate a network mathematical model to integrate the brain connectome data and examine the effect of the parameter involved in the Aβ clearance term. The AD status at the first treatment is also dependent on the AD progression. Therefore, we have also studied the solution depending on the initial conditions.

The organization of the rest of this paper is as follows. In Sect. 2, we describe the reaction-diffusion model and the network model. Simulation results are presented in Sect. 3 followed by conclusions in Sect. 4.

2   Models for AD

We consider $\Omega \subset \mathbb{R}^3$ is a spatial domain. For $\mathbf{x} \in \Omega$ and time $t \in \mathbb{R}^+$, we denote by $u = u(\mathbf{x}, t)$ and $v = v(\mathbf{x}, t)$, the concentrations of healthy Aβ and τP, respectively. Similarly, we denote by $\widetilde{u} = \widetilde{u}(\mathbf{x}, t)$ and $\widetilde{v} = \widetilde{v}(\mathbf{x}, t)$, the concentrations of toxic Aβ and τP, respectively. The evolution of concentrations of the four populations can then be given as follows [13,15]:

$$\frac{\partial u}{\partial t} = \nabla \cdot (\mathbf{D}_u \nabla u) + a_0 - a_1 u - a_2 u \widetilde{u}, \tag{1a}$$

$$\frac{\partial \widetilde{u}}{\partial t} = \nabla \cdot (\mathbf{D}_{\widetilde{u}} \nabla \widetilde{u}) - \widetilde{a}_1 \widetilde{u} + a_2 u \widetilde{u}, \tag{1b}$$

$$\frac{\partial v}{\partial t} = \nabla \cdot (\mathbf{D}_v \nabla v) + b_0 - b_1 v - b_2 v \widetilde{v} - b_3 \widetilde{u} v \widetilde{v}, \tag{1c}$$

$$\frac{\partial \widetilde{v}}{\partial t} = \nabla \cdot (\mathbf{D}_{\widetilde{v}} \nabla \widetilde{v}) - \widetilde{b}_1 \widetilde{v} + b_2 v \widetilde{v} + b_3 \widetilde{u} v \widetilde{v}, \tag{1d}$$

with non-negative initial conditions and no-flux boundary conditions. Here, the first two equations correspond to the usual heterodimer model for the healthy and toxic variants of the protein u and the last two equations are the same for v. The parameters a_0 and b_0 are the mean production rates of healthy proteins, $a_1, b_1, \widetilde{a}_1$ and $\widetilde{b}_1$ are the mean clearance rates of healthy and toxic proteins, and a_2 and b_2 represent the mean conversion rates of healthy proteins to toxic proteins. The parameter b_3 is the coupling between the two proteins $A\beta$ and τP. The first term in the right-hand side in all equations represent the diffusion tensors.

Astrocytes are present in the brain cells, and generally, they remain inactive till a sufficient accumulation of sticky protein (toxic amyloid-beta) in the brain. At the initial stage, brain cells send indications through which astrocytes start accumulations. After reaching a peak density, astrocytes damage the toxic amyloid-beta [16]. Here, we introduce such type of dynamics of astrocytes (by modifying $\widetilde{u}$), the above system (1) as follows:

$$\frac{\partial u}{\partial t} = \nabla \cdot (\mathbf{D}_u \nabla u) + a_0 - a_1 u - a_2 u \widetilde{u}, \tag{2a}$$

$$\frac{\partial \widetilde{u}}{\partial t} = \nabla \cdot (\mathbf{D}_{\widetilde{u}} \nabla \widetilde{u}) - \widetilde{a}_1 \widetilde{u} + a_2 u \widetilde{u} - \alpha w \widetilde{u}, \tag{2b}$$

$$\frac{\partial v}{\partial t} = \nabla \cdot (\mathbf{D}_v \nabla v) + b_0 - b_1 v - b_2 v \widetilde{v} - b_3 \widetilde{u} v \widetilde{v}, \tag{2c}$$

$$\frac{\partial \widetilde{v}}{\partial t} = \nabla \cdot (\mathbf{D}_{\widetilde{v}} \nabla \widetilde{v}) - \widetilde{b}_1 \widetilde{v} + b_2 v \widetilde{v} + b_3 \widetilde{u} v \widetilde{v}, \tag{2d}$$

$$\frac{\partial w}{\partial t} = \nabla \cdot (\mathbf{D}_w \nabla w) + w(c_0 - c_1 w)(w - \widetilde{u}). \tag{2e}$$

The second term in the right-hand side of the last equation of (2) represents the growth or decay of astrocytes. In the absence of toxic amyloid-beta, astrocytes increase their concentration and are saturated at c_0/c_1. If $w > \widetilde{u}$, then the term contributes to its growth and helps to decrease the toxic amyloid-beta levels. On the other hand, for $w < \widetilde{u}$, it drives the concentration of astrocytes to decay to 0. The last term in the right-hand side of the second equation of (2) represents the clearance of toxic $A\beta$ by astrocytes. This signifies that astrocytes can cure up to a certain level of toxic load in the brain, and after that, astrocytes can not decrease the toxic load, rather it helps in building the AD. The failing case does not contribute to the clearance of toxic $A\beta$. Hence, it supports increasing the toxic

Aβ concentration indirectly, and we call this as the astrocytes' activated stage. We analyze the role of astrocytes results with the help of numerical simulations.

2.1 Network Model for the Brain Connectome

Here, we formulate the network mathematical model corresponding to the modified model (2) for the brain connectome data [13,14,17]. Suppose, the brain data is represented by a graph $\mathcal{G}$ with V nodes and E edges. For the graph $\mathcal{G}$, we construct the adjacency matrix $\mathbf{A}$. This helps us to construct the Laplacian in the graph. We define the (i, j) $(i, j = 1, 2, 3, \ldots, V)$ element of the matrix $\mathbf{A}$ as

$$A_{ij} = \frac{n_{ij}}{l_{ij}^2},$$

where n_{ij} is the mean fiber number and l_{ij}^2 is the mean length squared between the nodes i and j. Now, we define the elements of the Laplacian matrix $\mathbf{L}$ as

$$L_{ij} = \rho(D_{ii} - A_{ij}), \quad i, j = 1, 2, 3, \ldots, V,$$

where ρ is the diffusion coefficient and $D_{ii} = \sum_{j=1}^{V} A_{ij}$ are the elements of the diagonal weighted-degree matrix. With the help of the Laplacian matrix, we derive a network mathematical model on the graph $\mathcal{G}$, whose dynamics at each node is given by

$$\frac{du_j}{dt} = -\sum_{k=1}^{V} L_{jk}^u u_k + a_0 - a_1 u_j - a_2 u_j \widetilde{u}_j, \tag{3a}$$

$$\frac{d\widetilde{u}_j}{dt} = -\sum_{k=1}^{V} L_{jk}^{\widetilde{u}} \widetilde{u}_k - \widetilde{a}_1 \widetilde{u}_j + a_2 u_j \widetilde{u}_j - \alpha w_j \widetilde{u}_j, \tag{3b}$$

$$\frac{dv_j}{dt} = -\sum_{k=1}^{V} L_{jk}^v v_k + b_0 - b_1 v_j - b_2 v_j \widetilde{v}_j - b_3 \widetilde{u}_j v_j \widetilde{v}_j, \tag{3c}$$

$$\frac{d\widetilde{v}_j}{dt} = -\sum_{k=1}^{V} L_{jk}^{\widetilde{v}} \widetilde{v}_k - \widetilde{b}_1 \widetilde{v}_j + b_2 v_j \widetilde{v}_j + b_3 \widetilde{u}_j v_j \widetilde{v}_j, \tag{3d}$$

$$\frac{dw_j}{dt} = -\sum_{k=1}^{V} L_{jk}^w w_k + w_j(c_0 - c_1 w_j)(w_j - \widetilde{u}_j), \tag{3e}$$

where u_j, $\widetilde{u}_j$, v_j, $\widetilde{v}_j$, and w_j denote the concentrations of Aβ, toxic Aβ, τP, toxic τP and astrocytes, respectively, at the node j. In the simulations, we have used non-negative initial conditions for all the variables.

2.2 Homogeneous System for the Network Model

The homogeneous system corresponding to the model (3) can be obtained by assuming the independence of spatial terms. This allows us to focus on the dynamics of AD propagations. Therefore, in this case, the system (3) reduces to

$$\frac{du}{dt} = a_0 - a_1 u - a_2 u\widetilde{u}, \tag{4a}$$

$$\frac{d\widetilde{u}}{dt} = -\widetilde{a}_1\widetilde{u} + a_2 u\widetilde{u} - \alpha w\widetilde{u}, \tag{4b}$$

$$\frac{dv}{dt} = b_0 - b_1 v - b_2 v\widetilde{v} - b_3\widetilde{u}v\widetilde{v}, \tag{4c}$$

$$\frac{d\widetilde{v}}{dt} = -\widetilde{b}_1\widetilde{v} + b_2 v\widetilde{v} + b_3\widetilde{u}v\widetilde{v}, \tag{4d}$$

$$\frac{dw}{dt} = w(c_0 - c_1 w)(w - \widetilde{u}), \tag{4e}$$

with non-negative initial conditions for all the variables. The model (4) provides us with a better us into the disease progression, as we demonstrate in the next section.

3   Results and Discussions

In this section, we analyze the models (3) and (4) numerically. We have adopted the parameter values for the amyloid-beta and tau protein interactions from [13]. Further, we have integrated the brain connectome data (freely available on https://braingraph.org [18]) in the network model. An in-house tool based on Matlab and C-language has been used for the simulations. We have used the SHARCNET (www.sharcnet.ca) high performance computational facilities to minimize the time in computations.

To date, AD treatment is still only symptomatic. As mentioned earlier, four drugs have been approved by the Food and Drug Administration (FDA) to treat AD. They help only in the symptoms' management, not to prevent any neuronal damage in the brain [2]. Due to the inefficacy of the drugs, researchers target the pathological features of the disease. Amyloid-beta and tau protein therapies remain the keys to mitigating symptoms from AD. According to the amyloid-beta hypothesis, accumulation of Aβ peptide, aggregation, and deposition in the form of Aβ plaques is the main reason for AD. Researchers studied different anti-amyloid therapies to slow down the AD progression in the brain.

Here, we focus on toxic Aβ and toxic τP clearances. For the toxic Aβ clearance, we increase the parameter values of α. On the other hand, we decrease the parameter values of b_3 in some parts of the brain connectome to account for the toxic τP clearance. We expect less toxic loads in the brain connectome in both the clearances, so that minor damage occur in the brain cells.

Depending on the parameter values, the homogeneous system (4) has many non-trivial equilibrium points. One may find those equilibrium points algebraically by solving the homogeneous system with taking the derivative terms as zero. We list two of them as $E_0 = (u_0, \widetilde{u}_0, v_0, \widetilde{v}_0, w_0) = (a_0/a_1, 0, b_0/b_1, 0, 0)$ and $E_1 = (u_1, \widetilde{u}_1, v_1, \widetilde{v}_1, w_1) = (a_0/a_1, 0, b_0/b_1, 0, c_0/c_1)$ and we find the other equilibrium points numerically later in this section. The equilibrium point E_1 is the healthy state as it has zero toxic loads with non-zero astrocytes' concentration. If the equilibrium component corresponding to astrocytes is larger than

the toxic amyloid beta and zero toxic loads of tau protein, then the equilibrium point is healthy; otherwise it is a disease state. Here, we analyze the disease development by varying some parameter values and different initial conditions, known as the initial stage of the treatment.

3.1   Focussing on the Dynamics of AD Propagation

In this section, we study the behaviour of the solutions of the system (4). We first consider the parameter α, the clearance by the astrocytes. All the fixed parameters are chosen from the Table 1 except the parameter α. These parameters are corresponding to the secondary tauopathy, studied earlier in [13–15] in the absence of astrocytes. For the primary tauopathy, amyloid-beta does not alter the onset of the regional pathology. We have considered the mixture of primary and secondary tauopathies parameters in the coming section. For $\alpha \in [0.1, 0.3]$, the total number of equilibrium points of the homogeneous system varies. But, for all the cases, two of them are locally asymptotically stable, and the rest are unstable.

Table 1. Fixed parameters values [13].

Parameter	Value	Parameter	Value	Parameter	Value	Parameter	Value
a_0	1.035	a_1	1.38	a_2	1.38	$\widetilde{a}_1$	0.828
b_0	0.69	b_1	1.38	b_2	1.035	$\widetilde{b}_1$	0.552
c_0	1.0	c_1	1.0	b_3	4.14	α	0.2

We fix $\alpha = 0.1$. The stable equilibrium points of the system (4) corresponding to $\alpha = 0.1$ are $(u_1^s, \widetilde{u}_1^s, v_1^s, \widetilde{v}_1^s, w_1^s) = (0.6, 0.25, 0.27, 0.58, 0)$ and $(u_2^s, \widetilde{u}_2^s, v_2^s, \widetilde{v}_2^s, w_2^s)$ $= (0.75, 0.007, 0.5, 0, 1)$. Both the stable equilibrium points represent the disease state due to the non-zero concentrations of toxic amyloid-beta and tau proteins. Depending on the initial conditions, the solution of the homogeneous system (4) converges to one of these stable equilibrium points. We plot their basin of attractions for different values of α in Fig. 1. In the simulations, we fix the initial conditions for u, v and $\widetilde{v}$ as a_0/a_1, b_0/b_1 and 0.05, respectively, and we vary $\widetilde{u}$ and w from 0.01 to 0.49 with all possible combinations. While it is possible to analyze the situation with a higher range in the initial conditions for $\widetilde{u}$ and w, but the mentioned range is sufficient for the goal of this paper. The solutions of the homogeneous system (4) with the initial condition region below the curve $\alpha = 0.1$ converge to $(u_1^s, \widetilde{u}_1^s, v_1^s, \widetilde{v}_1^s, w_1^s)$ while the solution for the upper region converges to the other stable equilibrium point.
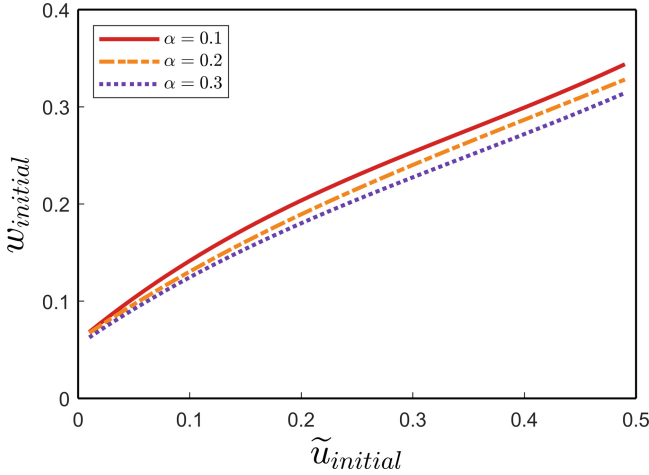
Fig. 1. Bifurcation curve which separates the basin of attractions of two stable equilibrium points for the homogeneous system with different values of α. (Color figure online)
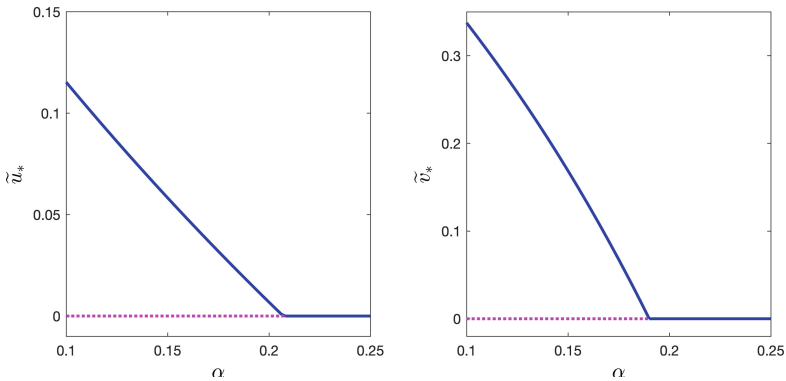
Fig. 2. Transcritical bifurcations of the equilibrium points of the homogeneous system (4). (Color figure online)

The equilibrium point $(u_1^s, \widetilde{u}_1^s, v_1^s, \widetilde{v}_1^s, w_1^s)$ has high concentrations of toxic amyloid-beta and toxic tau protein compared to the other stable equilibrium point. Hence, the solutions of the homogeneous system converge to the more disease state if the initial conditions are chosen from the lower region compared to the upper region, of the partition curve. With an increase in the parameter values α, the partition curves for the basin of attractions of the stable equilibrium points shift downwards. We observe that, for $\alpha = 0.3$, the solutions in the lower region converges to the disease state whereas the solution in the upper region converges to the healthy state. Therefore, the temporal model predicts that, with an increase in the damage rate of the toxic amyloid-beta by the astrocytes can

control the AD propagation in the brain. However, we verify this observation with the help of the network model (3) defined on the brain connectome for uniform and non-uniform parameter values in different brain regions.

Figure 2 depicts the two subcritical transcritical bifurcations occur at $\alpha = 0.192$ and $\alpha = 0.208$. Here, we have shown only the bifurcation of one stable equilibrium point, and the other stable equilibrium point does not exhibit any such type of bifurcation in the mentioned range. As we see, for $0.192 < \alpha < 0.208$, a non-zero concentration corresponding to the toxic Aβ exists. In this case, both the stable equilibrium points correspond to the disease state. For $\alpha > 0.208$, both the toxic concentrations become zero; hence, a healthy stable equilibrium occurs of the system (4).

3.2   AD Propagation in the Brain Connectome

Here, we integrate the brain connectome data and investigate the solution behaviours of the network model (3). The integrated brain connectome data consists of $V = 1015$ nodes and $E = 16,280$ edges. First, we set uniform parameter values [see Table 1] for all the regions in the brain connectome. We choose the diffusion coefficients for u, $\widetilde{u}$, v, $\widetilde{v}$ and w as 1.38, 0.138, 1.38, 0.014 and 1.38, respectively, and these are fixed throughout the paper (adopted from [13,14]). For all the nodes in the brain connectome, the chosen initial conditions for u, v and w are a_0/a_1, b_0/b_1 and 0.05, respectively.
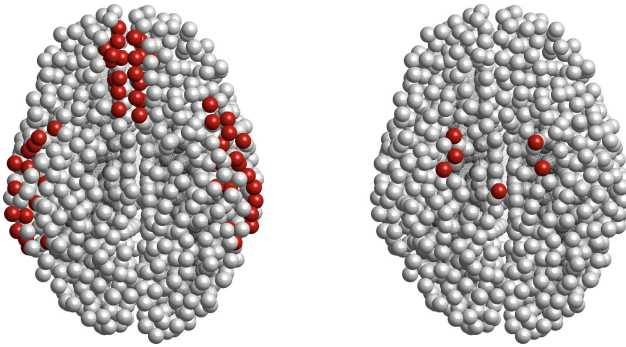
Fig. 3. Initial seeding sites for the toxic amyloid-beta and toxic tau proteins in the brain connectome. Red colors represent the non-zero concentration and gray colors represent the zero concentration. (Color figure online)

The initial seeding sites for the toxic amyloid-beta in the brain connectome are the temporobasal and frontomedial regions. On the other hand, the initial seeding sites for the toxic tau proteins are the locus coeruleus and transentorhinal associated regions [see Fig. 3]. The toxic loads for amyloid-beta and tau proteins

are 0.0375 and 0.0125, respectively, and these non-zero concentrations are the 5% of the healthy concentrations. We use these initial conditions for the rest of the paper.
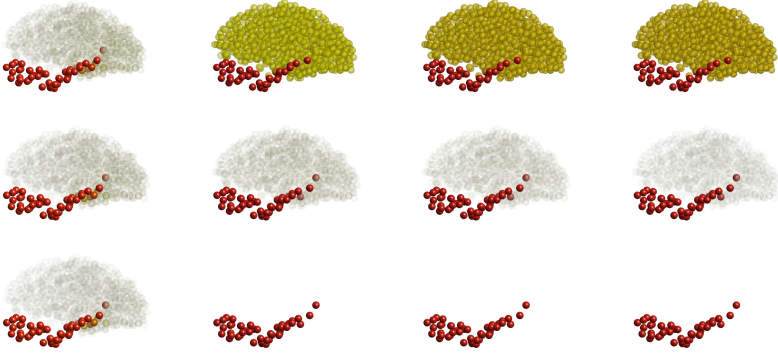
Fig. 4. Distributions of toxic amyloid-beta in the brain connectome for the network model at different time steps with different values of α. Top, middle and bottom panels are corresponding to $\alpha = 0.1, 0.2$ and 0.3. Left to right is corresponding to $t = 20, 50, 70$ and 120 for top to bottom panels. Red colors represent the high concentration, and gray colors represent the low concentration. (Color figure online)

We plot the simulation results for the network model corresponding to the toxic amyloid-beta in Fig. 4 for three different values of α. For $\alpha = 0.1$, we see the top panel in Fig. 4, some nodes converge to one steady-state, and the rest converge to the other. This bistability occurs in the network model due to two stable equilibrium points for the homogeneous system. With an increase in the parameter associated with the death of toxic amyloid-beta due to astrocytes, less toxic concentrations distribute in the brain connectome. Hence, minor damage occurs in the brain.

Now, we move forward to the case of non-uniform parameter values in the brain connectome. We use the general synthetic parameters values mentioned in Table 1 with some modifications in the parameters b_2 and b_3 in some regions of the brain connectome. The modified parameter values are mentioned in Tables 2 and 3. We observe that the solution corresponding to the toxic tau protein $\widetilde{v}$ converges to the different steady states at different nodes in the brain connectome [see Fig. 5]. The non-uniform distribution of 18F-AV-1451 radiotracer has been observed in [19].

Table 2. Modified b_3 parameter values in different regions [13].

Brain region and modified b_3 value			
Pars Opercularis	7.452	Rostral middle frontal gyrus	6.707
Superior frontal gyrus	7.452	Caudal middle frontal gyrus	7.452
Precentral gyrus	5.589	Postcentral gyrus	3.726
Lateral orbitofrontal cortex	6.486	Medial orbitofrontal cortex	6.486
Pars triangularis	5.520e-6	Rostral anterior cingulate	6.210e-6
Posterior cingulate cortex	3.45	Inferior temporal cortex	13.11
Middle temporal gyrus	11.04	Superior temporal sulcus	8.97
Superior temporal gyrus	8.28	Superior parietal lobule	12.42
Cuneus	13.8	Pericalcarine cortex	13.8
Inferior parietal lobule	11.73	Lateral occipital sulcus	15.18
Lingual gyrus	13.8	Fusiform gyrus	7.59
Parahippocampal gyrus	11.04	Temporal pole	1.104e-5

The non-zero steady-state corresponding to the toxic amyloid-beta does not depend on the parameters b_2 or b_3. Hence, the solution corresponding to toxic amyloid-beta remains uniform in most regions. An increase in the clearance rate of the toxic amyloid-beta by the astrocytes (i.e., α) decreases the toxic loads in most brain connectome regions. But, the toxic loads do not become zero for all the areas, i.e., the astrocytes can not clear the full toxic load. So, AD may start to propagate once we decrease the clearance rate, and it would be interesting to see in the future.

Table 3. Modified b_2 and b_3 parameter values in different brain regions [13].

Brain region	Entorhinal cortex	Pallidum	Locus coeruleus	Putamen	Precuneus
b_2	3.125	2.76	1.38	3.795	3.105
b_3	1.104e-5	2.76	1.38	3.795	3.105

We have not considered the clearance of toxic τP separately. Here, the parameter values of b_2 and b_3 are modified in most regions. This was an inherent clearance of toxic τP in the study.
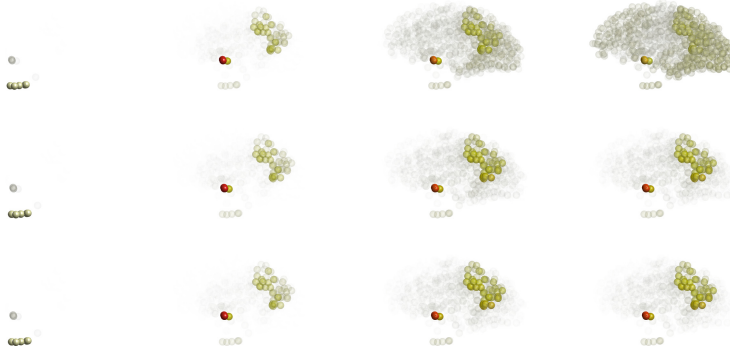
Fig. 5. Distributions of toxic tau protein in the brain connectome for the network model at different time steps with different values of α. Top, middle and bottom panels are corresponding to $\alpha = 0.1, 0.2$ and 0.3. Left to right is corresponding to $t = 20, 50, 70$ and 120 for top to bottom panels. Red colors represent the high concentration, and gray colors represent the low concentration. (Color figure online)

4   Conclusions

In this paper, we have introduced astrocytes' interactions with amyloid-beta and tau proteins and their toxic forms. We have considered a heterodimer model for the amyloid-beta and tau protein interactions [13]. Our modelling approach has allowed us to study the clearance of the toxic amyloid-beta by the astrocytes.

We have observed that the initial conditions play a crucial role in the resulting solutions. Further, with the help of brain connectome data applied to the network model, we have analyzed the AD progression in the brain. With an increase in the clearance rate of the toxic amyloid-beta by the astrocytes, the toxic load in the brain connectome is reduced significantly. This result is unaltered for uniform and non-uniform parameter values in different brain regions. Finally, a non-uniform toxic tau protein distribution in the brain connectome has been observed for different parameter values (related to τP) in distinct areas, confirming a good agreement obtained by the models developed here with experimental results (e.g., [19]). Therefore, the considered model suggests that the clearance of toxic amyloid-beta by astrocytes restricts the amyloid plaque distributions in the whole brain and keeps the brain safe from full-scale AD progression.

References

1. Alzheimer's Association: 2020 Alzheimer's disease facts and figures. Alzheimer's Dementia, pp. 391–460 (2020)
2. Vaz, M., Silvestre, S.: Alzheimer's disease: recent treatment strategies. Eur. J. Pharmacol. **887**, 173554 (2020)
3. Hardy, J.A., Higgins, G.A.: Alzheimer's disease: the amyloid cascade hypothesis. Science **256**, 184–186 (1992)
4. Götz, J., Halliday, G., Nisbet, R.M.: Molecular pathogenesis of the tauopathies. Annu. Rev. Pathol. **14**, 239–261 (2019)
5. Verkhratsky, A., et al.: Astrocytes in Alzheimer's disease. Neurother. Journal Am. Soc. Exp. Neurother. **7**, 399–412 (2010)
6. Trujillo-Estrada, L., et al.: Astrocytes: from the physiology to the disease. Curr. Alzheimer Res. **16**, 675–698 (2019)
7. Panatier, A., et al.: Glia-derived D-serine controls NMDA receptor activity and synaptic memory. Cell **125**, 775–784 (2006)
8. Ding, S., et al.: Enhanced astrocytic Ca2+ signals contribute to neuronal excitotoxicity after status epilepticus. J. Neurosci. **27**, 10674–10684 (2007)
9. González-Reyes, R.E., et al.: Involvement of astrocytes in Alzheimer's Disease from a neuroinflammatory and oxidative stress perspective. Front. Mol. Neurosci. **10**, 427 (2017)
10. Rodríguez-Arellano, J.J., et al.: Astrocytes in physiological aging and Alzheimer's disease. Neuroscience **323**, 170–182 (2016)
11. Parameshwaran, K., Dhanasekaran, M., Suppiramaniam, V.: Amyloid beta peptides and glutamatergic synaptic dysregulation. Exp. Neurol. **210**, 7–13 (2008)
12. Mota, S.I., Ferreira, I.L., Rego, A.C.: Dysfunctional synapse in Alzheimer's disease - a focus on NMDA receptors. Neuropharmacology **76**, 16–26 (2014)
13. Thompson, T.B., Chaggar, P., Kuhl, E., Goriely, A.: Protein-protein interactions in neurodegenerative diseases: a conspiracy theory. PLoS Comput. Biol. **16**, e1008267 (2020)
14. Pal, S., Melnik, R.: Nonlocal models in the analysis of brain neurodegenerative protein dynamics with application to Alzheimer's disease. Sci. Rep. **12**, 7328 (2022)
15. Pal, S., Melnik, R.: Pathology dynamics in healthy-toxic protein interaction and the multiscale analysis of neurodegenerative diseases. In: Paszynski, M., Kranzlmüller, D., Krzhizhanovskaya, V.V., Dongarra, J.J., Sloot, P.M.A. (eds.) ICCS 2021. LNCS, vol. 12746, pp. 528–540. Springer, Cham (2021). https://doi.org/10.1007/978-3-030-77977-1_42
16. Pekny, M., Michael, N.: Astrocyte activation and reactive gliosis. Glia **50**, 427–434 (2005)
17. Schäfer, A., et al.: Bayesian physics-based modeling of Tau propagation in Alzheimer's Disease. Front. Physiol. **12**, 702975 (2021)
18. Kerepesi, C., Szalkai, B., Varga, B., Grolmusz, V.: How to direct the edges of the connectomes: dynamics of the consensus connectomes and the development of the connections in the human brain. PLoS ONE **11**, e0158680 (2016)
19. Ossenkoppele, R., Rabinovici, G.D., Smith, R., Miller, B.L.: Discriminative Accuracy of [18F] flortaucipir positron emission tomography for Alzheimer Disease vs other neurodegenerative disorders. JAMA **320**, 1151–1162 (2018)

Effects of Random Inputs and Short-Term Synaptic Plasticity in a LIF Conductance Model for Working Memory Applications

Thi Kim Thoa Thieu[1] and Roderick Melnik[1,2(✉)]

[1] MS2Discovery Interdisciplinary Research Institute, Wilfrid Laurier University, 75 University Avenue West, Waterloo, ON N2L 3C5, Canada
{tthieu,rmelnik}@wlu.ca

[2] BCAM - Basque Center for Applied Mathematics, Bilbao, Spain

Abstract. Working memory (WM) has been intensively used to enable the temporary storing of information for processing purposes, playing an important role in the execution of various cognitive tasks. Recent studies have shown that information in WM is not only maintained through persistent recurrent activity but also can be stored in activity-silent states such as in short-term synaptic plasticity (STSP). Motivated by important applications of the STSP mechanisms in WM, the main focus of the present work is on the analysis of the effects of random inputs on a leaky integrate-and-fire (LIF) synaptic conductance neuron under STSP. Furthermore, the irregularity of spike trains can carry the information about previous stimulation in a neuron. A LIF conductance neuron with multiple inputs and coefficient of variation (CV) of the inter-spike-interval (ISI) can bring an output decoded neuron. Our numerical results show that an increase in the standard deviations in the random input current and the random refractory period can lead to an increased irregularity of spike trains of the output neuron.

Keywords: Working memory · Short-term synaptic plasticity · LIF · Langevin stochastic models · Spike time irregularity · Random input currents · Synaptic conductances · Neuron spiking activities · Uncertainty factors · Membrane and action potentials · Neuron refractory periods

1 Introduction

Human working memory (WM) is a crucial part of human brain studies. In general, the simplest assumption is that information in WM is maintained through persistent recurrent activity. However, recent studies have shown that information can be maintained without persistent firing, namely, information can be stored in activity-silent states. Short-term synaptic plasticity (STSP) is one of the candidate mechanisms for storing information in activity-silent states, STSP leads to rapid changes in the strength of connections between neurons that reflects new information being presented to the network system [1,2]. STSP

strongly affects the information processing in the nervous system. STSP is used to study by using the description of intracellular recordings of postsynaptic potentials or currents evoked by presynaptic spikes. However, STSP can also affect the statistics of postsynaptic spikes [3]. A comprehensive description of the combined effect of both short-term facilitation and depression on noise-induced memory degradation in one-dimensional continuous attractor models has been provided in [4]. STSP makes neurons sensitive to the distribution of presynaptic population firing rates [5]. On the other hand, the dynamics of firing rate and irregularity of single neurons are closely connected [6,7]. Using a computational model to study the formation of silent assemblies in a network of spiking neurons, the authors in [8] have found that even though the formed assemblies were silent in terms of mean firing rate, they had an increased coefficient of variation of inter-spike intervals.

In this paper, we consider the effects of random inputs to a LIF conductance neuron with STSP for applications in WM. In particular, we develop a LIF synaptic conductance model under a facilitation type of short-term synaptic plasticity dynamics. We study the effects of random external current inputs and random refractory periods on the spiking activities of neurons in a cell membrane potential setting of such LIF conductance neuron. Our analysis is carried out by considering a Langevin stochastic dynamic in a numerical setting for a cell membrane potential with random inputs. The numerical results demonstrate that the random inputs affect the spiking activity of the neuron. Under a weak excitatory input to the LIF conductance neuron together with the short-term facilitation, the memory can be reactivated. Furthermore, an increase in the standard deviations of Gaussian white noise inputs can lead to an increase in the irregularity of spike trains of the output neuron.

2   Synaptic Conductance Model Description

The simplest assumption in the modelling of synapses is that the synaptic weights are fixed. To get closer to the real situation, we will investigate synapses whose weights change in some input conditions. One of the candidates for such changes in the synaptic weights is the STSP. In general, STSP is a phenomenon in which synaptic efficacy changes over time in a way that reflects the history of presynaptic activity. There are two types of STP: Short-Term Depression (STD) and Short-Term Facilitation (STF), with opposite effects on synaptic efficacy, which have been experimentally observed.

The mathematical model of STSP is characterized by a limited pool of synaptic resources available for transmission R, which is the amount of available resources to the presynaptic neuron. For instance, the overall amount of synaptic vesicles at the presynaptic terminals. We know that the number of presynaptic resources changes in a dynamic fashion depending on the recent history of spikes. Specifically, at a presynaptic spike, the fraction u (the fraction of resources used each time a neuron fires) of the available pool to be utilized increases due to spike-induced calcium influx to the presynaptic terminal. Then, u is consumed

to increase the post-synaptic conductance. During each spike, u decays back to zero with time constant τf, while R recovers to 1 with time constant τd. We define the following dynamics of excitatory (subscript E) STSP (see, e.g., [2]):

$$\begin{cases} \frac{du_E}{dt} & = -\frac{U_0 - u_E}{\tau_f} + U_0(1 - u_E^-)\delta(1 - t_{sp}), \\ \frac{dR_E}{dt} & = \frac{1 - R_E}{\tau_d} - u_E^+ R_E^- \delta(1 - t_{sp}), \\ \frac{dg_E(t)}{dt} & = -\frac{g_E}{\tau_E} + \bar{g}_E u_E^+ R_E^- \delta(1 - t_{sp}), \end{cases} \quad (1)$$

where U_0 is a constant determining the increment of u, u_E^- and R_E^- represent the corresponding values before the arriving spike, while u_E^+ denotes the moment right after the spike. In (1), $\bar{g}_E$ represents the maximum excitatory conductance, while $g_E(t)$ is calculated for all spike times sp. Here, $\delta(\cdot)$ denotes the Dirac delta function, while τ_E is the given time constant. Moreover, the dynamics of inhibitory STSP can be described by replacing the subscript E with I in system (1).

STSP involves mechanisms for both facilitation of transmitter release, where synaptic strength increases with consecutive presynaptic spikes, and depression with synaptic strength decreases. The dynamics of u and R determine if the joint effect of uR is dominated by depression or facilitation. In the regime of $\tau_d \gg \tau_f$ and for large U_0, the synapse is STD-dominated due to an initial spike incurs a large drop in R that takes a long time to recover. In the regime of $\tau_d \ll \tau_f$ for small U_0, the synapse is STF-dominated since the synaptic efficacy is increased gradually by spikes. The kinetic dynamics of depressed and facilitated synapses observed in many cortical areas have been successfully reproduced by using such STSP phenomenological model. In this work, we consider a LIF synaptic conductance model with STSP for working memory. This model is sustained by calcium-mediated synaptic facilitation in the recurrent connections of neocortical networks. The facilitating transmission is displayed by all excitatory-to-excitatory connections in the system. Moreover the amount of available resources (R_E such that $0 \leq R_E \leq 1$) and the utilization parameter $u_E(x)$ modulate the synaptic efficacy. Such factors define the fraction of resources used by each spike, reflecting the residual calcium level. During a spike, the amount of $u_E R_E$ is used to produce the postsynaptic current, thus R_E reduces. This process is known as neurotransmitter depletion [1]. See, e.g., Figs. 1 and 2 for (STF) changes represented for firing rates of the presynaptic spike train. The amplitude synaptic conductance g changes with every incoming spike until it reaches its stationary state, and the ratio of the synaptic conductance corresponding to the 1st and 10th spikes changes as a function of the presynaptic firing rate in the STF case. In Fig. 2, we observe that the small fluctuations are visible in the data presented for the conductance corresponding to the 10th spike and the conductance ratio of the synaptic conductance corresponding to the 1st and 10th spikes. Such small fluctuations come from the fact that total synaptic resources are finite and recover in a finite time. Hence, at high frequency inputs, synaptic resources are rapidly neglected at a higher rate than their recovery. After the first few spikes, only a small number of synaptic resources are left. Therefore, the steady-state synaptic conductance at high frequency inputs decreases.
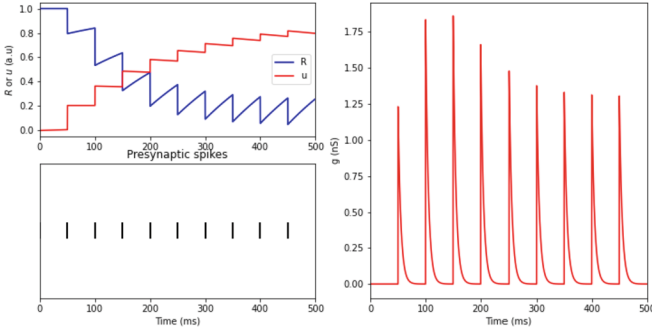
Fig. 1. Short-term synaptic facilitation (STF) changes for firing rates $r_i = r_e = 20$ of the presynaptic spike train and the amplitude synaptic conductance g changes with every incoming spike until it reaches its stationary state. (Color figure online)
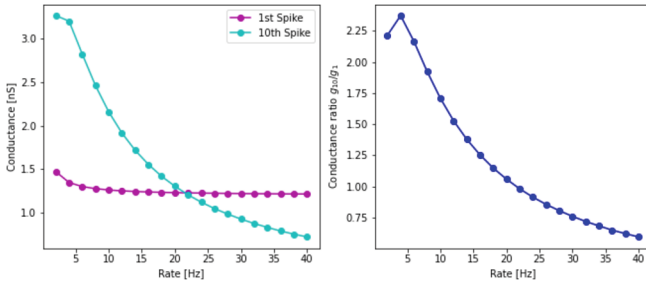
Fig. 2. The ratio of the synaptic conductance corresponding to the first and 10th spikes as a function of the presynaptic firing rate in the STF case. (Color figure online)

2.1 LIF Synaptic Conductance Dynamics

In this section, we consider a model of synaptic conductance dynamics under the STSP presented in (1). In particular, neurons receive myriad excitatory and inhibitory synaptic inputs at dendrites. To understand better the mechanisms underlying neuronal computation, we investigate the dynamics of STSP in a LIF neuron via electrophysiological recording techniques.

In general, the synaptic input in vivo is characterized by the combination of excitatory neurotransmitters. Such excitatory neurotransmitters depolarize the cell and drive it towards a spike threshold. Inhibitory neurotransmitters hyperpolarize it, driving it away from the spike threshold. These factors cause specific ion channels on the postsynaptic neuron to open. Then, the neuron's conductance changes. Therefore, the current will flow in or out of the cell (see, e.g., [9,10]). This synaptic conductance process can be modelled by assuming that the presynaptic neuron's spiking activity produces transient changes in the postsynaptic neuron's conductance $(g_{\mathrm{syn}}(t))$. Such conductance transients $(g_{\mathrm{syn}}(t))$ can be generated by using the system (1).

Using Ohm's law allows us to convert conductance changes to the current as follows:

$$I_{\text{syn}}(t) = g_{\text{syn}}(t)(V(t) - E_{\text{syn}}), \tag{2}$$

where E_{syn} denotes the direction of current flow of the excitatory (E_E) or inhibitory (E_I) of the synapse.

The total synaptic input current I_{syn} is the combination of both excitatory and inhibitory inputs. Suppose the total excitatory and inhibitory conductances received at time t are $g_E(t)$ and $g_I(t)$, and their corresponding reversal potentials are E_E and E_I, respectively. The total synaptic current can be defined as (see, e.g., [11]):

$$I_{\text{syn}}(V(t), t) = -g_E(t)(V - E_E) - g_I(t)(V - E_I). \tag{3}$$

Next, we note that the corresponding membrane potential dynamics of the LIF neuron under synaptic current can be described as follow (see, e.g., [11])

$$\tau_m \frac{d}{dt} V_m(t) = -(V_m(t) - E_L) - \frac{g_E(t)}{g_L}(V_m(t) - E_E) - \frac{g_I(t)}{g_L}(V_m(t) - E_I) + \frac{I_{\text{inj}}}{g_L}, \tag{4}$$

where V_m is the membrane potential, I_{inj} is the external input current, τ_m is the membrane time constant, g_L denotes the leak conductance, while E_L is the leak potential.

We consider a random synaptic input by introducing the following random input current (additive noise) $I_{\text{Inj}} = \mu_{\text{Inj}} + \sigma_{\text{Inj}}\eta(t)$ (pA), where η is the Gaussian white noise with mean μ_{Inj} and standard deviation σ_{Inj}.

By considering such Gaussian white noise input currents, the Eq. (4) can be considered as the following Langevin stochastic equation (see, e.g., [12]):

$$\tau_m \frac{d}{dt} V_m(t) = -(V_m(t) - E_L) - \frac{g_E(t)}{g_L}(V_m(t) - E_E) - \frac{g_I(t)}{g_L}(V_m(t) - E_I)$$
$$+ \frac{1}{g_L}(\mu_{\text{Inj}} + \sigma_{\text{Inj}}\eta(t)) \quad \text{if } V(t) \leq V_{\text{th}}. \tag{5}$$

In this paper we investigate the effects of random refractory periods. We define the random refractory periods t_{ref} with $t_{\text{ref}} = \mu_{\text{ref}} + \sigma_{\text{ref}}\mathcal{N}$, where $\mathcal{N}$ is the normal distribution.

In our model, to approximate the stochastic neuronal firings, we use the simplest input spikes with the Poisson process [10,13]. The input spikes will be added to the system via the quantity $\delta(t - t_{sp})$ in (1). We assume that the input spikes are given when every input spike arrives independently of other spikes. For designing a spike generator of spike train, we define the probability of firing a spike within a short interval (see, e.g. [14]) $P(1 \text{ spike during } \Delta t) = r_j \Delta t$, where $j = e, i$ with r_e, r_i representing the instantaneous excitatory and inhibitory firing rates, respectively. A Poisson spike train is generated by first subdividing time

into a group of short intervals through small time steps Δt. At each time step, we define a random variable x_{rand} with uniform distribution over the range between 0 and 1. Then, we compare this quantity with the probability of firing a spike, which reads:

$$\begin{cases} r_j \Delta t > x_{\mathrm{rand}}, & \text{generate a spike,} \\ r_j \Delta t \leq x_{\mathrm{rand}}, & \text{no spike is generated.} \end{cases} \tag{6}$$

2.2   Firing Rate and Spike Time Irregularity

In general, the irregularity of spike trains can carry information about previous stimulation in a neuron. A LIF conductance neuron with multiple inputs and coefficient of variation (CV) of the inter-spike-interval (ISI) can bring an output decoded neuron. In particular, we have found that the increase of σ_{Inj} and σ_{ref} can lead to an increase in the irregularity of the spike trains (see also [8]).

Spike regularity can be calculated as the following coefficient of variation of the inter-spike-interval (see, e.g., [8]):

$$CV_{\mathrm{ISI}} = \frac{\sigma_{\mathrm{ISI}}}{\mu_{\mathrm{ISI}}},$$

where σ_{ISI} is the standard deviation and μ_{ISI} is the mean of the ISI of an individual neuron.

In the next section, we plot and analyze the output firing rate as a function of Gaussian white noise mean or direct current value, known as the input-output transfer function of the neuron.

3   Numerical Results for the LIF Synaptic Conductance Model

In this subsection, we take a single pyramidal neuron at the dendrite and study how the neuron behaves under STF dynamics and when it is bombarded with both excitatory and inhibitory spike trains (see, e.g., [1,2,11]).

In what follows, the simulations have been carried out by a modification of the numerical method provided in the open source framework at https://github.com/ (see W2D3 Biological Neuron Models in the Neuromatch Academy directory).

In the simulations, we choose the parameter set as follows: $E_E = 70$ (mV), $E_L = -60$ (mV), $E_I = -10$ (mV), $V_{\mathrm{th}} = -55$ (mV), $V_{\mathrm{reset}} = -70$ (mV), $\Delta t = 0.1$, $\tau_m = 10$ (ms), $r_e = 20$, $r_i = 20$, $n_E = 20$ spikes, $n_I = 80$ spikes, $\bar{g}_E = 1.2 \times 4$ (nS), $\bar{g}_I = 1.6 \times 4$ (nS), $\tau_E = 5$ (ms), $\tau_I = 100$ (ms), $U_{0E} = U_{0I} = 0.2$, $\tau_{\mathrm{dE}} = \tau_{\mathrm{dI}} = 200$ (ms), $\tau_{\mathrm{fE}} = \tau_{\mathrm{fI}} = 1500$ (ms) . Here, n_E and n_I represent the number of excitatory and inhibitory presynaptic spike trains, respectively. These parameters have also been used in for dynamic clamp experiments and we take them for our model validation. In this section, we use the excitatory and

inhibitory conductances provided in Fig. 2 for all of our simulations. Further, we use the experimental data provided in [2] and [11] for our model validation.

The main numerical results of our analysis here are shown in Figs. 3, 4, 5, 6, 7, 8, 9, 10 and 11, where we have plotted the time evolution of the membrane potential calculated based on model (4), the input-output transfer function as well as the spike regularity profile of the neuron. We investigate the effects of random inputs on a LIF neuron under synaptic conductance dynamics and a facilitation type of short-term synaptic plasticity dynamics. By using a Poissonian spike input, we observe that the random external current and random refractory period influence the spiking activity of a neuron in the cell membrane potential. Our simulations demonstrate that as long as the synapses remain facilitated, the memory can be reactivated by presenting a weak excitatory input to the LIF conductance system, even though the neural activity is at the spontaneous level. Furthermore, the presence of random input current impacts the spiking activities of the system.
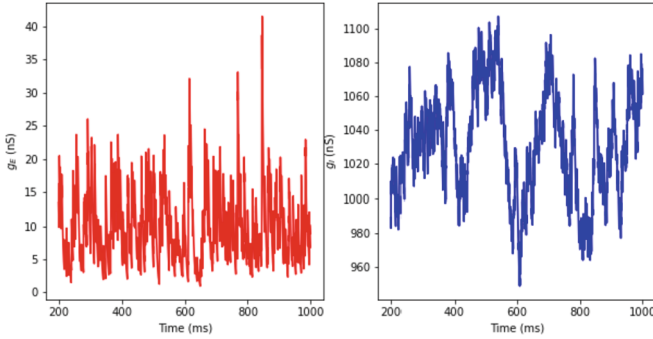
Fig. 3. Left: Excitatory conductances profile. Right: Inhibitory conductances profile. (Color figure online)

In particular, in Fig. 4, we have plotted the Gaussian white noise current profile, the time evolution of the membrane potential $V(t)$ with Gaussian white noise input current and direct input current ($I_{\text{inj}} = I_{\text{dc}} = 200$ (pA)). In the case with Gaussian white noise input current in the second row of Fig. 4, the neuron does not reach its threshold for a long time from 1 to nearly 1000 (ms). There are only the two spikes that come over the threshold. However, in the bottom row of Fig. 4, with the direct input current, we observe that the neuron fires a spike within an interval of about 20 (ms) (see, e.g., [1]). It is clear that the memory can be reactivated under a weak excitatory input to the LIF conductance system ($n_E = 20$ and $n_I = 80$ spikes). The presence of Gaussian white noise in the system increases the distance between each spike and decreases the spiking activity of the neuron compared with the case of direct input current.
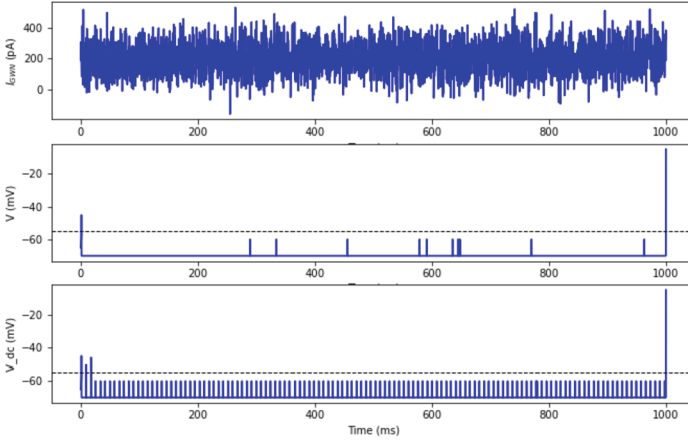
Fig. 4. Top row: Gaussian white noise current profile. Middle row: Time evolution of membrane potential $V(t)$ with Gaussian white noise current. Bottom row: Time evolution of membrane potential $V(t)$ with direct input. (Color figure online)

In Fig. 5, by increasing the values of $\tau_{dE} = \tau_{dI} = 1400$ (ms), we observe that the spiking activity of the neuron increases in both two cases: Gaussian white noise input and direct input currents. In the second row of Fig. 5, the spikes of the neuron increase compared to the cases presented in Fig. 4. Specifically, in the third row of Fig. 5, almost all spikes reach their threshold after a time of 570 (ms) in the case of direct input current. In the second row of Fig. 5, the presence of the random input current in the system leads to an increase in the distance between spikes that decrease the spiking activity in the system.

In Fig. 6, we have plotted the spike count profile as a function of average injected current. With $\sigma_{Inj} = 1$ and $t_{ref} = 8$ (ms), we have 124 spikes for both cases: Gaussian white noise input and direct input currents. There is no difference in the spike count between the two cases.

In Fig. 7, we consider the random refractory period for the case with Gaussian white noise current, and the standard refractory period v for the case with the direct input current. We observe that the spike count dramatically reduces in the case of random input current and random refractory period compared to the cases in Fig. 6. It is clear that the random refractory period affects the spiking activity of the system.
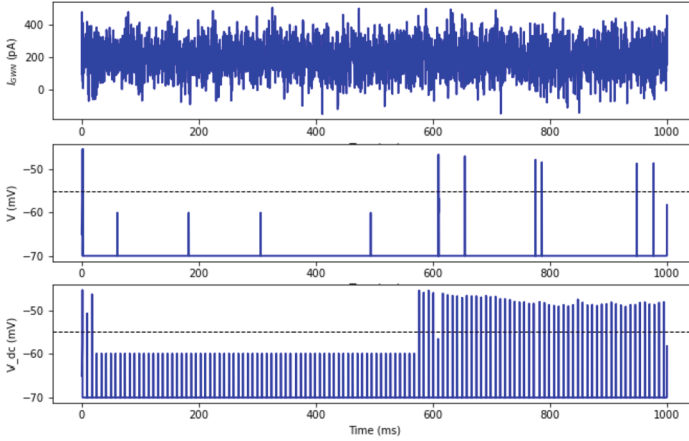
Fig. 5. Top row: Gaussian white noise current profile. Middle row: Time evolution of membrane potential $V(t)$ with Gaussian white noise current. Bottom row: Time evolution of membrane potential $V(t)$ with direct input. (Color figure online)
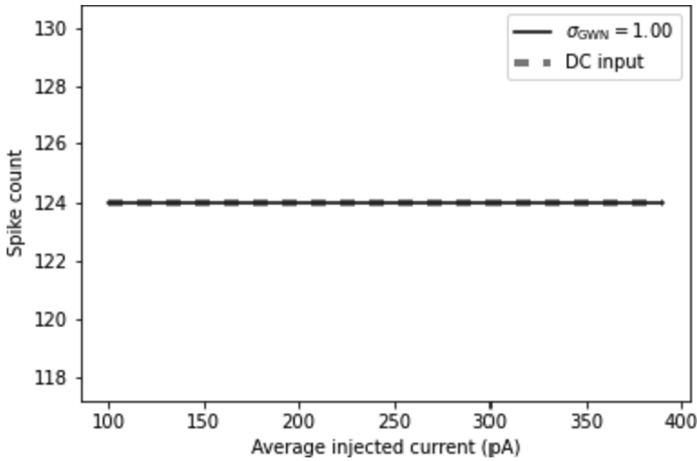
Fig. 6. The input-output transfer function of the neuron, output firing rate as a function of input mean. Parameters: direct input current $\sigma_{\text{Inj}} = 1$, $t_{\text{ref}} = 8$ (ms). (Color figure online)

In Fig. 8, using random refractory periods for both cases: Gaussian white noise and direct input current, we observe that the spikes decrease in both cases. In particular, the spike count remains the same (14 spikes) from $I_{\text{Inj}} = 100$ (pA) to $I_{\text{Inj}} = 380$ (pA). Then it reduces to 11 spikes in the case of Gaussian white noise input current. Similarly, from $I_{\text{Inj}} = 225$ (pA), the spike count decreases from 9 spikes to 6 spikes also in the case of direct input current. This effect is caused by the presence of a random refractory period in the system.
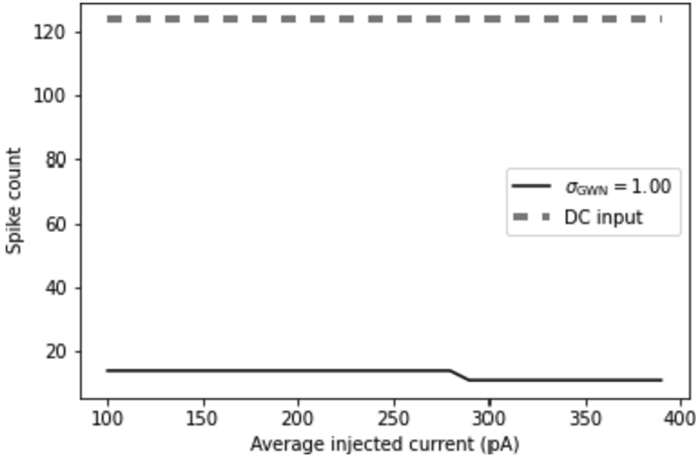
Fig. 7. The input-output transfer function of the neuron, output firing rate as a function of input mean. Parameters: $\sigma_{\mathrm{Inj}} = 1$, $\mu_{\mathrm{ref}} = 8$, $\sigma_{\mathrm{ref}} = 1$, $t_{\mathrm{ref}} = 8$ (ms) for direct input current. (Color figure online)
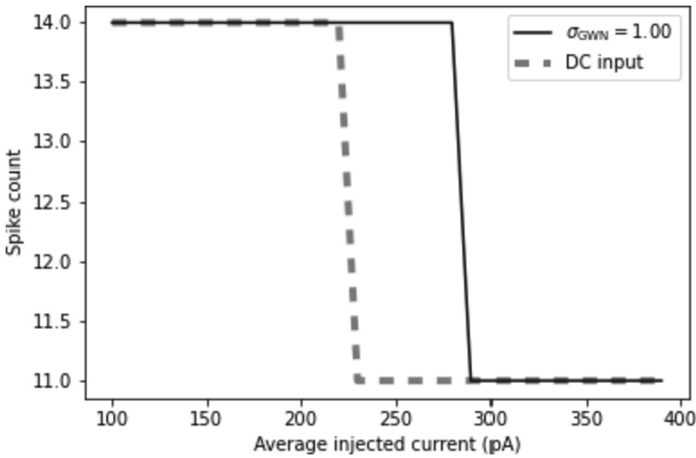
Fig. 8. The input-output transfer function of the neuron, output firing rate as a function of input mean. Parameters: $\sigma_{\mathrm{Inj}} = 1$, $\mu_{\mathrm{ref}} = 8$, $\sigma_{\mathrm{ref}} = 1$. (Color figure online)

In Fig. 9, we look at the corresponding spike irregularity profile of the spike count in Fig. 8. We see that there is not much change in the coefficient of variation of the inter-spike-interval with values around 0.9. There is a slight decrease of the spike irregularity from the average injected current with values from 280 (pA) to 400 (pA).
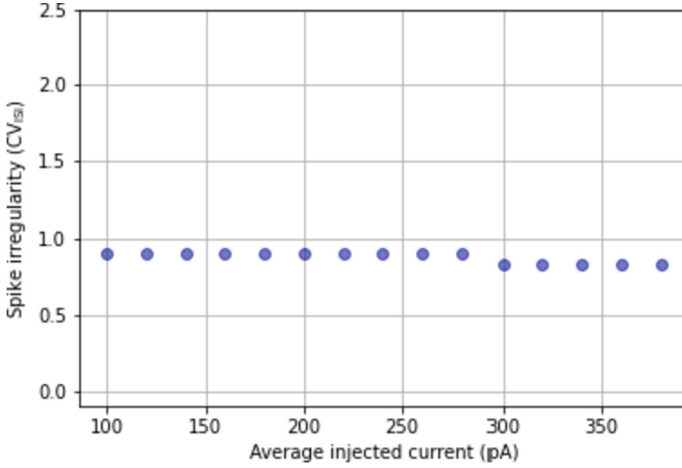
Fig. 9. Spike irregularity profile in the case with direct current. Parameters: $\sigma_{\text{Inj}} = 1$, $\mu_{\text{ref}} = 8$, $\sigma_{\text{ref}} = 1$. (Color figure online)
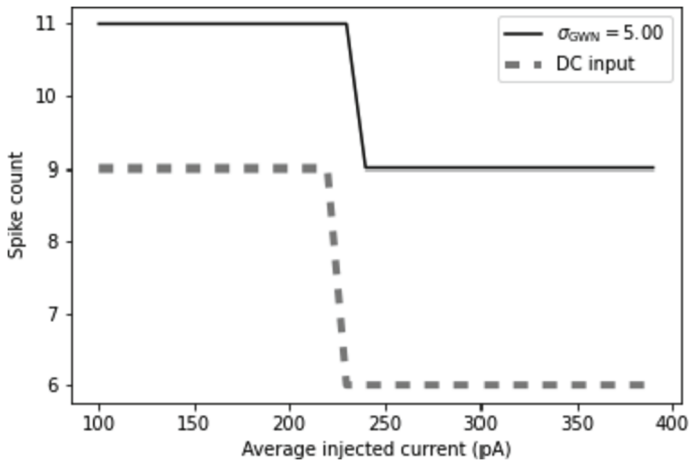
Fig. 10. The input-output transfer function of the neuron, output firing rate as a function of input mean. Parameters: $\sigma_{\text{Inj}} = 5$, $\mu_{\text{ref}} = 8$, $\sigma_{\text{ref}} = 2.5$. (Color figure online)

In Fig. 10, we consider the same cases as in Fig. 8. The only difference is that we increase the values of the standard deviations of the random input current and random refractory period to $\sigma_{\text{Inj}} = 5$ and $\sigma_{\text{ref}} = 2.5$. We observe that the spikes decrease when the average injected current increases. This is visible also in the corresponding spike irregularity profile in Fig. 11, at the average injected current of value 250 (pA), we see a decrease of the spike irregularity coefficient CV_{ISI} from 1.7 to 1.1. It is clear that even with a decrease in the spike irregularity the
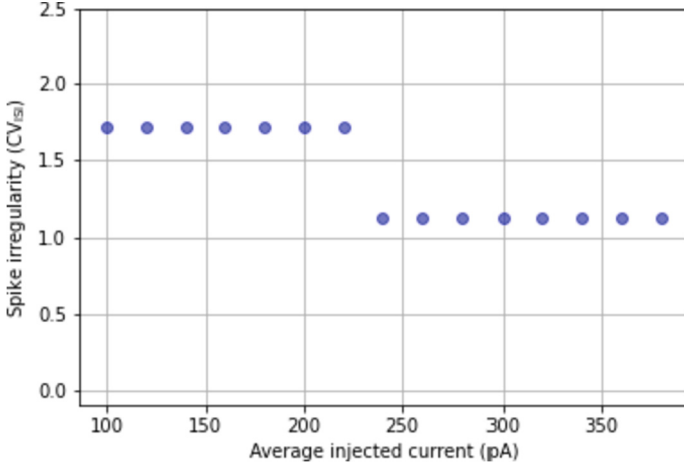
Fig. 11. Spike irregularity profile in the case with Gaussian white noise current. Parameters: $\sigma_{\mathrm{Inj}} = 5$, $\mu_{\mathrm{ref}} = 8$, $\sigma_{\mathrm{ref}} = 2.5$. (Color figure online)

coefficient $\mathrm{CV}_{\mathrm{ISI}}$, in this case, is still larger than in the cases presented in Fig. 9. This is due to the fact that when we increase the mean of the Gaussian white noise, at some point, the effective input means are above the spike threshold and then the neuron operates in the so-called mean-driven regime. Hence, as the input is sufficiently high, the neuron is charged up to the spike threshold and then it is reset. This essentially gives an almost regular spiking.

Additionally, we notice that the presence of a random refractory period increases the distance of the time interval between two nearest neighbor spikes as well as decreases the spiking activity in the system. However, with a weak excitatory input to the LIF conductance system together with the STF, the spiking activity of the neuron still occurs and the memory can be reactivated. Under suitable values of average injected current as well as the values of random input current and random refractory period, the irregularity of spike trains increases. This effect leads to an improvement in the carrying of information about previous stimulation in the neuron.

4   Conclusions

We have proposed and described a LIF synaptic conductance model with random inputs. Using the description based on the Langevin stochastic dynamics together with the STSP, we have analyzed the effects of noise in a cell membrane potential. In particular, we have provided details of the model along with representative numerical examples. Our computational experiments have demonstrated that the presence of random input current and random refractory period decrease the spiking activity of the neuron in the system. The memory can be reactivated under a weak excitatory input to the LIF conductance system with

STF. When the values of average injected current are large enough together with suitable values of the standard deviations of Gaussian white noise inputs, the irregularity of spike trains increases. A better understanding of uncertainty factors in LIF conductance neurons with STSP dynamics would contribute to further progress and model developments for WM in human brain studies.

References

1. Mongillo, G., Barak, O., Tsodyks, M.: Synaptic theory of working memory. Science **319**(5869), 1543–1546 (2008)
2. Pals, M., Stewart, T.C., Akyürek, E.G., Borst, J.P.: A functional spiking-neuron model of activity-silent working memory in humans based on calcium-mediated short-term synaptic plasticity. PLoS Comput. Biol. **16**(6), e1007936 (2020)
3. Ghanbari, A., Malyshev, A., Volgushev, M., Stevenson, I.H.: Estimating short-term synaptic plasticity from pre- and postsynaptic spiking. PLoS Comput. Biol. **13**(9), e1005738 (2017)
4. Seeholzer, A., Deger, M., Gerstner, W.: Stability of working memory in continuous attractor networks under the control of short-term plasticity. PLoS Comput. Biol. **15**(4), e1006928 (2019)
5. Tauffer, L., Kumar, A.: Short-term synaptic plasticity makes neurons sensitive to the distribution of presynaptic population firing rates. eNeuro **8**(2) (2019). ENEURO.0297-20.2021
6. Hamaguchi, K., Riehle, A., Brunel, N.: Estimating network parameters from combined dynamics of firing rate and irregularity of single neurons. J. Neurophysiol. **105**, 487–500 (2021)
7. Fitz, H., Uhlmann, M., van den Broek, D., Duarte, R., Hagoort, P., Petersson, K.M.: Neuronal spike-rate adaptation supports working memory in language processing. PNAS **117**(34), 20881–20889 (2020)
8. Gallinaro, J.V., Clopath, C.: Memories in a network with excitatory and inhibitory plasticity are encoded in the spiking irregularity. PLoS Comput. Biol. **17**(11), e1009593 (2021)
9. Gerstner, W., Kistler, W.M., Naud, R., Paninski, L.: Neuronal Dynamics: From Single Neurons to Networks and Models of Cognition. Cambridge University Press (2014)
10. Thieu, T.K.T., Melnik, R.: Effects of noise on leaky integrate-and-fire neuron models for neuromorphic computing applications (2022). https://doi.org/10.48550/arXiv.2202.09482
11. Li, S., Liu, N., Yao, L., Zhang, X., Zhou, D., Cai, D.: Determination of effective synaptic conductances using somatic voltage clamp. PLoS Comput. Biol. **15**(3), e1006871 (2019)
12. Roberts, J.A., Friston, K.J., Breakspear, M.: Clinical applications of stochastic dynamic models of the brain, part i: a primer. Biol. Psychiatry Cogn. Neurosci. Neuroimaging **2**, 216–224 (2017)

13. Teka, W., Marinov, T.M., Santamaria, F.: Neuronal integration of synaptic input in the fluctuation-driven regime. J. Neurosci. **24**(10), 2345–2356 (2004)
14. Dayan, P., Abbott, L.F.: Theoretical Neuroscience. The MIT Press Cambridge, Massachusetts London, England (2005)

Biomedical Engineering

Thermal Effects of Manual Therapy in Low Back Pain: A Pilot Study

Andrea Rosales-Hernandez[1], Daniela Vigueras-Becerril[1],
Arely G. Morales-Hernandez[1], Sandra M. Chavez-Monjaras[1],
Luis A. Morales-Hernandez[2], and Irving A. Cruz-Albarran[2(✉)]

[1] Physiotheraphy/Nursing Faculty, Autonomous University of Queretaro, Corregidora,
Queretaro, Mexico
{arely.morales,sandra.mariana.chavez}@uaq.mx

[2] Mechatronics/Engineering Faculty, Campus San Juan del Rio, Autonomous University of
Queretaro, San Juan del Rio, Queretaro, Mexico
{lamorales,icruz}@hspdigital.org

Abstract. The aim of this pilot study is to know the thermal impact that manual therapy has on the body temperature of the lower back and abdominal region in subjects with low back pain. It was conducted on ten patients, five of them diagnosed with low back pain and five without it. The intervention protocol was based on Richelli's instrumentalized manual therapy, it was carried out by a certified physical therapist, one session per week, for two weeks. Infrared Thermography was used to show the effects of this study. The regions of interest considered for the thermal analysis were the rectus abdominis, the obliques, the quadratus lumbar and the lumbar spine. The temperature difference between post and pre-intervention in patients with low back pain was higher in the first week, maintaining differences greater than 0.78, while in the second week the maximum difference was 0.52 in the lumbar area. As a result, the instrumentalized manual intervention technique tends to stabilize the temperature of the muscles, managing to favor the subjects with low back pain because this specific group achieved greater temperature stability in the intervened muscle groups. Infrared Thermography proved to be a useful tool for monitoring physiotherapeutic treatments.

Keywords: Thermography · Manual therapy · Low back pain · Abdominal muscles · Lumbar Region

1 Introduction

Low back pain is a symptom experienced by people of all ages, from childhood to adulthood (Hartvigsen et al. 2018). Its prevalence ranges from 4.2% for subjects between 24 and 39 years old to 19.6% for subjects between 20 and 59 years old (Barbari et al. 2020). For this reason, it has been attributed as one of the main causes of disability in many countries, as well as being among the main worldwide (Taylor and Bishop

2019). It has been documented that it has an extremely high recurrence, presenting within 12 months after his recovery (Da Silva et al. 2019). In general, the factors that are associated with low back pain are age, education, hypertension, smoking, work, ergonomic factors, marital status, among others (Frascareli et al. 2020).

Nowadays, for the treatment of low back pain, in addition to traditional medicine, procedures based on complementary or alternative medicine have also been adopted (Hartvigsen et al. 2018), for which pharmacological treatments are no longer used. Among the several non-pharmacological interventions that could found are acupuncture (Comachio et al. 2020; Godley and Smith 2020; Volpato et al. 2019), heat therapy (Freiwald et al. 2018; Laosee et al. 2020; Leemans et al. 2020), electrical stimulation (Leemans et al. 2020), exercise programs (Kim and Kim 2018; Pakbaz et al. 2019; Shariat et al. 2019; Sipaviciene and Kliziene 2019; Washif et al. 2019) and manual therapies (Toomey et al. 2020; Cashin et al. 2020; Toprak Celenay et al. 2019; Zafereo et al. 2018; Louw et al. 2016).

The objective of manual therapy is to produce therapeutic effects through the movement of the hands, creating different strokes, sometimes with the help of different instruments (Portillo-Soto et al. 2014), with which it is possible to produce an increase in oxygenation and nutrient intake to muscle tissue (Charles et al. 2019). For the diagnosis of low back pain, there are different methods, for example, radiography, computed tomography (CT), and magnetic resonance imaging (MRI) (Chou et al. 2011). However, these techniques are expensive and expose patients to unnecessary harm (Samuel et al. 2016). The temperature has been shown to be a natural indicator of abnormalities (Lahiri et al. 2012), for example, as a marker of a probable muscle injury (De Andrade Fernandes et al. 2017). Therefore, Infrared Thermography (IRT) is an indispensable tool for the detection of patients with musculoskeletal injuries (Marcon Alfieri et al. 2019; Hegmann et al. 2019; Morales Ríos 2011; Gutiérrez-Vargas 2017). Among the advantages of IRT are the following: it is a non-invasive, low-cost, light-invariant tool that can work in dark environments (Cruz-Albarran et al. 2018). For these reasons, research focused on low back pain and thermography has been carried out, for example, Marcon Alfieri et al. (2019) associated lumbar surface temperature and tolerance to pressure pain, obtained that the higher the perception of pain, the lower the pain tolerance and the higher the lumbar temperature. Polidori et al. (2018) used IRT as a diagnostic and recovery monitoring tool after osteopathic manipulative treatment. Samuel et al. (2016) carried out a study to find out if IRT could be used as an indicator of the result of interferential and laser treatment of low back pain, concluding that it can be used objectively. As can be seen, studies have been carried out that make use of IRT for the diagnosis and measurement of the results of different treatments for low back pain, however, a study that shows the thermal effects that manual therapy has on the structures involved in low back pain has not been carried out. Therefore, it is accurate to have a study that shows the impact of manual therapy in subjects with low back pain on body temperature, measured through IRT.

In the present work, a pilot study of the impact that manual therapy has on the body temperature of the lumbar and abdominal areas is shown. The protocol followed was Richelli's instrumentalized manual therapy. This therapy is applied both in the lumbar area and in the abdominal area. Therefore, the regions of interest (ROIs) that were

analyzed were, for the lumbar area, the lumbar squares (right and left), and for the abdominal area, the rectus abdominis, and the obliques (right and left).

2   Material and Methods

The general proposed methodology to carry out this exploratory study is shown in Fig. 1. The first stage consisted of the subjects, the space conditioning where the study was carried out, and the technological equipment used (FLIR A310 thermographic camera, Personal Computer (PC), FLUKE-975 air quality meter, and FLUKE 61 infrared thermometer). Subsequently, the first image was taken before the intervention. Then the application of manual therapy was carried out. Once this was finished, the final thermographic image was taken. Finally, the data analysis was done.
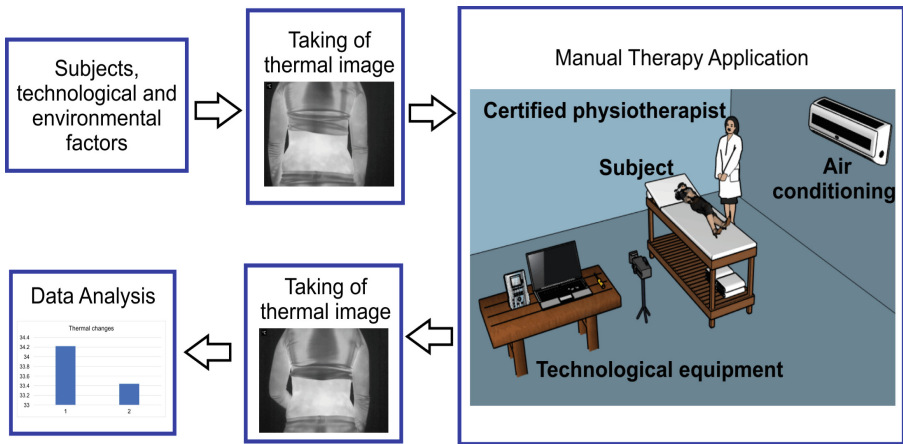
Fig. 1. General proposed methodology.

2.1   Subjects

The study was conducted on 10 female participants, with a mean age of 23.9 (standard deviation of 3.14) and an average body mass index of 22.83 (standard deviation of 2.38). Five of them were part of the control group, that is, they did not have any alteration of lumbar pain sensation and the other five were part of the intervention group (with lumbar pain sensation). Specific tests were performed on the recruited subjects to corroborate or rule out alteration in the sensation of low back pain of radicular origin. The following tests were performed: Lasegue test, Adam's test, Cram test, Gillette test, Sacroiliitis test, Oswestry questionnaire, Bragard's sign, and the measurement of the ranges of motion (ROM) was performed. The inclusion criteria to participate in the study were: voluntary participation, not using lotions, creams, cosmetics, and deodorants, not shaving the area of analysis, not having taken stimulant drinks, not smoking at least two hours before, not engaging in physical activity one hour before the study. The exclusion criteria dictated

by the protocol were: pregnancy, post-surgery, altered sensation in the lumbar region with radiating pain, fibromyalgia, rheumatoid arthritis during the initial or acute phases, medical contraindication, infectious skin diseases, carcinomas, and raynaud disease. The invitation to participate was open, the subjects interested in being part of the study were explained what the study consisted of, and those who decided to participate signed the informed consent letter. The study was conducted under the Declaration of Helsinki, in addition to complying with the guidelines of the Nuremberg Code. The research was approved by the ethics committee of the Faculty of Nursing of the Autonomous University of Querétaro.

2.2   Technological and Environmental Factors

The study was carried out in a 5×4-m room. A FLIR A310 camera was used for the taking of thermographic images, with a resolution of 320×240 pixels and a sensitivity of 0.05 °C to 30 °C, which works in the spectral range of 7.5 to 13 μm. For a correct measurement, it is necessary to have controlled environmental conditions, therefore, an air conditioner (Mini Split) was used, with which the ambient temperature was maintained at 20 ± 2 °C, with a relative humidity of 45–60% (measured with a FLUKE 975 air quality meter). To obtain the apparent reflected temperature of the subjects, a FLUKE 61 infrared thermometer was used.

2.3   Taking of Thermal Images

For the acquisition of thermographic images, the camera was positioned 1.2 m from the subject under study, the height was adjusted according to the height of each subject. First, the parameters of the camera were adjusted, that is, the ambient temperature, the reflected apparent temperature, and the relative humidity. Subsequently, 2 thermographic images were taken, a posterior thermogram for the lumbar area and an anterior thermogram for the abdominal area. This process was carried out by each subject before the application of manual therapy and after it.

2.4   Manual Therapy Application

Richelli's Instrumentalized Manual Therapy was used for this work. This technique is carried out with 2 tools called Pain Reliever and 3DThumb. The first is made up of foot, head, body, and hook; and the second by foot, head, body, and arm. Each shape, curve, and part of the tools are used to make specific passes over certain areas of the human body. The instruments are made of polyethylene 500, colored blue.

The intervention process was carried out by a physiotherapist previously certified in the instrumentalized manual technique. The intervention was carried out according to the next treatment, established by Richelli and Rodríguez (n.d.):

Lumbar Muscles

Paravertebral.

- Shallow and deep longitudinal strokes
- Shallow and deep longitudinal strokes with 3D foot
- Superficial and deep longitudinal lines (heterolateral)
- Hook without compression
- Hook with compression

Lumbar Square.

- Hooking with kneading
- Continuous deep pressure
- Shallow and deep longitudinal strokes with foot
- Shallow and deep longitudinal strokes with body

Abdominal Muscles

- Shallow and deep longitudinal strokes
- Shallow and deep cross lines
- Hook without compression
- Compression hook
- Hooking with kneading.

It was carried out by making 4 strokes, 3 with gentle pressure and one with deep pressure, on the lumbar squares (right and left), the rectus abdominis and the obliques (right and left). The intervention was carried out one day a week, for a period of two weeks.

An example of the longitudinal lines that were applied is shown in Fig. 2. Figure 2a shows the body of the Pain Reliever Tool on the lumbar fascia and Fig. 2b the foot of the 3D Thumb Tool on the lumbar fascia.

a)   b)
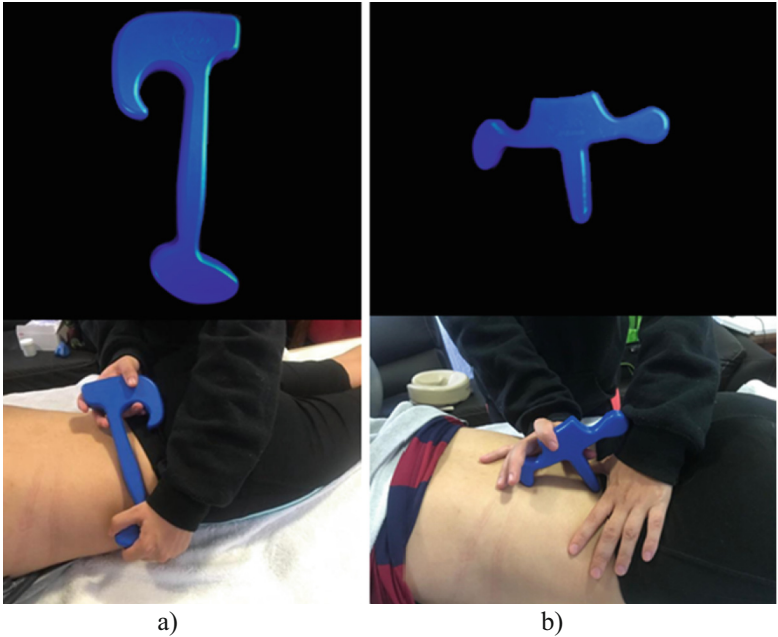
Fig. 2. Longitudinal strokes. a) With the body on the lumbar fascia (Pain Reliever Tool). b) With the foot on the lumbar fascia (3D Thumb Tool).

2.5 Data Analysis

For the temperature analysis, three ROIs were obtained for the abdomen area (Fig. 3a) and three for the lumbar area (Fig. 3b) (Cheung et al. 2020). To achieve this objective, free language software was developed, it allows obtaining statistical values (median, standard deviation, and variance) of the mentioned ROIs. Once these values were obtained for each subject, a database was created in SPSS software, version 22. Finally, a student

a)   b)
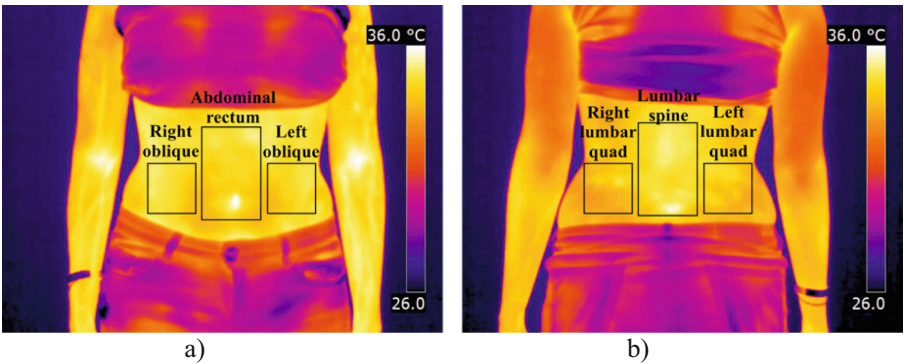
Fig. 3. Thermal ROIs. a) Abdominal region. b) Lumbar region.

t test (for both dependent and independent samples) and a Pearson correlation were performed.

3   Results

This section presents the results of the data analysis. Table 1 shows the ROI results of the thermal analysis carried out during the first and second sessions, in a pre-post way, both for subjects with low back pain and for subjects without it. Where M_pre represents the pre-intervention mean (in ℃) M_post, is the post-intervention mean (in °C), ΔT is the difference in temperature between pre and post (in °C) and ρ is the significance. The level of significance that was considered was 95% (Simon 1986). The cells shaded in red show the statistically significant values. For subjects with low back pain, a significant temperature decrease can be observed at week one in the right oblique and at week two in the lumbar spine. By analyzing the temperature increases in week one compared to week two, a significantly lower temperature decrease (ρ = 0.013) was obtained in the case of subjects with low back pain (ρ = 0.013) in week one (−1.76 °C), than in week two (−0.02 °C). On the other hand, for subjects without low back pain, there is a significant decrease in temperature in week one, both in the right and left oblique. With the analysis of the temperature increases between week one and two, a significantly lower

Table 1. Statistical values for subjects with and without low back pain.

With Low Back Pain							
	Week 1				Week 2		
ROI	M_{pre}	M_{post}	ΔT	**ρ**	M_{pre}	M_{post}	ΔT	**ρ**
Abdominal Rectum (AR)	34.22	33.44	-0.78	0.156	33.82	33.86	0.04	0.923
Left Oblique (LO)	34.64	33.80	-0.84	0.068	34.20	33.92	-0.28	0.449
Right Oblique (RO)	34.28	33.48	-0.80	0.037	34.00	34.00	0.00	1.000
Lumbar Spine (LS)	34.94	32.14	-2.80	0.317	34.52	34.00	-0.52	0.001
Left Lumbar Quad (LLQ)	34.34	31.64	-2.70	0.324	33.98	34.18	0.20	0.389
Right Lumbar Quad (RLQ)	34.30	31.62	-2.68	0.362	33.98	34.40	0.42	0.082
Without Low Back Pain							
	Week 1				Week 2		
ROI	M_{pre}	M_{post}	ΔT	ρ	M_{pre}	M_{post}	ΔT	ρ
Abdominal Rectum (AR)	34.14	32.78	-1.36	0.118	33.64	33.50	-0.14	0.750
Left Oblique (LO)	33.64	32.90	-0.74	0.020	33.74	33.62	-0.12	0.811
Right Oblique (RO)	33.62	33.04	-0.58	0.023	33.86	33.82	-0.04	0.928
Lumbar Spine (LS)	33.94	33.92	-0.02	0.902	33.28	34.08	0.80	0.090
Left Lumbar Quad (LLQ)	33.48	34.02	0.54	0.147	33.06	33.88	0.82	0.082
Right Lumbar Quad (RLQ)	33.36	33.66	0.30	0.270	32.90	33.64	0.74	0.106

temperature decrease ($\rho = 0.004$) was obtained in week one (-0.31 °C), compared to week 2 (0.34 °C).

Table 2 shows the results by ROI of the thermal analysis for independent samples carried out during the first and second sessions, in the form of subjects with low back pain vs subjects without low back pain, both for pre-intervention and for post-intervention Where M_w represents the mean of the subjects with low back pain (in °C), M_wo is the mean of subjects with low back pain (in °C), ΔT is the difference in temperature between both groups (in °C) and, ρ is the significance. The box marked in red shows the statistically significant value.

Table 2. Statistical values between subjects with low back pain and without low back pain (pre and post).

With Low Back Pain (w) vs Without Low Back Pain (wo) PRE							
	Week 1				Week 2		
ROI	M_w	M_{wo}	ΔT	ρ	M_w	M_{wo}	ΔT	ρ
Abdominal Rectum (AR)	34.22	34.14	-0.08	0.585	33.82	33.64	-0.18	0.556
Left Oblique (LO)	34.64	33.64	-1.00	0.572	34.20	33.74	-0.46	0.203
Right Oblique (RO)	34.28	33.62	-0.66	0.782	34.00	33.86	-0.14	0.327
Lumbar Spine (LS)	34.94	33.94	-1.00	0.269	34.52	33.28	-1.24	0.093
Left Lumbar Quad (LLQ)	34.34	33.48	-0.86	0.128	33.98	33.06	-0.92	0.218
Right Lumbar Quad (RLQ)	34.30	33.36	-0.94	0.283	33.98	32.90	-1.08	0.172
With Low Back Pain (w) vs Without Low Back Pain (wo) POST							
	Week 1				Week 2		
ROI	M_w	M_{wo}	ΔT	ρ	M_w	M_{wo}	ΔT	ρ
Abdominal Rectum (AR)	33.44	32.78	-0.66	0.309	33.86	33.50	-0.36	0.327
Left Oblique (LO)	33.80	32.90	-0.90	0.193	33.92	33.62	-0.30	0.678
Right Oblique (RO)	33.48	33.04	-0.44	0.418	34.00	33.82	-0.18	0.025
Lumbar Spine (LS)	32.14	33.92	1.78	0.106	34.66	34.08	-0.58	0.076
Left Lumbar Quad (LLQ)	31.64	34.02	2.38	0.102	34.18	33.88	-0.30	0.323
Right Lumbar Quad (RLQ)	31.62	33.66	2.04	0.094	34.44	33.64	-0.80	0.279

The results of the Pearson correlation between the different ROIs for the subjects with low back pain, both pre-intervention, and post-intervention, are shown in Table 3. Where the ROIs shaded in green correspond to the pre-intervention and the shaded in orange correspond to the post-intervention. The boxes shaded in yellow show the ROIs that have a significant positive correlation, where they mostly correspond to extremely high positive correlations. These results are only shown for week one because that was when the greatest impact of instrumentalized manual therapy was presented.

Table 3. Pearson's correlation and significance for subjects with low back pain.

		AR	LO	RO	LS	LLQ	RLQ	AR	LO	RO	LS	LLQ	RLQ
AR	Pearson	1											
	p												
LO	Pearson	.957	1										
	p	.011											
RO	Pearson	.894	.846	1									
	p	.041	.071										
LS	Pearson	.534	.742	.366	1								
	p	.354	.151	.545									
LLQ	Pearson	.560	.765	.394	.999	1							
	p	.326	.131	.512	.000								
RLQ	Pearson	.515	.705	.239	.958	.959	1						
	p	.375	.184	.699	.010	.010							
AR	Pearson	.520	.510	.443	.495	.471	.382	1					
	p	.369	.380	.455	.396	.424	.526						
LO	Pearson	.471	.380	.562	.165	.147	-.006	.898	1				
	p	.423	.528	.324	.791	.813	.992	.038					
RO	Pearson	.596	.456	.770	.008	.010	-.166	.687	.913	1			
	p	.289	.441	.128	.989	.987	.789	.200	.030				
LS	Pearson	.734	.511	.684	-.169	-.141	-.124	.227	.393	.633	1		
	p	.158	.379	.203	.785	.821	.843	.714	.513	.251			
LLQ	Pearson	.759	.541	.707	-.131	-.103	-.093	.274	.432	.660	.999	1	
	p	.136	.346	.182	.834	.869	.882	.655	.468	.225	.000		
RLQ	Pearson	.726	.501	.655	-.172	-.143	-.113	.219	.371	.604	.999	.997	1
	p	.165	.390	.230	.783	.818	.857	.724	.539	.281	.000	.000	

*. Correlation is significant at the 0.05 level (2-tailed).

**. Correlation is significant at the 0.01 level (2-tailed).

The results of the Pearson correlation between the different ROIs for the subjects without low back pain, both pre-intervention, and post-intervention, are shown in Table 4. The ROI's shaded in green correspond to the pre-intervention values and the shaded in orange correspond to post-intervention values. The boxes in yellow show the significant correlations between ROIs, whose value is extremely high, positive. Likewise, they only show up for week one.

A thermographic image shows the peripheral temperature obtained through the radiation produced by the human body. The visualization is done through color palettes, where each pixel is assigned a color, which represents a temperature, the upper limit shows the highest temperature and the lower limit the lowest temperature. Starting from the latter, as the color changes towards the top, the temperature increases. Some examples of the acquired thermographic images, both for subjects with low back pain and for subjects without low back pain, are presented in Fig. 4.

Table 4. Pearson's correlation and significance for subjects without low back pain.

		AR	LO	RO	LS	LLQ	RLQ	AR	LO	RO	LS	LLQ	RLQ
AR	Pearson	1											
	p												
LO	Pearson	.957*	1										
	p	.011											
RO	Pearson	.894*	.846	1									
	p	.041	.071										
LS	Pearson	.534	.742	.366	1								
	p	.354	.151	.545									
LLQ	Pearson	.560	.765	.394	.999**	1							
	p	.326	.131	.512	.000								
RLQ	Pearson	.515	.705	.239	.958*	.959**	1						
	p	.375	.184	.699	.010	.010							
AR	Pearson	.520	.510	.443	.495	.471	.382	1					
	p	.369	.380	.455	.396	.526							
LO	Pearson	.471	.380	.562	.165	.147	-.006	.898*	1				
	p	.423	.528	.324	.791	.813	.992	.038					
RO	Pearson	.596	.456	.770	.008	.010	-.166	.687	.913*	1			
	p	.289	.441	.128	.989	.987	.789	.200	.030				
LS	Pearson	.734	.511	.684	-.169	-.141	-.124	.227	.393	.633	1		
	p	.158	.379	.203	.785	.821	.843	.714	.513	.251			
LLQ	Pearson	.759	.541	.707	-.131	-.103	-.093	.274	.432	.660	.999**	1	
	p	.136	.346	.182	.834	.869	.882	.655	.468	.225	.000		
RLQ	Pearson	.726	.501	.655	-.172	-.143	-.113	.219	.371	.604	.999**	.997**	1
	p	.165	.390	.230	.783	.818	.857	.724	.539	.281	.000	.000	

*. Correlation is significant at the 0.05 level (2-tailed).

**. Correlation is significant at the 0.01 level (2-tailed).

		Pre - intervention		Post - intervention	
		Abdominal region	Lumbar region	Abdominal region	Lumbar region
With low back pain	Subject 1				
	Subject 2				
Without low back pain	Subject 1				
	Subject 2				

Fig. 4. Thermography images in subjects with and without low back pain, pre - intervention and post - intervention.

4 Discussion

The main objective was to know the thermal impact after the intervention through instrumentalized manual therapy in two groups, a control group (healthy subjects) and an experimental group (subjects with chronic low back pain). The temperature behavior for both study groups showed differences concerning the treated muscle area. Taking as a premise that the study in question looked for myofascial alterations and evaluated the thermal responses, it is important to clarify their pathophysiology. Recent research suggests that the pathophysiology and sequelae of myofascial trigger points begin with excessive stress or injury to muscle fibers (Paolini 2009). This results in a decrease in available oxygen and nutrients, which leads to muscle shortening, and ultimately an increase in metabolic demands. So far, it has been shown that, in the trunk and proximal parts of the body, the surface temperature is strongly influenced by internal organs, subcutaneous tissue and muscle activity, contraction-relaxation, which is the most important source of metabolic thermal increase, therefore pathological conditions such as muscle spasms or myofascial trigger points can become visible as regions of increased temperature (Chojnowski 2017). This is reflected in the data analysis shown in Table 3, where for week 1 pre-intervention, the mean temperature of the group with low back pain for all regions of interest is higher than the mean of the group without low back pain (values without statistical significance). On the other hand, it has been studied that the proposed intervention with instrumentalized manual therapy aims to increase the intake of oxygen and nutrients in muscle tissue, as mentioned above (Charles et al. 2019; Simons 2004). According to Simmons (2004), the autonomic responses derived from the intervention can modulate the increase in acetylcholine release and contribute to the positive feedback loop. This type of technique aims to reduce the pain caused by trigger points and produce significant hyperemia with histamine discharge within the tissues (Arranz Álvarez et al. 1999; Pennes 1948). Producing a pleasant response, relief, and relaxation, resulting in an increase in brain endorphin levels that causes the inhibition of substance P (pain neurotransmitter) which in turn inhibits T (transmitter) cells. When muscles are exercised or tissue is mobilized by instruments, an increase in heat develops in the muscle due to frictional forces imposed on the tissue and consequently increased metabolism. Increased blood flow to the muscle also contributes to increased heat to the area after exercise or manipulation. Because muscle is a relatively superficial tissue, surrounded by a layer of connective tissue, its temperature is usually between 32 °C and 33 °C, however, when blood flow to the exercised or manipulated muscle increases, this temperature approaches the central tissue temperature which is 37 °C (Ivanitsky et al. 2006; Pennes 1948). For both groups, in week 1 and taking pre-intervention, the right quadratus lumbar showed a decrease in temperature with significant values ($p = 0.037$; $p = 0.20$). This decrease can be attributed to muscle hyperactivity, which leads to mechanical compression of the blood vessels that supply the muscle, consequently reducing circulation and, in turn, skin temperature (Rodrigues-Bigaton et al. 2014). Unfortunately, a direct relationship between the intervention and the specific results for the right quadratus lumbar cannot be established. Likewise, the comparison between groups (Table 2) shows that the quadratus lumbar again decreases its mean temperature in week 2 post-intervention, the difference being the lowest, in comparison with the other results for this muscle.

On the other hand, Roy et al. (2010) studied the thermal changes after the intervention with manual spinal manipulation at the L5 level, the results showed an immediate increase in temperature and at 5 min after the manipulation. For this case, the authors attribute the heat transfer from the chiropractor's hand as a fundamental factor for the temperature variation in the immediate measurement. However, for this pilot test, an external instrument was used to prevent direct heat transfer by physical contact. For the consequent increase in temperature, a possible response of cytokines and other pro and anti-inflammatory mediators is discussed, as well as a neurological supraspinal control, a physiological cellular reaction of the blood vessels of the skin or deep tissue, or the immune systems. This leads to highlighting two important points in the conclusion of this study: 1) The tendency of the adjusted area to continue heating is probably a reflection of a positive inflammatory response that removes debris from the injured area through increased blood flow and 2) changes in surface temperature could be related to several factors, including axonal reflexes, the release of chronic muscle spasm, and normal tissue response to mechanical stimulation. It was observed that the difference in temperature between post and pre-intervention in patients with low back pain was higher in the first week, maintaining differences greater than 0.78, on the other hand, in the second week the maximum difference was in the lumbar area of 0.52, differences were managed in the other muscles less than 0.28, tending to the normality of the temperature of the treated muscles. The "law of the artery" (stated by Still AT) affirms that a properly vascularized tissue is considered healthy, and, on the contrary, when it does not receive the correct blood supply, the disturbance of this tissue occurs, referring to an injury or dysfunction neurovascular. Vertebral dysfunction causes a neurovascular alteration, and this, in turn, causes angiospasm and stasis or circulatory retention, thus producing an alteration in the anatomical elements located in the vascular territory, with ischemic pain and long-term tissue modifications (Almazán Campos 1998). The aforementioned is reflected in the results of Table 1 through the differences in temperature between week 1 post-intervention and week 2. This increase in blood flow is expected to return to normal within a couple of hours after surgery. Completion of instrumentalized manual therapy. However, when temperatures are still elevated 24 h after exercise or manual manipulation, it indicates that there is potential muscle damage. This muscle damage causes additional heat transfer from the muscle to the overlying skin, resulting in a thermographically detectable hot spot under the skin (Al-Nakhli et al. 2012).

However, despite the results, it is considered that future research will be necessary that includes microscopic indicators of the evaluated tissues, as well as a study with a larger sample.

5   Conclusion

The instrumentalized manual therapy intervention, both in healthy subjects and in subjects with low back pain, tends to stabilize the temperature of the muscles, managing to favor the subjects with low back pain, due to the fact that said group achieved greater temperature stability in the intervened muscle groups, since the averages of temperature for this group decreased, presenting statistically significant values in the decrease in temperature in week one in the right oblique and in week two in the lumbar spine. The

greatest impact of instrumentalized manual therapy was in week one. IRT proved to be a useful tool in the monitoring of physiotherapeutic treatments to determine predictable and specific objectives based on the patient's health condition.

Conflicts of Interest. The authors declare that there is no conflict of interest regarding the publication of this paper.

References

Almazán Campos, G.: Terapia manual y osteopatía. <<De la teoría a la técnica>>. Rev. Iberoam. Fisioter. Kinesiol. **1**(1), 47–59 (1998)

Al-Nakhli, H.H., Petrofsky, J.S., Laymon, M.S., Berk, L.S.: The use of thermal infra-red imaging to detect delayed onset muscle soreness. J. Vis. Exp. **59**, 1–11 (2012)

Arranz Álvarez, B.A., Tricás Moreno, J.M., Lucha López, M.O., Jiménez Lasanta, A.I., Domínguez Oliván, P., García, R.B.: Tratamiento del dolor. Rev. Iberoam. Fisioter. Kinesiol. **2**(3), 167–180 (1999)

Barbari, V., Storari, L., Ciuro, A., Testa, M.: Effectiveness of communicative and educative strategies in chronic low back pain patients: a systematic review. Patient Educ. Couns. **103**(5), 908–929 (2020)

Cashin, A.G., et al.: A systematic review highlights the need to improve the quality and applicability of trials of physical therapy interventions for low back pain. J. Clin. Epidemiol. **126**, 106–115 (2020)

Charles, D., Hudgins, T., Macnaughton, J., Newman, E., Tan, J., Wigger, M.: A systematic review of manual therapy techniques, dry cupping and dry needling in the reduction of myofascial pain and myofascial trigger points. J. Bodyw. Mov. Ther. **23**, 539–546 (2019)

Cheung, W.K., Cheung, J.P.Y., Lee, W.-N.: Role of ultrasound in low back pain: a review. Ultrasound Med. Biol. **46**(6), 1344–1358 (2020)

Chojnowski, M.: Infrared thermal imaging in connective tissue diseases. Reumatologia **55**(1), 38–43 (2017)

Chou, R., Qaseem, A., Owens, D.K., Shekelle, P.: Diagnostic imaging for low back pain: advice for high-value health care from the American college of physicians. Ann. Intern. Med. **154**, 181–189 (2011)

Comachio, J., Oliveira, C.C., Silva, I.F.R., Magalhães, M.O., Marques, A.P.: Effectiveness of manual and electrical acupuncture for chronic non-specific low back pain: a randomized controlled trial. J. Acupunct. Meridian Stud. **13**, 87–93 (2020)

Cruz-Albarran, I.A., Benitez-Rangel, J.P., Osornio-Rios, R.A., Dominguez-Trejo, B., Rodriguez-Medina, D.A., Morales-Hernandez, L.A.: A new approach to obtain a colour palette in thermographic images. Quant. Infrared Thermogr. J. **1**, 1–20 (2018)

Da Silva, T., et al.: Recurrence of low back pain is common: a prospective inception cohort study. J. Physiother. **65**, 159–165 (2019)

De Andrade, F.A., et al.: Effect of a professional soccer match in skin temperature of the lower limbs: a case study. J. Exerc. Rehab. **13**(3), 330–334 (2017)

Frascareli, T.P., dos Santos, C.V., Machado, N., Porfírio, G., Penteado, S., de Vitta, A.: Low back pain and some associated factors: is there any difference between genders? Braz. J. Phys. Ther. **24**(1), 79–87 (2020)

Freiwald, J., Hoppe, M.W., Beermann, W., Krajewski, J., Baumgart, C.: Effects of supplemental heart therapy in multimodal treated chronic low back pain patients on strength and flexibility. Clin. Biomech. **57**, 107–113 (2018)

Godley, E., Smith, M.A.: Efficacy of acupressure for chronic low back pain: a systematic review. Complement Ther. Clin. Pract. **39**, 101146 (2020)

Gutiérrez-Vargas, R., Ugalde-Ramírez, J.A., Rojas-Valverde, D., Salas-Cabrera, J., Rodríguez-Montero, A., Gutiérrez-Vargas, J.C.: La termografía infrarroja como herramienta efectiva para detectar áreas músculares dañadas después de correr una maratón. Rev. Fac. Med. **65**(4), 601–607 (2017)

Hartvigsen, J., et al.: What low back pain is and why we need to pay attention. The Lancet **391**, 2356–2367 (2018)

Hegmann, K.T., et al.: Diagnostic tests for low back disorders. J. Occup. Environ. Med. **61**(4), E155–E168 (2019)

Ivanitsky, G.R., Khizhnyak, E.P., Deev, A.A., Khizhnyak, L.N.: Thermal imaging in medicine: a comparative study of infrared systems operating in wavelength ranges of 3–5 and 8–12 μm as applied to diagnosis. Dokl. Biochem. Biophys. **407**(2), 258–262 (2006)

Kim, D.-H., Kim, T.-H.: Comparison of the effects of stability exercise and balance exercise on muscle activity in female patients with chronic low back pain. J. Exerc. Rehab. **14**(6), 1053–1058 (2018)

Lahiri, B.B., Bagavathiappan, S., Jayakumar, T., Philip, J.: Medical applications of infrared thermography: a review. Infrared. Phys. Technol. **55**, 221–235 (2012)

Laosee, O., Sritoomma, N., Wamontree, P., Rattanapan, C.: The effectiveness of traditional Thai massage versus massage with herbal compress among elderly patients with low back pain: a randomised controlled trial. Complement Ther. Med. **48**, 102253 (2020)

Leemans, L., et al.: Transcutaneous electrical nerve stimulation and heat to reduce pain in a chronic low back pain population: a randomized controlled clinical trial. Braz. J. Phys. Ther. **25**(1), 86–96 (2020)

Louw, A., et al.: The effect of manual therapy and neuroplasticity education on chronic low back pain: a randomized clinical trial. J. Man Manip Ther. **25**(5), 227–234 (2016)

Marcon Alfieri, F., Rodrigues Souto Lima, A., Rizo Battistella, L., Vargase Silva, N.C.O.: Superficial temperature and pain tolerance in patients with chronic low back pain. J. Bodyw. Mov. Ther. **23**(3), 583–587 (2019)

Morales Ríos, M., Medina Chacón, E., Carnevali Fernández, A., Orozco, G.E.: Termografía infrarroja y el estudio de riesgos de lesiones músculo esqueléticas. Ingen. Indust. **1**, 55–67 (2011)

Pakbaz, M., Hosseini, M.A., Aemmi, S.Z., Gholami, S.: Effectiveness of the backschool program on the low back pain and functional disability of Iranian nurse. J. Exerc. Rehab. **15**(1), 134–138 (2019)

Paolini, J.: Review of myofascial release as an effective massage therapy technique. Int. J. Athletic Therapy Train. **14**(5), 30–34 (2009)

Pennes, H.H.: Analysis of tissue and arterial blood temperatures in the resting human forearm. J. Appl. Physiol. **I**(2), 93–122 (1948)

Polidori, G., Kinne, M., Mereu, T., Beaumont, F., Kinne, M.: Medical infrared thermography in back pain osteopathic management. Complement Ther. Med. **39**, 19–23 (2018)

Portillo-Soto, A., Eberman, L.E., Demchak, T.J., Peebles, C.: Comparison of blood flow changes with soft tissue mobilization and massage therapy. J. Altern. Complement. Med. **20**(12), 932–936 (2014)

Richelli, S., Rodríguez, A.: Terapia Manual Instrumentalizada: Richelli's Pain Reliever y 3DThumb. International Board of Certification in Physiotherapy

Rodrigues-Bigaton, D., Dibai-Filho, A.V., Packer, A.C., Costa, A.C., de Castro, E.M.: Accuracy of two forms of infrared image analysis of the masticatory muscles in the diagnosis of myogenous temporomandibular disorder. J. Bodyw. Mov. Ther. **18**(1), 49–55 (2014)

Roy, R.A., Boucher, J.P., Comtois, A.S.: Paraspinal cutaneous temperature modification after spinal manipulation at L5. J Manipulat. Physiol. Ther. **33**(4), 308–314 (2010)

Samuel, S.R., Cg, S.K., Maiya, G.A.: Infrared thermal imaging as an outcome measure in low back pain. Res. J. Pharm. Biol. Chem. Sci. **7**(1), 1806–1810 (2016)

Shariat, A., et al.: The impact of modified exercise and relaxation therapy on chronic lower back pain in office workers: a randomized clinical trial. J. Exerc. Rehab. **15**(5), 703–708 (2019)

Simon, R.: Confidence intervals for reporting results of clinical trials. Ann. Intern. Med. **105**, 429–435 (1986)

Simons, D.G.: Review of enigmatic MTrPs as a common cause of enigmatic musculoskeletal pain and dysfunction. J Electromyogr Kinesiol **14**, 95–107 (2004)

Sipaviciene, S., Kliziene, I.: Effect of different exercise programs on non-specific chronic low back pain and disability in people who perform sedentary work. Clin. Biomech. **73**, 17–27 (2019)

Taylor, S., Bishop, A.: Patient and public beliefs about the role of imaging in the management of non-specific low back pain. Physiotherpy **107**, 224–233 (2019)

Toomey, D., Reid, D., White, S.: How manual therapy provided a gateway to a biopsychosocial management approach in an adult with chronic post-surgical low back pain: a case report. J. Man. Manip. Ther. **29**(2), 107–132 (2020)

Toprak Celenay, S., Ozer Kaya, D., Gunay, U.S.: Adding connective tissue manipulation to physiotherapy for chronic low back pain improves pain, mobility, and well-being: a randomized controlled trial. J. Exerc. Rehab. **15**(2), 308–315 (2019)

Volpato, M.P., et al.: Single cupping therapy session improves pain, sleep, and disability in patients with nonspecific chronic low back pain. J. Acupunct. Meridian Stud. 1–7 (2019)

Washif, J.A., Teichmann, J., Kok, L., Schmidtbleicher, D.: Using stochastic resonance and strength training as part of a rehabilitation programme for recurrent low back pain treatment: a case study. J. Exerc. Rehab. **15**(1), 139–147 (2019)

Zafereo, J., Wang-Price, S., Roddey, T., Brizzolara, K.: Regional manual therapy and motor control exercise for chronic low back pain: a randomized clinical trial. J. Man Manip. Ther. **26**(4), 193–202 (2018)

Bone Health Parameters in Young Adult Female Handball Players

Elie Maliha[1,2], Anthony Khawaja[1,3], Hechmi Toumi[4], Rachid Jennane[2], Antonio Pinti[5(✉)], and Rawad El Hage[1]

[1] Faculty of Arts and Sciences, Division of Education, Department of Physical Education, University of Balamand, Kelhat El-Koura, Lebanon
[2] IDP Laboratory, University of Orleans, UMR 7013, rue de Chartres, 45067 Orleans, France
[3] Faculty of Sport Sciences, Antonine University, Mejdlaya-Zgharta, Lebanon
[4] Translational Medicine Research Platform, PRIMMO, Regional Hospital of Orleans, 45007 Orleans, France
[5] Laboratoire LARSH DeVisu, Université Polytechnique Hauts-de-France (UPHF), Valenciennes, France
`antonio.pinti@uphf.fr`

Abstract. The main aim of this study was to compare bone health parameters (bone mineral content [BMC], bone mineral density [BMD], geometric indices of femoral neck [FN] strength (cross-sectional area [CSA], cross-sectional moment of inertia [CSMI], section modulus [Z], buckling ratio [BR] and strength index [SI]) and composite indices of FN strength (compression strength index [CSI], bending strength index [BSI], and impact strength index [ISI])) in young adult inactive women (n = 18) and young adult female handball players (n = 20). The participants of the study were 38 young adult women; their ages ranged from 20 to 32 years. Dual-energy X-ray absorptiometry (DXA) was used to evaluate body composition, BMC, BMD and geometric indices of FN strength. BMD measurements were completed for the whole body (WB), the lumbar spine (L1–L4), the total hip (TH) and the femoral neck (FN). Composite indices of femoral neck (FN) strength (CSI, BSI, and ISI) were calculated. Validated tests were used to evaluate maximal bench-press strength, maximal half-squat strength, maximal deadlift strength, vertical jump, horizontal jump, sprinting performance and maximal aerobic velocity. Validated questionnaires were used to evaluate sleep quality, daily protein and calcium intakes and physical activity level. Lean mass, WB BMC, WB BMD, L1–L4 BMD, TH BMD, FN BMD, CSMI, Z, physical activity level, daily protein intake, daily calcium intake, one-repetition maximum (1-RM) bench press, 1-RM half-squat and 1-RM deadlift were significantly higher in female handball players compared to inactive women. In conclusion, the present study suggests that handball practice is associated with better bone health parameters in young adult women.

Keywords: Peak bone mass · Team sports · Prevention of osteoporosis · Mechanical loading

1 Introduction

A frequent disorder in the bones is commonly known as osteoporosis, and its distinctive characteristics are low bone mineral density (BMD) as well as reduction signs of bone microarchitecture; these eventually result in a higher fracture risk [1]. As a matter of fact, 50% of women who are older than 50 years are affected by osteoporosis [2]. Bones, in general, reach 90% of their peak mass in people aged 20 years [2]. Therefore, a possible solution could be making sure there is maximal acquisition of bone mineral content (BMC) to compensate for the age-related bone loss [2]. There are a lot of effective preventive tools to prevent osteoporosis. One of the most effective strategies against osteoporosis is physical activity (PA) practice [1, 2]. In fact, PA ameliorates the acquisition of bone mass, expands the mass of muscles and eventually provides a balanced and healthy energy to the body [1, 2]. The best diagnosis known for osteoporosis is done by performing dual-energy X-ray absorptiometry (DXA) scan which measures BMD, and this is considered to be the reference standard for diagnosis. Although the leading indicator in measuring strength of bone is BMD [3, 4], it is only capable of explaining 50–70% of the strength of bone [5]. DXA can also measure geometric indices of bone resistance that can be evaluated in the area of the femoral neck (FN); these indices include cross-sectional area [CSA], cross-sectional moment of inertia [CSMI], section modulus [Z], buckling ratio [BR] and strength index [SI]) [6]. These indices are correlated with biomechanical bone strength and are predictors of osteoporotic fractures in the elderly [7–9]. FN width and bending strength are parameters which are also known to influence hip bone strength [10, 11]. Composite indices of FN strength (compression strength index [CSI], bending strength index [BSI], and impact strength index [ISI]) can be measured through hip scans taken by DXA, from which the risk of a future hip fracture can be predicted; this has been studied and confirmed by Karlamangla et al. [11]. FN size and body size merge with bone density due to these indices [12]. CSI, BSI, and ISI are a reflection of the FN's capacity to withstand axial compressive and bending forces and also its ability to retain the energy received from a collision [12]. Besides, in the elderly population, hip fracture risks as well as assessments of bone strength are improved by these indices [11–13]. Nowadays, the prevention of osteoporosis later in life is directly linked to the increase of peak BMD; therefore, it is essential to implement strategies which would increase peak BMD [14]. Several significant correlations have been demonstrated by several studies between BMD and the results of performances received through tests done physically for the evaluation of fitness components [15–18]. The findings of a study conducted on adult women [19] showed that vertical jump (VJ), maximum power (MP) of the lower limbs and maximal half-squat strength are positively associated with bone health parameters (BMD and geometric indices of hip bone strength). Likewise, another study which included young adults [20] demonstrated a positive association between VJ, MP and bone health parameters (BMD and geometric indices of hip bone strength). In addition, several studies conducted on young adults have found that PA levels are positive determinants of composite indices of the strength of the femoral neck [21–28]. Two previous studies conducted on prepubertal children [29] and adult women [30] are in conformity with these results. They have shown a positive association between the level of PA and CSI, BSI and ISI [29, 30]. Also, the findings of another recent study showed that inactive men aged more than 18 years in

comparison to their active peers have lower composite indices of FN strength [26]. A recent randomized controlled trial conducted on postmenopausal women [31] found a positive impact on bone turnover after a short period of practicing handball within a team and also positively affected the health of bone and postural balance; these positive effects were received even though the women did not have any previous training in handball. All this may help in preventing the risk of falling and having fractures. Another recent study conducted on adolescent females [2] showed that larger values of BMC were found in the women who had received more than one year of handball training compared to the women who had received training in soccer; both groups of women have higher values of BMC compared to women who were not engaged in sports. Similarly, a previous study has demonstrated that handball practice results in three positive effects; the first shows an improvement in physical fitness, the second shows an improvement in the lean mass and the bone mass, and the final one shows an improvement in the axial and appendicular BMD of young girls [15]. A recent study demonstrated that when young men practice handball, this results in a higher level of BMD and composite indices of femoral neck strength [32]. This study's aim is to verify whether such results are present in women. The aim of the present study was to compare bone health parameters (BMC, BMD, geometric indices of FN strength [CSA, CSMI, Z, BR, SI] and composite indices of FN strength [CSI, BSI and ISI]) in young adult inactive women and young female handball players. We hypothesized that young adult women who practice handball have greater bone health parameters compared to inactive females.

2 Material and Methods

2.1 Subjects and Study Design

The subjects who accepted to be in the present study are young adult women. They were 38 volunteers between the ages of 20 and 32. None of the subjects smoked, and none of them suffered from any considerable orthopedic problem or any disorder such as diabetes known to affect bone metabolism. Participants were excluded if they had a medical condition which could negatively affect bone metabolism. One example is a person who has a history of chronic disease involving a vital organ. Another criterion for exclusion is taking medications which could affect bone metabolism. In the current study, the participants were divided in two different groups: one group of 18 inactive women and another group of 20 female handball players. The practice of handball was the determinant for assigning the participants into the proper group. The women assigned to the inactive group were young adult inactive women. The definition of being inactive was "performing less than 150 min of moderate intensity PA or less than 75 min of vigorous-intensity PA or less than an equivalent combination of moderate- and vigorous-intensity activity a week accumulated across work, home, transport or discretionary domains" [33]. Moreover, the subjects in the inactive group had never regularly practiced a sport which was considered an impact sport any time during the years of adolescence or during childhood. The other group included the handball players who regularly participated in competitions nationally or regionally. Their training included at least 6 h every week (it sometimes went up to 9 h); they trained at their clubs between 4 and 6 times weekly; this training had been consistent for the past 5 years. All participants had very clear

knowledge of the study's aim and the advantages as well as the risks entailed in the participation. Therefore, the subjects were required to sign a consent form before participating in the study. The work described fits the requirements of the declaration of Helsinki (relating to experimenting on humans via the medical community which was proposed by the World Medical Association).

2.2 Anthropometrics

The participants were weighed through the use of a standard mechanical scale (which is precise to up to 100 g), and a standard stadiometer (which is precise to the nearest 0.5 cm) was used to measure their height. While they were being measured, the subjects were asked to wear very negligible clothing and to be barefoot. BMI was calculated as body weight divided by height squared (in kilogram per square meter) [34]. DXA (GE-Lunar iDXA, Madison, WI) assessed the composition of the body which included the lean mass (LM; Kg), and it also assessed FM (%, Kg).

2.3 Bone Measurements

Every participant was assessed by DXA (GE-Lunar iDXA, Madison, WI) to evaluate BMC (in grams) and BMD (in grams per square centimeter). DXA was used to complete the measurements of BMD for the whole body (WB), the lumbar spine (L1–L4), the total hip (TH), the FN and total radius BMD of the right side. Moreover, DXA calculated the geometric indices of FN strength (CSA, CSMI, Z, BR and SI). As Karlamangla et al. [11] had described, composite indices of FN strength (CSI, BSI and ISI) were calculated. The importance of the indices is that they are able to predict the possible risk of a hip fracture in an elderly individual [11–13]. CSI (CSI = [FN BMD * FN width/weight]) and BSI (BSI = [FN BMD * FN width^2]/[hip axis length * weight]) indicate the forces that the FN has to withstand in axial compressive and bending forces; however, ISI (ISI = [FN BMD * FN width * hip axis length]/[height * weight]) reveals how much energy FN can retain during impact from standing height [8–10]. All of the previously mentioned measurements done by DXA scans were performed by one certified technician (who holds a BS in medical imaging sciences) who used the same technique for all measurements. One DXA machine was used for the subjects of the study. At the laboratory, the variation coefficients were <1% for BMC and BMD. The variation coefficients for CSA and Z assessed through multiple measurements for 10 participants were <3%.

2.4 Procedures of Physical Performance Tests

An explanatory session was given to the participants of the study in order for them to understand and be familiar with the required equipment to be used while performing the physical tests as well as with the procedures of the tests; this was done before the procedures of evaluations began. When the tests began, they took place on 3 non-consecutive days. On the first day, the tests determined the time of the 20 m sprint and maximal aerobic velocity (MAV) using Luc-Léger shuttle-run test. On the second

day, vertical jump (VJ), horizontal jump (HJ), throwing velocity, force-velocity power (FV) on cycle ergometer, squat-jump (SJ) and counter movement jump (CMJ) were appropriately measured. On the third day, the tests determined one-repetition maximum (1-RM) of bench press, leg extension, leg curl, half-squat, and deadlift.

2.5   Sprinting Performance

The measurement of time of the sprint of 20 m took place with the use of 2 pairs of photoelectric cells which were linked to an electronic timer (BROWER Timing Systems). For proper measurement, pair number 1 was placed at the starting line (0 m), and pair number 2 was placed at the 20-m finish line. A specific warm-up was performed by the subjects of the study before beginning the evaluation process. The assessment was made up of a 20 m maximal sprint to be done four times; after every maximal sprint, the subjects passively rested for 3 consecutive minutes, and then they went for another sprint. Every sprint's time was recorded, and out of the four times, the best one was chosen to be evaluated as previously described [35].

2.6   Jumping Performance

The jump and reach Sargent test [35] was used to measure VJ height. A specific warm-up was performed by the participants before beginning the process of evaluation. The subjects of the study carried out a CMJ with free movements of the upper limbs. The number of times that the participants jumped was 3; they rested for 2 consecutive minutes between each jump, and the value of the highest jump was taken. The best recorded value of the VJ was taken for the calculation of the peak power of the lower limb; this was done by using the Lewis Formula [36]. HJ was also calculated. The HJ was performed by all subjects; they began standing up. They started the jump by swinging their upper limbs. For precision, the participants positioned their feet, which were in a shoulder-width position, immediately before the line which had been previously drawn. A metric tape was used to measure the length of the jump; it was done by measuring the distance from the take-off line to the nearest landing point, which is considered as where the heels touch. Three attempts were performed by every participant, and the attempt with the longest distance achieved was the one chosen. CMJ and squat-jump performances were measured using a Myotest device.

2.7   Maximal Strength Measurements

Every one of the subjects performed the half-squat, the bench press, the leg extension, the leg curl and the leg extension following the protocol established by the National Strength and Conditioning Association (NSCA) [37]. Direct evaluations of 1-RM have been done for all the above-mentioned exercises. Prior to the beginning of the test, the subjects warmed-up by following a specific standardized routine. If the participant was not able to perform the exercise in its full range of motion, then the test was stopped. While performing the half-squats, the participants had to squat till they reached a 90-degree knee angle; this had to be done in all the attempts.

2.8 Questionnaires

Sleep Quality
The quality of sleep and the sleep disturbances were evaluated by the Pittsburgh Sleep Quality Index (PSQI); this took place for 30 days. Scores were given for 7 "components" which are related to subjective sleep quality, sleep latency, sleep duration, habitual sleep efficiency, sleep disturbances, use of sleeping medication, and daytime dysfunction. The scores of the 7 components were added, and the sum received [38] was evaluated. If the PSQI score was high, it meant that sleep quality was bad; therefore, the lower the score, the better the sleep quality. Because a significant correlation has been shown between parameters [39–41] of bone health and sleep quality in several preceding studies, sleep quality was evaluated.

Daily Calcium and Protein Intakes
The participants had to fill authenticated questionnaires about their food frequency [42–44]; those were semi-quantitative, and they evaluated the DCI, which is daily calcium intake and DPI, which is daily protein intake. The assessment of the consumption of milk and dairy products such as yoghurt, cheese and chocolate, and other products such as eggs, meat, fish, cereals, bread, vegetables and fruits [42] was done through the DCI questionnaire. As for the DPI questionnaire, it gives the participants the opportunity for quantifying or assessing their food intake through which the large quantity of proteins is provided [44]. The participants did not require any help in filling in the DCI and DPI questionnaires. The participants in the study were not taking any supplements.

Physical Activity
For the evaluation of the PA duration for every week, the global PA questionnaire was used; it checks for the number of hours of PA per week [45]. 16 questions are included in the questionnaire; the answers result in knowing more about the PA being done while working, traveling and doing recreational activities. It provides details of intensity, duration and frequency of physical activities.

Statistical Analysis
Calculations were done to find the means and standard deviations for all clinical, physical performance and bone parameters. The Shapiro-Wilk test was used to evaluate for normality of all variables. The inactive group was compared to the handball group, but this was done after checking for Gaussian distribution. The use of unpaired t-tests was required in case Gaussian distribution was found. If not, Mann-Whitney U-tests were used. Pearson's Test was used to compute correlations. Statistical analyses were performed using the SigmaStat 3.1 Program (Jandel Corp., San Rafael, CA). A level of significance of $p < 0.05$ was used.

3   Results

3.1   Clinical Characteristics and Bone Data of the Study Population

Age, weight, BMI, FM, CSA, SI, CSI, BSI, ISI and PSQI were not significantly different between the 2 groups. LM, WB BMC, WB BMD, L1–L4 BMD, TH BMD, FN BMD, CSMI, Z, DPI and DCI were significantly higher in handball players compared to inactive women. Height, FM percentage and BR were significantly higher in inactive women compared to handball players (Table 1).

Table 1. Clinical characteristics and bone variables ofthe study population.

	Handball players (n = 20)	Controls (n = 18)	p-value
	Mean ± SD	Mean ± SD	
Age (years)	25.9 ± 3.7	24.2 ± 1.9	0.101
Weight (kg)	64.8 ± 9.4	67.6 ± 8.8	0.352
Height (cm)	**164.3 ± 5.3**	**168.2 ± 3.7**	**0.013**
BMI (kg/m^2)	24.0 ± 3.5	23.9 ± 3.1	0.902
Lean mass (Kg)	**38.990 ± 3.223**	**31.046 ± 2.457**	**<0.001**
Fat mass (Kg)	24.604 ± 5.629	25.858 ± 1.939	0.376
Fat mass (%)	**34.6 ± 3.3**	**38.4 ± 1.4**	**<0.001**
WB BMC (g)	**2358 ± 234**	**2183 ± 235**	**0.028**
WB BMD (g/cm^2)	**1.152 ± 0.084**	**1.054 ± 0.107**	**0.003**
L1-L4 BMD (g/cm^2)	**1.247 ± 0.106**	**1.098 ± 0.079**	**<0.001**
TH BMD (g/cm^2)	**1.064 ± 0.064**	**0.961 ± 0.021**	**<0.001**
FN BMD (g/cm^2)	**1.072 ± 0.101**	**0.942 ± 0.024**	**<0.001**
CSA (mm^2)	155 ± 16	149 ± 5	0.123
CSMI (mm^4)	**10.93 ± 1.07**	**9.85 ± 1.37**	**0.010**
Z (mm^3)	**649 ± 71**	**590 ± 35**	**0.003**
BR	**2.61 ± 0.33**	**3.97 ± 0.94**	**<0.001**
SI	1.84 ± 0.34	1.68 ± 0.07	0.068
CSI (g/kg-m)	5.14 ± 0.82	5.06 ± 0.55	0.722
BSI (g/kg-m)	1.58 ± 0.26	1.66 ± 0.16	0.255
ISI (g/kg-m)	0.312 ± 0.046	0.328 ± 0.035	0.237
1-RM bench press (kg)	**28.750 ± 3.837**	**12.944 ± 1.474**	**<0.001**
1-RM leg extension (kg)	**37.750 ± 3.864**	**13.333 ± 1.534**	**<0.001**
1-RM leg curl (kg)	**28.100 ± 4.303**	**8.944 ± 1.830**	**<0.001**

(*continued*)

Table 1. (*continued*)

	Handball players (n = 20)	Controls (n = 18)	p-value
	Mean ± SD	Mean ± SD	
1-RM squat (kg)	**59.650 ± 5.537**	**22.056 ± 3.404**	**<0.001**
1-RM deadlift (kg)	**58.250 ± 5.098**	**33.056 ± 2.838**	**<0.001**
VJ (cm)	**33.000 ± 4.365**	**22.000 ± 1.372**	**<0.001**
HJ (m)	**1.567 ± 0.0863**	**1.158 ± 0.0618**	**<0.001**
20 m sprint (s)	**3.878 ± 0.048**	**4.009 ± 0.050**	**<0.001**
Throwing velocity (km/h)	**32.400 ± 1.818**	**27.833 ± 0.786**	**<0.001**
FV power (watts)	**567.150 ± 27.410**	**471.167 ± 16.797**	**<0.001**
MAV (km/h)	**10.800 ± 0.696**	**8.333 ± 0.485**	**<0.001**
SJ (cm)	**19.515 ± 1.695**	**11.782 ± 0.464**	**<0.001**
CMJ (cm)	**27.330 ± 1.677**	**17.166 ± 0.306**	**<0.001**
DPI (g/day)	**95.6 ± 6.7**	**63.5 ± 9.0**	**<0.001**
DCI (mg/day)	**1064.0 ± 89.8**	**870.3 ± 63.3**	**<0.001**
PSQI	9.0 ± 2.1	9.1 ± 0.3	0.751

SD, standard deviation; BMI, body mass index; WB, whole body; BMC, bone mineral content; BMD, bone mineral density; L1–L4, Lumbar spine; TH, total hip; FN, femoral neck; CSA, cross-sectional area; CSMI, cross-sectional moment of inertia; Z, section modulus; BR, buckling ratio; SI, strength index; CSI, compression strength index; BSI, bending strength index; ISI, impact strength index; RM, repetition maximum; VJ, vertical jump; HJ, horizontal jump; FV, force-velocity; CMJ, counter movement jump; DPI, daily protein intake; DCI, daily calcium intake; PSQI, Pittsburgh sleep quality index. In bold, significant differences between the 2 groups.

3.2 Physical Performance Variables of the Study Population

1-RM bench press, 1-RM leg extension, 1-RM leg curl, 1-RM half-squat, 1-RM deadlift, VJ, HJ, throwing velocity, FV power, MAV, SJ and CMJ were significantly higher in handball players compared to inactive women. 20 m sprint duration was significantly higher in inactive women compared to handball players (Table 1).

3.3 Correlations Between Clinical Variables and Bone Variables Characteristics of the Study Population

Age was positively correlated to WB BMC, WB BMD, L1–L4 BMD, TH BMD, FN BMD, CSA, Z and SI. Age was negatively correlated to BR. Weight was negatively correlated to SI, CSI, BSI and ISI. Height was positively correlated to WB BMD, L1–L4 BMD and BR. Height was negatively correlated to WB BMC and TH BMD. BMI was positively correlated to WB BMC and WB BMD. BMI was negatively correlated to SI, CSI, BSI and ISI. LM was positively correlated to WB BMC, WB BMD, L1–L4 BMD,

TH BMD, FN BMD and Z. LM was negatively correlated to BR. FM was positively correlated to WB BMC. FM was negatively correlated to SI, CSI, BSI and ISI. FM percentage was positively correlated to BR. FM percentage was negatively correlated to L1–L4 BMD, TH BMD, FN BMD, SI and CSI. ST was negatively correlated to WB BMC, WB BMD, L1–L4 BMD, TH BMD, FN BMD and Z. ST was positively correlated to BR. PA was positively correlated to WB BMC, WB BMD, L1–L4 BMD, TH BMD, FN BMD and Z. PA was negatively correlated to BR. DPI was positively correlated to WB BMC, WB BMD, L1–L4 BMD, TH BMD, FN BMD and Z. DPI was negatively correlated to BR, BSI and ISI. DCI was positively correlated to WB BMC, WB BMD, L1–L4 BMD, TH BMD, FN BMD and Z. DCI was negatively correlated to BR (Table 2).

3.4 Correlations Between Physical Performance Variables and Bone Characteristics of the Study Population

1-RM bench press was positively correlated to WB BMC, WB BMD, L1–L4 BMD, TH BMD, FN BMD, CSA, Z and CSMI. 1-RM bench press was negatively correlated to BR. 1-RM leg extension was positively correlated to WB BMC, WB BMD, L1–L4 BMD, TH BMD, FN BMD, CSA, Z and SI. 1-RM leg extension was negatively correlated to BR. 1-RM leg curl was positively correlated to WB BMC, WB BMD, L1–L4 BMD, TH BMD, FN BMD, CSA, Z and SI. 1-RM leg curl was negatively correlated to BR. 1-RM half-squat was positively correlated to WB BMC, WB BMD, L1–L4 BMD, TH BMD, FN BMD, Z and SI. 1-RM half-squat was negatively correlated to BR. 1-RM deadlift was positively correlated to WB BMC, WB BMD, L1–L4 BMD, TH BMD, FN BMD, CSA, Z and SI. 1-RM deadlift was negatively correlated to BR. VJ was positively correlated to L1–L4 BMD, TH BMD, FN BMD and SI. VJ was negatively correlated to BR. HJ was positively correlated to WB BMD, L1–L4 BMD, TH BMD, FN BMD and SI. HJ was negatively correlated to BR. 20 m sprint duration was positively correlated to BR. 20 m sprint duration was negatively correlated to WB BMD, L1–L4 BMD, TH BMD and FN BMD. Throwing velocity was positively correlated to WB BMC, WB BMD, L1–L4 BMD, TH BMD, FN BMD, CSA and Z. Throwing velocity was negatively correlated to BR. FV power was positively correlated to WB BMC, WB BMD, L1–L4 BMD, TH BMD, FN BMD, CSA and Z. FV power was negatively correlated to BR. MAV was positively correlated to WB BMD, L1–L4 BMD, TH BMD, FN BMD and Z. MAV was negatively correlated to BR. SJ was positively correlated to WB BMD, L1–L4 BMD, TH BMD, FN BMD and SI. SJ was negatively correlated to BR. CMJ was positively correlated to WB BMD, L1–L4 BMD, TH BMD, FN BMD, Z and SI. CMJ was negatively correlated to BR (Table 2).

Table 2. Correlations between clinical characteristics and bone variables in the whole population.

	WB BMC (g)	WB BMD (g/cm²)	L1–L4 BMD (g/cm²)	TH BMD (g/cm²)	FN BMD (g/cm²)	CSA (mm²)	CSMI (mm⁴)	Z (mm³)	BR	SI	CSI (g/kg−m)	BSI (g/kg−m)	ISI (g/kg−m)
Age (yr)	0.38 *	0.48 **	0.55 ***	0.59 ***	0.61 ***	0.52 ***	0.12	0.42 **	−0.38 *	0.47 **	0.28	0.20	0.19
Weight (kg)	0.22	0.22	−0.12	−0.04	−0.05	0.17	−0.18	0.19	0.02	−0.37 *	−0.77 ***	−0.57 ***	−0.74 ***
Height (m)	−0.42 **	0.49 **	0.61 ***	−0.47 **	−0.25	0.08	0.05	−0.003	0.33 *	−0.08	0.01	0.29	−0.02
BMI (kg/m²)	0.41 **	0.42 **	0.14	0.16	0.05	0.13	−0.20	0.19	−0.11	−0.34 *	−0.78 ***	−0.70 ***	−0.73 ***
Lean mass (Kg)	0.35 *	0.43 **	0.53 ***	0.61 ***	0.55 ***	0.26	0.08	0.44 **	−0.65 ***	0.21	−0.06	−0.25	−0.30
Fat mass (Kg)	0.40 *	0.18	0.01	0.04	−0.05	0.19	−0.34 *	0.06	0.02	−0.41 **	−0.58 ***	−0.48 **	−0.50 **
Fat mass %	−0.04	−0.22	−0.37 *	−0.42 **	−0.44 **	−0.08	−0.38 *	−0.25	0.38 *	−0.41 *	−0.44 **	−0.24	−0.27
1-RM bench press (kg)	0.40 *	0.55 ***	0.69 ***	0.83 ***	0.81 ***	0.39 *	0.40 *	0.58 ***	−0.73 ***	0.38 *	0.18	−0.03	−0.08
1-RM leg extension (kg)	0.43 **	0.54 ***	0.71 ***	0.82 ***	0.76 ***	0.32 *	0.41 **	0.51 ***	−0.73 ***	0.36 *	0.14	−0.10	−0.10
1-RM leg curl (kg)	0.44 **	0.56 ***	0.73 ***	0.84 ***	0.78 ***	0.37 *	0.39 *	0.53 ***	−0.71 ***	0.37 *	0.15	−0.08	−0.10
1-RM half-squat (kg)	0.40 *	0.50 **	0.69 ***	0.79 ***	0.71 ***	0.26	0.36 *	0.45 **	−0.72 ***	0.33 *	0.06	−0.18 *	−0.17
1-RM deadlift (kg)	0.42 **	0.58 ***	0.73 ***	0.84 ***	0.77 ***	0.34 *	0.36 *	0.51 ***	−0.74 ***	0.37 *	0.08	−0.14	−0.15
VJ (cm)	0.10	0.30	0.53 ***	0.57 ***	0.46 **	−0.03	0.18	0.13	−0.61 ***	0.42 **	0.15	−0.12	−0.05

Table 2. (*continued*)

	WB BMC (g)	WB BMD (g/cm²)	L1–L4 BMD (g/cm²)	TH BMD (g/cm²)	FN BMD (g/cm²)	CSA (mm²)	CSMI (mm⁴)	Z (mm³)	BR	SI	CSI (g/kg−m)	BSI (g/kg−m)	ISI (g/kg−m)
HJ (m)	0.28	0.39 *	0.59 ***	0.63 ***	0.52 ***	0.05	0.38 *	0.30	−0.63 ***	0.34 *	0.14	−0.15	−0.07
20 m Sprint (s)	−0.31	−0.40 *	−0.65 ***	−0.74 ***	−0.66 ***	−0.23	−0.34 *	−0.30	0.78 ***	−0.26 *	−0.18	0.09	−0.02
Throwing velocity (Km/h)	0.61 ***	0.68 ***	0.81 ***	0.91 ***	0.82 ***	0.47 **	0.40 *	0.59 ***	−0.75 ***	0.27	0.06	−0.15	−0.14
FV power (watts)	0.54 ***	0.60 ***	0.72 ***	0.84 ***	0.77 ***	0.42 **	0.46 **	0.58 ***	−0.74 ***	0.25	0.03	−0.19	−0.21
MAV (km/h)	0.28	0.44 **	0.60 ***	0.66 ***	0.60 ***	0.11	0.24	0.36 *	−0.67 ***	0.25	0.11	−0.13	−0.12
SJ (cm)	0.24	0.41 *	0.60 ***	0.67 ***	0.58 ***	0.10	0.34 *	0.31	−0.68 ***	0.41 **	0.14	−0.13	−0.09
CMJ (cm)	0.27	0.41 **	0.61 ***	0.69 ***	0.61 ***	0.13	0.36 *	0.36 *	−0.69 ***	0.38 *	0.14	−0.13	−0.10
ST (h/day)	−0.39 *	−0.39 *	−0.55 ***	−0.70 ***	−0.64 ***	−0.26	−0.43 **	−0.46 **	0.73 ***	−0.11	0.00	0.20	0.25
PA (h/week)	0.33 *	0.39 *	0.52 ***	0.61 ***	0.54 ***	0.14	0.39 *	0.41 **	−0.67 ***	0.16	−0.05	−0.27	−0.30
DPI (g/day)	0.42 **	0.56 ***	0.60 ***	0.73 ***	0.64 ***	0.30	0.27	0.50 **	−0.65 ***	0.18	−0.17	−0.38 *	−0.40 *
DCI (g/day)	0.40 *	0.42 **	0.61 ***	0.64 ***	0.60 ***	0.27	0.28	0.40 *	−0.49 **	0.17	0.17	−0.04	−0.00
PSQI	−0.26	−0.10	−0.10	−0.08	−0.10	−0.13	−0.09	−0.16	0.06	0.26	0.03	0.02	−0.00

BMI, body mass index; WB, whole body; BMC, bone mineral content; BMD, bone mineral density; L1–L4, Lumbar spine; TH, total hip; FN, femoral neck; CSA, cross sectional area; CSMI, cross-sectional moment of inertia; Z, section modulus; BR, buckling ratio; SI, strength index; CSI, compression strength index; BSI, bending strength index; RM, repetition maximum; VJ, vertical jump; HJ, horizontal jump; FV, force-velocity; SJ, squat-jump; CMJ, counter movement jump; ST, siting time; PA, physical activity; DPI, daily protein intake; DCI, daily calcium intake; PSQI, Pittsburgh sleep quality index. *p < 0.05. **p < 0.01. ***p < 0.001.

4   Discussion

In the present study, two groups of young adult women were compared (handball players vs. inactive young adult women). We noticed a clear difference in the results regarding various bone health parameters such as WB BMC, BMD and Z which had a remarkably greater value in female handball players compared to inactive women. Similarly, LM, PA, DPI and DCI had a remarkably greater value in handball players compared to inactive women. In contrast, FM percentage, BR and ST had a remarkably greater value in inactive women compared to handball players. However, age, weight, BMI, FM, CSA, SI, CSI, BSI, ISI and sleep quality did not show any significant differences when comparing the 2 groups.

Our results seem logical and are in compliance with those of many other studies which showed that handball players have significantly greater bone health parameters compared to non-athlete controls [2, 31]. The results of three recent studies conducted on adolescent females [2, 15] and postmenopausal women [31] are in accordance with those received in this study. Pereira et al. [31] performed a trial which was random and controlled and aimed at evaluating the outcome of recreational team handball on bone health, postural balance and body composition in inactive postmenopausal women. Sixty-seven postmenopausal women (68.3 ± 6.2 years) were subjects of the study [31]. They were randomized into handball team (n = 41) and control group (n = 26) [31]. The intervention stretched through a period of 16 weeks during which the handball team performed two to three 60-min training sessions per week; as for the control group, they did not change their routine of PA [31]. They noticed a positive impact on bone turnover after a short period of practicing handball within a team and also positively affected the health of bone and postural balance; these positive effects were received even though the women did not have any previous training in handball. All this may help in preventing the risk of falling and having fractures [31]. Another current study by Fagundes et al. [2] aimed to compare the bone mass content, bone mass density and LM of young female soccer players (odd-impact loading exercise), handball players (high-impact loading exercises) and non-athletes. One hundred and fifteen female handball players (15.5 ± 1.3 years) and one hundred forty-two soccer players (15.5 ± 1.5 years) were evaluated for body composition using a dual-emission X-ray absorptiometry system, and one hundred thirty-six female non-athletes (data from NHANES) (15.1 ± 1.32 years) were considered as the control group [2]. They showed that the lowest BMC values were for the non-athletes, followed by higher values for the adolescents who practiced soccer; the highest recorded values were for the adolescent females practicing handball for at least one year [2]. These results justify the choice of practicing a specific sport to increase bone mass gain in this population [2]. Vicente-Rodriguez et al. [15] have evaluated the effect of PA on the BMC and BMD of 51 adolescent girls (14.2 ± 0.4 yr). They have demonstrated that handball practice results in three positive effects; the first shows an improvement in physical fitness, the second shows an improvement in the lean mass and the bone mass, and the final one shows an improvement in the axial and appendicular BMD of adolescent girls [15]. They also suggested that they could identify girls who have lower values of bone mass through the use of the combination of anthropometric and fitness-related variables [15].

Our results showed clear differences in several physical performance variables. 1-RM bench press, 1-RM leg extension, 1-RM leg curl, 1-RM squat, 1-RM deadlift, VJ, HJ, throwing velocity, FV power, MAV, SJ and CMJ had a remarkably greater value for the handball players compared to inactive women. These results seem to be logical since practicing handball improves jumping performance, lower limb strength and upper limb strength. On the other hand, 20 m sprint duration (seconds) yielded a higher score in inactive women compared to handball players.

The present study demonstrated that weight was negatively correlated to SI, CSI, BSI and ISI. BMI was positively correlated to WB BMC and WB BMD but negatively correlated to SI, CSI, BSI and ISI. FM was positively correlated to WB BMC but negatively correlated to SI, CSI, BSI and ISI. FM percentage was positively correlated to BR but negatively correlated to L1–L4 BMD, TH BMD, FN BMD, SI and CSI. Our results are in accordance with the results of many preceding studies which were done on young adults that have showed that body weight, BMI and FM were negatively associated to composite indices of FN strength [21–28, 46]. The excess of FM may negatively affect FN strength composite indices. For this reason, the implementation of strategies aiming at reducing FM excess should be done to prevent the incidents of fractures associated to in a later phase of life to osteoporosis.

Furthermore, our findings are a confirmation of the influence of LM on bone health in young adult women. LM was positively correlated to WB BMC, BMD and Z but negatively correlated to BR. ST was negatively correlated to WB BMC, BMD and Z but positively correlated to BR. PA was positively correlated to WB BMC, BMD and Z but negatively correlated to BR. These findings confirm the findings of studies that were done previously on young adults that have shown significant associations between LM, PA and bone health parameters [26, 28, 47–49]. Accordingly, putting into effect a plan which would augment LM is crucial for young adult women because it would help in the lack of occurrence of osteoporotic fractures later in life. Our results are the same as the results founded by several pre-ceding studies that suggested that LM is an important determinant of WB BMC, FN CSA and FN Z [50–57]. A cross-sectional study in which 70 osteoporotic and menopausal women participated, has found a significant association between LM and bone health parameters (BMC and BMD) [58]. The study has shown that FN BMD and femur BMD were correlated to LM [58]. Another study [59] which was done on a group of young adults has demonstrated a positive association between LM and WB BMC and WB BMD in both young men and women. Our results confirm the relation between DPI and DCI with bone health parameters. DPI and DCI were positively correlated to WB BMC, BMD and Z but negatively correlated to BR. The associations between DPI and DCI with bone variables have been demonstrated by two previous studies conducted on young adults [59, 60]. The yielded results affirm the importance of protein and daily calcium intakes for bone health.

Our findings showed that 1-RM squat was positively correlated to WB BMC, BMD, Z but negatively correlated to BR. Several authors have demonstrated that 1-RM half-squat was significantly associated with bone variables in adult women who were overweight and obese [19], in overweight men [61], in men who are middle-aged [28], in elderly men [62] and in elderly women [63]. 1-RM bench press was positively correlated to WB BMC, BMD, CSA and Z but negatively correlated to BR. These findings are similar

to other findings from a current study which was done on middle-aged men [28]. The current study is the pioneer in finding several significant associations. 1-RM leg extension and leg curl were positively correlated to WB BMC, BMD, CSA, and Z but negatively correlated to BR. The current study demonstrated that VJ was positively correlated to L1–L4 BMD, TH BMD, FN BMD and SI but negatively correlated to BR. HJ, and SJ were positively correlated to BMD and SI but negatively correlated to BR. CMJ was positively correlated to BMD, Z and SI but negatively correlated to BR. The goal of these physical tests is to call attention to the relative power. These findings are in conformity with the findings of previously done studies by our research team on young adults that have found positive associations between VJ and bone health parameters [19, 20, 64]. Similarly, a previous study conducted by our research team suggested that HJ and counter movement jump were positively correlated to several bone health parameters in middle-aged men [28]. Thus, the results that we found call attention to the necessity of increasing jumping performance of the lower limbs to prevent osteoporosis later in life. 20 m sprint duration was negatively correlated to BMD. Similarly, a previous recent study conducted on middle-aged men has demonstrated a negative correlation between sprinting performance and several bone health parameters [28]. They showed that the performance of sprinting best determined the composite indices in this population [28]. Longitudinal studies to be done in the future ought to confirm the impact of sprint training on bone health parameters. The current study was the first to show significant associations between throwing velocity, FV power, MAV and bone health parameters in young adults. We noticed that throwing velocity was positively correlated to WB BMC, BMD, CSA and Z but negatively correlated to BR. FV power was positively correlated to WB BMC, BMD, CSA and Z but negatively correlated to BR. MAV was positively correlated to BMD and Z but negatively correlated to BR. The latter highlights the importance of improving cardiovascular endurance to prevent osteoporosis later in life. These results have clinical implications since high BR values have a close association with a higher fracture risk in the elderly.

Despite our study being an original one, it presents various limitations. The first limitation is that the study's nature is cross-sectional, and therefore, a causal relationship between handball practice and bone health parameters cannot be confirmed. The second limitation is that the number of subjects is low in both groups; however, there were enough power values which made running the analyses and testing the differences between the 2 groups regarding bone health parameters possible and credible. The third limitation is that we did not assess many bone health correlates (such as hormones and vitamin D levels). The fourth limitation of our study is that visceral FM was not evaluated. It is well known that visceral fat has a deleterious effect on bone health parameters [65, 66]. The last limitation was the lack of use of a specific PA questionnaire to measure the effect of mechanical strain on BMD [67, 68]. Nevertheless, based on our knowledge, comparing bone health parameters (BMC, BMD, geometric indices of FN strength [CSA, CSMI, Z, BR, SI] and composite indices of FN strength [CSI, BSI, and ISI]) in inactive young adult women and young female handball players has been done for the first time in the current study.

5   Conclusion

To conclude, our study suggests that handball training is affiliated with greater bone health parameters in young adult women. As a result, practicing handball during young adulthood years could protect from the risk of contracting osteoporotic fractures later in life. Finally, selecting proper training programs in the duration of young adult years ought to be adapted accordingly.

Disclosure of Interest.   None of the authors reported a conflict of interest related to the study.

References

1. Castrogiovanni, P., Trovato, F.M., Szychlinska, M.A., Nsir, H., Imbesi, R., Musumeci, G.: The importance of physical activity in osteoporosis. From the molecular pathways to the clinical evidence. Histol. Histopathol. **31**, 1183–1194 (2016)
2. Fagundes, U., Vancini, R.L., Seffrin, A., et al.: Adolescent female handball players present greater bone mass content than soccer players: a cross-sectional study. Bone **154**, 116217 (2022). https://doi.org/10.1016/j.bone.2021.116217
3. World Health Organization: Assessment of fracture risk and its application to screening for postmenopausal osteoporosis. Report of a WHO Study Group. World Health Organ. Tech. Rep. Ser. **843**, 1–129 (1994)
4. Kanis, J.A., McCloskey, E.V., Johansson, H., Oden, A., Melton 3rd., J., Khaltaev, N.: A reference standard for the description of osteoporosis. Bone **42**, 467–475 (2008)
5. Stone, K.L., Seeley, D.G., Lui, L.Y., et al.: BMD at multiple sites and risk of fracture of multiple types: long-term results from the study of osteoporotic fractures. J. Bone Miner. Res. **18**, 1947–1954 (2003)
6. Beck, T.J., Ruff, C.B., Warden, K.E., Scott Jr., W.W., Rao, G.U.: Predicting femoral neck strength from bone mineral data. A structural approach. Invest. Radiol. **25**(1), 6–18 (1990)
7. Beck, T.J.: Extending DXA beyond bone mineral density: understanding hip structure analysis. Curr. Osteoporos. Rep. **5**(2), 49–55 (2007)
8. Kaptoge, S., Da Silva, J.A., Brixen, K., et al.: Geographical variation in DXA bone mineral density in young European men and women. Results from the Network in Europe on Male Osteoporosis (NEMO) study. Bone **43**(2), 332–339 (2008)
9. LaCroix, A.Z., Beck, T.J., Cauley, J.A., et al.: Hip structural geometry and incidence of hip fracture in postmenopausal women: what does it add to conventional bone mineral density? Osteoporos. Int. **21**(6), 919–929 (2010)
10. Black, D.M., Bouxsein, M.L., Marshall, L.M., et al.: Proximal femoral structure and the prediction of hip fracture in men: a large prospective study using QCT. J. Bone Miner. Res. **23**, 1326–1333 (2008)
11. Karlamangla, A.S., Barrett-Connor, E., Young, J., Grenndale, G.A.: Hip fracture risk assessment using composite indices of femoral neck strength: the Rancho Bernardo study. Osteoporos. Int. **15**, 62–70 (2004)
12. Yu, N., Liu, Y.J., Pei, Y., et al.: Evaluation of compressive strength index of the femoral neck in Caucasians and Chinese. Calcif. Tissue Int. **87**, 324–332 (2010)
13. Ayoub, M.L., Maalouf, G., Bachour, F., et al.: DXA-based variables and osteoporotic fractures in Lebanese postmenopausal women. Orthop. Traumatol. Surg. Res. **100**(8), 855–858 (2014)
14. Nilsen, O.A., Ahmed, L.A., Winther, A., et al.: Changes and tracking of bone mineral density in late adolescence: the Tromsø study. Fit futures. Arch. Osteoporos. **12**(1), 37 (2017)

15. Vicente-Rodriguez, G., Dorado, C., Perez-Gomez, J., Gonzalez-Henriquez, J.J., Calbet, J.A.: Enhanced bone mass and physical fitness in young female handball players. Bone **35**, 1208–1215 (2004)
16. Dixon, W.G., Lunt, M., Pye, S.R., et al.: Low grip strength is associated with bone mineral density and vertebral fracture in women. Rheumatology (Oxford) **44**(5), 642–646 (2005)
17. Sirola, J., Rikkonen, T., Tuppurainen, M., Jurvelin, J.S., Alhava, E., Kröger, H.: Grip strength may facilitate fracture prediction in perimenopausal women with normal BMD: a 15-year population based study. Calcif. Tissue Int. **83**, 93–100 (2008)
18. Sherk, V.D., Palmer, I.J., Bemben, M.G., Bemben, D.A.: Relationships between body composition, muscular strength, and bone mineral density in estrogen-deficient postmenopausal women. J. Clin. Densitom. **12**, 292–298 (2009)
19. Berro, A.J., Al Rassy, N., Ahmaidi, S., et al.: Physical performance variables and bone parameters in a group of young overweight and obese women. J. Clin. Densitom. **22**(2), 293–299 (2019)
20. Khawaja, A., Sabbagh, P., Prioux, J., et al.: Does muscular power predict bone mineral density in young adults? J. Clin. Densitom. **22**(3), 311–320 (2019)
21. El Hage, R.: Composite indices of femoral neck strength in adult female soccer players. J. Clin. Densitom. **17**, 212–213 (2014)
22. El Hage, R., Zakhem, E., Zunquin, G., Theunynck, D., Moussa, E., Maalouf, G.: Does soccer practice influence compressive strength, bending strength, and impact strength indices of the femoral neck in young men? J. Clin. Densitom. **17**(1), 213–214 (2014)
23. Berro, A.-J., et al.: Maximal oxygen consumption and composite indices of femoral neck strength in a group of young women. In: Rojas, I., Ortuño, F. (eds.) IWBBIO 2017. LNCS, vol. 10208, pp. 369–375. Springer, Cham (2017). https://doi.org/10.1007/978-3-319-56148-6_32
24. El Khoury, C., Toumi, H., Lespessailles, E., et al.: Decreased composite indices of femoral neck strength in young obese men. J. Clin. Densitom. **20**(2), 268–270 (2017)
25. El Khoury, G., Zouhal, H., Cabagno, G., et al.: Maximal oxygen consumption and composite indices of femoral neck strength in a group of young overweight and obese men. J. Clin. Densitom. **21**(2), 310–311 (2018)
26. Zakhem, E., Sabbagh, P., Ghanem-Zakhem, A., et al.: Influence of physical activity level on composite indices of femoral neck strength in a group of young overweight. J. Clin. Densitom. **23**(4), 596–603 (2020)
27. Zakhem, E., Sabbagh, P., El Khoury, C., Zunquin, G., Baquet, G., El Hage, R.: Positive correlations between physical activity level and composite indices of femoral neck strength in a group of young overweight and obese men. Sci. Sports (2020). https://doi.org/10.1016/j.scispo.2020.06.010
28. Finianos, B., Zunquin, G., El Hage, R.: Composite indices of femoral neck strength in middle-aged inactive subjects vs former football players. J. Clin. Densitom. **24**(2), 214–224 (2021)
29. Sardinha, L.B., Baptista, F., Ekelund, U.: Objectively measured physical activity and bone strength in 9-year-old boys and girls. Pediatrics **122**(3), e728–e736 (2008)
30. Mori, T., et al.: Physical activity as determinant of femoral neck strength relative to load in adult women: findings from the hip strength across the menopause transition study. Osteoporos. Int. **25**(1), 265–272 (2013). https://doi.org/10.1007/s00198-013-2429-z
31. Pereira, R., Krustrup, P., Castagna, C., et al.: Effects of recreational team handball on bone health, postural balance and body composition in inactive postmenopausal women - a randomised controlled trial. Bone **145**, 115847 (2021). https://doi.org/10.1016/j.bone.2021.115847
32. Maliha, E., Pinti, A., Bassim, P., Toumi, H., El Hage, R.: Composite indices of femoral neck strength in young adult male handball players. J. Clin. Densitom. (2021). https://doi.org/10.1016/j.jocd.2021.11.012

33. World Health Organization. Global Recommendations on Physical Activity for Health. World Health Organization (2010)

34. Sabbagh, P., et al.: Relationships between muscular power and bone health parameters in a group of young Lebanese adults. In: Rojas, I., Valenzuela, O., Rojas, F., Herrera, L.J., Ortuño, F. (eds.) Bioinformatics and Biomedical Engineering: 8th International Work-Conference, IWBBIO 2020, Granada, Spain, May 6–8, 2020, Proceedings, pp. 119–129. Springer, Cham (2020). https://doi.org/10.1007/978-3-030-45385-5_11

35. Finianos, B., Sabbagh, P., Zunquin, G., El Hage, R.: Muscular power and maximum oxygen consumption predict bone density in a group of middle-aged men. J. Musculoskelet. Neuronal. Interact. **20**(1), 53–61 (2020)

36. Harman, E., Rosenstein, M., Frykman, P., Rosenstein, R., Kraemer, W.: Estimation of human power output from vertical jump. J. Strength Cond. Res. **5**(3), 116 (1991)

37. Haff, G.G., Triplett, N.T. (eds.): Essentials of Strength Training and Conditioning, 4th edn. Human kinetics (2015)

38. Buysse, D.J., Reynolds, C.F., 3rd., Monk, T.H., Berman, S.R., Kupfer, D.J.: The Pittsburgh sleep quality index: a new instrument for psychiatric practice and research. Psychiatry Res. **28**(2), 193–213 (1989)

39. Zakhem, E., El Hage, R., Zunquin, G., Jacob, C., Moussa, E., Theunynck, D.: Sleep quality is a determinant of hip bone mineral density in a group of young Lebanese men. J. Med. Liban. **62**(4), 213–216 (2014)

40. Bonjour, J.P., Chevalley, T., Ferrari, S., Rizzoli, R.: The importance and relevance of peak bone mass in the prevalence of osteoporosis. Salud. Publ. Mex. **51**(Suppl 1), S5-17 (2009)

41. Lucassen, E.A., de Mutsert, R., le Cessie, S., et al.: Poor sleep quality and later sleep timing are risk factors for osteopenia and sarcopenia in middle-aged men and women: the NEO study. PLoS ONE **12**(5), e0176685 (2017)

42. Fardellone, P., Sebert, J.L., Bouraya, M., et al.: Evaluation of the calcium content of diet by frequential self-questionnaire. Rev. Rhum. Mal. Osteoartic. **58**(2), 99–103 (1991)

43. El Hage, R., Jacob, C., Moussa, E., Jaffré, C., Benhamou, C.L.: Daily calcium intake and body mass index in a group of Lebanese adolescents. J. Med. Liban. **57**(4), 253–257 (2009)

44. Morin, P., Herrmann, F., Ammann, P., Uebelhart, B., Rizzoli, R.: A rapid self-administered food frequency questionnaire for the evaluation of dietary protein intake. Clin. Nutr. **24**(5), 768–774 (2005)

45. Armstrong, T., Bull, F.: Development of the global physical activity questionnaire (GPAQ). J. Publ. Health **14**, 66–70 (2006)

46. Kim, H., Lee, S.H., Kim, B.J., Koh, J.M.: Association between obesity and femoral neck strength according to age, sex, and fat distribution. Osteoporos. Int. **28**(7), 2137–2146 (2017)

47. El Hage, R., Zakhem, E., Zunquin, G., Theunynck, D., Moussa, E., Maalouf, G.: Does soccer practice influence compressive strength, bending strength, and impact strength indices of the femoral neck in young men? J. Clin. Densitom. **17**(1), 213–214 (2014)

48. El Hage, R., Bachour, F., Sebaaly, A., Issa, M., Zakhem, E., Maalouf, G.: The influence of weight status on radial bone mineral density in Lebanese women. Calcif. Tissue Int. **94**(4), 465–467 (2014)

49. El Hage, R., Khairallah, W., Bachour, F., et al.: Influence of age, morphological characteristics, and lumbar spine bone mineral density on lumbar spine trabecular bone score in Lebanese women. J. Clin. Densitom. **17**(3), 434–435 (2014)

50. El Khoury, C., Pinti, A., Lespessailles, E., et al.: Physical performance variables and bone mineral density in a group of young overweight and obese men. J. Clin. Densitom. **21**(1), 41–47 (2018)

51. Petit, M.A., Beck, T.J., Hughes, J.M., Lin, H.M., Bentley, C., Lloyd, T.: Proximal femur mechanical adaptation to weight gain in late adolescence: a six-year longitudinal study. J. Bone Miner. Res. **23**, 180–188 (2008)

52. Shea, K.L., Gozansky, W.S., Sherk, V.D., et al.: Loss of bone strength in response to exercise-induced weight loss in obese postmenopausal women: results from a pilot study. J. Musculoskelet. Neuronal Interact. **14**(2), 229–238 (2014)
53. MacKelvie, K.J., McKay, H.A., Petit, M.A., Moran, O., Khan, K.M.: Bone mineral response to a 7-month randomized controlled, school-based jumping intervention in 121 prepubertal boys: associations with ethnicity and body mass index. J. Bone Miner. Res. **17**(5), 834–844 (2002)
54. Nikander, R., Sievänen, H., Heinonen, A., Kannus, P.: Femoral neck structure in adult female athletes subjected to different loading modalities. J. Bone Miner. Res. **20**(3), 520–528 (2005)
55. Lorentzon, M., Mellström, D., Ohlsson, C.: Association of amount of physical activity with cortical bone size and trabecular volumetric BMD in young adult men: the GOOD study. J. Bone Miner. Res. **20**(11), 1936–1943 (2005)
56. Bonjour, J.P., Chevalley, T., Rizzoli, R., Ferrari, S.: Gene environment interactions in the skeletal response to nutrition and exercise during growth. Med. Sport Sci. **51**, 64–80 (2007)
57. El Hage, R., Jacob, C., Moussa, E., Youssef, H., Jaffré, C.: Effects of 12 weeks of endurance training on bone mineral content and bone mineral density in obese, overweight and normal weight adolescent girls. Sci. Sports **24**(3–4), 210–213 (2009)
58. Genaro, P.S., Pereira, G.A., Pinheiro, M.M., Szejnfeld, V.L., Martini, L.A.: Influence of body composition on bone mass in postmenopausal osteoporotic women. Arch. Gerontol. Geriatr. **51**(3), 295–298 (2010)
59. Zakhem, E., El Khoury, G., Feghaly, L., et al.: Performance physique et densité minérale osseuse chez de jeunes adultes libanais. J. Med. Liban. **64**(4), 193–199 (2016)
60. El Khoury, G., Zouhal, H., Cabagno, G., et al.: Bone variables in active overweight/obese men and sedentary overweight/obese men. J. Clin. Densitom. **20**(2), 239–246 (2017)
61. Khawaja, A., Sabbagh, P., Prioux, J., Pinti, A., El Khoury, G., El Hage, R.: Relation between maximal half squat strength and bone variables in a group of young overweight men. In: International Conference on Bioinformatics and Biomedical Engineering, pp. 374–384. Springer, Cham (2019). https://doi.org/10.1007/978-3-030-17935-9_34
62. Nasr, R., Al Rassy, N., Watelain, E., Ishac, S., Abdul Al, O., El Hage, R.: Muscular maximal strength indices and bone variables in a group of elderly men. Sci. Sports **34**(1), 56–58 (2019)
63. Nasr, R., Al Rassy, N., Watelain, E., et al.: Muscular maximal strength indices and bone variables in a group of elderly women. J. Clin. Densitom. **23**(3), 465–471 (2018)
64. Khawaja, A., Kamlé, P., Maliha, E., et al.: Relationships between vertical jump and composite indices of femoral neck strength in a group of young women. In: International Conference on Bioinformatics and Biomedical Engineering, pp. 27–38. Springer, Cham (2021). https://doi.org/10.1007/978-3-030-88163-4_3
65. El Hage, R., Jacob, C., Moussa, E., Baddoura, R.: Relative importance of lean mass and fat mass on bone mineral density in a group of Lebanese postmenopausal women. J. Clin. Densitom. **14**(3), 326–331 (2011)
66. El Hage, R., El Hage, Z., Moussa, E., Jacob, C., Zunquin, G., Theunynck, D.: Geometric indices of hip bone strength in obese, overweight, and normal-weight adolescent girls. J. Clin. Densitom. **16**(3), 313–319 (2013)
67. Dolan, S.H., Williams, D.P., Ainsworth, B.E., Shaw, J.M.: Development and reproducibility of the bone loading history questionnaire. Med. Sci. Sports Exerc. **38**(6), 1121–1131 (2006)
68. Kemper, H.C.G., Bakker, I., Twisk, J.W.R., van Mechelen, W.: Validation of a physical activity questionnaire to measure the effect of mechanical strain on bone mass. Bone **30**(5), 799–804 (2002)

Adaptative Modelling of the Corneal Architecture in a Free-of-Stress State in Incipient Keratoconus

Francisco Cavas[1]([✉]) [iD], Carmelo Gómez[2] [iD], José S. Velázquez[1] [iD], David Piñero[3] [iD], Francisco L. Sáez-Gutiérrez[1] [iD], and Jorge Alió[4] [iD]

[1] Department of Structures, Construction and Graphic Expression, Technical University of Cartagena, 30202 Cartagena, Spain
`francisco.cavas@upct.es`
[2] International School of Doctorate, Technical University of Cartagena, 30202 Cartagena, Spain
[3] Grupo de Óptica y Percepción Visual, Universidad de Alicante, 03690 Alicante, Spain
[4] Keratoconus Unit of Vissum Corporation Alicante, 03016 Alicante, Spain

Abstract. Finite element models (FEM) have been a breakthrough in the field of medicine for a wide variety of applications. They have been used, for example, for predicting the behaviour of many biological structures, as well as to foresee the possible outcomes of some types of operations. One of the basic problems when modelling biological structures is finding a way to determine the initial geometric parameters with a sufficient degree of precision, so that the results are representative. In the case of computational models used for the study of corneal biomechanics, the knowledge of initial conditions defined in a finite element model become critical, since they represent the in-vivo state of the biological structure by means of a computer simulation. There is a lack of consensus among the investigations carried out to date regarding whether the initial status in the FEM models should be considered or not. In this research work, two approaches that aim to determine the geometry of the in-vivo state of the cornea with mild keratoconus have been compared: the so-called stress-free geometry on the one side, and the initial tension state on the other side. The results obtained allow comparisons between them, and validate both approaches when they are used to obtain corneal geometry in initial stress-free conditions for a FEM model when incipient keratoconus.

Keywords: Corneal biomechanics · FEM · Inverse geometry · Biological structure

1 Introduction

The cornea is a fundamental part of the human eye. It is a complex, heterogeneous, aspherical and thin tissue, which is part of the anterior part of the eye, and it is in contact with the outside environment in one of its areas. In a conventional scenario, without the presence of pathological alterations, both the anterior and posterior parts of the cornea present a very particular morphology, derived from the balance between stresses and

deformations, which generate a very stable geometric surface. This geometry can be structured in-vivo by corneal tomographers [1].

In the early 1990s, following the publication of the first case of iatrogenic ectasia, a rising interest in biomechanical modelling emerged, aiming to use it to predict, by means of a numerical model developed by the Finite Element Method (FEM), the response of the cornea to various situations, such as pathological surgeries and non-surgical treatments, whether they were invasive or not [2].

The reliability of these behavioral models depends on both the fixed geometry of the cornea and the goodness of fit to the reality of the parameters that define the composition of the material at both microscopic and macroscopic levels [3]. Therefore, it would be of the highest interest determining the stress-free geometric state in the initial FEM model for incipient keratoconus.

The first works in the field of biomechanics considered asymmetric two-dimensional geometric models [4, 5]. Later approximations to corneal geometry were based on the use of different optical models, and different approaches to the basic geometry of the cornea could be adopted depending on the model being considered. In all cases, the objective is to obtain a model capable of representing the essential characteristics of the mean cornea, i.e., using as an approximation to the corneal surface a model based on a conical or biconical surface plus a residue, the so-called Navarro model [6]. However, these models do not register true specific geometry of the patient, and therefore they do not capture the defining structural irregularities of each patient, and those that are inherent to corneal pathologies.

In addition, our research group has introduced the concept of "patient-specific geometry", that consists in the development of a patient-specific 3D model that can effectively record the characteristic geometrical alterations of corneal pathologies. This model has been validated for the both the detection and diagnosis of corneal ectasia. The 3D model has recently been used for the first time in a FEM model for the characterization of corneal biomechanics [7].

As mentioned above, the reliability of the numerical simulation models used for the study of corneal biomechanics depends on the initial conditions defined in the FEM model, since they are responsible for representing the in-vivo state of the biological structure using a computer simulation. Among the investigations to date, there are differences as to whether or not to consider the initial state in the FEM models.

In this research work two approaches are compared to determine the geometry of the in-vivo state of the cornea with incipient keratoconus according to the Amsler-Krumeich classification [1], the so-called stress-free geometry and the initial stress state.

2   Materials and Methods

2.1   Participants

This study involved 12 patients aged between 19 and 61 years (38% men, 72% women).

All patients were selected, according to the Amsler-Krumiech grading, basing on the level of myopia, central keratometry, minimum pachymetry and the presence of other signs such as scars or steepening.

Inclusion criteria were: patients diagnosed as having Grade I KC eyes (up to – 5D astigmatism, ≤48D values of central mean keratometry, lack of scarring and eccentrical localized steepening).

The exclusion criteria were the following: any previous eye surgery in clinical history, ocular surface inflammation, moderate to severe dry eye or other active ocular comorbidity, or use of contact lenses within the four weeks prior to the first visit.

The participants signed an informed consent to participate in the clinical study that was carried out according to the ethical standards agreed by the Declaration of Helsinki (7th revision, October 2013, Fortaleza, Brazil).

The patients were part of the Iberia Biobank (Universidad Miguel Hernández de Elche, OFTARED-ISCIII). The study was approved by the UPCT ethics committee (CEI21_001).

2.2 Anisotropic Properties of the Cornea

Since the last century, it is well known that the human cornea is formed by a complex grouping of structured collagen fibres, that are interwoven, in a very precise way, within a matrix [2]. From a numerical point of view, the effect of considering a fibre-reinforced continuum is important, and that is why most studies in this field consider anisotropic models for their analysis. In general, there is agreement on the distribution of collagen fibres in the most important components of the human eye:

- The cornea has two preferential directions: nasal-temporal and upper-lower
- Limbo presents a preferential direction: circumferential
- The sclera, for numerical purposes, is considered as an isotropic material.

2.3 Material Parameters

Through experimental test, mechanical behavior of any type of material can be characterized, an experimental study on corneal biomechanics with few test is a poorly conditioned problem [8, 9].

However, some studies promoted by some authors present a sufficient set of data to perform the study of mechanical characterization of the cornea, in our study we have considered a hyperelastic anisotropic material with incompressible behavior [10].

2.4 Meshing

To optimize the time required for calculations, as well as the quality of the solution, the right mesh size should be found. For such problems, it has been found that the mesh size based on a minimum of 4 elements thick and 6 to model the dynamic fluid coupling [10].

Finally, for the mesh the total number of elements is 1024 and 6138 nodes. The type of element used for the analysis has been SOLID186.

2.5 Displacement Method

This method allows obtaining the stress-free geometry by means of an iterative process, in which that geometry is firstly assumed, and then intraocular pressure is applied. The resulting geometry is compared to the geometry measured with the topographer until the difference between them two is below a certain fixed threshold.

This technique was initially proposed by A. Pandolfi and G.A. Holzapfel [11] and was later modified by Elsheikh et al. [12] basing on a loop-like iterative process. Initially, the cornea is under the influence of the intraocular pressure (IOP), being X_0 the coordinates of the nodes of the stressed mesh. After applying pressure equal to the IOP, the material is deformed, moving the coordinates a quantity u:

$$x = X + u \tag{1}$$

so, it can be affirmed that

$$x_1 = x = X + u \tag{2}$$

The process begins by assuming that the coordinates in the first iteration x_1, are equal to the deformed configuration, and applying a pressure equal to the PIO it can be determined the displacement field in iteration 1, u_1, with which can be calculated the coordinates of the deformed geometry, x_1 according to Eq. (3):

$$x_1 = X_1 + u_1 \tag{3}$$

An overall measure of error could be estimated from the vector standard of differences between the deformed coordinates after the application of the IOP and the initial configuration, as shown in Eq. (4):

$$e_1 = \|x_1 - X_0\| = \|X_1 + u_1 - X_0\| \tag{4}$$

Finally, the material coordinates can be updated with the iteration in Eq. (5):

$$X_2 = X_0 - u_1 \tag{5}$$

The process will end when, in iteration k, e_k error is

$$e_k = \|x_k - X_0\| = \|X_k + u_k - X_0\| < \varepsilon \tag{6}$$

being ε a preset value between orders 10^{-6} and 10^{-9} (Fig. 1).
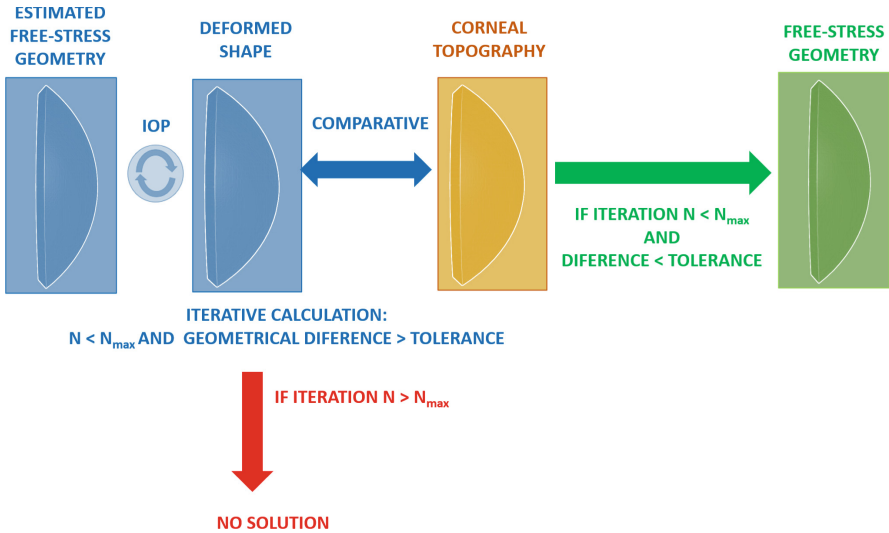
Fig. 1. Displacement method (schematic process).

2.6 Pre-stress Method

The pre-stress method does not allow calculating stress-free geometry by itself. It looks for the initial pre-stress of the tissue that makes deformation almost null when the intraocular pressure is applied, and therefore the resulting geometry practically coincides with the one of the topographer. If only that stress is considered as a load once calculated, stress-free geometry can be obtained.

This methodology was proposed by E. Lanchares in 2018 [13], and is based on finding the stresses to which the cornea is subjected when the IOP is present.

The ultimate goal is to determine what is the stress field that makes nodal shifts null or, in other words, find the stress field that balances the IOP.

The algorithm of this implementation is based on solving the static problem as many times as necessary for the displacement field to be overridden.

To do this, assuming that the iterator is in iteration $k > 0$, then this iteration will have as inputs the following parameters:

- The initial iteration mesh
- The assigned IOP (about 15 mmHg)
- The stress field solution for iteration $k-1$

When $k = 0$, the only entry will be the assigned IOP, given an initial mesh.
The natural trend is that this algorithm converges after about 20 iterations (Fig. 2).
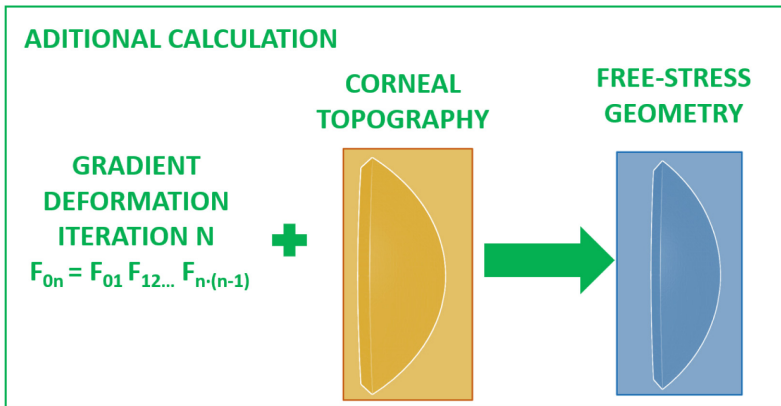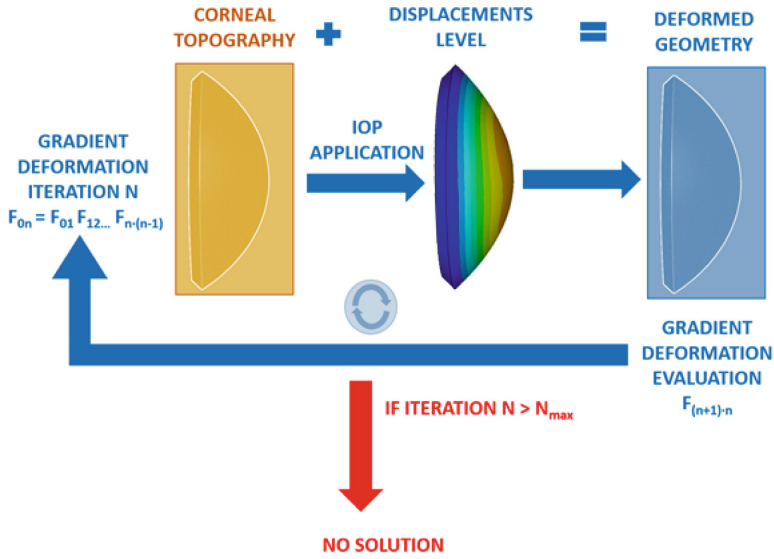
Fig. 2. Pre-stress method (schematic process).

2.7 Statistical Analysis

The statistical analysis of the outcomes obtained was performed using the software SPSS version 15.0 for Windows (SPSS, Chicago, IL). Normality of all data distributions was confirmed by means of the Kolmogorov–Smirnov test. Then, parametric statistics was always applied. Differences between X, Y and Z positions calculated with the displacement and pre-stress methods for the different point evaluated were analyzed using the paired Student t test. All statistical tests were two-tailed, and p-values less than 0.05 were considered statistically significant.

3   Results

Table 1 summarizes the results of the comparison of the simulations obtained with the two methods of simulation, displacement and pre-stress, in the keratoconus cornea grade I. As shown, significant differences between methods were only detected in the Z position of points on the anterior corneal surface (p = 0.004).

Table 1. Comparison of the results of the simulations performed in the keratoconus grade I cornea with the displacement and pre-stress methods.

Mean (SD) range	Displacement method	Pre-stress method	P-value
Anterior corneal surface			
X (mm)	−0.0170 (3.0552) −5.82 to 5.68	−0.0170 (3.0554) −5.82 to 5.68	0.999
Y (mm)	0.0109 (3.0791) −5.84 to 5.98	0.0111 (3.0799) −5.84 to 5.98	0.659
Z (mm)	1.5660 (1.0450) 0.20 to 3.15	1.5677 (1.0447) 0.20 to 3.15	0.004
Posterior corneal surface			
X (mm)	0.0096 (2.7665) −5.19 to 5.33	0.0105 (2.7647) −5.19 to 5.33	0.168
Y (mm)	0.0021 (2.7407) −5.07 to 5.20	0.0018 (2.7392) −5.07 to 5.20	0.532
Z (mm)	2.1393 (1.1178) 0.70 to 3.90	2.1398 (1.1165) 0.70 to 3.90	0.366

Only significant correlations of the differences in X (r = −0.288, p = 0.030) and Z (r = −0.254, p = 0.046) coordinates calculated with the displacement and pre-stress methods on the posterior corneal surface in the keratoconus grade I eye were found with the distance of location of the point evaluated (Fig. 3).

Maximum difference reached 7.32 microns per point (anterior surface). Mean value of total difference between inverse geometries calculated between methods 2.88 (standard deviation 2.00 microns).

Maximum difference reached 7.90 microns per point (posterior surface). Mean value of total difference between inverse geometries calculated between methods 0.04 (standard deviation 0.03 microns).
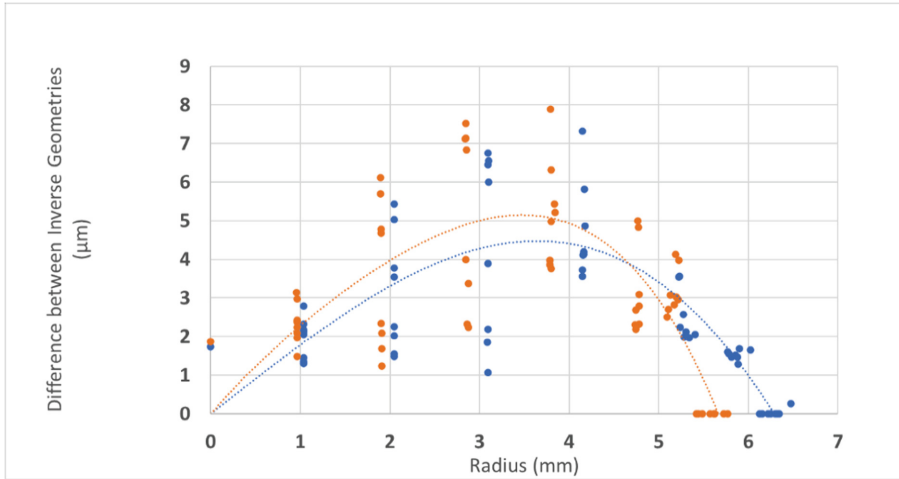
Fig. 3. Difference between Inverse Geometries to Keratoconus Grade I. Blue (Anterior surface difference), Orange (Posterior surface difference).

4   Discussion

In the field of modelling and numerical simulation of corneal biomechanics, the main objective is usually predicting the response of this structure in several different situations, whether they are invasive or non-invasive. Works can be found in the scientific literature presenting applications related with the behavior of the cornea in a healthy scenario [14], the analysis of its behavior before an ocular surgery [11], corneal structural alterations induced by physical phenomena, such as tonometry for the measurement of IOP [15], the evaluation of structural alterations before pathologies such as keratoconus [16], or even their incorporation into the biomechanical assessment of visual acuity optic models after a treatment. For all these applications, a real geometrical model of the corneal architecture must be developed, including both its anterior and posterior surfaces [1].

In a physiological state, when a biological structure is captured in-vivo, as it is the case of the cornea, it is subjected to a series of internal and external forces that force it to acquire a specific geometry, as a result of an equilibrium between them. In the case of the cornea, it is the IOP and the atmospheric pressure the ones which are balanced to generate the patient-specific geometry captured by the corneal tomographs [1].

There are discrepancies among current investigators regarding whether initial status should be considered or not. The general rule is that the problem of conditions is not mentioned, however, there are certain works that do contemplate it. To take into account the in-vivo state of the cornea two approaches can be observed: the stress-free geometry or the displacement method [11] and the initial tension state or pre-stress method [13].

Both methods present significant differences with respect to the coordinates of height Z or point of maximum curvature on the anterior surface, especially in the paracentral region, coinciding these results with those obtained by other authors on 3D models [17, 18].

With respect to the posterior face, there are no differences between both methods for the Cartesian coordinates (X, Y, Z), this behavior is aligned with the mean values of the total differences obtained between both methods for the inverse geometry, that is just 0.04 ± 0.03 microns.

With respect to the displacement method, the main advantage is that it allows to obtain the inverse geometry directly, and then the real IOP can be applied for each patient to obtain its physiological geometry (Fig. 4). Another feature of this method is that it can be implemented in any FEM code, so it does not depend on the material or the type of geometry.
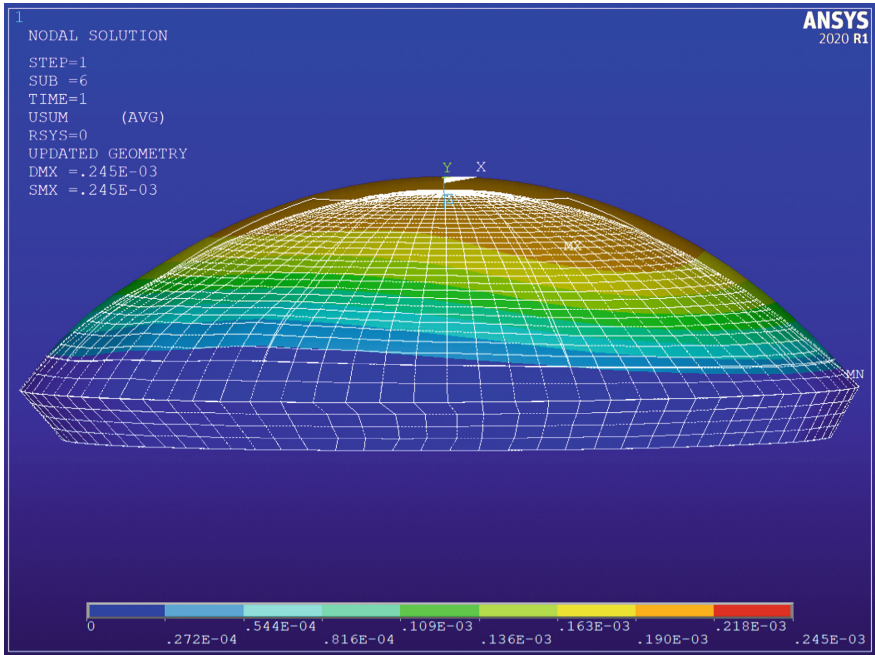
Fig. 4. Physiological geometry obtained by FEM after applying IOP to stress-free geometry

With respect to the pre-stress method, it presents an important limitation, consisting in the fact that it does not allow to calculate the stress-free geometry by itself, but it carries one more step (Fig. 2) to obtain such geometry. The method allows to obtain the tension field that balances the IOP or, in other words, the stress field that makes the nodal displacements null, and consequently it entails a greater computational cost. Then, inverse geometry can be obtained from this point.

5   Conclusion

Due to the non-linearity of corneal tissues and the exponential character of the behavior curve, failure to include residual stresses or not from the stress-free geometric model in computational numeric models can lead to calculation errors.

In this study we compared two methods to obtain stress-free or inverse geometry for corneas with incipient keratoconus. Both methodologies are valid to obtain the free geometry for these pathological corneas, but the displacement method is an inverse method more agile and with lower computational cost.

References

1. Cavas-Martínez, F., De la Cruz Sánchez, E., Nieto Martínez, J., Fernández Cañavate, F.J., Fernández-Pacheco, D.G.: Corneal topography in keratoconus: state of the art. Eye Vis. (London, England) **3**(5) (2016). https://doi.org/10.1186/s40662-016-0036-8

2. Ma, J., Wang, Y., Wei, P., Jhanji, V.: Biomechanics and structure of the cornea: implications and association with corneal disorders. Surv. Ophthalmol. **63**, 851–861 (2018). https://doi.org/10.1016/j.survophthal.2018.05.004

3. Kling, S., Hafezi, F.: Corneal biomechanics - a review. Ophthalmic Physiol. Opt. J. Br. Coll. Ophthalmic Opt. (Optom.) **37**, 240–252 (2017). https://doi.org/10.1111/opo.12345

4. Bryant, M.R., McDonnell, P.J.: Constitutive laws for biomechanical modeling of refractive surgery. J. Biomech. Eng. **118**, 473–481 (1996). https://doi.org/10.1115/1.2796033

5. Buzard, K.A.: Introduction to biomechanics of the cornea. Refract. Corneal Surg. **8**, 127–138 (1992)

6. Navarro, R., González, L., Hernández, J.L.: Optics of the average normal cornea from general and canonical representations of its surface topography. J. Opt. Soc. Am. A Opt. Image Sci. Vis. **23**, 219–232 (2006). https://doi.org/10.1364/josaa.23.000219

7. Gómez, C., Piñero, D.P., Paredes, M., Alió, J.L., Cavas, F.: Iterative methods for the biomechanical evaluation of corneal response. A case study in the measurement phase. Appl. Sci. **11**, 10819 (2021)

8. Ariza-Gracia, M., Ortillés, Á., Cristóbal, J., Rodríguez Matas, J.F., Calvo, B.: A numerical-experimental protocol to characterize corneal tissue with an application to predict astigmatic keratotomy surgery. J. Mech. Behav. Biomed. Mater. **74**, 304–314 (2017). https://doi.org/10.1016/j.jmbbm.2017.06.017

9. Ariza-Gracia, M.Á., Zurita, J., Piñero, D.P., Calvo, B., Rodríguez-Matas, J.F.: Automatized patient-specific methodology for numerical determination of biomechanical corneal response. Ann. Biomed. Eng. **44**(5), 1753–1772 (2015). https://doi.org/10.1007/s10439-015-1426-0

10. Pandolfi, A.: Cornea modelling. Eye Vis. (London, England) **7**, 2 (2020). https://doi.org/10.1186/s40662-019-0166-x

11. Pandolfi, A., Holzapfel, G.A.: Three-dimensional modeling and computational analysis of the human cornea considering distributed collagen fibril orientations. J. Biomech. Eng. **130**, 061006 (2008). https://doi.org/10.1115/1.2982251

12. Elsheikh, A., Whitford, C., Hamarashid, R., Kassem, W., Joda, A., Büchler, P.: Stress free configuration of the human eye. Med. Eng. Phys. **35**, 211–216 (2013). https://doi.org/10.1016/j.medengphy.2012.09.006

13. Lanchares, E., Calvo, B., Cristóbal, J.A., Doblaré, M.: Finite element simulation of arcuates for astigmatism correction. J. Biomech. **41**, 797–805 (2008). https://doi.org/10.1016/j.jbiomech.2007.11.010

14. Alastrué, V., Calvo, B., Peña, E., Doblaré, M.: Biomechanical modeling of refractive corneal surgery. J. Biomech. Eng. **128**, 150–160 (2006). https://doi.org/10.1115/1.2132368
15. Elsheikh, A., Wang, D., Kotecha, A., Brown, M., Garway-Heath, D.: Evaluation of Goldmann applanation tonometry using a nonlinear finite element ocular model. Ann. Biomed. Eng. **34**, 1628–1640 (2006). https://doi.org/10.1007/s10439-006-9191-8
16. Navarro, R., Palos, F., Lanchares, E., Calvo, B., Cristóbal, J.A.: Lower- and higher-order aberrations predicted by an optomechanical model of arcuate keratotomy for astigmatism. J. Cataract Refract. Surg. **35**, 158–165 (2009). https://doi.org/10.1016/j.jcrs.2008.09.015
17. Alifa, R., Piñero, D., Velázquez, J., Alió Del Barrio, J.L., Cavas, F., Alió, J.L.: Changes in the 3D corneal structure and morphogeometric properties in keratoconus after corneal collagen crosslinking. Diagnostics (Basel, Switzerland) **10**, 397 (2020). https://doi.org/10.3390/diagnostics10060397
18. Toprak, I., Cavas, F., Velázquez, J.S., Alió Del Barrio, J.L., Alió, J.L.: Three-dimensional morphogeometric and volumetric characterization of cornea in pediatric patients with early keratoconus. Am. J. Ophthalmol. **222**, 102–111 (2021). https://doi.org/10.1016/j.ajo.2020.09.031

Design of an Analysis Method for the Human Cornea's Bilateral Symmetry. A Case-Study in Healthy Patients

Francisco Cavas[1(✉)] [ID], José S. Velázquez[1] [ID], Carmelo Gómez[2] [ID], Jorge Mira[2], Francisco L. Sáez-Gutiérrez[1] [ID], and Jorge Alió[3] [ID]

[1] Department of Structures, Construction and Graphic Expression, Technical University of Cartagena, 30202 Cartagena, Spain
`francisco.cavas@upct.es`
[2] International School of Doctorate, Technical University of Cartagena, 30202 Cartagena, Spain
[3] Keratoconus Unit of Vissum Corporation Alicante, 03016 Alicante, Spain

Abstract. Bilateral symmetry in the human body is a necessary feature for our body to function more efficiently. Apparently, it could be thought that the ocular structure presents a bilateral symmetrical structure, however this does not occur in all cases, especially in those that are pathological. In many cases, symmetry is essential for the achievement of certain optical tasks. This study presents a method for evaluating bilateral symmetry (direct vs mirror) from the differences between the Cartesian coordinates (OD vs OS) in healthy corneas using customized patient-specific models and unprocessed data from corneal tomographs. The results obtained in the central and paracentral regions of the corneas evaluated show that the bilateral mirror symmetry presents differences below 10 microns and the direct bilateral symmetry reaches differences of the order of 30 microns at spatial coordinates level. This study shows that the level of asymmetry in healthy corneas can be evaluated by direct or mirror symmetry, and that the presence of asymmetric anomalies can be useful as a clinical diagnostic tool.

Keywords: 3D modelling · Computational modelling · Ophthalmology · Biological morphology

1 Introduction

The bilateral symmetry of the human body with respect to its sagittal plane is a necessary feature for our organism to function more efficiently [1]. In the scientific literature, several studies have been carried out on this subject, which have served, among other things, for the detection and diagnosis of diseases [1].

In the case of the ocular structure, it could apparently be thought that it presents a bilateral symmetrical architecture, however this does not occur in all cases, especially in those that are pathological [2]. This asymmetry can also occur in nonpathological eyes and can severely affect the visual quality of the patient, reaching situations of amblyopia,

commonly known as lazy eye, or nystagmus, a phenomenon through which the visual axes are very dissimilar [3].

The presence of certain bilateral symmetry in non-pathological eyes is important as it may affect visual ability by its influence on the field of vision [4], stereosepsis [5], utrocular discrimination [6] and allelotropia [7].

Several studies have evaluated bilateral symmetry in healthy eyes from indices obtained from corneal tomographs [8–10]. These technologies are well accepted in clinical practice for corneal topographies [11] because their measurements are accurate and repeatable. However, these studies present different results since they have been made from data processed by different commercial solutions. In addition, the indices used to evaluate the asymmetries are specific to each technology, and therefore they are difficult to compare. In this scenario, it would be of great interest to define metrics that could allow measurement of bilateral symmetry that were independent of each commercial solution using pre-processed data.

A few studies have used pre-processed data or raw data obtained from corneal tomographs. Some authors [12] analysed bilateral symmetry from corneal apex in healthy eyes using raw data, however it was not easy to locate the point of maximum curvature as it varies for each patient, therefore it is not a fixed point for comparing bilateral symmetries. Other authors evaluated the bilateral symmetry in healthy eyes from the repeatability of the measurements made by corneal tomographs [13], comparing the raw data obtained in each measure with reference points, concluding that the measurements made were stable and could define a measure of corneal symmetry based on a possible misalignment between successive measurements between partner eyes. Therefore, these studies showed that raw data is reliable data for the evaluation of bilateral symmetry.

Bilateral symmetry can be evaluated through so-called direct symmetry or through mirror symmetry. There are some studies that have evaluated both symmetries in non-pathological eyes [10, 14], however their results did not coincide, nor did they present data on the prevalence of one symmetry or another in healthy eyes, as the measurement technologies used in their studies presented different sensitivity for obtaining raw data.

In this study we present a method for evaluating bilateral symmetry (direct vs mirror) from the differences between the cartesian-radial coordinates, in pre-processed format or raw data, in healthy corneas (Right Eye vs Left Eye), using specific patient customized models.

2   Materials and Methods

2.1   Participants

This study involved 19 patients aged between 26 and 59 years (48% men, 52% women). The inclusion criteria were: both eyes healthy and no previous clinical history of eye surgery. The participants signed an informed consent to participate in the clinical study that was carried out according to the ethical standards agreed by the Declaration of Helsinki (7th revision, October 2013, Fortaleza, Brazil). The patients were part of the Iberia Biobank (Universidad Miguel Hernández de Elche, OFTARED-ISCIII). The study was approved by the UPCT ethics committee (CEI21_001).

2.2 Data Acquisition

The equipment used for the complete examination of each patient's eyes was the Sirius tomographer (CSO, Italy), based on Scheimpflug technology. Raw spatial data can be exported from the machine vision algorithm of the equipment in. csv format [2].

A protocol was defined for data acquisition, consisting in taking four consecutive measures per patient according to the following order: Right eye (DO), Left eye (OS), Right eye (DO) and Left eye (OS). All measurements were taken in the same session and were performed by an experienced optometrist. For each measurement, the patient was aligned and positioned according to a quality index that the tomograph includes, to check the reliability of acquisition of the measurement (quality measurement acquisition index, QMAI). Of all the measurements made, the one with the lowest QMAI was selected and extrinsic errors were eliminated when possible.

2.3 Methods

The artificial vision algorithm of the corneal tomographer allows scanning the anterior and posterior corneal surfaces in the form of points with a radial distribution, these spatial radial points are the result of the projection of the Plácido discs on the corneal surfaces and make up the so-called raw data [2]. These data are obtained in matrix form, and have been successfully used by our research team in several previous studies for the morpho-geometrical characterization of the human cornea [15, 16].

This study proposes to evaluate bilateral symmetry basing on direct symmetry and mirror symmetry in nonpathological eyes. To do so, we initially divided into 8 quadrants or octants the radial projections of the Placid Discs, for both the right eye and the left eye in direct symmetry (Fig. 1) and mirror symmetry (Fig. 2).
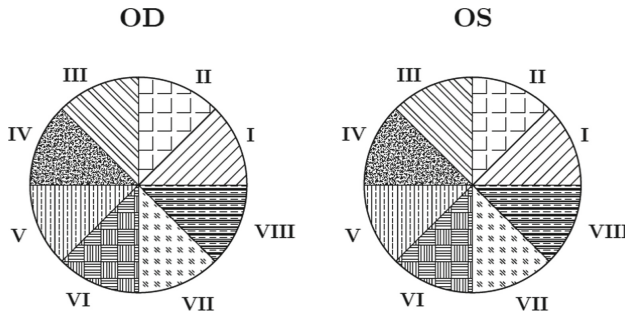
Fig. 1. Graphic representation of the octants of both eyes of a healthy patient in the case of direct symmetry.
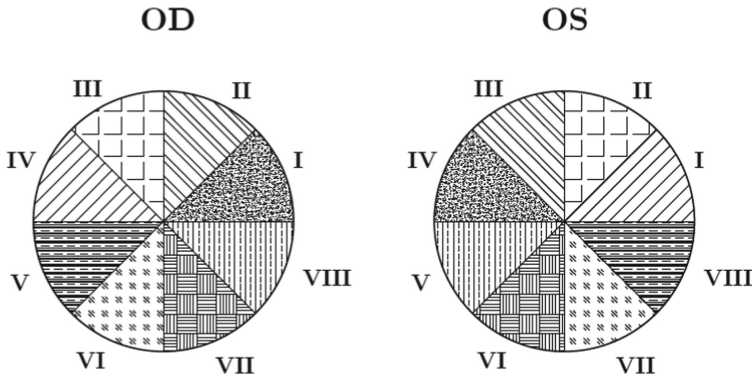
Fig. 2. Graphic representation of the octants of both eyes of a healthy patient in the case of mirror symmetry.

The direct symmetry consists in calculating the difference between the values of dimension z for each spatial coordinate (raw data) corresponding to the same quadrants, both for the right eye (DO) and for the left eye (OS) (Table 1).

Table 1. Protocol for the differences in direct symmetry.

Difference	Resulting matrix
$Z_{OD_I} - Z_{OS_I}$	$Z_{direct}(I)$
$Z_{OD_{II}} - Z_{OS_{II}}$	$Z_{direct}(II)$
$Z_{OD_{III}} - Z_{OS_{III}}$	$Z_{direct}(III)$
$Z_{OD_{IV}} - Z_{OS_{IV}}$	$Z_{direct}(IV)$
$Z_{OD_V} - Z_{OS_V}$	$Z_{direct}(V)$
$Z_{OD_{VI}} - Z_{OS_{VI}}$	$Z_{direct}(VI)$
$Z_{OD_{VII}} - Z_{OS_{VII}}$	$Z_{direct}(VII)$
$Z_{OD_{VIII}} - Z_{OS_{VIII}}$	$Z_{direct}(VIII)$

Mirror symmetry consists in taking the difference between the z-dimension values for each spatial coordinate (raw data) corresponding to mirror quadrants, for both the right rye (DO) and the left eye (OS) (Table 2). In other words, it is obtaining the difference between points located in diametrically opposed quadrants: I with IV, II with III, III with II, IV with I, etc.

To obtain the differences for both symmetries, a routine with the name "differences" was designed and programmed (Fig. 3) using Matlab software (Matworks, USA). It is necessary that raw input data is expressed in the form of the Z array for this function to work properly.

Table 2. Protocol for the differences in mirror symmetry.

Difference	Resulting matrix
$Z_{OD_I} - Z_{OS_{IV}}$	$Z_{mirror}(I - IV)$
$Z_{OD_{II}} - Z_{OS_{III}}$	$Z_{mirror}(II - III)$
$Z_{OD_{III}} - Z_{OS_{II}}$	$Z_{mirror}(III - II)$
$Z_{OD_{IV}} - Z_{OS_I}$	$Z_{mirror}(IV - I)$
$Z_{OD_V} - Z_{OS_{VIII}}$	$Z_{mirror}(V - VIII)$
$Z_{OD_{VI}} - Z_{OS_{VII}}$	$Z_{direct}(VI - VII)$
$Z_{OD_{VII}} - Z_{OS_{VI}}$	$Z_{direct}(VII - VI)$
$Z_{OD_{VIII}} - Z_{OS_V}$	$Z_{direct}(VIII - V)$
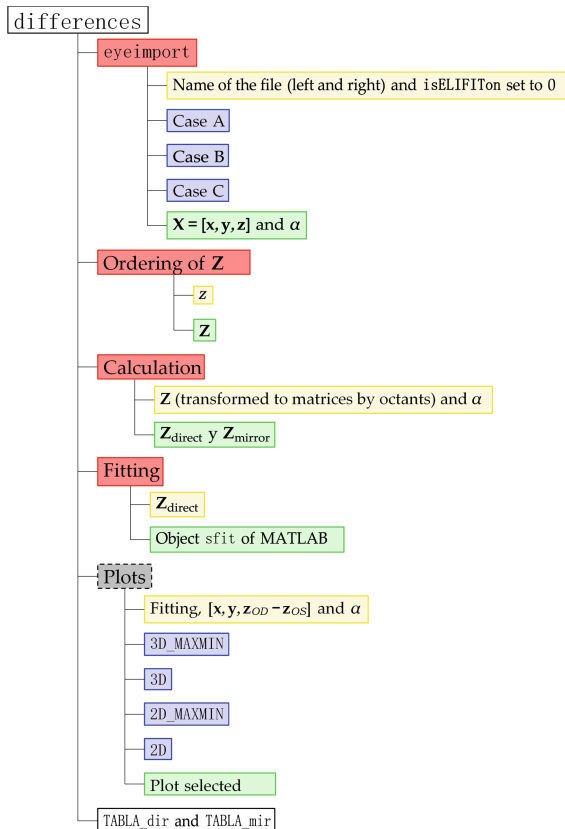
Fig. 3. Internal subroutines that make up the routine differences. Optional subroutines are displayed in grey with a dashed line box, needed subroutines are displayed in red, input options for the subroutine are depicted in blue, inputs are shown in yellow and outputs in green. The final numeric output is shown in white. (Color figure online)

The routine "differences" takes as input data the names of the files where the raw data obtained from the corneal tomographer is. The routine is divided into subsections that involve a code development (Fig. 2), these are:

- Ordering and reading of files (via eyeimport)
- Arrangement of the elevation matrix, Z
- Calculation
- Fitting
- Plots

2.3.1   Ordering and Reading of Files (eyeimport)

This function is responsible for importing to MATLAB the data (x, y, z) in three vectors x, y and z, which are in a file in format.csv. The data received by this function do not always have the same amount of information, being able to give three different cases, denoted by A, B and C.

2.3.2   Ordering of the Elevation Matrix, Z

The original elevation matrix could be understood as a vector composed of the elevations of all Placido disks, located one after the other. With this structure, it is considerably more difficult to identify in which octant and disc a certain point is located.

Therefore, the structure of this vector has been changed, creating a matrix called "elevation matrix, Z". The distribution of the elevation matrix will be 256 rows and 20 columns, so that in each column 256 points of a Placid disc of radius r, which oscillates between 0 and 4 mm, could be found. That means that, if we define Z as an "l x k" array, where l = 256 and k = 20, Eq. (1) is obtained:

$$\begin{bmatrix} z_1 & z_{257} & \cdots & z_{lk+1} \\ z_2 & z_{258} & \cdots & z_{lk+2} \\ \vdots & \vdots & \ddots & \vdots \\ z_l & z_{2l} & \cdots & z_{lk+l} \end{bmatrix} \tag{1}$$

To know the radius of the corresponding Placido disc, Eq. (2) is used

$$r_k = 0.2k \tag{2}$$

where k is a column of matrix Z, and its value can be any natural number within the range [1,20].

2.3.3   Calculation

To calculate the differences, both mirror and direct, the matrix Z of each corneal surface was divided into 8 parts, referring to the octants.

Also, and thanks to the structuring with which Z was created, identifying octants is a trivial task, since as there are 256 points, each octant will be composed of 32 points.

Thus, it has been established that the classification by octants follows the following Eq. (3):

$$Octant\ Limits = \left[\frac{l}{8}(O-1)+1,\ \frac{lO}{8} \right] \tag{3}$$

where O represents the octant in which the limits are to be calculated and $l = 256$. If $O = 1$, the limits will be [1, 32], and likewise could be calculated for any other octant.

Once the matrices of all the octants are obtained, the differences can be calculated, which depending on whether it is direct (Fig. 1) or mirror (Fig. 2). In these figures, octants with the same grating pattern will be differentiated. Tables 1 and 2 show the operations to be performed, as well as the matrices that are generated from these differences.

2.3.4 Fitting

For the adjustment of surfaces from raw data, MATLAB software has several types of algorithms internally implemented. This study focuses only in obtaining a map of elevations, therefore the objective is finding a surface that fits well with raw data, in this case and since there is no apparent pattern with the cloud of points, the adjustment used was based on the cubic interpolation method [17]. This interpolation is composed of fragment-defined functions, and therefore, it is very flexible. This function has been selected because it is a very fast interpolation function, with a good fit even for complex surfaces (Fig. 4).

In the case of mirror symmetry, this paper focuses only in numerical results, so there will be no graphical representations.

(A) 3D_MAXMIN   (B) 3D

(C) 2D_MAXMIN   (D) 2D
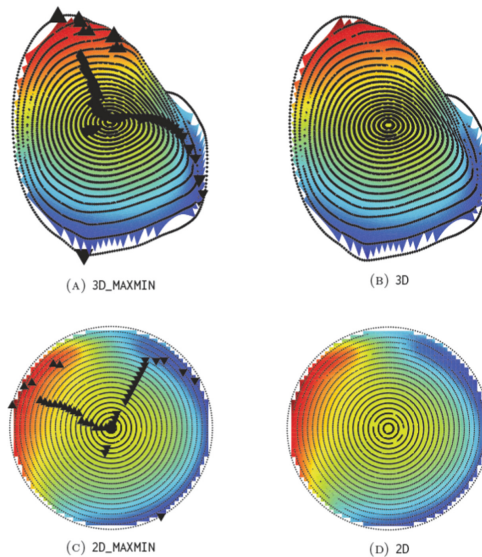
Fig. 4. Interpolated surfaces from the cubic interpolation function. Representation of maximum and minimum points (triangle up and down) in 2D/3D.

2.3.5 Plots

The "differences" routine is capable of generating a number of figures, related to direct symmetry. Depending on the **PLOTSon** parameter, we can find the following possibilities:

– 3D_MAXMIN (Fig. 4a). A three-dimensional elevation map is generated with maximum and minimum indicators (up triangles and down triangles, respectively)
– 3D (Fig. 4b). A three-dimensional elevation map is generated without maximum and minimum indicators
– 2D_MAXMIN (Fig. 4c). A two-dimensional elevation map is generated with indicators of maxima and minima (up triangles and down triangles, respectively)
– 2D (Fig. 4d). A two-dimensional elevation map is generated without indicators of maxima and minima.

2.3.6 Output

The data output is made by using the matrices "TABLA_dir" and "TABLA_mir". They are generated automatically, through temporary submatrices, which are introduced into "TABLA_dir" and "TABLA_mir". This makes the routine independent of the number of corneas being studied. The structure of each table is different, so it is necessary to differentiate between both.

- TABLA_dir. Considering the column value, the internal structure of this matrix would be as shown in Eq. (4). In this equation, $\Delta_{SEGr}(I)$ is a vector that contains the 256 differences of the SEG corneal face (anterior, ANT, or posterior, POST), Placido disk of radius r and for the number of the cornea l. Additionally, at the end of this vector, we can observe the maximum and minimum difference, their angular position and the corresponding octant.

$$TABLA_{dir} = \begin{bmatrix} \Delta_{ANT_{0.2}}(1)^T & \Delta_{ANT_{0.4}}(1)^T & \cdots & \Delta_{ANT_{3.8}}(1)^T & \Delta_{ANT_{4.0}}(1)^T \\ 0 & 0 & \cdots & 0 & 0 \\ \Delta_{POST_{0.2}}(1)^T & \Delta_{POST_{0.4}}(1)^T & \cdots & \Delta_{POST_{3.8}}(1)^T & \Delta_{POST_{4.0}}(1)^T \\ 0 & 0 & \cdots & 0 & 0 \\ 0 & 0 & \cdots & 0 & 0 \\ \Delta_{ANT_{0.2}}(2)^T & \Delta_{ANT_{0.4}}(2)^T & \cdots & \Delta_{ANT_{3.8}}(2)^T & \Delta_{ANT_{4.0}}(2)^T \\ 0 & 0 & \cdots & 0 & 0 \\ \Delta_{POST_{0.2}}(2)^T & \Delta_{POST_{0.4}}(2)^T & \cdots & \Delta_{POST_{3.8}}(2)^T & \Delta_{POST_{4.0}}(2)^T \\ 0 & 0 & \cdots & 0 & 0 \\ 0 & 0 & \cdots & 0 & 0 \\ \vdots & \vdots & \cdots & \vdots & \vdots \\ \Delta_{ANT_{0.2}}(l)^T & \Delta_{ANT_{0.4}}(l)^T & \cdots & \Delta_{ANT_{3.8}}(l)^T & \Delta_{ANT_{4.0}}(l)^T \\ 0 & 0 & \cdots & 0 & 0 \\ \Delta_{POST_{0.2}}(l)^T & \Delta_{POST_{0.4}}(l)^T & \cdots & \Delta_{POST_{3.8}}(l)^T & \Delta_{POST_{4.0}}(l)^T \\ 0 & 0 & \cdots & 0 & 0 \\ 0 & 0 & \cdots & 0 & 0 \end{bmatrix} \quad (4)$$

(4)

- TABLA_mir. The internal structure of this matrix can be seen in Eq. (5). where $Z_{SEG}(I)$ are blocks of matrices of the form shown in the table, with zeros between each row of this table.

$$Tabla_{mir} = \begin{bmatrix} Z_{ANT}(1) \\ 0 \\ 0 \\ Z_{POST}(1) \\ 0 \\ 0 \\ 0 \\ Z_{ANT}(2) \\ 0 \\ 0 \\ Z_{POST}(2) \\ \vdots \\ Z_{ANT}(l) \\ 0 \\ 0 \\ Z_{POST}(l) \\ 0 \\ 0 \\ 0 \end{bmatrix} \quad (5)$$

2.4 Statistical Analysis

Descriptive statistical analysis was performed with Excel software (Microsoft, USA). For this study, it has been calculated the mean value and the standard deviation of the differences for each coordinate z for each radius projected in both direct and mirror symmetry.

3 Results

Placido radii projected by the corneal tomographer can cover the entire central and paracentral region, going from r = 0 to r = 4 in steps of 0.2 mm, which includes 20 radii per corneal surface. Therefore, there will be 40 radii, which corresponds to a very large volume of data, and consequently present study has been limited to evaluating the spatial differences in direct and mirror symmetries just for the radii r = 1, 2, 3 and 4 of the anterior and posterior surfaces of the cornea.

With respect to direct symmetry and based on the protocol defined in Table 1, the results are presented in Table 2. Mirror symmetry results are presented in Table 3.

Table 3. Results for the direct symmetry model.

Difference (µm)	r = 1	r = 2	r = 3	r = 4
	Mean (SD)	Mean (SD)	Mean (SD)	Mean (SD)
Anterior surface				
I	−0.11 (0.71)	−1.14 (2.74)	−5.055 (6.95)	−18.22 (20.13)
II	−0.14 (0.79)	−0.94 (3.33)	−3.75 (8.35)	−10.12 (23.061)
III	−0.066 (0.65)	0.21 (2.90)	1.96 (6.78)	7.71 (18.48)
IV	0.064 (0.77)	0.75 (3.23)	4.00 (8.58)	17.11 (24.056)
V	0.025 (0.75)	0.22 (2.90)	1.97 (7.66)	12.26 (19.32)
VI	−0.20 (0.85)	−0.98 (3.61)	−2.024 (8.35)	−0.67 (16.93)
VII	−0.20 (0.55)	−1.11 (2.57)	−3.51 (6.60)	−10.32 (14.96)
VIII	0.0028 (0.67)	−0.73 (2.81)	−3.94 (7.13)	−16.66 (17.30)
Posterior surface				
I	10.15 (16.44)	22.74 (25.19)	34.44 (35.33)	23.80 (53.43)
II	2.25 (13.00)	6.50 (17.19)	10.093 (22.47)	−9.33 (45.027)
III	−6.28 (12.35)	−9.45 (16.19)	−10.39 (22.84)	3.15 (36.78)
IV	−14.044 (15.46)	−25.56 (25.084)	−34.71 (37.053)	−23.35 (55.70)
V	−14.62 (15.37)	−27.29 (24.47)	−42.33 (35.99)	−50.86 (53.55)
VI	−8.83 (12.99)	16.19 (17.61)	−24.43 (25.086)	−29.80 (35.88)
VII	1.85 (13.34)	6.26 (17.41)	11.49 (25.00)	15.053 (35.32)
VIII	8.23 (16.50)	20.34 (25.28)	34.64 (37.82)	43.037 (53.40)

Table 4. Results for the mirror symmetry model.

Difference (µm)	r = 1	r = 2	r = 3	r = 4
	Mean (SD)	Mean (SD)	Mean (SD)	Mean (SD)
Anterior surface				
I–IV	−0.022 (0.74)	−0.27 (3.10)	−1.043 (7.30)	−2.49 (16.97)
II–III	−0.13 (0.72)	−0.45 (3.25)	−1.20 (8.66)	−1.50 (21.40)
III–II	−0.081 (0.85)	−0.29 (3.56)	−0.59 (8.084)	−0.92 (16.30)
IV–I	−0.028 (0.83)	−0.12 (3.31)	−0.012 (7.95)	1.38 (16.77)
V–VIII	−0.10 (0.71)	−0.56 (2.79)	1.47 (6.42)	−2.17 (12.50)
VI–VII	−0.31 (0.79)	−1.24 (3.21)	−3.00 (7.31)	−5.12 (14.40)
VII–VI	−0.090 (0.87)	−0.84 (3.47)	−2.54 (8.33)	−5.87 (17.95)

(*continued*)

Table 4. (*continued*)

Difference (μm)	r = 1	r = 2	r = 3	r = 4
	Mean (SD)	Mean (SD)	Mean (SD)	Mean (SD)
VIII–V	0.13 (0.87)	0.057 (3.41)	−0.49 (8.20)	−2.22 (19.91)
Posterior surface				
I–IV	−2.42 (12.65)	−2.64 (16.22)	−2.47 (24.36)	−0.13 (32.12)
II–III	−2.53 (11.93)	−3.17 (14.89)	−2.81 (20.63)	−5.51 (37.11)
III–II	−1.51 (12.86)	0.22 (18.92)	2.52 (29.21)	−0.67 (37.90)
IV–I	−1.48 (13.25)	−0.19 (19.43)	2.19 (30.83)	0.58 (45.31)
V–VIII	−3.11 (11.51)	−3.55 (12.61)	−4.67 (16.85)	−8.37 (28.39)
VI–VII	−3.59 (12.25)	−5.46 (16.66)	−7.51 (25.28)	−11.63 (36.70)
VII–VI	−3.38 (12.74)	−4.47 (15.44)	5.43 (22.079)	−3.12 (31.55)
VIII–V	−3.28 (13.49)	−3.40 (16.31)	−3.022 (23.54)	0.54 (36.42)

In addition, regarding direct symmetry, a map of three-dimensional (3D_MAXMIN) and two-dimensional (2D_MAXMIN) elevations can be obtained. The maxima and minima obtained (upward triangles and downward triangles, respectively) correspond to the 20 Placid disks covering the corneal region from r = 0 to r = 4 mm for both healthy (Fig. 5) and keratoconus corneas (Fig. 6) (Table 4).
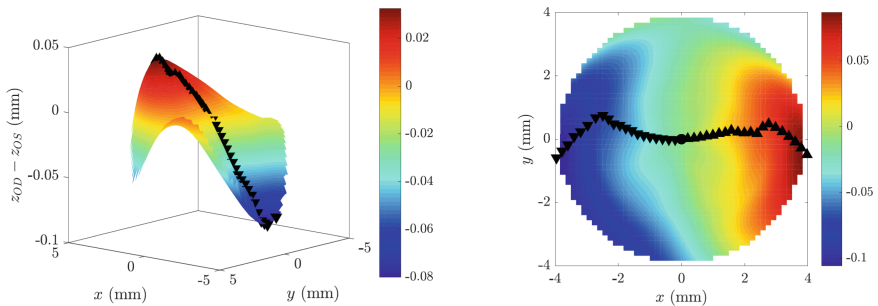
Fig. 5. Depiction of the direct differences in healthy cornea number 16. Differences 3D (left) and 2D (right).
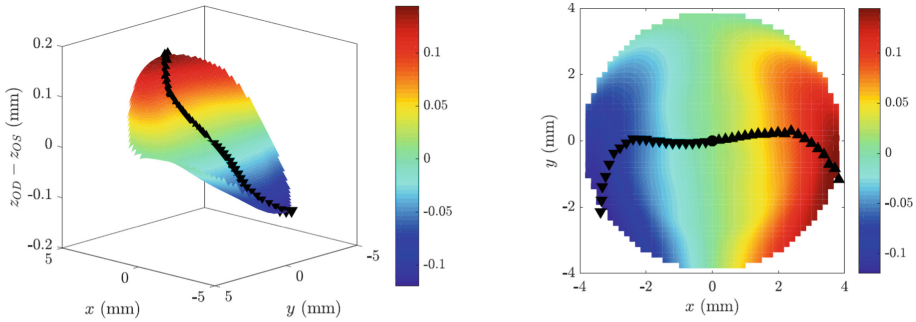
Fig. 6. Depiction of the direct differences in healthy diseased number 62. Differences 3D (left) and 2D (right).

4   Discussion

The morphological characterization of the cornea in clinical practice has experienced a growing demand lately, due to the importance of its study to understand how certain changes in the cornea affect the visual quality of patients, to the evolution, diagnosis and treatment of certain corneal pathologies, as well as to the planning of ophthalmological surgeries [11].

The modelling of the corneal structure can be done under two different approaches: using Generic models and Custom models. The first group includes those models that are designed aiming to the study of populations with one or more common characteristics, depending on the particular model. The second group aims to obtain particular results for a given patient, being very common to find customized models for patients with severe pathologies, on which it is very difficult to find generic models that capture the specific corneal morphology that they present [11].

In this research work, it has been evaluated both direct and mirror symmetry in terms of corneal elevation from the spatial coordinates resulting from the projection of Placido disks.

With regard to direct symmetry, the results obtained in the central and paracentral regions of the evaluated corneas reach the maximum differences in octants IV and V (radii 3 and 4) for the anterior surface. No significant differences existed in the rest of the corneal region. With respect to the posterior surface, differences were observed in octants VII and VIII (radii 2, 3 and 4), suggesting higher levels of asymmetry. This difference in direct symmetry on the posterior surface with respect to the anterior surface may be due to the potential effect of structural readjustment during the blinking phase [18].

With respect to mirror symmetry, the results obtained for the anterior surface present a high level of symmetry in both the anterior and posterior surfaces, we believe that the absence of significant differences in terms of height z between mirror octants, suggests a homogeneous distribution of corneal geometry in nonpathological corneas.

In addition, a map of direct differences (direct symmetry) has been made showing the value of the differences at each point, as well as the location of the maximum and minimum difference for each radius, both in 2D and 3D (Figs. 5 and 6), allowing the

results obtained to locate the greatest differences in the temporal zone, and the minimum ones in the nasal zone. These results coincide with those presented by other authors [12, 13].

5 Conclusion

In conclusion, there is a certain level of direct asymmetry in the corneal surfaces, especially in the posterior surfaces of the cornea, however the corneas in this study present mirror symmetry, which leads us to believe that healthy corneas have a relatively uniform geometry distribution, especially on the anterior corneal surface. Future studies should confirm the validity of present research for the detection of pathologies affecting the corneal structure, or to evaluate its biomechanical behaviour.

References

1. Roguin, A.L., Roguin, A., Roguin, N.: Historical advancements and evolution in understanding human anatomy and pathology: the contribution of the middle ages. Adv. Anat. Pathol. **28**, 171–177 (2021). https://doi.org/10.1097/pap.0000000000000296
2. Tubbs, R.S.: Anatomy, the eye of medicine. Clin. Anatomy (New York, N.Y.) **34**, 821 (2021). https://doi.org/10.1002/ca.23766
3. Park, S.H.: Current management of childhood Amblyopia. Korean J. Ophthalmol. KJO **33**, 557–568 (2019). https://doi.org/10.3341/kjo.2019.0061
4. Schwarzkopf, D.S., Schindler, A., Rees, G.: Knowing with which eye we see: utrocular discrimination and eye-specific signals in human visual cortex. PLoS ONE **5**, e13775 (2010). https://doi.org/10.1371/journal.pone.0013775
5. Poggio, G.F., Poggio, T.: The analysis of stereopsis. Annu. Rev. Neurosci. **7**, 379–412 (1984). https://doi.org/10.1146/annurev.ne.07.030184.002115
6. Arba Mosquera, S., Verma, S.: Bilateral symmetry in vision and influence of ocular surgical procedures on binocular vision: a topical review. J. Optometry **9**, 219–230 (2016). https://doi.org/10.1016/j.optom.2016.01.005
7. Erkelens, C.J., Muijs, A.J., van Ee, R.: Binocular alignment in different depth planes. Vis. Res. **36**, 2141–2147 (1996). https://doi.org/10.1016/0042-6989(95)00268-5
8. Zha, Y., Feng, W., Han, X., Cai, J.: Evaluation of myopic corneal diameter with the Orbscan II topography system. Graefe's archive for clinical and experimental ophthalmology = Albrecht von Graefes Archiv fur klinische und experimentelle Ophthalmologie **251**, 537–541 (2013). https://doi.org/10.1007/s00417-012-2069-6
9. Prakash, G., Ashok Kumar, D., Agarwal, A., Sarvanan, Y., Jacob, S., Agarwal, A.: Evaluation of bilateral minimum thickness of normal corneas based on Fourier-domain optical coherence tomography. J. Cataract Refract. Surg. **36**, 1365–1372 (2010). https://doi.org/10.1016/j.jcrs.2010.02.023
10. Hashemi, H., et al.: Enantiomorphism and rule similarity in the astigmatism axes of fellow eyes: a population-based study. J. Optometry **12**, 44–54 (2019). https://doi.org/10.1016/j.optom.2017.12.002

11. Cavas-Martínez, F., De la Cruz Sánchez, E., Nieto Martínez, J., Fernández Cañavate, F.J., Fernández-Pacheco, D.G.: Corneal topography in keratoconus: state of the art. Eye Vis. (London, England) **3**, 5 (2016). https://doi.org/10.1186/s40662-016-0036-8
12. Bao, F., et al.: Evaluation of the shape symmetry of bilateral normal corneas in a Chinese population. PLoS ONE **8**, e73412 (2013). https://doi.org/10.1371/journal.pone.0073412
13. Li, Y., Bao, F.J.: Interocular symmetry analysis of bilateral eyes. J. Med. Eng. Technol. **38**, 179–187 (2014). https://doi.org/10.3109/03091902.2014.899401
14. Zheng, X., Bao, F., Geraghty, B., Huang, J., Yu, A., Wang, Q.: High intercorneal symmetry in corneal biomechanical metrics. Eye Vis. (London, England) **3**, 7 (2016). https://doi.org/10.1186/s40662-016-0037-7
15. Velázquez, J.S., Cavas, F., Piñero, D.P., Cañavate, F.J.F., Alio del Barrio, J., Alio, J.L.: Morphogeometric analysis for characterization of keratoconus considering the spatial localization and projection of apex and minimum corneal thickness point. J. Adv. Res. **24**, 261–271 (2020). https://doi.org/10.1016/j.jare.2020.03.012
16. Toprak, I., Cavas, F., Velázquez, J.S., Alio del Barrio, J.L., Alio, J.L.: Subclinical keratoconus detection with three-dimensional (3-D) morphogeometric and volumetric analysis. Acta Ophthalmologica **98**, e933–e942 (2020). https://doi.org/10.1111/aos.14433
17. De Boor, C., De Boor, C.: A Practical Guide to Splines, vol. 27. Springer, New York (1978)
18. Savino, G., Battendieri, R., Riso, M., Traina, S., Poscia, A., D'Amico, G., Caporossi, A.: Corneal topographic changes after eyelid ptosis surgery. Cornea **35**, 501–505 (2016). https://doi.org/10.1097/ico.0000000000000729

Biomedical Signal Analysis

Automated TTC Image-Based Analysis of Mouse Brain Lesions

Gerasimos Damigos[1,2], Nefeli Zerva[2], Angelos Pavlopoulos[2],
Konstantina Chatzikyrkou[2], Argyro Koumenti[2], Konstantinos Moustakas[1],
Constantinos Pantos[2], Iordanis Mourouzis[2], Athanasios Lourbopoulos[2,3],
and Evangelia I. Zacharaki[1(✉)]

[1] VVR Group, Department of Electrical and Computer Engineering,
University of Patras, 26504 Rio, Greece
moustakas@ece.upatras.gr, ezachar@upatras.gr
[2] Department of Pharmacology, Athens Medical School, 11527 Athens, Greece
{cpantos,imour}@med.uoa.gr
[3] Institute for Stroke and Dementia Research (ISD), University of Munich Medical
Center, Munich, Germany

Abstract. Small animals stroke models have widely been used to study
the mechanisms of ischemic brain damage in controllable experimental set-
tings. The evaluation of stroke lesions mainly relies on visual inspection of
tissue samples collected after brain sectioning, slice staining and scanning,
a procedure that is highly subjective and prone to human error. In this
study we developed a machine-learning based methodology for automatic
segmentation of lesions in mouse brain tissue samples, stained with Triph-
enyltetrazolium chloride (2% TTC). Our approach relies on the creation of
a statistical mouse brain atlas of healthy TTC slices that was lacking in the
literature. For this purpose we applied tissue clustering and Markov Ran-
dom Fields (MRF) for brain tissue detection followed by deformable image
registration for spatial normalization. The obtained statistical atlas is then
exploited by outlier detection techniques and Random Forest classifica-
tion to extract lesion probability maps in new slices. The good agreement
between our segmentation results and expert-based lesion delineation on
12 mouse brains highlights the potential of the proposed approach to auto-
mate stroke volumetry analysis, thereby contributing to increased trans-
lational capacity of experimental stroke.

1 Introduction

Experimental mice models provide the means to understand the pathophysiol-
ogy of brain infarction and subsequent mechanisms of neuronal survival, which
is crucial for the development of therapeutic interventions. A deep insight into
the spatio-temporal microstructural damage and perfusional alterations can be
obtained using in vivo advanced magnetic resonance imaging (MRI) techniques,
such as diffusion and perfusion weighted imaging. However the availability of

---

A. Lourbopoulos and E. I. Zacharaki–Contributed equally to the work.

such imaging techniques, especially for small animals requiring dedicated micro-tomographs, is very limited. Therefore, the most common approach has been histopathological and immunohistochemical analysis, in which case the standard procedure for lesion quantification is based on manual measurements performed by human experts through inspection of the scanned brain slices [5]. Common parameters of interest are the hemispheric infarction volume and edema of the infarcted hemisphere, whereas more dedicated ones include the cortical and striatal infarction areas at each coronal level [5]. This quantification procedure is time consuming and labor intensive, highly subjective, prone to human error and non-reproducible.

To automate this process, in the case of in vivo assement of lesions and pathologies in human brains, many methods have been proposed that exploit high resolution medical imaging information. A widely recognized approach is based on spatial normalization of the brain volume to a standard stereotaxic space using linear or non-linear registration techniques, and then performing voxel-wise statistical tests [11] or multi-variate pattern analysis [3,13]. Voxel-based morphometry and statistical analysis techniques have also been combined with supervised classification methods in brain pathology segmentation problems. These methods use manually delineated samples and aim to train a predictive model using as features the original image intensities or other attributes derived from image filtering, transformations or decomposition techniques. Classification models, such as support vector machines (SVM), random forest (RF) and neural networks, can subsequently be trained upon these features to assign labels to new samples.

All the above mentioned methods have been implemented for lesion segmentation in high resolution images of the human brain, while works on lesion detection in ex vivo mouse brain tissue slices is very limited. Efforts to improve lesion quantification have used semi-automated analysis of TTC-stained sections with ImageJ, which results in faster and less human-dependent (thus "objective") stroke volumetry data [6], though still subjected to significant detection errors (false-positive) due to a "simplified" binary transformation analysis approach of the ischemic lesion. Moreover, the only available anatomic reference atlases are constructed utilizing 3D high resolution modalities, thus being unsuitable for comparison with 2D low resolution TTC slices. Additionally for TTC-stained tissue slices, no prior work has aimed to encode the spatial variation in the anatomy that is present not only due to anatomical differences across mice, but also caused due to the experimental procedure in the preparation of the tissue slices.

In this study, we present a novel framework developed for quantitative mouse brain lesion analysis in slices stained with TTC. Our method is based on learning the statistical variation of pixel intensities in pathology free samples, co-registered in a common space, and then use these for new TTC-stained tissue slices with ischemic lesion to calculate statistical maps, that express pixel-wise deviation from normality. For segmentation refinement, the obtained statistical maps are also combined with multiple color pixel intensities in a binary

random forest (RF) classifier. Additional topological constraints are used to eliminate most false positive detections, leading to a compact region with tissue pathology, ready for quantitative volumetric analysis. Our methodology has been already assessed in two separate experimental sets [1], showing improved performance over all previous TTC-volumetry approaches used for comparison. In this paper we present the overall methodology and algorithmic implementation, while further information on the experimental procedure and exploitation of our framework for infarct volumetry can be found in [1].

2   Methodology Overview

The aim of our framework is to detect and analyze stroke lesions in coronal TTC-slices of mouse brain. Since brain lesions show a similar intensity profile with healthy tissue in some anatomical areas, such as the corpus callosum and white matter tracts, automatic segmentation fails if it relies only on imaging information. Therefore, we incorporated anatomical information by transforming intensities to pixel-wise probabilistic scores using a statistical atlas. With the term "atlas" we refer to a statistical representation of spatial intensities at each 2D slice (defined by a coronal plane at the anteroposterior axis), that consists of an average TTC image and a standard deviation image representing the variation of normal brain anatomy. As no reference statistics for TTC-stained images (TTC-atlas) exist so far, we constructed it de novo from 2D coronal slices from normal (naive) C57/bl6 mice. A subsequent semi-automated registration of the Allen mouse brain atlas [2] to the TTC atlas space allowed to map the Allens anatomical regions to the TTC-atlas space, necessary for neuroanatomical mapping of the stroke lesions.

Then, in order to segment infarcts in scanned TTC-slides, we developed and evaluated an automated lesion analysis framework based on outlier detection and machine learning (Fig. 1). Specifically, lesion detection is conducted in two main steps: (1) An outlier tissue probability map is constructed which localizes deviations from normality expressed by the statistical atlas. A thresholding operation is then used to evaluate the affected lesion, restricted in the respective hemisphere (as only unilateral stroke-lesions are considered), identified by utilizing the constructed TTC atlas. (2) The outlier map is introduced to a machine learning model along with tissue intensity information to estimate the affected areas. Topological constraints are enforced on the obtained segmentation mask through morphological operations (e.g. to remove isolated pixels). The schematic diagram of the two methodological components, i.e. the construction of the TTC atlas using healthy brains and the segmentation of lesions in diseased brains, is illustrated in Fig. 1 and analyzed with more details in the subsequent sections.

2.1   Preprocessing and Background Segmentation

Let's consider the intensities of a TTC slice for each pixel $x \in R^2$ as a 2D image $I(x)$, and also let the set of segmentation labels be $S = \{s_1, s_2, s_3\}$ for *background* (BG), *healthy* (HL) brain tissue (reddish region in TTC) and *lesion* (LS)
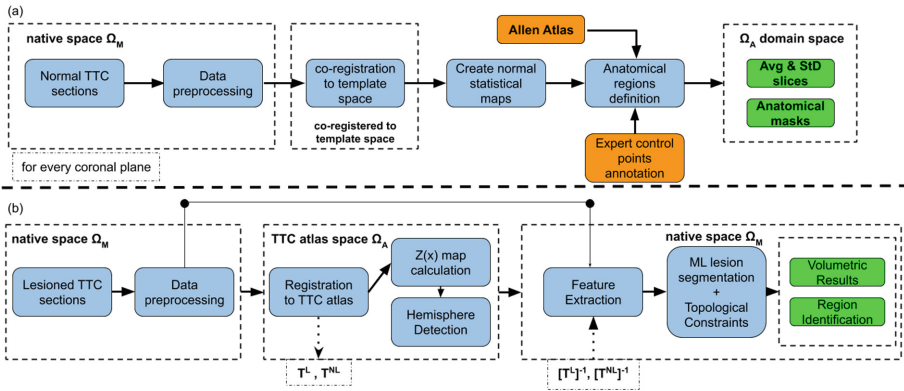
Fig. 1. Proposed lesion segmentation framework. a) TTC atlas construction. b) Automated lesion segmentation.

class (infarcted brain tissue with bright near-white color in TTC). Preprocessing begins with background extraction for non tissue regions removal. This is performed through multiple steps. Initially we divide the input image in superpixels to encapsulate local neighborhood information [4] and then apply K-means classification with three centers to assign a class label s_i to every superpixel. Markov Random Fields (MRF) [8] optimization is subsequently performed to reduce spatial incoherence in classification. An example of 3 class (i.e. brain, lesion, background) segmentation before and after the application of MRFs is shown in Fig. 2. The complementary of the background mask $(M_{BG}(x))$ is then used to extract the brain (healthy and infarcted) tissue, i.e. $I_{brain}(x) = I(x) \circ \overline{M_{BG}(x)}$, where "$\circ$" is the Hadamard product.

Fig. 2. Segmentation example of a TTC slice (left) with kmeans before (middle) and after (right) Markov Random Fields. The colors indicate the hyper-intense region part of which is lesion (blue), the healthy brain tissue (orange), and the background (black). (Color figure online)

Preprocessing is concluded with spatial normalization of all tissue samples which includes image centering based on the center of mass and removal of large rotational misalignment caused by differences in placement of the tissue samples in the scanner. For global alignment we perform Principal Components Analysis

[10] on the binary brain tissue mask $(\overline{M_{BG}(x)})$ and rotate the corresponding image slice $I_{brain}(x)$ according to the orientation indicated by the first principal component.

2.2   TTC Atlas Construction

The developed 2D TTC-atlas encapsulates statistical information for the image intensity of healthy (pathology-free) brains at each anatomical location. We inherited a coordinate system with anterior-superior-right orientation similar to Paxinos coordinates [9], where every slice is represented by a coronal plane at an index i, with $i = 0$ defining the plane of bregma ($i > 0$ indicates a plane anterior to bregma and $i < 0$ posterior to bregma). Thereby, every coronal plane (slice) of the TTC atlas is represented in its own space $\Omega_A^j, j = 1, ..., K$, where K is the number of slices of the TTC atlas. Assuming that image intensity for every tissue follows a Gaussian distribution, we can parametrize the distribution by the average and standard deviation values which together define the TTC atlas. To calculate these values from given samples, the images have to be first coregistered so that each pixel corresponds to the same anatomical location across mouse brains. Therefore, for every coronal plane j we selected one of the available image slices as template ($I_A^j \in \Omega_A^j$) and registered the corresponding slices of the remaining mouse brains ($I_M^j \in \Omega_M^j$) to it. The registration problem seeks to find a transformation $T^j : \Omega_M^j \to \Omega_A^j$ that spatially aligns the moving image to the reference image space. Omitting the index j for simplicity, we define the transformation $T(x)$ as a composition of a linear ($T^L(x)$) and a non-linear (deformable) (T^{NL}) mapping: $T(x) = T^{NL} \circ T^L(x)$). The linear component (affine in our case) accounts for translation, rotation and shearing differences due to the experimental setup and global variations in the mouse brain anatomies, whereas the non-linear component corrects local deformities and is obtained with Dramms [7] deformable mapping algorithm.

Eventually, after co-registration of all available brain slices for each coronal plane, we compute the pixel-wise average ($AVG(x)$) and standard deviation ($STD(x)$) across brains to quantify the maximum-likelihood estimate of each TTC-slice spatial intensity. The methodology for the TTC atlas calculation is shown in Fig. 1-a, whereas their utilization for lesion detection in new brains is shown in Fig. 1-b.

Definition of Anatomical Areas on the TTC-atlas. After the completion of the TTC atlas construction we need to define the anatomical regions at each TTC atlas coronal plane. This is essential for the acquisition of anatomical information of the lesioned areas. We map anatomical information from Allen Brain Atlas (ABA) [2] to the TTC atlas by transforming ABA's and TTC's atlas corresponding coronal slices. This mapping is a semi-automated registration process, as an expert researcher manually annotates corresponding control points in few slices. We utilize the annotated points and a Local Weighted Mean transformation to map the ABA's anatomical masks to TTC atlas space.

2.3   Atlas-Based Abnormality Detection

Lesion detection is automatically performed by detecting abnormality regions based on the spatial likelihood of the tissue being healthy. Let $I(x)$ denote the intensity of the pixel x in a 2D coronal slice. Assuming Gaussian distribution, we use as abnormality score the z-score, $Z(x) = \frac{I(x)-AVG(x)}{STD(x)}$, which is a metric proportional to the log-likelihood of observing the intensity I at pixel x if the brain is healthy, where $AVG(x)$ and $STD(x)$ are the mean and standard deviation values at pixel x of the TTC atlas. Thresholding of this abnormality score provides an initial lesion segmentation mask, $M_{LS}^0(x)$. The threshold value is determined empirically based on a few left-out brain slices with stroke. At this step the mask includes many false positives at the boundary of each slice, which have image intensities almost identical to those of the infarct and are mainly due to the local staining procedure. An example is shown in Fig. 3). Thereby, for a robust LS segmentation approach, we take into account that in our experimental procedure only unilateral stroke-lesions are considered, thus the identification of the affected hemisphere will allow to reduce the search space. Thereby, the hemisphere with significantly more *abnormal tissue* (as quantified by the mask M_{LS}^0) is considered as being the one affected.

In order to identify the boundary separating the two brain hemispheres, the midline of a coronal slice (symmetry line) has to be extracted. For extraction of the midline we seek and identify the axis of brain symmetry utilizing the ABA's anatomical masks. Midline calculation on the original ABA masks is a relative simple process as ABA is a "rotation free" atlas constructed in perfect symmetry. We later transform the constructed hemisphere masks using the transformations obtained as described in Sect. 2.2. After hemisphere segmentation, the abnormality map is masked out retaining only the part in the affected hemisphere (denoted as $Z_H(x)$) and its values are introduced as features for the next and final step of the segmentation process, as presented next.

2.4   Lesion Segmentation Based on Machine Learning (ML)

The second step of our methodology is formulated as a binary classification problem of the identified LS regions into actual lesion or non-lesion tissue (false positives) and solved using a random forest (RF) classifier [12]. For this purpose three types of features are combined and introduced to RF:

– 3 intensity features from each of the 3 RGB color channels (thus 9 features in total), i.e. the original pixel intensity and the values obtained after median filtering within a 3×3 kernel and after Gaussian filtering with $sigma = 2$ for the kernel. The respective kernel parameters were experimentally optimized.
– 2 features expressing lesion probability in respect to healthy mouse brain population, i.e. the original probability value $Z_H(x)$ and the value after median filtering
– 2 features expressing lesion probability in respect to brain symmetry calculated as the difference in $Z(x)$ between the two hemispheres.

The combined 13 features are used to train an RF classifier by minimizing the expected misclassification cost among lesion and healthy tissue classes. Finally, remaining false positives are further reduced by applying morphological operations producing our final lesion segmentation for each brain slice. The concatenation of the lesions masks at each coronal index provides eventually the stroke volumetry and neuroanatomical region identification.

3   Results and Conclusions

The dataset included 517 slices (after excluding those with strong artefacts produced during the experimental procedure) from 83 healthy mouse brains for the construction of the TTC atlas, and 77 slices from 14 mouse brains with induced ischemic stroke lesions [1]. The dataset with lesions was split into two parts for training (5 slices) and testing (72 slices) of the RF classifier, respectively. It should be noted that with the adopted experimental procedure – including slice cutting, tissue staining, scanning and digitization – some of the tissue slices used for testing had proper quality ($n = 47$), whereas others were of low quality ($n = 25$). Segmentation accuracy was assessed against manual delineation provided by an expert using data with mixed image quality (all 72 testing slices) or only good image quality. The average and standard deviation (across all samples) of the dice coefficient, false positive rate and true positive rate of the proposed method were respectively 0.79 ± 0.10, 0.02 ± 0.02, 0.80 ± 0.12 for mixed quality data, and 0.90 ± 0.06, 0.02 ± 0.02, 0.89 ± 0.07 for good quality data. The corresponding overlap metrics for atlas-based segmentation of mixed quality data without the ML component were 0.70 ± 0.11, 0.03 ± 0.02 and 0.69 ± 0.14, respectively. An example is illustrated in Fig. 3. A more comprehensive set of results of lesion volume analysis on an independent cohort of animals and evaluation of the whole methodology in respect to image-acquisition modalities and resolutions can be found in [1].
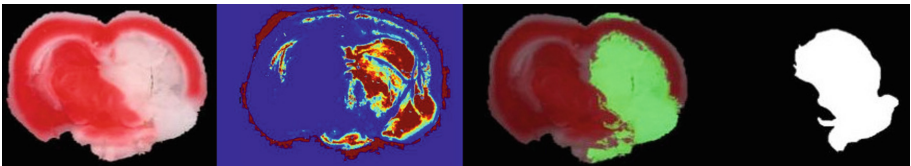
Fig. 3. Example of a coronal slice of a mouse brain with stroke. From left to right: Image after BG extraction and PCA-based spatial standardization, atlas-based abnormality map ($Z(x)$), final LS segmentation (in green), expert-based annotation used as ground truth. (Color figure online)

Concluding, in this paper we presented an automated methodology that fuses features describing outlier probability, brain symmetry, expert knowledge and topological constraints into a lesion detection scheme designed (for the first

time) for TTC-stained slices. The good volume overlap agreement with manually annotated lesion masks indicates that the developed tool has a high potential in replacing the current practice which is based on non-reproducible visual inspection.

References

1. Damigos, G., et al.: Machine learning based analysis of stroke lesions on mouse tissue sections. J. Cereb. Blood Flow Metab., 1–15 (2022)
2. Dong, H.: The Allen Reference Atlas: A Digital Color Brain Atlas of the C57Bl/6J Male Mouse. Wiley (2008)
3. Erus, G., Zacharaki, E., Davatzikos, C.: Individualized statistical learning from medical image databases: application to identification of brain lesions. Med. Image Anal. **18**(3), 542–554 (2014)
4. Fulkerson, B., Vedaldi, A., Soatto, S.: Class segmentation and object localization with superpixel neighborhoods. In: 2009 IEEE 12th International Conference on Computer Vision, pp. 670–677. IEEE (2009)
5. Lourbopoulos, A., Karacostas, D., Artemis, N., Milonas, I., Grigoriadis, N.: Effectiveness of a new modified intraluminal suture for temporary middle cerebral artery occlusion in rats of various weight. J. Neurosci. Meth. **173**(2), 225–234 (2008)
6. Macleod, M., et al.: Risk of bias in reports of in vivo research: a focus for improvement. PLoS Biol. **13**(10), e1002273 (2015)
7. Ou, Y., Sotiras, A., Paragios, N., Davatzikos, C.: DRAMMS: deformable registration via attribute matching and mutual-saliency weighting. Med. Image Anal. **15**(4), 622–639 (2011)
8. Paragios, N., Ferrante, E., Glocker, B., Komodakis, N., Parisot, S., Zacharaki, E.: (Hyper)-graphical models in biomedical image analysis. Med. Image Anal. **33**, 102–106 (2016)
9. Paxinos, G., Franklin, K.B.: Paxinos and Franklin's the Mouse brain in Stereotaxic Coordinates. Academic Press (2019)
10. Rehman, H., Lee, S.: Automatic image alignment using principal component analysis. IEEE Access **6**, 72063–72072 (2018)
11. Rorden, C., Brett, M.: Stereotaxic display of brain lesions. Behav. Neurol. **12**(4), 191–200 (2000)
12. Touw, W., et al.: Data mining in the life sciences with random forest: a walk in the park or lost in the jungle? Brief. Bioinform. **14**(3), 315–326 (2013)
13. Zacharaki, E.I., Bezerianos, A.: Abnormality segmentation in brain images via distributed estimation. IEEE Trans. Inf. Technol. Biomed. **16**(3), 330–338 (2012)

PET-Neuroimaging and Neuropsychological Study for Early Cognitive Impairment in Parkinson's Disease

Sergey Lytaev[1,2(✉)]

[1] St. Petersburg State Pediatric Medical University, St. Petersburg 194100, Russia
physiology@gpmu.org
[2] St. Petersburg Federal Research Center of the Russian Academy of Science, St. Petersburg 199178, Russia

Abstract. To present time, the world science has accumulated a sufficient amount of information on the quantitative changes in the rate of glucose utilization according to positron emission tomography (PET) with 18-fluorodeoxyglucose (FDG) in Parkinson's disease (PD) with dementia. It was found that in the early stages of dementia with PD, there is a dysfunction of the frontal lobes, while PET examination of patients with PD with dementia shows the quantitative changes in the rate of glucose utilization. On this basis, it seems relevant to compare the functional state of the brain structures and the results of neuropsychological studies in patients with PD with varying severity of cognitive impairment. The present research was aimed to investigate the relationship between early cognitive violations according to neuropsychological research and the rate of glucose metabolism in different brain areas during PET scanning in patients with Parkinson's disease. Neuropsychological testing consisted of clinical interviews, observation, questioning, Mini-Mental State Exam (MMSE) and frontal assessment battery (FAB). According to the research outcomes, it was found that with initial cognitive impairment, determined by FAB, a quantitative change in the rate of glucose utilization is observed, similar to the pattern found in patients with cognitive disorders in PD. Four factors were established: factor 1 – dorsal system of attention (voluntary attention), factor 2 – ventral system of attention (involuntary attention), factor 3 – system of the state of operational rest, factor 4 – visual projective zone. The precentral cortex of the frontal areas and the upper half of the parietal zones of big brain are constitute the 1st factor. The anterior third of the convexital part of the frontal areas and the lower half of the parietal zones are the 2nd factor. The 3rd factor includes the 23, 36, 29 and 30 cytoarchitectonic Brodmann fields (the posterior cingulate gyrus). Primary visual area (17th Brodmann's field) is the 4th factor.

Keywords: Parkinson's disease · Positron emission tomography · 18-fluorodeoxyglucose · Cognitive disorders · Lewy body · Dementia

1 Introduction

Parkinson's disease is one of the most general neurodegenerative diseases. The incidence in different countries is 150–200 cases per 100,000 population. The peak incidence is at 60–65 years [15]. Traditionally, PD is associated with a deficiency of the dopaminergic system, which manifests itself in extrapyramidal movement disorders. In addition, this disease is accompanied by a wide differences of not only movement violations, but also autonomic, mental, cognitive, dyssomnic and sensory disorders. As the progression progresses, some of these symptoms may become dominant [4, 7, 10, 23].

The level of preservation of person cognitive functions covers a wide range - from normal to severely retarded. Differential diagnosis of such violations often causes clinical difficulties, the solution of which increases the value of neuroimaging tools in this area. The most common causes of dementia are neurodegenerative disorders, among which the most common are Alzheimer's and Parkinson's, which are accompanied by significant changes in brain metabolism with devastating neurological as well as economic, social and clinical consequences. Such changes are noticeable through positron emission tomography (PET) already at the earliest period of disease [9, 12, 13, 21].

Most often, PET brain researches in neurodegenerative disorders are performed using [18F] fluorodeoxyglucose (FDG) – an imaged radiopharmaceutical. Such researches demonstrate diagnostic and prognostic value in assessing cognitive impairments and differential diagnosis of primary neurodegenerative disorders with a different etiology of changes in cognitive functions [2, 3, 15, 23].

Dementia affects about 24 million people worldwide, of which about 5 million new cases are recorded annually [23, 27]. The most common cause of decline that ultimately leads to dementia, and the most well-studied is Alzheimer's disease (AD). This condition occurs in 10–15% of people over 65 and 40–50% of all over 85. Other causes of cognitive decline are also considered dementia with Lewy bodies, Parkinson's disease, cerebrovascular disease, fronto-temporal dementia, Creutzfeldt-Jakob disease, HIV-related dementia, neurosyphilis, normal pressure hydrocephalus, and dementia due to exposure to current – septic substances (heavy metals, alcohol, other drugs), metabolic disorders or mental disorders.

Cognitive impairments, including mild cognitive violations and dementia in Parkinson's disease, are among the most common non-movement violations in PD. Cognitive impairment manifests itself in more than 80% of patients after about 15 years of illness [10], and the risk of dementia in PD patients is several times higher than in the general population [9].

Considering the problem of dementia in PD, first of all, it is required to carry out a differential diagnosis between PD and dementia with Lewy bodies. Most often in clinical practice, they rely on indicators of the onset of cognitive impairment and the presence of visual hallucinations during the first year of the disease [9]. Often there is a comorbid existence of PD and Alzheimer's disease, as well as PD and manifestations of discirculatory encephalopathy. It is also important to note that therapy for motor disorders in PD is not sufficient to prevent the development of dementia in PD [22].

Lewy body dementia (DLB) and Parkinson's disease dementia (PDD) are the next most common neurodegenerative dementia after Alzheimer's disease (AD) in the elderly

[9, 27]. DLB and PDD, conceptualized as spectrum disorders, are associated with abnormal accumulation of α-synuclein and have clinical and pathological overlap with variations in the temporal set of motor and cognitive symptoms [11]. The prevalence of DLB ranges from 15 to 25% of diagnoses [8], but the clinical manifestation is much lower. Less than half of cases can be correctly identified by routine clinical examination [21]. Updating the DLB diagnostic criteria involves the use of validated and recommended biomarkers, but a significant lack of compliance complicates the assessment of DLB prevalence.

Patients with DLB make up from 0 to 30.5% of cases of elderly people with dementia in clinical trials [9], while PDD is 3.6–30% [1, 24, 25] with more than 80% in patients with BP [6]. DLB prevalence among various population studies ranges from 0 to 26% of all cases of dementia, which is in line with the population prevalence (about 10%) in a rural island town in East Asia [9].

Cognitive impairments in the early stages of PD are mainly characterized by signs of mild disorder of executive functions, requiring action planning and switching from one task to another [13]. To determine such disorders, various neuropsychological tests are traditionally used to assess the functions of the frontal lobes and executive functions [7, 15, 16].

Today, positron emission tomography of the brain is practically a necessary application for clinical diagnosis and assessment of changes in cognitive abilities. The degree of preservation of human cognitive functioning is a wide range. This can vary from normal for a given person to a violation of subjective perception, which has not been objectively tested in neuropsychological research. At the same time, subjective disorders can represent the earliest stages of a decrease in minimally disturbed states with neuropsychological functioning to an intermediate state - "mild cognitive impairment" (MCI) [23]. And this is already a state of mild, moderate or severe dementia. At the same time, some people suffering from milder forms of impairment are on the path of a progressive decline, others will have stable or reversible forms of impairment, which greatly complicates the differential diagnosis with the real cause, which is often difficult to determine clinically.

Recently, for differential diagnosis, they increasingly resort to various neuroimaging methods that determine both the structural integrity and the functional activity of different parts of the brain. The advantages of functional neuroimaging methods, such as PET, single-photon computed tomography, functional magnetic resonance imaging and magnetic resonance spectroscopy, include their early sensitivity to dysfunction of visualized structures before the onset of atrophic changes [14, 17, 28]. Information has been accumulated on the pattern of changes in the rate of glucose metabolism according to PET with 18-fluorodeoxyglucose (FDG) in PD with dementia [22]. It was found that in the early stages of dementia with PD, there is a dysfunction of the frontal lobes, while PET examination of patients with PD with dementia shows a characteristic pattern of changes in the rate of glucose metabolism.

Based on the foregoing, it seems relevant to compare the functional state of the brain structures and the results of neuropsychological studies in patients with PD with varying severity of cognitive impairments. This study was aimed to research the relationship between early cognitive impairment according to neuropsychological research and the

rate of glucose metabolism in different parts of the brain in patients with Parkinson's disease.

2 Methods

The study group consisted of patients (31 people) with verified Parkinson's disease, aged 41 to 77 years, who underwent inpatient and/or outpatient treatment in a hospital clinic. The exclusion criteria were gross morphological changes on MRI and PET, as well as severe cognitive impairment (MMSE < 23). The control group consisted of patients of the same age group without cognitive impairment. The exclusion criterion for this group of patients was also pronounced morphological changes according to MRI and PET.

To assess the rate of glucose metabolism, a standard technique was used – immediately before the study, a radiopharmaceutical [18F] – fluorodeoxyglucose was synthesized, which was injected intravenously at a dose of 3 to 5 mCi in 8 ml of saline. During the accumulation of the radiopharmaceutical, the patient was in a room with dim light, low noise level and minimal motor activity. PET scanning was performed 30–40 min after injection for 20 min [26].

The analysis of the obtained PET images was carried out as follows. At the first stage, in order to further select standardized regions of interest (RI) that collectively cover the entire volume of the brain, individual images were reduced to a standard form in accordance with the coordinate space of the Talairak stereotaxic atlas [26]. For this, the SPM software package was used, and then for RI corresponding to Brodmann's fields and subcortical structures, using the WFU PicAtlas software, the average values of the accumulated FDG activity were calculated.

The level of accumulated activity in the OI recorded during the scan is associated with the rate of glucose metabolism in this area. To exclude a number of "technical" reasons for the variability of the recorded accumulated activity, including the activity of the radiopharmaceutical administered during the injection, the duration of scanning, and inaccuracies in patient positioning in the camera's field of view (the depth of field of view of the PC2048-15B tomograph, equal to 96 mm, was not always sufficient for scanning the entire brain simultaneously), a procedure was used to normalize the accumulated activity in the RI to the average accumulated activity in the reference area.

As this area, the bilateral insular cortex was used, due to its anatomical location present in PET images of all patients. For neuropsychological testing [15], a complex of psychological techniques was applied, consisting of a clinical interview, observation, questioning and testing according to the methods of Mini-Mental State Exam (MMSE) and frontal assessment battery. The MMSE test consists of 9 items, was first proposed in 1975 by Folstein [7] and is currently one of the most common methods for screening and assessing the dynamics of cognitive impairment. The overall score on the test results can range from 0 to 30. Values in the range of 26–30 points are considered normal, 21–25 - mild cognitive impairment, below 20 - moderate, and from 0 to 9 - severe cognitive impairment. The Frontal Assessment Battery (FAB) test is applied to assess frontal lobe function and is widely used in the differential diagnosis of Alzheimer's disease and frontotemporal dementia. The test consists of 6 tasks and is assessed on an 18-point scale. If a patient scores a total of 16–18 points during testing, it is considered that the frontal functions are completely preserved [5].

The data of neuropsychological research and the results of PET-scanning were processed using factor analysis by the method of principal components by the method of varimax-rotation. The factor was included in the factorial solution if the Kaiser criterion was met (i.e., if its eigenvalue was greater than 1). A variable with a load on the factor greater than 0.45 was regarded as included in the factor.

In Fig. 1 shows the typical distribution of 18-FDG in MRI scanning in patients of the two study groups with PD.
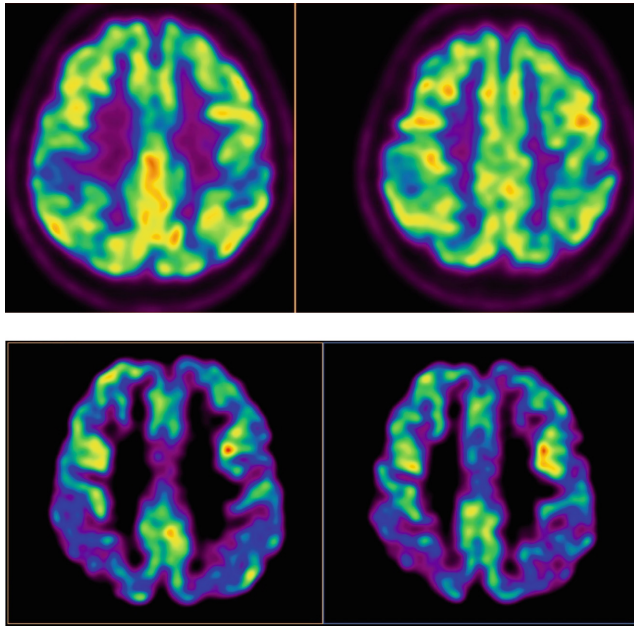
Fig. 1. Original. Distribution of the utilization of the radionuclide glucose - [18F] - fluorodeoxyglucose in the brain regions according to the data of the PET-scan without cognitive disorders (top figure) and with cognitive disorders (bottom figure).

3   Outcomes

The results of the MMSE test showed that in the majority of patients (78%) the level of cognitive impairment was within the age norm. Mild cognitive impairments were observed in 22% of patients. The results of the BPD test showed that in 55% of patients the total number of points was in the range of 16–18 – the preservation of the functions of the frontal areas was recorded. In the remaining 45% of patients from main group, according to the test results, the score was below 16. This made it possible to divide the study group into two subgroups (Table 1). When comparing the studied subgroups and the control group, a decrease in the rate of glucose utilization in the associative visual zone of both cerebral hemispheres (18th, 19th and 37th Brodmann's fields bilaterally) was observed (Fig. 2).

Table 1. Clinical and anamnestic characteristics of the examined groups

№ group	Group characteristics	n, people	Age	MMSE	FAB
Research group					
1	PD 1	17 (9 W, 8 M)	$60,2 \pm 2,4$	25–30	≥ 16
2	PD 2	14 (10 W, 4 M)	$65,5 \pm 2,6$	23–30	<16
Control group					
3	Patients without dementia	15 (6 W, 9 M)	$59,7 \pm 3,2$	26–29	≥ 16
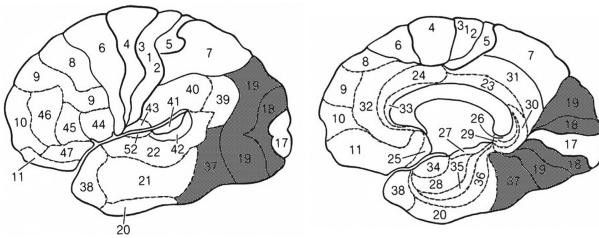
Fig. 2. PET data in PD patients compared with the control group. Areas of bilateral decrease in the rate of glucose utilization are marked by gray. Left – lateral cortex of the cerebral hemispheres, on the right – the medial one. Figures – fields according to Brodman.
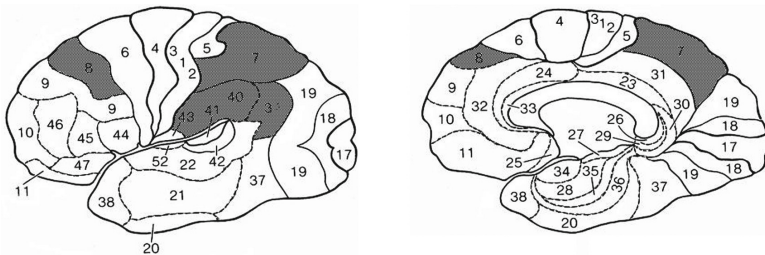
Fig. 3. PET data in patients with PD of the 2nd group compared with the 1st group. Areas of bilateral decrease in the rate of glucose utilization are marked by gray. Left – lateral cortex of the cerebral hemispheres. On the right is the medial one. Figures – fields according to Brodman.

In the second subgroup of patients with PD (PD2), when compared with the results of PET of the first subgroup of patients with PD (PD1) and the control group, there was a significant decrease in the rate of glucose utilization in the middle third of the frontal areas bilaterally (8th Brodmann's field), a similar decrease in the level of functional National activity was recorded in the lateral and medial cortex of the parietal lobes of both cerebral hemispheres (7, 39, 40 Brodmann's fields) (Fig. 3). The decrease in functional activity in the associative visual cortex in PD patients in our study can be explained by a number of reasons. First of all, a well-known symptom of visual hallucinations, which quite often

accompanies the course of Parkinson's disease. A number of authors also associate functional changes in the associative visual cortex not only with visual hallucinations, but also with sleep disorders [2, 7].

Factor Analysis Results. In order to assess the integration of the frontal and parietal areas based on the analysis of PET data on glucose utilization, the research of the self-organizing functioning of neuroanatomical systems was continued. Following four systems were developed. 1) The state of operational rest (brain default system); 2) The dorsal system of attention; 3) The ventral system of attention and 4) the visual system in normal conditions and in patients with cognitive violations of varying severity and genesis and other pathologies.
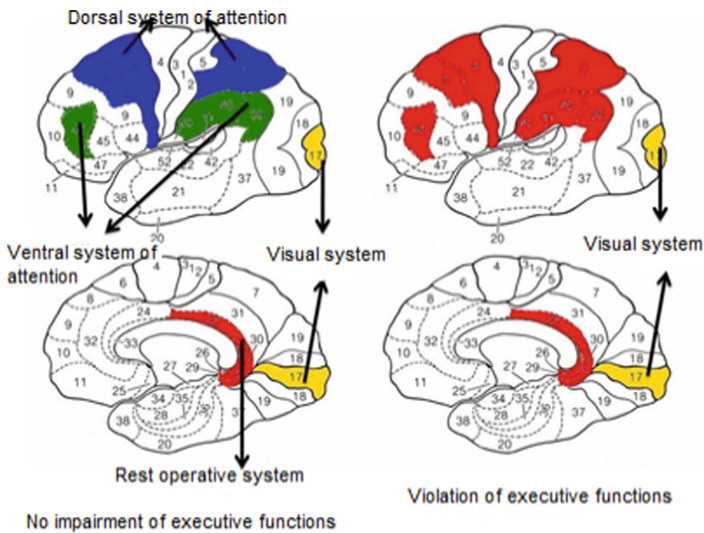
Fig. 4. Factor structure of self-organizing functioning of neuroanatomical systems for patients without impaired executive functions (left) and with syndrome of impaired executive functions (right).

It was found that the factorial structure of data on regional areas of glucose utilization in subjects of different nosology's, but without cognitive impairments, is stable from the point of view of the composition of factors included in the factorial solution. These factors may be discussed in accordance with the belonging of the cerebral regions, which have the greatest load on the factor, to one or another neuromorphological zone.

Thus, 4 factors were established that can be interpreted as: factor 1 – dorsal system of attention (voluntary attention), factor 2 – ventral system of attention (involuntary attention), factor 3 – system of the state of operational rest, factor 4 – visual area. The first factor includes the 6, 7 and 8 cytoarchitectonic fields of Brodmann (the precentral cortex of the frontal areas and the upper half of the parietal zones of both cerebral hemispheres). The second factor includes 46 and 40, 39 of Brodmann's fields (the anterior third of the convexital part of the frontal areas and the lower half of the parietal zones). The third

factor includes the 23, 36, 29 and 30 cytoarchitectonic Brodmann fields (the posterior cingulate gyrus). The fourth factor is the 17th Brodmann field (primary visual zone).

According to the outcomes of factor analysis, it was revealed that in patients with Parkinson's disease, but without the syndrome of impaired executive functions, a factor structure is determined that includes all four factors. The same factor structure was recorded in patients in the control group and in healthy young patients. In the group of patients with Parkinson's disease with syndrome of impaired executive functions and in the group of patients with vascular dementia, reorganization of the ventral and dorsal systems of attention, as well as the system of operative rest was observed (Fig. 4).

4   Discussion

Dynamics in the parameters of cerebral blood flow allows in psychophysiological studies to assess the possibility of quantitative participation of certain brain areas in providing cognitive activity.

Positron emission tomography is one of the most modern, promising and powerful neuroimaging methods. Today it is called a "functional neuroanatomy of the human brain." The first publications on PET date back to 1975–1979, but the main stream of work appeared in the 80s. The main purpose of PET-scan is to study the distribution in the living brain of various (more than 200) chemicals it utilizes in order to assess one or another of its functions. Among them are blood flow, pH, metabolism, molecular diffusion, protein synthesis, activity of membrane receptors, and a number of others. Amino acids, carboxylic acids, amines, sugars, steroids, metabolites, drugs, and their derivatives are used as injected substances. The principle of the method is registration of radioactive decay (positron emission) of short-lived (2–110 min) isotopes (C, N, O or F), combined with a substance-tracer. Based on the principles of computed tomography, a three-dimensional display of brain radioactivity is constructed, consisting of huge number (up to 230 thousand) discrete points. The sensitivity of PET is very high – it allows the detection of test substances in the brain in concentrations of up to several picomoles per gram [12, 17, 18, 25].

A line of studies have described a metabolic pattern that characterizes the initial signs of mild cognitive impairment, and then dementia in PD. This pattern is characterized by a decrease in the rate of glucose utilization in the middle third of the frontal and parietal cortex bilaterally [22]. In our study, a similar pattern was recorded in patients with signs of an initial decrease in the function of the frontal lobes according to the battery of frontal dysfunction. The obtained data suggest that the frontal dysfunction battery technique is valid for the early diagnosis of cognitive violations in PD.

Also, pattern of a decrease in the rate of glucose metabolism in the occipital lobes in Lewy body dementia, often associated with PD, cannot be ignored. There is an opinion that from the point of view of the mechanisms of dementia formation, PD and dementia with Lewy bodies should be considered not as two separate diseases, but as two nosological forms or two syndromes of the same neurodegenerative process [9, 20].

Behavioral and psychological symptoms (BPSD) have been reported to be common in patients with DLB, PDD, and AD. This overlap of symptoms (psychological, psychological and cognitive) often makes it difficult to make an accurate diagnosis. Thus,

hallucinations in AD can occur in any sensory modality, and the frequency of BPSD depends on the stage of AD. With low rates of psychosis in the prodromal and early periods of asthma and higher rates in the middle and late stages [19, 20]. Therefore, there are some difficulties even in the diagnosis of visual hallucinations. It is believed that patients with PDD and DLB are relatively weaker and BPSD in them is reduced faster than in patients with AD, in visuospatial ability, but did not differ from each other (DLB ≈ PDD < AD). Interestingly, similar symptoms according to PET scan with 18-FDG were described in cobalt intoxication resulting from joint arthroplasty [2].

Thus, the decrease in the rate of glucose utilization in the occipital areas observed in our study in PD patients confirms this point of view. A decrease in the rate of glucose metabolism in the middle third of the frontal zones bilaterally (Brodmann's field 8) in the group of patients with impaired frontal functions (in the PD2 group) is quite expected. The simultaneous decrease in functional activity in the parietal cortex in this group of patients can be explained by the formation of a dementia pattern in Parkinson's disease.

5   Conclusion

As article outcome, let us consider the importance of PET-scan with other methods of clinical neurophysiology of brain imaging (Fig. 5) [17]. Levels of study may be are divide from the brain to cells and synapses. Time of research may vary from milliseconds to long time – several years. The general feature of clinical neurophysiology diagnostics is time, as rule – on time. Traditionally, these are fractions of a second (Event-Related Potentials), seconds (EEG, Magneto Encephalography, Electrocorticography, etc.), minutes (fMRI). Only positron emission tomography reflects the brain status over several days, which is associated with the life cycle of radioactive isotopes. The research level corresponds to the whole brain, maps, microelectrode (neural activity) allow you to explore individual neurons and nerve centers – nuclei.

The results of PET and neuropsychological studies allowed us to distinguish two groups of patients with PD in our research. The first subgroup consisted of patients without cognitive violations (according to the results of the frontal dysfunction battery test), and the second – with an initial disorder of the frontal area function. In the second subgroup, the quantitative changes in the rate of glucose utilization, characteristic of patients with cognitive impairments in PD, was recorded. Thus, a characteristic change in the rate of glucose utilization was recorded already at the early period of dysfunction of the frontal areas. Our outcomes suggest a high sensitivity of the frontal dysfunction battery test for the early diagnosis of cognitive violations in PD.

Four factors were identified, named accordingly: factor I – the dorsal system of attention (voluntary attention), factor II – the ventral system of attention (involuntary attention), factor III – the system of the state of operational rest, factor IV – the visual zone. First factor includes the 6, 7 and 8 cytoarchitectonic fields of Brodmann (the precentral cortex of the frontal areas and the upper half of the parietal zones of both cerebral hemispheres). Second factor includes 39 and 36, 40 of Brodmann's fields (the anterior third of the convexosital part of the frontal areas and the lower half of the parietal zones). Third factor includes 23, 36, 29 and 30 Brodmann's fields (posterior cingulate gyrus). Fourth factor is Brodmann's 17 field (primary visual system).

Research in time	Research level				
	Brain	**Mapping**	**Layers/ Nuclei**	**Cells**	**Synapses**
Milliseconds/ seconds	EEG, ERPs, MEG, ECoG		Neural activity		Biophysics
Seconds/ hours	fMRI, USDG, NIRS, EDA		Vascular video microscopy		
Days	PET-scan		Angiography		Molecular biology
Years	CT, MRI				

Fig. 5. PET-scan compared with diagnostic methods for brain mapping.

According to the results of factor analysis, it was revealed that in patients with Parkinson's disease without executive dysfunction syndrome, a factor structure is determined that includes all four factors. Also similar factor pattern in the control group and in healthy young subjects is recorded. In the group of patients with PD with the syndrome of impaired executive functions and in the group of patients with vascular dementia, a reorganization of the ventral and dorsal systems of attention, as well as the system of operative rest, was observed.

References

1. Aarsland, D., Zaccai, J., Brayne, C.: A systematic review of prevalence studies of dementia in Parkinson's disease. Mov. Disord. **20**, 1255–1263 (2005)
2. Bridges, R.L., Cho, C.S., Beck, M.R., Gessner, B.D., Tower, S.S.: F-18 FDG PET brain imaging in symptomatic arthroprosthetic cobaltism. Eur. J. Nucl. Med. Mol. Imaging **47**(8), 1961–1970 (2019). https://doi.org/10.1007/s00259-019-04648-2
3. Buchert, R., Buhmann, C., Apostolova, I., Meyer, P.T., Gallinat, J.: Nuclear imaging in the diagnosis of clinically uncertain parkinsonian syndromes. Dtsch. Arztebl. Int. **116**, 747–754 (2019)
4. Campoy, A.-D.T., Liang, C., Ladwa, R.M., et al.: [18F] Nifene PET/CT imaging in mice: improved methods and preliminary studies of α4β2* nicotinic acetylcholinergic receptors in transgenic A53T mouse model of α-synucleinopathy and post-mortem human Parkinson's disease. Molecules **26**, 7360 (2021)
5. Cohen, O.S., Vakil, E., Tanne, D., et al.: The frontal assessment battery as a tool for evaluation of frontal lobe dysfunction in patients with Parkinson disease. J. Geriatr. Psychiatry Neurol. **2**, 71–77 (2012)
6. Ferri, C.P., Prince, M., Brayne, C., et al.: Global prevalence of dementia: a Delphi consensus study. Lancet **366**, 2112–2117 (2005)
7. Folstein, M.F., Folstein, S.E., McHugh, P.R.: Mini-mental state: a practical method for grading the cognitive state of patients for the clinician. J. Psychiatric Res. **2**, 189–198 (1975)
8. Fujimi, K., Sasaki, K., Noda, K., et al.: Clinicopathological outline of dementia with Lewy bodies applying the revised criteria: the Hisayama study. Brain Pathol. (Zurich, Switzerland). **18**, 317–325 (2008)
9. Gan, J., Liu, S., Wang, X., et al.: Clinical characteristics of Lewy body dementia in Chinese memory clinics. BMC Neurol. **21**, 144 (2021)
10. Hely, M.A., Morris, J.G., Reid, W.G.: Sydney multicenter study of Parkinson's disease: non-L-dopa-responsive problems dominate at 15 years. Mov. Disord. **3**, 190–199 (2005)

11. Kane, J.P.M., Surendranathan, A., Bentley, A., et al.: Clinical prevalence of Lewy body dementia. Alz. Res. Ther. **10**, 19 (2018). https://doi.org/10.1186/s13195-018-0350-6
12. Khil'ko, V., Shostak, V., Khlunovskiǐ, A., et al.: The topographic mapping of evoked bioelectrical activity and other methods for the functional neural visualization of the brain. Vestn. Ross. Akad. Med. Nauk **3**, 36–41 (1993)
13. Leh, S.E., Petrides, M., Strafella, A.P.: The neural circuitry of executive functions in healthy subjects and Parkinson's disease. Neuropsychopharmacology **1**, 70–85 (2010)
14. Loane, C., Politis, M.: Positron emission tomography neuroimaging in Parkinson's disease. Am. J. Transl. Res. **3**, 323–341 (2011)
15. Lytaev, S.A., Susin, D.S.: PET-diagnostics of cognitive impairment in patients with Parkinson's disease. Pediatrician **7**, 63–68 (2016)
16. Lytaev, S., Aleksandrov, M., Popovich, T., Lytaev, M.: Auditory evoked potentials and PET-scan: early and late mechanisms of selective attention. Adv. Intell. Syst. Comput. **775**, 169–178 (2019)
17. Lytaev, S.: Modern neurophysiological research of the human brain in clinic and psychophysiology. In: Rojas, I., Castillo-Secilla, D., Herrera, L.J., Pomares, H. (eds.) BIOMESIP 2021. LNCS, vol. 12940, pp. 231–241. Springer, Cham (2021). https://doi.org/10.1007/978-3-030-88163-4_21
18. Lytaev, S.: Modeling and estimation of physiological, psychological and sensory indicators for working capacity. Adv. Intell. Syst. Comput. **1201**, 207–213 (2021)
19. Lytaev, S.: Long-latency event-related potentials (300–1000 ms) of the visual insight. Sensors **22**, 1323 (2022)
20. Murray, P.S., Kumar, S., Demichele-Sweet, M.A., Sweet, R.A.: Psychosis in Alzheimer's disease. Biol. Psychiatry **75**, 542–552 (2014)
21. Palmqvist, S., Hansson, O., Minthon, L., Londos, E.: Practical suggestions on how to differentiate dementia with Lewy bodies from Alzheimer's disease with common cognitive tests. Int. J. Geriatr. Psychiatry **24**, 1405–1412 (2009)
22. Poston, K.L., Eidelberg, D.: FDG PET in the evaluation of Parkinson's disease. PET Clin. **1**, 55–64 (2010)
23. Silverman, D.H.S., Mosconi, L., Ercoli, L., et al.: PET scans obtained for evaluation of cognitive dysfunction. Semin. Nucl. Med. **38**, 251–261 (2008)
24. Surendranathan, A., Kane, J.P.M., Bentley, A., et al.: Clinical diagnosis of Lewy body dementia. BJPsych Open **6**, e61 (2020)
25. Szeto, J.Y.Y., Walton, C.C., Rizos, A., et al.: Dementia in long-term Parkinson's disease patients: a multicentre retrospective study. NPJ Parkinson's Dis. **6**, 2 (2020)
26. Talairach, J., Tournoux, P.: Co-planar stereotactic atlas of the human brain. In: 3-Dimensional Proportional System: An Approach to Cerebral Imaging, pp. 5–15. Thieme, New York (1988)
27. Taylor, J.P., McKeith, I.G., Burn, D.J., et al.: New evidence on the management of Lewy body dementia. Lancet Neurol. **19**, 157–169 (2020)
28. Thompson, E., Marrett, C., et al.: Performance evaluation of the PC-2048: a new 15-slice encoded-crystal PET scanner for neurological studies. IEEE Trans. Med. Imaging **2**, 90–95 (1991)

Architecture and Calibration of a Multi-channel Electrical Impedance Myographer

Edson Rodrigues[(✉)], Erick Dario León Bueno de Camargo[(✉)], and Olavo Luppi Silva[(✉)]

Universidade Federal do ABC - UFABC, São Bernardo do Campo, Brazil
rodgraneiro@gmail.com, {erick.leon,olavo.luppi}@ufabc.edu.br
https://www.ufabc.edu.br/

Abstract. Electrical impedance myography (EIM) is a non-invasive measurement technique capable of determining physiological and morphological changes in skeletal muscle tissue. The method consists of applying an alternating current on the skin through two electrodes to determine the bioimpedance of the medium. EIM has contributed to the study of degenerative diseases that changes the electrical properties of muscle tissue during its evolution of the disease. The objective of this work is to develop a portable and low-cost impedance measurement instrument to assist in activities related to the study and diagnosis of muscle diseases. We present a modular hardware architecture that allows the impedance measurement of multiple muscles at the same time, but in the present work we test the performance of the prototype with a single impedance measurement channel implemented. The tests were performed with known theoretical impedance calculated to evaluate the accuracy of the impedance meter, as well as other performance tests of the system.

Keywords: Electrical impedance myography · Instrumentation · Hardware design

1 Introduction

Bioimpedance can be defined as the opposition to the passage of electrical current in biological tissues. The smallest building block of life is the cell that in a living tissue is filled and surrounded by fluids containing diluted ions necessary for metabolism. The cell can be modeled mathematically by an association of resistors, representing internal and external fluids, and by capacitors representing the lipid layers of cell membranes and organelles [9]. In this way, biological tissue is not a purely resistive medium to the passage of alternating current and has capacitive reactance that is dependent on frequency. Therefore, more vascularized tissues such as muscles contain a greater amount of ions in their structure making them good conductors of current, on the other hand, less capillaryized bone and fat tissues are poor conductors. Therefore, it is possible to distinguish

the different biological tissues by determining the impedance of the region of interest. The advantage of this measurement technique is that it reduces the costs of biomedical equipment used for monitoring and diagnosing patients.

There is an increasing number of researches associated with the study of the electrical properties of biological tissues, such as muscle dynamics and physiology [17]; degenerative muscle diseases such as amyotrophic lateral sclerosis [4,15] and muscle fatigue related to sports activities [2,5]. Due to the large number of researches interested in the analysis of the electrical properties of biological tissues, there is a demand for measuring instruments to meet this need.

Some commercial instruments for impedance measurement have been used in these researches. The mScan^{TM} EIM manufactured by the Myolex company [13] is a portable single-channel measuring instrument with a 50 kHz biological tissue excitation current. Another equipment used in the research is the Quantum V Segmental BIA from the company RJL Systems [14], which has 12 multiplexed measurement channels with an excitation frequency also of 50 kHz. Both equipments are designed to measure arm, leg, torso muscles, including the upper and lower regions of the human body.

Although this work presents the development of the concept of a single measurement channel, we adopted a modular design criterion with the aim of developing in the future an EIM hardware with multiple measurement channels to study different muscle groups simultaneously. Thus, this project aims to build a portable and autonomous equipment to measure the bioimpedance of skeletal muscle tissue using electrodes installed on the patient's skin with a excitation current 31.5 kHz.

2   Background

Electrical impedance myography can be used to study skeletal muscle through the electrical properties of this tissue [16]. The method consists of applying a sinusoidal current excitation signal of known amplitude and frequency through two electrodes in the region of interest, while the electrical voltage generated by this current is measured in the same electrodes. Once the current and voltage are known, it is possible to determine the bioimpedance of the medium using Ohm's Law. Thus, EIM has the potential to study the evolution of neuromuscular degenerative diseases by analyzing changes in muscle tissue bioimpedance.

The Fig. 1 shows an electronic model of the cell tissue [9] composed of the resistivity of the extra-cellular fluid R_e; by the resistance R_m and capacitance C_m of the lipid layer of the membrane; and the resistivity of the fluids and organelles inside the cell with resistance R_i. The equivalent electronic circuit of the model can be reduced according to the Fig. 1 and represented by the Eq. 1, where Z_{eq} is the total equivalent impedance; $Z_e = R_e + j0$ is the external fluids impedance; $Z_i = R_i + j0$ is the internal fluid impedance and Z_m is total cell membrane impedance representing the parallel association of resistance R_m and capacitance jX_{C_m}, according to Eq. 2.
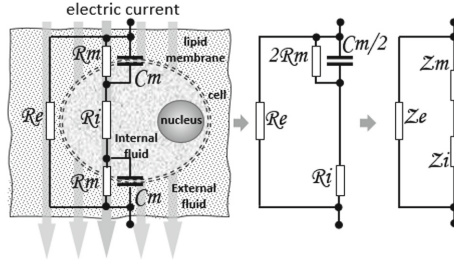
Fig. 1. Equivalent cell model, adapted from [9].

$$Z_{eq} = \left(\frac{1}{Z_e} + \frac{1}{Z_i + Z_m} \right)^{-1} \tag{1}$$

$$Z_m = \left(\frac{1}{2R_m} + j\frac{2}{X_{Cm}} \right)^{-1} \tag{2}$$

The excitation signal of the sinusoidal electric current is typically applied at frequencies that vary from 10 Hz to a few MHz in order to adjust the frequency response according to the object under study. At low frequencies, the reactive component of the impedance, due to the capacitance of the muscle cell membrane tends to be much larger (open circuit) than the resistive component. Therefore, the current bypasses the cellular membrane and flows mostly in the extracellular fluid. At high frequencies the capacitive reactance becomes much smaller (short-circuit) than the resistive component inside the cell, increasing the current intensity in the intracellular fluid. Once the amplitude, frequency and phase of the applied excitation signal are known, it is possible to determine the impedance of the muscle by analyzing changes in the amplitude and phase of the voltage and current measured in the region of interest.

With the EIM it is possible to analyze the impedance changes in healthy muscle tissue by determining the impedance distributed in the longitudinal and transverse axes. Thus, the progression or regression of muscle diseases such as amyotrophic lateral sclerosis, injuries, fat rate, etc. can be monitored [10,15] by analyzing the changes in muscle tissue impedance.

3 Proposed Architecture

3.1 Overview

The design approach adopted was to develop the equipment in electronic modules where each acquisition channel measures an analog voltage signal. This concept allows simultaneous impedance measurement of N samples through $N + 1$ modules, being that N channels are responsible to measure the voltages and one channel to indirectly determines the current by measuring the voltage across a sentinel resistor of known value.

A single voltage-controlled current source individually excites all samples by an analog multiplexer. The maximum number of measurement channels is related to the model of the multiplexer installed in the system. The sinusoidal excitation signal from the current source can be generated either by an internal circuit or by an external signal generator.

The electrode signal is conditioned and filtered in the first stages of the module. The objective is to reduce 50/60 Hz noise from the power supply and also noise with frequencies above the frequency band of interest. Then, the conditioned signal is sent to the next stage composed by an analog-to-digital converter (ADC) circuit. The ADC is the AD7762 integrated circuit manufactured by the company Analog Devices®, whose main characteristics are: (i) differential input of the modulator; (ii) 24-bit resolution; (iii) sampling frequency of 625 kSPS (kilo Samples Per Second) and (iv) signal-to-noise ratio (SNR) of 106 dB [3]. The microcontroller of the channel acquires the sample data discretized by the ADC. The microcontroller used is the 32-bit Atmel SAM3X8E ARM Cortex-M3 which is embedded into the Arduino Due open source platform. The functional block diagram of the Impedance Meter is shown in the Fig. 2.
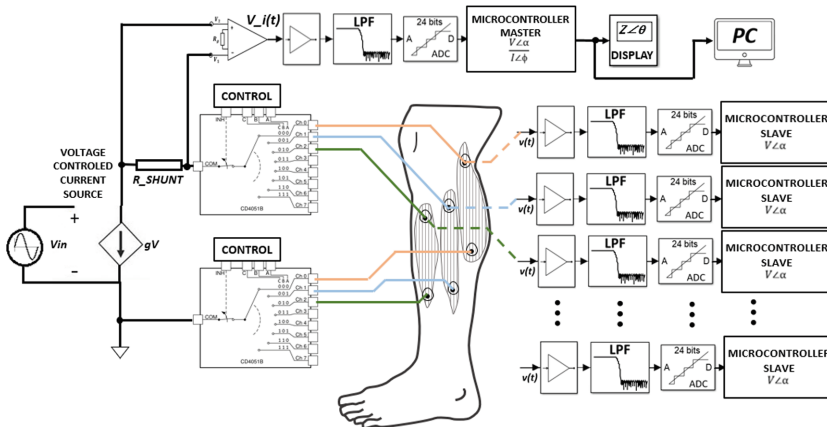
Fig. 2. Functional block diagram of the impedance meter with multiple channels

The design approach shown in Fig. 2 is convenient to implement an impedance meter with any number of simultaneous measuring channels depending only on the choice of the number of channels of the mux integrated circuit. In the present work we have implemented only one impedance measuring channel as a proof of concept. The following subsections detail the implementation of this prototype.

3.2   Acquisition Channels

Hardware Description. The constructed impedance meter prototype have two different types of measurement channels: one called the master channel that

is responsible to measure the current and the other is called slave channel responsible to measure the voltage. The hardware of master and slave channels are similar, the difference between them is the addition of an IC INA129 instrumentation amplifier circuit in the master channel. It is used to amplify the low voltage across the sentinel resistor (Fig. 3). A first order high pass filter (HPF) with 150 Hz of cutoff frequency is placed between the terminals of the sentinel resistor and the inputs V^+ and V^- of the preamplifier INA129 in order to eliminate any DC component from the previous stage.

Notice that the hardware of the master and slave channels is identical except for the presence of the preamplifier on the master channel. Since the PCB of both circuits are the same, we use a jumper to bypass the leads of the preamplifier.

The next stage consists of a first order low pass filter with cutoff frequency of 300 kHz to reduce high frequency noise. In sequence, the next stage is a single-ended to differential signal converter circuit. This circuit is based on a unity gain inverting amplifier with one input and two outputs V_{in}^+ and V_{in}^-, where V_{in}^+ is the original input and V_{in}^- is the input shifted by 180 °C. These outputs will serve as inputs of the ADC. Since the AD7762 ADC has differential inputs, so this adaption circuit through the AD8021 operational amplifier is mandatory [3].

To determine the current it is necessary to measure the voltage drop across the sentinel resistor ($R_{SHUNT} = 56\,\Omega$). Since this voltage drop is small, it is necessary to introduce a preamplifier. The implemented current source supplies from 1 to 10 mA, then the maximum voltage over R_{SHUNT} is only 560 mV. Therefore, the preamplifier multiply this voltage to optimize the input range of ADC which is ±3.6 V. In the implemented circuit, the signal is amplified with a gain factor of 5 through the instrumentation operational amplifier INA129 [7] as seen in the Fig. 3. It is worth noting that only the master channel needs this circuit.
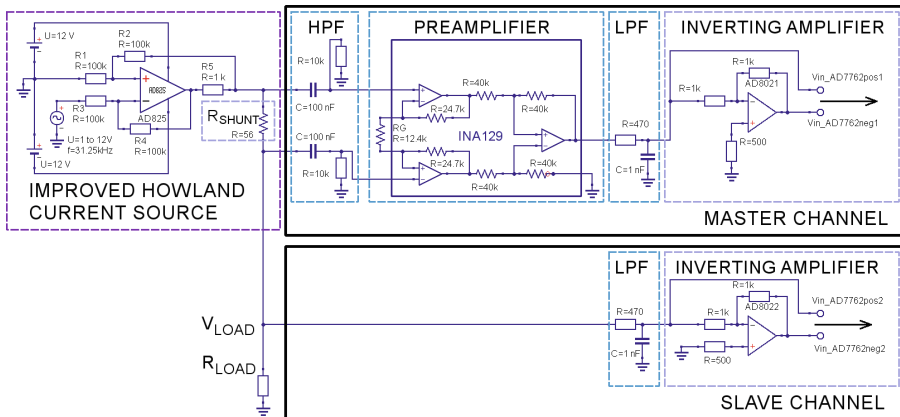
Fig. 3. Electronic schematic of Howland current source and Master/Slave channels signal Conditioners.

Software Description. Regarding the algorithm, the IDE (Integrated Development Environment) of the Arduino microcontroller is divided into two parts. In the first part `void setup()` are inserted the system initialization and configuration instructions that will be executed only once. In the second part `void loop()` are inserted the instructions that are executed continuously by the main program.

First, in `void setup()`, it is necessary to configure the ADC, which remains turned off in default mode, sending the commands that will determine the component's operation settings to Control Registers 1 and 2, such as: power-on; sampling frequency; clock division factor; filter configuration, etc. At this stage, the microcontroller sends 16-bit address words to Control Registers 1 and 2 signaling that it will write data to it. AD7762 understands that the word following the address is a data control word and stored it in the respective register [3]. It is worth noting that the sampling frequency of 312.5 kHz is determined at this stage. Then, still at this stage, the master microcontroller sends data to initialize the display, informs the operator that the equipment is ready to perform an impedance measurement and finishes the setup procedure.

In `void loop()`, once a measurement is triggered, the microcontroller reads two 16-bit words from the sample acquired by the ADC at that instant. This data is rearranged into a single 24-bit word and stored in memory. This digital word contains the 16 bits of the Most Significant Word (MSW) and the 8 bits of the Least Significant Word (LSW) of the discretized sample value. The microcontrollers - master and slaves - reads 10 samples for each period of the sinusoidal signal and exits looping. Next, it determines the amplitude and phase angle of the voltage and current, respectively, using the quadrature demodulation process [19] (see details in Appendix A). The microcontroller of the master channel reads the data from the ADC_{master} and then, it requests the slave channel to send the amplitude and phase of the voltage over the load $V_{load} \angle \phi^\circ$ calculated in that channel. With these data the master channel calculates the impedance $Z_{load} \angle \theta^\circ$ by dividing the voltage of the load by the current and sends the value to a LCD display or microcomputer. Communications between the microcontroller of the master channel and the slave channels are carried out by the I^2C (Inter-Integrated Circuit) protocol. In addition, each channel can connect with the personal computer via the USB (Universal Serial Bus) port.

3.3   Analog-to-Digital Converter

The electronic circuit of the analog acquisition channel has as main component the integrated circuit AD7762. As mentioned in Sect. 3.1, it is a 24-bit resolution analog-to-digital converter capable of data acquisition at 625 kSPS and signal-to-noise ratio (SNR) of the order of 106 dB. This is a high-performance ADC designed under the Σ-Δ (sigma-delta) architecture where samples are oversampled at an acquisition rate much higher than the Nyquist frequency. The sample discretizes the 24 bits in two steps, or rather, in two 16-bit words. When the ADC finishes the discretized conversion of a sample, the DRDY (Data Ready Output - pin 38) control signal of the ADC goes to logic level '0' indicating that

the most significant 16 bits of the word (MSW) are available for reading in the buffer.

To perform the reading, the microcontroller must send a signal of logic level '0' to the CS (Chip Select - pin 40) and RD/WD (Read/Write - pin 39) pins, respectively, for at least 6 cycles of clock and acquire the 16 bits MSW from word. After this time interval, the microcontroller resets logic level '1' on the CS and RD/WR control pins for the same period of 6 cycles, in this way, the ADC provides the second part of the word with the 8 least significant bits LSW of the converted signal, along with 8 bits of the STATUS of the conversion. Again, the microcontroller sends logic level 0 for 6 cycles to the CS and DR/WR control pins to read the second part of the word, returning to logic level '1' after reading. Note that the DRDY signal goes to logic level 0 only once for each valid 24-bit data. The microcontroller then rearranges the 16 MSW bits of the first part of the word with the 8 most significant bits of the second part (LSW) to store the signal discretization in just a 24-bit word. The 8 least significant bits of the LSW word present the status of the discretization performed, and each bit informs a certain condition, for example: DVALID (valid data); OVR (overload), among others. Once the reading cycle is completed, the microcontroller waits for signaling from the DRDY pin to read a new sample.

3.4   Current Source

The current source used is built around the design known as the Discrete Improved Howland Current Pump described by TEXAS INSTRUMENTS [6,8]. This type of current source is highly used in bioimpedance analysis applications due to its high output impedance and has a constant amplitude over a wide range of frequency [1]. It uses just one op-amp and five resistors to supply and control the current in the load resistor R_{LOAD} as seen in the Fig. 3. The load current I_{LOAD} can be calculated using Eq. 3 and the circuit gain G is given by Eq. 4.

$$I_{LOAD} = \frac{G(V_p - V_n)}{R_5} \tag{3}$$

$$G = \frac{R_2}{R_1} = \frac{R_4 + R_5}{R_3} \tag{4}$$

The current source was tested to verify its performance over different loads. This test was initially performed only with resistive loads to determine the current source capacity as a function of the load. The test consisted of injecting the current supplied by the source in a determined load resistor and measuring the voltage drop with an oscilloscope Minipa model MVB-DSO de 100 MHz [11]. The actual values of the resistors were obtained using a digital multimeter Tektronix model TEK DMM 830 [18]. In the test, the current source excitation signal is generated by the function signal generator model Minipa MFG-4202 [12]. Figure 4 presents the experimental survey of the current delivered by the source as a function of load for the range of interest from zero to 1 kΩ. Analyzing

the behavior test data, we verified that the current source enters the non-linear region for resistance values above $5\,\text{k}\Omega$.
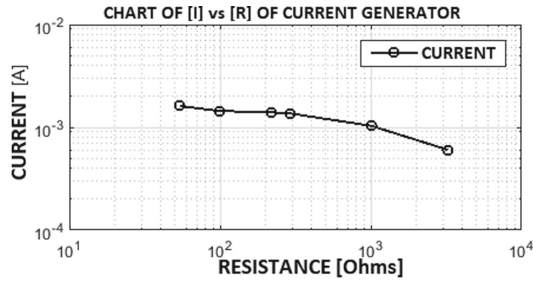
Fig. 4. Experimental test of current source and resistive load.

4   Testing Protocols

In the following subsections we describe some tests that were performed to evaluate the performance of the impedance meter after the construction of the first prototype was finished.

4.1   Sample Rate Performance Test

The AD7762 can be programmed to operate at four different sampling frequencies depending on the desired application: $625\,\text{kSPS}$, $312.5\,\text{kSPS}$, $15.75\,\text{kSPS}$ and $7.875\,\text{kSPS}$. However, as demonstrated in Sect. 3.3, the microcontroller has to read two 16-bit words on the ADC data bus, interpret this information and store the discretized sample value in a 24-bit word. For the fastest sampling rate of $625\,\text{kSPS}$ the microcontroller has $1.6\,\mu\text{s}$ to accomplish this task. Since the microcontroller chosen is the Arduino Due, a test was performed with each of these sampling frequencies and voltage of $1\,\text{V}$ peak amplitude to verify the performance of the ADC-Arduino combination. In this test, we verified that the Arduino does not behave properly only for the sampling frequency of $625\,\text{kSPS}$, without prejudice to the other frequencies. Data were stored on the computer in text mode. In this step, we verified that the Arduino Due microcontroller presented the best performance of discretization of input signals for a sampling rate of $312.5\,\text{kSPS}$. Therefore, we adopted this sampling frequency for the operation of the system.

4.2   Excitation Frequency Performance Test

In the next step, analog signals generated with the Minipa generator were acquired. Four signals were generated to perform the tests with the amplitudes in the values of $150\,\text{mV}_\text{p}$, $500\,\text{mV}_\text{p}$, $1\,\text{V}_\text{p}$ and $1.6\,\text{V}_\text{p}$, respectively. The sampling

rate was 312.5 kHz for all signals. The signals were generated at the frequencies of 10 kHz, 31.25 kHz, 50 kHz and 125 kHz totalizing 16 different measurements. The graphs in the Fig. 5 show an example of these measurements for the voltage of 500 mV$_p$ in the range of 100 μs. Analyzing these data, we decided to adopt the frequency of 31.25 kHz for the excitation of the sample under test and to acquire ten points per sinusoidal period since the sampling frequency is 312.5 kHz.

The stored signals were analyzed in the MATLAB® software to determine the total harmonic distortion rate (THD) and the FFT of the discretized signals. The THD varied between 1.01% and 3.7% increasing distortion with increasing amplitude. The THD was calculated in the Matlab program using the function $[r, harmpow, harmfreq] = thd(x, fs, n)$ where: r is the value of the THD in dB; $harmpow$ is the harmonic power value; $harmfreq$ is the harmonic frequency; thd is the function that calculates the THD; x is the name of the file with the discretized data; fs is the sampling frequency; and n and the desired harmonic iteration number. It is worth noting that the THD also depends on the quality of the signal generator to maintain the monotonicity of the sine wave. In the case of the Minipa MFG-4202 function generator, the manual [12] informs that the sine wave distortion is less than 2% (10 kHz, 5 Vpp). Figure 6 present an example demonstrating these analyses.
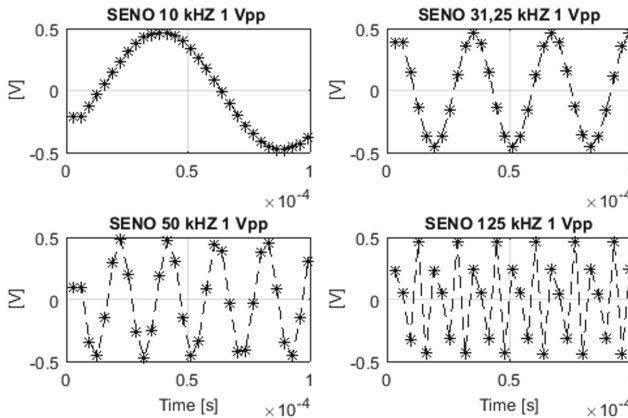
Fig. 5. Example of 4 discretized samples - sample Rate 312.5 kHz.

4.3   Impedance Accuracy Test

Subsequently, measurements of previously known impedances were performed. The impedances were produced through associations in parallel between capacitors and resistors. The actual values of the components were measured with the multimeter model TEK DMM 830 and these data were used to theoretically determine the impedances through the Eqs. 5. A theoretical table with 28 different impedances was created using the values of the real components, with
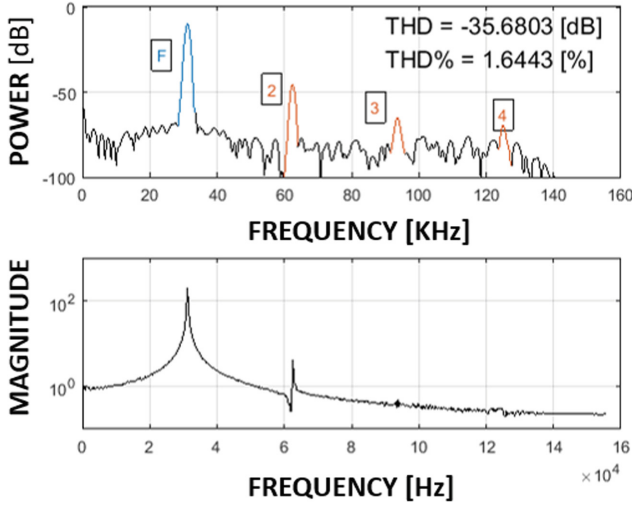
Fig. 6. THD sinusoidal signal 500 mVp 31.23 kHz. - sample rate 312.5 kHz.

associations in parallel and an excitation frequency of 31.25 kHz. The calculation of the resulting impedance of a resistor R in parallel with capacitor with reactance X is given by Eq. 5:

$$Z = \frac{jRX}{R + jX} = \frac{RX^2}{R^2 + X^2} + j\frac{R^2 X}{R^2 + X^2} \; , \tag{5}$$

In the test, we deliver to the load the highest possible current for the impedance in the analysis. The amplitudes of the excitation currents varied from 1 to 10 mA, and the ratio of the amplitudes of the signals sent to the inputs of the ADC's is the highest possible, reducing discretization errors.

The test is performed with the help of the oscilloscope Minipa MVB-DSO and the function generator Minipa MFG-4202. Since the current is controlled as a function of the voltage drop across the sentinel resistor, we install the oscilloscope probe across the terminals of this resistor. Then, through the generator, a low-amplitude voltage is applied to the input of the current source and the voltage amplitude (V_{in}) is gradually increased until reaching the best relationship between voltage and sentinel resistor. Then, measurement tests were performed having as standard reference the impedances calculated according to the Eq. 5. Resistors with values 55.1 Ω, 100.0 Ω, 220.0 Ω, 292.4 Ω, 497.0 Ω, 668.0 Ω and 994.0 Ω were used. The resistors were associated in parallel with each of the following capacitors: $C_1 = 1.5$ nF, $C_2 = 3.3$ nF and $C_3 = 4.4$ nF. The Table 1 presents a summary of the actual impedance measurements performed with the impedance meter [M] and its respective theoretical [T] value calculated.

Table 1. Difference between the theoretical impedance, marked as [**T**] and the measured impedance, marked as [**M**]. The second column show a purely resistive load with resistor R while third to fifth column shows a capacitive load with R in parallel with capacitors $C_1 = 1.5$ nF, $C_2 = 3.3$ nF and $C_3 = 4.4$ nF.

		Impedance Association			
		R [Ω]	$R\|C_1$ [Ω]	$R\|C_2$ [Ω]	$R\|C_3$ [Ω]
* $R = 55.1\,\Omega$	**T**	$55.1\angle 0.0°$	$55.1\angle{-0.9°}$	$55.1\angle{-2.0°}$	$55.0\angle{-2.7°}$
	M	$56.1\angle 1.5°$	$56.1\angle 0.4°$	$55.3\angle{-1.3°}$	$55.8\angle{-2.5°}$
* $R = 100.0\,\Omega$	**T**	$100.0\angle 0.0°$	$99.9\angle{-1.7°}$	$99.7\angle{-3.7°}$	$99.6\angle{-4.9°}$
	M	$102.0\angle 0.6°$	$102.7\angle{-1.5°}$	$101.3\angle{-3.1°}$	$100.8\angle{-3.5°}$
* $R = 220.0\,\Omega$	**T**	$220.0\angle 0.0°$	$219.5\angle{-3.7°}$	$217.8\angle{-8.1°}$	$216.1\angle{-10.8°}$
	M	$225.9\angle 0.1°$	$223.5\angle{-2.6°}$	$222.3\angle{-7.3°}$	$220.6\angle{-9.8°}$
* $R = 292.4\,\Omega$	**T**	$292.4\angle 0.0°$	$291.3\angle{-4.9°}$	$287.3\angle{-10.7°}$	$283.5\angle{-14.2°}$
	M	$297.9\angle{-0.9°}$	$298.8\angle{-4.7°}$	$291.8\angle{-10.4°}$	$285.6\angle{-14.3°}$
* $R = 497.0\,\Omega$	**T**	$497.0\angle 0.0°$	$491.8\angle{-8.3°}$	$473.1\angle{-17.9°}$	$456.7\angle{-23.2°}$
	M	$498.3\angle{-2.2°}$	$490.6\angle{-7.6°}$	$472.6\angle{-16.9°}$	$461.2\angle{-23.6°}$
* $R = 668.0\,\Omega$	**T**	$668.0\angle 0.0°$	$655.4\angle{-11.1°}$	$613.0\angle{-23.4°}$	$578.6\angle{-30.0°}$
	M	$662.8\angle{-3.4°}$	$660.1\angle{-9.9°}$	$619.9\angle{-22.1°}$	$569.4\angle{-31.1°}$
* $R = 994.0\,\Omega$	**T**	$994.0\angle 0.0°$	$953.9\angle{-16.3°}$	$835.7\angle{-32.8°}$	$741.1\angle{-40.7°}$
	M	$1003.6\angle{-4.3°}$	$923.4\angle{-17.9°}$	$849.9\angle{-31.5°}$	$721.4\angle{-42.3°}$

Each sample measured in the Table 1 is the trimmed mean of 100 impedance measurements acquired in the tests. In this procedure, the upper and lower end quartiles of the sample set were eliminated to calculate the trimmed mean. The quartile was calculated as follows. As these are complex numbers, firstly, the modules were sorted, which have greater weight in the polar form, where 12.5% of the samples at the upper and lower ends were eliminated at this stage, resulting in a new data set. In this reduced data set, a new sort was performed, only this time the angles were sorted, and again 12.5% of the upper and lower samples were eliminated, resulting in a set with 50 valid data in polar form. Then, these data were converted from polar to rectangular form to calculate the average. The data was converted back to polar form as seen in Table 1.

The graphs in the Figs. 7 and 8 show a comparison between the measured impedance values as a function of the theoretical values with the same data presented in Table 1. The graph of Fig. 7 presents the data in polar form while in Fig. 8 in rectangular form.

The Fig. 9 presents the 2100 values of all impedance measurements performed in the test without any form of data treatment where we can observe the clouds of impedance measurements compared with the theoretical values represented in polar form.
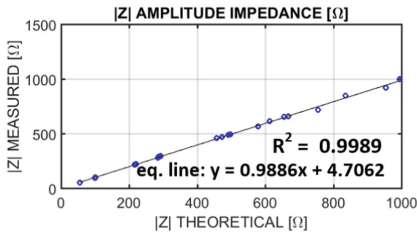
(a) Amplitude impedance $[\Omega]$
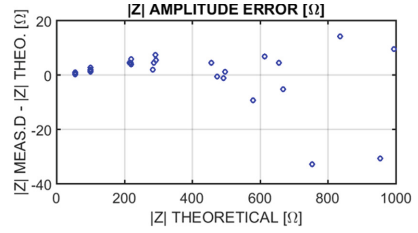
(b) Amplitude error $[\Omega]$
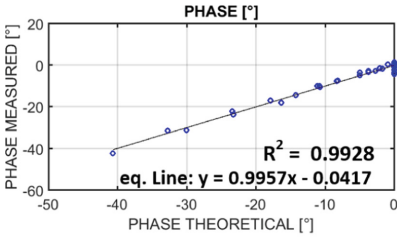
(c) Phase angle $[°]$
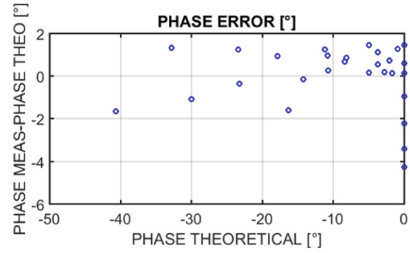
(d) Phase error angle $[°]$

Fig. 7. Impedance error in polar mode.
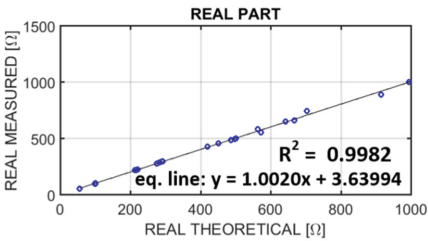
(a) Real part impedance $[\Omega]$
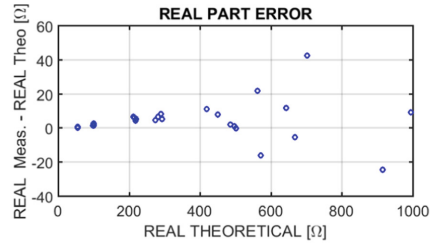
(b) Real part impedance error $[\Omega]$
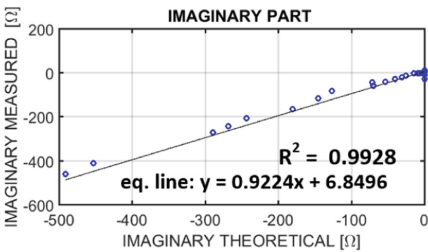
(c) Imaginary part impedance $[\Omega]$
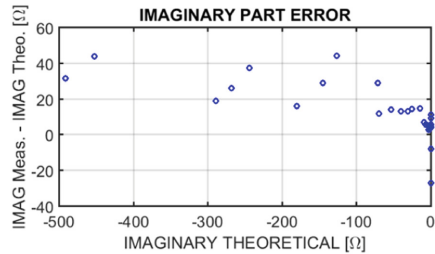
(d) Imaginary part impedance error $[\Omega]$

Fig. 8. Impedance error in rectangular mode.
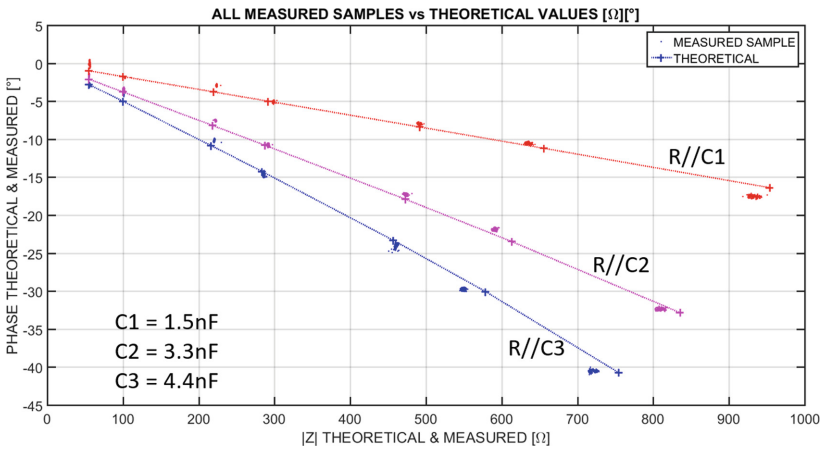
Fig. 9. All measured samples vs theoretical values

5   Discussion and Conclusion

Analyzing the measured and theoretical impedance results presented in the Figs. 7 and 8, we verified a correlation with Pearson's coefficient of $r = 0.9981 + 0.0134j$ indicating a positive linear relationship of the order of 99%. The amplitude of the standard deviation of the measured modules was $\pm 15.0175\,\Omega$, the average error was $\pm 1.8946\,\Omega$. Regarding the impedance phase of the measurement, the standard deviation found was $\pm 0.3458°$ and an average error of $\pm 0.2786°$.

The project is currently in its initial concept stage and only a prototype was built to analyze the effectiveness of the proposed architecture through experimental tests on phantoms. In the next stage, we will perform impedance measurements in biological tissues *ex-vivo* to compare these data with the impedance values known in the literature for the tissue under analysis. Then it is necessary to adapt the electrical insulation of the equipment to meet the safety requirements necessary for application in human beings.

Some changes must be made to achieve these goals. First, the volume of the impedance meter has to be reduced. A printed circuit board (PCB) is being developed to accommodate only the electronic components necessary for the project, avoiding the use of open source platforms and redundant electronic circuits. The concept of this modular architecture allows the implementation of multiple measurement channels. However, the maximum number of possible channels is 127, limited only by the Arduino's I^2C communication capability with the peripherals.

In summary, we believe that the impedance meter can be a viable alternative to contribute to studies related to electrical impedance myography.

A   Quadrature Demodulation Algorithm

To determine the amplitude, phase and offset parameters, the algorithm developed by Zhang [19] known as quadrature demodulation is used. Quadrature demodulation is a high performance algorithm developed to determine the four parameters of a sine wave discretized in time in digitization processes. The algorithm is based on the iterative method of total least squares widely used in digital signal processing for linearization and function adjustment. However, quadrature demodulation is a non-iterative method that provides fast results with low computational load, reducing processing time. In this way, the amplitude, phase and offset of a sine wave can be easily determined by:

$$s = A\sin\left(\alpha + \beta\right) + c = A\sin\left(\alpha\right)\cos\left(\beta\right) + A\cos\left(\alpha\right)\sin\left(\beta\right) + c \tag{6}$$

By rearranging Eq. 6 in matrix form, we can previously calculate a E matrix with known points of unit amplitude sines and cosines, phase α and with the same sampling frequency (31.25 kHz) as the discretized signal, we have:

$$[s] = \begin{bmatrix}\sin\left(\alpha\right) & \cos\left(\alpha\right) & 1\end{bmatrix}_{N\times 3} \begin{bmatrix}A\cos\left(\beta\right) \\ A\sin\left(\beta\right) \\ c\end{bmatrix}_{3\times 1} = E\begin{bmatrix}a \\ b \\ c\end{bmatrix} = Ep \tag{7}$$

Then;

$$[s] = [E][p] \tag{8}$$

The pseudo-inverse of E can also be previously calculated because it is the matrix with the values of the known points of sines and cosines with unitary amplitude. Thus, we can find the coefficients of the matrix p by multiplying both sides of the Eq. 8 by the pseudo-inverse matrix $E^{\dagger}$, so we have:

$$[p] = [E^{\dagger}][s] \tag{9}$$

Then, the amplitude, phase and offset of the discretized sine wave are determined by the equations:

$$A = \sqrt{a^2 + b^2} \tag{10}$$

$$\theta = \arctan\frac{b}{a} \tag{11}$$

$$c = \mathit{offset} \tag{12}$$

References

1. Bertemes-Filho, P., Felipe, A., Vincence, V.C.: High accurate Howland current source: output constraints analysis. Circ. Syst. **04**(07), 451–458 (2013)
2. Honorato, R.C., Ferraz, A.S.M., Kassiano, W., Carvalho, D.P., Ceccatto, V.M.: Test-retest reliability of electrical impedance myography in hamstrings of healthy young men. J. Electromyogr. Kinesiol. **56**, 102511 (2021). https://doi.org/10.1016/j.jelekin.2020.102511
3. Analog Devices. Data sheet - AD7762 - 625 kSPS, 24-Bit, 109 dB Sigma-Delta ADC With On-Chip Buffer (2014). https://www.analog.com/media/en/technical-documentation/data-sheets/AD7762.pdf
4. Hobson-Webb, L.D., Zwelling, P.J., Raja, S.S., Pifer, A.N., Kishnani, P.S.: Quantitative muscle ultrasound and electrical impedance myography in late onset Pompe disease: a pilot study of reliability, longitudinal change and correlation with function. Mol. Genet. Metab. Rep. **28**, 100785 (2021)
5. Huang, L.K., Huang, L.N., Gao, Y.M., Lucev Vasic, Z., Cifrek, M., Du, M.: Electrical impedance myography applied to monitoring of muscle fatigue during dynamic contractions. IEEE Access **8**, 13056–13065 (2020)
6. Texas Instruments. An-1515 a comprehensive study of the Howland current pump. Application report SNOA474A (2008)
7. Texas Instruments. Datasheet - INA129-EP Precision, Low Power Instrumentation Amplifiers. Texas Instruments Incorporated (2009–2015)
8. Texas Instruments. Analysis of improved Howland current pump configurations. Application report SBOA437 - October 2020 (2020)
9. Ivorra, A.: Bioimpedance monitoring for physicians: an overview. Centre Nacional de Microelectrònica Biomedical Applications Group, vol. 11, p. 17 (2003)
10. Lah, L.Y.M.: Avaliação de atividade muscular do bíceps braquial por miografia de impedância elétrica. Master's thesis, Universidade Federal do ABC, São Bernardo do Campo (2017)
11. Minipa. Manual - OSCILOSCÓPIO DIGITAL. Minipa do Brasil Ltda. (2014)
12. Minipa. Manual - MFG-4202-FUNCTION SIGNSL GENERATORs. Minipa do Brasil Ltda. (2019)
13. Myolex. Quantitative muscle health measurement for lower costs and improved standard of care (2022). Accessed 22 Mar 2017
14. RJL Systems Inc.: Quantum v segmental bia-bioelectrical impedance analyzer (2022). Accessed 22 Mar 2017
15. Rutkove, S.: Electrical impedance myography as a biomarker for ALS. Lancet Neurol. **8**(3), 226 (2009)
16. Rutkove, S.B.: Electrical impedance myography: background, current state, and future directions. Muscle Nerve **40**(6), 936–946 (2009)
17. Silva, O.L.: Muscle contraction detection using Electrical Impedance Tomography. Ph.D. thesis, Universidade de São Paulo (2012)
18. Tektronix. Manual - DMM800 Series Digital Multimeters. Tektronix Inc. (1992)
19. Zhang, J.Q., Xinmin, Z., Xiao, H., Jinwei, S.: Sinewave fit algorithm based on total least-squares method with application to ADC effective bits measurement. IEEE Trans. Instrum. Meas. **46**(4), 1026–1030 (1997)

Biomedicine. New Advances and Applications

Advanced Incremental Attribute Learning Clustering Algorithm for Medical and Healthcare Applications

Siwar Gorrab[(✉)], Fahmi Ben Rejab, and Kaouther Nouira

Université de Tunis, ISGT, LR99ES04 BESTMOD, Tunis, Tunisia
`siwarg9@gmail.com`

Abstract. Data-driven science and its consequences in the extensive field of artificial intelligence and especially in machine learning have the potential to drive important changes in medicine. Therewith, new instances including new incoming mixed features are unceasingly emerged at high rate as data streams. Hence, big data promises immense advantages for medical and healthcare research. Aiming to analyse these medical data streams in the lastly mentioned fields, this paper provides a better insight into an advanced incremental attribute and object learning k-prototypes algorithm for healthcare and medical applications. Experiments performed on various real mixed healthcare data sets show that the proposed real-time healthcare/medical application is efficient and may cover different medical case studies such as patient monitoring, disease control, and clinical support systems for better prediction of diseases. The measured evaluation criteria accentuate the efficiency of the proposed method compared to the conventional k-prototypes method.

Keywords: Big data · Mixed data stream · Incremental k-prototypes · Merge · Medical and healthcare applications

1 Introduction

Nowadays, artificial intelligence is unceasingly growing to change the healthcare system, driven by the juxtaposition of big data and potent machine learning techniques. Medicine, like many other fields, is experiencing a confluence of two recent developments: the rise of big data, and the growth of advanced artificial intelligence and machine learning techniques that can be further used to find complex patterns among those data [1]. Into the bargain, data mining applications can significantly benefit the medicine and healthcare industry with developing multiple tools to advance medical research and to improve the process of clinical care as well as their efficiency. These tools count on algorithms and machine learning programs, created from healthcare data that can make future predictions and recommendations. The big data revolution in healthcare is well underway, driven by exponential growth in available data in the form of data streams [2]. The huge amounts of these data generated by media sensors in health

monitoring systems, by medical diagnosis that produce both numerical as well as categorical contents, and from health service providers are too complex and enormous to be processed and analyzed by traditional data mining methods [3]. So, mining these massive data sets faster and more accurately and making it fluently accessible for predictive analysis remains a key challenge of the health care and medical industry. For example, imagine you are a doctor and a patient you once saw in your practice who was affected by a rare condition or unique set of comorbidities. You wondered if there were similar patients in your medical system hoping to gain insight into their disease progression or therapeutic outcomes [2]. Actually, this doctor is handling dynamic attribute and object spaces when ceaselessly new patients' parameters have to be tracked, new analysis have to be done, and results should be stored and suitably analyzed in order to ensure the best patient's followup. To do so, many data mining techniques such as classification, clustering, and association rules are used for making a decision regarding the continuously emerging patient's health conditions in order to provide benefits for grouping patients having similar type of diseases or health issues so that to provide them with effective treatments [3]. This paper focuses on proposing an advanced incremental attribute learning clustering method based on k-prototypes algorithm in the interest of enhancing healthcare applications for efficient patient care and disease assessment constraints when dealing with big data in medicine and healthcare fields. In point of fact, our aim is to build a real-time framework that dynamically handles the differences in numerical and categorical features in an emerging data stream environment and groups them into similar clusters while tackling the incremental object and attribute learning spaces at the same deal. This would be a medical/healthcare application based on the proposed IK-prototypes method proposed in [4]. Simply put, this application is capable of handling a bulk of updates owing to the mixed healthcare training samples which become available one after another over time. Hence, this new proposed medical/healthcare application searches to enhance medicine and to improve healthcare quality. It can be applied where ever new data streams emerge escorted with new features. For instance, to detect unknown diseases, causes of diseases, and identification of medical treatment methods. It also helps medical researchers in constructing drug recommendation systems, developing health profiles of patients, understanding new diseases and therapies, predicting outcomes at earlier stages and making real-time decisions. We validate the effectiveness of our proposal through comparisons, conducted between the IHK-prototypes and the conventional k-prototypes method on four mixed medical as well as healthcare data sets. The quality of the solutions offered by each method is rated in terms of run time value and similarity between and within clusters measures. The rest of this paper is structured in this way: Sect. 2 provides background on conventional k-prototypes algorithm and related works. Section 3 presents our proposed approach. Section 4 illustrates the experimental study and discusses the corresponding results and Sect. 5 concludes the paper.

2   K-Prototypes Algorithm and Related Works

2.1   Theoretical Concepts of K-Prototypes Algorithm

Proposed in [5] which integrates both k-means [6] and k-modes [7] algorithms for clustering data, the k-prototypes algorithm is practically more useful for mixed-type objects. Given a data set $X = \{x_1...x_n\}$ of n data points containing m_r numeric attributes and m_t categorical attributes, the focal objective of the k-prototype algorithm is to group the data set X into k different clusters while minimizing the following cost function in Eq. (1):

$$J = \sum_{i=1}^{n} \sum_{j=1}^{k} u_{ij} d(x_i - c_j), \tag{1}$$

where $u_{ij} \in \{0,1\}$ is an element of the partition matrix U_{n*k}, indicating the membership of data point i in cluster j ; $c_j \in C = \{c_1...c_k\}$ is the center of the cluster j and $d(x_i - c_j)$ is the dissimilarity measure defined in Eq. (2):

$$d(x_i - c_j) = \sum_{r=1}^{m_r} \sqrt{(x_{ir} - c_{jr})^2} + \sum_{t=1}^{m_t} \delta(x_{it}, c_{jt}), \tag{2}$$

where x_{ir} and x_{it} represent respectively the values of the numeric attribute r and the categorical attribute t for a data point i; c_{jr} represents the mean of the numeric attribute r and cluster j.

Algorithm 1. K-prototypes algorithm

1: **Input:** X: data set, k: number of clusters
2: **Output:** Cluster centers
3: **Begin**
4:     **Choose** randomly k initial cluster centres from the data set X.
5:     **Attribute** each data point in X to its nearest cluster center using Eq. (2).
6:     **Update** the cluster centres after each allocation using.
7:     If the updated cluster centers are identical to the previous ones then terminate, otherwise, go back to step 5.
8: **End.**

2.2   Related Works

Medical and Healthcare Applications
F. Ben Rejab et al. proposed a health monitoring system based on parallel-APPROX SVM [9] to deal with the high rate of false alarms generated by the health monitoring system in intensive care units. In [10], Dong et al. proposed a Hadoop/MapReduce architecture for large scale clinical informatics applications, which provides a scalable solution to meet the rapidly increasing, imperative big data needs of clinical research. Mehre et al. presents in [11] a content-based image retrieval (CBIR) system for pulmonary nodules using optimal feature sets and class membership-based retrieval to enhance the performance of

retrieval. Additionally, Dhara et al. have proposed [12] a Content-Based Image Retrieval System for Pulmonary Nodules to assist radiologists in self-learning and diagnosis of lung cancer where the pulmonary nodules are segmented using a semi-automated technique. Moreover, a dermatologist-level classification of skin cancer with deep neural networks has been proposed in [13] and approved that the CNN achieves performance on par with all tested experts, demonstrating an artificial intelligence capable of classifying skin cancer with a level of competence comparable to dermatologists. Recently, instagram photos reveal predictive markers of depression, in [14], with applying machine learning tools to successfully identify them and resulting models outperformed general practitioners' average unassisted diagnostic success rate for depression. Moreover, in [15], Zhong and Zhang have developed an uncertainty-aware INVASE to quantify predictive confidence of healthcare problem and which enhances breast cancer diagnosis based on feature selection.

Clustering and Healthcare Applications
The huge amount of healthcare data, coupled with the need for data analysis and decision making tools has made data mining interesting research areas. Specifically, the unsupervised clustering technique helps to discover and understand hidden patterns in a healthcare data set. Presently, a large number of clustering algorithms are available for clustering healthcare data In [16], visual topic models for healthcare data clustering has been proposed by Prasad et al. to properly extract health topics for analyzing discriminative and coherent latent features of tweet documents in healthcare applications. Also in [17], a cluster based outlier detection algorithm has been proposed so that to detect and remove outliers. Furthermore, in [3], an enhanced k-Means clustering algorithm for pattern discovery, namely G-means, has been developed based on a greedy approach to produce the preliminary centroids and then takes k or lesser passes over the data set to adjust these center points.

Although some successful and developed classification/clustering algorithms for mining big data healthcare fields, the k-prototypes algorithm has not been yet evaluated to handle medical data. Thus, here is a requirement to upgrade the unsupervised techniques with the ability to tackle the incremental numeric and categorical attribute learning task in the healthcare and medical fields. Add it to that, our proposal is capable of handling continuously emerging mixed data streams within memory and time restrictions, compared to these previously mentioned state of the art healthcare applications and methods.

3   Proposed Approach

In this section, we cover our proposed big data solution in medicine and healthcare fields, through incremental attribute learning (IAL) context. This is proposed towards handling mixed large scale data in the form of continuously emerging data streams. We also shed light on implementations.

3.1   Definition and Approach Presentation

The main purpose and the essence behind our proposed healthcare/medical application that is to facilitate and to improve healthcare applications for efficient patient care and disease assessment constraints in a streaming data environment. It is based on the previously proposed IK-prototypes method [4], founded on the merge procedure. Likewise, in the purpose of constructing a real-time healthcare/medical solution that dynamically handles the differences in numerical and categorical healthcare features, arriving with emerging data streams, our proposed method groups them into similar clusters while tackling jointly the incremental object and attribute learning tasks. For greater understanding, non-incremental clustering algorithms require to store and process all the input data pattern matrix in the memory, which generally need the complete input data being loaded into memory and thus results in high requirements of memory space. Nevertheless, we are managing a dynamic scope of big data in healthcare and medical fields through which doctors and medical staff should handle these data streams by means of advanced data mining techniques. So, our proposal is supposed to cluster continuously arriving mixed data, with newly joined attributes, within memory and time restrictions. Bearing these restrictions in mind, our proposed solution for clustering mixed medical data streams is able to ideally fulfill the following requirements:

– Provide timely results by performing fast and incremental processing of incoming data objects and without retraining from the scratch.
– Rapidly adapt to changing dynamics of the data, and performs well at the emergence of new attributes in addition to the old set ones. That is to scale to the number of objects that are continuously incoming, escorted with new mixed patient's features.
– Provide a model representation which is not only compact, but also does not grow with the number of objects processed.

Figure 1 provides a better insight into the focal concept behind our proposed healthcare/medical IHK-prototypes method, established in three steps which we will be detailed lately.

   For illustrative purposes, doctors are handling a dynamic space when ceaselessly new patients' parameters have to be tracked, new analysis have to be done, and results should be stored and suitably analyzed in order to ensure the best patient's followup. To do so, we have developed a medical/healthcare application based on IK-prototypes [4] method that well performs as a healthcare/medical service provider for making as suitable decisions as possible regarding patient health conditions. It is able to group patients having similar type of diseases or health issues so that the doctors or healthcare organizations can provide them with effective treatments. At an early stage, an input patient's data is firstly accessible, which we are supposed to learn using the conventional k-prototypes algorithm. The result here is k different clusters such as similar instances are joined together in one cluster. The learning process could end up at this level with a coherent clustering result. Secondly, the sequentially arriving chunks of
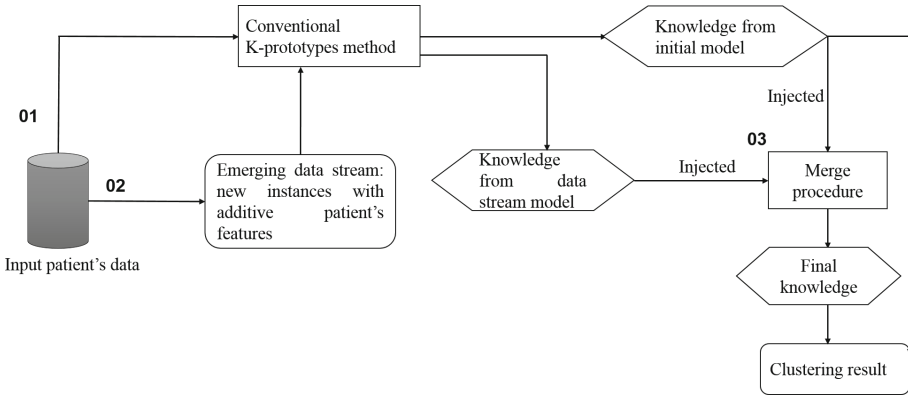
Fig. 1. The proposed healthcare and medical Incremental K-prototypes method through incremental attribute learning context

data namely data streams, as being the main source of big data, will be processed independently in the learning phase using the conventional k-prototypes method. Simply put, at the arrival of new patient's instances escorted with new features, we suggest to keep in background the conventional k-prototypes algorithm which would, in this step, learn only these incoming data streams. Hence, we aim to create k' clusters using the same k-prototypes algorithm and then save the obtained results as a second knowledge from the data stream model. Thereafter, the merge procedure processes the set of gained clusters k and k' from both initial and data stream model in order to generate the final cluster centers and to achieve the incremental attribute learning task. Consequently, we first gained knowledge from the merge procedure, namely k cluster centres resulting from all data accessible at that time. So, the learning process could end up at this level with a coherent clustering result. Our proposed IK-prototypes algorithm for healthcare and medical applications is detailed in the following Algorithm 2:

One may ask a question: how can we integrate the acquired results derived from both models in such a manner to get a coherent model?

We are going to provide a consistent answer to this question and to deeply explain the mechanism while illustrating the merge procedure in the next subsection.

3.2   Merge Procedure

Aiming to achieve the incremental attribute and object learning tasks, the main idea was to merge knowledge coming from both initial and data stream models (corresponding to k and k' clusters) such as each similar couple of clusters are fused in one resulting cluster, grouping the most likely instances together. In order to showcase the merge process, the focal challenge remains in selecting the most suitable couple of clusters to be combined from the present distribution

Algorithm 2. Incremental Healthcare K-prototypes algorithm

1: **Input:** X: patients' data set, k: number of clusters
2: **Output:** k cluster centers
3: **Begin**
4: **Choose** randomly k initial prototypes from each arriving healthcare data stream X
5: **Attribute** each data point in X to its nearest cluster center using Eq. (2).
6: **Update** the cluster centres after each allocation.
7: If the updated cluster centers are identical to the previous ones then terminate, otherwise, go back to step 5.
8: **If** a new data stream emerges, escorted with new attributes patient's then go back to step 5,
    Merge the resulting clusters from initial and data stream models, otherwise, terminate.
9: **End.**

$K = k + k'$ clusters and while guaranteeing the return to the initial number of clusters k because this work deals only with incremental object and attribute learning spaces and not with incremental class learning space. To calculate the similarity between clusters, two significant indexes are used as follows:

1. Davies-Bouldin index (DB) [18]: the similarity measure here is based on a comparison between the distance between clusters and the size of the clusters themselves (DB values closer to zero relate to a better partition of clusters). It is calculated using Eq. (3):

$$DB = \frac{1}{k} \sum_{i=1}^{k} \max(\frac{s_i + s_j}{d_{ij}}); i \neq j \tag{3}$$

   DB is defined as the average similarity between each cluster C_i for $i = 1, ..., k$ and its most similar one is C_j, Where s_i is the cluster diameter that represents the average distance between the point i/j and it's cluster center and d_{ij} represents the distance between both cluster centers i and j.

2. Calinski-Harabasz score (CH) [19]: also known as the variance ratio criterion, calculates the ratio of the sum of between-clusters dispersion and of inter-cluster dispersion for all clusters. An upper CH value relates to a model with better defined clusters. It is calculated as follows in Eq. (4):

$$s = \frac{tr(\sum_{q=1}^{k} \sum_{x \in C_q} (x - c_q)(x - c_q)^T)}{tr(\sum_{q=1}^{k} n_q (C_q - c_E)(C_q - c_E)^T)} * \frac{n_E - k}{k - 1} \tag{4}$$

   where n_E is the size of the set of data **E**, k is the number of clusters, n_q is the number of points in cluster q and c_q and c_E are respectively the centers of the cluster q and of E.

However, the highest DB index and the lowest CH scores may not be related to the same cluster. Means, once in a while the highest DB and the lowest CH may result in different combination of clusters. So, they may not be the best choices for the merge procedure. In such a case, our algorithm will carry on with merging both clusters resulting from the two calculated indexes and ends up with maintaining the cluster with the lowest Sum of Squared Error (SSE) value that determines the dispersion of elements of a cluster in relation with their centroids. Besides, the more it is closer to zero, the more clusters are well defined and its calculation is as follows in Eq. (5) :

$$SSE_{x \in C} = \sum_{i=1}^{n} \sum_{j=1}^{m} (x_{kj} - c_j) \tag{5}$$

where c_j is the centre of the cluster j.

Specifically, in our study, the merge procedure is based on the following three consecutive steps:

1. Calculate the DB index and the CH score for each cluster.
2. Determine the most similar couple of clusters to be merged.
3. Merge the selected clusters until reaching the initial k.

In reference to the merge algorithm, illustrated in Algorithm 3, we will explain the functions that have been used there.

– **Compute (cluster):**
  - **Input:** Clusters.
  - **Output:** Davies-Bouldin index and Calinski-Harabasz scores of corresponding clusters.

  It is the key function of the merge procedure because it determines the best couple of clusters that will be merged. Actually, it computes the DB index and the CH score of each cluster, provided ultimately in the two symmetric matrices.
– **Max (DB/CH), Min (DB/CH) :**
  - **Input:** Matrix of corresponding calculated indexes.
  - **Output:** Highest and/or lowest scores.

  As indicated by their names, they determine respectively the highest and the lowest indexes from the input matrices.
– **Merge (clusters):**
  - **Input:** cluster i, cluster j.
  - **Output:** one cluster ij.

  This function permits to fuse the most two likely clusters in such a manner to result in one single cluster, incorporating elements from both initial clusters.
– **Delete(cluster):**
  - **Input:** clusters.

  Once merging the most suitable clusters together in one resulting cluster, removing each single one of them is required so that to avoid redundancy.

Algorithm 3. Merge algorithm

1: **Input: clusters** $= \{c_1, c_2, ..c_k\}$
2: **Output: clusters** $= \{c'_{i..k}\}$
3: **Begin**
4:   **For** each cluster A_i in $\{c_1, c_2, c_k\}$ **do**
5:   **For** each cluster B_j in $\{c_4, c_5, c_{k'}\}$ **do**
6:     $DB \leftarrow computeDaviesBouldinIndex(A_i, B_j)$
7:     $CH \leftarrow computeCalinskiHarabaszIndex(A_i, B_j)$
8:   **end For**
9:   **end For**
10:   **For** each cluster A_i in $\{c_1, c_2, c_k\}$ **do**
11:   **For** each cluster B_j in $\{c_4, c_5, c_{k'}\}$ **do**
12:     **If** $DB(A_i, B_j) = \text{Max(DB)}$ **then**
13:       $Cluster1 \leftarrow A_i$
14:       $Cluster2 \leftarrow B_j$
15:     **end If**
16:     **If** $CH(A_i, B_j) = \text{Min(CH)}$ **then**
17:       $Cluster3 \leftarrow A_i$
18:       $Cluster4 \leftarrow B_j$
19:     **end If**
20:   **end For**
21:   **end For**
22:   **For** i in $[1..k]$ **do**
23:   **If** (Cluster1=Cluster3) and (Cluster2=Cluster4) **then**
24:     $c'_i \leftarrow Merge(Cluster1, Cluster2)$
25:     Delete (Cluster1)
26:     Delete (Cluster2)
27:     i=i+1
28:   **end If**
29:     $SSE1 \leftarrow SSE(Merge(Cluster1, Cluster2))$
30:     $SSE2 \leftarrow SSE(Merge(Cluster3, Cluster4))$
31:   **If** SSE1 < SSE2 **then**
32:     $c'_i \leftarrow Merge(Cluster1, Cluster2)$
33:     Delete (Cluster1)
34:     Delete (Cluster2)
35:   **Else**
36:     $c'_i \leftarrow Merge(Cluster3, Cluster4)$
37:     Delete (Cluster1)
38:     Delete (Cluster2)
39:   **end If**
40:   **end For**
41: **Return** clusters $= \{c'_{i..k}\}$
42: **End.**

4   Simulation Experiments and Performance Analysis

In this section, number of experiments are conducted on several real mixed data sets to compare our proposal with the conventional k-prototypes method.

4.1   Simulation Environment

We have implemented our proposed healthcare/medical IHK-prototypes method using python 3.7 language and executed on an Intel i5 processor (2.5 GHz) with 4 GB memory running on windows 7 operating system. Aiming to assess our proposal's performance and capability, we have applied the IHK-prototypes method as well as the conventional k-prototypes method to cluster the following four real-world mixed data sets from both medical and healthcare fields:

- **Stroke Prediction (SP)**: this data set, composed of 5110 instances, is used to predict whether a patient is likely to get stroke based on the 12 input parameters (7 numerical and 5 categorical ones). SP is also derived from Kaggle[1].
- **Pharmaceutical Drug Spending by countries (PDS)**: it describes the total pharmaceutical drug spending for specific countries, having 1036 objects described by 7 attributes (5 numerical and 2 categorical). PDS is derived from Kaggle[2].
- **Breast Cancer Wisconsin (BCW)**: it is a diagnostic wisconsin breast cancer data set, imported from U.C.I repository? BCW holds 569 instances and 32 attributes (31 numerical and 1 categorical). Features are computed from a digitized image of a fine needle aspirate of a breast mass where they describe characteristics of the cell nuclei present in the image.
- **Personality Scale Analysis (PSA)**: is a scoring-based personality scale analysis. PSA is composed of 315 objects, described by 8 attributes (6 numerical and 2 categorical) and imported from Kaggle[3].

For a better understanding, we take for instance the SP data set to deeply explain the philosophy of our proposal's implementation. Admitting that SP contains 5110 instances and 12 attributes describing the patients, we start by introducing an input data composed of 1000 objects and 9 attributes. As time proceeds, a data stream came to join the learning process with 4110 instances and 12 attributes (9 old attributes and 3 new ones). Our proposed solution keeps learning these new added samples escorted with newly joined features. It is supposed to apply the conventional k-prototypes algorithm only on this recently joined mixed data stream.

4.2   Evaluation Measures

In order to estimate the validity of our unsupervised IAL clustering algorithm for healthcare and medical fields, we have opted to use indices that estimate the cluster cohesion and the cluster separation and combine them to compute a quality measure. Also, we have attributed an up or down arrow to each abbreviation in which the down arrow denotes that a lower value of that index reflects a better partition between clusters and/or the lower index is better. Contrary to the up arrow which means exactly the opposite.

---

[1] https://www.kaggle.com/fedesoriano/stroke-prediction-dataset.
[2] https://www.kaggle.com/tunguz/pharmaceutical-drug-spending-by-countries.
[3] https://www.kaggle.com/brsdincer/personality-scale-analysis.

1. The run time (RT ↓): it is, in all, the time needed to maintain the final clustering result (instances are divided between k clusters) starting from the beginning of the learning process.
2. The Sum of Squared Error (SSE ↓): it enlightens the inter-cluster and the intra-cluster similarity with calculating the sum of squared errors of each object to its nearest cluster center. SSE is defined by Eq. (5).
3. The Silhouette Coefficient [20] (SC ↑): it is bounded between −1 for incorrect clustering and +1 for highly dense clustering. A higher SC score relates to a model with better defined clusters. SC is composed of two scores a and b and calculated using Eq. (6):

$$s = \frac{b - a}{\max(a, b)} \tag{6}$$

Having a: is the mean distance between a sample and all other points in the same cluster; b: is the mean distance between a sample and all other points in the next nearest cluster.

These measured evaluation criteria accentuate the efficiency of the proposal compared to the conventional k-prototypes method.

4.3   Results Analysis and Discussion

Table 1. The SSE, SC and RT values of conventional k-prototypes vs. Incremental Healthcare K-prototypes methods per data set

Data sets	Conventional K-prototypes			Incremental K-prototypes		
	RT (second)	SSE	SC	RT (second)	SSE	SC
SP	87.788	1.920	0.363	56.229	1.651	0.388
PDS	11.090	1.956	0.469	6.772	1.577	0.523
BCW	7.188	2.130	0.457	4.543	1.547	0.467
PSA	2.956	2.587	0.487	1.794	1.682	0.576

Now, we proceed by detailing the experimental results in Table 1 and further discussing them after having compared the performance of our proposal versus the conventional k-prototypes method. Effectively, the healthcare/medical IHK-prototypes algorithm accomplishes the incremental attribute and object learning tasks when dealing with continuously emerging mixed medical and healthcare data streams incrementally and without retraining from the scratch. Still, the conventional k-prototypes method requires to retrain the model from the scratch once new chunk of data escorted with newly joined attributes than the old set ones becomes accessible over time. Consequently, this latter requires to firstly stop the program, then to fuse the initial input data and the new emerging data stream with its new added attributes, describing patients, and finally to retrain from scratch with re-applying the k-prototypes algorithm.

1. **Run Time Results Analysis:** Table 1 displays the RT results after comparing the IHK-prototypes method to the conventional k-prototypes method. We may notice that our proposed IHK-prototypes requires almost less the half time for its execution compared to the conventional k-prototypes and the offset is proportional to the size of the data set. By way of illustration, the PDS data set requires for its learning process respectively 11.09 s and 6.772 s using by order the k-prototypes and the IK-prototypes. In other words, to learn the pharmaceutical drug spending input data and the corresponding emerging data streams, joined with new features that better describe the affair as learning proceeds, we need almost less by half time to achieve a predictive data mining analysis and opting for a coherent decision making.
2. **Sum Of Squared Error Results Analysis:** Table 1 underlines the fact that we have acquired the lowest SSE values, when using IHK-prototypes method for all used data sets which lead to better defined clusters: the maximum similarity within clusters and the minimum similarity between clusters are gained.
3. **Silhouette Coefficient Results Analysis:** Analyzing the SC results, detailed in Table 1, we can confirm that our proposal outperforms the conventional k-prototypes when dealing with incremental object and attribute tasks in medical field since it gained the highest SC score for all used data sets and further highlight our proposal relevance in IAL context.

In sum, it is crucial and essential to provide the memory and time restrictions when learning mixed data streams incrementally. Here, the conventional k-prototypes method needs the complete input data being loaded into the memory which results in elevated need of memory space and time consuming. The value of our proposal can be translated into understanding and predicting diseases and outcomes at earlier stages, making real-time decisions, promoting patients' health, enhancing medicine, reducing cost and improving life expectancy and healthcare quality.

5   Conclusion

In this paper, we have presented an application of the proposed incremental k-prototypes algorithm for clustering big data in medicine. We aim to enhance to offer advanced healthcare monitoring systems, services and medical applications such as helping in early detection of diseases, treatment recommendations, and clinical services to doctors. The conducted experiments affirm that the proposal outperforms the conventional k-prototypes algorithm based on different evaluation measures. As for future work, we plan on forming an enhanced version of the IK-prototypes algorithm, capable to deal with evolving feature and object spaces, means to append it with the decremental aspect.

References

1. Price, I.I., Nicholson, W.: Artificial intelligence in health care: applications and legal issues (2017)

2. Austin, C., Kusumoto, F.: The application of Big Data in medicine: current implications and future directions. J. Interv. Cardiac Electrophysiol. **47**(1), 51–59 (2016)

3. Haraty, R.A., Dimishkieh, M., Masud, M.: An enhanced k-means clustering algorithm for pattern discovery in healthcare data. Int. J. Distrib. Sens. Netw. **11**(6), 615–740 (2015). SAGE Publications Sage UK: London, England

4. Gorrab, S., Rejab, F.B.: IK-prototypes: incremental mixed attribute learning based on K-prototypes algorithm, a new method. In: Abraham, A., Piuri, V., Gandhi, N., Siarry, P., Kaklauskas, A., Madureira, A. (eds.) ISDA 2020. AISC, vol. 1351, pp. 880–890. Springer, Cham (2021). https://doi.org/10.1007/978-3-030-71187-0_81

5. Huang, Z.: Extensions to the k-means algorithm for clustering large data sets with categorical values. Data Mining Knowl. Discov. **2**(3), 283–304 (1998)

6. MacQueen, J.: Some methods for classification and analysis of multivariate observations. In: Proceedings of the Fifth Berkeley Symposium on Mathematical Statistics and Probability, vol. 1(14), pp. 281–297 (1967)

7. Huang, Z.: A fast clustering algorithm to cluster very large categorical data sets in data mining. DMKD **3**(8), 34–39 (1997)

8. Uddin, M.F., Gupta, N.: Seven V's of Big Data understanding Big Data to extract value. In: Proceedings of the 2014 Zone 1 Conference of the American Society for Engineering Education, pp. 1–5. IEEE (2014)

9. Ben Rejab, F., Ksiaâ, W., Nouira, K.: Health monitoring system based on parallel-APPROX SVM. In: Rojas, I., Ortuño, F. (eds.) IWBBIO 2017. LNCS, vol. 10208, pp. 3–14. Springer, Cham (2017). https://doi.org/10.1007/978-3-319-56148-6_1

10. Dong, X., et al.: Leverage Hadoop framework for large scale clinical informatics applications. In: AMIA Joint Summits on Translational Science Proceedings, p. 53 (2013)

11. Mehre, S.A., Dhara, A.K., Garg, M., Kalra, N., Khandelwal, N., Mukhopadhyay, S.: Content-based image retrieval system for pulmonary nodules using optimal feature sets and class membership-based retrieval. J. Digit. Imaging **32**(3), 362–385 (2019)

12. Dhara, A.K., Mukhopadhyay, S., Dutta, A., Garg, M., Khandelwal, N.: Content-based image retrieval system for pulmonary nodules: assisting radiologists in self-learning and diagnosis of lung cancer. J. Digit. Imaging **30**(1), 63–77 (2017)

13. Esteva, A.: Dermatologist-level classification of skin cancer with deep neural networks. Nature **542**(7639), 115–118 (2017)

14. Reece, A.G., Danforth, C.M.: Instagram photos reveal predictive markers of depression. EPJ Data Sci. **6**, 1–12 (2017)

15. Zhong, J.X., Zhang, H.: Uncertainty-aware INVASE: enhanced Breast Cancer diagnosis feature selection. arXiv preprint arXiv:2105.02693 (2021)

16. Rajendra Prasad, K., Mohammed, M., Noorullah, R.M.: Visual topic models for healthcare data clustering. Evol. Intell. **14**(2), 545–562 (2021)

17. Christy, A., Gandhi, G.M., Vaithyasubramanian, S.: Cluster based outlier detection algorithm for healthcare data. Procedia Comput. Sci. **50**, 209–215 (2015)

18. Davies, D.L., Bouldin, D.W.: A cluster separation measure. IEEE Trans. Pattern Anal. Mach. Intell. **2**, 224–227 (1979)

19. Caliński, T., Harabasz, J.: A dendrite method for cluster analysis. Commun. Stat. Theory Methods **3**(1), 1–27 (1974)

20. Rousseeuw, P.J.: Silhouettes: a graphical aid to the interpretation and validation of cluster analysis. J. Comput. Appl. Math. **20**, 53–65 (1987)

Assessment of Inflammation in Non-calcified Artery Plaques with Dynamic 18F-FDG-PET/CT: CT Alone, Does-It Detect the Vulnerable Plaque?

Mamdouh S. Al-enezi[1,2], Abdelouahed Khalil[3], Tamas Fulop[3], Éric Turcotte[1], and M'hamed Bentourkia[1(✉)]

[1] Department of Nuclear Medicine and Radiobiology, Faculty of Medicine and Health Sciences, 3001, 12th Avenue North, Sherbrooke, QC J1H5N4, Canada
Mhamed.Bentourkia@USherbrooke.ca

[2] Department of Diagnostic Radiology, Faculty of Applied Medical Science, University of Hail, Hail, Saudi Arabia

[3] Department of Medicine, Faculty of Medicine and Health Sciences, 3001, 12th Avenue North, Sherbrooke, QC J1H5N4, Canada

Abstract. Background: The goal of this work was to measure artery inflammation in aged volunteers with atherosclerosis using computed tomography (CT) and positron emission tomography (PET) with 18F-FDG. The artery plaques are composed of lipid rich fibrous tissue and foamy macrophages and are the most vulnerable for detachment. Such plaques can be differentiated by their density with CT imaging. Methods: A healthy artery (NAR) was considered with no plaque on a CT images and with density between 51 and 130 Hounsfield Units (HU). A non-calcified plaque (NCP) and a calcified plaque (CP) were respectively identified as having a density $\leq$ 50 HU and >130 HU. In the calcified arteries, the calcification area divided by the artery area (RCA) and the calcification score (ACS) were classified with Hierarchical K-means algorithm into 4 clusters and were correlated with the metabolic rate of 18F-FDG (MRG). Results: we found MRG statistically higher in NCP in comparison to NAR and CP in subjects without medication ($P < 0.05$). In subjects under-medication, NCP values were found the lowest. MRG of NCP in non-medication subjects was statistically significantly different from CP with small area but not from CP with large areas ($P = 0.40$). In under-medication subjects, no statistical differences were found between NCP and CP independently of plaque area and density. Conclusion: Since the low-density plaque was reported as the vulnerable plaque, based on the present work, this latter can be simply identified on CT images with intensity between 30 HU and 50 HU.

Keywords: Atherosclerosis · Artery inflammation · Kinetic modeling · Computed tomography · Positron emission tomography

1   Introduction

Atherosclerosis especially affects elderly and it is the most common type of cardiovascular complications causing mortality and morbidity [1]. The disease starts by forming an atherosclerotic plaque in the large arteries, due mainly to lipid accumulation and oxidation [2].

Computed tomography (CT) provides quantification of calcified plaques (CP) and non-calcified plaques (NCP) by means of diverse techniques [3, 4]. Besides, NCP was the most prone to rupture as reported in several works [5–7]. This has led to the concept of the "*vulnerable plaque*" describing atherosclerotic plaques with high risk of rupture. Intravascular ultrasound (IVUS) and optical coherence tomography are able to identify the NCP and to measure the fibrous cap thickness with a good accuracy and a high spatial resolution [8]. However, these modalities are invasive and lack the penetration depth, adding difficulties to assess plaque morphology [9]. Magnetic resonance imaging (MRI) has a great potential to assess atherosclerosis. Several studies reported the ability of MRI to differentiate fibrous cap and lipid core components of the atherosclerotic plaque [10–12]. Nevertheless, a need of longer imaging times to enhance signal to noise ratio and MRI environment not suitable for patients with claustrophobia, pacemakers, defibrillators, and certain aneurysm clips are of major limitations [13].

In recent years, several studies using CT imaging identified the NCP and investigated its morphology, localizing it below 30 HU and in other studies below 50 HU [14–17]. The non-invasiveness, fast acquisition, availability and low cost of CT imaging offers several privileges in plaque measurement based on its density. In combination with CT, positron emission tomography (PET) imaging is noninvasively able to assess high-risk features of unstable plaque with superior sensitivity up to the picomolar of tracer concentration with respect to other non-invasive imaging modalities [18]. ^{18}F-FDG and PET are widely used in research and the clinic and have been reported to locate artery plaque inflammation [19–21]. PET with ^{18}F-FDG was shown to detect the inflammation within the fibrous cap in NCP [22]. The two-tissue compartment model of ^{18}F-FDG offers the calculation of the metabolic rate of glucose (MRG) [23], although it is not often used in the clinic principally due to its lengthy measurement [24–26].

It has been reported that plaque lipid rich and fibrous tissue can be discriminated based on its density on CT images [3, 27, 28], and that the lipid rich plaques are the most vulnerable for detachment [3]. Other investigations showed that heterogeneous NCP are associated with high risk detachment [16, 29], while homogeneous NCP are stable [16]. The density of the lipid rich plaque was found between 30 and 60 HU [15, 30], distinctive from the normal artery tissue which has higher density. Backed by these results, in this study, we classified arteries with NCP on CT images with a threshold of 50 HU and calculated their metabolism in terms of MRG and SUVmax in aged volunteers. We also report MRG and SUVmax of CP in comparison to calcification area and density.

2 Methods

2.1 Study Design and Population

We prospectively recruited three groups of subjects for this study. In group 1, 4 subjects were healthy volunteers and 2 of them were measured twice at 12 months of interval (T0 and T12) with CT and PET-^{18}F-FDG. In group 2, 4 subjects were diagnosed with hypercholesterolemia prior to this study and all 4 were measured twice at T0 and T12. In group 3, 3 subjects were recently diagnosed with chest angina (less than 6 months) and 2 of them were measured twice at T0 and T12. Since the goal of this study was not to compare between groups of subjects, but to collect enough images of arteries extending from healthy to those with calcification and/or inflammation, and from subjects taking or not medication in order to correlate the inflammation as measured with PET-^{18}F-FDG to artery density on CT images, to ultimately deduce artery plaque vulnerability from CT images. For this reason, all the artery transaxial images considered on the image slice basis were assembled in two groups for with and without medication.

For medication, group 1 of healthy volunteers and the 4 subjects with hypercholesterolemia measured at T0 were having no medication, making a total of 10 subjects. The 4 subjects with hypercholesterolemia measured at T12, plus those 3 subjects with chest angina with 2 of them measured twice making a total of 9 subjects having medication. In the rest of this paper, a measurement is considered as a subject. These 19 subjects consisted of 11 females and 9 males and they were aged between 65 and 85 years.

The subjects with hypercholesterolemia in group 2 measured at T12 were taking a medication of 20 mg/day of Rosuvastatin against artery inflammation. The subjects with chest angina were taking their prescribed medication consisting of beta-blockers, antihypertensive drugs, statins and antiaggregant drugs [31].

The exclusion criteria for subjects' recruitment were diabetes, chronic inflammatory diseases, chronic kidney disease (serum creatinine level > 250 μM/L), cancer, subjects taking anti-inflammatory drugs or immunomodulator agents. All procedures were approved by the Ethics Committee of the University Institute of Geriatrics of Sherbrooke (#2009-19). Informed written consent was obtained from all individual participants included in the study.

All participants fasted for more than 6 h before glycemia measurements and CT/PET scans. The scans started with a low-dose CT followed by a dynamic PET image acquisition for 30 min after an intravenous injection of ^{18}F-FDG bolus (3.7 to 10 mCi depending on subject's weight) and the images were reconstructed into 26 frames: 12×10 s, 8×30 s and 6×240 s. The 30 min scan duration was reported to be greatly correlated to a standard PET acquisition time of 60 min [32]. CT and PET acquisitions were performed with a PET/CT system (Philips Gemini TF 16) and the images were reconstructed in a matrix of a $144 \times 144 \times 45$ for PET with a voxel size of 4 mm $\times$ 4 mm $\times$ 4 mm, and in a matrix $512 \times 512 \times 138$ with a voxel size of 1 mm $\times$ 1 mm $\times$ 5 mm for CT, and the PET images were reconstructed with the iterative 3D row action maximum likelihood reconstruction algorithm. The arteries studied in this work were the aorta and iliacs analyzed on the transaxial PET images. Each transaxial image slice of the artery was considered as an independent artery segment.

2.2 Analysis of CT Images

The arteries on the transaxial image slices were segmented using the algorithm of active contour technique to find an optimal object boundary [33]. The technique of histogram thresholding was used to isolate NCP with intensities less than 50 HU, and to set CP with intensities greater than 130 HU in areas having at least 4 adjacent pixels [34, 35]. An artery with no plaque observed on the artery segment or with intensities between 51 HU and 130 HU was considered as a normal artery (NAR).

The artery wall on the images was determined by a second region of interest (ROI) deduced from the firstly drawn with active contour on the whole artery, by displacing the latter by 3 pixels inward for aorta and 2 pixels for iliac artery. The justification of using 3 and 2 pixels was deduced from the average thickness of artery calcification.

The calcification area ratio (RCA) was assessed as the calcification area divided by the artery area [34], and classified in four clusters RCA1-4. The calcification scores (ACS) were calculated using the maximum pixel density in each calcification area assigned a level from 1 to 4: 1 for density between 131 and 199 HU, 2 for 200–299 HU, 3 for 300–399 HU, and 4 for ≥400 HU. The ACS were finally obtained by multiplying these levels with their corresponding RCA [38–40]. We also defined the maximal density in HU in each calcification area and classified these densities in four levels similar to ACS as density levels (DL) from 1 to 4.

The Hierarchical K-means algorithm (AHK) with the precision of hierarchical clustering [36] in the combination with silhouette-coefficient [37] were used for calcification areas, scores and densities clustering. At the end, the clusters of RCA1 to 4, ACS1 to 4, DL1 to 4, NCP and NAR formed the independent variables for PET MRG and SUVmax comparison.

2.3 Analysis of PET Images

Images of artery segments were classified based on the early frames of PET dynamic images where the activity in blood was well defined after the bolus injection of ^{18}F-FDG. The artery image segmentation was performed with active contours including the whole artery from the transaxial image slices. Similar to CT images, each artery slice was considered as an independent artery segment with or without calcification and/or inflammation. No coregistration of CT and PET images was necessary in order to avoid uncertainties introduced by interpolations. In fact, the artery slices were matched between CT and PET depending on their location on the scanner bed positioning as indicated in the image file header.

In order to extract the tissue blood volume (BV(t)) of the artery images which was subsequently used in the kinetic modeling, the dynamic image sequence was decomposed in tissue and blood image components with factor analysis [41, 42]. The time-activity curve of each artery segment was fitted with the modified two-tissue compartment model [41]. In the classical compartmental model of ^{18}F-FDG, tissue blood volume is assumed as a fraction $k_5 < 1$ of the input function IF(t), i.e. $BV(t) = k_5 IF(t)$, and k_5 is fitted together with the four rate constant $K_1 - k_4$ to the time-activity curve of the artery [23]. In the modified model i.e. the model without blood sampling (WOBS), BV(t) is taken from the blood component obtained with factor analysis, from which IF(t) is deduced

as $IF(t) = BV(t)/k_5 = vBV(t)$ with $v > 1$. It is to be remembered that both the artery time-activity curve and BV(t) are determined from the same region of interest (ROI) on the artery, the first on the measured image, and the second on the blood component image. The model WOBS is efficient because it does not need an experimental IF(t) nor the correction for partial volume effect (PVE) since BV(t) and the tissue time-activity curve are derived from the same ROI. The equations below summarize the WOBS model. The standard ^{18}F-FDG model introduced by Phelps et al. [23] is written as:

$$C_{PET}(t) = \frac{K_1}{\alpha_2 - \alpha_1}\left[(k_3 + k_4 - \alpha_1)e^{-\alpha_1 t} + (\alpha_2 - k_3 - k_4)e^{-\alpha_2 t}\right]$$
$$\otimes IF(t) + k_5 IF(t)$$

In this equation, the last term $k_5 IF(t)$ represents BV(t) in the ROI. When the image is decomposed with factor analysis or with other algorithms to provide separate images of blood and tissue, the tissue blood volume can then be extracted from the blood image component, thus $BV(t) = k_5 IF(t)$, from which IF(t) is extracted as $IF(t) = BV(t)/k_5 = vBV(t)$, giving finally a modification to the equation above [41]:

$$C_{PET}(t) = \frac{K_1}{\alpha_2 - \alpha_1}\left[(k_3 + k_4 - \alpha_1)e^{-\alpha_1 t} + (\alpha_2 - k_3 - k_4)e^{-\alpha_2 t}\right]$$
$$\otimes vBV(t) + BV(t)$$

The same approach of fitting the time-activity curve with the standard model works with WOBS for ROIs or on the pixel basis.

Note that fitting the time-activity curve of an artery from the measured image sequence or from the tissue component is equivalent. In the latter form, the term BV(t) in the last equation must be omitted as there should be no blood in the tissue images.

Although the measured artery time-activity curve contains more radiotracer in blood than in artery wall depending on the time of the measurement, this ratio is taken into account during the fitting by accurately determining the fraction k_5 or the factor v.

2.4 Statistical Analysis

The data were tested for normality using the D'Agostino-Pearson omnibus test. The parametric variables were expressed as mean ± standard deviation and compared using Student's t test and expressed as mean ± standard deviation. Non-parametric data were compared using Mann-Whitney U test and the results were expressed as median, quartiles and interquartile range (IQR) with the statistical significance level chosen as 5%.

3   Results

Figure 1a shows an example of an aorta coronal view with the iliac bifurcation. Each 4 mm length of the aorta and iliacs formed a segment on the PET transaxial images. The WOBS model accurately fitted the artery time-activity curves as shown in Fig. 1b. The fit to each artery segment provided the MRG values. A single subject CT transaxial image without apparent calcification and its corresponding PET slice are shown in Fig. 2a and Fig. 2b, respectively. In fact, this is an example of an artery having an NCP. In Fig. 2c and 2d from another subject, the calcification around the aorta nearly occupied the full artery wall. Although the calcification was more intense at three spots as seen in Fig. 2d, the whole wall was affected by calcification at different density levels evidenced by thresholding or by pixel reading on the image. The ROI around the artery and the extent of the calcification allowed to delimit the arterial wall with an inner ROI providing a ring-like ROI from which RCA, ACS and DL were estimated.

The total number of artery segments on CT transaxial images in all 19 subjects was 1741 with 354 of them having calcification, with a mean RCA of 0.21 ± 0.14 (Median, 0.18; IQR, 0.20; IQR range, 0.10–0.30), and ACS of 0.74 ± 0.59 (mean $\pm$ SD) (Median, 0.61; IQR, 0.92; IQR range, 0.21–1.14).

In Table 1, are presented the MRG values in units of μmoles/100 g/min and SUVmax for NAR, NCP and CP and for subjects without medication and subjects with medication. The median MRG values are reported in Fig. 3 still for NAR, NCP and CP comparing the medication effect which was found statistically different in each artery type. All the values in the three artery types and for non-medication and under-medication were statistically significantly different between each other except NCP and CP in under-medication. The data shows that NCP had the highest MRG value which was more abruptly lowered by the medication, suggesting that this type of plaque is sensitive to inflammation which is prone to rupture.
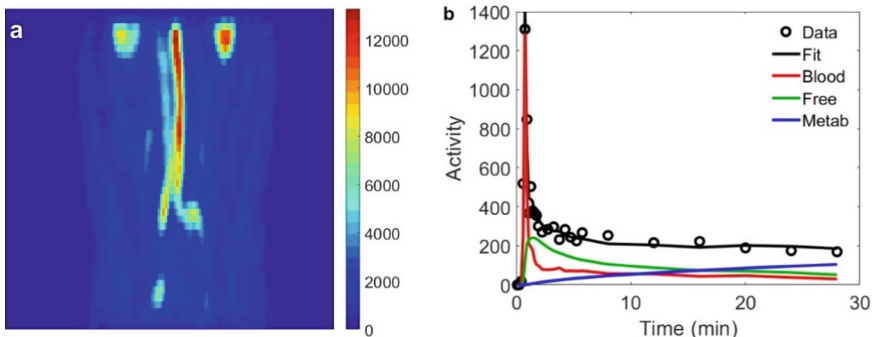
Fig. 1. a) Aorta image from PET in coronal view. The red color represents high concentration of 18F-FDG. b) Time-activity curve fit with WOBS model for an aorta segment. Free is for free 18F-FDG compartment, and Metab is for metabolized 18F-FDG.
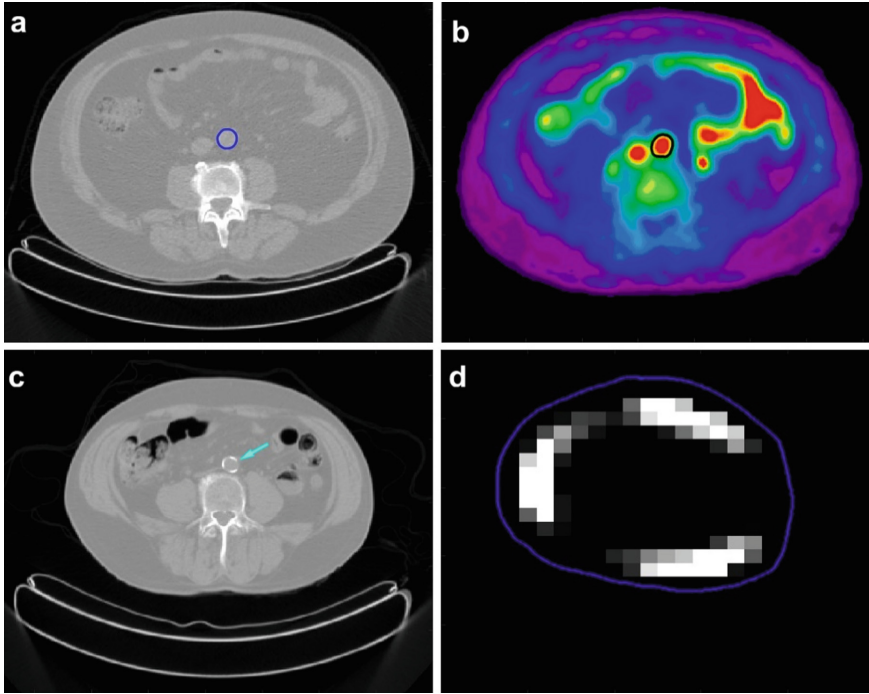
Fig. 2. a) Image of the aorta from CT with non-calcified plaque having 32 HU and an area of 89.3 mm^3 (blue ROI). b) PET image of the same aorta (black ROI). c) Image of aorta with nearly the whole wall calcified (blue arrow). d) Same aorta image as in (c) where only the calcification was isolated, having a calcification area ratio of 0.329. Different zooms were used on the pairs of figures. (Color figure online)

Table 1. MRG values in units of *μmoles/100g/min* and SUVmax for NAR, NCP and CP, from subjects without medication and subjects with medication.

Artery state	Parameters	Without medication		With medication	
		MRG	SUVmax	MRG	SUVmax
NAR	Mean ± SD	1.50 ± 0.91	1.94 ± 0.40	1.22 ± 0.77	1.80 ± 0.36
	Median	1.32	1.97	1.10	1.84
	Quartiles	0.74–2.08	1.74–2.17	0.61–1.70	1.57–2.02
	IQR	1.34	0.43	1.09	0.46
NCP	Mean ± SD	1.70 ± 0.83	2.42 ± 0.50	0.74 ± 0.45	2.26 ± 0.45

Table 1. (*continued*)

Artery state	Parameters	Without medication		With medication	
		MRG	SUVmax	MRG	SUVmax
	Median	1.52	2.46	0.70	2.30
	Quartiles	1.10–2.32	2.18–2.72	0.35–1.05	1.96–2.53
	IQR	1.22	0.54	0.70	0.57
CP	Mean ± SD	1.20 ± 0.88	1.91 ± 0.55	0.82 ± 0.47	1.70 ± 0.53
	Median	0.99	1.90	0.75	1.70
	Quartiles	0.45–1.74	1.59–2.27	0.40–1.16	1.31–2.05
	IQR	1.29	0.68	0.75	0.74
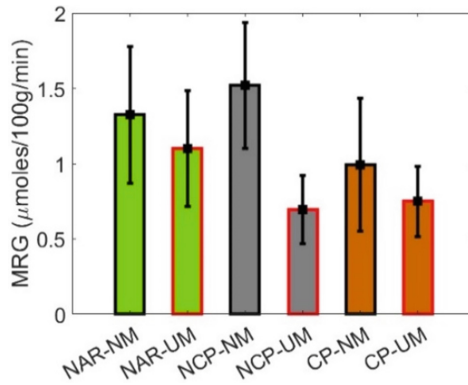
Fig. 3. Glucose metabolism as median MRG values for the three artery types NAR, NCP and CP with non-medicated (NM) and under-medication (UM). The three groups of arteries were statistically significantly different between non-medication and under-medication, and between each other, except NCP-UM and CP-UM.

The median MRG values for RCA, DL and ACS in comparison with NAR and NCP are reported in Fig. 4, for non-medicated subjects (left column) and subjects under-medication (right column). NCP appears with a higher MRG than NAR (Mean: 1.70 versus 1.50, Median 1.52 versus 1.32, see also Table 1, P = 0.032) confirming the effect of inflammation in NCP, and in Fig. 4b the values in NCP were lowered by the medication (Mean: 0.74 versus 1.22 in NAR, Median 0.70 versus 1.10, see Table 1, P = $3.48.10^{-5}$). As shown in Fig. 4, when the calcification area is large (larger RCA and ACS), the medication lowers MRG indicating an active plaque. This was not the case for DL levels where only the intensity was taken into account.
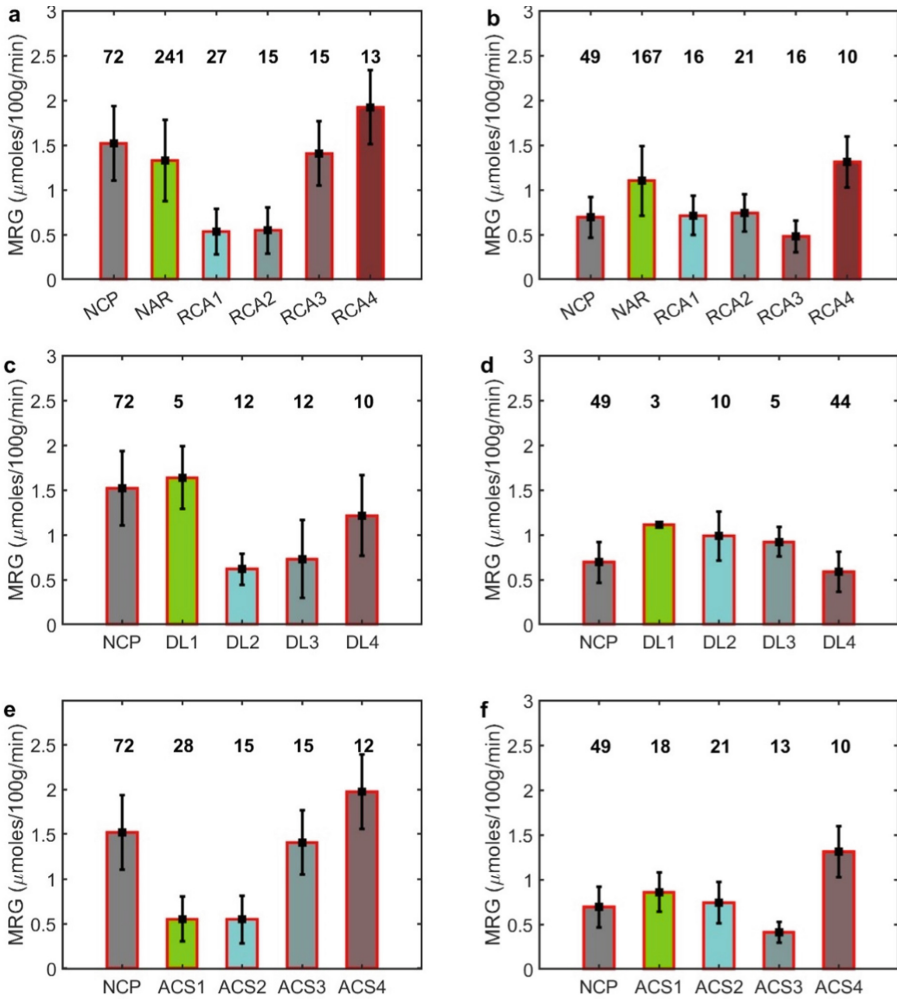
Fig. 4. Glucose metabolism for (a) NCP, NAR and RCA clusters in non-medicated subjects, (b), Same as (a) for subjects under medication. c) and d) Same as (a) and (b), respectively, but for the four density levels (DL) (NAR was omitted since it was the same as in (a) and (b)). e) and f) same as in c) and d) for NCP in comparison to ACSs. The digits above each bar is for the number of artery segments.

4 Discussion

CT modality is extensively used in imaging of atherosclerosis. The peripheral arteries can be imaged for the calcification density and extent and for stenoses. It was reported that the plaque even calcified does not provoke local stenoses, and the high calcification density was associated with plaque stability, while the non-calcified plaque and the larger plaque were described as active and probably prone to detach. Even the non-calcified plaque cannot be seen on CT images, it can be detected with PET and ^{18}F-NaF

[6, 43]. The radiotracer ^{18}F-NaF is thus capable of detecting the microcalcifications and inflammation [43]. The present study is therefore in agreement with the literature in addition to the exploitation of the dynamic imaging mode with PET-^{18}F-FDG to accurately trace artery inflammation.

NCP with values below 50 HU was found to be metabolically more active compared to densities below 30 HU in the agreement with other studies [3, 6, 27]. The metabolism in NCP was also found significantly higher in comparison to CP and even when assessed with SUVmax (Table 1 and Fig. 3). NCP was found with high metabolism (MRG) in non-medication subjects compared to the normal artery wall (NAR) assumed to have CT densities between 51 HU and 130 HU (Table 1, Fig. 3 and Fig. 4a), denoting its inflammation. This observation was confirmed in subjects under medication where the metabolism was drastically reduced in NCP denoting the response to inflammation (Table 1, Fig. 3 and Fig. 4b). NAR was also found statistically significantly different between non-medication and under-medication subjects (P = 0.023).

Based on the literature, the area but not the density was cited to be associated with atherosclerosis [44]. Unsurprisingly, the calcification scores in Agatston approach were in the same arrangement as the areas where the scores were influenced more by area (same statistical differences between NCP and RCAs vs NCP and ACSs). The effect of medication was clearly demonstrated in NCP and RCA clusters as shown in Figs. 3 and 4 in accordance with the literature [45].

The limitation of the present study was mainly due to the limited number of subjects, 10 without medication and 9 under medication. However, the main conclusions are more drawn from NCP versus NAR and CP globally which have more than 50 artery segments. As discussed above, the plaque density has a lesser impact on the inflammation, the thresholding of NCP to below 50 HU as reported in the literature depends on the statistics in the CT images which are influenced by several parameters such as beam flux and photon energy spectrum, photon scattering, image reconstruction filtering, artery movement and artery image segmentation. Keeping a gap between 50 HU and 130 HU, where this latter is the start of the calcification, assures somehow the assumption of the homogeneity of the vulnerable plaque. Another remark concerns the kinetic modeling when using WOBS, which makes the ^{18}F-FDG uptake depending on the same ROI for the input function and for the tissue time-activity curve, thus intrinsically reducing the uncertainties, and at the same time, the model avoid the partial volume effect. In usual pharmacokinetic modeling, the input function can be determined from artery images, to fit the artery time-activity curve, i.e. itself, while external blood sampling is tedious and risky.

5 Conclusion

The correlation of CT and PET-^{18}F-FDG in the detection of the active plaque was conducted in subjects under and without medication. The artery segments determined on the transaxial images were studied for their plaque density and area, with and without calcification. The metabolism was assessed with a pharmacokinetic model which does not need a prior correction for partial volume effect.

The correspondence between CT densities and inflammation reported with PET-^{18}F-FDG possibly leads to the use of CT alone to detect the active plaques not being calcified

yet. The larger calcification areas were also found active and these calcifications present a mixture of low and high density and these are also detected with CT alone.

References

1. Agnelli, G., Belch, J.J.F., Baumgartner, I., Giovas, P., Hoffmann, U.: Morbidity and mortality associated with atherosclerotic peripheral artery disease: a systematic review. Atherosclerosis **293**, 94–100 (2020). https://doi.org/10.1016/j.atherosclerosis.2019.09.012
2. Rafieian-Kopaei, M., Setorki, M., Doudi, M., Baradaran, A., Nasri, H.: Atherosclerosis: process, indicators, risk factors and new hopes. Int. J. Prev. Med. **5**, 927–946 (2014)
3. Saremi, F., Achenbach, S.: Coronary plaque characterization using CT. Am. J. Roentgenol. **204**, W249–W260 (2015). https://doi.org/10.2214/AJR.14.13760
4. Owen, D.R.J., Lindsay, A.C., Choudhury, R.P., Fayad, Z.A.: Imaging of atherosclerosis. Annu. Rev. Med. **62**, 25–40 (2011). https://doi.org/10.1146/annurev-med-041709-133809
5. Li, X., et al.: Association between osteogenesis and inflammation during the progression of calcified plaque evaluated by 18F-Fluoride and 18F-FDG. J. Nucl. Med. **58**, 968–974 (2017). https://doi.org/10.2967/jnumed.116.182790
6. Kitagawa, T., et al.: 18F-sodium fluoride positron emission tomography for molecular imaging of coronary atherosclerosis based on computed tomography analysis. Atherosclerosis **263**, 385–392 (2017). https://doi.org/10.1016/j.atherosclerosis.2017.04.024
7. Blomberg, B.A., et al.: Thoracic aorta calcification but not inflammation is associated with increased cardiovascular disease risk: results of the CAMONA study. Eur. J. Nucl. Med. Mol. Imaging **44**(2), 249–258 (2016). https://doi.org/10.1007/s00259-016-3552-9
8. Miyamoto, Y., et al.: Plaque characteristics of thin-cap fibroatheroma evaluated by OCT and IVUS. JACC Cardiovasc. Imaging **4**, 638–646 (2011). https://doi.org/10.1016/j.jcmg.2011.03.014
9. Ehara, S., et al.: Spotty calcification typifies the culprit plaque in patients with acute myocardial infarction: an intravascular ultrasound study. Circulation **110**, 3424–3429 (2004). https://doi.org/10.1161/01.CIR.0000148131.41425.E9
10. Chai, J.T., et al.: Quantification of lipid-rich core in carotid atherosclerosis using magnetic resonance T2 mapping: relation to clinical presentation. JACC Cardiovasc. Imaging **10**, 747–756 (2017). https://doi.org/10.1016/j.jcmg.2016.06.013
11. Trivedi, R.A., et al.: MRI-derived measurements of fibrous-cap and lipid-core thickness: the potential for identifying vulnerable carotid plaques in vivo. Neuroradiology **46**, 738–743 (2004). https://doi.org/10.1007/s00234-004-1247-6
12. Corti, R., Fuster, V.: Imaging of atherosclerosis: magnetic resonance imaging. Eur. Heart J. **32**, 1709–1719 (2011). https://doi.org/10.1093/eurheartj/ehr068
13. Kramer, C.M., Anderson, J.D.: MRI of atherosclerosis: diagnosis and monitoring therapy. Expert Rev. Cardiovasc. Ther. **5**, 69–80 (2007). https://doi.org/10.1586/14779072.5.1.69
14. Motoyama, S., et al.: Multislice computed tomographic characteristics of coronary lesions in acute coronary syndromes. J. Am. Coll. Cardiol. **50**, 319–326 (2007). https://doi.org/10.1016/j.jacc.2007.03.044
15. Marwan, M., et al.: In vivo CT detection of lipid-rich coronary artery atherosclerotic plaques using quantitative histogram analysis: a head to head comparison with IVUS. Atherosclerosis **215**, 110–115 (2011). https://doi.org/10.1016/j.atherosclerosis.2010.12.006
16. Maurovich-Horvat, P., et al.: The napkin-ring sign indicates advanced atherosclerotic lesions in coronary CT angiography. JACC Cardiovasc. Imaging **5**, 1243–1252 (2012). https://doi.org/10.1016/j.jcmg.2012.03.019

17. Tzolos, E., et al.: Repeatability of quantitative pericoronary adipose tissue attenuation and coronary plaque burden from coronary CT angiography. J. Cardiovasc. Comput. Tomogr. **15**, 81–84 (2021). https://doi.org/10.1016/j.jcct.2020.03.007

18. Tarkin, J.M., Joshi, F.R., Rudd, J.H.F.: PET imaging of inflammation in atherosclerosis. Nat. Rev. Cardiol. **11**, 443–457 (2014). https://doi.org/10.1038/nrcardio.2014.80

19. Tarkin, J.M., et al.: Detection of atherosclerotic inflammation by 68Ga-DOTATATE PET compared to [18F]FDG PET imaging. J. Am. Coll. Cardiol. **69**, 1774–1791 (2017). https://doi.org/10.1016/j.jacc.2017.01.060

20. Moghbel, M., Al-Zaghal, A., Werner, T.J., Constantinescu, C.M., Høilund-Carlsen, P.F., Alavi, A.: The role of PET in evaluating atherosclerosis: a critical review. Semin. Nucl. Med. **48**, 488–497 (2018). https://doi.org/10.1053/j.semnuclmed.2018.07.001

21. Leccisotti, L., Nicoletti, P., Cappiello, C., Indovina, L., Giordano, A.: PET imaging of vulnerable coronary artery plaques. Clin. Transl. Imaging **7**(4), 267–284 (2019). https://doi.org/10.1007/s40336-019-00334-3

22. Saito, H., et al.: Validity of dual MRI and F-FDG PET imaging in predicting vulnerable and inflamed carotid plaque. Cerebrovasc. Dis. **35**, 370–377 (2013). https://doi.org/10.1159/000348846

23. Phelps, M.E.E., Huang, S.C.C., Hoffman, E.J.J., Selin, C., Sokoloff, L., Kuhl, D.E.E.: Tomographic measurement of local cerebral glucose metabolic rate in humans with (F-18)2-fluoro-2-deoxy-D-glucose: validation of method. Ann. Neurol. **6**, 371–388 (1979). https://doi.org/10.1002/ana.410060502

24. Chen, W., Dilsizian, V.: PET assessment of vascular inflammation and atherosclerotic plaques: SUV or TBR? J. Nucl. Med. **56**, 503–504 (2015). https://doi.org/10.2967/jnumed.115.154385

25. Rudd, J.H.F., et al.: Atherosclerosis inflammation imaging with 18F-FDG PET: carotid, iliac, and femoral uptake reproducibility, quantification methods, and recommendations. J. Nucl. Med. **49**, 871–878 (2008). https://doi.org/10.2967/jnumed.107.050294

26. Lammertsma, A.A.: Forward to the past: the case for quantitative PET imaging. J. Nucl. Med. **58**, 1019–1024 (2017). https://doi.org/10.2967/jnumed.116.188029

27. Achenbach, S., Raggi, P.: Imaging of coronary atherosclerosis by computed tomography. Eur. Heart J. **31**, 1442–1448 (2010). https://doi.org/10.1093/eurheartj/ehq150

28. Kitagawa, T., et al.: Characterization of noncalcified coronary plaques and identification of culprit lesions in patients with acute coronary syndrome by 64-slice computed tomography. JACC Cardiovasc. Imaging **2**, 153–160 (2009). https://doi.org/10.1016/j.jcmg.2008.09.015

29. Schroeder, S., et al.: Reliability of differentiating human coronary plaque morphology using contrast-enhanced multislice spiral computed tomography: a comparison with histology. J. Comput. Assist. Tomogr. **28**, 449–454 (2004). https://doi.org/10.1097/00004728-200407000-00003

30. Schlett, C.L., et al.: Histogram analysis of lipid-core plaques in coronary computed tomographic angiography: ex vivo validation against histology. Invest. Radiol. **48**, 646–653 (2013). https://doi.org/10.1097/RLI.0b013e31828fdf9f

31. Khalil, A., Orellana, M.R.M., Fulop, T., Turcotte, E.E., Bentourkia, M.: Positron emission tomography imaging for vascular inflammation evaluation in elderly subjects with different risk factors for cardiovascular diseases. Am. J. Nucl. Med. Mol. Imaging **4**, 283 (2014)

32. Torizuka, T., et al.: Short dynamic FDG-PET imaging protocol for patients with lung cancer. Eur. J. Nucl. Med. **27**(10), 1538–1542 (2000). https://doi.org/10.1007/s002590000312

33. Caselles, V., Kimmel, R., Sapiro, G.: Geodesic active contours. Int. J. Comput. Vis. **22**, 61–79 (1997). https://doi.org/10.1023/A:1007979827043

34. Derlin, T., et al.: In vivo imaging of mineral deposition in carotid plaque using 18F-sodium fluoride PET/CT: correlation with atherogenic risk factors. J. Nucl. Med. **52**, 362–368 (2011). https://doi.org/10.2967/jnumed.110.081208

35. Ohya, M., et al.: Vascular calcification estimated by aortic calcification area index is a significant predictive parameter of cardiovascular mortality in hemodialysis patients. Clin. Exp. Nephrol. **15**, 877–883 (2011). https://doi.org/10.1007/s10157-011-0517-y

36. Arai, K., Ridho Barakbah, A.: Hierarchical K-means: an algorithm for centroids initialization for K-means (2007)

37. Rousseeuw, P.J.: Silhouettes: a graphical aid to the interpretation and validation of cluster analysis. J. Comput. Appl. Math. **20**, 53–65 (1987). https://doi.org/10.1016/0377-0427(87)90125-7

38. Agatston, A.S., Janowitz, W.R., Hildner, F.J., Zusmer, N.R., Viamonte, M., Detrano, R.: Quantification of coronary artery calcium using ultrafast computed tomography. J. Am. Coll. Cardiol. **15**, 827–832 (1990). https://doi.org/10.1016/0735-1097(90)90282-T

39. Van Der Bijl, N., et al.: Assessment of Agatston coronary artery calcium score using contrast-enhanced CT coronary angiography. Am. J. Roentgenol. **195**, 1299–1305 (2010). https://doi.org/10.2214/AJR.09.3734

40. McEvoy, J.W., et al.: Coronary artery calcium progression: an important clinical measurement? J. Am. Coll. Cardiol. **56**, 1613–1622 (2010). https://doi.org/10.1016/j.jacc.2010.06.038

41. Bentourkia, M.: Kinetic modeling of PET data without blood sampling. IEEE Trans. Nucl. Sci. **52**, 697–702 (2005). https://doi.org/10.1109/TNS.2005.851442

42. De Geus-Oei, L.F., et al.: Comparison of image-derived and arterial input functions for estimating the rate of glucose metabolism in therapy-monitoring 18F-FDG PET studies. J. Nucl. Med. **47**, 945–949 (2006)

43. Chen, W., Dilsizian, V.: Targeted PET/CT imaging of vulnerable atherosclerotic plaques: microcalcification with sodium fluoride and inflammation with fluorodeoxyglucose. Curr. Cardiol. Rep. **15**(6), 1–6 (2013). https://doi.org/10.1007/s11886-013-0364-4

44. Blaha, M.J., Mortensen, M.B., Kianoush, S., Tota-Maharaj, R., Cainzos-Achirica, M.: Coronary artery calcium scoring: is it time for a change in methodology? JACC Cardiovasc. Imaging **10**, 923–937 (2017). https://doi.org/10.1016/j.jcmg.2017.05.007

45. Li, Z., et al.: Effects of statin therapy on progression of mild noncalcified coronary plaque assessed by serial coronary computed tomography angiography: a multicenter prospective study. Am. Heart J. **180**, 29–38 (2016). https://doi.org/10.1016/j.ahj.2016.06.023

Comparative Analysis of the Spatial Structure Chloroplasts and Cyanobacteria Photosynthetic Systems I and II Genes

Maria Senashova[1] and Michael Sadovsky[1,2,3(✉)]

[1] Institute of Computational Modelling of the Siberian Branch of the Russian Academy of Sciences, Krasnoyarsk, Russia
msad@icm.krasn.ru
[2] V.F. Voino-Yasenetsky Krasnoyarsk State Medical University, Krasnoyarsk, Russia
[3] Federal Siberian Research and Clinical Center of FMBA of Russia, Krasnoyarsk, Russia

Abstract. Statistically revealed inner structuredness of bacterial vs. chloroplast phototsynthetic genes is studied. To do it, we analysed the cyanobacterial genes responsible for a light consumption. A sounding difference in the spatial pattern specific for chloroplast photosystem genes, and bacterial photosystem genes is found. Thus, the bacterial genes yield another type of symmetry of the distribution of the genes converted into triplet frequency dictionaries in 63-dimensional Euclidean space of triplets.

Keywords: Triplet frequency · Clustering · Elastic map · Structure

1 Introduction

Sun is the primary source of energy on Earth. A number of organisms adapted to use it. Plants, algae, and cyanobacteria grow due to their ability to consume sunlight to extract electrons from water. In elementary words, that is how photosynthesis and, accordingly, phototrophic nutrition works. Photosynthetic organisms comprise phototrophic bacteria and green plants. The study of the photosynthetic system's structure and function is of great value since the plants' role in oxygen and food supply. Recently, significant progress has been reported [15] in determining the spatial structures of the chloroplast photosystem of both terrestrial plants and cyanobacteria. However, a lot could be done more. Many papers are devoted to studying various aspects of the structure of photosynthetic systems I and II, implying both mathematical and biological methods [1–4, 6, 11–14, 16–20, 23–27].

Chloroplasts seem to be the most widely spread "machine" to consume sun energy and convert it into organic chemical compounds. However, there are some ancient organisms who also are able to utilize sun light for organic matter production while they have no chloroplasts. The most popular theory of chloroplast origin says that these latter take the origin from ancient photosynthetic bacteria.

In such a capacity, a tight comparison of formally identified spatial structured-ness may bring a lot in understanding of various aspects in structure–function–evolution interplay of photosynthetic organisms.

Here we comparatively study the spatial structure of chloroplast and cyanobacteria genes belonging to photosynthetic systems I and II. The structure is understood as triplet composition of the sequences of corresponding genes, and the spatial structure refers to the distribution of points representing spe-cific frequency dictionaries of the genes of the photosynthetic system in the 64-dimensional triplet space. This approach differs from an idea of a structure of genes commonly spread in biology.

2   Materials and Methods

2.1   Frequency Dictionary

We consider the photosynthetic system genes as symbol sequences of various lengths from the four-letter alphabet $\aleph = \{\mathsf{A}, \mathsf{C}, \mathsf{G}, \mathsf{T}\}$. No other symbols are stipulated to be in a gene sequence, and if yes then they were eliminated so that the total length of the sequence is reduced by the number of eliminated symbols. Each sequence is then converted into a frequency dictionary $W^{(j)}$ of thickness 3; index j enlists the genes. This dictionary is a list of all triplets $\omega = \nu_1\nu_2\nu_3$ of three neighboring nucleotides where each triplet is provided with its frequency. There are 64 triplets, totally. Frequency f_ω is the ratio of the number of copies n_ω of a given triplet to the total number N of all triplets, where N is the sum of all n_ω:

$$f_\omega = \frac{n_\omega}{N}. \tag{1}$$

More rigorously, to develop a triplet frequency dictionary, one must fix the parameter t, $t \geq 1$, which is the step length of a reading frame shift along a sequence. Placing a reading frame at the first symbol of a sequence, one iden-tifies a triplet ω. Moving right (for a determinacy) the reading frame with the step t and counting the triplets identified by the reading frame, one gets a finite dictionary. Finally, changing the numbers of triplets with their frequency due to (1), one gets the frequency dictionary $W_t^{(j)}$, where j enlists the genetic enti-ties, and t is the reading frame shift. Obviously, t different (in general) frequency dictionaries are obtained for $1 \leq k \leq t$ where k is the starting position of the reading frame. Everywhere further we shall use $t = 3$; it resembles the triplet frequency dictionary counted for codons, meanwhile that is not so exactly, since the introns are counted here as well.

Any frequency dictionary $W^{(j)}$ maps a symbol sequence into a 64-dimensional metric space. The proximity of two genomes is given in a natural way: for exam-ple, as the proximity of two points in the Euclidean metric:

$$\rho\left(W^{(j)}, W^{(k)}\right) = \sqrt{\sum_{\omega=\mathsf{AAA}}^{\mathsf{TTT}} \left(f_\omega^{(j)} - f_\omega^{(k)}\right)^2}. \tag{2}$$

The transformation maps symbol sequences into much more convenient mathematical objects that are the points in metric space, thus allowing to implement the effective methods of analysis.

2.2 Genetic Material

Photosynthetic system I and II genes were isolated for 570 chloroplast genomes currently available in the EMBL bank. The following genes were found in the studied set of genomes: *psa*A, *psa*B, *psa*C, *psa*I, *psa*J, *psa*M, *psb*A, *psb*B, *psb*C, *psb*D, *psb*E, *psb*F, *psb*G, *psb*H, *psb*I, *psb*J, *psb*K, *psb*L, *psb*M, *psb*N, *psb*T. The following genes were found in the 45 genomes of cyanobacteria examined in addition to those indicated above: *psa*D, *psa*E, *psa*F, *psa*K, *psa*L, *psa*X, *psb*O, *psb*P, *psb*Q, *psb*U, *psb*V, *psb*W, *psb*X, *psb*Y, *psb*Z.

2.3 Clustering Methods

To reveal the structure in the set of genes, we converted each gene sequence into a point in a 64-dimensional space of triplets frequency, as described above. Also, each frequency dictionary was labeled with the name of the gene and the name of the species. Besides, the strand bearing the gene (direct or reverse) is indicated and GC-content of the gene. Based on the obtained set of points, the *VidaExpert* freely distributed software[1] was used to construct the data view in the space of the leading three principal components determined in 64-dimensional space of triplets frequency. To visualize the distribution, we developed two-dimensional projections of that latter, for the first and the second principal components, and for the second and the third principal components [8–10].

Thus, we investigate the distribution of the points corresponding to genetic sequences in this metric space revealing patterns and clusters, if any. The idea of this method consists in jamming the originally plain manifold (a square in our case) in the manner to minimize the total deformation energy of the elastic manifold, and mathematical springs connected to the manifold in the projection points. It is highly powerful and efficient method to cluster multidimensional data and visualize them.

3 Results

It was found that both for chloroplast photosystem genes and cyanobacteria photosystem genes the set of points yields two large clusters; the former comprises the points referred to the forward strand, and the latter comprises the points referred to the reverse strand (Fig. 1). It differs the spatial structure of the genes of photosynthetic systems I and II of chloroplasts and cyanobacteria from the spatial structure observed for a complete genome of chloroplasts, mitochondria, and bacteria, where such clustering is not observed [7, 22]. Moreover, the cyanobacteria genes belonging to the same strand can be well approximated

---

[1] http://bioinfo-out.curie.fr/projects/vidaexpert/.
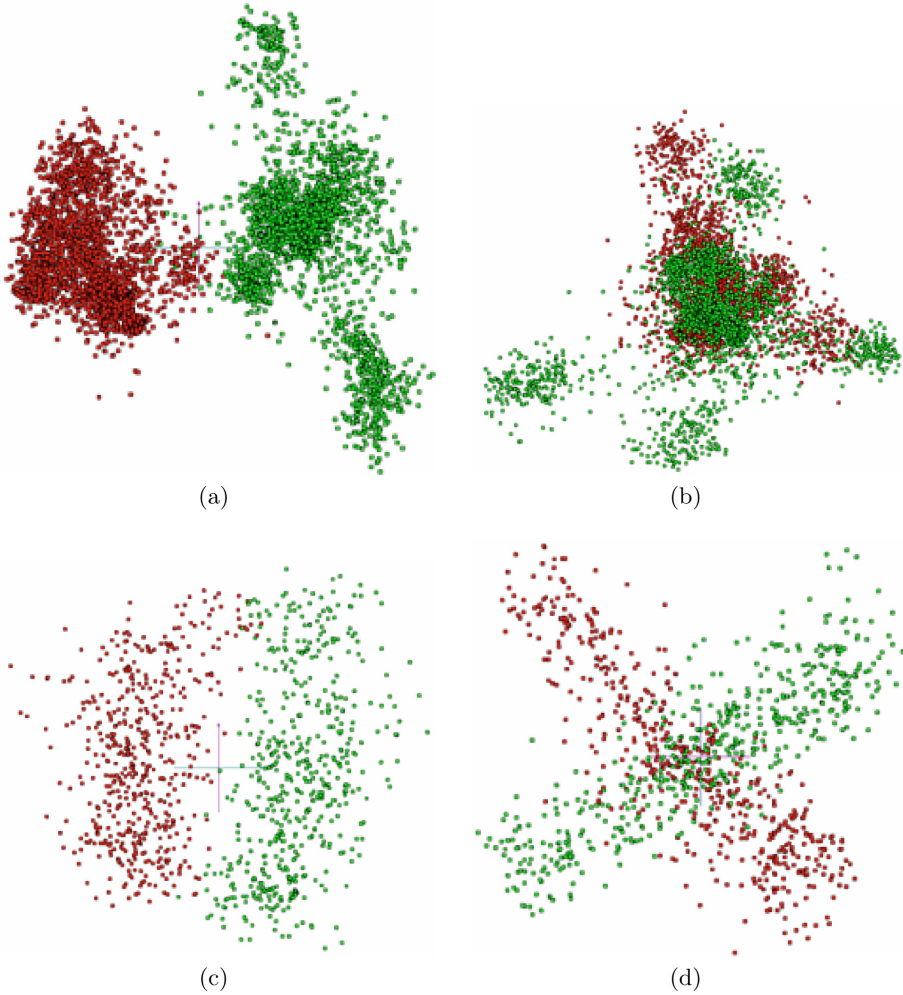
Fig. 1. Projection of chloroplast photosystem genes onto the plane of the first and the second principal components (Fig. 1(a)) and the second and the third principal components (Fig. 1(b)). Projection of the genes of the cyanobacterial photosystem into the plane of the first and the second principal components (Fig. 1(c)) and into the plane of the second and the third principal components (Fig. 1(d)). The genes from the forward strand are shown in red, and the genes from the reverse strand are shown in green. (Color figure online)

by an embedded plane. The planes corresponding to the points of each strand are perpendicular (Fig. 1d). Previously, such pattern was observed neither for complete genomes, nor for individual genes.

It was found that besides two main clusters chloroplast photosystem genes exhibit six groups of points quite distant from the main clusters. These groups

(a)   (b)
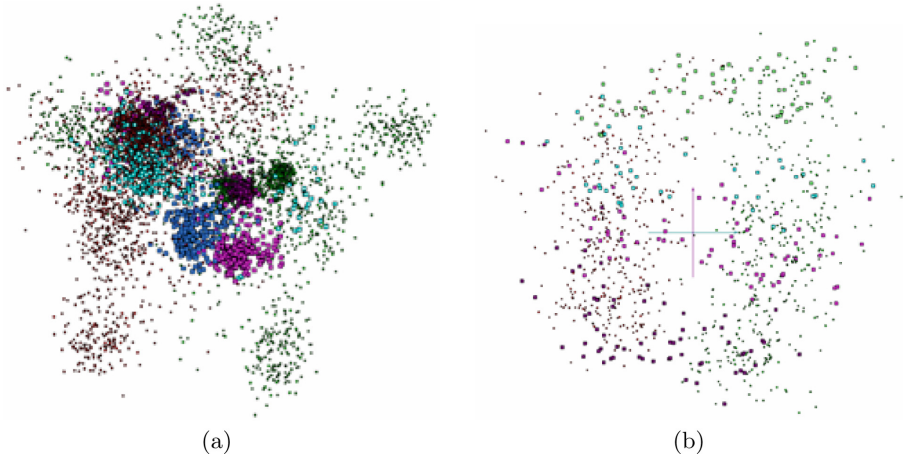
Fig. 2. Clustering of photosystem genes for chloroplasts (Fig. 2(a)) with respect to gene function and for cyanobacteria (Fig. 2(b)) with respect to the organism. (Color figure online)

of points correspond to genes *psa*I and *psb*I belonging to the forward strand (Fig. 1(a)), and genes *psb*F, *psb*G, *psb*L and *psb*N belonging to the reverse strand (Fig. 1(b)). The points are colored as follows: *psa*I points are blue, *psb*I are orange, *psb*F are turquoise, *psb*J are raspberry, *psb*L are light green and *psb*N are violet. All other points are colored according to the strand and have a smaller size marker for clarity. The mentioned genes are also present in the cluster belonging to the direct strand, but their abundance is low.

The gene *psb*F in higher plants comprises about 38 amino acids, the β-subunit of cytochrome b559. *psb*O gene plays important role in PS II assembly and regulates the electron flux to the pool of plastoquinones. The gene *psb*L is important for proper operation of the Q_a site preventing the return of an electron from the Q_b site to Q_a. The gene *psb*N is involved in the assembly of the reaction center of photosystem II. The gene *psa*I interacts with the gene *psa*H and binds to the light harvesting complex of photosystem II. The gene *psb*N is essential for the assembly and function of photosystem II. The reason why these genes are located so far from the core clusters requires further study.

The genes of cyanobacteria photosystem do not form separate groups. The criteria ruling the group aggregation also differ. A gene type is the leading factor in clustering of the chloroplast photosystem genes. It should be noted that genes of the same type in chloroplasts are located very compactly, even if they are found in large clusters belonging to the forward and reverse strands. They are more likely to "neighbor" than to overlap the genes of other types. Small red and green squares label the points related to the forward and reverse strands, respectively, in Fig. 2. For clarity, several types of chloroplast genes are highlighted in color: *psa*E is colored in raspberry, *psb*K iscolored in turquoise, *psa*B is colored in purple and *psa*C is colored in blue. On the contrary, cyanobacteria genes

(a)   (b)
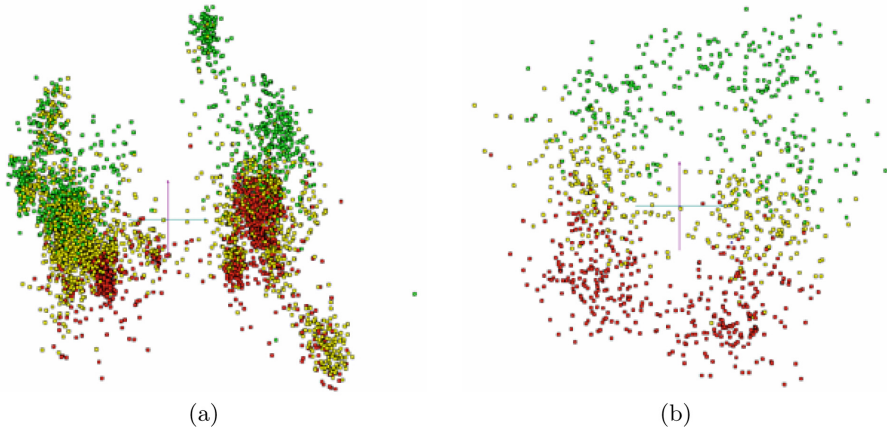
Fig. 3. Spatial distribution of GC-content values for photosynthetic systems genes of chloroplasts (Fig. 3(a)) and cyanobacteria (Fig. 3(b)) in the plane of the first and second principal components. (Color figure online)

form the groups within the strands. Figure 1(b) shows the genes of *Gloeobacter kilaueensis* (AC CP003587 in EMBL-bank) and *Gloeobacter violaceus* (AC BA000045), colored in purple, *Synechocystis sp.* (AC AP012205, AP012276, AP012277, AP012278, BA000022 and CP003265), *Nostoc spp.* (AC CP003552, BA000019, CP003548 and CP001037) are colored in turquoise, *Prochlorococcus marinus* (AC CP000551, CP00552 and CP000553) are shown in light green.

The spatial distribution of GC-content values for the photosystem genes of chloroplasts and cyanobacteria was considered. GC-content was determined for each gene. It is the ratio of the number of nucleotides G and C to the total number of nucleotides in the gene. The points corresponding to genes with GC-content value less than the average are marked in Fig. 3 in green, points corresponding to genes with an average GC-content value are indicated in yellow, and points with GC-content value above the average are indicated in red. No order was observed in the distribution of the GC-content of the genes of the photosynthetic systems of chloroplasts. It also distinguishes the genes under consideration from the complete genomes of chloroplasts, mitochondria, and bacteria characterized by two types of distribution: gradient and central symmetry. There is a gradient distribution in the space of triplet frequencies for the GC-content value of the photosystem genes of cyanobacteria. This type of distribution is often found in complete genomes. In particular, it occurs in the genomes of chloroplasts [22], in the mitochondrial genomes of higher plants, algae, mosses, lichens, and fungi, and in GC-rich bacteria.

4 Conclusion

The spatial structures of the chloroplasts and cyanobacteria photosynthetic system genes in the triplet frequency space differs from each other. Also, these

structures differ from similar ones of previously studied complete genomes of chloroplasts, mitochondria, bacteria, and genes possessing the same function.

The leading role of the strand (forward vs. reverse one) occurrence of individual genes in cluster pattern was found for the first time, for the genes of photosystems of chloroplasts and cyanobacteria. Previously a direct role of taxonomy in whole genome triplet dictionaries clustering was reported [21], while function is the leading factor in a cluster composition for individual genes distribution [5]. However, for cyanobacteria photosystem genes follows the taxonomy, not gene function. This fact distinguishes them from the other organisms. Paper [22] reports that complete genomes exhibit a gradient or central symmetry distribution of GC-content values of the formally identified fragments. A gradient distribution of GC-content values also was found in cyanobacteria photosystem genes, but no order in the GC-content values of the chloroplast photosystem genes was observed. Thus, the spatial structure of chloroplasts and cyanobacteria photosystem genes is significantly different. It may indicate that chloroplasts and cyanobacteria separated a long time ago in their evolution from a common ancestor and took their evolution trajectory independently.

References

1. Allen, J.F., de Paula, W.B., Puthiyaveetil, S., Nield, J.: A structural phylogenetic map for chloroplast photosynthesis. Trends Plant Sci. **16**(12), 645–655 (2011)
2. Anderson, J.M., Melis, A.: Localization of different photosystems in separate regions of chloroplast membranes. Proc. Natl. Acad. Sci. **80**(3), 745–749 (1983)
3. Casella, S., et al.: Dissecting the native architecture and dynamics of cyanobacterial photosynthetic machinery. Mol. Plant **10**(11), 1434–1448 (2017)
4. Chowdhury, F.A., Trudeau, M.L., Guo, H., Mi, Z.: A photochemical diode artificial photosynthesis system for unassisted high efficiency overall pure water splitting. Nat. Commun. **9**(1), 1–9 (2018)
5. Fedotovskaya, V., Sadovsky, M., Kolesnikova, A., Shpagina, T., Putintseva, Y.: Function vs. taxonomy: further reading from fungal mitochondrial atp synthases. In: IWBBIO, pp. 438–444 (2020)
6. Gabdulkhakov, A.G., Dontsova, M.V.: Structural studies on photosystem II of cyanobacteria. Biochemistry (Moscow) **78**(13), 1524–1538 (2013). https://doi.org/10.1134/S0006297913130105
7. Gorban, A.N., Popova, T.G., Zinovyev, A.Y.: Four basic symmetry types in the universal 7-cluster structure of microbial genomic sequences. In Silico Biol. **5**(3), 265–282 (2005). http://content.iospress.com/articles/in-silico-biology/isb00185
8. Gorban, A.N., Zinovyev, A.: Principal manifolds and graphs in practice: from molecular biology to dynamical systems. Int. J. Neural Syst. **20**(03), 219–232 (2010). https://doi.org/10.1142/S0129065710002383. pMID: 20556849
9. Gorban, A.N., Zinovyev, A.Y.: Fast and user-friendly non-linear principal manifold learning by method of elastic maps. In: 2015 IEEE International Conference on Data Science and Advanced Analytics, DSAA 2015, Campus des Cordeliers, Paris, France, 19–21 October 2015, pp. 1–9 (2015). https://doi.org/10.1109/DSAA.2015.7344818
10. Gorban, A., Sumner, N., Zinovyev, A.: Topological grammars for data approximation. Appl. Math. Lett. **20**(4), 382–386 (2007)

11. Hankamer, B., Barber, J., Boekema, E.J.: Structure and membrane organization of photosystem II in green plants. Annu. Rev. Plant Biol. **48**(1), 641–671 (1997)
12. Heinz, S., Liauw, P., Nickelsen, J., Nowaczyk, M.: Analysis of photosystem II biogenesis in cyanobacteria. Biochimica Et Biophysica Acta (BBA)-Bioenergetics **1857**(3), 274–287 (2016)
13. Inoue-Kashino, N., Kashino, Y., Satoh, K., Terashima, I., Pakrasi, H.B.: PSBU provides a stable architecture for the oxygen-evolving system in cyanobacterial photosystem II. Biochemistry **44**(36), 12214–12228 (2005)
14. Karapetyan, N.: Photosystem I of cyanobacteria: organization and functions. Adv. Biol. Chem. **41**, 39–76 (2001)
15. Kirchhoff, H.: Structure-function relationships in photosynthetic membranes: challenges and emerging fields. Plant Sci. **266**, 76–82 (2018)
16. Kirchhoff, H., Haase, W., Wegner, S., Danielsson, R., Ackermann, R., Albertsson, P.A.: Low-light-induced formation of semicrystalline photosystem II arrays in higher plant chloroplasts. Biochemistry **46**(39), 11169–11176 (2007)
17. Kirchhoff, H., Tremmel, I., Haase, W., Kubitscheck, U.: Supramolecular photosystem II organization in grana thylakoid membranes: evidence for a structured arrangement. Biochemistry **43**(28), 9204–9213 (2004)
18. Mabbitt, P.D., Wilbanks, S.M., Eaton-Rye, J.J.: Structure and function of the hydrophilic photosystem II assembly proteins: Psb27, Psb28 and Ycf48. Plant Physiol. Biochem. **81**, 96–107 (2014)
19. Nelson, N., Ben-Shem, A.: The complex architecture of oxygenic photosynthesis. Nat. Rev. Mol. Cell Biol. **5**(12), 971–982 (2004)
20. Nelson, N., Yocum, C.F.: Structure and function of photosystems I and II. Annu. Rev. Plant Biol. **57**, 521–565 (2006)
21. Sadovsky, M., Putintseva, Y., Chernyshova, A., Fedotova, V.: Genome structure of organelles strongly relates to taxonomy of bearers. In: Ortuño, F., Rojas, I. (eds.) Bioinformatics and Biomedical Engineering, pp. 481–490. Springer, Cham (2015). https://doi.org/10.1007/978-3-319-16483-0_47
22. Sadovsky, M.G., Senashova, M.Y., Malyshev, A.V.: Amazing symmetrical clustering in chloroplast genomes. BMC Bioinform. **21**(2), 1–14 (2020)
23. Shen, J.R.: The structure of photosystem II and the mechanism of water oxidation in photosynthesis. Annu. Rev. Plant Biol. **66**, 23–48 (2015)
24. Staehelin, L.A., Arntzen, C.J.: Regulation of chloroplast membrane function: protein phosphorylation changes the spatial organization of membrane components. J. Cell Biol. **97**(5), 1327–1337 (1983)
25. Wang, Y., Wu, Y., Sun, K., Mi, Z.: A quadruple-band metal-nitride nanowire artificial photosynthesis system for high efficiency photocatalytic overall solar water splitting. Mater. Horizons **6**(7), 1454–1462 (2019)
26. Zhang, S., Wang, S., Guo, L., Chen, H., Tan, B., Jin, S.: An artificial photosynthesis system comprising a covalent triazine framework as an electron relay facilitator for photochemical carbon dioxide reduction. J. Mater. Chem. C **8**(1), 192–200 (2020)
27. Zlenko, D.V., Galochkina, T.V., Krasilnikov, P.M., Stadnichuk, I.N.: Coupled rows of PBS cores and PSII dimers in cyanobacteria: symmetry and structure. Photosynth. Res. **133**(1), 245–260 (2017)

Unsupervised Classification of Some Bacteria with 16S RNA Genes

Agnia Teterleva[1] , Vladislav Abramov[4] , Andrey Morgun[3] ,
Irina Larionova[3] , and Michael Sadovsky[2,3,4(✉)]

[1] School of Fundamental Biology and Biotechnology of Siberian Federal University,
Krasnoyarsk, Russia
[2] Institute of Computational Modelling of the Siberian Branch of the Russian
Academy of Sciences, Krasnoyarsk, Russia
msad@icm.krasn.ru
[3] Krasnoyarsk State Medical University named after Prof. V.F. Voino-Yasenetsky,
Krasnoyarsk, Russia
[4] Federal Siberian Research and Clinical Center of FMBA of Russia,
Krasnoyarsk, Russia

Abstract. We used unsupervised nonlinear clustering to reveal the interplay between structure of nucleotide sequences and the taxonomy of their bearers. Triplet frequency composition is referred to a structure, and taxonomy is determined through standard morphology and physiology of bacteria. Soft 16×16 elastic map has been used for clustering. Some preliminary results are presented here approving the high efficiency of such approach to phylogeny analysis. Further applications to medicine are discussed.

Keywords: Triplet frequency · Clustering · Elastic map · Structure

1 Introduction

An interplay between structure and function of genetic entities, and the taxonomy of their bearers still challenges researchers. A lot has been done here (see e.g., [4–6,14,20] and much more others). Obviously, the answer depends on the genetic matter taken into consideration: some entities show the strong prevalence of the taxonomy over function [19], while another matter shows the prevalence of the function over taxonomy [3]. This paper aims to further the studies of the interplay mentioned above.

Here we study the relation of the structure encoded in 16 SRNA (that is a triplet frequency dictionary) to taxonomy of the bearers of those moleculae. In general, there are three entities: structure of a genetic sequence, the function encoded in it, and taxonomy of the bearer of that former. Ultimately, we aim to study an interplay between all of them. To do it, one must define rigorously what is a structure. Hereafter we shall refer a structure as a triplet frequency dictionary $W^{(j)}$ of the jth 16 SRNA sequence.

The index j enlists the genetic entities to be considered, with respect to their taxonomy. Frequency dictionary (also known as k-mer ensemble) is well-known

object in the studies of nucleotide sequences; it opposes to the widely spread sequences comparison methods based on alignment. The main disadvantage of alignment consists in the necessity to set up some informally determined parameters. On the contrary, k-mer based methods are free from that disadvantage thus providing a researcher with more reliable and formally defined results. The k-mer approach to sequence comparison has a long story and still goes through a progress. We use here classical approach based on the count of the triplet frequency determined over a sequence; however, some expansions of the method could be found in [13], see also papers [1,2,21].

One may not expect a dependence on a function of the anticipated patterns in interplay; here the function is the same. Indeed, we study the ribosomal RNA (16S RNA, specifically) genes, hence all of them encode the same function. Thus, we aim to reveal the dependence between triplet composition of the genes and the taxonomy of their bearers.

To reveal the interplay between structure and taxonomy, we do the following steps:

– choose the genetic entities with clearly determined and controlled function;
– convert them into a triplet frequency dictionary $W^{(j)}$ each;
– use up-to-date and powerful methods to cluster the points (frequency dictionaries) in the relevant metric space and identify the clusters;
– check whether a taxonomy of DNA donoring organisms or determine the composition of the clusters (if any).

Suppose, the clusters are observed (otherwise no interplay takes place). Here three possible outputs may be:

1. the clusters are apparent, and each cluster comprises the sequences belonging to a specific taxon (or taxa);
2. the clusters are apparent, and each cluster comprises the sequences belonging to organisms of various taxa (maybe, rather distant);
3. an hierarchy in the clusters composition takes place: e.g. there are super-clusters gathering the higher taxa with fine pattern of each super-cluster determined by lower taxonomy position of the organisms.

Here we present some preliminary results on the study of the relation between triplet composition of 16S RNA genes and taxonomy of some bacteria. Ultimately, this work aims to reveal the medically sounding effects in such pattern appearance.

The medical value of a tool to retrieve knowledge from 16S pyrosequencing and the determination of patterns characterizing healthy people vs. patients with various neurological diseases or their predisposition is very high. The reliable changes in qualitative and quantitative diversity of the microbiota for inflammatory bowel diseases (Crohn's disease and ulcerative colitis, Parkinson's disease, Alzheimer's disease, multiple sclerosis, and other neurodegenerative and neuroinflammatory diseases) are reported.

However, the lack of correct and convenient interpretation follows in a severe expansion of time spent on analysis; one must rigorously follow the same protocol that is not always possible elsewhere. However, a diagnosis of a number of

gastroenterological, neurological, and possibly other diseases may be improved. In the future, it will significantly contribute the personalized medical care based on microbiota records. The most ambitious goal here is to create a preventive strategy to correct the human microbiota due to targeted drugs prescription: either eliminating harmful microflora or activating the necessary one. It is necessary to assess the adequacy of the correction being carried out during this treatment procedure.

2 Materials and Methods

2.1 Genetic Material

To reveal the interplay between structure and taxonomy over a set of 16S RNA bacterial genes we use SILVA database[1]. It is freely accessible database gathering SRNAs of a great variety of organisms, including bacteria. For the purposes of our study we downloaded 52474 sequences of large subunits of bacterial 16S RNA. The distribution of the genes over taxons is extremely inhomogeneous: some of higher taxa comprise a few species (or strains), while others comprise hundreds or more. Such bias results in a "signal loss": numerous entries representing higher taxa with few species fail to produce a signal, but make a noise just deteriorating a cluster pattern. To avoid this effect, we hashed the database: we eliminated both over-represented and under-represented taxa. Finally, we tried to balance the representativeness of various taxa in the dataset, so that the entries representing various lower taxa ranged in number from a hundred to tens. The final size of the database was 2143 entries. Taxonomic composition of the database is shown in Table 1. Of course, the composition of the dataset is far from an ideally balanced; however, it represents to some extent the natural distribution of taxa. it should be borne in mind that any database is filled not according to nature, but following the preferences in the choice of species to be sequenced.

2.2 Triplet Frequency Dictionary

Triplet frequency dictionary $W^{(j)}$ is the list of all 64 triplets ω_k, $k = \mathsf{AAA}, \ldots,$ TTT accompanied with their frequency f_{ω_k}; index j here enlists the sequences in the dataset. To make a dictionary, place the reading frame of the length 3 at the very beginning of a sequence and count all the triplets identified by the frame as it moves along a sequence from left to right (for determinacy), with the given step t. Within this paper, $t = 1$. Obvious constraint

$$\sum_{k=\mathsf{AAA}}^{\mathsf{TTT}} f_\omega = 1 \tag{1}$$

holds true.

---

[1] https://www.arb-silva.de/.

Table 1. Abundances of various taxa and genetic entries in the dataset; N stands for the number of genetic entities in the family.

Subdomain	Class*	Order	Family	N
Acidobacteriota	*Acidobacteriae*	*Acidobacteriales*	*Acidobacteriaceae*	31
Acidobacteriota	*Acidobacteriae*	*Acidobacteriales*	*Koribacteraceae*	1
Acidobacteriota	*Acidobacteriae*	*Solibacterales*	*Solibacteraceae*	2
Actinobacteriota	*Acidimicrobiia*	*Acidimicrobiales*	*Acidimicrobiaceae*	24
Verrucomicrobiota	*Chlamydiae*	*Chlamydiales*	*Chlamydiaceae*	49
Verrucomicrobiota	*Chlamydiae*	*Chlamydiales*	*Parachlamydiaceae*	39
Firmicutes	*Bacilli*	*Mycoplasmatales*	*Mycoplasmataceae*	13
Bacteroidota	*Bacteroidia*	*Bacteroidales*	*Bacteroidaceae*	163
Verrucomicrobiota	*Chlamydiae*	*Chlamydiales*	*Chlamydiaceae*	101
Bacteroidota	*Bacteroidia*	*Bacteroidales*	*Prevotellaceae*	147
Bacteroidota	*Bacteroidia*	*Bacteroidales*	*Tannerellaceae*	94
Bacteroidota	*Bacteroidia*	*Bacteroidales*	*Porphyromonadaceae*	106
Bacteroidota	*Bacteroidia*	*Bacteroidales*	*Rikenellaceae*	69
Bacteroidota	*Bacteroidia*	*Bacteroidales*	*Dysgonomonadaceae*	58
Bacteroidota	*Bacteroidia*	*Bacteroidales*	*Marinifilaceae*	58
Firmicutes	*Bacilli*	*Staphylococcales*	*Staphylococcaceae*	150
Firmicutes	*Bacilli*	*Bacillales*	*Bacillaceae*	151
Firmicutes	*Bacilli*	*Lactobacillales*	*Listeriaceae*	148
Firmicutes	*Bacilli*	*Paenibacillales*	*Paenibacillaceae*	124
Firmicutes	*Bacilli*	*Bacillales*	*Planococcaceae*	101
Firmicutes	*Bacilli*	*Brevibacillales*	*Brevibacillaceae*	147
Firmicutes	*Bacilli*	*Exiguobacterales*	*Exiguobacteraceae*	191
Firmicutes	*Bacilli*	*Alicyclobacillales*	*Alicyclobacillaceae*	176

*We use the term *class* to denote any subdomain higher than *order*

The transformation of a sequence into the triplet frequency dictionary converts that latter into a point in 63-dimensional metric space; the constraint (1) allows to eliminate a triplet, since there are 63 ones linearly independent only. In theory, any triplet might be excluded from the analysis; practically, we have excluded the triplet CAC, since it has the least standard deviation figure determined over the dataset. An idea standing behind such choice is that the triplet with the minimal standard deviation contributes less of all into the distinguishability of the genetic entities.

The transformation maps symbol sequence into more convenient mathematical object that is the points in metric space, thus allowing to implement the effective methods of analysis. To do it, one must introduce a metrics; further, we use Euclidean metrics

$$\rho\left(W_j, W_l\right) = \sqrt{\sum_{k=\mathsf{AAA}}^{\mathsf{TTT}} \left(f_k^{(j)} - f_k^{(l)}\right)^2}. \tag{2}$$

Thus, we investigate the distribution of the points corresponding to genetic sequences in this metric space revealing patterns and clusters, if any.

2.3   Clustering and Visualization

A variety of methods to cluster the multidimensional data is huge. We used k-means and elastic map technique to cluster the data. k-means is well known linear classification method [7,9], so let's focus on elastic map technique. It is the non-linear statistics method based on the approximation of the multidimensional data by a manifold of the lower dimension; further we shall use two-dimensional manifolds [8].

The idea of this method consists in jamming the originally plain manifold (a square in our case) in the manner to minimise the total deformation energy of the elastic manifold, and mathematical springs connected to the manifold in the projection points. It is highly powerful and efficient method to cluster multidimensional data and visualise them.

Non-linear clustering of genes was provided by local density technique. In simple words, local density is a specific number of point in a small site on map. To calculate the local density, we supply each point on the map with bell-shaped function

$$h\left(r, r^{(j)}\right) = \exp\left\{-\frac{(r - r^{(j)})^2}{\sigma^2}\right\}, \tag{3}$$

where r is a point position on the map, $r^{(j)}$ is the coordinate of a gene converted into a point through triplet frequency transformation, and σ is the contrast parameter. The function (3) looks like a normal distribution function, however it is not.

As soon as all the points on the map are supplied with the function (3), one should calculate the sum

$$H(r) = \sum_{j \in \Omega} h\left(r, r^{(j)}\right). \tag{4}$$

Here Ω is the set of all the points from the dataset. One should plot the function (4) over the map to see the density of the points distribution (see Fig. 1(b)); Ω is the set all the points representing the considered genes.

3   Results and Discussion

16 SRNAs are typically used in the studies of the relations (phylogeny as well) of bacteria [10,18,22]. Usually, the comparison of the sequences is provided by alignment; here we present some preliminary results of the structure identification provided through the implementation of alignment-free approach, namely the unsupervised clustering based on elastic map technique.

Speaking in advance, we tried the unsupervised clustering to reveal a pattern in taxa distribution of some bacteria; we aimed mainly to prove that such pattern

(a)   (b)
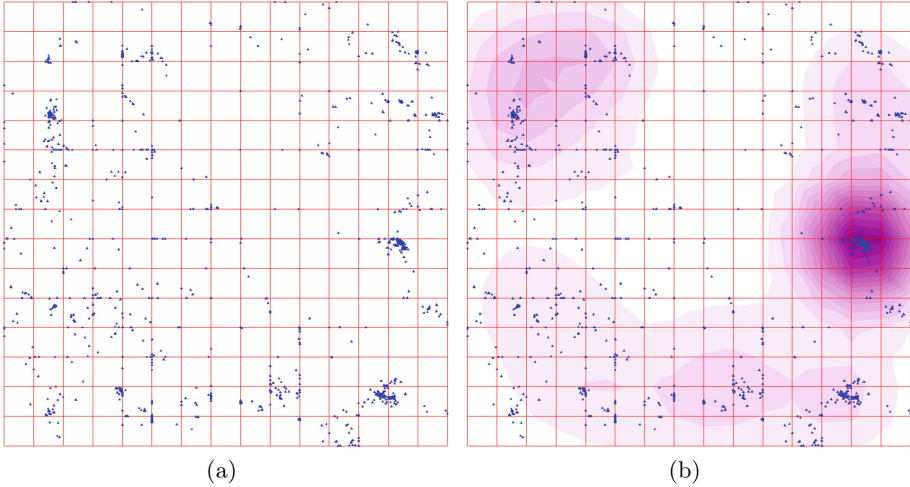
Fig. 1. A distribution of 2143 points over the elastic map with no local density indication (Fig. 1(a)) and with that former (Fig. 1(b)).

exists. Figure 1 shows the raw distribution of 2143 genes of 16S RNA over the soft elastic map. Figure 1(a) shows the distribution itself, and Fig. 1(b) shows the same distribution over the local density mapped at the same map.

Figure 1 shows the overall distribution of the genes over the soft elastic map 16×16 (Fig. 1(a)). To compare with, Fig. 1(b) shows this distribution together with the local density. Of course, the cluster pattern depends on the contrast radius σ from (3); the choice of that latter is quite informal. We used by default figure of 0.25 for this parameter. Doubtlessly, there is one highly dense cluster located at the right of the map. There are three to four clusters more, as well.

Figure 2 shows the individual distributions of specific orders over the elastic map. To do it, we made all markers of genes except those belonging to a specific order invisible; however, the elastic map as well as the local density chart is developed for the entire set of genes (these are 2143 entries). For technical reasons, we had to merge two orders (these are *Mycoplasmatales* and *Solibacterales*) into a single map (see Fig. 2(i)).

We explored the distinguishability of rather high taxa through the clustering of 16S RNA bacterial genes converted into triplet frequency dictionaries. Thus, a question arises what happens with lower taxa? In other words, if one implements the same procedure for the set of genes belonging, say to the same order, then what kind of clustering could be observed? Again, here two options may take place: the former is that lower taxa yield the distinct clustering (regardless of the peculiarities of the clusters composition, at the first step), and the latter is a decomposition of a cluster pattern resulting in more or less uniform distribution of the genes over the elastic map.

(a) *Acidimicrobiales*

(b) *Alicyclobacillales*

(c) *Bacillales*

(d) *Bacteroidales*

(e) *Brevibacillales*

(f) *Chlamydiales*

(g) *Exiguobacterales*

(h) *Lactobacillales*

(i) *Mycopl+Solibact.*⋆

(j) *Paenibacillales*

(k) *Acidobacteriales*

(l) *Staphylococcales*
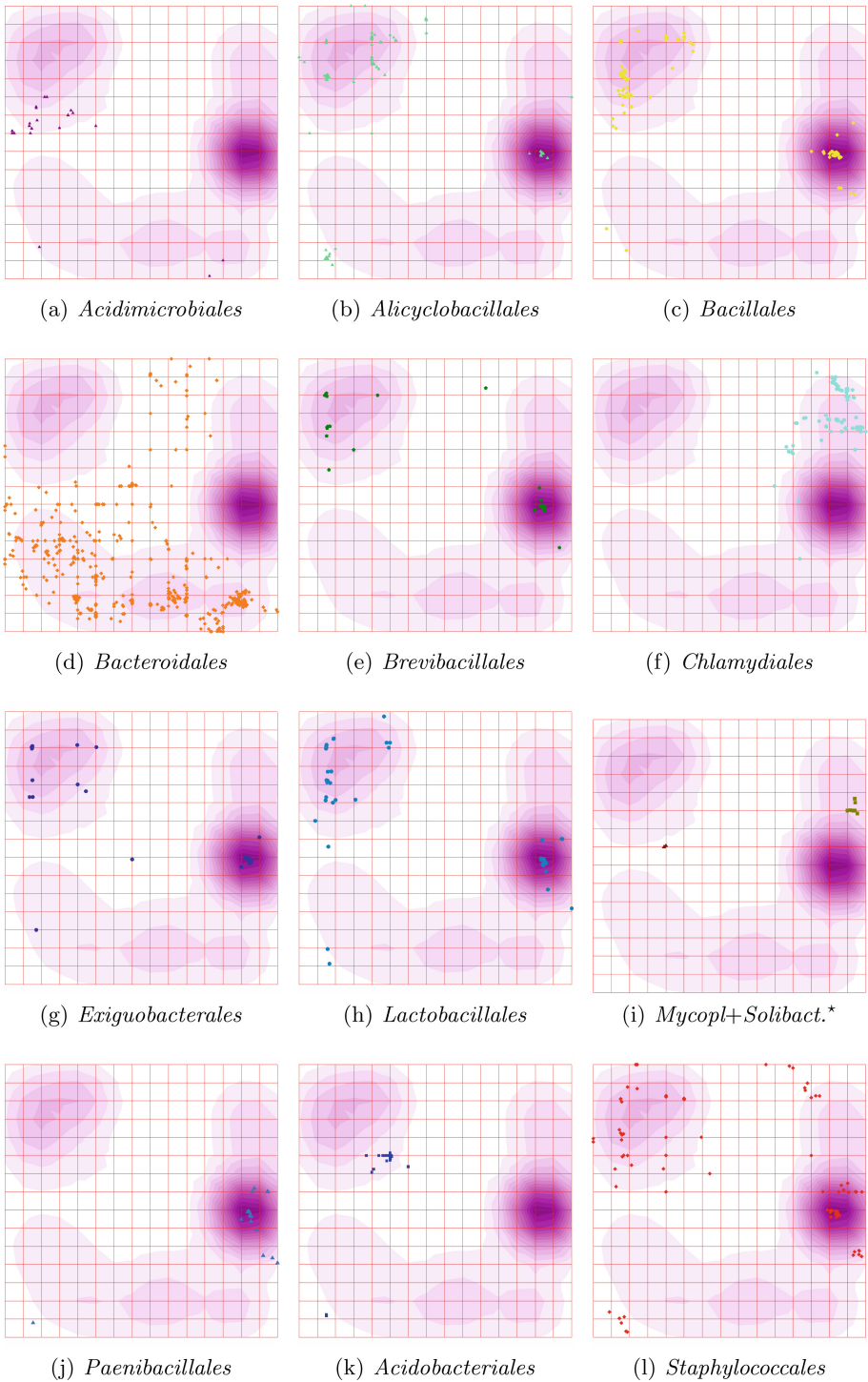
Fig. 2. Individual distributions of various orders.

(a) *Chl. chlamidacea*   (b) *Chl. mycoplasmataceae*   (c) *Chl. parachlamydiaceae*
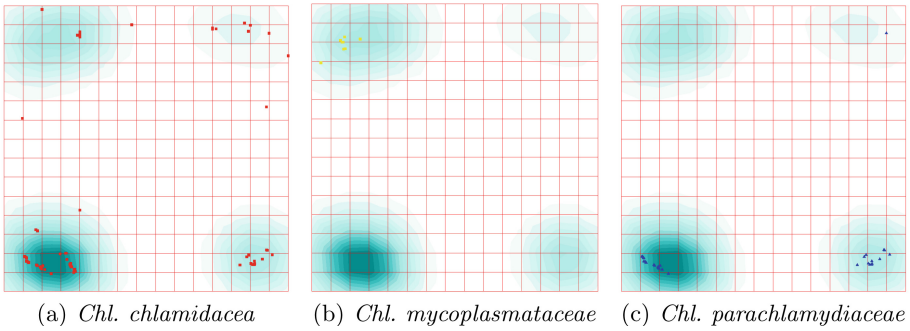
Fig. 3. Family distributions of *Clhlamydiales* order.

The first option means a scalability of the cluster pattern observed through the triplet composition analysis of the genes; the second one means the absence of fine structure in the lower taxa distributions developed due to triplet composition approach. Figure 3 illustrates the lower level distinguishability of the genes, for *chlamydiales* order. There are three families comprised into the dataset, for this order. Obviously, the distribution of the families is highly specific and the species show significant speciality in the mutual location over the elastic map. The orders *Acidobacteriales* and *Acidomicrobiales* comprise a single lower suborder with 34 and 24 entries each, respectively, so we just omitted these orders from consideration here.

Space limitation makes it impossible to show the in-order distribution for all five orders shown above; however, two other orders (these are *Bacillales*, 1118 entries and *Bacteroidia*, 695 entries) have eight and seven families each, so we studied the distribution of the families for them. Surprisingly, these two orders show opposite patterns in the behaviour. *Bacillales* order shows three apparent clusters: the first one is the most dense, are two others are less dense. So, the distribution of the families over the clusters is pretty close to a uniform one: the genders belonging to various families are distributed quite homogeneously over these three clusters. It means that no dependence between lower taxonomy and triplet composition of the genes for this order is observed.

The cluster comprising *Chlamydiales* order makes a clear and apparent group located separately from other considered bacteria orders, in elastic map (see Fig. 3(f) and 3). Such isolation of pathogenic bacteria makes a promising result concerning the reliable diagnostics, in future. On the contrary, the order *Bacteroidia* exhibits very good and clear speciality in the cluster composition. It comprises seven families and they are distributed over the elastic map separately. The genes of this order yield four clusters; however, the genes are separated, for each family.

The ultimate goal is to identify and verify the early predictors of some neurological diseases, in particular the multiple sclerosis through the analysis of microbiota [11, 12, 15–17]. This ambitious goal requires an implementation of

the tool for fast and efficient analysis of some genetic markers of the microbiota, and 16S RNA seems to be the best one here. A diagnostics of the mentioned diseases requires a study of a normal pattern of the gut microbiota occurrence; hence, we prove an efficiency in the microbial population investigation and a reference value, for further medically sounding studies. The method of clustering and/or classification could complement the currently practising techniques of for diagnostics and curation strategy implementation.

Here we present some preliminary results aimed to demonstrate the feasibility and efficiency of the diagnostics based on 16S RNA analysis of the microbiota of healthy and sick people. To implement such diagnostic tool, one should make sure that a genetic marker used to distinguish sick people from healthy ones really supports this distinguishability. The results provided here unambiguously prove the efficiency of such approach, in principle. Doubtlessly, our current results to not comprise a diagnostic tool; they just approve the feasibility of the tool if it is implemented.

4   Conclusion

Here we explored the interplay between triplet composition of 16S RNA bacterial genes of five orders and taxonomy of those bacteria. Some preliminary results are present aimed to approve the feasibility of triplet composition based clustering of 16S RNA bacterial genes to identify the distinguishability of various taxa in the 63-dimensional Euclidean space of triplets frequency. The results unambiguously show that various taxa differ in terms of the triplets frequency so that more detailed and exhaustive investigation of the interplay for sure makes sense and may bring a lot. Moreover, the interplay is *scalable*: a transition from higher taxon to lower ones reveals the new and more fine structuredness in the clustering.

The study of interplay between taxonomy and k-tipple composition of genes is of great interest and value itself. However, these studies may contribute a lot in various applied areas including e.g. medicine.

Thus, a design and implementation of a tool for early diagnostics such hard to detect diseases based on comparative analysis of formally identified structures in bacterial 16S RNA is feasible.

References

1. Bonnici, V., Cracco, A., Franco, G.: A k-mer based sequence similarity for pangenomic analyses. In: International Conference on Machine Learning, Optimization, and Data Science, pp. 31–44. Springer, Cham (2021). https://doi.org/10.1007/978-3-030-95470-3_3
2. Das, S., Das, A., Bhattacharya, D., Tibarewala, D.: A new graph-theoretic approach to determine the similarity of genome sequences based on nucleotide triplets. Genomics **112**(6), 4701–4714 (2020)

3. Fedotovskaya, V., Sadovsky, M., Kolesnikova, A., Shpagina, T., Putintseva, Y.: Function vs. taxonomy: further reading from fungal mitochondrial ATP synthases. In: IWBBIO, pp. 438–444 (2020)

4. Frappat, L., Sciarrino, A.: Conspiracy in bacterial genomes. Physica A Stat. Mech. Appl. **369**(2), 699–713 (2006)

5. Gorban, A.N., Zinovyev, A.Y.: The mystery of two straight lines in bacterial genome statistics. Bull. Math. Biol. **69**(7), 2429–2442 (2007)

6. Gorban, A., Popova, T., Zinovyev, A.: Codon usage trajectories and 7-cluster structure of 143 complete bacterial genomic sequences. Physica A Stat. Mech. Appl. **353**, 365–387 (2005)

7. Gorban, A.N., Zinovyev, A.: Principal manifolds and graphs in practice: from molecular biology to dynamical systems. Int. J. Neural Syst. **20**(03), 219–232 (2010). https://doi.org/10.1142/S0129065710002383. pMID: 20556849

8. Gorban, A.N., Zinovyev, A.Y.: Fast and user-friendly non-linear principal manifold learning by method of elastic maps. In: 2015 IEEE International Conference on Data Science and Advanced Analytics, DSAA 2015, Campus des Cordeliers, Paris, France, 19–21 October 2015, pp. 1–9 (2015). https://doi.org/10.1109/DSAA.2015.7344818

9. Gorban, A., Sumner, N., Zinovyev, A.: Topological grammars for data approximation. Appl. Math. Lett. **20**(4), 382–386 (2007)

10. Janda, J.M., Abbott, S.L.: 16S RRNA gene sequencing for bacterial identification in the diagnostic laboratory: pluses, perils, and pitfalls. J. Clin. Microbiol. **45**(9), 2761–2764 (2007)

11. Kozhieva, M., Naumova, N., Alikina, T., Boyko, A., Vlassov, V., Kabilov, M.R.: Primary progressive multiple sclerosis in a Russian cohort: relationship with gut bacterial diversity. BMC Microbiol. **19**(1), 1–9 (2019)

12. Li, B., et al.: Mild cognitive impairment has similar alterations as Alzheimer's disease in gut microbiota. Alzheimer's Dement. **15**(10), 1357–1366 (2019)

13. Luczak, B.B., James, B.T., Girgis, H.Z.: A survey and evaluations of histogram-based statistics in alignment-free sequence comparison. Brief. Bioinform. **20**(4), 1222–1237 (2019)

14. Mascher, M., Schubert, I., Scholz, U., Friedel, S.: Patterns of nucleotide asymmetries in plant and animal genomes. Biosystems **111**(3), 181–189 (2013)

15. Mirza, A., et al.: The multiple sclerosis gut microbiota: a systematic review. Multiple Sclerosis Related Disorders **37**, 101427 (2020)

16. Mulak, A., Bonaz, B.: Brain-gut-microbiota axis in Parkinson's disease. World J. Gastroenterol. WJG **21**(37), 10609 (2015)

17. Nair, A.T., Ramachandran, V., Joghee, N.M., Antony, S., Ramalingam, G.: Gut microbiota dysfunction as reliable non-invasive early diagnostic biomarkers in the pathophysiology of Parkinson's disease: a critical review. J. Neurogastroenterol. Motil. **24**(1), 30 (2018)

18. Purkhold, U., Pommerening-Röser, A., Juretschko, S., Schmid, M.C., Koops, H.P., Wagner, M.: Phylogeny of all recognized species of ammonia oxidizers based on comparative 16S RRNA and AMOA sequence analysis: implications for molecular diversity surveys. Appl. Environ. Microbiol. **66**(12), 5368–5382 (2000)

19. Sadovsky, M., Putintseva, Y., Chernyshova, A., Fedotova, V.: Genome structure of organelles strongly relates to taxonomy of bearers. In: Ortuño, F., Rojas, I. (eds.) Bioinform. Biomed. Eng., pp. 481–490. Springer, Cham (2015). https://doi.org/10.1007/978-3-319-16483-0_47

20. Sadovsky, M.G., Putintseva, J.A., Shchepanovsky, A.S.: Genes, information and sense: complexity and knowledge retrieval. Theory Biosci. **127**(2), 69–78 (2008)

21. Sievers, A., Wenz, F., Hausmann, M., Hildenbrand, G.: Conservation of k-mer composition and correlation contribution between introns and intergenic regions of animalia genomes. Genes **9**(10), 482 (2018)
22. Yang, B., Wang, Y., Qian, P.Y.: Sensitivity and correlation of hypervariable regions in 16S RRNA genes in phylogenetic analysis. BMC Bioinform. **17**(1), 1–8 (2016)

Modern Approaches to Cancer Treatment

Snezhana M. Bakalova[1] , Milena Georgieva[2(✉)] , and Jose Kaneti[1]

[1] Institute of Organic Chemistry with Centre of Phytochemistry, Bulgarian Academy of Sciences, 1113 Sofia, Bulgaria

[2] Institute of Molecular Biology "Acad. R. Tsanev", Bulgarian Academy of Sciences, Sofia 1113, Bulgaria

`milenageorgy@gmail.com`

Abstract. Cancer remains the most common worldwide problem with the highest impact on global health. It is the second leading cause of death, due to the lack of early diagnosis and high recurrence rate after conventional therapies. Although every year several new therapeutic approaches are proposed the urgent need for more effective therapeutic strategies to improve the survival rate and life expectancy of cancer patients rapidly grows.

A recent promising anticancer strategy is based on multinuclear heterocycles as widely investigated bioactive molecules, considered important synthetic targets for the development of novel therapeutic agents. Many nitrogen heterocycles are known for a long time as natural alkaloids, known to possess the broad and diverse biological activity and medicinal applicability. Nowadays however novel multinuclear drug-like heterocyclic structures are generated by methods of artificial intelligence. Novel approaches are required as more expeditious ways of studying their biological activity, capable of more than explaining their activity, and even prognosticating it.

This study highlights our and other authors' recent results on the biological activity of multinuclear heterocyclic molecules on cancer cells, explicitly based on their capacity to bind to G-quadruplexes. It further stresses the need for novel G-quadruplex binding compounds, with elucidated biochemical mechanisms of action for biomedical applications, namely in anticancer therapies.

Keywords: Cancer · Heterocycles · Bioactive molecules · G-quadruplexes

1   Cancer – The Hidden Pandemic

Cancer is a generic term for a large group of diseases that can affect any part of the body [1]. The common feature of all cancer types is the rapid creation of abnormal cells that grow beyond their usual boundaries, which can then invade adjoining parts of the body and spread to other organs through the process of metastasizing (National Cancer Institute, 2020). Metastases are a major cause of death from cancer. Late-stage presentation and inaccessible diagnosis and treatment are common. In 2017, only 26% of low-income countries reported having pathology services generally available in the public sector. More than 90% of high-income countries reported treatment services are

available compared to less than 30% of low-income countries. The economic impact of cancer is significant and is increasing. The total annual economic cost of cancer in 2010 was estimated at approximately US\$ 1.16 trillion (WHO, 2020). A correct cancer diagnosis is essential for adequate and effective treatment because every cancer type requires a specific treatment regimen that encompasses one or more modalities such as surgery, radiotherapy, and chemotherapy. Determining the goals of treatment and palliative care is an important first step, and health services should be integrated and people-centered (WHO, 2020 Report on cancer). The primary goal is generally to cure cancer or to considerably prolong life.

In 2017, the World Health Assembly approved the resolution for Cancer Prevention and Control through an Integrated Approach (WHA70.12), which urges governments and WHO to accelerate action to achieve the targets specified in the Global Action Plan and 2030 UN Agenda for Sustainable Development to reduce premature mortality from cancer. Therefore, the search for novel, effective and cancer-selective therapeutics is of utmost interest to each country.

2 The G-quadruplexes: Characteristics and Properties

DNA can spontaneously fold into several secondary structures besides the classic double helix, so-called non-canonical secondary structures. The G-quadruplex (G4) received huge attention in recent years [2]. Strands of RNA that contain at least four stretches of two or more adjacent guanine nucleotides are also able to form G4. These G4s can either be intramolecular, forming from a single strand of DNA or RNA or intermolecular, forming from either two or four separate nucleic acid strands. In terms of structure, the basic unit of the G4 is the G-quartet/tetrad, an approximately planar array of four Hoogsteen-bonded guanine bases, which may stack on top of one another to form the G4 structure itself [3], stabilised by monovalent cations (principally thought to be K^+ or Na^+ within cells). This is the first precise X-ray structural proof of the G-quartet [3].

Initially considered a structural curiosity, now G4s are found all over the human genome and are suspected of being involved in a wide range of biological processes. G4s are most frequently present at the end of chromosomes, the telomeres, as well as in proto-oncogenes regulating their expression. G4s are involved in the replication and transcription of DNA [4]. G4s, formed under physiological conditions are as stable as, or even more stable than, duplex DNA. It must be acknowledged that some of the evidence that supports roles for G4s in nucleic acid biology are tentative, which is not surprising given the technical challenges associated with demonstrating G4s in biology (G4s are transient and therefore difficult to identify directly in living cells). In 2013 Cambridge researchers published a paper proving evidence that G-quadruplexes also existed within the human genome [5]. They developed a highly specific DNA G-quadruplex antibody and employed it to visualize G-quadruplex structures in the DNA of human cells. As a result, they demonstrated that the formation of G-quadruplexes is dynamically sensitive to the cell cycle, and showed by direct visualization that a small-molecule ligand (pyridostatin, PDS) traps these structures in cells. We study these structures computationally at the currently possible level of accuracy. The problem of computing reliable stacking stabilization energies of G4s with relatively small molecular ligands requires the use

of quantum mechanical approaches to achieve chemical precision, which systematically leads to uncertainties in calculated energy differences less than ± 1 kcal mol^{-1}. Figures 1 and 2 provide G-quartet structures and their stacking together in two or more layers to model the observable G-quadruplexes [20].
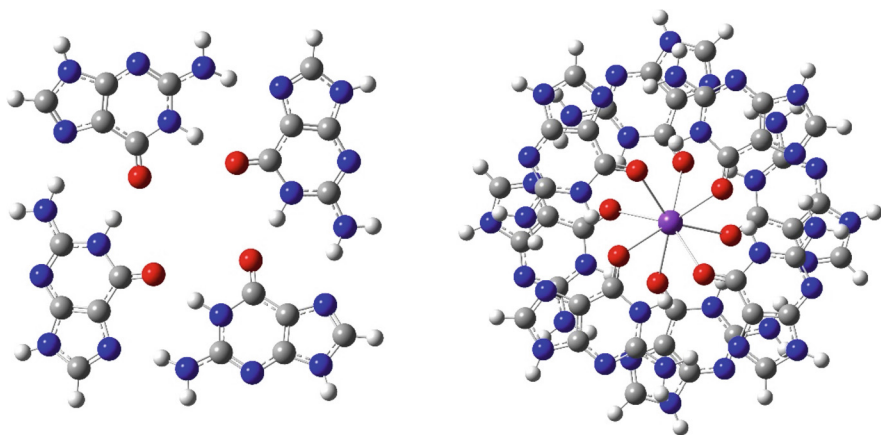
Fig. 1. A G-quartet, and a two-layered quadruplex with a stabilizing K+ ion, the purple centre atom, view along the symmetry axis. Nitrogen atoms are blue, and oxygen atoms are red. (Color figure online)

G-quadruplexes turned out to be amazingly multifunctional. Regulation of telomerase – helicase pair is a most typical example of G-quadruplex functionality. While participation in NA processing might seem easy to surmise as a "NA internal", G4-regulation is observed further away in the control of protein synthesis [6]. Several oncogene protein promoter genes, like c-MYC, c-KIT, etc., are known to include G-quadruplexes within their secondary structures and are susceptible to control by small molecules [7]. The working hypothesis of complex formation with the small (or potential candidate) drug molecule has first been confirmed by an X-ray study of the daunomycin complex with a telomeric G-quadruplex [8]. π-π stacking the planes, Fig. 2, of small molecules to G-quadruplexes is being confirmed by a steadily increasing number of X-ray crystal and NMR solution structural studies [9–11].

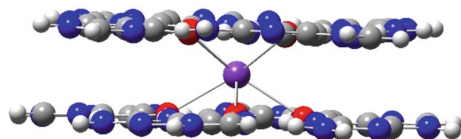**Fig. 2.** Another view of a two-layered G-quadruplex with a stabilizing K+ ion, the purple centre atom. Nitrogen atoms are blue, and oxygen atoms are red. (Color figure online)

The significant participation of π-π interactions in stacked complexes of heterocyclic drug candidates and G-quadruplexes, Fig. 3, offers the opportunity to study their interaction energies theoretically in considerable detail [12, 13]. A great variety of molecular mechanic (MM) and/or molecular dynamic (MD) studies of G-quadruplexes has been used to elucidate the 3D-spatial and temporal properties of G-quadruplexes [13, 14]. While relatively affordable, the MM/MD calculations suffer some important shortcomings in terms of the accuracy of computed interaction energies. These shortcomings preclude to a certain extent the use of MM computational models for molecular design, in particular their use in the direction of QSAR.

Further, significantly more accurate (or "chemically precise") quantum mechanical, QM, studies of G-quadruplex structures belong to the class of large scale computations. The most robust contemporary models [15] of various G-quadruplex structural varieties utilize density functional theory, DFT, to provide "unique insights into the H-bonding, stacking, ion binding, and backbone conformations of nucleic acids" [15]. Currently, there are, as might be expected, two directions in the more accurate, but tedious QM studies of G-quadruplexes: the use of relatively small models to reveal basic structural trends, [16, 17] and complete size models, ultimately directed to QSAR [18–20].

The recent pair of decades have seen significant efforts to select better methodological approaches in the computations of interaction energies within the structures relevant to G-quartet formations and complexes. Components of the interaction energy are accurately represented by DFT as

$$\Delta E_{int} = \Delta V_{elstat} + \Delta E_{exch} + \Delta E_{overlap} + \Delta E_{disp} \tag{1}$$

where elstat, exch, overlap and disp are the electrostatic, exchange, overlap, and dispersion components of interaction energy. As common with molecular DFT computations, accurate results may be produced with a careful selection of parameterized DFT functionals, where long-range and dispersion interactions are properly accounted for. For this reason, we select the hybrid wB97XD functional, accounting for both dispersion and long range interactions [21]. Our model to produce stacking interaction energies of potential anticancer candidates includes a two- or three-layered G-quadruplex, stripped off pentose-phosphate residues [20]. The stacking interaction energy of potential drug ligands and a model G-quadruplex provides the ligand affinity, which should be related to its activity, is defined as

$$\Delta E_{LG} = E_L + E_G - E_{LG} \tag{2}$$

where L denotes the ligand, G – the model G-quadruplex, and LG – the (stacked) complex thereof.

In our research we used the following computational protocol to reproduce the above simple expressions of energies of ligand – G4-quadruplex adducts, and derive the necessary ligand – G-quadruplex, G4, affinities ΔE_{LG} with an example of known anticancer agent, quarfloxin [8]. The protocol that we have provided include the following steps:

1. Compute G4 energy, and the energy of a quadruplex with a K+ ion, using complete function minimization concerning all molecular coordinates at the wB97-XD/6-31G(d,p) quantum chemical level, Fig. 2: −4939.424689 a.u.

2. Compute ligand L energy, with complete function minimization concerning all molecular coordinates using wB97-XD/6-31G(d,p) – in this case, quarfloxin, Fig. 3. [9]: -2007.047343 a.u.
3. Build a stacked ligand – quadruplex complex using primitive molecular docking
4. Compute full LG energy of the complex using complete function minimization with respect to all molecular coordinates at the wB97XD/6-31G (d,p) level of DFT, Fig. 4: -6946.563341 a.u.
5. Evaluate ΔE_{LG} from values of 1, 2, and 4, Eq. 2: -0.091309 a.u. $= -57.3$ kcal·mol^{-1}
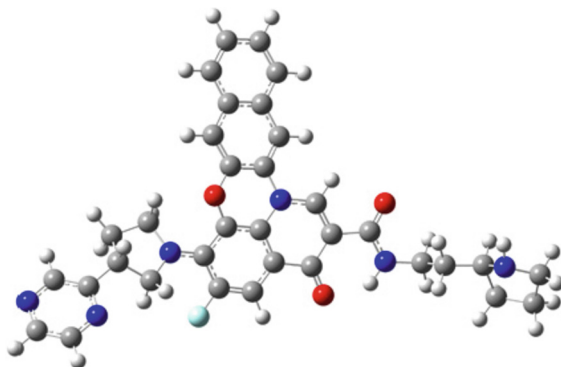
Fig. 3. Quarfloxin, or CX-3543, is an anticancer drug candidate [8].
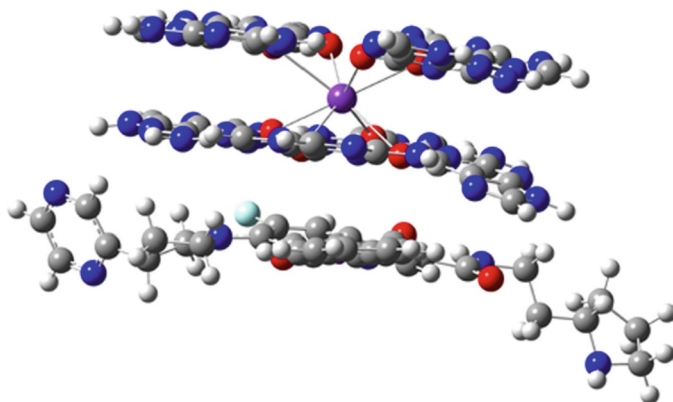
Fig. 4. The G4 - Quarfloxin, or CX-3543, complex, wB97XD/6-31G(d,p).

The above energy values may conveniently be rectified at another more accurate level of quantum chemical computations, RI-MP2/6-31G (d,p), with an auxiliary SVP basis for projecting atomic wave functions [20].

The same operation with structures, produced by AI methods, has one more complication arising from the large number of generated potentially active compounds. The

process must obviously involve the selection of molecular structures, closest to the mechanistic hypothesis underlying the drug relation with the biomolecular activity of interest. In the present case, we assume stacking interaction of molecules with a G-quadruplex, which supposedly would be preferred with multinuclear heterocycles. A compound, similar to the molecules studied in this laboratory, is marked as P108610048. (Otava chem) Its computed wB97-XD/6-31G(d,p) energy is -1162.914367 a.u., which is stage 2 at the procedure, outlined above, Fig. 5.

Computed ligand – complex total energy is -6102.429463 a.u.

The affinity of G4 to P108610048 is -0.090407 a.u. = -56.7 kcal.mol^{-1}.

Another AI generated compound is P0107740024, Fig. 6. Calculated wB97-XD/6-31G(d,p) energy values for this compound and G4 complex are respectively, -1112.694009 a.u. and -6052.179028 a.u. The affinity of 0107740024 to the G-quadruplex is -0.060330 a.u., or -37.9 kcal·mol^{-1}, Fig. 6.
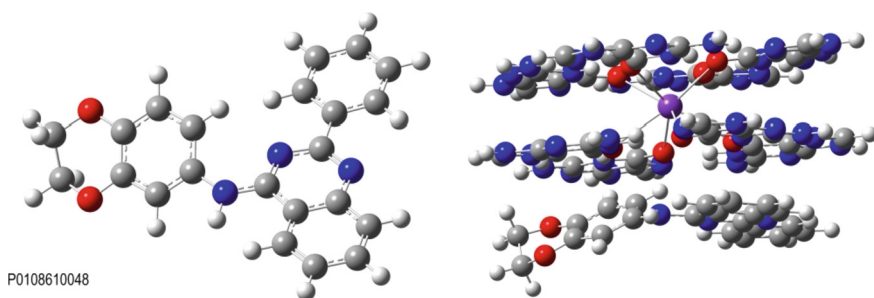
Fig. 5. Compound P0108610048 from an AI database, [Otava chem., 2021], and its G4-complex, wB97XD/6-31G(d,p).

As seen from the given examples, the experimentally proven active anticancer compound does really have a significantly higher G-quadruplex affinity. The affinity of the 4-arylaminosubstituted quinazoline P0108610048 is marginally lower, while that of P0107740024 is much lower, rendering the latter compound insignificant.

3 The G4 Motifs as Targets in Anticancer Therapy

In 2020 it was discovered that G4 forms are preserved in tumour tissues and biopsies of breast cancer [22]. The authors concluded that the abundance and location of G-quadruplexes in these biopsies give a clue to their importance in cancer biology and the heterogeneity of breast cancers. There are numerous G4 motifs in the human genome (over 350,000 allowing loops of 1–7 nt, and over 700,000 allowing loops up to 12 nt in length), especially abundant in specific chromosomal domains, genomic regions, and genes [23], but we do not yet know if every genomic G4 motif forms a quadruplex in a living cell. G4s have recently gathered a lot of attention as potential therapeutic targets, particularly in anticancer drug design [24]. Small compounds able to bind and stabilize these structures have been synthesized and their potential to interfere with telomeric functions and/or oncogene expression has been demonstrated [25]. Several
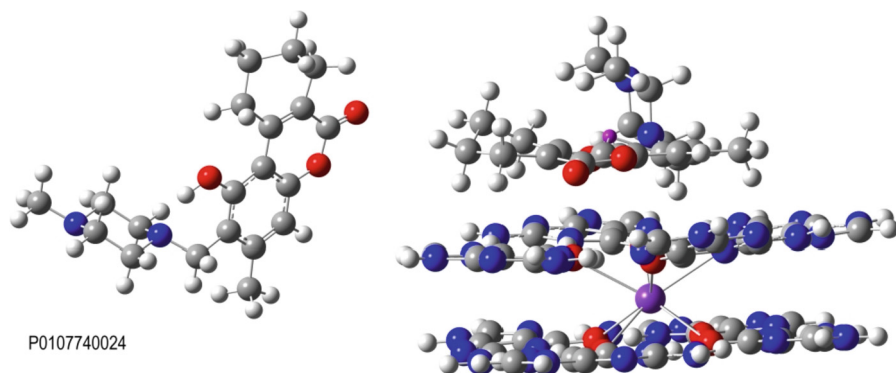
Fig. 6. Compound P0107740028 from an AI database, [Otava chem., 2021] and its G4-complex, wB97XD/6-31G(d,p).

classes of ligands are described as binding and stabilizing G4 [26]. Aggressive cancer cells, such as the MDA breast cancer line, are known to be sensitive to the presence of G4 [27]. Pyridostatin (CX-5461), a G4-stabilizer toxic against tumours, and quarfloxin have been shown to effectively kill BRCA-deficient cancer cells [28]. The authors proved that tumour cells, exposed to CX-5461, experienced replication stress and accumulation of ssDNA breaks. The CX-5461-induced DNA damage and failure to repair led tumor cells death, thus reinforcing the idea of G4 targeting as a beneficial approach in anti-tumor therapies especially for DNA repair deficient cancer types. CH-5461 and its related drug CX-3543 are in advanced phase clinical trials.

As a general phenomenon in cancer, there is an increased requirement for rDNA transcription to meet the greater protein synthesis demand in cancer cells [29]. G4s increase the tendency for DNA damage to occur, by impeding DNA polymerase and DNA damage repair processes [30]. Pyridostatin (CX-5461), quarfloxin (CX-3543) and BMH-21 (a benzopyridoquinazoline-carboxamide) are inhibitors of rDNA transcription. CX-3543 binds to G4 sequences and disrupts the interaction of rDNA G4 structures with nucleolin (the major nucleolar protein of growing eukaryotic cells, associated with intranuclear chromatin and pre-ribosomal particles), thereby inhibiting Polymerase I transcription and inducing apoptotic death in cancer cells [31].

Hundreds of ligands are reported to bind G4 sequences with high specificity and affinity. The pioneering works, that accelerated the development of G4-selective synthetic molecules, along with the advance in methods/techniques to characterize the binding profiles of such G4 ligands, are on the so-called "global" G4-selective ligands [32]. Such ligands are 2,6-diamido-anthraquinone derivatives (interacting with telomere G4s) [33], TMPyP4 (a cationic porphyrin) [34], telomestatin (a macrocycle naturally occurring in *Streptomyces annulatus*) [35]. Several commercially available G4 ligands, such as BRACO 19 [36], pyridostatin [37], Phen-DC3 [38], L2H2-6OTD [39], and L1H1-7OTD [40], are indispensable to biochemical, biophysical, and chemical biology studies of G4s. All of these have negligible binding affinities to duplex DNAs [32].

Based on the organization of their structural elements, G4 ligands can be roughly divided into three major families: (1) fused heteroaromatic polycyclic systems (such

as the indoloquinoline); (2) macrocycles (such as hexaoxazole L2H2-6M(2)OTD [40]; (3) modular aromatic compounds (nonfused aromatic systems) [41]. The design of G4 ligands, including our efforts [20] emerged as the answer to achieve not only more drug-like compounds but also to find more selective ligands taking in mind the diversity of the G4 loops and grooves.

Combinations of *in silico/in vitro* approaches to identify novel inhibitors against (bio)targets have the potential to become a popular discovery tool. Stages in a typical drug discovery process include target selection, hit identification, lead optimization, and preclinical and clinical studies. Hit identification and lead optimization are very intertwined with computational modelling. Structure-based virtual screening (VS), also known as target-based virtual screening (TBVS), attempts to predict the best interaction between ligands against a molecular target to form a complex. It has been a staple for more than a decade in drug discovery with its underlying computational technique, docking extensively studied [42]. VS strategies have been building momentum in G4 drug discovery both as a low-cost enrichment step and as a lead development step in the discovery pipeline. In a recent review of the past decade of G-quadruplex virtual drug discovery approaches and campaigns, the relevant virtual screening platforms have been analysed [43]. Among common VS screening strategies, extensively used in lig- and discovery, including docking and pharmacophore screening, however, there is no "universal" strategy specifically targeting G4s.

4   Conclusions

The reported findings appear to support our recent mechanistic suggestion that at least some anticancer agents manifest their activity thanks to complex formation with important G-quadruplexes, thus stabilizing these structures and modifying their regulation of cell proliferation, and metabolism and functioning in general. This could as well be the explanation for their anticancer activity, which may then be correlated to the affinity of these molecules to stack with G-quadruplexes in QSAR. Three test cases, one of which known as anticancer compound, outline the novel suggestion numerically.

Websites:

https://www.who.int/health-topics/cancer
https://www.who.int/health
https://apps.who.int/gb/ebwha/pdf_files/WHA70/A70_R12-en.pdf
https://otavachemicals.com/products/targeted-libraries-and-focused-libraries

References

1. Hanahan, D., Weinberg, R.A.: Hallmarks of cancer: the next generation. Cell **144**, 646–674 (2011)
2. Spiegel, J., Adhikari, S., Balasubramanian, S.: The structure and function of DNA G-quadruplexes. Trends Chem. **2**, 123–136 (2020)
3. Gellert, M., Lipsett, M.N., Davies, D.R.: Helix formation by guanylic acid. Proc. Natl. Acad. Sci. U.S.A. **48**, 2013 (1962)
4. Simone, R., Fratta, P., Neidle, S., Parkinson, G.N., Isaacs, A.M.: G-quadruplexes: emerging roles in neurodegenerative diseases and the non-coding transcriptome. FEBS Lett. **589**, 1653–1668 (2015)
5. Biffi, G., Tannahill, D., McCafferty, J., Balasubramanian, S.: Quantitative visualization of DNA G-quadruplex structures inhuman cells. Nat. Chem. **5**(3), 182–186 (2013)
6. Masai, H., Tanaka, T.: G-quadruplex DNA and RNA: their roles in regulation of DNA replication and other biological functions. Biochem. Biophys. Res. Commun. **531**, 25–38 (2020)
7. Wang, K.-B., Elsayed, M.S.A., Wu, G., Deng, N., Cushman, M., Yang, D.: Indenoisoquinoline topoisomerase inhibitors strongly bind and stabilize the MYC promoter G-quadruplex and downregulate MYC. J. Am. Chem. Soc. **141**, 11059–11070 (2019)
8. Clark, G.R., Pytel, P.D., Squire, C.J., Neidle, S.: Structure of the first parallel DNA quadruplex-drug complex. J. Am. Chem. Soc. **125**, 4066–4067 (2003)
9. Drygin, D., et al.: Anticancer activity of CX-3543: a direct inhibitor of rRNA biogenesis. Can. Res. **69**, 7653–7661 (2009)
10. Neidle, S.: Quadruplex nucleic acids as novel therapeutic targets. J. Med. Chem. **59**, 5987–6011 (2016)
11. Cushman, M.: Design and synthesis of indenoisoquinolines targeting topoisomerase I and other biological macromolecules for cancer chemotherapy. J. Med. Chem. **64**, 17572–17600 (2021)
12. Xiao, X., Cushman, M.: An ab initio quantum mechanics calculation that correlates with ligand orientation and DNA cleavage site selectivity in Camptothecin− DNA− Topoisomerase I ternary cleavage complexes. J. Am. Chem. Soc. **127**, 9960–9961 (2005)
13. Haider, S.: Computational methods to study G-quadruplex–ligand complexes. J. Indian Inst. Sci. **98**, 325–339 (2018)
14. Clay, E.H., Gould, I.R.: A combined QM and MM investigation into guanine quadruplexes. J. Mol. Graph. Model. **24**, 138–146 (2005)
15. Gkionis, K., Kruse, H., Sponer, J.: Derivation of reliable geometries in QM calculations of DNA structures: explicit solvent QM/MM and restrained implicit solvent QM optimizations of G-quadruplexes. J. Chem. Theory Comput. **12**, 2000–2016 (2016)
16. Zaccaria, F., van der Lubbe, S.C., Nieuwland, C., Hamlin, T.A., Fonseca Guerra, C.: How divalent cations interact with the internal channel site of guanine quadruplexes. ChemPhysChem **22**, 2286–2296 (2021)
17. Zaccaria, F., Fonseca Guerra, C.: RNA versus DNA G-quadruplex: the origin of increased stability. Chem. Eur. J. **24**, 16315–16322 (2018)
18. Islam, B., Stadlbauer, P., Neidle, S., Haider, S., Sponer, J.: Can we execute reliable MM-PBSA free energy computations of relative stabilities of different guanine quadruplex folds? J. Phys. Chem. B **120**, 2899–2912 (2016)
19. Sponer, J., Mladek, A., Spackova, N., Cang, X., Cheatham III, T.E., Grimme, S.: Relative stability of different DNA guanine quadruplex stem topologies derived using large-scale quantum-chemical computations. J. Am. Chem. Soc. **135**, 9785–9796 (2013)

20. Kaneti, J., et al.: Biological activity of quinazoline analogues and molecular modeling of their interactions with G-quadruplexes. Biochim. Biophys. Acta Gen. Subj. **1865**, 129773 (2021)
21. Chai, J.-D., Head-Gordon, M.: Long-range corrected hybrid density functionals with damped atom–atom dispersion corrections. Phys. Chem. Chem. Phys. **10**, 6615–6620 (2008)
22. Hänsel-Hertsch, R., et al.: Landscape of G-quadruplex DNA structural regions in breast cancer. Nat. Genet. **52**, 878–883 (2020)
23. Maizels, N., Gray, L.T.: The G4 genome. PLoS Genet. **9**, e1003468 (2013)
24. Neidle, S.: Quadruplex nucleic acids as novel therapeutic targets. J. Med. Chem. **59**, 5987–6011 (2016)
25. Roxo, C., Kotkowiak, W., Pasternak, A.: G4 matters-the influence of G-quadruplex structural elements on the antiproliferative properties of G-rich oligonucleotides. Int. J. Mol. Sci. **22**, 4941 (2021)
26. Monchaud, D., Teulade-Fichou, M.-P.: A hitchhiker's guide to G-quadruplex ligands. Org. Biomol. Chem. **6**, 627–636 (2008)
27. Di Somma, S., et al.: G-quadruplex binders induce immunogenic cell death markers in aggressive breast cancer cells. Cancers (Basel) **11**, 1797 (2019)
28. Xu, H., et al.: CX-5461 is a DNA G-quadruplex stabilizer with selective lethality in BRCA1/2 deficient tumours. Nat. Commun. **8**, 14432 (2017)
29. Derenzini, M., Trerè, D., Pession, A., Govoni, M., Sirri, V., Chieco, P.: Nucleolar size indicates the rapidity of cell proliferation in cancer tissues. J. Pathol. **191**, 181–186 (2000)
30. Duan, W., et al.: Design and synthesis of fluoroquinophenoxazines that interact with human telomeric G-quadruplexes and their biological effects. Mol. Cancer Ther. **1**, 103–120 (2001)
31. Bywater, M.J., et al.: Inhibition of RNA polymerase I as a therapeutic strategy to promote cancer-specific activation of p53. Cancer Cell **22**, 51–65 (2012)
32. Asamitsu, S., Obata, S., Yu, Z., Bando, T., Sugiyama, H.: Recent progress of targeted G-quadruplex-preferred ligands toward cancer therapy. Molecules (Basel, Switzerland) **24**, 429 (2019)
33. Sun, D., et al.: Inhibition of human telomerase by a G-quadruplex-interactive compound. J. Med. Chem. **40**, 2113–2116 (1997)
34. Anantha, N.V., Azam, M., Sheardy, R.D.: Porphyrin binding to quadrupled T4G4. Biochemistry **37**, 2709–2714 (1998)
35. Kim, M.Y., Vankayalapati, H., Shin-Ya, K., Wierzba, K., Hurley, L.H.: Telomestatin, a potent telomerase inhibitor that interacts quite specifically with the human telomeric intramolecular g-quadruplex. J. Am. Chem. Soc. **124**, 2098–2099 (2002)
36. Burger, A.M., et al.: The G-quadruplex-interactive molecule BRACO-19 inhibits tumor growth, consistent with telomere targeting and interference with telomerase function. Cancer Res. **65**, 1489–1496 (2005)
37. Rodriguez, R., Müller, S., Yeoman, J.A., Trentesaux, C., Riou, J.F., Balasubramanian, S.: A novel small molecule that alters shelterin integrity and triggers a DNA-damage response at telomeres. J. Am. Chem. Soc. **130**, 15758–15759 (2008)
38. De Cian, A., Delemos, E., Mergny, J.L., Teulade-Fichou, M.P., Monchaud, D.: Highly efficient G-quadruplex recognition by bisquinolinium compounds. J. Am. Chem. Soc. **129**, 1856–1857 (2007)
39. Tera, M., Ishizuka, H., Takagi, M., Suganuma, M., Shin-ya, K., Nagasawa, K.: Macrocyclic hexaoxazoles as sequence- and mode-selective G-quadruplex binders. Angew. Chem. Int. Ed. Engl. **47**, 5557–5560 (2008)
40. Chung, W.J., Heddi, B., Tera, M., Iida, K., Nagasawa, K., Phan, A.T.: Solution structure of an intramolecular (3 + 1) human telomeric G-quadruplex bound to a telomestatin derivative. J. Am. Chem. Soc. **135**, 13495–13501 (2013)
41. Duarte, A.R., Cadoni, E., Ressurreição, A.S., Moreira, R., Paulo, A.: Design of modular G-quadruplex ligands. ChemMedChem **13**, 869–893 (2018)

42. Maia, E.H.B., Assis, L.C., de Oliveira, T.A., da Silva, A.M., Taranto, A.G.: Structure-based virtual screening: from classical to artificial intelligence. Front. Chem. **8**, 343 (2020)
43. Monsen, R.C., Trent, J.O.: G-quadruplex virtual drug screening: a review. Biochimie **152**, 134–148 (2018)

A Service for Flexible Management and Analysis of Heterogeneous Clinical Data

Sandro Hurtado[1,2,3] , José García-Nieto[1,2,3(✉)] ,
and Ismael Navas-Delgado[1,2,3]

[1] Departamento de Lenguajes y Ciencias de la Computación, Universidad de Málaga,
Málaga, Spain
{sandrohr,jnieto}@uma.es
[2] ITIS Software, Arquitecto Francisco Peñalosa 18, 29071 Málaga, Spain
[3] Biomedical Research Institute of Málaga (IBIMA), Málaga, Spain

Abstract. This paper describes FIMED 2.0, a Service for Flexible Management and Analysis of Heterogeneous Clinical Data. This software tool allows flexible clinical data management from multiple trials, which can help to improve the quality of clinical data and ease in clinical trials. The proposed service has been developed on top of a NoSQL Database (MongoDB), which allows for collecting and integrating clinical data in dynamic and incremental schemes based on their needs and clinical research requirements. Building upon our experiences with Flexible Management of Biomedical Data (FIMED), we have developed this new version of the tool aiming not only at replicating the former one but also including further gene regulatory network analysis and data visualization oriented to annotate gene functionality and identify hub genes. This version allows the practitioner to use four different network construction methods such as data assimilation, linear interpolation, tree-based ensemble or Gradient Boosting Machine regression. You may find a free version of this tool on the web at https://khaos.uma.es/fimedV2. A demo user account has been created to provide user demonstration, *"iwbbio"*, using the password *"demo"*. A real-world use case for a clinical assay in Melanoma disease is also included in this demo, which has been indeed anonymized.

Keywords: Clinical research · Clinical trial management systems · NoSQL Database · Gene expression data analysis · Gene regulatory network inference

1 Introduction

Next-generation sequencing (NGS) has improved clinical genetics by allowing researchers to investigate hundreds of genes at once compared to conventional Sanger sequencing [17]. To conduct more in-depth analysis, clinical researchers

integrate these data with other patients' clinical and personal information, such as electronic health records, habits, inheritance, and environmental factors [16]. In this regard, advanced data management and analysis systems in clinical study and personalised medicine have been developed over the last few years. Even with the tremendous advancement in NGS technology and bioinformatics software tools, more improvements are required to deal with complicated and genetically heterogeneous diseases.

There are many software packages already available for clinical data management software and some of them are freely available to clinicians as found in [1–3,6,9,15]. The majority of these clinical data management systems are web-based platforms adapted to the requirements of a particular clinical trial, where clinicians have to design electronic Case Report Forms (eCRF) in any spreadsheet software and upload them through the user interface. Due to the heterogeneity of clinical data and the possibility for changes in different studies, clinicians must continually load forms into the system. In this sense, these systems lack flexibility and extensibility due to the database limitations in terms of development.

In addition, almost none of these systems allow the analysis of patients' clinical data to diagnose clinical diseases, so they are limited in filling the gap among bioinformatics, molecular geneticists and clinicians.

In this paper, we present FIMED 2.0, a software tool for the flexible management and analysis of clinical data. Our motivation for developing FIMED 2.0 stems from our experience with FIMED [7]. Our goal is provide users with new functionalities in order to preform new and more accurate analysis. In this new version, we place our interest in the analysis of Gene regulatory networks (GRNs) inference incorporating new GRNs algorithms for the sake of a principled comparison among GRNs gene network reconstructions. Also, an ensemble of GRNs has been proposed based on a voting system to allow users rank the most important gene interactions (top-k genes/edges) between the similar outputs of a set of GRNs. So, this can indicate the gene pairs that are most important in the regulatory process. Moreover, visualization tools have been added to the tool to provide users with a deep insight into the networks through a better graphic plotting. As a result, the primary goal would be to establish links between genes that are expressed similarly, which would lead to the discovery of novel therapeutic targets or biomarkers for the patient's expected treatment progression.

We demonstrated the advantages of the new functionalities of FIMED 2.0 in a practical use case using real expression data from metastatic Melanoma patients used in previous works [7,14].

The remaining of this article is organized as follows. Section 2 describes the system architecture, detailing the gene expression pre-processing and gene regulatory inference methodology. In Sect. 3, a use case is reported, to illustrate the usability of the proposed service, and finally, in Sect. 4, the key conclusions and future directions of effort.

2   System Architecture

FIMED 2.0 is an extension of FIMED that internally implements a workflow as depicted in Fig. 1, which consists of several phases: data collection, integration, clinical data analysis and data visualization. Thanks to the web interface, the user is guided through this workflow, so internal data mappings and adaptations are automatically conducted. This section summarises the architecture of this tool, making special emphasis on the new elements included in this extension.
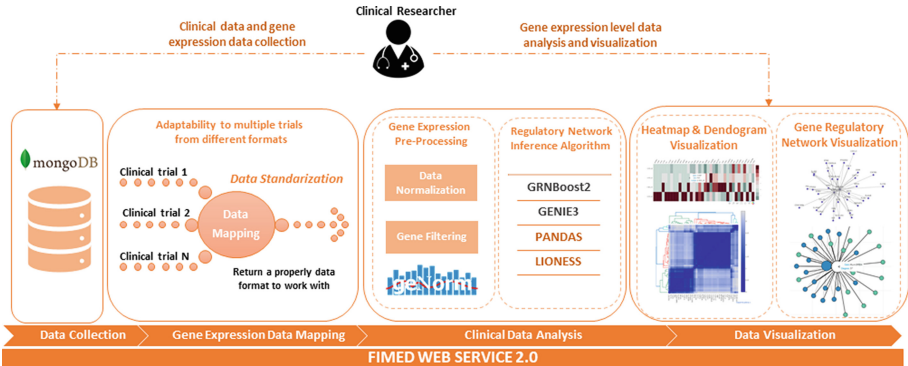
Fig. 1. FIMED 2.0 Workflow is made up of several phases: (I) Data collection, (II) Mapping data which guarantee the adaptability to multiple trials, (III) Clinical Data analysis through several algorithms and (IV) Data Visualization

2.1   Data Collection

The core of the data integration and management is a MongoDB database that provides a flexible way of dealing with clinical information such as gene expression data. The database schema is shown in the JSON Code Snipped 1.1. The database is organised into one collection of users. So, each user is represented as a BSON document. In this schema, the users are the clinicians, and so, each data entry includes the list of patients related to them. This means usually that for each clinician we have the patients participating in a clinical trial. The information associated with each patient is stored together, including general information for statistical studies, as well as any additional files related to the clinical trial (gene expression data, informed consent, blood sample reports).

However, end-users are not expected to directly interact with MongoDB database. Thus, FIMED provided a Web Graphical User Interface for easing the management of the clinical trial information. FIMED 2.0 has extended not only the list of available algorithms but also the visual tools provided to the end-users.

The Web GUI provides a dynamic visualization of the information that can modify the internal database schema depending on the clinical trial needs. Thus, if a user needs to include a new data field in the clinical trial, they only have

to add it in the user interface and this will automatically update the implicit schema of the MongoDB database.

This tool also takes into account the previous experience of clinicians, so the data fields of previous patients is obtained and provided at the time of adding new patients. This automatic process accelerates the data collection process reducing the database maintenance procedures done by technicians to the minimum.

Code Snippet 1.1. Core JSON Schema. It is the initial document structure from which the database adds new items and updates existing ones progressively.

```
{   "_id": <ObjectId()>,
    "Name": <String>,
    "Surname": <String>,
    "Password": <String>,
    "Patients": [{
            "_id": <ObjectId()>,
            "_patientInformation": <Object>,
            "_files": [
            {
                "filename": <String>,
                "metadata": <Object>,
                "gridFS": <Object>
            }],
            "_clinicalSamples": [
            {
                "sample_name": <String>,
                "metadata": <Object>,
                "gridFS": <Object>
            }]
        }],
    "Form": <Object>,
    "Analysis_results": [
        {
            "name_analysis": <String>,
            "results": <String>
        }]
}
```

As far as this tool is managing sensible data, some security elements are included to reduce the risk of adding these data into the service. Patients' information is secured in the whole database. Advanced Encryption Standard (AES) is used to protect the stored data. This encryption algorithm [4] uses a secret key to encrypt and decrypt the data. The 256-bit keys are used to achieve robust data security. This key is automatically generated during the registration process at the server side.

Additionally, the cryptography keys are stored in a MinIO[1] cluster. This cluster has been deployed in an internal network only accessible from the server where the APIs are allocated, taking also advantage of the security layers provided by MinIO. This reduces the risk of cyber-attacks to the database.

2.2   Gene Expression Data Mapping

Gene expression data is loaded into FIMED 2.0 by uploading files with the output provided by the different providers. Once the user indicates that an uploaded file corresponds to gene expression data, this data is parsed and translated to a shared internal representation. Thus, it is possible to uniformly manage and analyse different NGS file formats from various providers such as Nanostring, Affymetrix, etc.

The load of such data in FIMED 2.0 ends with a shared structure storing the gene names, class names and gene expression values. In this way, the components analysing such data will be able to translate them to a gene expression matrix. This means, that for each data file we will have the expression levels for each gene included in the specific panel.

FIMED supports RCC (*Reporter Code Count*) format independently of the Nanostring^{TM} panel used. These files provide Code Class, Gene Name, Accession and Count that are directly translated to the shared format. However, this process is not limited to parsing and translation. The translation process includes specific normalization processes that are aware of the essential lane attributes provided by Nanostring^{TM}. At the end of this step, the system will have homogeneous gene expression data as well as other transformations will be conducted to assure high-quality results.

This process can be extended for further versions of the software, adapting the processes for reading the files and normalizing the data to the documentation provided by the providers.

2.3   Gene Expression Pre-processing

Gene expression data pre-processing is mainly focused on the normalization process. Hence, the main objective is to reduce the possible noise that is produced in the gene sequencing. FIMED 2.0 uses a standard normalization process. This process is essential as any noise in the data used for a given analysis will be translated to the analysis results.

RCC files contain quality control flags as positive and negative control genes. Positive control linearity ensures that the samples have a consistent linear relationship. Background correction is conducted with the use of negative control samples. The process done for RCC files is based on the algorithm *geNorm*[2] [12] provided by Nanostring^{TM}.

---

[1] https://min.io/.
[2] https://genorm.cmgg.be/.

2.4   Gene Regulatory Network Inference Analysis

Gene regulatory network inference is used to construct gene regulatory networks from previously pre-processed gene expression data. GRNs models are used to represent and predict dependencies between molecular entities [11]. These are composed of genes, in which interactions between genes are represented within a graph model focused on transcription factors (TFs).

In this sense, FIMED 2.0 improve the analysis capabilities of FIMED in the context of efficient statistical and machine learning approaches for GRN inference. Originally FIMED integrated two distinguished algorithms (GENIE3 and GRNBoost2) provided in the *arboretum* Python package.[3] However, this version of the tool includes two new gene inference algorithms that will provide the user with a broader comparison of the results in order to improve their analysis capacity. Moreover, FIMED 2.0 provides an ensemble gene regularity inference functionality that enables users examine which algorithms produced similar reconstructions.

GENIE3 is a generic and straightforward algorithm based on feature selection with tree-based ensemble methods. It breaks down the prediction of a regulatory network involving p genes into p separate regression problems. The expression pattern of one of the genes (target gene) is predicted from the expression patterns of all the other genes (input genes) in each regression problem. The importance of an input gene in predicting the expression pattern of a target gene is interpreted as a possible regulatory connection. The network is then recreated by aggregating putative regulatory relationships across all genes to generate a ranking of interactions [8].

GRNBoost2 uses Gradient Boosting Machine regression with early-stopping regularisation to estimate regulatory networks. A tree-based regression model is trained for each gene in the dataset to predict its expression profile using the expression values of a collection of putative transcription factors (TFs). This algorithm is based on the GENIE3 architecture [13].

PANDA (Passing Attributes between Networks for Data Assimilation) is a message-passing model that integrates protein-protein interaction, gene expression, and sequence motif data to reconstruct genome-wide, condition-specific regulatory networks as a model. In this regard, the networks that are generated are more accurate than those constructed using individual data sets. Gene regulatory network generating with PANDA can also capture information about specific biological mechanisms and pathways that other methodologies had ignored [5].

LIONESS is a linear framework to relate a set of networks, each representing a different biological sample. The average of individual component networks

---

reflecting the contributions of each member in the input sample set can be thought of as an "aggregate" network predicted from a collection of N samples [10].

Gene Regulatory Network Ensemble. For further analysis, an ensemble approach has been developed in this proposal as a gene regulatory network inference made from the four prior networks (GENIE3, GRNBoost2, PANDA, LIONESS).

The ensemble approach has been designed since network inference algorithms are naturally noisy, it remains a challenge to identify whether these changes represent real cellular responses or whether they emerged by random coincidence. In this sense, the ensemble internally develops a voting system in order to rank the top-k edges compose by the similar outputs of a set of GRNs, thus users can examine the top-k edges produced by similar reconstructions of the GRN algorithms.

2.5 Gene Regulatory Network Inference Visualization

One of the advantages of FIMED 2.0 is its power related to visualization features thanks to the availability of better graphic plotting, where users can interactively explore the constructed network. Many interactive visualizations allow users to actively move the network and examine the connections between nodes, allowing users to see the network's structure in detail. In this sense, users can choose from different network representation layouts: Circular layout or Force-directed layout, as shown in Fig. 2. It is worth noting that FIMED 2.0 offers a new graph visualisation in which clicking on a given gene will highlight this gene and its related neighbours and the information associated with them (Fig. 2C).

These rich set of visualization tools allow users to observe the most important nodes representing genes and arcs representing interactions between them. By changing the arc form or length, the arcs can express the strength of the interaction. Users can compare different patient samples or patients at the same stage of sickness in this way.

Additionally, as mentioned before, an ensemble powerful visualization tool has been developed combining various GRNs models, where users can examine the top-k edges between gene interactions. Each similar reconstructions are represented in different edges colors. In this way, users can observe edges frequency in different colours to see the most important gene interaction in the ensemble voting system as depicted in Fig. 2D, where grey edge colour represent frequency of 1, blue edge frequency of 2, green edge colour frequency of 3 and red edge colour frequency of 4.

3 Use Cases

With the aim of showing the potential of using the new functionalities of FIMED 2.0, the tool has been tested with real-world scenarios involving patients with
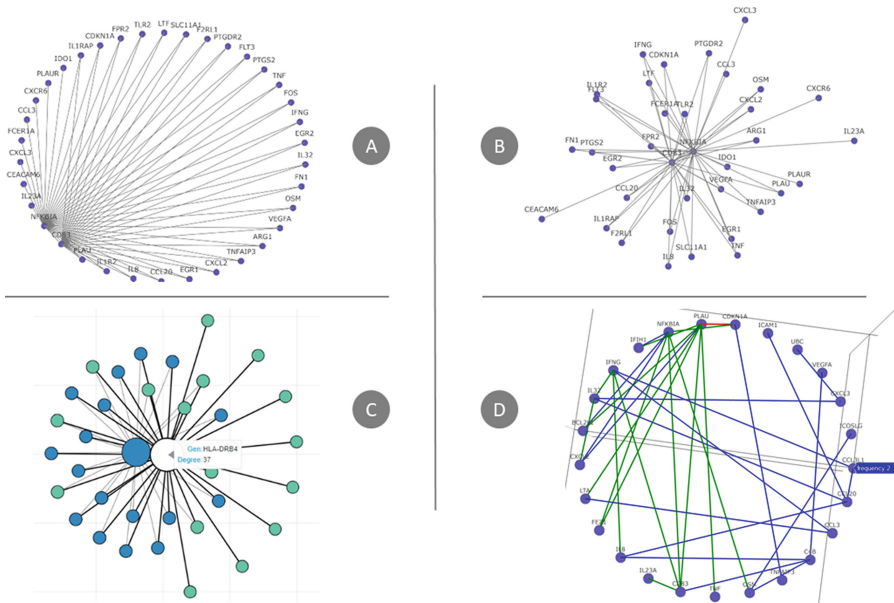
Fig. 2. Gene regulatory network representations with different layouts: Circular layout or Force-directed, and dynamic plotting (Color figure online)

advanced melanoma [14], as in the previous version of FIMED. Thus, we have validated the new analytical functionalities and visualisation techniques producing appropriate analysis and visualisation in cancer research. For this proposal, we have used the FIMED 2.0 online interface to enter the clinical information of two Melanoma patients. In this sense, for this clinical trial, we designed a customised Electronic Case Report Form (eCRF). Then, the clinical information of the patients was entered into the tool. As seen in Code Snippet 1.2, this clinical case comprises six simple fields and one composed field. Thanks to MongoDB's flexibility, the primary database structure can be increased in a customised manner.

In addition, other files providing gene expression assays related to the patient have been loaded in FIMED2.0. As a result, new meta-data fields in the gene expression files have been introduced to offer more information to the samples.

Gene expression data from Melanoma cancer have been taken from a specific panel (Immune Profiling Panel Nanostring^{TM}) in RCC format (under MIT License). These files have been normalised through a housekeeping method. Users can find 12 RCC files with the gene counts stored in FIMED 2.0 (*Help section*: *Supplementary material*). Each file has associated with the experiment date and the patient's code.

FIMED 2.0 has been deployed on our servers to enable users to explore the new functionalities, where users can manage their patient data or test ittest it

using sample data given by the demo user provided.[4] This demo user includes anonymized patient data to allow new users to see an example of how their databases may be built. Users can also establish a new free account in which each user will have an independent workspace to design a particular database schema for their clinical trial.

Code Snippet 1.2. Data Schema in Melanoma use cases

```
{   "Form":
    {
        "_id":<ObjectId()>,
        "Attributes":
        {
            "Patient Code": <Number>,
            "Sex": <String>,
            "Birth Date": <Date>,
            "Treatment response": <String>,
            "Observations": <String>,
            "Diabetes": <Checkbox>,
            "Hospital admission":
            {
                "Hospital name": <String>,
                "Hospital address": <String>
            }
        }
    }
}
```

3.1   Use Case: Gene Regulatory Network

In this section, the new functionalities in FIMED 2.0 are shown from the GRNs point of view. As exposed above, new GRNs algorithms have been added to the tool, as well as new features in the visualization part that improves the ability of users to discover important gene-to-gene interactions and to inspect the topology of the network thanks to the availability of better graphic plotting.

In Fig. 3 can be observed the selection panel of FIMED 2.0 that allow users to perform gene regulatory network analysis and visualizations. Five GRNs visualizations have been performed, corresponding to each of the GRNs algorithms provided in FIMED 2.0. An experiment has been carried out which consist in inferring a set of different networks (GENIE3, GRNBoost2, PANDA, LIONESS) and compare the results of each of the networks. Besides, the ensemble algorithm based in a voting system has been executed in order to provide users an entirely deep insight of the most important gene interactions coming from the similar reconstructions of the GRNs algorithms.

Users will then be able to distinguish the frequency that each interactions between genes are repeated through similar GRNs outputs since each frequency

---

[4] Demo user grants: username *"iwbbio"* and password *"demo"*.

is represented with a different edge colour (frequency 1: grey, frequency 2: blue, frequency 3: green, frequency 4: red). Therefore, the most important gene interactions (highest frequency) are represented with a red edge colour.

Furthermore, only the most variable gene expression levels as a fraction of the total number of genes in the panel can be extracted using a sliding parameter. A statistical cutoff parameter is also supplied to limit the maximum number of linkages in the network, which improves visualisation because it focuses only on the most relevant genes and their interactions. It's worth mentioning that these features might provide clinicians with new information for improving treatment outcomes by allowing users to find genes and gene interactions that could be utilised as diagnostic and prognostic indicators and focused therapy.
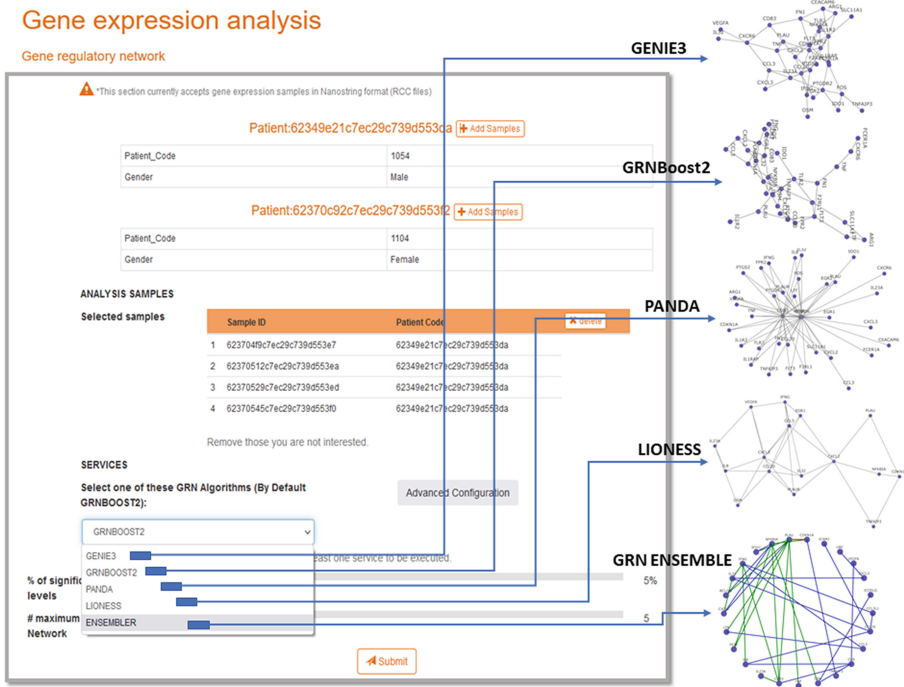
Fig. 3. Selection panel of FIMED 2.0 that allow users to perform gene regulatory network analysis and visualizations from gene expression data

4   Conclusion

In this paper, we present FIMED 2.0, a software tool for flexible clinical data collection, management, analysis and visualization of gene expression data in the practice of clinical assays in different studied diseases. It is released freely available on the web for the community at https://khaos.uma.es/fimedV2/.

The current version improves the previous version of FIMED in terms of Gene Regulatory analysis inference. New distinguished GRNs algorithms (PANDA and LIONESS) have been integrated in the tool that will provide users with better analysis capacities in order to increase their GRNs understanding. Besides, an ensemble has been designed based on a voting system of the similar reconstructions network from a set of four GRNs algorithms (GENIE3, GRNBoost2, PANDA and LIONESS). Moreover, new visualization features have been added guaranteeing users new ways of exploring gene networks to clearly inspect the topology of the network, thanks to the availability of better graphic plotting.

All these new functionalities of the tool have been tested in a use case conducted with real-world gene expression data from Melanoma cancer. These data have been stored in FIMED 2.0 so that users can explore the tool with a demo user *"iwbbio"* and password *"demo"*.

Specific lines of future work include incorporating the compatibility with additional use cases. Thus, integrating adaptability for more gene expression file formats, other clinical studies on different diseases, and other algorithms such as clinical image analysis.

References

1. Brandt, C., et al.: TrialDB: a web-based clinical study data management system. In: AMIA Annual Symposium Proceedings, vol. 2003, p. 794. American Medical Informatics Association (2003)
2. Cavelaars, M., et al.: OpenClinica. J. Clin. Bioinform. **5**, S2 (2015)
3. Cramon, P., et al.: Development and implementation of PROgmatic: a clinical trial management system for pragmatic multi-centre trials, optimised for electronic data capture and patient-reported outcomes. Clin. Trials **11**(3), 344–354 (2014)
4. Daemen, J., Rijmen, V.: The Design of Rijndael: AES-the Advanced Encryption Standard. Springer, Heidelberg (2013). https://doi.org/10.1007/978-3-662-04722-4
5. Glass, K., Huttenhower, C., Quackenbush, J., Yuan, G.C.: Passing messages between biological networks to refine predicted interactions. PLoS ONE **8**(5), e64832 (2013)
6. Harris, P.A., Taylor, R., Thielke, R., Payne, J., Gonzalez, N., Conde, J.G.: Research electronic data capture (REDCap)-a metadata-driven methodology and workflow process for providing translational research informatics support. J. Biomed. Inform. **42**(2), 377–381 (2009)
7. Hurtado, S., García-Nieto, J., Navas-Delgado, I., Aldana-Montes, J.F.: FIMED: flexible management of biomedical data. Comput. Methods Programs Biomed. **212**, 106496 (2021)
8. Huynh-Thu, V.A., Irrthum, A., Wehenkel, L., Geurts, P.: Inferring regulatory networks from expression data using tree-based methods. PLoS ONE **5**(9), e12776 (2010)

9. Krenn, R.: Design and development of a web-based clinical trial management system (2014)
10. Kuijjer, M.L., Tung, M.G., Yuan, G., Quackenbush, J., Glass, K.: Estimating sample-specific regulatory networks. iScience **14**, 226–240 (2019)
11. McCall, M.N.: Estimation of gene regulatory networks. PostDoc J. J. Postdoc. Res. Postdoc. Affairs **1**(1), 60 (2013)
12. Mestdagh, P., et al.: A novel and universal method for microRNA RT-QPCR data normalization. Genome Biol. **10**(6), R64 (2009)
13. Moerman, T., et al.: GRNBoost2 and Arboreto: efficient and scalable inference of gene regulatory networks. Bioinformatics **35**(12), 2159–2161 (2018)
14. Navas-Delgado, I., et al.: VIGLA-M: visual gene expression data analytics. BMC Bioinform. **20**(4), 150 (2019)
15. Nguyen, L., et al.: Dados-prospective: an open source application for web-based prospective data collection. Source Code Biol. Med. **1**(1), 7 (2006). https://doi.org/10.1186/1751-0473-1-7
16. Ou, M., et al.: Database.bio: a web application for interpreting human variations. Bioinformatics **31**(24), 4035–4037 (2015)
17. Pereira, R., Oliveira, J., Sousa, M.: Bioinformatics and computational tools for next-generation sequencing analysis in clinical genetics. J. Clin. Med. **9**(1), 132 (2020). https://doi.org/10.3390/jcm9010132, https://www.mdpi.com/2077-0383/9/1/132

Biosensors and Data Acquisition

Reconfigurable Arduino Shield for Biosignal Acquisition

Leozítor Floro de Souza, Fábio Iaione[(✉)] [ORCID], and Shih Ting Ju

Faculty of Computing-Federal University of Mato Grosso do Sul,
Campo Grande, MS 79070-900, Brazil
`iaione@facom.ufms.br`
`http://www.facom.ufms.br`

Abstract. There are several situations where it is necessary to acquire analog signals, like sensors outputs and bioelectrical signals, with different amplitudes and frequency ranges. The FPAA (Field Programmable Analog Array) is a semiconductor device that allows the creation of several analog circuits. The Arduino is a platform for rapid development with microcontrollers, well known and widely used to build experimental and commercial equipment. Given the above, the objective of this work was to create a hardware board (shield) and a software library to use an FPAA in conjunction with Arduino boards. In one test, we implemented a band-pass filter and obtained between the projected and measured frequency response an average error of 0.027 dB (SD = 0.163 dB). The maximum error was 0.265 dB. In another test, we implemented a circuit to capture the ECG signal. The results of the ECG test were satisfactory. This research introduces a significant contribution to bioelectrical signal acquisition since similar works do not exist.

Keywords: Biosignal acquisition · Reconfigurable analog circuit · Arduino shield

1 Introduction

Many types of equipment register analog signals, such as ECG (electrocardiogram), EEG (electroencephalogram), voice, and sensors. Then, analyze them and deliver useful information. The common approach today is to use a specific device for each case. Using an FPAA (Field Programmable Analog Array), it is possible to create reconfigurable analog circuits to capture different analog signals used in different applications [15]. The Arduino [6,21] is a well-known low cost platform for fast development with microcontrollers. This platform is widely used to build different experimental and commercial equipment, applied in the problem's solution in several areas of knowledge [7,9,11,13,14,16,19,22,24]. The work [10] showed a great increase in the number of articles with the terms "Arduino" and "Raspberry Pi" between 2010 and 2016 in databases of scientific papers.

We performed a search for scientific articles in dozens of databases, such as ACM Digital Library, IEEE Xplore, SciELO, ScienceDirect, and others. We used the search string: Arduino AND (biosignal OR bioelectrical OR ECG OR Electroencephalogram OR EEG OR Electroencephalogram OR EMG OR Electromyogram OR EOG OR Electrooculogram OR ERG OR Electroretinogram OR EGG Electrogastrogram), applied to the title. Five articles were found in English, which are analyzed below.

Work [23] developed a system for the acquisition of 12 ECG leads. The built-in analog circuit has eight acquisition channels connected to eight analog inputs of an Arduino Leonardo board. Four ECG leads are reconstructed by software. Each of the eight channels consists of an instrumentation amplifier, high-pass filter, low-pass filter, band-reject filter, and offset circuit. The authors built all electronic circuits, except the instrumentation amplifier, with operational amplifiers, resistors, and capacitors. ECG signals are visualized and stored in a personal computer through software developed in Labview, which also performs digital signal filtering. Work [17] developed a system for acquiring an ECG lead. The built-in analog circuit includes an instrumentation amplifier, high-pass filter, low-pass filter, notch filter, and voltage shifter circuit. The authors built all electronic circuits, except the instrumentation amplifier, with operational amplifiers, resistors, and capacitors. The ECG signal, digitized by an ATMega328P microcontroller, is stored in an SD card and viewed on a personal computer through a developed application. Work [20] developed a system for acquiring 16 EEG leads. Each acquisition channel consists of an instrumentation amplifier, notch filter, high-pass filter, and low-pass filter. The authors built all circuits using operational amplifiers, resistors, and capacitors. The ECG signal is digitized by an Arduino Mega 1280 board and processed in a personal computer using the EEGAnalyzer application. The three works cited do not inform if the printed circuit board was built and the cost of the prototypes.

Work [12] used the E-Health Sensor Platform v2.0. This platform is an Arduino shield, compatible with the Uno model. It is capable of capturing the ECG and EMG through three electrodes, in addition to other non-electrical physiological parameters. Currently, the E-Health Medical Development Platform replaced the E-Health Sensor Platform v2.0, the complete model has a cost of USD1,795.00. Work [18] used an Arduino DUE to digitally filter a simulated ECG signal without using a circuit to acquire bioelectrical signals.

Considering that we did not find a similar scientific study, this work aims to create an electronic circuit (Arduino shield) and a software library to use an FPAA in conjunction with Arduino boards. The Arduino shield will allow the implemented signal acquisition circuit to be reconfigurable and applied to solve different problems, such as the acquisition of bioelectrical signals. Researchers who need to acquire bioelectrical signals can use the shield. A consequence of the shield usage is the reduction of financial expenses with the purchase of signals acquisition equipment. Also, the industrial sector can use it to develop electromedical equipment.

1.1 Summary of Contributions

The main contributions of this work are:

– Arduino shield (hardware board) containing an FPAA;
– Software library for the Arduino platform containing functions to use the "shield";
– Shield and library test results, including ECG signal acquisition.

2 Materials and Methods

Figure 1 shows the block diagram of the developed system. The shield contains an FPAA (AN221E04), a micro SD card socket, an LED, resistors, capacitors, and connectors. We implement the analog circuits using the AnadigmDesigner2 application [3] on a computer, and the configuration files generated by the software are stored on a micro SD card. The Arduino® initializes the FPAA, reads the configuration data from the micro SD card through the SPI bus, and sends it to the FPAA also through SPI. Once configured, the FPAA receives the input signal that passes through the implemented analog circuit and is read by the Arduino's® analog inputs.

Fig. 1. System block diagram.
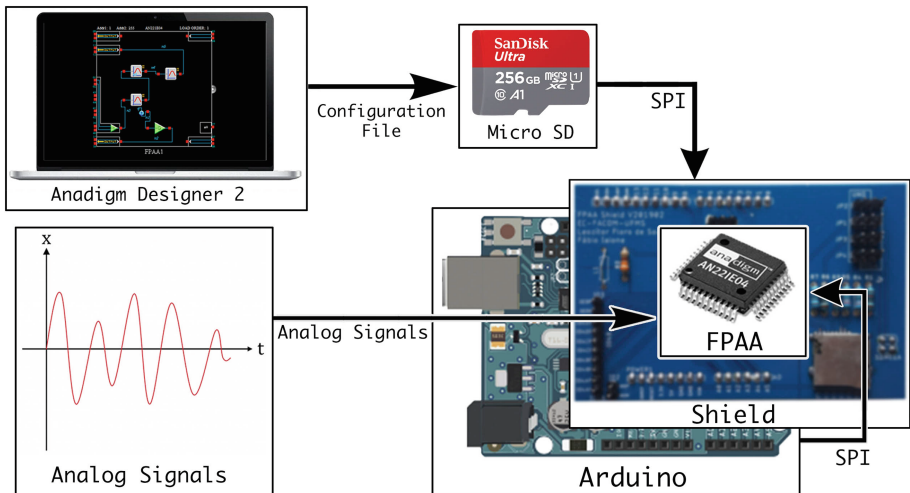
Field Programmable Analog Arrays (FPAAs) are semiconductor devices that have several configurable analog circuits internally (capacitor switching filters, multiplexers, operational amplifiers, and others). The FPAA used in this work [1,2] has the following elements internally: four configurable analog blocks (CAB), six configurable I/O cells (two specifics for output), 256 bytes

LUT (Look-up-table), voltage references, crystal oscillator circuit (external crystal) and configurable frequency dividers, configuration interface, configuration SRAM memory (stores the current FPAA configuration), shadow SRAM memory (stores the new FPAA configuration), and analog switches (connect any CAB to any I/O cell). Each CAB has the following analog devices internally: two operational amplifiers, one voltage comparator, and eight capacitors, in addition to analog switches that interconnect these devices. The two SRAM memories allow reconfiguration on the fly, in which a new configuration is sent to the FPAA while the current one is in operation, and the configuration change occurs without the need for the FPAA restart. If the configuration process is successful, the FPAA turns on a LED in the shield.

The FPAA requires two clock signals, one for the digital communication interface (DCLK) and another for analog circuits (ACLK). The two clocks have a maximum value of 40 MHz. Arduino generates the DCLK clock by software (SPI bit-banging). The ACLK frequency, in conjunction with internal frequency dividers, defines the cutoff frequency limits of the filters implemented in the FPAA (filters with switched capacitors). As the FPAA internal frequency dividers have a limited range, it is necessary to use a configurable ACLK signal. Thus, there is great flexibility in the cutoff frequency of the filters in the FPAA. Therefore, we decided to generate the ACLK signal through Arduino. Arduino Uno and Arduino Mega are two widely used boards, mainly due to their low cost, so we selected these two models.

The clock generated by Arduino® using the function *tone (pin, frequency)*, already existing in one of its libraries, generates a square wave (*duty cycle of 50%*) with a maximum frequency 65535 Hz. Due to the microcontrollers on the Arduino Uno and Mega boards having 16 MHz crystal oscillators, we realized the possibility of generating an ACLK signal greater 65535 Hz. As these two Arduino models have different microcontrollers, the solution for each is slightly different, such as the use of timers, output pins of the generated clock signal, and connection to the micro SD card.

2.1   Arduino Timers

The microcontrollers [4, 5] from Arduino Boards used has 8-bit and 16-bit timers, working similarly but changing the maximum count value, 255 and 65535, respectively. Timers can work in different modes, with CTC mode (*Clear Timer on Compare Match*) being the most suitable for generating a clock signal. In this mode, the counter (TCNTn) increases until it reaches the OCRnA value, then it is reset, and inversion occurs in the logic level of a determined pin (OCnA). Thus, the frequency of the output square wave depends on the value stored in the OCRnA. Figure 2 shows the TCNTn increasing until reaching the OCRnA value and TCNTn set to zero, generating the inversion of the logical level in OCnA and the desired output.

Therefore, the maximum frequency that can be generated, considering the clock frequency of the microcontrollers (fClock = 16 MHz), is 8 MHz, as defined by the Eq. 1.
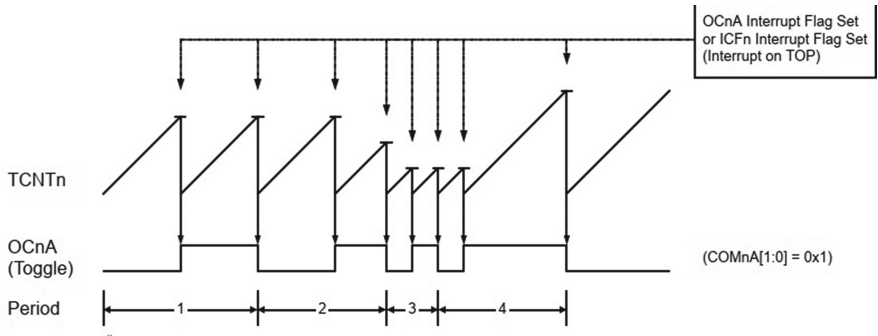
Fig. 2. Timing diagram. Source [5].

$$fOC1A = \frac{fClock}{2 \times N \times (1 + OCR1A)} \tag{1}$$

N is the clock division factor (*prescaler*) that reduces the frequency of the oscillator by different values: 1 (without reduction), 8, 64, 256, and 1024.

It was possible to solve the maximum clock limitation of the function *tone (pin, frequency)* by directly manipulating the timers. However, due to the differences between the microcontrollers of the two Arduino boards, it was necessary to use different timers so that the same pin on both boards outputs the clock signal.

2.2 Clock Selection Function

We created the function *setClock (frequency)* in the FPAA library for the configuration of the ACLK signal, allowing up to 8 MHz clocks on pin 3 of the Arduino. Therefore, for the definition of the desired frequency (which must be a multiple of 2) using the function *setClock (frequency)*, a table of *defines* was created to be used as an argument of the function, allowing 16 different frequencies, from 1.95 kHz to 8 MHz. Each table item has an integer value assigned to it. This value is used in the OCRnA register to define the maximum count value and generate the desired clock. Due to a difference in configuration between the Mega and Uno boards and the timer used, the user must also configure "*#define MEGA*" or "*#define UNO*" in the FPAA.h file to select the board used.

2.3 Library for Arduino

The library that we created to use the shield in Arduino has four main functions. Below we describe these functions.

a) FPAA.begin ("*.ahf file*"): initializes the SPI bus, the SD card, and the FPAA, sending the configuration data from the file contained in the file .ahf to the FPAA, and returning a boolean value (true = success, false = failure);

b) FPAA.setClock (freq): sets the frequency of the FPAA ACKL clock generated by Arduino and allows the following values: F8M (8 MHz), F4M, F2_666M, F2M, F1_6M, F1_333M, F1M, F500K (500 kHz), F250K, F125K, F62_5K, F31_250K, F15_625K, F7_8125K, F3_90625K and F1_953125K;

c) FPAA.update ("·.ahf file"): sends reconfiguration data to the FPAA without the need for restart (on-the-fly), allowing automatic configuration oriented through states that use different configuration settings;

d) FPAA.read (pinA, pinB, VREF): returns the difference between the analog voltages applied to pins A and B, considering the reference voltage of the Arduino ADC in Volts (VREF). pinA and pinB can assume the values: FPAA.O1P (Arduino A0 pin), FPAA.O1N (A1), FPAA.O2P (A2), FPAA.O2N (A3), FPAA.IO1P (A4), and FPAA.IO1N (A5). This function returns the difference of the voltages because the FPAA has differential outputs.

2.4   Printed Circuit Board

The printed circuit board, shown in Fig. 3, was designed using the AutoDesk Eagle—PCB Design Software, considering all good practices on PCI design and the recommendations of the FPAA manufacturer, such as the separation of digital and analog GNDs, interconnected by a ferrite "bead" minimizing the incidence on the analog part of the EMI generated by digital section.
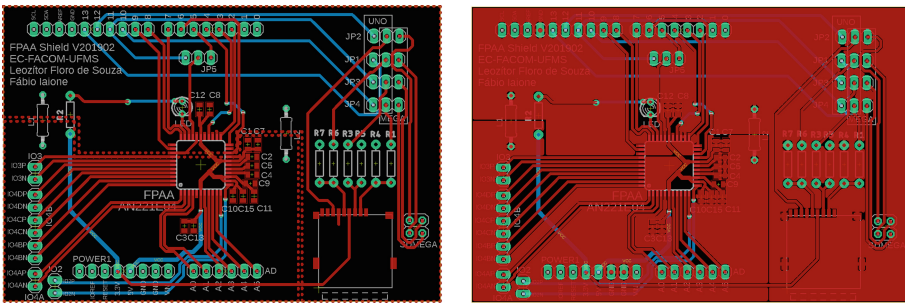
Fig. 3. Dual-layer PCB layout developed using Eagle software. Layout without ground planes (left) and complete layout (right).

Figure 4 shows a photo of the Printed Circuit Board of the shield, attached to an Arduino® Uno, manufactured in FR-4 (Flame Retardant 4) of 1.53 mm with layers 0.035 mm copper, with all components assembled.

3   Results

We performed three tests to verify the functioning of the shield and library. One checks the correctness of the clock generated to the FPAA (ACLK). Another
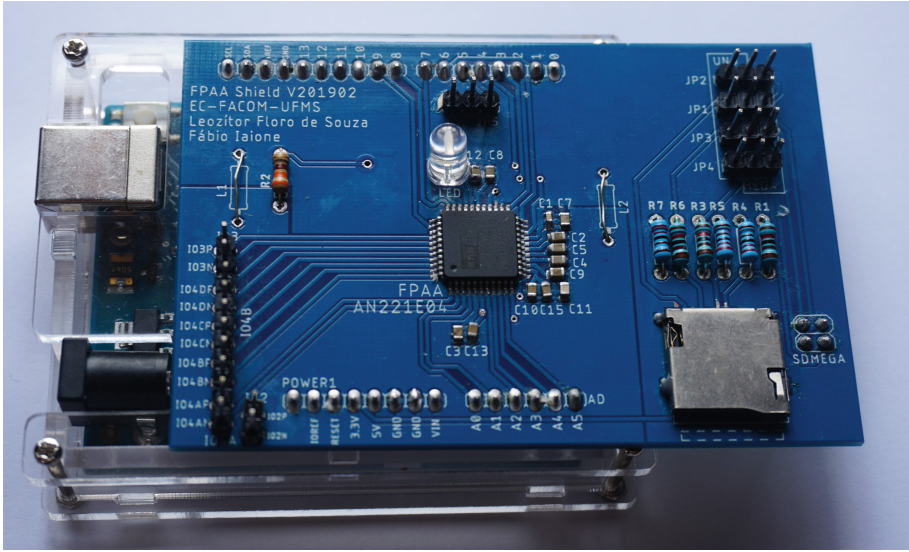
Fig. 4. FPAA Shield attached to an Arduino Uno.

builds an arbitrary filter in the FPAA, and the last implements a circuit to acquire the ECG signal.

3.1 Clock Test

We used a digital oscilloscope Tektronix TDS-1001C-EDU for analyzing the clock generated by the function *setClock()* in Arduino®. We made three measurements and calculated the maximum percentage error for each of sixteen frequencies. Then, we calculated the average and standard deviation of the sixteen maximum percentage errors. Table 1 shows the results of the tests performed.

3.2 Filter Implementation Test

We used a band-pass filter for test filter implementation in the FPAA, which we designed in the AnadigmFilter tool available in the AnadigmDesigner2 application. This filter was arbitrarily designed with the following characteristics: passband ripple = 3 dB, passband gain = 0 dB, stopband attenuation = −30 dB, center frequency = 100 Hz, pass bandwidth = 100 Hz, stop bandwidth = 500 Hz, and with Butterworth approximation, resulting in the block diagram shown in Fig. 5. The FPAA ACLK clock, generated by Arduino, was set to 8 MHz.

The FPAA configuration file (.ahf), generated by the AnadigmDesigner2 application on a desktop computer (AMD, RYZEN 7 1800 3.0 GHz, 16 GB, WINDOWS 10), was recorded on the micro SD card (32 GB), which we inserted later into the shield. The filter circuit consumed the following internal FPAA resources: three I/O cells, seven op-amps, 28 capacitors, one DC voltage source.

Table 1. Maximum Error (ME) obtained for each frequency of the clock signal (ACLK) generated by Arduino. We made three measurements (M1, M2, and M3). The average maximum percentage error was −0.45%, and the standard deviation was 0.16%.

F (Hz)	M1 (Hz)	M2 (Hz)	M3 (Hz)	ME (Hz)	ME(%)
1953.125	1938	1942	1942	−15.1	−0.8
3906.25	3876	3873	3870	−36.3	−0.9
7812.5	7785	7777	7776	−36.5	−0.5
15625	15570	15570	15580	−55	−0.4
31250	31130	31130	31130	−120	−0.4
62500	62250	62260	62260	−250	−0.4
125000	124500	124500	124500	−500	−0.4
250000	249100	249100	249100	−900	−0.4
500000	498100	498100	498100	−1900	−0.4
1000000	996200	996200	996100	−3900	−0.4
1333000	1328000	1328000	1328000	−5000	−0.4
1600000	1594000	1594000	1594000	−6000	−0.4
2000000	1993000	1992000	1992000	−8000	−0.4
2666000	2657000	2657000	2658000	−9000	−0.3
4000000	3980000	3984000	3986000	−20000	−0.5
8000000	7974000	7968000	7968000	−32000	−0.4

The resulting configuration file (.ahf) had 1124 bytes. The following internal resources remained: three I/O cells, one op-amp, four capacitors, four comparators, one counter, one LUT (Luck Up Table), and four SARs (Successive Approximation Registers). We tested the filter implemented in the FPAA using the myDAQ data acquisition system (National Instruments) in conjunction with the BodeAnalyzer application. We connected myDAQ to the FPAA to assess the frequency response. We connected myDAQ output (signal injection) to FPAA input and myDAQ input (signal measurement) to the FPAA output. The graph in Fig. 6 shows the overlapping projected and measured frequency responses, resulting in an average error of 0.027 dB (SD = 0.163) and a maximum error of 0.265 dB.

3.3 ECG Acquisition Circuit Test

We tested a few different configurations in the FPAA to implement the ECG signal acquisition circuit. Figure 7 shows the one that produced the best result.
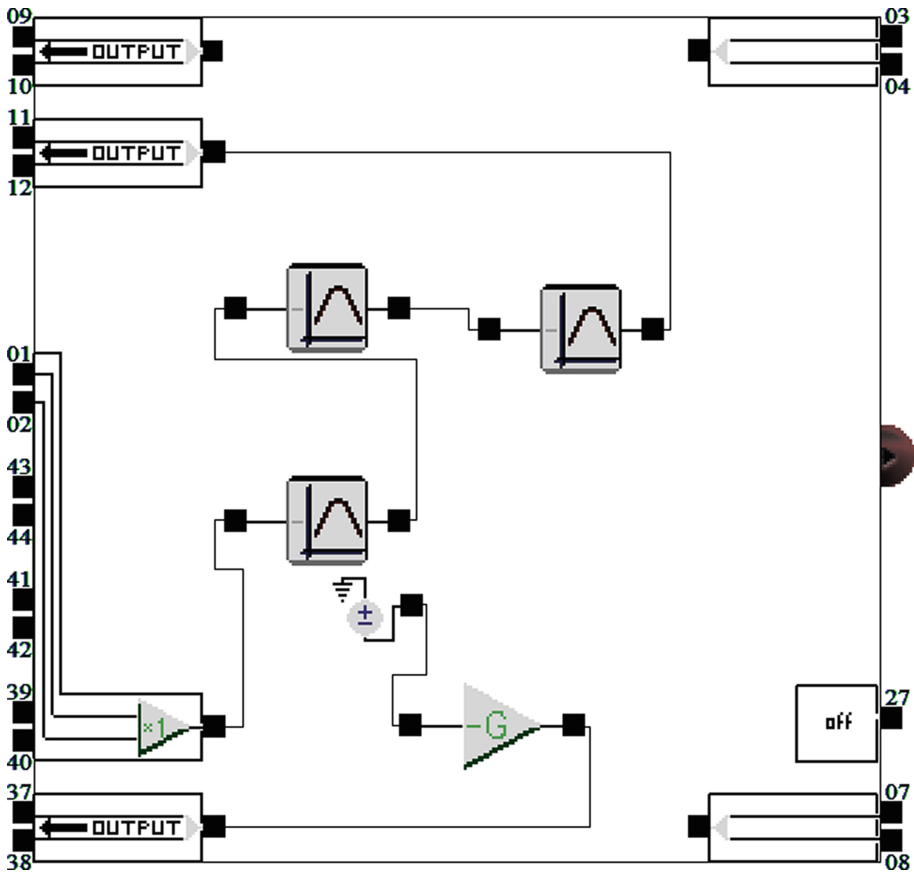
Fig. 5. Block diagram of the circuit generated by the AnadigmFilter tool in the Anadig-mDesigner2 application to implement the desired band-pass filter.

This circuit configuration uses the following I/O cells:

a- I/O cell: input differential mode, low offset chopper amplifier (gain = 128), low pass filter (Fc = 76 kHz). We connected the two electrodes that capture the ECG signal to this cell. We use the highest possible gain (128) and the lowest possible corner frequency (Fc = 76 kHz). The low pass filter eliminates radio frequency interference.

b- Output cell: low pass filter (Fc = 76 kHz). We connected the positive output (03 pin) to Arduino's A0 analog input. And the negative output (04 pin) to A1 analog input. The lowest possible corner frequency (Fc) was used (76 kHz).

c- I/O cell: output differential mode. We connected the third electrode to one of the pins of this cell. This electrode works as a reference, keeping the common-mode voltage at the amplifier inputs (a) with approximately 2 V (referenced to GND).
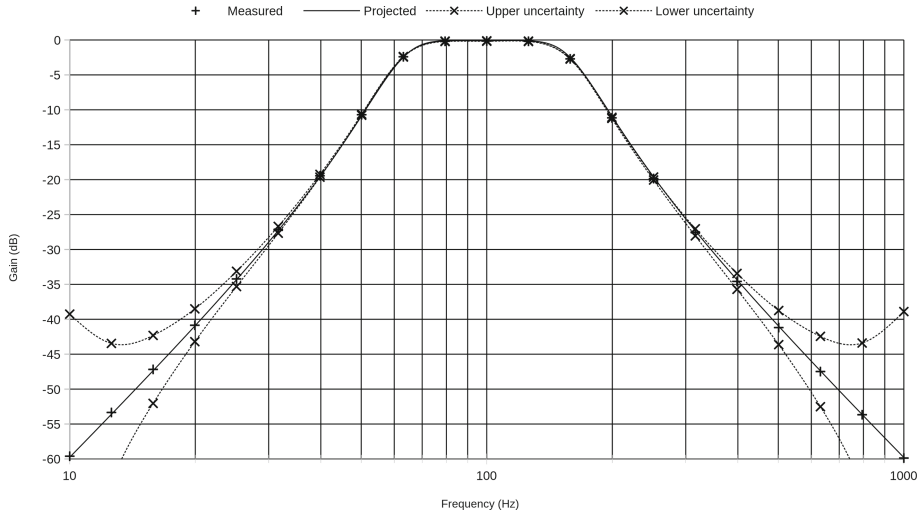
Fig. 6. The graph shows projected and measured frequency responses, and the lower and upper limits, considering the measurement uncertainty of the used device. The average error was 0.027 dB (SD = 0.163 dB) and the maximum error was 0.265 dB.

We used the following analog modules, in addition to the I/O cells.

d- Inverter amplifier: gain = 4. We used this amplifier to increase the gain applied to the input signal.

e- Bilinear filter: high pass (Fc = 0.504 Hz). This filter eliminates the DC and low-frequency components from the signal. We use an Fc that respects ANSI/AAMI [8].

f- Biquadratic filter: low pass (Fc = 40 Hz, gain = 6). This filter works as an anti-aliasing filter and limits the signal band according to ANSI/AAMI [8].

g- Voltage source: voltage = +3 V. Internally, the FPAA works only in differential mode, using a voltage of 2 V as reference (referenced to GND). Therefore, connected to an output cell (differential), this +3 V voltage source corresponds to 3.5 V on the positive pin and 0.5 V on the negative pin, both relative to GND (3.5 V − 0.5 V = +3 V).

h- Inverter amplifier: gain = 0.01. This amplifier transforms the source voltage from +3 V to −0.03 V. Thus, the voltages present on pins 11 and 12 (differential output) of the FPAA will be 1.985 V, and 2.015 V (1.985 V − 2.015 V = −0.03 V). Therefore, either pin 11 or pin 12 can be the reference electrode, keeping the body at approximately 2V (referenced to GND).
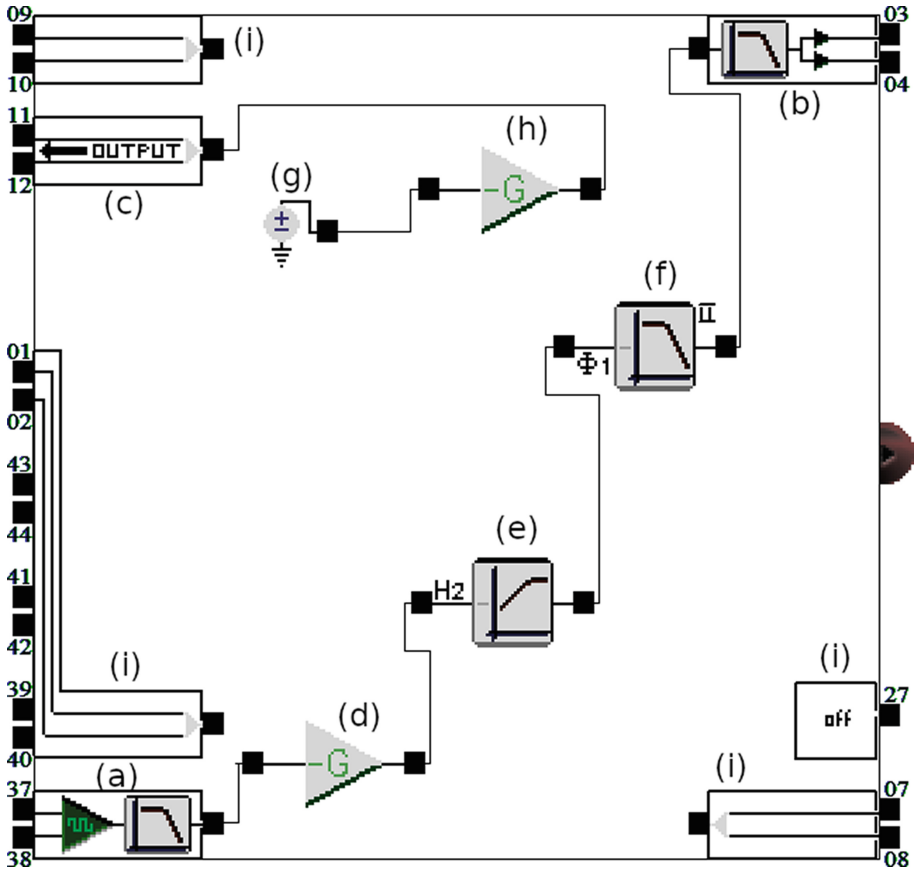
Fig. 7. Circuit's block diagram for ECG signal acquisition. The blocks marked with (i) appear by default and are not used. The ACLK utilized was 125 kHz.

We built the firmware in Fig. 8 to test the ECG recording and used the free Better Serial Plotter V0.1.0 app to display the signal on a netbook (Intel(R) Atom(TM) @ 1, 44 GHz, 4 GB RAM, 32GB SSD, Windows 10 Home). We do not use the FPAA.read() function because the ECG has very fast amplitude variations. Arduino has only one ADC with multiplexed inputs. Thus FPAA.read() reads the two analog inputs (differential input) at slightly different times. This characteristic is suitable only for DC or slow variations signals.

Figure 9 shows the ECG signal recorded in a healthy person. We always used the notebook disconnected from the power grid while recording ECG.

```
#include "FPAA.h"
#include "TimerOne.h"

void setup(){
Serial.begin(57600);
while (!Serial);
if(FPAA.begin("ECG3.ahf")) Serial.println("FPAA_configuration_OK");
  else Serial.println("FPAA_configuration_Error");
FPAA.setClock(F125K);
Timer1.initialize(1000); // Ts=1ms -> Fs=1000 samples/s
Timer1.attachInterrupt(Timer1_ISR);
}

void Timer1_ISR(){
  int ECG_sample = analogRead(A0);
  Serial.println(ECG_sample>>2);
}

void loop(){
while(1);
}
```

Fig. 8. Firmware designed for Arduino. The 2 bits right-shift transforms a 10-bit digitized value (ECG_sample) into an 8-bit value. Thus, each sample becomes a 0 to 255 value.
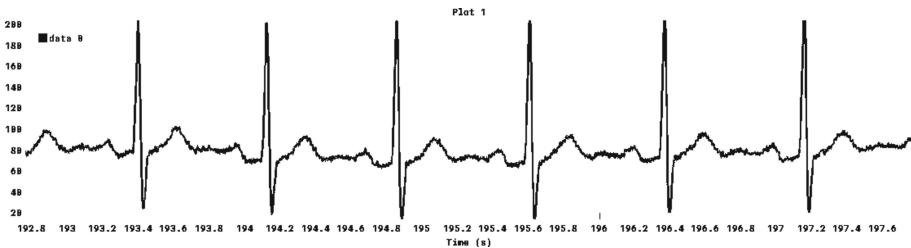
Fig. 9. Application image showing the ECG signal recorded on the netbook (lead DII).

4   Conclusion

This work described the creation of a shield for Arduino containing an FPAA, which allows the implementation of the most different analog circuits using an application on a desktop computer. This flexibility enables implementing amplifiers, filters, linearizers, rectifiers, and other electronic circuits. Gains, cutoff frequencies, and other characteristics are configurable in the computer application. The software library created for the Arduino platform allows easy configuration and shield usage.

The clock generation tests showed an average maximum percentage error to the frequency of -0.45%, with a standard deviation of 0.16% and a maximum of -0.9%.

The filter implementation test showed an average error of 0.027 dB, a standard deviation of 0.163 dB, and a maximum error of 0.265 dB, between the projected and measured frequency response.

The errors obtained in these two tests are relatively small. We attributed them to the measurement uncertainties of the meters (oscilloscope and myDAQ) and intrinsic errors of Arduino and FPAA.

The test of the ECG signal acquisition circuit showed promising results. The recorded signal had little noise, a surprising result since we used unshielded 1.3 m cables to connect the three electrodes to the shield.

A limitation of the shield is its current consumption (average of 50 mA), which added to Arduino consumption (average of 75 mA–Mega 2560) difficult to use in applications powered by small batteries (e.g., 9V PP3 size). However, most applications can use power supplied by the USB port of a notebook or netbook.

We will develop the configurations for acquiring different bioelectrical signals such as EMG and EEG, for example, in future works. And also a website for disseminating information and details about the shield.

This work contributed to the biomedical engineering area and the embedded system area. We did not find similar work.

References

1. AN121E04, AN221E04 field programmable analog arrays - user manual. Technical Report, UM021200-U007g. Anadigm, Inc. (2003). https://www.anadigm.com/_doc/UM021200-U007.pdf
2. AN221E04 dynamically reconfigurable FPAA with enhanced i/o. Technical Report, DS030100-U006c. Anadigm, Inc. (2003). http://www.anadigm.com/_doc/DS030100-U006.pdf
3. AnadigmDesigner 2 user manual. Technical Report, UM020800-U001o. Anadigm, Inc. (2004). https://www.anadigm.com/_doc/UM020800-U001.pdf
4. ATmega640/V-1280/V-1281/V-2560/V-2561/V - 8-bit Atmel microcontroller with 16/32/64KB in-system programmable flash. Technical Report, 2549Q-AVR-02/2014. Atmel Corporation (2014). https://ww1.microchip.com/downloads/en/devicedoc/atmel-2549-8-bit-avr-microcontroller-atmega640-1280-1281-2560-2561_datasheet.pdf, rev.2549Q
5. ATmega48A/PA/88A/PA/168A/PA/328/P - megaAVR data sheet. Technical Report, DS40002061A. Microchip Technology Inc. (2018). http://ww1.microchip.com/downloads/en/DeviceDoc/ATmega48A-PA-88A-PA-168A-PA-328-P-DS-DS40002061A.pdf, rev. A
6. Arduino - home, June 2021. https://www.arduino.cc
7. Ain, K., Wibowo, R., Soelistiono, S., Muniroh, L., Ariwanto, B.: Design and development of a low-cost Arduino-based electrical bioimpedance spectrometer. J. Med. Signals Sens. **10**(2), 125–133 (2020). https://doi.org/10.4103/jmss.JMSS_24_19,http://www.jmssjournal.net/article.asp?issn=2228-7477;year=2020;volume=10;issue=2;spage=125;epage=133;aulast=Ain;t=6

8. American National Standards Institute/Association for the Advancement of Medical Instrumentation - ANSI/AAMI, United States: EC13:2002 - Cardiac monitors, heart rate meters, and alarms (2002)

9. Chen, C.L., Chen, T.R., Chiu, S.H., Urban, P.L.: Dual robotic arm "production line" mass spectrometry assay guided by multiple Arduino-type microcontrollers. Sens. Actuators B Chem. **239**, 608–616 (2017)

10. Cressey, D.: Age of the Arduino. Nature **544**(7648), 125–126 (2017)

11. Călinoiu, D., Ionel, R., Lascu, M., Cioablă, A.: Arduino and labVIEW in educational remote monitoring applications. In: 2014 IEEE Frontiers in Education Conference (FIE) Proceedings, pp. 1–5 (2014)

12. Dioren Rumpa, L., Suluh, S., Hendrika Ramopoly, I., Jefriyanto, W.: Development of ECG sensor using Arduino Uno and e-health sensor platform: mood detection from heartbeat. In: Journal of Physics. Conference Series, vol. 1528, no. 1, p. 12043 (2020)

13. Jahns, M., et al.: An arduino based mössbauer spectrometer. Nucl. Instrum. Methods Phys. Res. A: Accel. Spectrom. Detect. Assoc. Equip. **940**, 116–118 (2019). https://doi.org/10.1016/j.nima.2019.06.003, http://www.sciencedirect.com/science/article/pii/S0168900219308204

14. Jumaat, S.A., Othman, M.H.: Solar energy measurement using Arduino. In: MATEC Web of Conferences, vol. 150, p. 01007 (2018). https://doi.org/10.1051/matecconf/201815001007

15. Kay, M.S., Iaione, F.: Reconfigurable embedded system for ECG signal acquisition. In: Proceedings of the 2015 IEEE 28th International Symposium on Computer-Based Medical Systems, CBMS 2015, pp. 25–26. IEEE Computer Society, USA (2015). https://doi.org/10.1109/CBMS.2015.58

16. Mahajan, R., Bansal, D.: Real time EEG based cognitive brain computer interface for control applications via Arduino interfacing. Procedia Comput. Sci. **115**, 812–820 (2017). https://doi.org/10.1016/j.procs.2017.09.158, http://www.sciencedirect.com/science/article/pii/S1877050917319919. 7th International Conference on Advances in Computing & Communications, ICACC-2017, 22–24 August 2017, Cochin, India

17. Wijaya, N.H., Rahmat, J., Wibowo, S.A.: Modification of Holter ECG monitoring based on Arduino Uno with data storage. Int. J. Recent Technol. Eng. **8**(4), 2819–2824 (2019)

18. Rahmatillah, A.: Ataulkarim: IIR digital filter design for powerline noise cancellation of ECG signal using Arduino platform. In: Journal of Physics. Conference Series, vol. 853, no. 1, p. 12009 (2017)

19. Rosa, T.R., Betim, F.S., de Queiroz Ferreira, R.: Development and application of a labmade apparatus using open-source "Arduino" hardware for the electrochemical pretreatment of boron-doped diamond electrodes. Electrochimica Acta **231**, 185–189 (2017)

20. Saptono, D., Wahyudi, B., Irawan, B.: Design of EEG signal acquisition system using Arduino MEGA1280 and EEGAnalyzer. In: MATEC Web of Conferences, vol. 75, p. 4003 (2016)

21. Severance, C.: Massimo Banzi: building Arduino. Computer **47**(01), 11–12 (2014). https://doi.org/10.1109/MC.2014.19

22. Sheinin, A., Lavi, A., Michaelevski, I.: StimDuino: an Arduino-based electrophysiological stimulus isolator. J. Neurosci. Meth. **243**, 8–17 (2015). https://doi.org/10.1016/j.jneumeth.2015.01.016, http://www.sciencedirect.com/science/article/pii/S0165027015000175

23. Van, S.N., Nguyen, D.T., Hoai, G.N.: Development of a low-cost Arduino-based 12-lead ECG acquisition system and accompanied labview application. Int. J. Eng. Adv. Technol. **9**(1), 1641–1648 (2019)
24. Zachariadou, K., Yiasemides, K., Trougkakos, N.: A low-cost computer-controlled Arduino-based educational laboratory system for teaching the fundamentals of photovoltaic cells. Eur. J. Phys. **33**(6), 1599–1610 (2012). https://doi.org/10.1088/0143-0807/33/6/1599

Smart Watch for Smart Health Monitoring: A Literature Review

Avnish Singh Jat [ID] and Tor-Morten Grønli[(✉)] [ID]

Mobile Technology Lab, Department of Information Technology, Kristiania University College, Oslo, Norway
Tor-Morten.Gronli@kristiania.no

Abstract. This review paper focuses on analyzing research work related to the utilization of smartwatches in health informatics. In recent years, we have seen an ascent in life expectancy due to considerable innovations in the healthcare industry. Sicknesses identified with the cardiovascular framework, eye, respiratory framework, skin, and emotional well-being are inescapable around the world. Most of these sicknesses can be kept away from or potentially appropriately overseen through consistent examining. To empower ceaseless well-being checking to serve developing medical care needs, moderate, non-intrusive, and simple to-utilize medical services arrangements are basic. The increasing use of wearables watches coupled with health monitoring sensors makes it an essential tech for a continuous and remote health examination. In this paper, we present a comprehensive review of different research work on the utilization of smartwatches to deal with various diseases. For this, we have screened 370 research publications related to smartwatches in health informatics and selected 20 journals for the review that matched our selection criteria. Finally, we discussed future research perspectives and concerns regarding smartwatch-enabled healthcare architecture.

Keywords: Healthcare informatics · Smart watch · Remote health monitoring · Wearable devices

1 Introduction

1.1 Background

A smartwatch is a small smartphone-like device that is worn on the wrist. It gets connected to a smartphone through Bluetooth and provides assistance to some essential functions of mobile like picking up the call, messaging, music control, and camera control. The users can run the smartwatch using a touchscreen, buttons, or a blend of the two. Smartwatches have sensors like ECG (electrocardiography), SpO2, and Accelerometer to assist consumers in monitoring their health. The wrist is a convenient place to display all vital information as the arm moves several times compared to all other body parts. Hence, it is able to trace all the motions of the body, and also, the wrist has veins and arteries to measure pulse, and the skin is thin enough for sensors to detect blood pressure.

Wearable smartwatches can be considered a boon to healthcare technology. It provides patient monitoring, diagnosis, and assistance with treatment. It is capable of monitoring blood pressure, Oxygen saturation, heartbeats, pulse rate, sleep habits, physical activities, etc. It can also be used as an alarm for daily routines like exercises, taking medicines, etc. It can track physical movements like daily step counter and location. There is no doubt that smartwatches have entered our lives, particularly among early adopters. Various organizations have put resources into creating wearables with novel functionalities to gain adequate access to buyer markets. A smartwatch can be characterized as a portable gadget worn as an adornment or inconspicuously implanted in the client's attire [1]. For the most part, wearable gadgets embrace the advances of modern biosensors and remote information correspondence that permit the wearer to get to and send data in all areas of human undertaking. Given the usefulness of scaled-down biosensors equipped for remote correspondence, these gadgets are created to be imaginative, non-obtrusive observing innovations for ceaseless and independent transmission of physiological information [2]. As smartwatch multiplies in the healthcare area, they can give parental figures the data required to work on the nature of the medical field, analyze and work with the healthcare work process, oversee and treat patients distantly, gather more prominent wellbeing information, and convey more significant medical care to patients [3]. For functional use, Zhang's examination bunch noticed a few key factors that ought to be created to carry out wearable gadgets, including scaling down, reconciliation, systems administration, digitalization, and normalization [4]. A new appearance to the quickly developing business sector of wearable gadgets is savvy. With its scaled-down structure factor plan and figuring innovation, a savvy can be worn persistently without intruding on the client's everyday movement. Albeit PDAs have turned into a piece of our day-to-day routines and may be viewed as wearable, these gadgets regularly dwell in a pocket or satchel. In contrast to PDAs, keen watches can be genuinely wearable without intruding on our day-to-day routines. Likewise, they can fill in as a promptly available augmentation of the advanced mobile phone [3]. With the potential for boundless reception in the medical care area, smartwatches outfitted with biosensors can possibly give significant medical services data to patients and their suppliers.

1.2 Objectives

This article intends to survey the research work concerning medical care utilization of smartwatches and the ongoing exploration projects enrolled in the public authority clinical preliminaries site. Additionally, we examined the everyday uses and restrictions of smartwatches in medical services architecture.

2 Selection Method

2.1 Literature Search

The review process ought to be all around created and intended to diminish biases and dispose of unessential and inferior quality investigations. The means for carrying out a systematic review include incorporating (i) accurately figuring out the framing of a "foreground" research question using PICO (population, intervention, control, and outcomes) process, (ii) fostering a convention (consideration and rejection measures), (iii) execute detailed research search and (iv) screening the abstracts of the research recognized in the pursuit, For the systematic review, we utilized PRISMA methodology [10]. Most of the publications were screened from the PubMed database and ACM Digital Libraries, followed by IEEE Xplore. All data sets were looked at by utilizing the keywords "Smart Watch; Health care" or "Smartwatch; Healthcare" alongside the brand of the smartwatches.

2.2 Selection Criteria

Published studies were identified through 'pearl growing' [5], citation chasing, a search of published using the systematic review methods filter [6], and our topic knowledge. Inclusion and exclusion criteria are mentioned below (Table 1):

Table 1. Inclusion and Exclusion Criteria.

Inclusion criteria	Exclusion criteria
• Title is related to the question. Studies should report on marginal and internal fit • Included studies must be related to study design • Included studies must have been published between 2016 and 2021	• Study related to food and diet monitoring through the smartwatch • Study with no citation count • Study was published in a language other than English

3 Result

We screened 370 research publications, which were published between 2016 and 2021. Out of which, 346 didn't match our selection criteria and were excluded. A total of 24 publications' full text was reviewed. Finally, 20 publications were included and summarized in Table 2.

Table 2. Characteristics of articles for utilization of smartwatch for healthcare

Title	Study design	Target population	No. of participants/patients	Smart watch type	Sensors type
Inferring physical agitation in dementia using smartwatch and sequential behavior models	Experimental study	People Suffering from Dementia	8	Pebble, Android	Accelerometer
HIPAA Compliant Wireless Sensing Smartwatch Application for the Self-Management of Pediatric Asthma	Proposed Framework	People Suffering from Asthma	1	Samsung Gear Live, Android	Dust Sensor, Spirometer
Posttraumatic Stress Disorder Hyperarousal Event Detection Using Smartwatch Physiological and Activity Data	Observational study	United States veterans diagnosed with PTSD	99	Moto 360 Gen 1 & Gen 2, Apple Watch Series 3 & 4	Accelerometer, photoplethysmography sensor
Use of a Smart Watch for Early Detection of Paroxysmal Atrial Fibrillation: Validation Study	Experimental study	Patients who underwent cardiac surgery	40	Apple Watch 3, Fitbit Charge HR	photoplethysmography sensor
Validation of Single Centre Pre-Mobile Atrial Fibrillation Apps for Continuous Monitoring of Atrial Fibrillation in a Real-World Setting: Pilot Cohort Study	Controlled Trial	People aged ≥ 18 years	200	Huawei WatchGT, Honor Watch, Honor Band 4	photoplethysmography sensor
Feasibility of Using a Smartwatch to Intensively Monitor Patients With Chronic Obstructive Pulmonary Disease: Prospective Cohort Study	Observational study	Old age people suffering from COPD	28	LG Watch Urbane W150, Moto 360 2nd Generation	Accelerometer, photoplethysmography sensor

Table 2. (*continued*)

Title	Study design	Target population	No. of participants/patients	Smart watch type	Sensors type
Real-time mental stress detection based on a smartwatch	Proposed framework	Young people with a mean age of 24	10	Android Wear	Accelerometer, photoplethysmography (PPG) sensor
Validation of Blood Pressure Measurement Using a Smartwatch in Patients With Parkinson's Disease	Experimental study	Old age patients with Parkinson's Disease	56	SM-R850	Photoplethysmography (PPG) sensor
Building a Cardiovascular Disease Prediction Model for Smartwatch Users Using Machine Learning: Based on the Korea National Health and Nutrition Examination Survey	Observational study	Participants with a mean age of 47.57	6170	Samsung smartwatch	blood pressure, ECG (electrocardiography) sensor, SpO2, and blood glucose
Novel Use of Apple Watch 4 to Obtain 3-Lead Electrocardiogram and Detect Cardiac Ischemia	Proposed Framework	Old age patient with chest pain	2	Apple Watch 4	ECG (electrocardiography) sensor
DeepHeart: Semi-Supervised Sequence Learning for Cardiovascular Risk Prediction	Controlled Trial	People aged ≥ 18 years	14,011	Apple Watch	ECG (electrocardiography) sensor
ParkNosis: Diagnosing Parkinson's Disease Using Mobile Phones	Proposed Framework	People aged between 30 and 60	11	Moto 360 2nd Generation	Accelerometer
Cognitive IoT-Cloud Integration for Smart Healthcare: Case Study for Epileptic Seizure Detection and Monitoring	Proposed Framework	People aged between 10 and 22	23	Android Smartwatch	EEG, ECG (electrocardiography) sensor, SpO2, and blood glucose

Table 2. (*continued*)

Title	Study design	Target population	No. of participants/patients	Smart watch type	Sensors type
Pre-symptomatic detection of COVID-19 from smartwatch data	Observational study	People aged ≥ 18 years	5262	Fitbit, Apple Watch, Gramin,	ECG (electrocardiography) sensor, SpO2, and Accelerometer
Smartwatch PPG Peak Detection Method for Sinus Rhythm and Cardiac Arrhythmia	Proposed Framework	63–88 years old	16	–	–
Passive Detection of Atrial Fibrillation Using a Commercially Available Smartwatch	Observational study	People aged ≥ 18 years	9750	Apple Watch	Accelerometer, photoplethysmography (PPG) sensor
FOQUS: A Smartwatch Application for Individuals with ADHD and Mental Health Challenges	Proposed Framework	People aged between 20 and 30	10	Samsung Gear 2	Accelerometer, photoplethysmography (PPG) sensor
A Machine Learning Implementation for Mental Health Care. Application: Smart Watch for Depression Detection	Experimental study	People aged ≥ 18 years	334	Wear OS	Accelerometer, photoplethysmography (PPG) sensor, Gyroscopes
H-Watch: An Open, Connected Platform for AI-Enhanced COVID19 Infection Symptoms Monitoring and Contact Tracing	Proposed Framework	–	–	H-watch	photoplethysmography (PPG), SpO2
Wearable sensor data and self-reported symptoms for COVID-19 detection	Observational study	People aged ≥ 18 years	30,529	Fitbit, Apple Watch	ECG (electrocardiography) sensor, SpO2

Most of the papers selected were published in 2021 (6, 30%), followed by 2018 (5, 25%). There were three publications chosen in 2016, 2019, and 2020 (15%), and the least was from 2017 (1, 5%). The research works related to smartwatches in healthcare are booming with researchers working on projects ready to be deployed to users, which can be stated by the fact that the study design for most of the selected research work is a proposed framework (8, 40%). This is followed by an observational study (30%), experimental study (20%), and controlled trial (10%). Figure 1 shows several publications in different study designs.

Many of the selected research was focused on disease while choosing their target population (7, 35%) rather than determining the age of selected participants. Also, much research was open to all adults (6, 30%). This could be due to the fact that the popularity of smartwatches among youngsters is more as compared to older people. Among selected publications, there are six publications specifically targeted at old age people (30%) and three publications targeted explicitly at youngsters (15%). With the advancement of heart rate monitoring in smartwatches, most of the selected research works were focused on cardiovascular disease (9, 45%). There are four publications related to mental health (20%) and two publications associated with Parkinson's (10%). Three publications illustrated the importance of smartwatches in fighting pandemics and were focused on the utilization of smartwatches for predicting symptoms of Covid-19. With the introduction of Electrocardiography (ECG) in smartwatches, many selected publications utilized this sensor for their research (6, 30%), and the Photoplethysmography sensor (PPG) was used in nine research works (45%). Oxygen saturation monitor (SpO2) was also utilized in many research publications (5, 25%). Most of the research work presented a user-centric design ready to be utilized in real-life scenarios (8, 40%) and consolidates the importance of a smartwatch in health care.
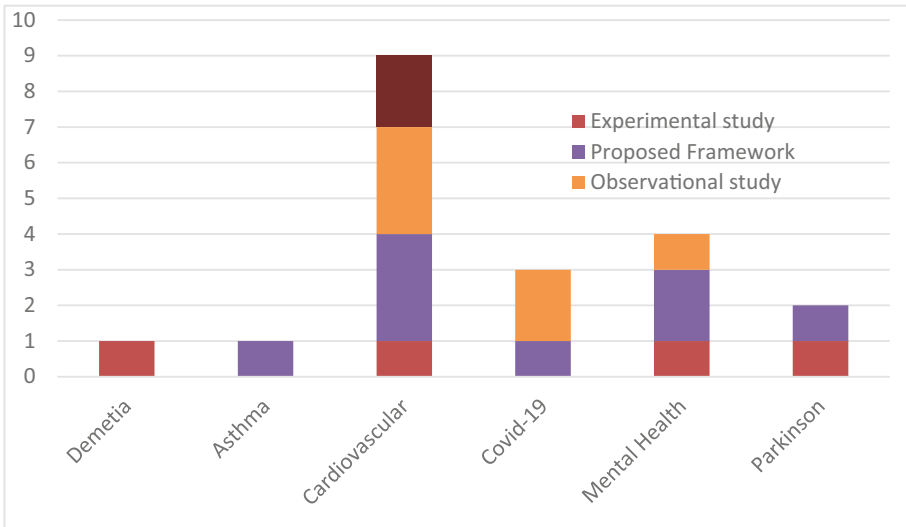

Fig. 1. Number of selected publications based on different disease and study types

4   Discussion

In our literature survey, 370 research publications were screened, and 20 were selected based on our inclusion criteria. Our literature survey intends to depict the recent research work on the utilization of smartwatches in healthcare. Our review showed that there is a vast difference in terms of study design and targeted population, and the same is represented in Fig. 1. This section will discuss the platform utilized and diseases targeted in selected publications, which will present a direction of current research work for the utilization of smartwatches in healthcare.

Android wear (9, 45%) was used nearly in half of the selected research works; this could be due to open-source availability for developers and researchers in android wear makes it feasible to utilize as per the research requirements. Six publications utilized the apple watch (30%); although there is a limitation to accessing the apple watch's health data, but its accuracy is considered better than others. In terms of functionality, the recent release of both platforms provides a SpO2 sensor, an ECG sensor, and a GPS. GPS and heart rate observing precision of smartwatches is up there with some decent dedicated trackers. The recent series of the Apple Watch's [7] healthcare monitoring facility isn't still medical grade, so there is a scope for improvement in both apple watch and Android watches.

As mentioned earlier, most of the publications reviewed were related to the utilization of smartwatches in cardiovascular disease. The regular ECG machine gives an exact evaluation of "cardiovascular arrhythmias." In any case, it offers just a "depiction" of electrical signals and cannot detect arrhythmias that happen when patients are not monitored. Thus, continuous monitoring of ECG through a smartwatch could be helpful to compensate for this limitation. The utilization of machine learning (ML) has additionally improved the job of these gadgets. It provides a practical, moderately reasonable, and straightforwardly open technique for cardiovascular checking to the overall population.

Patient acknowledgment is vital for effective computerized mental well-being mediations to keep away from dismissal or discontinuation. The expanded simple entry in recording practices, more noteworthy explicitness of update setting, and further developed input and representation of practices over the long haul might work with use and commitment with the treatment for depression. Continuous monitoring provided by wearable advances increments the precision and culmination of data assortment, which can assist with educating our agreement regarding the connection between disposition, practices, and clinical results. Moreover, programmed observing of rest or movement levels can diminish the patient's weight of making sure to report.

From the COVID-19 pandemic, we have understood that assuming healthcare frameworks had sped up the reception of innovation accessible throughout recent years, the magnitude of the current pandemic would probably have been significantly less extreme. As of now, we observe there are now numerous smartwatches available; various arrangements are at the trying stage, and various wearables have been proposed by specialists. There were three selected publications (15%) that present the utilization of smartwatch in the prediction and prevention of the Covid-19. With computerized arrangements moving towards low power utilization and little structure factor gadgets, multi-sensors may cover different physiological and contact tracing parameters, making advanced information

bases, giving admittance to clinical professionals, utilizing cloud or edge administrations to examine the impact of treatment, or surveying the patients (Table 3).

Table 3. Study intervention of articles selected for review

Author & year	Study Intervention
Anahita Hosseini 2016	The research work depicts a start to finish asthma attack risk prediction framework that educates people regarding their general danger of asthma attacks through a straightforward UI on a smartwatch. The proposed framework saves clients' wellbeing-related information through a HIPPA consistent cryptographic structure and limits the requirement for e-journal demands through automated wireless detecting and RESTful APIs [8]
Ridwan Alam 2018	The objective of this work is to capably surmise agitation episodes from wearable sensor information in genuine arrangements [7]
Mahnoosh Sadeghi 2021	This research assesses machine learning algorithms to foresee PTSD hyperarousal occasions among veterans utilizing smartwatch-based heart rate and accelerometer data. This article used scientific methods to identify the most important features contributing to such detection, thus, working on understanding the results and moving towards logical ML devices for PTSD observation. Trained data on four different algorithms, including Random Forest, SVM, Logistic Regression, and XGBoost. The XGBoost was the most robust algorithm among the developed algorithms, which yielded an AUC of 0.70 and over 81% accuracy. The initial analysis from the SHAP summary plot and SHAP dependence plots show that heart rate and body acceleration features have nonlinear relationships with PTSD episodes [9]
Robert Wu 2018	Feasibility study to decide whether patients with Chronic Obstructive Pulmonary Disease would utilize a smartwatch regularly and whether the transmitted data from the smartwatch is reliable [11]
Lucio Ciabattoni 2017	The research proposes live detection of stress during various intellectual errands. The Framework was proposed to gather and break down biosignal information (for example, HR, GSR, and BT) for continuous monitoring and for minimal price mental stress conditions during day-to-day activities. Results unveil a general grouping precision of 84:5%. A misclassification error of 26% was found in perceiving stress while the participant was relaxed. Research pointed out that a smartwatch can precisely detect mental stress conditions [12]
Jong Hyeon Ahn, 2021	Research focuses on determining the precision of Blood Pressure (BP) monitoring by utilizing a smartwatch in patients with Parkinson's Disease (PD) [13]

(*continued*)

Table 3. (*continued*)

Author & year	Study Intervention
Min-Jeong Kim 2021	The objective of this research is to foster an architecture that depicts the commonness of cardiovascular illness utilizing wellbeing-related information that smartwatch clients can effectively estimate. Nonetheless, on account of the pressure list, it is hard to say that it is adequately identified with the consequence of the Korea National Health and Nutrition Examination Survey. Like this, since the pressure list variable impedes this review, it is essential to remaking the prescient model utilizing an exact estimation worth or measurement according to an incorporated viewpoint on the pressure record later on [14]
Abdulwahab Sahyoun 2016	This paper intends to give a Parkinson's Disease (PD) manifestations appraisal instrument utilizing an Android cell phone application that permits PD patients to survey their side effects using both quantitative and subjective tests. Mobile Application is intended to give a single click analysis and identify early PD side effects. With the help of specialists, the application can ultimately turn out to be essential for continuous clinical examination tools for instant response and feedback [15]
Musaed Alhussein 2018	This review proposes a cognitive medical care monitoring system dependent on the IoT and the cloud. Epileptic seizure detection and classification framework inside the system is fabricated utilizing profound CNN and stacked autoencoders [16]
Tejaswini Mishra 2020	The study recommends that movement following and wellbeing observing through buyer wearable gadgets might be utilized for the enormous scope, constant discovery of respiratory diseases, regularly pre-apparently. Of the 25 instances of COVID-19 with recognized physiological changes for which we had side effect data, 22 were diagnosed previously (or at) manifestation beginning, with four cases identified around nine days sooner. Utilizing review smartwatch information, we show that 63% of the COVID-19 instances might have been distinguished before side effects beginning continuously through a two-layered admonition framework dependent on the event of outrageous rises in resting pulse compared with the singular gauge [17]
Dong Han 2019	The proposed PPG peak detection algorithm gives better pinnacle discovery exactness to sinus cadence and cardiovascular arrhythmias. The SWEPD strategy depends on the waveform envelope technique and a clever Poincaré plot component to naturally address fast arrhythmia beats, brings about critical decreases in the RMSE esteems and undetected moments, and ultimately gives better pinnacle discovery exactness over the looked at strategy (DATPD) [18]

Table 3. (*continued*)

Author & year	Study Intervention
Geoffrey H. Tison 2018	This investigation discovered that a PPG sensor combined with a profound machine learning algorithm could inactively recognize AF with some deficiency of affectability and explicitness against a basis standard ECG. The affectability, particularity, and beneficiary working trademark C measurement for the algorithm to identify AF were produced [19]
Victor Dibia 2016	This paper covers the development of focus, an application running on a smartwatch to help grown-ups with psychological well-being conditions like ADHD, and gentle types of consideration inadequacy through two primary courses – devices to cultivate stretched out concentration and devices to lessen uneasiness/stress. A smartwatch application intended to assist clients with working on their capacity to zero in on undertakings (through an adaptable execution of the Pomodoro time usage strategy), lessen their tension using careful reflection, and further develop their emotional well-being through sure message preparation was planned and carried out [20]
Piyush Kumar 2021	The precision rate accomplished was over 90%, yet while averaging out, it was referenced that gathering model 1 (K-NN, Support Vector Machine and Logistic Regression) is superior to troupe model 2 (Decision Tree calculation, Naïve Bayes classifier) for foreseeing individuals experiencing depression [21]
Tommaso Polonelli 2021	Results exhibited just 5.9 mW of average power utilization, prompting a long period of 9 days on a bit of watch battery. All the equipment and the product, including an AI on the MCU tool compartment, are given open-source, permitting the researchers to construct and utilize the H-Watch [22]
Giorgio Quer 2021	The research investigates whether individual sensor data gathered over the long run might assist with distinguishing subtle changes showing a disease, for example, in patients with COVID-19. Researchers have surveyed whether side effects and sensor data can separate COVID-19 [23]

5   Conclusion

For the smartwatch to acquire wide acknowledgment by health experts, a thorough examination of their precision, culmination, and impact on the work process should be directed before smartwatches are coordinated in the healthcare industry. Practical use cases to examine usefulness, UI plan, and ease of use for an assortment of health-care architecture are required. Deep exploration is needed to comprehend the impact of applications on Healthcare Informatics. Generally, the smartwatch and its clinical applications stay invigorating yet doubtful. At present, the innovation has all the ear-marks of being protected, fills in as promoted, and connects with patients outside of the average patient-supplier office experience. While there are legitimate worries about

adding new surges of clinical data of indistinct advantage onto currently overburdened jobs, notwithstanding concerns about information security and protection, doctors need to get ready for an undeniably associated insight with patients and their information.

References

1. Wissinger, E.: Wearable tech, bodies, and gender. Sociol. Compass **11**, e12514 (2017)
2. Ajami, S., Teimouri, F.: Features and application of wearable biosensors in medical care. J. Res. Med. Sci. **20**(12), 1208–1215 (2015)
3. Lu, T.-C., et al.: Healthcare applications of smart watches. A systematic review. Appl. Clin. Inf. **7**(3), 850–869 (2016). https://doi.org/10.4338/ACI-2016-03-R-0042
4. Poon, C.C., Zhang, Y.T.: Perspectives on high technologies for low-cost healthcare. IEEE Eng. Med. Biol. Mag. **27**, 42–47 (2008)
5. Pearl Growing. In: Wikipedia (2021). https://en.wikipedia.org/wiki/Pearl_growing. Accessed 3 Feb 2022
6. Systematic reviews: creating a search strategy. In: Research Guides. https://guides.lib.umich.edu/c.php?g=283340&p=2126706. Accessed 3 Feb 2022
7. Alam, R., et al. Inferring physical agitation in dementia using smartwatch and sequential behavior models. In: 2018 IEEE EMBS International Conference on Biomedical & Health Informatics (BHI). IEEE (2018)
8. Hosseini, A., et al.: HIPAA compliant wireless sensing smartwatch application for the self-management of pediatric asthma. In: 2016 IEEE 13th International Conference on Wearable and Implantable Body Sensor Networks (BSN). IEEE (2016)
9. Sadeghi, M., McDonald, A.D., Sasangohar, F.: Posttraumatic Stress Disorder Hyperarousal Event Detection Using Smartwatch Physiological and Activity Data. arXiv preprint arXiv: 2109.14743 (2021)
10. Inui, T., et al.: Use of a smart watch for early detection of paroxysmal atrial fibrillation: validation study. JMIR Cardio **4**(1), e14857 (2020)
11. Wu, R., et al.: Feasibility of using a smartwatch to intensively monitor patients with chronic obstructive pulmonary disease: prospective cohort study. JMIR mHealth and uHealth **6**(6), e10046 (2018)
12. Ciabattoni, L., et al.: Real-time mental stress detection based on smartwatch. In: 2017 IEEE International Conference on Consumer Electronics (ICCE). IEEE (2017)
13. Ahn, J.H., et al.: Validation of blood pressure measurement using a smartwatch in patients with Parkinson's disease. Front. Neurol. **12** (2021)
14. Kim, M.-J.: Building a cardiovascular disease prediction model for smartwatch users using machine learning: based on the Korea National Health and Nutrition Examination Survey. Biosensors **11**(7), 228 (2021)
15. Sahyoun, A., et al.: ParkNosis: diagnosing Parkinson's disease using mobile phones. In: 2016 IEEE 18th International Conference on e-Health Networking, Applications and Services (Healthcom). IEEE (2016)
16. Alhussein, M., et al.: Cognitive IoT-cloud integration for smart healthcare: case study for epileptic seizure detection and monitoring. Mob. Netw. Appl. **23**(6), 1624–1635 (2018)
17. Mishra, T., et al.: Pre-symptomatic detection of COVID-19 from smartwatch data. Nat. Biomed. Eng. **4**(12), 1208–1220 (2020)
18. Han, D., et al.: Smartwatch PPG peak detection method for sinus rhythm and cardiac arrhythmia. In: 2019 41st Annual International Conference of the IEEE Engineering in Medicine and Biology Society (EMBC). IEEE (2019)

19. Tison, G.H., et al.: Passive detection of atrial fibrillation using a commercially available smartwatch. JAMA Cardiol. **3**(5), 409–416 (2018)
20. Dibia, V.: Foqus: a smartwatch application for individuals with adhd and mental health challenges. In: Proceedings of the 18th International ACM SIGACCESS Conference on Computers and Accessibility (2016)
21. Kumar, P., et al.: A machine learning implementation for mental health care. Application: smart watch for depression detection. In: 2021 11th International Conference on Cloud Computing, Data Science and Engineering (Confluence). IEEE (2021)
22. Polonelli, T., et al.: H-Watch: an open, connected platform for AI-enhanced COVID19 infection symptoms monitoring and contact tracing. In: 2021 IEEE International Symposium on Circuits and Systems (ISCAS). IEEE (2021)
23. Quer, G., Radin, J.M., Gadaleta, M., et al.: Wearable sensor data and self-reported symptoms for COVID-19 detection

Data Quality Enhancement for Machine Learning on Wearable ECGs

Balázs Molnár[1]([✉])[iD], László Micsinyei[1], Gábor Perlaki[2,3], Gergely Orsi[2,3], László Hejjel[4], Tamás Dóczi[5], József Janszky[2,3], Norbert Laky[1], and Ákos Tényi[1]

[1] Smart Data Group, E-Group ICT Software Zrt., Budapest, Hungary
balazs.molnar@egroup.hu
[2] Department of Neurology, University of Pécs, Medical School, Pécs, Hungary
[3] MTA-PTE Clinical Neuroscience MR Research Group, Eötvös Loránd Research Network (ELKH), Pécs, Hungary
[4] Heart Institute, University of Pécs, Medical School, Pécs, Hungary
[5] Department of Neurosurgery, University of Pécs, Medical School, Pécs, Hungary

Abstract. With the exponentially growing amount of data collected by wearable medical devices, there is an expansion of opportunities to exploit machine learning methods in monitoring patient health and predicting events that may need medical attention. Wearable ECG devices provide a more comfortable alternative compared to the usual monitoring devices used in clinical settings, at the cost of inferior information density and signal quality. Notwithstanding, recent studies suggest that machine learning methods are able to work with wearable data, and for specific tasks, even medical grade devices are now available (e.g. detection of cardiac arrhythmias). This paper focuses on improving the quality of machine learning data, as part of an ongoing research of automating pipelines that allow for building robust models based on wearable ECG signals. While our efforts in general also consider the mainstream machine learning task of heartbeat classification, this work instead (exploiting the long-term ECG data) contributes to the development of models to learn features much longer than a single heartbeat. For the extraction of such features, R-peak detectors are considered and evaluated with respect to sensitivity and robustness to noise. Noise stress tests show that a combination of global filters can improve the performance of detectors, efficiently dealing with typical noises almost always present in wearable ECG signals. Also, local noise detection models are demonstrated to be promising methods to handle heavy noises that can not be resolved by the global filters.

Keywords: Machine learning · ECG · Wearable devices

1 Introduction

With health-related big data currently being gravely under-utilized, smart data solutions to analyze, evaluate and extract interpretive information are especially

called for. With the typical trend of machine learning (ML) models moving towards more complex, deep architectures, the amount of training data rarely seems sufficient. Nevertheless, even in the case of a single modality, the collected data is still largely unused: each year, hundreds of millions of electrocardiogram (ECG) recordings are collected, but only a small fraction of them is ever used to train a machine learning model. Wearable sensors further escalate the data flow to an unprecedented level, but also mean an opportunity for the early detection of diseases expanding the clinical application of ML methods [1]. Automated, end-to-end solutions thus become more important. For the heartbeat classification problem, a comprehensive study was conducted in [6]. For other tasks that consider longer-term features, the challenge typically lies in handling un-standardized data picked up by devices with various settings, and the typically poor signal-to-noise ratio of wearables. These issues often manifest in the machine learning model having high false positive rate (FPR) [3] hindering the clinical applicability of such ML-based alarm systems. The standardization of ML data and sophisticated noise detection algorithms can help to remedy the situation, which gives the motivation for this paper.

2   Methods

Following the agile, iterative methodology of the Team Data Science Process proposed by Microsoft, we execute standard data science tasks to develop an automated pipeline to load, transform and process long-term ECG data and train a machine learning model without the need of an expert review of the data. The challenge of such development is to make sure the ML model is always supplied with proper input, i.e. processing of signals is robust to noise and the variability of signal acquisition settings. In this paper, we focus on the methodology of data exploration (Data acquisition and understanding) and feature engineering (Modeling), depicted in Fig. 1.

2.1   Data Acquisition and Understanding

Data for this paper was collected from several sources, including public databases available for internet download and synthetic data as can be seen in Fig. 2.

The frequently used ML training set of the MIT-BIH Arrhythmia detection database [10] was firstly considered for the development and evaluation of our algorithms. The database contains 48 half-hour recordings of ambulatory ECG recordings, digitized at the frequency of 360 Hz. The database contains expert annotation of heartbeats, usually used to train an ML model for a heartbeat classification task. Within our perspective, since we are motivated in learning long-term features, R-peak locations were the only annotations we used from this dataset. These annotations, however, could not be identified in noisy segments of the signal, as the curation protocol was to exclude such segments where annotations could have been uncertain. Thus for noise detection tests, this particular dataset is not ideal.
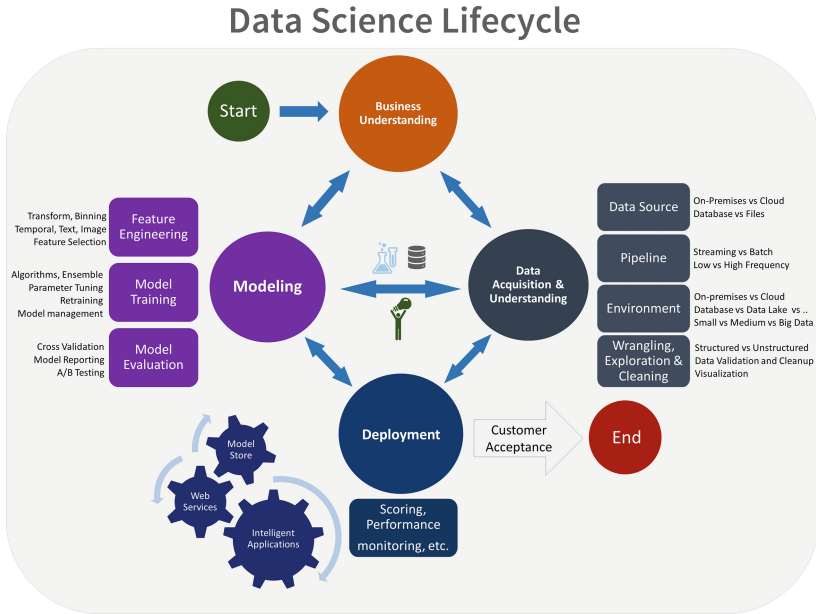
Fig. 1. Overview of the Team Data Science Process (Microsoft) methodology used in the broader context of our research/development. The scope of this work lies in the area of data exploration (Data acquisition and understanding) and feature engineering (Modeling)

To assess the performance of noise detectors, the MIT-BIH noise stress test database [12] was considered. The dataset contains 12 half-hour ECG recordings and 3 half-hour recordings of noise typical in ambulatory ECGs: baseline wander, muscle artifact and electrode motion artifact. Noises were added to two clean signals leaving two-minute clean intervals between two-minute noisy segments while also varying the amplitude of added noise, yielding 6 records with different signal-to-noise ratio for each of the two clean recordings.

By generating normal sinus rhythms and various noises, we created a synthetic database, containing 15×5-minute recordings each with 1000 samples per second. The recordings were created by adding noise to 3 records: one clean record with constant beat-to-beat intervals and two with different amplitude of respiratory sinus arrhythmia (RSA) of 0.2 Hz. 5 type of noises were simulated including baseline wander, motion artifact, random noise (with two different amplitudes) and powerline noise.

2.2 Modeling

The concept for an automated processing of ECG signals consists of 5 steps depicted in Fig. 3. First, measurement data goes through an extract, transform, and load (ETL) pipeline which yields a database of collected signal data and
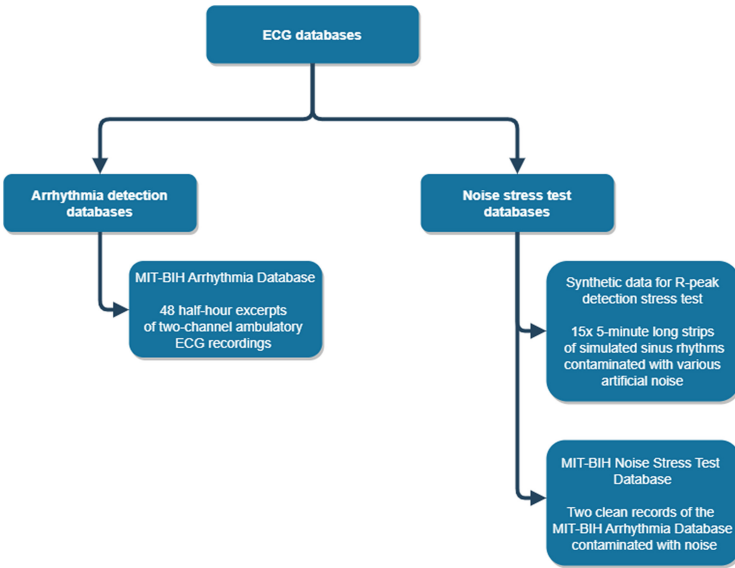
Fig. 2. ECG databases used in this paper

other metadata. The database is then queried to retrieve raw measurement data to be analyzed, based on query conditions. The preprocessing of raw signals standardizes and filters the data, removes noises that can not be resolved when extracting features. This step ensures that the captured features are independent of the acquisition settings and noises. Feature extraction step is where long-term features are extracted, meaning that, in general, the filtered and standardized ECG signal is transformed into a lower dimensional feature space. A typical example is when the signal is transformed to a time-series of beat-to-beat-intervals called a tachogram, and parameters such as the heart rate are extracted. In the scope of this paper, we only deal with the preprocessing and feature extraction step of the processing pipeline, highlighted in the figure.
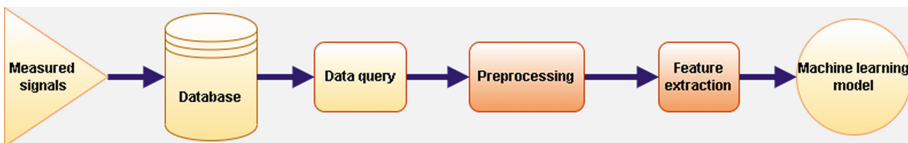

Fig. 3. The automated ECG data processing pipeline, highlighting the preprocessing and feature extraction steps addressed in this paper

Preprocessing - Noise Reduction/Removal. For noise removal, we consider global and local filters. Global filters affect the whole signal, while local filters leave most of the signal intact, but mark/remove part of the signal where noise can not be resolved by the global filters. Among globally acting filters we implemented powerline and baseline filters in the frequency domain by designing a notch filter of 50/60 Hz critical frequency, and a Butterworth low-pass filter with 0.5 Hz critical frequency, respectively. Time domain filters such as moving average (with window size typically set between 5 and 50 ms) and moving median detrending filters (with window size typically set between 100 and 300 ms) were also implemented, the first to remove high-frequency noises, the second to further reduce baseline wander.

Local filters are based on decomposing the signal in a few seconds long segments. The idea is that with a proper measure, noisy and clean segments can be distinguished. One favorable measure based on [9], is the distance of autocorrelation functions of the segments. The autocorrelation function (ACF) of segments exhibit a unique shape if the segment has good signal-to-noise ratio and this shape is invariant to the scaling of the waveform, but is particularly sensitive to noise. In other words, the ACF can be a good discriminator between clean and noisy segments, demonstrated in Fig. 4.

First, the signal is decomposed into (typically) 5 s long segments, which are then transformed by taking the ACF of segments. The detection is initialized by finding some segments that are sure to be clean based on the stability of R-peak detections. All other segments are initially assumed to be noisy. The detection then analyzes each segment's ACF and compare to the average of clean ACFs by taking the L2 distance between the ACFs. If the difference is within the preset threshold, the segment is classified as clean and the average clean ACF is updated. This is repeated until convergence (no new clean segment is found).

Feature Extraction. For machine learning tasks targeted by our research, long-term features were derived from the ECG signal. Without the loss of generality, specific parameters were not considered and our analysis only relies on transforming the signal to the time series of beat-to-beat intervals. The time series can be constructed by detecting R-peaks in the signal, for that, several methods exist, summarized by Table 1. From R-peak detections, beat-to-beat intervals are calculated by simply taking the time difference of consecutive R-peak locations.

3   Results and Discussion

Having long-term ambulatory ECG data, machine learning methods can be trained for various tasks. While in general, our algorithms could contribute to other ML models (such as heartbeat classification models), the results shown here are valuable in the context of ML tasks where the learning process focuses on long-term features rather than the morphology of heartbeats. Our results showcase the evaluation of preprocessing and feature extraction algorithms, including the performance assessment of several algorithms that identify R-peaks in
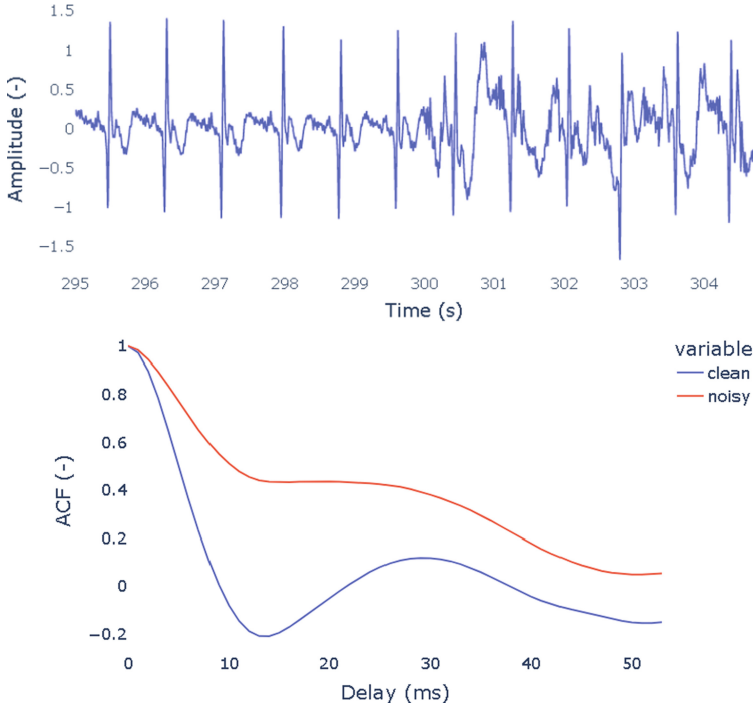
Fig. 4. An example of distinguishing clean and noisy segments of an ECG record based on the autocorrelation function of segments. Figure shows a 2×5 s long part of the signal (top) and the autocorrelation function of 5 s long segments (bottom). The ACF of a clean segment exhibits a unique shape which is extremely sensitive to noise (but is invariant to dilation and translation) giving the opportunity to classify segments.

the signal, evaluating global noise reduction algorithms and demonstrating the applicability of an autocorrelation-based noise detection method.

3.1   R-Peak Detection Performance Benchmark

Long-term features having clinical significance include parameters that can be derived from the time series of beat-to-beat intervals, i.e. the evolution of the elapsed time between consecutive heartbeats. Such time-series can be constructed by detecting R-peaks in the signal and taking the time difference between consecutive detections. We evaluated some common R-peak detectors with respect to their sensitivity and their robustness to noise. Table 1 shows 7 R-peak detectors, including the filtering, detection and post-detection algorithms applied by the detectors. In some cases, the detector does not in fact mark the R-peak in the signal (due to a consistent delay caused by the filters), but this does not impact the evaluation since we are only interested in the time difference of detections. Two benchmark tests were designed to measure the

performance and robustness of R-peak detectors: the first, entitled 'noise stress test' in Table 1, is a binary measure of noise tolerance indicating whether the detector trends to break down (detection accuracy below 50%) under poor signal quality conditions. This test was carried out by applying the detectors on the synthetic dataset described in Sect. 2.1. The second measure is the sensitivity of detectors assuming good signal quality, but employing a strict tolerance (under 5 ms) for detection precision. This is to ensure that the uncertainty of features extracted from beat-to-beat interval series are minimal. This test was carried out on a record from the MIT-BIH Arrhythmia Detection dataset. In both cases, to account for the delay of detections when the detector does not mark the R-peak, the median delay (with respect to the ground truth R-peak locations) was subtracted from the actual detections. Other than the intrinsic filters of R-peak detectors, no filters/pre-processing were applied.

From Table 1, we see that most of the detectors break down under poor signal quality conditions, meaning that the detection accuracy fell below 50%. The test signal chosen from the synthetic dataset contained a wide spectrum of noises including motion artifacts, powerline noise, baseline wander and gaussian random noise. Two of the detectors, WFDB and Christov however, proved to have a high tolerance against these types of noises, suggesting that these detectors would be strong candidates to be considered to move on with, regarding real world wearable ECG data. Figure 5 shows detections of the WFDB detector. We see that the test signal is indeed of a very bad quality, unsurprisingly breaking down most of the detectors, but we also note that the human eye would identify all R-peaks without difficulties.
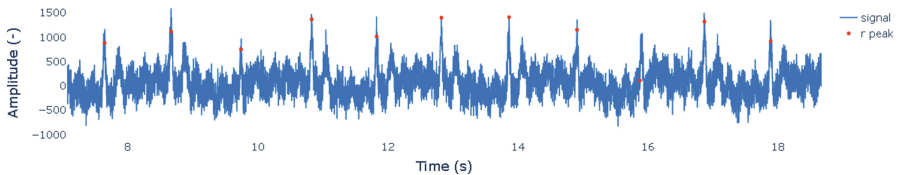

Fig. 5. A sample from the synthetic stress test data testing the R-peak detectors, with detections of the best performing WFDB detector. The synthetic data contains a wide range of noises: RSA, baseline wander, motion artifact, random (gaussian) noise and powerline noise.

The sensitivity of detectors were obtained by calculating the true positive rate of detections on one of the clean record (containing only normal sinus beats) of the MIT-BIH Arrhythmia Detection database (Sect. 2.1). Positive detections were identified if the detection was within the 5 ms range of the true R-peak location given by the annotation of the record. We found that WFDB and EngZee detectors exhibited excellent performance, while other detectors were evaluated as unacceptable, due to the amount of uncertainty propagated to the ML task of learning long-term features derived from the detections.

Table 1. The benchmark of common R-peak detectors.

	Long name	Filtering	Detection	Post detection	Marks R-peak?	Passed noise stress test?	MIT-BIH sensitivity (tolerance of 5 ms)
WFDB [11]	Waveform database	Second order Butterworth IIR filter with a passband of 5–20, moving wave integration with ricker wavelet	Maximum search, adaptive threshold (with learning to initialize thresholds)	Missed beat backsearch, refractory period rejection	Yes	Yes	100%
2avg [4]	Two moving averages	Second order Butterworth IIR filter with a passband of 8–20, 120 and 600 ms moving average windows	First MA amplitude > second MA amplitude. Maximum search	Refractory period rejection	No	No	93%
SWT [7]	Stationary wavelet transform	Bandpass 5–15 Hz, Daubechies 3 wavelet, squared	Adaptive threshold		No	No	94%
EngZee [8]	Englese and Zeelenberg	50 Hz powerline, differentiate, five tap FIR windowed smoothing filter	Adaptive threshold	Peak correction on the unfiltered signal	Yes	No	99.80%
Christov [2]	Christov's adaptive threshold	20, 28 ms moving average, differentiate, rectify, 40 ms moving average	Combination of adaptive thresholds		No	Yes	86%
Hamilton [5]	Hamilton	First order Butterworth IIR bandpass 8–16 Hz, differentiate, rectify, 80 ms moving average	Adaptive threshold	Refractory period rejection	No	No	74%
Tompkins [13]	Pan-Tompkins	First order Butterworth IIR bandpass 5–15 Hz, differentiate, square, 150 ms moving average	Adaptive threshold	Missed beat backsearch, refractory period rejection	No	No	69%

3.2   Noise Stress Test of Global Filters

Testing the global filters, the synthetic dataset was systematically evaluated with respect to the ability of filters to resolve noises. The constant and RSA records, contaminated by noises of different types, were filtered with global filters of both frequency-domain (baseline and powerline filters) and time-domain (moving average and moving median de-trend). We evaluated the performance of global filtering by measuring the accuracy of beat-to-beat intervals that can be generated from detections of the best performing R-peak detector (WFDB detector) on the filtered signal. The accuracy was calculated by taking the absolute error of beat-to-beat intervals with respect to ground truth. The errors were also calculated in the case of detecting peaks on the unfiltered (raw) data. Results are shown in Table 2. As we see, motion artefact and baseline wander did not cause any issue for the R-peak detector, also, unsurprisingly, powerline noise was easily resolved by the global filters, since one of them is designed to cut out

50 Hz frequency band. We found random noise to be the most difficult for the detector to handle, due to spikes on the signal which can be falsely detected as peaks and confusing the detection threshold. These noises were also successfully resolved by the global filters, presumably by the moving average filters. Figure 6 shows an 8 s long segment of the original clean record, and the detection on the noisy, unfiltered data as well as on the filtered data.

We conclude that the global filters were able to resolve all types of noises that were generated within acceptable tolerance. Based on R-peak detection tolerance of 5 ms, the tolerance for the difference of consecutive R-peak locations should be $\sqrt{2}$ times 5 ms, which is an upper bound for the global filtered errors in Table 2.

Table 2. Testing the global filters with synthetic data. The table shows the absolute error of beat-to-beat interval calculations from R-peak detections on raw and filtered data in the presence of various noises. Errors are in the unit of milliseconds.

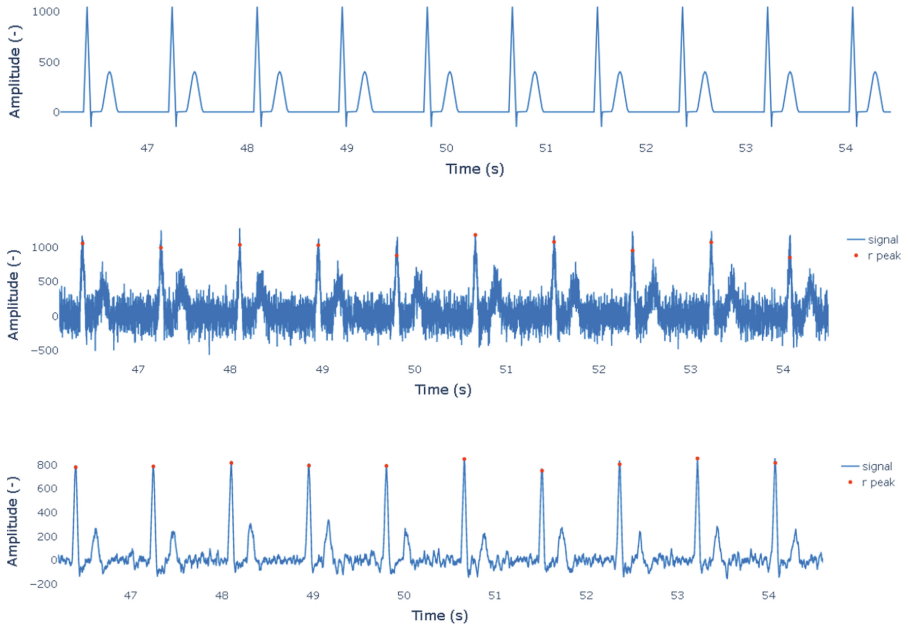|	Constant rhythm		Respiratory sinus arrhythmia (RSA)	
	With raw data	With global filters	With raw data	With global filters
Motion artefact	0	0	1	1
Random noise	36	5	92	6
Baseline wander	0	0	1	1
Powerline noise	6	0	7	1

Fig. 6. Clean synthetic data (top), synthetic data with random noise (middle), filtered data (bottom) and R-peak detections of the WFDB detector.

3.3   Signal Quality Assessment and the Local Noise Filter

Signals picked up by wearable ECGs are exposed to noises that cause signal distortion that can not be resolved by global filters. Most of the times however, signal distortion is only local, as in the case of increased physical activity of the wearer causing baseline jumps, heavy muscle artefacts and even signal losses. Such localized noises should be cropped out from the signal before any feature extraction can be made, since they would typically break down algorithms such as R-peak detectors. To this end, we have developed a local noise filter that can remove noisy segments from the signal while leaving clean segments intact, described in Sect. 2.2. In this example, 5 s long segments were classified as either noisy or clean. In the scope of this paper, we only show preliminary results, while a more detailed analysis is on the way, featuring a larger validation set of real world data with expert annotations. Demonstrating the application of the method, Fig. 7 shows the detection of noisy segments on the dataset of the MIT-BIH stress test database (cf. Sect. 2.1). A shorter segment of the data was already shown in Fig. 4, where the signal can be observed from a closer view. We found that noisy segments were indeed detected with a small number false positives. A more extensive validation is however needed, both regarding quantitative assessment and testing different noise types. This will be targeted by future research.
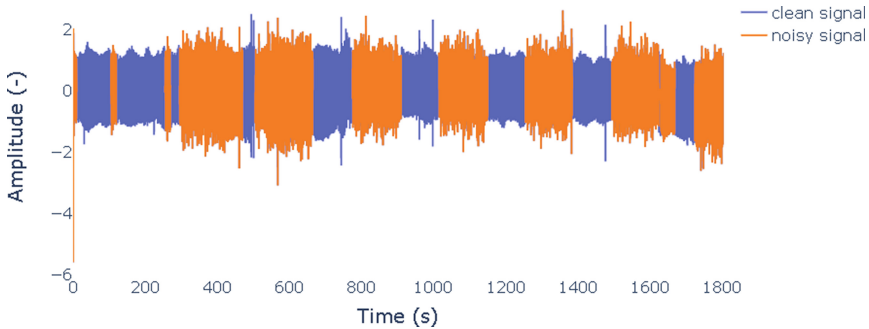

Fig. 7. Qualitative performance assessment of the local noise filter on the MIT-BIH noise stress test dataset. A shorter segment of the data was already shown in Fig. 4, where the signal can be observed from a closer view.

4   Conclusion and Future Work

With the exponentially growing amount of data obtained by wearable ECG devices, automated pipelines to analyze and interpret the data are called for. Machine learning solutions proved to be applicable even in the context of wearable devices, with a significant challenge of tackling poor signal quality scenarios. We have shown that with a combination of global and local filters, typical noises in wearable ECG signals can be reduced/removed in a way that the extracted

features for machine learning tasks contain minimal uncertainty. Our findings can help to build robust machine learning models with lower false positive rate, paving the way towards clinical applications.

Next step in our research focuses on validation and testing on real world data. Data is currently being collected by wearable devices acquiring single channel ECGs. The proposed noise detection methodology is to be further improved in the future by implementing an unsupervised learning method for the classification of noisy and clean segments. A comprehensive validation analysis is also on the way in this respect.

References

1. Beniczky, S., Karoly, P., Nurse, E., Ryvlin, P., Cook, M.: Machine learning and wearable devices of the future. Epilepsia (2020). https://doi.org/10.1111/epi.16555
2. Christov, I.I.: Real time electrocardiogram QRS detection using combined adaptive threshold. BioMed. Eng. OnLine **3**(1), 1–9 (2004). https://doi.org/10.1186/1475-925x-3-28
3. De Cooman, T., Kjær, T.W., Van Huffel, S., Sorensen, H.B.: Adaptive heart rate-based epileptic seizure detection using real-time user feedback. Physiol. Meas. **39**(1), 014005 (2018). https://doi.org/10.1088/1361-6579/aaa216
4. Elgendi, M., Jonkman, M.F.D.: Frequency bands effects on QRS detection. In: Proceedings of the Third International Conference on Bio-inspired Systems and Signal Processing. SciTePress - Science and and Technology Publications (2010). https://doi.org/10.5220/0002742704280431
5. Hamilton, P.: Open source ECG analysis. In: Computers in Cardiology. IEEE (2002). https://doi.org/10.1109/cic.2002.1166717
6. Hannun, A.Y., et al.: Cardiologist-level arrhythmia detection and classification in ambulatory electrocardiograms using a deep neural network. Nat. Med. **25**(1), 65–69 (2019). https://doi.org/10.1038/s41591-018-0268-3
7. Kalidas, V., Tamil, L.: Real-time QRS detector using stationary wavelet transform for automated ECG analysis. In: 2017 IEEE 17th International Conference on Bioinformatics and Bioengineering (BIBE). IEEE, October 2017. https://doi.org/10.1109/bibe.2017.00-12
8. Lourenco, A., Silva, H., Leite, P., Lourenço, R., Fred, A.L.: Real time electrocardiogram segmentation for finger based ECG biometrics. In: Proceedings of the International Conference on Bio-inspired Systems and Signal Processing. SciTePress - Science and and Technology Publications (2012). https://doi.org/10.5220/0003777300490054
9. Moeyersons, J., et al.: Artefact detection and quality assessment of ambulatory ECG Signals **182**, 105050. https://doi.org/10.1016/j.cmpb.2019.105050
10. Moody, G., Mark, R.: The impact of the MIT-BIH arrhythmia database **20**(3), 45–50. https://doi.org/10.1109/51.932724
11. Moody, G.B.: WFDB applications guide. Harvard-MIT Div. Health Sci. Technol. **10**, 30–31 (2003)
12. Moody, G.B., Muldrow, W.E., Roger, M.: A noise stress test for arrhythmia detectors. Comput. Cardiol. **11**, 381–384 (1984)
13. Pan, J., Tompkins, W.J.: A real-time QRS detection algorithm. IEEE Trans. Biomed. Eng. BME **32**(3), 230–236 (1985). https://doi.org/10.1109/tbme.1985.325532

Image Visualization and Signal Analysis in Biomedical Applications

Measurable Difference Between Malignant and Benign Tumor of the Thyroid Gland Recognizable Using Echogenicity Index in Ultrasound B-MODE Imaging: An Experimental Blind Study

Jiri Blahuta[1,2]([✉]), Tomas Soukup[1,2], Jan Lavrincik[1], Lukas Pavlik[1], and Zuzana Repaska[1]

[1] Moravská vysoká škola Olomouc, o.p.s.tř. Kosmonautů 1288/1, 77900 Olomouc, Czech Republic
{jiri.blahuta,jan.lavrincik,lukas.pavlik,zuzana.repaska}@mvso.cz,
{jiri.blahuta}@fpf.slu.cz
[2] Slezská univerzita v Opavě, Filozoficko-přírodovědecká fakulta Masarykova třída 343/37, 74601 Opava, Czech Republic
http://www.mvso.cz/en, https://www.slu.cz/fpf/en

Abstract. The presented paper is focused on possibility to evaluate echogenicity grade on ultrasound B-images of the thyroid gland tumor. We use our developed software tool which has been originally designed for analysis of ultrasound B-images in neurology. Currently, the goal of this research is to decide if this software is also useful for different ultrasound B-images, in this case in endocrinology. To evaluate it, the Echo-Index parameter is used. The core principle of the algorithm is based on computing area and computed echogenicity index. The paper has two main parts. The first one is focused on general assessment of the reproducibility of computed Echo-Index between two independent, non-experienced observers. The second part is concentrated on changes of the echogenicity index (Echo-Index) in the case of malignant tumor and in the case of benign tumor. The general reproducibility is almost perfect, level of agreement based on correlation coefficient is higher than 0.98 and the absolute average error does not exceeds 15% between two observers. Subsequent analysis between malignant and benign tumor images evinces the Echo-Index is different.

Keywords: Thyroid gland ultrasound · Echogenicity index · Thyroid echogenicity · Thyroid sonography · Thyroid tumors ultrasound

1   Thyroid Gland, Its Role and Using Sonography in Endocrinology

Many organs and structures and their normal functions inside the human body are inseparable part of our everyday life. Brain, heart, liver, lungs, arteries and veins, etc. The thyroid gland, a part of the endocrine system may be overlooked sometimes. Nevertheless, the normal function of the thyroid gland and related tissues is really important for our life.

Thyroid gland is one part of human endocrine system of glands that produce endocrine secretions that help to control bodily metabolic activity, see Fig. 1 where the gland is located with its connected surrounding structures.
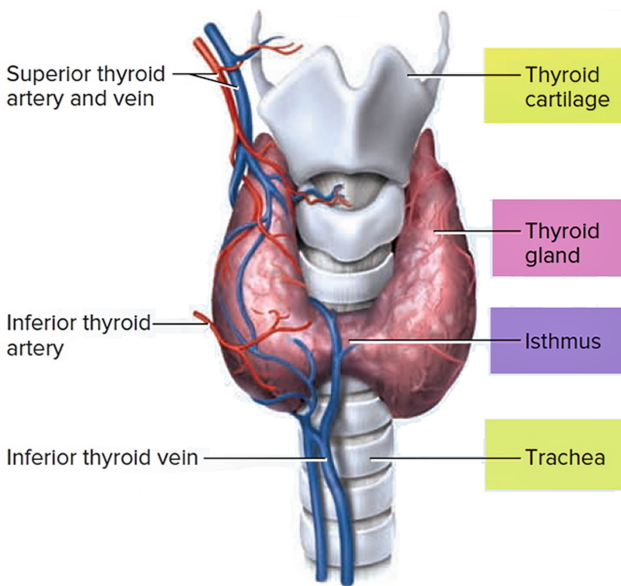

Fig. 1. Position of the thyroid gland and the surrounding structures (Source: https://healthjade.com/wp-content/uploads/2017/10/thyroid-gland-anatomy.jpg)

It is located in the front of the neck, right below the larynx and next to and around to the trachea. Thyroid gland has a butterfly shape consisting of two lobes connected by a piece of tissue, called the isthmus. Its functions like protein synthesis, long bones growth regulation, degrading of the cholesterol and triglycerides, increasing metabolic rate, heart contraction stimulation and another functions are essential in our life. More anatomic and function details, information about diseases of the thyroid gland and related structures are stated in [1]. Specific symptoms have hypothyroidism and hyperthyroidism. Thyroid gland tumors, especially malignant carcinoma, pose a threat to anyone and their number is increasing. Thus, early tumor diagnostics is really important.
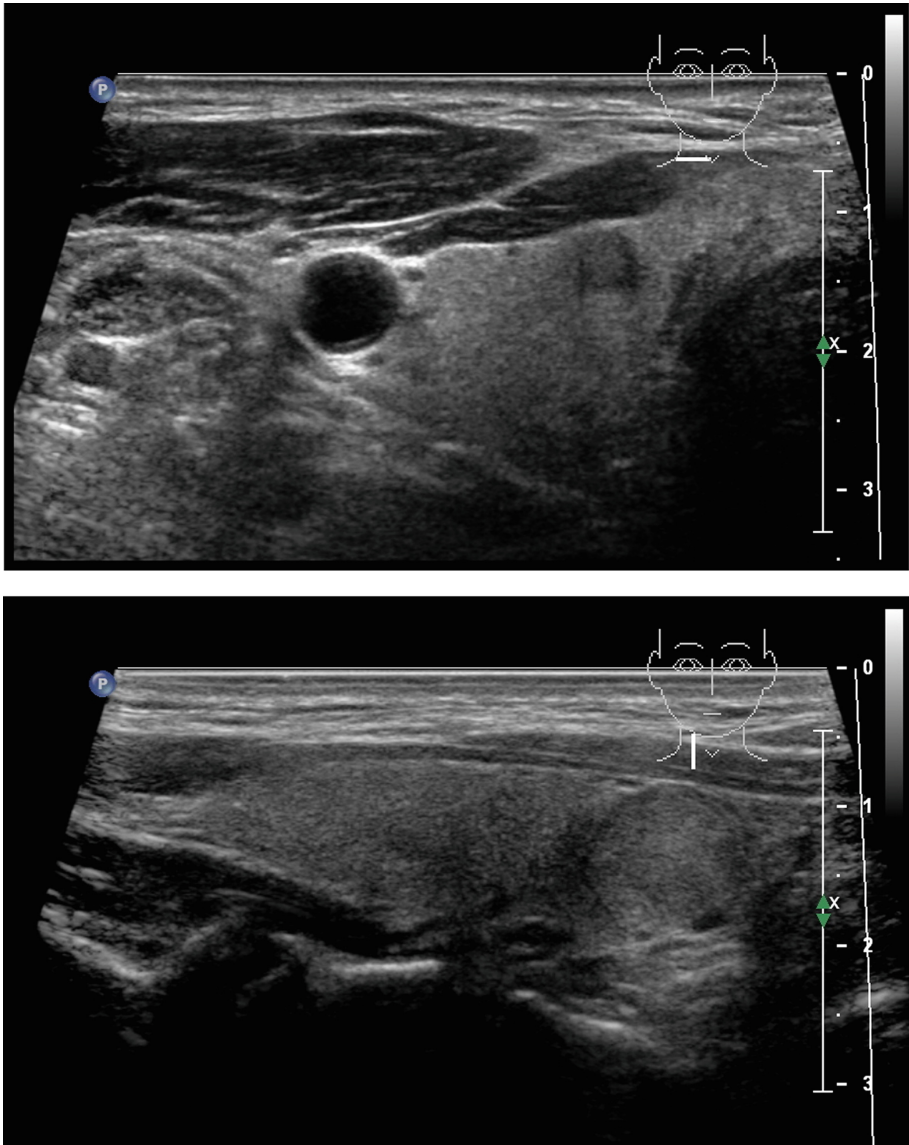
Fig. 2. Longitudinal (above) and transversal (below) section of thyroid gland tumor in US B-images

In contemporary endocrinology, diagnostic ultrasound imaging is used as a helpful tool to display thyroid gland and surrounding structures. Transversal and longitudinal sections with visible grayscale and measuring scale are used in our study, see an example in Fig. 2.

To get more information about principles and using high-resolution thyroid ultrasonography from the clinical point of view, you can read in [2]. In this study, there are used B-imaging, color-coded doppler ultrasonography and ultrasound elastography.

2   Input Image Data

Overall of 106 ultrasound B-images were analyzed within this study. In cooperation with an experienced endocrinologist, two groups were determined; images with malign tumor and images with benign tumor. In this image set, 46 images represent benign tumor and in 60 images a malignant tumor is displayed in marked ROI.

Firstly, the markers from taking of blood have been detected. The sonography is the second phase for all patients. Subsequently, selected patients are observed in long-time period. When a malignant tumor is detected, surgical intervention is inevitable as soon as possible. For this purpose, we have no anamnestic and/or demographic data about the patients; only information about tumor type within the image set.

In Fig. 3, an example of benign and malignant thyroid gland in ultrasound B-image, is displayed.

a benign tumor   **a malignant tumor**
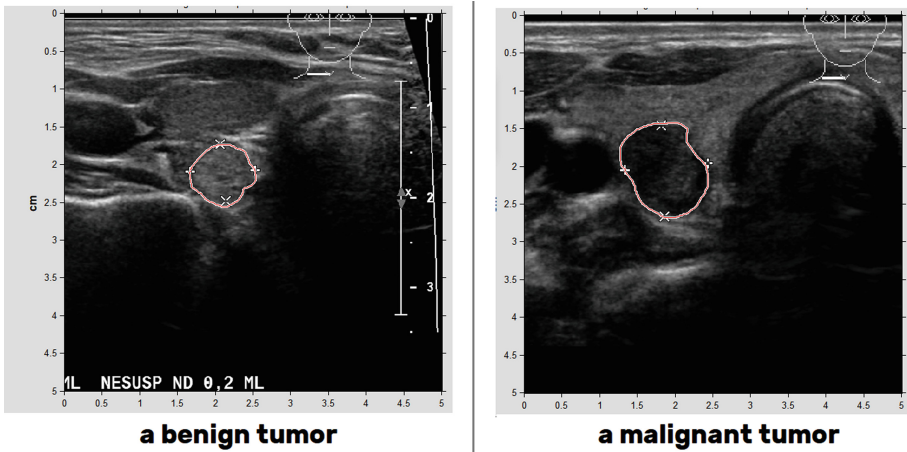
Fig. 3. A malignant tumor and a benign tumor of the thyroid gland in ultrasound B-image in longitudinal section

At first sight, it seems the echogenicity grade is significantly different. This idea is generally observed according to ultrasound examination of the thyroid tumors; generally hyperechoic are benign, commonly malignant tumors are hypoechoic or isoechoic [3].

In 2011, a study focused on segmentation and area measurement of the thyroid in ultrasound has been published [4]. This is a different approach to analysis thyroid tissue using ultrasound B-imaging including image enhancement algorithms. On the website Ultrasoundcases.info, there are examples of different benign and malignant thyroid tumors in ultrasound B-images [5] and much more.

3   Echo-Index Principle and Computation

The principle of ultrasound B-imaging is based on different echogenicity grade of the structures according to ultrasound beam reflection from the tissue. In our software we have developed an idea of Echo-Index value which should correspond with the echogenicity grade of the selected tissue. The idea of the Echo-Index is to express echogenicity grade of the structure by one numeric value.

Our software is based on computation of the area given by binary thresholding algorithm. More details about this core processing, see [6] and [7]. The Echo-Index was firstly used to analyze echogenicity grade of atherosclerotic plaques using B-MODE ultrasound imaging [7].

We have designed our algorithm which was first used in 2012. The first version has been developed to analysis of the echogenicity grade of the substantia nigra to predict probability of Parkinson's Disease according to increased echogenicity [8,9] what is considered as one of the visual markers in ultrasound B-images to Parkinson's Disease progress. Later, the algorithm has been improved with new features, e.g. using free-hand draw ROI.

The principle of the algorithm is based on binary thresholding in a selectable ROI. In US B-image, each pixel has an intensity value $H \in \langle 0; 255 \rangle$. Thus, the processing is based on thresholding for each H value and computing the remaining area after each thresholding step. Finally, all computed areas are summated and divided by 100 to obtain echogenicity index, called Echo-Index in our study.

In the software, to obtain Echo-Index, there are the following steps:

1. Loading an input image in native DICOM file or in bitmap format (like JPEG or PNG)
2. Select a window in which the examined ROI is visible (examined tissue; in this case, whole image size is selected)
3. Draw a free-hand closed ROI as in Fig. 3
4. Inside the ROI the area A_T is computed according to the threshold T:
   (a) The area is computed as the number of remaining pixels after binary thresholding
   (b) For each threshold T in the range of 0 to 255. The number of pixels is computed and finally is converted into real mm^2 according to displayed scale, i.e. the window size in step 2
5. Output values of the area for all 256 thresholds are represented in a graphical form (256 isolated values) as in Fig. 4.
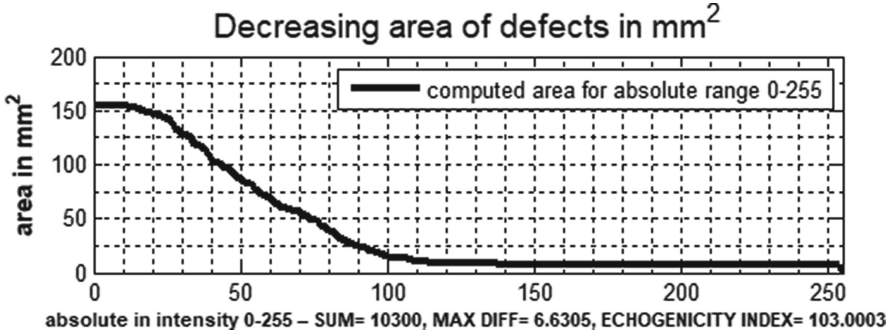
Fig. 4. Graphical representation of the descending area and computed Echo-Index

This is basic core algorithm designed originally for substantia nigra echogenity grade analysis using binary thresholding principle.

Let H is the brightness value of a pixel and T to be the threshold then A_T is the computed area for each threshold T in the range of $0 \leq T \leq 255$. The sum $AREASUM$ is computed as

$$AREASUM = \sum_{T=0}^{255} A_T \tag{1}$$

and this number is divided by 100 to obtain Echo-Index value

$$Echo - Index = \frac{AREASUM}{100} \tag{2}$$

Due to the principle of binary thresholding, for lower echogenicity grade, the Echo-Index should be lower and for higher echogenicity the Echo-Index should be higher. This is an assumption by the principle of binary thresholding. Thus, in the case of low echogenicity, for low T threshold the computed area should be very low and vice versa. In consequence of this principle, the sum for low echogenicity should be low and for high echogenic ROI the sum should be higher.

4   Analysis of Echo-Index Reproducibility and Changing According to Tumor Type

There are two main parts of this research; reproducibility assessment and analysis of Echo-Index changing in malignant and benign tumor.

4.1   General Reproducibility Assessment

In our last research, the reproducibility of the Echo-Index has been judged in US B-images of the atherosclerotic plaques [10,11], in which the plaques have been analyzed classified into 4 classes according to visual assessment in comparison

with computer analysis. Unfortunately, no reliable correlation between Echo-Index and visual evaluation has been found. However, general reproducibility between two independent observers has been evaluated as highly correlated so the level of agreement is satisfied. In this study focused on thyroid gland US images, the same reproducibility assessment is necessary for future clinical studies. In this part, all images were analyzed with no distinguishing malignant tumor and benign tumor.

In accordance with achieved results, Echo-Index can be considered as well reproducible parameter in general; similarly as for atherosclerotic plaques. The following Table 1 shows a sample of Echo-Index values for 35 randomly selected images.

To reproducibility assessment, achieved results shown that Echo-Index can be considered as well reproducible in general. One of the main descriptors is average absolute error between observers. The absolute error has been computed from difference between measurements in absolute value as difference between observers; there is not important if the difference is negative or positive, only absolute value is crucial. The absolute error in percent is given by

$$ERR_{abs} = |[(EI_{O1} - EI_{O2}/EI_{O1})] \times 100| \qquad (3)$$

where EI_{O1} and EI_{O2} are Echo-Index values from the first and from the second observer. The maximum error of 41.26% and the minimum error $< 0.5\%$ have been detected. The average absolute error of 14.88% has been detected from all 106 analyzed images.

Although in some measurements the error exceeds 35%, average absolute error does not exceed 15%. Also the correlation coefficient $r = 0.98$ can be considered as almost perfect level of agreement between observers.

4.2   Differences Between Malignant and Benign Tumor

Based on the results obtained, we can state that there is in principle a significant difference between Echo-Index values for benign tumor and for malignant tumor. It seems that Echo-Index could be useful tool to classify tumor type. However, to evaluate this assumption, more images should be analyzed by an experienced sonographer in endocrinology.

In the case of benign tumors, the average value of Echo-Index is 207.85 and in the case of malignant tumor images, average Echo-Index is 87.54, so 2.3× higher. In Fig. 5 there are six tumors with their computed Echo-Index.

In Table 2 there are 15 randomly selected Echo-Index values for benign tumors and 15 randomly selected Echo-Index values for malignant tumors. It seems, the values for malignant cases are lower in general.

Table 1. Randomly selected Echo-Index values obtained between two observers

| Echo-Index 1	Echo-Index 2	Absolute difference in %
212.69	169.68	20.22
202.91	179.3	11.64
313.45	263.93	15.80
99.03	75.45	23.81
113.3	81.40	28.16
137.94	96.68	29.91
116.46	98.02	15.83
174.46	161.27	7.56
140.54	117.48	16.41
80.00	78.58	1.78
78.28	59.35	24.18
69.66	58.28	16.34
59.58	48.61	18.41
326.12	357.42	9.60
315.89	339.63	7.52
57.53	73.87	28.40
63.51	48.62	23.45
55.59	52.13	6.22
62.14	63.55	2.27
83.11	71.89	13.50
50.14	52.72	5.15
54.09	56.53	4.51
55.43	60.07	8.37
61.82	60.95	1.41
79.85	66.16	17.14
66.07	67.02	1.44
149.88	159.55	6.45
92.54	100.23	8.31
115.42	90.03	22.00
86.52	76.02	12.14
72.70	51.68	28.91
55.66	50.98	8.41
53.38	51.42	3.67
53.78	41.67	22.52
76.16	66.98	12.05
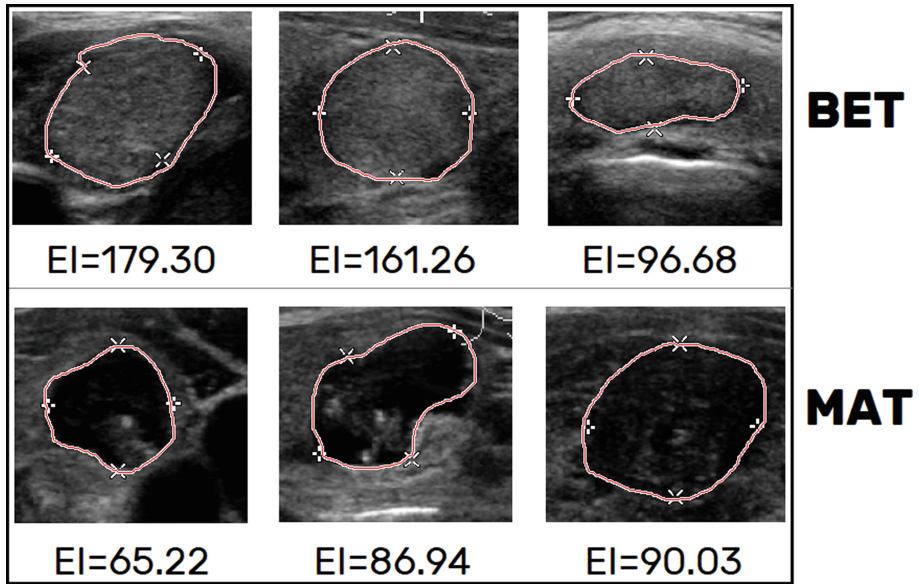
Fig. 5. Echo-Index for 3 benign tumors (BET) and 3 malignant tumors (MAT) in B in US B-images

Table 2. Example of 17 Echo-Index values for benign tumor (BET) and for malignant tumor (MAT)

BET Echo-Index	MAT Echo-Index
164.29	52.72
169.68	56.53
179.30	60.07
263.93	60.95
213.25	66.16
75.45	67.02
81.40	90.03
96.68	76.02
98.02	51.68
161.27	50.98
117.48	51.42
78.58	57.56
59.35	53.61
58.28	120.69
100.61	80.62
137.94	55.43
110.82	83.31

4.3   Known Limitations

Although the results meet idea about Echo-Index changing in accordance with
tumor type, there are two key limitation. ROI is selected by a free-hand shape
and the area is different for each image. Due to this limitation, a larger ROI
but with low echogenicity could has higher Echo-Index than smaller ROI with
higher echogenicity grade. Thus, Echo-Index in free-hand ROI is not simply
comparable; it is main difference in comparison with substantia nigra analysis,
in which the ROI has predefined shape and size so the initial value of the area
was equal in all images. The same limitation has been discussed in the case or
atherosclerotic plaques in our previous study, especially in our last paper, see
[12]. For example, in Fig. 6, two malignant tumors are displayed with different
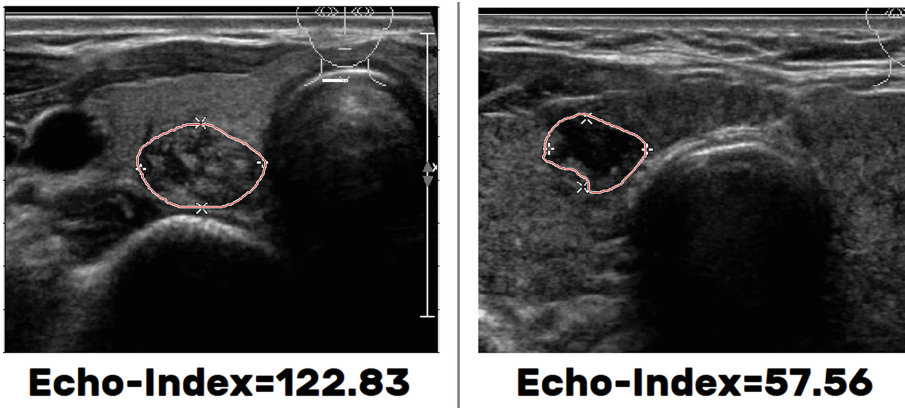Echo-Index values.

Echo-Index=122.83   **Echo-Index=57.56**

Fig. 6. Echo-Index difference for two malignant tumors with different ROI area

In the case of free-hand ROI, the size of the area is probably very important
factor to evaluate Echo-Index. In the case of static predefined ROI like for sub-
stantia nigra [4,5], the Echo-Index is better comparable because the initial area
of the ROI is equal in each image. The first clinical study using our algorithm
has been published in 2014 [7] to further development of the software including
new features like free-hand ROI using.

The second limitation is concerned about manual brightness enhancement.
Let consider when the brightness of the images is manually increased. To better
find the ROI the brightness adjustment could be helpful but the echogenicity
grade is visually higher so the Echo-Index should be higher too. Nevertheless,
if the brightness adjustment is constant for all images, Echo-Index should be
constantly higher. In other words, the boundary between malignant and benign
tumor will be constantly higher for all images.

4.4   A Tumor Rule-Based Classifier and Automatic ROI Detection

If the Echo-Index will be verified as reliable value to classification tumor types with required reliability (probably $\leq 90\%$), a software classifier could be created. In our previous study, a classifier for atherosclerotic plaques has been discussed, see [10,11]. Similarly, for the thyroid gland tumors, the classifier could be designed as IF-THEN rule-based system according to the Echo-Index value to estimate tumor type. The level of agreement of this conclusion with visual assessment and real diagnosis is closely related with settings of Echo-Index value ranges. Furthermore, this classifier could be adaptive (new and/or modified values). However, this system should be deeply tested by independent experienced users on many different images. To create the classifier based on Echo-Index IF-THEN rules, there is essential condition that all images must have the same default brightness level. If not, a special functionality to set brightness level ($+$ or $-$) to avoid false results. Echo-Index of the images which have different default brightness settings, should not be compared. In Fig. 7, there are two levels of the brightness for the same image, the Echo-Index can be different.
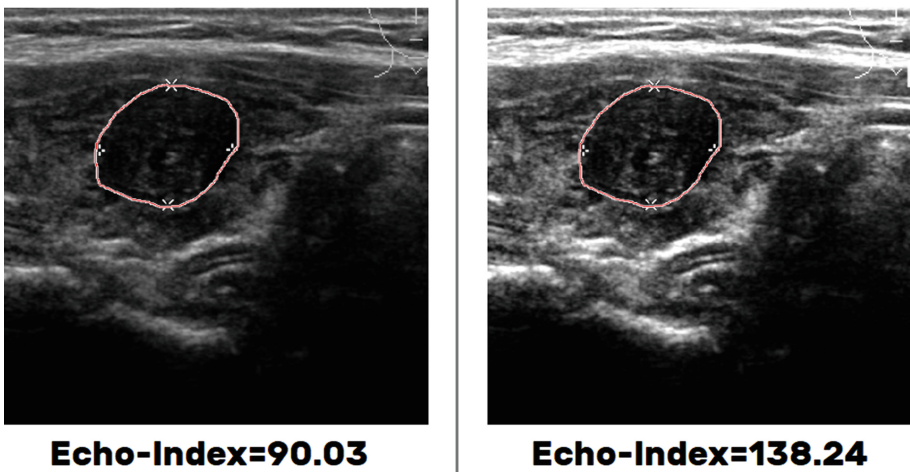

Echo-Index=90.03   **Echo-Index=138.24**

Fig. 7. Echo-Index: Original image (left) and with increased brightness $+50$ (right)

In this recent paper focused on atherosclerotic plaques, we have also discussed how to automatically select the plaque using a convolutional artificial neural network [13] and also using Active Contour Model (ACM) algorithm to detect border of the ROI. This experimental method has never been used in our software but there is a way to simplify ROI selection. ROI could be automatically selected instead of manual drawing the border. Within a discussion with an experienced sonographer in endocrinology, the idea about automatic ROI selection could be a useful solution to faster work. However, there is question about accuracy of

the selection in comparison with manual drawing. Similarly as for atherosclerotic plaques, we also have tried to apply ACM to detect tumor (ROI) border using ACM. Unfortunately, current result is really not usable, see an example in Fig. 8. To reliable results using ACM and/or convolutional neural network, long-term learning to set optimal ACM parameters (number of iterations, threshold level).
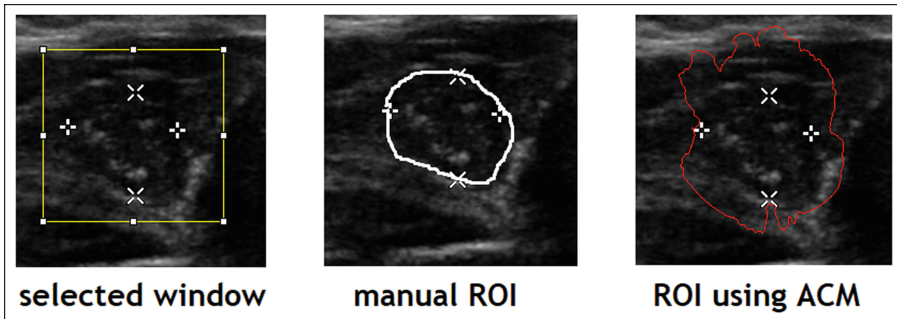

Fig. 8. Selected window, manual ROI drawn and ROI using iterative ACM

Although the experienced sonographer has the idea to have semi-automatic solution, this task is time-consuming due to complex structure of US B-images. It is a hard question if the development of this automatic ROI selection is priority for future work. Automatic segmentation techniques using artificial intelligence approach is desired in modern diagnostics. For inspiration, a study from 2019 shows how to use ACM with convolutional neural network to automatic finding breast tumor in ultrasound images, look at [15]. Recently, many papers focused on using automatic segmentation processing in modern radiology have been published.

5   Conclusions and Future Studies

Diagnostic ultrasound in contemporary endocrinology has an important role for early diagnostics, differential diagnostics and peri-operative using. Our paper is focused on using B-MODE ultrasound imaging based on our developed software tool. We have designed the Echo-Index value which should correlate with echogenicity grade of the tissue. This research is focused on analysis on echogenicity of thyroid gland tumors. Totally of 106 images were processed in our software and output numerical data were analyzed in a spreadsheet.

There are two main parts of this study. In the first one, the reproducibility of Echo-Index is judged according to results from two independent, in sonography non-experienced observers. In this phase, the level of agreement is almost perfect; correlation coefficient $r = 0.98$ and average difference (error) does not exceed 15%.

The second part is focused on analysis if the Echo-Index is different according to visual assessment of the echogenicity grade. We have analyzed 46 images with benign tumor and 60 images with malignant tumor. In general, average Echo-Index for benign tumors is $2.3\times$ lower than for malignant tumors. So, the Echo-index could be useful to distinguish benign and malignant tumors. However, there is one important limitation. To Echo-Index computation, the free-hand ROI is used and small highly echogenic area can has lower Echo-Index than larger ROI with low echogenic (or hypoechoic) echogenicity grade.

This is an experimental study focused on Echo-Index analysis from technical point of view. The echogenicity grade should be different between malignant and benign tumors on the basis on of experience in sonography. It seems, the Echo-Index could correlates with the echogenicity according to tumor class.

To publish future clinical studies, an experienced sonographer in endocrinology must prove that the Echo-Index really correlate with echogenicity grade to distinguish malignant from benign tumors. If the level of agreement exceeds 90%, the Echo-Index could be useful parameter in early diagnostic of thyroid gland tumors using ultrasound B-imaging.

Finally, two questions arose. The first one about future development simple IF-THEN classifier based on Echo-Index values. The classifier could classify tumors based on Echo-Index value. The second question has been asked by the experienced sonographer to create a semi-automatic solution including automatic ROI selection; finding the boundary of the tumor. In our previous study devoted to atherosclerotic plaques, we have discussed using a convolutional neural network and Active Contour Algorithm. Unfortunately, learning is really time-consuming task and optimal settings of ACM parameters must be found due to complexity US B-images. Athough, it could be one part of the future development to speedup using software.

References

1. Murray, G.R.: Diseases of Thyroid Gland, 194p. Hard Press Publishing (2012). ISBN:978-1407678511
2. Chaudhary, V., Bano, S.: Thyroid ultrasound. Indian J. Endocrinol. Metab. **17**(2), 219–227 (2013)
3. Ultrasoundpaedia.com. https://ultrasoundpaedia.com/thyroid-pathology
4. Mahmood, H.M., Rusli, A.H.: Segmentation and area measurement for thyroid ultrasound image. Int. J. Sci. Eng. Res. **2**(12) (2011). ISSN:2229-5718
5. Ultrasoundcases.info. https://www.ultrasoundcases.info/cases/head-and-neck/thyroid-gland

6. Školoudík, D., Herzig, R., Blahuta, J., Langová, K.: Comparison of automatic and manual transcranial sonographic morphometric measurement of the substantia Nigra. Neurology **80**(7 Supplement) (2013)

7. Blahuta, J., Čermák, P., Soukup, T., Večerek, M.: A Reproducible Application to B-MODE Transcranial Ultrasound Based on Echogenicity Evaluation Analysis in Defined Area of Interest, pp. 393–400. IEEE Press, Tunisia (2014). ISBN:978-1-4799-5934-4

8. Blahuta, J., Bártová, P., Jelínková, M., Čermák, P., Herzig, R., Školoudík, D.: A new program for highly reproducible automatic evaluation of the substantia Nigra from transcranial sonographic images. Biomed. Pap. **158**(4), 621–627 (2014). https://doi.org/10.5507/bp.2013.029

9. Blahuta, J., Čermák, P., Dušek, Z., Novák, D., Večerek, M.: Statistical Deviations and Characteristics of Echogenicity Level in Substantia Nigra Due to Different Contrast of Structures in B-Images, pp. 100–105. WSEAS Press, Brasov (2014). ISBN:978-960-474-387-2

10. Blahuta, J., Soukup, T. Čermák, P.: How to detect and analyze atherosclerotic plaques in B-MODE ultrasound images: a pilot study of reproducibility of computer analysis. In: Dichev, C., Agre, G. (eds.) Artificial Intelligence: Methodology, Systems, and Applications. AIMSA 2016. Lecture Notes in Computer Science, Vol. 9883, pp. 360–363. Springer, Cham (2016). https://doi.org/10.1007/978-3-319-44748-3_37

11. Blahuta, J., Soukup, T., Sosík, P.: Approach to automatic segmentation of atherosclerotic plaque in B-images using active contour algorithm adapted by convolutional neural network to echogenicity index computation. In: CEUR Workshop Proceedings, vol. 2718, pp. 223–229 (2020). ISSN:1613-0073

12. Blahuta, J., Soukup, T., Pavlík, L.: The classification of the progression of atherosclerotic plaques in B-images between computer image analysis using echogenicity index and visual assessment. In: Proceeding of SGEM 2020, pp. 341–348 (2020). ISSN:1314-2704

13. Yamashita, R., Nishio, M., Do, R.K.G., Togashi, K.: Convolutional neural networks: an overview and application in radiology. Insights Imag. **9**(4), 611–629 (2018). https://doi.org/10.1007/s13244-018-0639-9

14. Hu, Y., Guo, Y., Wang, Y., Yu, J., Li, J., Zhou, S., Chang, C.: Automatic tumor segmentation in breast ultrasound images using a dilated fully convolutional network combined with an active contour model. Med. Phys. **46**(1), 215–228 (2019). https://doi.org/10.1002/mp.13268

Initial Prototype of Low-Cost Stool Monitoring System for Early Detection of Diseases

José Luis López-Ruiz⬤, David Díaz-Jiménez⬤, Alicia Montoro-Lendínez(✉)⬤, and Macarena Espinilla⬤

Department of Computer Science, University of Jaén, 23071 Jaén, Spain
{llopez,mestevez}@ujaen.es {aml00074,ddj00003}@red.ujaen.es

Abstract. Even though cancer is one of the most common diseases in the 21st century, early detection tests are still expensive and invasive. In this work, a initial stool monitoring prototype for the early detection of this disease is proposed. The emerging and growing concept of Internet of Things has been considered for the implementation of this prototype. So, MOX (Metal OXide, metal-oxide-semiconductor type) sensors to detect volatile organic compounds (VOCs) and a thermal camera are integrated into different development boards, which send the collected data of stool to monitoring it by means of an IoT platform. With the result of this initial prototype, a proof of concept has been obtained for testing with cancer experts.

Keywords: Stool monitoring system · Volatile organic compounds (VOCs) · MOX sensors · Thermal camera · Internet of Things

1 Introduction

Colorectal cancer (CRC) is the third most common tumour worldwide (1.93 million cases) and was the second most common cause of death in 2020 (935,000 deaths). Early detection and early treatment have been shown to reduce cancer mortality. To achieve this, population-based screening is carried out to identify people who may have the disease on the basis of age and risk factors. Some of these risk factors include unhealthy diet, smoking, physical inactivity and obesity [24].

However, the most common screening tests currently available for CRC pose significant disadvantages, as they are invasive, painful, costly for the healthcare system and, in some cases, require patient preparation and sedation [23,25].

Scientific evidence has shown the power of canine olfactory systems to detect volatile organic compounds (VOCs), which differ in patients suffering from CRC and healthy patients [19]. Due to dogs' ability to identify VOCs, they can detect tumours with a high degree of accuracy and even at early stages. These VOCs differ in each person, making up their olfactory fingerprint. They can be detected

through breath or intestinal gas and have been analysed and found to be a tool of great potential, not only for the diagnosis of CRC but also for diabetes or Alzheimer's disease, among others [4,5].

Therefore, the analysis of gases from both the breath and the stool or changes in stool temperature can provide evidence to help to design a system capable of early detection of diseases such as CRC, with many advantages over the early detection tests which have been used to date [16].

An analysis of the low-cost systems currently available for population screening has shown that the main methods for early detection are fecal occult blood test (FOBT), colonoscopy, sigmoidoscopy, faecal immunochemical test (FIT), stool DNA testing and computed tomography colonography [3]. FOBT is the test of choice because of its lower cost compared to other screening tests. However, it requires good infrastructure, a large amount of material and human resources (administrative staff, nurses, digestive tract specialists, anaesthesia, preventive medicine, etc.). All this has a high cost for the healthcare system [18]. In recent years, the Internet of Things (IoT) has emerged as a new paradigm which can overcome these limitations and which has been of great use to the healthcare sector [1,12,13,20]. Among the many benefits that this paradigm brings to the healthcare sector are cost reduction and real-time monitoring.

This work proposes an initial system prototype based on the IoT paradigm to monitor the stool of patients at home with the aim of being the first prototype to detect anomalies. The initial system prototype will be composed of different development boards, sensors and actuators which will be placed on the toilet lid to collect data of interest related to gases and thermal images. The data collected by the sensors will be sent by wireless means to a central sink node which will store the information in a cloud server for persistence and send the information to an IoT platform for display. The main advantages of the proposal are that it is small scale, low-cost and non-invasive, with low power consumption.

The structure of this paper is as follows. Section 2 reviews the works related to gas and temperature monitoring for the early detection of diseases and low-cost monitoring systems for disease prevention or diagnosis. Section 3 presents the architecture of the system, describing all its components and the information flows within the system. Section 4 sets out the information processing proposed for the collection of sensor data, persistence in the cloud server and data display on the IoT platform. Finally, Sect. 5 presents the conclusions drawn and future lines of work.

2   Related Works

This section reviews the literature on the use of devices, sensors and intelligent systems to monitor gases and temperature for the early detection or diagnosis of diseases. To this end, firstly, we will review works related to devices with gas and temperature monitoring sensors for the early detection of diseases and, subsequently, systems which use sensors of this nature.

2.1 Gas and Temperature Sensor Devices for Early Detection of Diseases

The literature has shown the importance of gas sampling and stool temperature monitoring as fundamental functions to be implemented in our IoT system.

Regarding devices that monitor gases, the work presented by Malagú et al. [11] gives clues on the detection of VOCs. They use a series of MOX (Metal OXide, metal-oxide-semiconductor type) sensors which can detect VOCs even in conditions of low and high humidity and in low concentrations.

Benara et al. [2] show the first steps taken to manufacture a sensor capable of detecting methane (CH_4) at low concentrations. Analysis of this gas could be useful for identifying patients suffering from CRC. One disadvantage would be related to breath samples, which may require previous drying.

Movilla-Quesada et al. and Hofstetter et al. [7,14] present the use of MQ sensors for the collection of measurements of different types of gases in different projects such as the analysis of greenhouse gas emissions in asphalt mixtures with recycled materials or for the analysis of ammonia concentrations in the environment and its possible effects on poultry.

In terms of temperature monitoring, thermal cameras are an excellent option for the detection of a multitude of health-related problems [8,9], as well as being a good low-cost option [17]. Kaczmarek et al. [8] review the use of thermal cameras in medical applications such as analysing the severity of a body burn and its healing or the healing of a wound after cardiac surgery. All this has been validated by obtaining thermal camera images in different clinical studies.

Lahiri et al. [9] review medical applications where the successful use of thermal cameras has been proven for the diagnosis of breast cancer or diabetes related to vascular disorders as well as applications in dentistry, for example, for the determination of the common cracked tooth syndrome, which is very complicated to diagnose. Another use is the detection of fever, the most common symptom of COVID-19, with the aim of preventing massive spread of the virus.

2.2 Low-Cost Monitoring Systems for Prevention or Diagnosis of Diseases

In view of the type of commercial sensors which could be compatible with our purpose, a review of the corresponding literature has been carried out. Some of the most prominent examples are shown below.

In the literature, it is quite common to find the use of E-Nose technology for the design of disease prevention or diagnosis systems. This type of E-Nose technology simply consists of an array of sensors, usually MOX type sensors, with the ability to detect different types of VOCs. Liu et al. [10] designed a diabetes diagnosis system, from which the breath of participants was analysed to decide whether they were suffering from diabetes.

The analysis of VOCs for the early detection of cancer has also been studied by Thriumani et al. [21] to try to detected lung cancer based on an already marketed E-Nose and using classifiers for machine learning. To do this, samples

of cancerous cells from both breast and lung cancer were cultivated and analysed by the E-Nose together with healthy cells, showing that it is capable of identifying a high percentage of healthy or cancerous cell tissue.

Finally, given the recent coronavirus disease 2019 (COVID-19), work has been carried out on monitoring systems in this highly topical area. Ullah et al. [22] try to monitor the state of health of a patient with COVID-19 and also check whether their quarantine is being carried out correctly. This is done through electrocardiograms (ECG), blood oxygen measurements (SpO_2), body temperature, respiration sensors, accelerometers and gyroscopes. The collected data is sent to a cloud server where it is analysed using machine learning techniques and previous historical data. In addition, through a web application, they displayed the data analysed by their system and showed it to professionals and even to the patients themselves.

Thanks to the literature, it was possible to gain insights such as what type of VOCs are related to CRC, that MOX-type sensors are the most suitable for detecting VOCs and that VOCs from the intestine do not need a previous preparation phase, which are fundamental aspects for the design of our IoT system.

3   Architecture of the System

In this section, first of all, the architecture of our initial system prototype is presented, which will be composed of the different development boards, sensors and actuators in charge of collecting the key data (gases and thermal images) of the depositions from the toilet lid. Subsequently, we show how this data has been serialised and transmitted wirelessly to a central sink node, which will store the data in a cloud server for data persistence while sending the information to the IoT platform for visualisation.

In this overview in Fig. 1, it can be seen that the initial system prototype is made up of two very different parts: hardware and software. Both are responsible for ensuring that the system meets our key objectives.

The hardware is made up of the following elements:

- **Lolin32 Lite (ESP32) development board:** The main function of this board is to be the master of the NodeMcu V3 and to send the signal which interrupts the sleep mode (deep sleep mode) of the NodeMcu V3, thus reducing consumption considerably, as well as to process the alarm signal of the passive buzzer. This module already incorporates Wi-Fi, which will be very useful for transmitting the data collected (referring to user interaction with respect to the start and end of sample collection) without the need to purchase an external module, simplifying the process of building the initial system prototype. Another advantage is its Serial-USB converter, which allows the board to be connected directly to the computer for programming.
- **NodeMcu V3 (ESP8266) development board:** The slave. This development board model was chosen due to the need to supply 5 V to the gas sensor and it has a 5V output pin. As well as its small size, like the previous
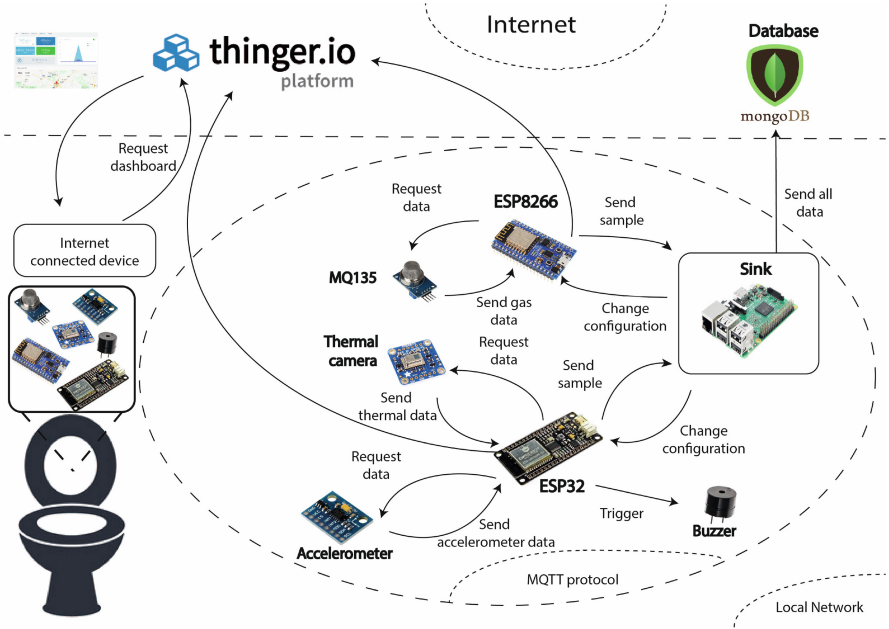
Fig. 1. Initial system prototype diagram

board, it incorporates Wi-Fi and a Serial-USB converter which allows it to be powered and programmed. The Wi-Fi feature has been a determining factor in our decision to choose this model among all the possibilities offered by the market.

– **Raspberry Pi 3 Model B+ development board:** Its main advantage is its significant computational capacity for its small size. Its purpose is to manage the data flow between the ESP32 and ESP8266 boards (the so-called central sink node).

– **Adafruit AMG8833 IR thermal camera sensor:** This sensor is formed by an 8×8 matrix of infrared thermal sensors, providing a low-resolution image of the deposition made by the monitored person. Its low resolution (8×8 pixels for a total of 64 pixels) could be thought to be a limiting factor; however, in our initial system prototype, given the nature of the images to be captured, it is actually an advantage as it provides anonymity, protecting the privacy of the monitored individual. Additionally, this type of infrared image capture device currently has a high cost, which tends to increase proportionally as the resolution increases. Given its limited resolution, the price of this sensor has been significantly reduced.

– **Accelerometer sensor MMA8451:** This sensor detects movement, tilt and orientation. It was included in the initial system prototype to determine when the person to be monitored is ready to use the toilet. Its purpose is to determine the start and end of the action in order to increase sample

collection and determine the time elapsed, giving the alarm signal with the
passive buzzer.
– **MQ2 gas sensor:** It measures the concentration of different gases present in
the air. It is a MOX sensor and can detect Liquefied Petroleum Gas (LPG),
smoke, alcohol, propane, hydrogen, methane and carbon monoxide, making
it useful for collecting gas samples in depositions. One of the major disad-
vantages of using this sensor was its power consumption, which is 150 mAh.
Although this may seem small considering that it is a battery-powered sys-
tem, this is a factor to be taken into account.
– **MQ135 gas sensor:** Allows detection of ammonia, benzene and alcohol gas,
but is also sensitive to smoke and other toxic gases.
– **Passive buzzer:** This actuator, which transforms electrical signals into
sound waves, has been used to alert the monitored person that the data
collection is complete and the toilet can now be flushed.

The software is made up of the following elements:

– **Visual Studio Code:** This is the chosen environment to program the ESP32
and ESP8266 development boards, as it offers more advanced functionalities
than the common Arduino IDE and can be complemented by adding exten-
sions. In our case, we have added C++, Python and PlatformIO IDE.
– **MongoDB:** This NoQSL database is usually used for IoT data management,
the different entities have been stored in it. This database provides a number
of advantages: it allows the creation of indexes to speed up searches, which
is very useful when the volume of data is significantly large, it has tools for
automatic data analysis, due to its focus on IoT, and thanks to the fact that
it is a document-based data model, it allows the definition of structures that
group different fields.
– **Thinger.io:** IoT platform used to display the data collection in real time,
through visual elements such as line graphs, among others. Although it is a
commercial tool for which we must purchase a licence, the free version that
allows us to connect up to two devices (gas sensor MQ2 and MQ135) has
been more than enough in this prototype.

3.1   Data Transmission

The protocol used is the Message Queuing Telemetry Transport (MQTT), a
network protocol based on publication and subscription that is ideal for low-
resource devices such as our development boards. To implement this protocol in
our initial system prototype we have used a library developed for that purpose
[15]. However, it has disadvantages such as not allowing the configuration of
access control to the server through certificates or the Quality of Service (QoS)
of the messages. The format of the data packets exchanged via MQTT contains:

– An initial part found in all types, called fixed header. Among the information
it can provide is the QoS, the type of message or the number of bytes of the
remaining packet.

– A variable header only present in some MQTT packets.
– A payload, also optional, of variable length and with all the information to be sent.

Using this protocol, the development boards publish the data collected by the sensors and the Raspberry Pi is in charge of subscribing to access this data.

3.2 Data Serialisation

The device will have to transmit the collected data to an external platform via Wi-Fi connection. By serialising the objects within the memory to convert complex structures into text strings, it is possible to send all the data in a single message, considerably reducing the subsequent processing of the data and therefore reducing the load on the MQTT server. The Java Script Object Notation (JSON) text format has been used, which provides multiple advantages: it is easy to understand, lighter in transmissions, and has high processing speed.

4 Information Processing

This section presents the proposal for processing the information in our initial system prototype. For this, firstly, the data collection process is described, followed by how this data is stored for persistence, and finally, how it is displayed using an IoT platform.

4.1 Data Collection

Having broadly discussed the protocols, connections and data format, the steps to be followed in collecting the data are:

– When the monitored person opens the toilet lid, the ESP32 (master) sends a signal to the ESP8266 (slave) for connection to the Wi-Fi network, the MQTT server and the Thinger platform.
– Data from the gas sensor is collected and sent until the ESP32 sends an end of action signal to the ESP8266 when the monitored person lowers the toilet lid.
– The ESP8266 disconnects and enters deep sleep mode until the ESP32 restarts the cycle, returning to step one.

Another mode of operation with programmed data collection regardless of the person to be monitored has also been implemented. This operating mode starts when a predetermined time is reached, as long as the ESP8266 board is in deep sleep mode. Then, an image of the values detected by the gas sensor is captured. This sample collection is performed every 60 s, although this parameter can be modified in the configuration file. This mode of operation is required to regularly monitor the values under "normal" and "abnormal" conditions. An "abnormal"

Fig. 2. Final prototype

condition could be the use of cleaning agents in the toilet, whose gases could persist after use and thus significantly alter the actual values (Fig. 2).

The sensors used (MQ2 and MQ135) have required the use of a library for their implementation [6] to find out which gases play the most relevant role in this type of detection. Obtaining measurements from this type of sensor is very simple, but obtaining accurate measurements requires preparation, taking into account the preheating time, which can range from minutes to hours.

Concerning the MQ135 sensor, it must be taken into account that the CO2 measurements in normal conditions are 400 parts per million (ppm) and this is the baseline for our reading value collected in the ADC (Analog-to-Digital Converter) of the ESP8266, so in the library it is always increased by 400 to produce the real value.

To avoid applying any type of formula, the sensor data can be read in raw values. This is what we have done in this project, carrying out a study to identify the threshold that detects whether the user is making a deposition or not.

These collected values require further processing, taking into account that the ESP8266 has a resolution of 10 bits, and that the voltage provided by the sensor will be a value between 0–1024. If we want to obtain the number of ppm, a simple conversion is carried out, as the minimum to be detected is 300 ppm and the maximum is 10000 ppm.

Regarding the number of samples to be collected with the sensor, intervals of one second have been estimated to be the most appropriate. However, this parameter can be modified in the configuration file. It should also be taken into account that measurements are collected every second even if the user is not using the toilet.

The temperature data obtained from the thermal camera, on an 8×8 matrix, was used to perform the analysis. It was then transformed into images for debugging to check that the camera was working correctly. To transform temperature data into images, a simple procedure has been followed whereby the minimum temperature value is associated with a colour value and the maximum

temperature value is associated with another colour, along with an intermediate colour scale for intermediate temperatures.

4.2 Database

As mentioned previously, the database chosen is MongoDB. Four unrelated entities were used to store the information. As for the entities, we have selected thermal data, data for the opening of the lid, values obtained by the gas sensor (raw readings) and finally, test results with the MQ135 and MQ2 sensors. These are sent using JSON format and each data collection will have its own structure. However, they will all have the following fields in common in the structure: an identifier (id), the name of the sensor, the measurement and the date of collection. Table 1 shows some of them.

Table 1. Data collection for the entity THERMAL DATA and USE DATA.

Thermal data	Description	Variable type
Id	Unique identifier	ObjectId
Sensor	Sensor identifier	String
Thermal array	List of temperature values collected by the sensor	Array
Img id	Image sequence number	Integer
Control data	Indicates whether the data is a control sample	Boolean
Date	Date and time in international format	ISODate
Use data	Description	Variable type
Id	Unique identifier	ObjectId
Sensor	Sensor identifier	String
Toilet id	Indicates whether the toilet lid has been opened or closed	String
Minutes	Number of minutes the lid has been open	Integer
Seconds	Number of seconds remaining	Integer
Date	Date and time in international format	ISODate

4.3 Data Visualisation as Decision Support for Detection

As discussed in previous sections, the IoT platform that has been chosen is Thinger.io. Figure 3 shows the dashboard created to display the data on Thinger.io. This dashboard is composed of three line graphs: the first one shows the history of maximum and minimum temperatures recorded by the thermal camera, the second one shows the history of values collected by the gas sensor and a third one represents the toilet usage log. Two meters have also been included, one to show the last raw value obtained by the gas sensor and the other to show it in ppm units.

Fig. 3. Dashboard

5   Conclusions

In this work, we have proposed a first prototype of a system to monitor from home the stool of patients with the aim of creating a first prototype to detect anomalies. To do this, firstly, the architecture of the system has been presented, consisting of the development boards, ESP32 and ESP8266 (both located on the lid of the toilet and responsible for collecting data), as well as Raspberry Pi 3 (the central sink node), the MQ2 and MQ135 sensors, the thermal camera and the passive buzzer actuator. Subsequently, the protocol for wireless data transmission was presented, where limitations were found as the ESP32 has random wireless connection losses due to an error in the libraries to establish the connection and the MQTT broker slows down if the time between sample collection decreases. Finally, the processing carried out from the data collection has been proposed for its subsequent storage in the MongoDB database, which provides data persistence, and visualisation on the IoT platform Thinger.io.

This prototype stool gas and temperature monitoring system aims to be a first step in the early detection of cancer. It is clear that the creation of such low-cost IoT systems to monitor VOCs not only in stool but also in exhaled air samples is a great step forward in this area and could reduce the mortality rate of this type of tumours, which, if detected early, are more likely to be treated successfully. In addition, it is an example of the benefits of bringing IoT and health together. Our future work focuses, on the one hand, on testing the initial prototype with cancer experts with the aim of a clinical trial, taking into account

the variability of the population (control group) and the different places where it will be performed (clinic, laboratory or home), and on the other hand, on the challenge of finding sensors with greater range, sensitivity and accuracy to improve the current prototype.

References

1. Albín-Rodríguez, A.P., Ricoy-Cano, A.J., de-la Fuente-Robles, Y.M., Espinilla-Estévez, M.: Fuzzy protoform for hyperactive behaviour detection based on commercial devices. Int. J. Environ. Res. Publ. Health **17**(18), 6752 (2020). https://doi.org/10.3390/IJERPH17186752
2. Benara, K., et al.: Fabrication of a sensor to detect low concentration of methane: a bio-marker of colon cancer. In: 2016 IEEE Annual India Conference (INDICON), pp. 1–4. IEEE (2016). https://doi.org/10.1109/INDICON.2016.7838944
3. Bénard, F., Barkun, A.N., Martel, M., von Renteln, D.: Systematic review of colorectal cancer screening guidelines for average-risk adults: summarizing the current global recommendations. World J. Gastroenterol. **24**(1), 124 (2018). https://doi.org/10.3748/wjg.v24.i1.124
4. Boots, A.W., van Berkel, J.J.B.N., Dallinga, J.W., Smolinska, A., Wouters, E.F., van Schooten, F.J.: The versatile use of exhaled volatile organic compounds in human health and disease. J. Breath Res. **6**(2), 027108 (2012). https://doi.org/10.1088/1752-7155/6/2/027108
5. Buszewski, B., Kęsy, M., Ligor, T., Amann, A.: Human exhaled air analytics: biomarkers of diseases. Biomed. Chromatogr. **21**(6), 553–566 (2007). https://doi.org/10.1002/BMC.835
6. Califa Urquiza, M.A., Contreras Contreras, G., Carrillo Amado, Y.R.: Mqsensorslib v1.03. https://zenodo.org/record/3384301#.YcX3NWjMLIU. Accessed 09 Mar 2022
7. Hofstetter, D., Fabian, E., Lorenzoni, A.G.: Ammonia generation system for poultry health research using Arduino. Sensors **21**(19), 6664 (2021). https://doi.org/10.3390/s21196664
8. Kaczmarek, M., Nowakowski, A.: Active IR-thermal imaging in medicine. J. Nondestruct. Eval. **35**(1), 1–16 (2016). https://doi.org/10.1007/s10921-016-0335-y
9. Lahiri, B., Bagavathiappan, S., Jayakumar, T., Philip, J.: Medical applications of infrared thermography: a review. Infrared Phys. Technol. **55**(4), 221–235 (2012). https://doi.org/10.1016/J.INFRARED.2012.03.007
10. Liu, A., Tian, Y.: Design and implementation of oral odor detection system for diabetic patients. Chem. Eng. Trans. **68**, 385–390 (2018). https://doi.org/10.3303/CET1868065
11. Malagù, C., et al.: Chemoresistive gas sensors for the detection of colorectal cancer biomarkers. Sensors **14**(10), 18982–18992 (2014). https://doi.org/10.3390/S141018982
12. Medina, J., Espinilla, M., García-Fernández, Á., Martínez, L.: Intelligent multi-dose medication controller for fever: From wearable devices to remote dispensers. Comput. Electr. Eng. **65**, 400–412 (2018). https://doi.org/10.1016/j.compeleceng.2017.03.012
13. Medina Quero, J., Fernandez Olmo, M.R., Pelaez Aguilera, M.D., Espinilla Estevez, M.: Real-time monitoring in home-based cardiac rehabilitation using wrist-worn heart rate devices. Sensors **17**(12), 2892 (2017). https://doi.org/10.3390/s17122892

14. Movilla Quesada, D., Lagos Varas, M., Raposeiras, A.C., Muñoz Cáceres, O., Andrés Valeri, V.C., Aguilar Vidal, C.: Analysis of greenhouse gas emissions and the environmental impact of the production of asphalt mixes modified with recycled materials. Sustainability **13**(14), 8081 (2021). https://doi.org/10.3390/SU13148081

15. O'Leary, N.: Arduino client for mqtt. https://pubsubclient.knolleary.net/. Accessed 09 Mar 2022

16. Politi, L., et al.: Discriminant profiles of volatile compounds in the alveolar air of patients with squamous cell lung cancer, lung adenocarcinoma or colon cancer. Molecules **26**(3), 550 (2021). https://doi.org/10.3390/MOLECULES26030550

17. Rai, M., Maity, T., Yadav, R.: Thermal imaging system and its real time applications: a survey. J. Eng. Technol. **6**(2), 290–303 (2017)

18. van Rossum, L.G., et al.: Colorectal cancer screening comparing no screening, immunochemical and guaiac fecal occult blood tests: a cost-effectiveness analysis. Int. J. Cancer **128**(8), 1908–1917 (2011). https://doi.org/10.1002/ijc.25530

19. Schoon, G.A.A., De Jonge, D., Hilverink, P.: How dogs learn to detect colon cancer-optimizing the use of training aids. J. Veter. Behav. **35**, 38–44 (2020). https://doi.org/10.1016/J.JVEB.2019.10.006

20. Sengan, S., Khalaf, O.I., Priyadarsini, S., Sharma, D.K., Amarendra, K., Hamad, A.A.: Smart healthcare security device on medical IOT using raspberry pi. Int. J. Reliab. Qual. E-Healthc. **11**(3), 1–11 (2022). https://doi.org/10.4018/ijrqeh.289177

21. Thriumani, R., et al.: A preliminary study on in-vitro lung cancer detection using e-nose technology. In: 2014 IEEE International Conference on Control System, Computing and Engineering (ICCSCE 2014), pp. 601–605. IEEE (2014). https://doi.org/10.1109/ICCSCE.2014.7072789

22. Ullah, F., Haq, H.U., Khan, J., Safeer, A.A., Asif, U., Lee, S.: Wearable IOTs and geo-fencing based framework for covid-19 remote patient health monitoring and quarantine management to control the pandemic. Electronics **10**(16), 2035 (2021). https://doi.org/10.3390/ELECTRONICS10162035

23. Winawer, S., Zauber, A., Homn, E.: Prevention of colorectal cancer by colonoscopic polypectomy. New Engl. J. Med. **329**(27), 329 (1977). https://doi.org/10.1056/NEJM199312303292701

24. World Health Organization: Cancer. https://www.who.int/news-room/fact-sheets/detail/cancer (2022). Accessed 09 Mar 2022

25. Zavoral, M., et al.: Colorectal cancer screening in Europe. World J. Gastroenterol. **15**(47), 5907 (2009). https://doi.org/10.3748/WJG.15.5907

Cerebral Activation in Subjects with Developmental Coordination Disorder: A Pilot Study with PET Imaging

Marie Farmer[1], Bernard Echenne[2], and M'hamed Bentourkia[1(✉)]

[1] Department of Nuclear Medicine and Radiobiology, Faculty of Medicine and Health Sciences, 3001, 12th Avenue North, Sherbrooke, QC J1H5N4, Canada
Mhamed.Bentourkia@USherbrooke.ca

[2] Service de Neurologie Pédiatrique, Université de Montpellier I, Montpellier, France

Abstract. Background: Developmental coordination disorder (DCD) is a neurodevelopmental disorder encountered in about 6% of children at school age. DCD mostly affects motor task automatization and it persists in adulthood. Several brain structures were supposed to be involved in DCD pathophysiology. Quantitative imaging techniques have the potential to investigate these connected brain regions associated with motor tasks. Methods: In the present work, we studied with 18F-fluorodeoxyglucose (18F-FDG) and positron emission tomography imaging (PET) brain metabolism in subjects with DCD versus control in resting state and during repetitive and standardized finger movements of the left non-dominant hand. We analyzed 42 brain structures in the right and left hemispheres and the data were statistically assessed by the Ward clustering approach to detect the activated/non-activated/deactivated brain regions. Results: The images obtained with PET clearly showed different uptake of 18F-FDG in subjects with DCD with respect to control subjects. The statistics showed less brain regions activated and more deactivated in subjects with DCD than in control. Among other differences, the right thalamus was activated in DCD subjects as both caudate nuclei were deactivated for a possible compensation for basal ganglia dysfunction or deficit. Conclusions: This first PET study of DCD found significant thalamus activation as previous studies on finger movement tasks comparing PET and fMRI in normal subjects. The Ward clustering in DCD images allowed to identify activated/non-activated/deactivated brain structures in subjects with DCD versus control.

Keywords: Developmental coordination disorder · Movement disorder · Brain development · Cerebral activation · PET imaging

1 Introduction

Developmental coordination disorder (DCD) concerns 6% of the population of children. It affects mostly boys [1], and it implies a lack for tasks automatization. This neurodevelopmental anomaly persists in adulthood [2]. Many clinical observations to date

hypothesize that neural networks between frontal cortex, striatum and cerebellum might be involved in DCD pathophysiology [3]. The cerebellum is thought to be implicated, among other tasks, in motor timing, in motor coordination and in emotional regulation [4]. Many other authors reported the involvement of a connection of several brain regions depending on the executed task, e.g. in the performance of visual tasks, such as the parietal-occipital lobe, the frontal lobe, the cerebellum, the basal ganglia, the brainstem, or during overt movement execution involving the parietal, premotor cortices, the basal ganglia and the cerebellum [5]. Licari et al. reported results on cortical functioning with functional magnetic resonance imaging (fMRI) during finger tapping and hand clenching, and concluded that there was no activation deficit in the DCD group, while they reported decreased activation in left superior and inferior frontal gyrus, and noticed increased activation in the right postcentral gyrus [6].

Studies implying finger movements reported that contralateral motor and somatosensory cortices were activated and that supplementary motor area was implicated in each hand movement in right-handed participants [7]. For the supplementary motor area implication, the importance of activation depends on the difficulty of the tasks: the more complicated is the task to accomplish, the more activation is seen in supplementary motor area [8]. Basal ganglia are also implicated in finger movements: the putamen is activated in finger movement execution of unusual self-initiated tasks [9]. The cerebellum was found having no activation when the participant initiated finger movements in a positron emission tomography (PET) study of 7 participants [10], but another study found ipsilateral activation of two cerebellar regions during passive and active finger movements [11]. More interestingly, Zeng et al. reported that activation intensity in the left motor area is reduced with right hand finger movement [12], and Wu et al. found that the ipsilateral primary motor cortex was deactivated for the non-dominant hand finger movement [13].

A recent review paper reported works on DCD imaging with MRI, single photon emission computed tomography (SPECT) and electroencephalography/evoked potential (EEG/EP) [14]. There was no PET imaging among these works.

In the present work we investigated the cerebral brain structures involved in DCD. We performed a PET study comparing DCD and non-DCD young adult participants, at rest and during brain activation consisting of determined and repetitive finger movement sequences. Prior to the PET study, we focused on DCD clinical signs in order to possibly select homogeneous participants with DCD. Unfortunately, since DCD is a spectral disorder, each participant with DCD presents his own symptomatology, and although statistics are available, signs and consequences differ from one participant to another due to familial and personal background and individual compensation strategies [15]. We mention also, as DCD persisting in adulthood, that we measured in this study young adults with DCD in comparison to young normal adults to avoid exposing children, and specifically control children, to radiation during computed tomography (CT) and PET measurements. We assure that the participants with DCD were clinically assessed for DCD without comorbidity prior to this study based on our clinical procedures and on questionnaire [16]. These participants were also diagnosed for DCD earlier in their childhood.

2 Materials and Methods

2.1 Participants

Four male volunteers participated in this study, two DCD and two controls, aged 21 to 27 years (24.5 ± 3 years). They were all right-handed according to the Edinburgh Handedness Inventory [17]. They had no history of neurological pathology and no diabetes; they had no intellectual deficit (IQ over 85). Written consent was obtained from all participants and the study was approved by the clinical research center's ethic committee, Faculty of Medicine and Health Sciences, University of Sherbrooke, Canada, under number 13–148. Both participants were clinically confirmed for DCD prior to imaging. The control participants were both university students with a Master degree. They had both IQ over 85, and were in good health, with no history of neurological or psychiatric diseases and no ADHD.

2.2 Experimental Procedures

All participants were fasting for 8 h prior to PET acquisition. Since neuronal activity fully relies on brain glucose metabolism, we designed the experiment to use 18F-fluorodeoxyglucose (18F-FDG). Two PET measurements were performed for each participant: the first one in resting state, and the second, on a separate day, while tapping their fingers of the left non-dominant hand. The scans were performed on two days to avoid contamination of remnant radiotracer from the first to the second acquisition, and to avoid discomfort to the participants for a longer scanning time which could affect the data, while optimally maintaining the two-day scans in similar environments. We mention also that the participants did not previously know about the task in order to prevent any learning or practicing before imaging. The use of the non-dominant hand for finger tapping was expected to add planning and motor difficulties. All PET acquisitions were done at the same moment of the day in order to have the same conditions for all images, without nyctohemeral interaction.

PET scans were obtained with a PET/CT (Philips TF 16). The participants were injected with a 5 mCi (185 MBq) of 18F-FDG bolus and PET was initiated in dynamic mode for 42.5 min. The rate of glucose in blood plasma was obtained in each participant. The dynamic scans were reconstructed with OSEM algorithm in 28 image frames of 1 × 30 s; 12 × 10 s; 6 × 30 s; 4 × 180 s; 5 × 300 s.

2.3 Data Analysis

Regions of interest (ROIs) were manually drawn on several brain image transaxial slices by reference to an electronic anatomic brain atlas (imaios.com) producing 42 volumes, extending on several slices, of 42 brain structures (Table 1). All regions were paired left and right relative to brain hemispheres. Time-activity curves (TAC) were obtained for each brain structure and glucose metabolism was assessed by the standard uptake value (SUV) [18]:

$$SUV = \frac{ROI\left[Bq/mg\ of\ tissue\right]}{Injected\ activity\ \left[Bq\right]/patient\ weight\ \left[kg\right]} \tag{1}$$

and participant weight was replaced by the body surface area (BSA) as [19]:

$$BSA = \sqrt{weight \ \times \ height/3600} \qquad (2)$$

The ROI value in (1) was evaluated as the average of the last five image frames of the brain structure, i.e. at the 5 frames of 300 s, and the SUV was multiplied by the rate of plasma glucose.

In order to compare the behavior of each brain structure to each other, and between rest and activation measurements, we normalized each structure SUV by the total SUV over all brain structures in each measurement. Moreover, and in order to compare the relative response to the activation, we evaluated the relative difference (SUV_r) as:

$$SUV_r = (SUV_{activation} - SUV_{rest})/SUV_{rest} \qquad (3)$$

2.4 Statistics

We used the Bartlett's test for variance differences between rest and activation and between subjects with DCD and control. We used the t-test for mean differences of the groups, and by clustering with Ward linkage method. We hypothesized that there could be brain structures which metabolize more glucose during activation (positive SUV_r), others could be deactivated (negative SUV_r), and some structures could remain unaffected by the activation (SUV_r around 0), and hence we decided to partition the data into three clusters.

Table 1. List of the 21 brain structures. These structures were identified on both left and right brain hemispheres. The abbreviations between parentheses were appended with L for left and R for right brain hemispheres in the results section. Ant for anterior, inf for inferior, post for posterior, med for medium

Brain structure	Brain structure	Brain structure
1. corona radiata (cr)	8. precentral (pc)	15. putamen (put)
2. superior frontal gyrus (sfg)	9. cuneus (cun)	16. inf occipital lobe (iol)
3. frontal mesial gyrus (fmg)	10. ant frontal pole (afp)	17. ant temporal pole (atp)
4. inferior frontal gyrus (fig)	11. med frontal pole (mfp)	18. med temporal pole (mtp)
5. angular gyrus (ag)	12. post frontal pole (pfp)	19. post temporal pole (ptp)
6. postcentral gyrus (pcg)	13. thalamus (thal)	20. superior cerebellum (sc)
7. superior parietal lobe (psl)	14. caudate nucleus (cn)	21. cerebellum (cer)

3 Results

Figure 1 shows a set of brain image slices extracted from the 90 image slices of the whole brain at the last frame time during the activation state (i.e. at 37.5 min after radiotracer

injection, duration of the frame 300 s). Figures 1a (DCD) and 1b (Control) were selected through the mid brain to show the differences in the cortices and nuclei, and Figs. 1c (DCD) and 1d (Control) depict the comparison in the slices including the cerebellum. The intensity of the signal in the structures clearly varied between the participant with DCD and the control. Glucose metabolism across the structures was spatially differently distributed in the participant with DCD than in the normal participant, where in the participant with DCD there was less uptake of 18F-FDG in the posterior brain than in the front.

The Bartlett test for variance difference in SUV_r (3) is reported in Fig. 2 where the participants with DCD showed larger variance but this variance was not found statistically different from the control (p = 0.057).

Using SUV_r (3) we calculated three clusters with Ward clustering approach to determine the activated, non-activated and deactivated brain structures (Fig. 3). We identified the three clusters in the two groups and the results are grouped in Table 2. Knowing that the left hand was used for finger tapping, the data did not significantly demonstrate differences in activated or deactivated structures relative to left and right brain hemispheres in either the participants with DCD or the control.
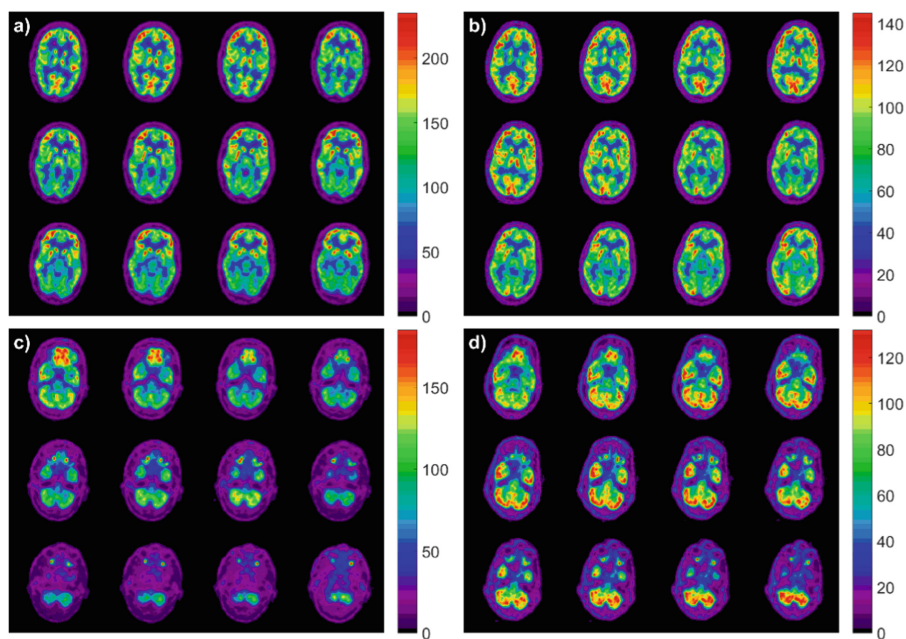
Fig. 1. A set of 18F-FDG PET images through the mid-brain (a and b) and through the cerebellum (c and d) for participants with DCD (a and c) and control (b and d) during the activation state. Images from the participant with DCD showed less intense uptake of 18F-FDG in comparison to the control. The right side of the participant is on the left side of the reader.
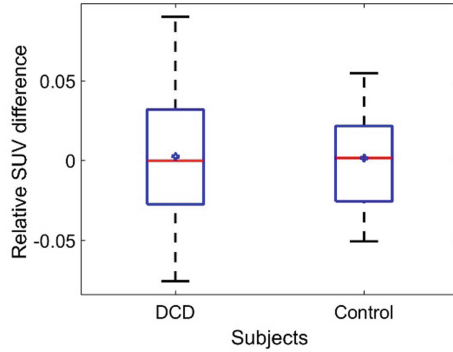
Fig. 2. Variance in the relative difference between rest-activation in the two groups of participants. The variance was not significantly different between the two groups (p = 0.057). The mid-line and marker "o" represent respectively the median and mean of the data in each group.
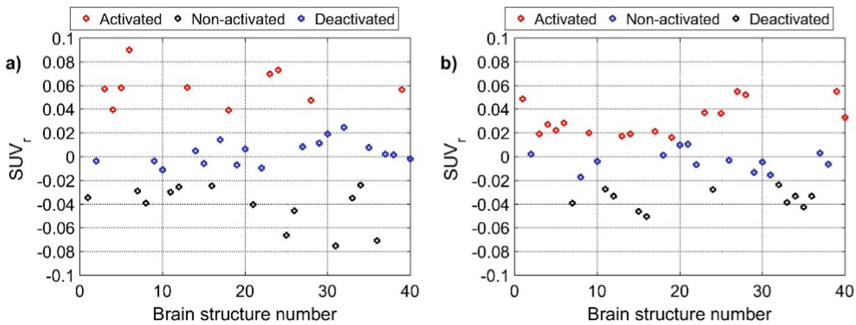

Fig. 3. Clustering of relative values of SUV_r in participants with DCD (a) and in control (b). The three clusters can be assumed as activated brain structures (+), not activated (o) and deactivated (*). These clusters were identified to corresponding brain structures and were reported in Table 2. The list of brain structures with numbers were listed in Table 1.

Table 2. Clusters of brain structures classified as activated, not activated and deactivated in the two groups of participants. The symbol + indicates common state of activation in both groups for that structure.

Participants with DCD			Control		
Activated	Not activated	Deactivated	Activated	Not activated	Deactivated
fmgL +	sfgR +	sfgL	sfgL	sfgR +	agL +
fmgR +	pcgL	agL +	fmgL +	agR	pslL +
figL +	pcgR +	agR	fmgR +	pcgR +	pslR +

(*continued*)

Table 2. (*continued*)

Participants with DCD			Control		
Activated	Not activated	Deactivated	Activated	Not activated	Deactivated
figR +	pcR	pslL +	figL +	afpR	cunL
pcL +	cunL	pslR +	figR +	mfpR +	cunR +
afpR	afpL	cunR +	pcgL	pfpL	thalR
thalL +	mfpL	pfpL	pcL +	pfpR	atpR
thalR	mfpR +	cnL	pcR	cnR	mtpL +
putR +	pfpR +	cnR	afpL	iolL +	mtpR +
cerL +	putL	atpL	mfpL	iolR +	ptpL
	iolL +	mtpL +	thalL +	atpL	ptpR +
	iolR +	mtpR +	cnL	scL +	
	atpR	ptpR +	putL	scR	
	ptpL		putR +		
	scL +		cerL +		
	scR +		cerR		
	cerR				

4 Discussion

Our study revealed differences in activation of brain structures comparing participants with DCD against controls. Participants with DCD showed activation of the right anterior frontal pole and the right thalamus during activation task. These participants showed deactivation of the left superior frontal gyrus, right angular gyrus, left posterior frontal lobe, bilateral caudate nuclei and left anterior temporal pole. They had no activation of many regions such as left precentral gyrus, left cuneus, left anterior and medium frontal poles, right anterior and left posterior temporal poles, left putamen and left cerebellum. Participants with DCD presented overall less activated regions than control participants but more deactivated regions.

The frontal region (right anterior frontal pole) is implicated with planning and initiating movements of left limbs and body parts and it was not activated in control participants while it was activated in participants with DCD. A potential valid explanation is that participants with DCD showed less automatization and therefore needed to plan and execute movements with attention control [20, 21], as if they could not learn it before and were always in learning process, explaining part of their cognitive surcharge.

Activation of the right thalamus in participants with DCD was fitting with a deficit of corticostriatal pathway [3, 20], and with the need for participants with DCD to keep conscious attention on their movements even they were repetitive. Another explanation could be a cognitive surcharge noticed in participants with DCD.

The left superior frontal gyrus was deactivated in participants with DCD and suggests a key deficit of activation that was significant between DCD and control participants and might be considered as a key difference between the 2 groups. Movements of the non-dominant hand should activate more cognitive areas for novel action planning as frontal lobe, as it is noticed with control participants.

These findings were expected as pathophysiology hypothesis for DCD corticostriatal and corticocerebellar deficits or dysfunction [3, 20, 22, 23].

In control participants, the right cerebellum was activated compared to participants with DCD where the right cerebellum was not activated. This is what was found in previous studies of DCD and in finger movement studies performed with "normal participants" [7, 22, 24].

The main limitation in this study was the limited number of participants. If the activation in the control participants can be confirmed from several reports in the literature either by PET or MRI for some brain structures, those obtained in participants with DCD certainly remains questionable. However, knowing that DCD is a wide spectrum, it becomes difficult to screen several participants from whom homogeneous participants with comparable DCD effects can be selected for imaging.

5   Conclusions

This study of repetitive finger movements with the non-dominant hand during PET acquisition found differences between DCD and control participants: less brain areas were activated in participants with DCD and more areas were not activated. Right thalamus was activated in participants with DCD as both caudate nuclei were deactivated for a possible compensation for basal ganglia dysfunction or deficit. More areas usually implicated in finger movements in control participants were deactivated in participants with DCD. This first PET study of DCD found significant thalamus activation as previous studies on finger movement tasks comparing PET and fMRI in normal participants. A study with more homogeneous participants with DCD would allow drawing more formal conclusions.

References

1. Farmer, M., Echenne, B., Bentourkia, M.: Study of clinical characteristics in young subjects with developmental coordination disorder. Brain Dev. **38**, 538–547 (2016). https://doi.org/10.1016/j.braindev.2015.12.010

2. Kirby, A., Edwards, L., Sugden, D.: Emerging adulthood and developmental co-ordination disorder. J. Adult Dev. **18**, 107–113 (2011). https://doi.org/10.1007/s10804-011-9123-1

3. Nicolson, R.I., Fawcett, A.J.: Dyslexia, dysgraphia, procedural learning and the cerebellum. Cortex **47**, 117–127 (2011). https://doi.org/10.1016/j.cortex.2009.08.016

4. Schutter, D.J.L.G., Van Honk, J.: The cerebellum in emotion regulation: a repetitive transcranial magnetic stimulation study. Cerebellum **8**, 28–34 (2009). https://doi.org/10.1007/s12311-008-0056-6

5. Gomez, A., Sirigu, A.: Developmental coordination disorder: core sensori-motor deficits, neurobiology and etiology. Neuropsychologia **79**, 272–287 (2015). https://doi.org/10.1016/j.neuropsychologia.2015.09.032

6. Licari, M.K., et al.: Cortical functioning in children with developmental coordination disorder: a motor overflow study. Exp. Brain Res. **233**(6), 1703–1710 (2015). https://doi.org/10.1007/s00221-015-4243-7

7. Catalan, M.J., Honda, M., Weeks, R.A., Cohen, L.G., Hallett, M.: The functional neuroanatomy of simple and complex sequential finger movements: a PET study. Brain **121**, 253–264 (1998). https://doi.org/10.1093/brain/121.2.253

8. Erdler, M., et al.: Dissociation of supplementary motor area and primary motor cortex in human subjects when comparing index and little finger movements with functional magnetic resonance imaging. Neurosci. Lett. **313**, 5–8 (2001). https://doi.org/10.1016/S0304-3940(01)02167-X

9. François-Brosseau, F.E., Martinu, K., Strafella, A.P., Petrides, M., Simard, F., Monchi, O.: Basal ganglia and frontal involvement in self-generated and externally-triggered finger movements in the dominant and non-dominant hand. Eur. J. Neurosci. **29**, 1277–1286 (2009). https://doi.org/10.1111/j.1460-9568.2009.06671.x

10. Blouin, J.S., Bard, C., Paillard, J.: Contribution of the cerebellum to self-initiated synchronized movements: a PET study. Exp. Brain Res. **155**, 63–68 (2004). https://doi.org/10.1007/s00221-003-1709-9

11. Thickbroom, G.W., Byrnes, M.L., Mastaglia, F.L.: Dual representation of the hand in the cerebellum: activation with voluntary and passive finger movement. Neuroimage **18**, 670–674 (2003). https://doi.org/10.1016/S1053-8119(02)00055-1

12. Zeng, L., Chen, H., Ouyang, L., Yao, D., Gao, J.H.: Quantitative analysis of asymmetrical cortical activity in motor areas during sequential finger movement. Magn. Reson. Imaging. **25**, 1370–1375 (2007). https://doi.org/10.1016/j.mri.2007.03.024

13. Wu, X., et al.: Ipsilateral brain deactivation specific to the nondominant hand during simple finger movements. NeuroReport **19**, 483–486 (2008). https://doi.org/10.1097/WNR.0b013e3282f6030b

14. Brown-Lum, M., Zwicker, J.G.: Brain imaging increases our understanding of developmental coordination disorder: a review of literature and future directions. Curr. Dev. Disord. Rep. **2**(2), 131–140 (2015). https://doi.org/10.1007/s40474-015-0046-6

15. Bo, J., Lee, C.M.: Motor skill learning in children with Developmental Coordination Disorder, Res. Dev. Disabil. **34**, 2047–2055 (2013). https://doi.org/10.1016/j.ridd.2013.03.012

16. Kirby, A., Edwards, L., Sugden, D., Rosenblum, S.: The development and standardization of the adult developmental co-ordination disorders/Dyspraxia checklist (ADC). Res. Dev. Disabil. **31**, 131–139 (2010). https://doi.org/10.1016/j.ridd.2009.08.010

17. Oldfield, R.C.: The assessment and analysis of handedness: the Edinburgh inventory. Neuropsychologia **9**, 97–113 (1971). https://doi.org/10.1016/0028-3932(71)90067-4

18. Thie, J.A.: Understanding the standardized uptake value, its methods, and implications for usage. J. Nucl. Med. **45**, 1431–1434 (2004)

19. Verbraecken, J., Van De Heyning, P., De Backer, W., Van Gaal, L.: Body surface area in normal-weight, overweight, and obese adults. A comparison study. Metabolism **281**, E586–E591 (2006). https://doi.org/10.1016/j.metabol.2005.11.004

20. Albaret, J.M., Chaix, Y.: Neurobiological bases and neurophysiological correlates of developmental coordination disorders. Neurophysiol. Clin. **42**, 11–17 (2012). https://doi.org/10.1016/j.neucli.2011.07.001

21. Fassbender, C., et al.: A topography of executive functions and their interactions revealed by functional magnetic resonance imaging. Cogn. Brain Res. **20**, 132–143 (2004). https://doi.org/10.1016/j.cogbrainres.2004.02.007

22. Zwicker, J.G., Missiuna, C., Harris, S.R., Boyd, L.A.: Brain activation of children with developmental coordination disorder is different than peers. Pediatrics **126**, 678–686 (2010). https://doi.org/10.1542/peds.2010-0059

23. Querne, L., et al.: Dysfunction of the attentional brain network in children with Developmental Coordination Disorder: a fMRI study. Brain Res. **1244**, 89–102 (2008). https://doi.org/10.1016/j.brainres.2008.07.066

24. Allison, J.D., Meador, K.J., Loring, D.W., Figueroa, R.E., Wright, J.C.: Functional MRI cerebral activation and deactivation during finger movement. Neurology **54**, 135 (2000). https://doi.org/10.1212/wnl.54.1.135

On the Use of Explainable Artificial Intelligence for the Differential Diagnosis of Pigmented Skin Lesions

Sandro Hurtado[1,2,3], Hossein Nematzadeh[1,2,4], José García-Nieto[1,2,3(✉)],
Miguel-Ángel Berciano-Guerrero[3,5], and Ismael Navas-Delgado[1,2,3]

[1] Department de Lenguajes y Ciencias de la Computación,
Universidad de Málaga, Málaga, Spain
{sandrohr,jnieto}@uma.es
[2] ITIS Software, Arquitecto Francisco Peñalosa 18, 29071 Málaga, Spain
[3] Biomedical Research Institute of Málaga (IBIMA), Málaga, Spain
[4] Department of Computer Engineering, Sari Branch,
Islamic Azad University, Sari, Iran
[5] Medical Oncology Intercenter Unit, Regional and Virgen de la Victoria University
Hospitals, Málaga, Spain

Abstract. In the last few years, eXplainable Artificial Intelligence
(XAI) has been attracting attention in data analytics, as it shows great
potential in interpreting the results of complex machine learning models
in the application of medical problems. The nutshell is that the outcome
of the machine learning-based applications should be understood by end
users, specially in medical data context where decisions have to be care-
fully taken. As such, many efforts have been carried out to explain the
outcome of a deep learning complex model in processes where image
recognition and classification are involved, as in the case of Melanoma
cancer. This paper represents a first attempt (to the best of our knowl-
edge) to experimentally and technically investigate the explainability of
modern XAI methods Local Interpretable Model-Agnostic Explanations
(LIME) and Shapley Additive exPlanations (SHAP), in terms of repro-
ducibility of results and execution time on a Melanoma image classifica-
tion data set. This paper shows that XAI methods provide advantages
on model result interpretation in Melanoma image classification. Con-
cretely, LIME performs better than SHAP gradient explainer in terms
of reproducibility and execution time.

Keywords: eXplainable Artificial Intelligence · Melanoma medical
image classification · LIME · SHAP · Deep Learning

1 Introduction

Explainable AI (XAI) is an artificial intelligence approach oriented to explain the
results of complex machine learning algorithms [2]. Generally, it is believed that
as the complexity of a machine learning algorithm increases, the understandabil-
ity of the results become harder [3]. Previously, the robustness of a classification

algorithm was evaluated using well-known criteria such as accuracy, precision, recall, Fscore, and etc. However, in real-world scenarios, human experts usually prefer the use of understandable algorithms, even though they usually have moderate, sometimes limited, performance that other complex black-box techniques, such as deep learners. In fact, explainability besides accuracy are two important factors to assess the output of any machine learning algorithms [9]. One of the main categories of explainers are post hoc model-agnostic. Post hoc refers to those methods that are applied after training the model and not at the middle of the model training process. Model-agnostic refers to the group of explainers that are not specifically designed for a certain machine learning algorithm. XAI specifically well-adapted to provide explanation ability to deep learning output on medical datasets [5], where Melanoma cancer is not an exception.

Melanoma is the most aggressive skin tumour, with a 5-year survival rate of 93% if diagnosed in early stages, but only 27% if diagnosed at an advanced stage with the presence of metastatic disease[1]. In Spain, 6,108 cases of melanoma were estimated in 2021 (2,480 men and 3,678 women), being the fifth most frequent cancer in men and women[2]. Diagnosis in the early stages is what allows better survival rates, although it entails the difficulty of differentiating it from other pigmented skin lesions (nevus and seborrheic keratosis, mainly), which are followed up. The inclusion of artificial intelligence in the diagnosis would allow a more accurate diagnosis. In concrete, there are many efforts to melanoma diagnosis using deep learning [1,7]. In order to realize trustworthy AI, XAI can be used as a technical method to ensure transparency of deep learning by helping better understand the neural network's underlying mechanisms and explaining system behaviours to users (in our case clinicians).

This paper is, to the best of our knowledge, a first attempt to evaluate two well-known post hoc model-agnostic methods in XAI, namely: Local Interpretable Model-Agnostic Explanations (LIME) [8] and SHapley Additive exPlanations (SHAP) [6], on explaining the deep learning prediction on Melanoma image dataset technically. Reproducibility and execution time are introduced as two major criteria for comparing LIME and SHAP. This paper finally concludes which of the aforementioned method is most suitable for explanation of Melanoma detection from an engineering point of view. The rest of this paper is organized as follow. Section 2 provides related information for LIME and SHAP. Section 3 demonstrates the methodology and the results achieved. Finally, Sect. 4 concludes the paper by summarizing the findings.

2   Preliminaries

This research focuses on the model-agnostic AI explainers, which provide post-hoc interpretability i.e. why the prediction model predicted its output through

---

providing after-the-fact evidence for the outputs. These explainers are probably the most popular ones in the current literature, which consist in Local Interpretable Model-Agnostic Explanations (LIME) [8] and SHapley Additive exPlanations (SHAP), both comprising a group of techniques that help humans visualize what an already-trained model thinks is important.

LIME uses Eq. 1 to minimize $\xi(x)$ so that f is the prediction model which is assumed as black box, g is a model in G as a class of potentially interpretable models that tries to approximate f, Π_x is used to define the locality around the sample to be explained ξ (perturbations from x), and $\Omega(g)$ represents the complexity of explanation that should be minimized as well as $L(f, g, \Pi_x)$.

$$\xi(x) = argmin_{g \in G} L(f, g, \Pi_x) + \Omega(g) \tag{1}$$

SHAP values are concepts coming from game theory [6]. Shapely quantifies to what extent each player (features) contributes to the game (output of prediction model). Shapely creates a power set of features firstly. The cardinality of power set is 2^n where n is the total number of features. Likewise, SHAP also requires to train 2^n models with different set of features according to the power set. It is obvious that as the number of features is higher the number of models to be trained increases exponentially, which is treated by Lundberg et al.[6] through some approximations and samplings. Basically, calculating SHAP values has two steps, namely calculating marginal contributions of each feature and weighing the marginal contributions which can be shown in general in Eq. 2, so that F is the entire number of (f) features and $set = 1, ..., F$.

$$SHAP_f(x) = \sum_{f \in set} [|set| \times \binom{F}{|set|}]^{-1} [Predict_{set}(x) - Predict_{set/f}(x)] \tag{2}$$

Figure 1 illustrates the difference between SHAP and LIME in general. According to this figure, LIME initially perturbs the sample to explain x to create the set $Z = z_1, z_2, ..., z_m$. Next, it selects an interpretable model (such as linear regression) to calculate the importance of features (calculating the coefficients related to each feature) via $g(Z)$. LIME finally selects the most effective features (through sorting coefficients if g is linear regression). However, SHAP build SHAP values by calculating the marginal contribution of features and weighing them. Effective features are those with greater SHAP values. Moreover, summing the SHAP values gives exactly the difference between the output of full model and null model, which shows the additive explanations of SHAP.

While SHAP explainers are model agnostic, there exists two variations that could be used for deep learning, namely deep explainer and gradient explainer. Deep explainer approximates the conditional expectations of SHAP values using a selection of background samples, while gradient explainer explains a model using expected gradients which reformulates the integral as an expectation and combines that expectation with sampling reference values from the background dataset.
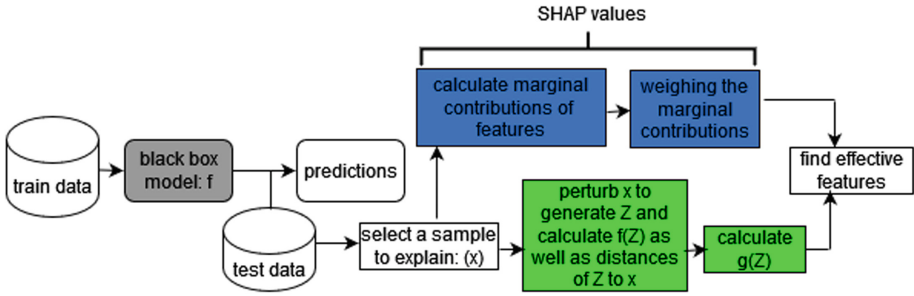
Fig. 1. General workflow of SHAP and LIME

3   Methodology

The methodology of the paper is illustrated using a pipeline in Fig. 2. The image dataset is online available in Kaggle Skin Lesion Images for Melanoma Classification (ISIC2019) repository[3]. It comprises more than 25,000 images with imbalanced classes (the majority of training data is nevus) which could cause an erroneous accuracy and incorrect predictions. There are many methods to balance training data including undersampling the majority class, oversampling the minority classes, applying SMOTE, and etc. depending on the dataset. However, our experiments reveal that the best technique for image datasets like Melanoma is the combination of random oversampling the minority classes following by applying data augmentation.

Fig. 2. Proposed methodology.

Thus, in the preprocessing step, the distribution of classes were equalized using random oversampling initially. Oversampling solely can lead to overoptimism in prediction. Assuming the training data is split into train and validation sets. It is expected that some images in the training data appear in the validation set, since there exist multiple replicated images as a result of random oversampling the minority classes. As such overfitting could happen where the model prediction will be high in training data, but very low in unseen data. Here data augmentation could alleviate overfitting. The data augmentation in this study is done through rescaling, rotating, width-shift, height-shift, and horizontal-flip

---

[3] In URL https://www.kaggle.com/andrewmvd/isic-2019.

augmentation. The pipeline in Fig. 2 follows by applying pre-trained ResNet [4] convolutional Deep Learning model and saving the best weights. Then, model agnostic post hoc explainers (SHAP with Deep and Gradient explainers, LIME with three well-known segmentation algorithms) are used to evaluate the results based on reproducibility of the results and execution time.

Reproducibility means the ability of the method to successfully reproduce same explanations in multiple runs. Likewise, execution time refers to the elapsed time starting from creating the explainer until calculating the explanation and generating the pictorial results. Table 1 also shows the main characteristics of the Melanoma dataset prior to oversampling and augmentation. After oversampling the distribution of each class in training set is equal to 1,372 so that the the entire training set contains 4,116 observations.

Table 1. Melanoma dataset description after oversampling class imbalance

Data	#Observations	Distribution of observations
Train	2000	374/Melanoma, 1372/Nevus, 254/Seborrheic-keratosis
Validation	150	30/Melanoma, 78/Nevus, 42/Seborrheic-keratosis
Test	600	117/Melanoma, 393/Nevus, 90/Seborrheic-keratosis

Table 2. Description of four selected samples for experimentation

Test observation	Real label	Melanoma	Nevus	Seborrheic-keratosis
Sample 1	Nevus	0.31	0.57	0.12
Sample 2	Melanoma	1.00	0.00	0.00
Sample 3	Nevus	0.00	1.00	0.00
Sample 4	Seborrheic-keratosis	0.00	0.00	1.00

3.1 Evaluation

This section provides related information for calculated metrics. All the experiments have been conducted in a virtualization environment running on a private high-performance cluster computing platform. This infrastructure is located at the Ada Byron Research Center at the University of Málaga (Spain), and comprises a number of IBM hosting racks for storage, units of virtualization, server compounds and backup services. Our virtualization platform is hosted in this computational environment. Concretely, this platform is made up of a CPU with Intel(R) Xeon(R) Gold 6130 @ 2.10 GHz, maximum 2 TB of HDD, maximum 64 GB of RAM, and Ubuntu 20.04.3 LTS(GNU/Linux 5.4.0-1049-kvm x86_64).

Since it is impossible to illustrate the entire test samples four test samples were selected to investigate the reproducibility and execution time analysis as explained in Table 2, so that for each sample the real labeling and the prediction of deep learning are shown.

3.2   Evaluation of LIME

Figure 3 illustrates the reproducibility of LIME using three well-known segmentation algorithm namely, quick shift, Simple Linear Iterative Clustering (SLIC) and felzenswalb. Quick shift uses approximation of kernelized mean-shift and it belongs to the family of local mode-seeking algorithms. SLIC uses k-means which is a simpler clustering method in comparison with the clustering method in quick shift. In contrast, felzenswalb uses a graph-based approach for image segmentation.

Figure 3 is the result of 5 multiple runs of LIME algorithm for 5 top features with different number of perturbations regarding each of the four images in Table 2. The original segmentation is illustrated for each image using quick shift, SLIC, and felzenswalb in Fig. 3 initially, so that the segmentation algorithms are tuned to contain roughly same number of segments for each algorithm, to have a fair comparison between them. Under each image is a fraction that shows how many times LIME is able to generate exactly same 5 top features in 5 multiple runs using each segmentation algorithm. For example, 4/5 for sample 1 with quick shift algorithm and 5,000 perturbations means the result of LIME in 4 runs from 5 runs are exactly same. As such, sample 1 achieves 1/5 for 100 perturbations using quick shift algorithm, which means that there are five unique results so that one of them is selected randomly.

It is noteworthy mentioning that, quick shift and SLIC have relatively same segmentation trend in comparison with felzenswalb so that this last sometimes results in segments with sizes that vary greatly as in sample 2 and sample 3. This may affect the reproducibility of LIME either positively in sample 3 or negatively in sample 2.

While Fig. 3 analyzes reproducibility strictly, Fig. 4 checks the reproducibility of LIME more gently by calculating the number of features in each perturbation (100, 500, and 1,000) that have also been observed when the perturbation is 5,000. Figure 4 shows that as the number of perturbation increases from 100 to 1,000, more features from that perturbation are observed within 5,000 perturbation. If two superpixels are equally good at explaining, LIME may pick an arbitrary one which sometimes result in not reproducible explanations. Figure 4 shows that by increasing the number of perturbation, LIME converges to reproducibility.

Recalling that good segmentation often depends on the application, illustrations in Figs. 3 and 4 show that the reproducibility in LIME mostly increases while the number of perturbation increases from 500 to 5,000 using any segmentation algorithm (the default number of perturbation in LIME is 1,000). While increasing number of perturbations has a positive effect in reproducibility of LIME, another approach is to fix the random seed to initialize the random number generator. This way, using any number of perturbations the explainability results are same. Nonetheless, greater number of perturbations together with fixed random seed result in better accuracy as well. Nonetheless, Fig. 5 shows how successfully LIME recognizes regions contributed to target label by increasing the number of perturbations and using fixed random seed. This last
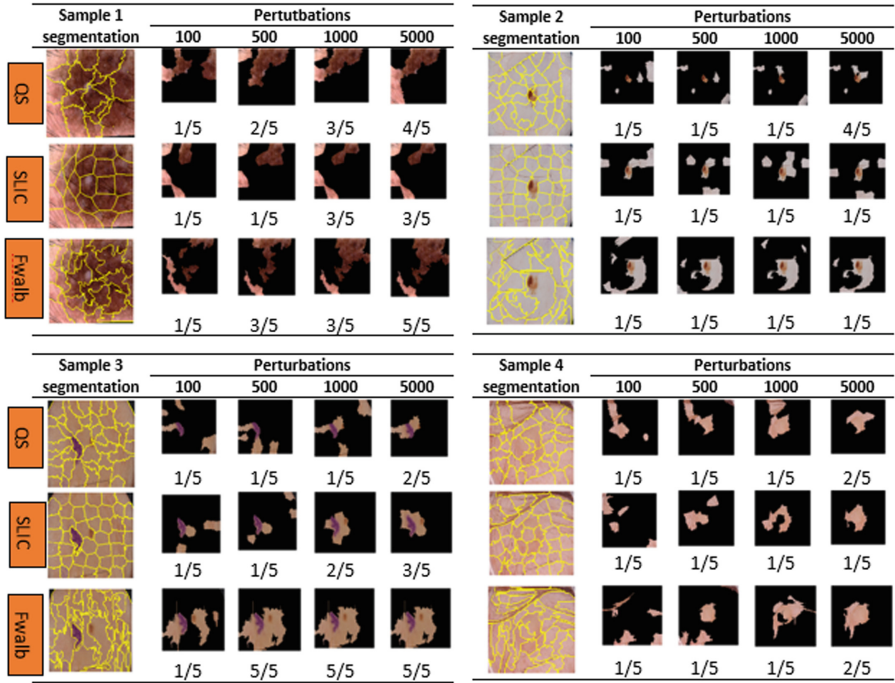
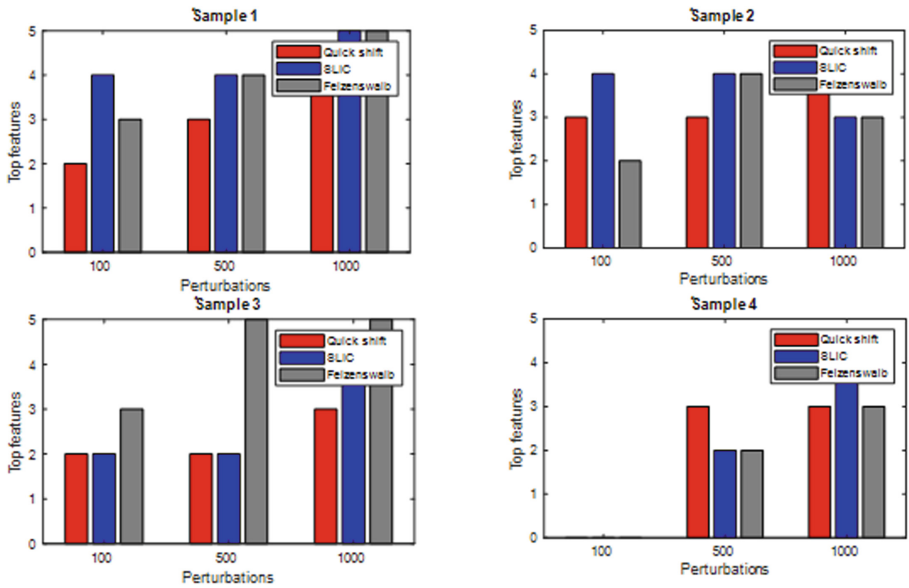**Fig. 3.** Strict analysis of LIME reproducibility by increasing number of perturbations

Fig. 4. Gentle analysis of LIME reproducibility by increasing number of perturbations

figure also reveals that LIME intelligently did not recognize mm scale and hair as effective features, but considers the stain in sample 3 within 5 most important superpixels.
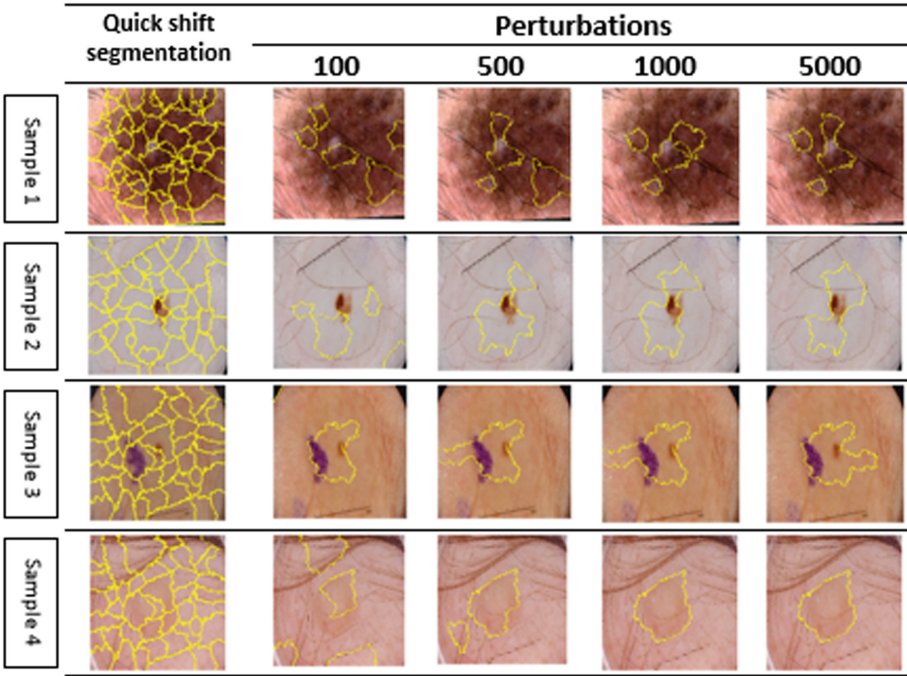

Fig. 5. Reproducibility analysis of LIME using fixed random seed and variable number of perturbations

3.3 Evaluation of SHAP

As commented before, there exists two variations of SHAP optimized for deep learning, namely gradient explainer and deep explainer. The SHAP kernel explainer could also be used because it works for all models, but is slower than the other model type-specific algorithms, as it makes no assumptions about the model type. Thus, to avoid redundancy of figures with same results and for the sake of hardware limitation (passing more than 100 background data was unreasonably expensive), the reproducibility of SHAP has been tested using solely with gradient explainer, shown in Fig. 6. Generally, pink pixels contribute to the model output and blue pixels contribute not being of that class. The intensity of color shows the intensity of contribution. Since gradient and deep explainer explains the prediction using pixels and not superpixels, it is difficult to trace the reproducibility numerically as it was done for LIME.

The nsamples parameter in gradient explainer (by default = 200) indicates the number of samples are taken to compute the expectation and shows accuracy

of explanation. This gives better estimates of SHAP values as the nsamples increases, which leads to low variate estimation of the SHAP values, however the execution time increases. Figure 6 shows that as the nsamples increases from 100 to 5,000 the explainability becomes a bit more reproducible, which is less obvious in sample 1 because the deep learning model is not completely sure about its prediction. Figure 6 also shows that gradient explainer considers the stain in sample 3 same as LIME in Fig. 5. The gradient explainer in Fig. 6 uses the entire 4,116 images in train set as a background data (the random seed in calculation of SHAP values is set to 42).
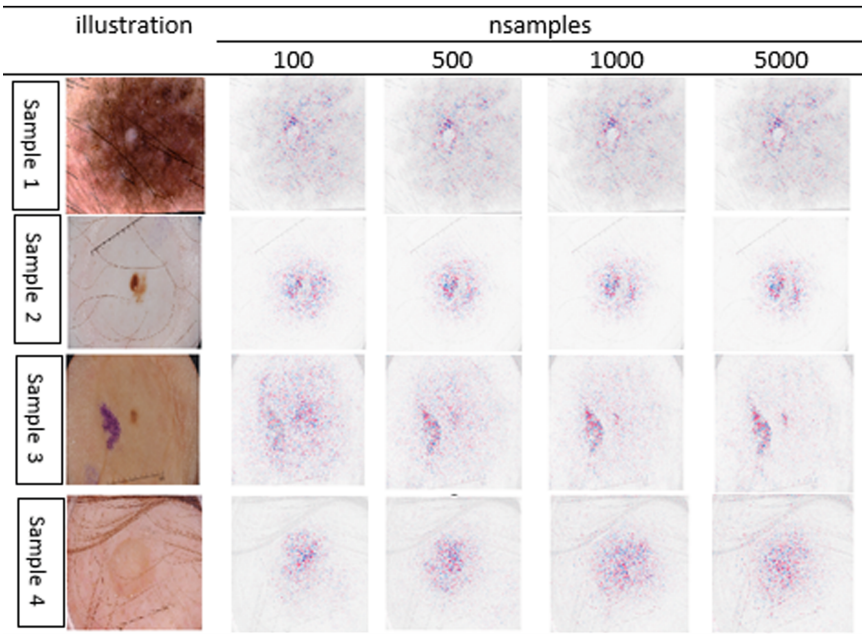
Fig. 6. Visual reproducibility analysis of SHAP gradient explainer

3.4 Computational Effort

From the point of view of the computational effort, Fig. 7 compares LIME (using quick shift) and SHAP gradient explainer in terms of execution time, so that N is the number of perturbation and nsamples for LIME and SHAP, respectively. It is clear that LIME spends less amount of time for explainability as N increases, while SHAP gradient explainer is almost three times slower than LIME. It is noteworthy mentioning that changing the segmentation algorithm does not have a considerable difference in execution time of LIME. SLIC is very competitively faster than quick shift and also quick shift is very closely faster than felzenswalb. Thus, Fig. 7 the better performance in terms of execution time of LIME using quick shift as a moderate segmentation algorithm. Technically speaking, LIME

has more reproducibility power and is almost much faster than SHAP gradient on melanoma dataset. Thus, there are sufficient engineering justifications to use LIME for explanability of deep learning on melanoma dataset for a single prediction rather than SHAP gradient explainer.
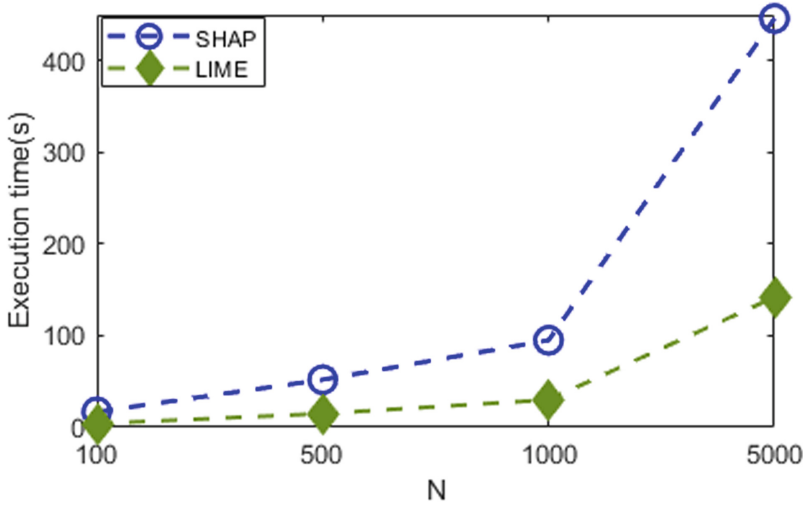

Fig. 7. Efficiency of LIME Vs SHAP

4   Conclusion

This paper investigated the explainability of Local Interpretable Model-Agnostic Explanations (LIME) and SHapley Additive exPlanations (SHAP) in order to help in the differential diagnosis of pigmented skin lesions. The evaluation criteria focuses on the reproducibility of the results, as well as the execution time. Three variations of LIME (using three well-known segmentation algorithms) are used and gradient explainer is selected for SHAP. From the engineering point of view, LIME was faster than SHAP. The idea is that while acceptable results are achieved by LIME in the case of differential diagnosis of pigmented skin lesions, there is no need to use SHAP because of its expensive efficiency. LIME works with super pixels and the reproducibility of results were more controllable than SHAP gradient explainer. Thus, it can be concluded that XAI methods show potentials in providing interpretable results for the specific case of pigmented skin lesions classification, in the context of Melanoma cancer diagnosis. Specifically, LIME shows better performance than SHAP gradient explainer in terms of reproducibility and execution time.

The general idea for future work is to approach explainability of deep learning on melanoma data set through improving LIME, as well as to tacking with other different kind of medical image datasets.

References

1. Banerjee, S., Singh, S.K., Chakraborty, A., Das, A., Bag, R.: Melanoma diagnosis using deep learning and fuzzy logic. Diagnostics **10**(8), 557 (2020). https://doi.org/10.3390/diagnostics10080577
2. Barredo Arrieta, A., et al.: Explainable artificial intelligence (XAI): concepts, taxonomies, opportunities and challenges toward responsible AI. Inf. Fusion **58**, 82–115 (2020). https://doi.org/10.1016/j.inffus.2019.12.012
3. Gulum, M.A., Trombley, C.M., Kantardzic, M.: A review of explainable deep learning cancer detection models in medical imaging. Appl. Sci. **11**(10) (2021)
4. He, K., Zhang, X., Ren, S., Sun, J.: Deep residual learning for image recognition. In: 2016 IEEE Conference on Computer Vision and Pattern Recognition (CVPR), pp. 770–778 (2016). https://doi.org/10.1109/CVPR.2016.90
5. Knapič, S., Malhi, A., Saluja, R., Främling, K.: Explainable artificial intelligence for human decision support system in the medical domain. Mach. Learn. Knowl. Extract. **3**(3), 740–770 (2021)
6. Lundberg, S.M., Lee, S.I.: A unified approach to interpreting model predictions. In: Proceedings of the 31st International Conference on Neural Information Processing Systems (NIPS 2017), pp. 4768–4777. Curran Associates Inc., Red Hook (2017)
7. Naeem, A., Farooq, M.S., Khelifi, A., Abid, A.: Malignant melanoma classification using deep learning: datasets, performance measurements, challenges and opportunities. IEEE Access **8**, 110575–110597 (2020). https://doi.org/10.1109/ACCESS.2020.3001507
8. Ribeiro, M.T., Singh, S., Guestrin, C.: Why Should I Trust You?: Explaining the Predictions of Any Classifier. Association for Computing Machinery (2016)
9. Samek, W., Montavon, G., Lapuschkin, S., Anders, C.J., Müller, K.: Toward interpretable machine learning: transparent deep neural networks and beyond. arXiv preprint arXiv:2003.07631 (2020)

Estimating Frontal Body Landmarks from Thermal Sensors Using Residual Neural Networks

Aurora Polo-Rodríguez[1]([✉]), Marcos Lupión[2], Pilar M. Ortigosa[2], and Javier Medina-Quero[1]

[1] Department of Computer Science, University of Jaén, Jaén, Spain
{apolo,jmquero}@ujaen.es
[2] Department of Informatics, University of Almería. CeIA3, Almería, Spain
{marcoslupion,ortigosa}@ual.es

Abstract. In this work, we propose the use of thermal vision sensors to estimate the frontal body landmarks of an inhabitant. The use of thermal sensors is being promoted to collect human patterns while protecting inhabitants' privacy in smart environments. On the other hand, deep learning approaches have provided encouraging results in estimating body, hand and facial landmarks. Here, we present a residual neural network which produces body landmarks from images collected by a low cost thermal sensor. In order to solve the problems of capturing and labeling data, which hinder learning in deep learning models, we propose an auto-labeling approach with dual visible-spectrum and thermal cameras, including the recognition of keypoints by the OpenPose model. A case study developed with four inhabitants in different poses shows encouraging results.

Keywords: Thermal sensor · Residual neural network · Body landmark

1 Introduction

Smart environments enable monitoring of human activities in an increasingly less invasive way [2]. They have the potential to improve the quality of healthcare and social services whilst allowing people to live independently at home and social centres in a secure and controlled way [7]. Smart environments are supported by the integration of sensors in the related field of Internet of Things (IoT) [1]. First, binary sensors were deployed as low-cost devices to collect human interactions in spaces and with objects within smart environment settings [20]. Next, wearable devices were applied to provide a first-person perspective of human activity, enabling recognition of activities and gestures in Activity Recognition [22] using mainly inertial sensors. New trends have incorporated vision sensors, which have been proposed together with computer vision models to analyse visual observations for pattern recognition in inhabitants [34]. More recently, thermal vision sensors have been proposed because they offer a degree of privacy not provided

by traditional camera methods, as occupants cannot be identified. This approach has the potential for a more positive acceptance than standard vision cameras [28].

The proliferation of deep learning approaches has enabled state-of-the-art sensor processing in activity recognition [31]. In the context of computer vision, deep learning drives the most prominent cases and results [30]. In this work, real-time multi-person 2D estimation of body landmarks has been achieved using complex structure models in the visible spectrum combining deep learning and affinity part methods [4]. The results have been promising.

Additionally, residual networks [10,32] have been successfully applied in many computer vision and natural language processing tasks, achieving state-of-the-art performance with deeper and wider architectures and with a low number of configuration parameters based on the creation of residual blocks with predefined inner-layers.

Moreover, in order to avoid learning from scratch, we propose combining learning from visible spectrum models for landmark estimation. To this end, domain adaptation methods are proposed to map between the source and target data distribution [24]. This approach has been proposed in several visual applications [6] and IoT sensors in smart environments [25].

The aim of this work is to compute the 2D estimation of frontal body landmarks from thermal sensors using the labeling of a different domain, which is thermal vision frames. We propose using a lighter Neural Network which can be deployed in IoT boards. The extension of this initial approach will serve as base for solving complex deployments in real-time conditions with occlusions, identifications of partial body parts and individual segmentation.

In order to reach this outcome, our approach is based on following key points:

– To collect a straightforward dataset, a pair of vision devices is proposed, integrating a thermal and visible-spectrum sensor. An IoT board is embedded with the dual vision devices to store paired images from both domains.
– OpenPose model is applied over the frames from the visible-spectrum sensor to obtain the body landmarks. The body landmarks proposed are MPI keypoints which describe the body's pose using 15 keypoints. These keypoints of body landmarks generated by OpenPose provide an automatic labelling of images representing the ground truth to be learned by the neural network model.
– A Residual Neural Network designed for this work is proposed to develop a regression of the body landmarks. The input of the model is composed of thermal vision images and the labeling is represented by 30 values of MPI keypoints computed by OpenPose, respectively.

The remainder of the paper is organised as follows: In Sect. 2, we review related works and methodologies; in Sect. 3, we describe the devices, architecture, and methodology of the approach; in Sect. 4, we present the results of a case study; in Sect. 5, we detail our conclusions and ongoing work.

2 Related Works

The emergence of thermal vision sensors is an excellent non-invasive and privacy-friendly approach to monitor people in their homes [8]; [21]. However, most work in the scientific literature makes use of visible-spectrum sensors, due to the encouraging performance of deep learning in multimedia data analysis using IoT [12]. However, many concerns around privacy have been raised by their deployment indoors [26].

For the acceptance of such technologies to be possible, it is essential to present the user with a scenario where they feel safe [16]. In this work, we have opted for an IoT device that integrates a dual vision/thermal sensor that offers greater guarantees regarding the user's privacy, depending on the context and sensitivity. Moreover, thermal sensors almost completely solve the problems related to light and shadows presented by visible-spectrum cameras [9]. In fact, numerous proposals have recently appeared where these devices stand out for their performance, mainly in fall detection [20] and activity and pose classification [18].

If we delve into landmark estimation, in the scientific literature we can find multiple examples of their use with visible-spectrum sensors such as Kinect [14]. Estimating these landmarks in the human body is very tedious, as existing datasets include incomplete annotations, leading to the assembly of different deep models trained independently on different datasets [15]. This reality is compounded by differences in the patterns collected between visible-spectrum images and thermal images, which means that visible-spectrum models cannot be applied to thermal images with great results. This makes it even more difficult to find scientific proposals that make use of thermal vision sensors for pose estimation.

The use of deep learning models is the best-performing method for this purpose, mostly with the use of lightweight and fast CNNs [19]. In fact, OpenPose has been the first real-time multi-person system to jointly detect human body, hand, facial, and foot keypoints (in total 135 keypoints) in single images, and has been used in numerous proposals with excellent results [3]. Such is the importance and impact of lightweight models such as OpenPose for IoT and real-time devices, that networks have already been proposed that improve its performance by estimating all points of the body simultaneously [11] or that have been optimised to be lighter [23].

3 Materials and Methods

This section presents a novel method to estimate the landmarks of a body using a thermal camera. The estimation of landmarks or points of interest has been covered extensively in the scientific literature on visible-spectrum vision sensors. The reason for including a landmark estimation method based on thermal camera images is to address privacy concerns. Such concerns are especially relevant when it comes to vision sensors deployed in hygienic environments and in domestic environments in general, where they should not capture as much sharpness

or resolution. However, due to differences in the patterns collected, models for estimating landmarks based on the visible spectrum have not achieved robust results when applied to the thermal domain.

3.1 IoT Device with Dual-Vision Thermal and Visible-Spectrum Sensors

To carry out the data collection and paring of images from the visible spectrum and the thermal domain, we have designed an IoT device consisting of a thermal vision sensor and a visible-spectrum sensor directly connected to a Raspberry Pi 4. It is described below:

– The visible-spectrum sensor selected is **Raspberry Pi NoIR Camera Module V2**. It is a low-cost sensor (around €30) that is able to take images in the dark because it does not use an infrared sensor (NoIr = No InfraRed) (Fig. 1).

Fig. 1. Raspberry Pi NoIR Camera Module V2

– The thermal vision sensor selected is **FLIR Lepton 3.5, integrated with the PureThermal 2 Smart IO Module** (see Fig. 2), which is a hackable USB thermal webcam for the FLIR Lepton thermal imaging camera core. It is a Long Wavelength Infra-Red camera that captures accurate, calibrated, non-contact temperature data at every pixel of every image and is priced at around €350.
  Both cameras collect 160×120 pixel images through a Python application that has been implemented, so the data collection is performed simultaneously on both devices. Figure 3 shows the final configuration of the devices with a case modeled for a 3D printer.
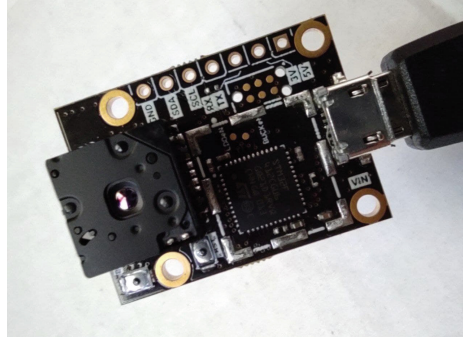
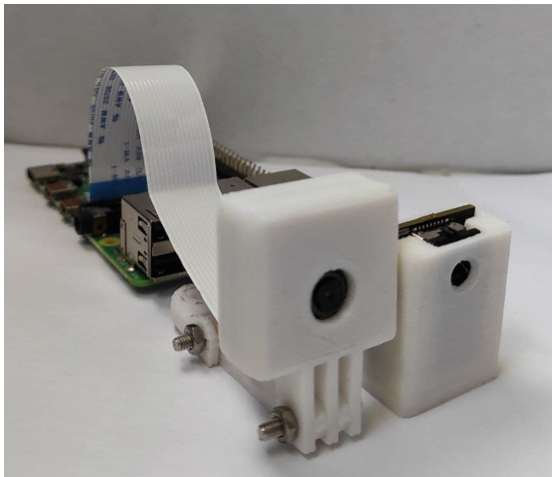**Fig. 2.** PureThermal 2 Smart I/O Module + FLIR Lepton 3.5

Fig. 3. (Left) Raspberry Pi NoIR Camera Module V2 (Right) PureThermal 2 Smart I/O Module + FLIR Lepton 3.5 (Back) Raspberry Pi 4

3.2 OpenPose Auto-Labelling, Homography Calibration, Data Augmentation and Data Pre-processing

The use of deep learning models to perform this estimation of landmarks is the method with the best performance [5]. One problem with deep learning models is that they need a large amount of data for learning. This required a huge data set where each thermal image would also have to be labeled by a human observer. To solve this problem, we propose a novel self-labeling system in the learning phase (not in the final deployment phase):

– IoT device with dual-vision thermal and visible-spectrum sensors collect paired images. A fuzzy membership function $\mu_{N(x_i)}$ is applied on the pixels x_i of the thermal data: i) to normalize data between [0,1], and ii) to

remove background noise (Fig. 4). This pre-processing step outperforms the learning of the network using raw thermal images. The membership function is defined by a left trapezoidal shape to normalize and remove background context from raw thermal pixels:

$$\mu_{N(x)} = TL(x)[l_1, l_2] = \begin{cases} 0 & x \leq l_1 \\ (x - l_1)/(l_2 - l_1) & l_1 \leq x \leq l_2 \\ 1 & l_2 \leq x \end{cases}$$

– Labeling of the visible-spectrum image is included using stable deep learning models: OpenPose [4].
– Labeling of the visible spectrum is related to the thermal camera using homography H.
– The process is repeated collecting samples in a domestic environment automatically in real time (with various poses and the user).
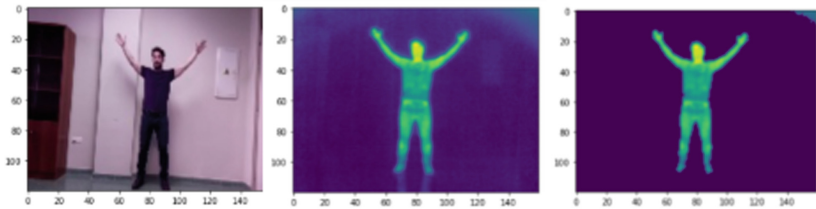
Fig. 4. Background segmentation

First, OpenPose developed an estimation of body landmarks from the visible-spectrum sensor images using the 15 keypoints approach developed in MPI. Specifically, we used the MPI model with 4 stages: a variation of the MPI model with the number of CNN stages reduced to 4, which is faster but less accurate for real-time purposes. This automatic labeling represents the ground truth which will be learned by the residual neural network.

Second, homography estimation between thermal and spectrum visible images was computed using the Ransac method [17]. So, from paired thermal and visible-spectrum images, we selected 10 related keypoints in the image which correspond to the same location. The homography between both cameras was performed with a manual selection of related points. Next, the Ransac method computed the homography which was applied from visible spectrum to thermal to obtain an accurate relation of keypoints.

Third, a data augmentation method [27] allowed us to solve the problem of learning with large volumes of labeled data. In this case, we carried out a data augmentation process, where each original image was transformed to generate several synthetic images. The method consisted of scaling, horizontal and vertical flip, rotation and translation of points of the original image. These rotation, translation, and scaling processes are performed in random parameters and must applied to the final homography for the labeling and source images to be correlated.

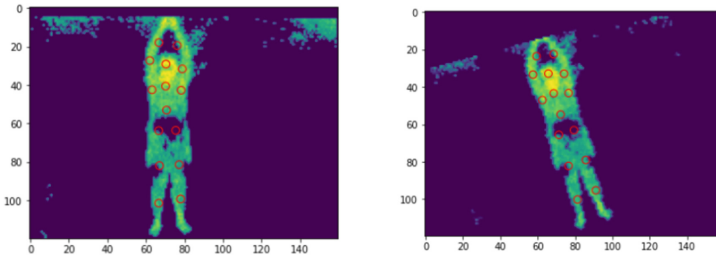Figure 5 shows an example of data augmentation for the same image:

Fig. 5. Original image and synthetic image generated by data augmentation along with related landmarks

3.3   Residual Neural Network Configuration

In this section we describe the modeling of the residual neural network which has been developed and optimized for this work. The following key points are highlighted: i) it is a lighter model to be deployed in non-deep design IoT boards. ii) it includes a dropout layer in residual blocks to avoid overfitting. iii) a progressive multi-layer regressor has been developed from flatten layer to 30 values which represents the coordinates x, y of 15 MPI keypoints from the body landmarks.

The estimation of the landmark points is computed as a regression (15 points of x, y coordinates) on an output of 30 values. For this purpose, a residual network model has been proposed [10]. A residual neural network, also well know as ResNet, is an artificial neural network that is based on pyramidal cell constructs similar to that of the cerebral cortex. Residual neural networks develop their architecture by using jump connections or shortcuts to jump over some layers. Typical ResNet models are implemented with layer breaks that contain value normalization and filtering. In our case, it was key to provide the dropout layer in ResNet blocks. Dropout was first introduced in [29] and was then adopted by many successful architectures, such as [33], in broad models that had a large number of parameters to prevent feature coadaptation and overfitting.

The creation of the residual networks is done by means of blocks that encapsulate the filters and reductions of classic filters. These networks have been some of the best-performing in pattern recognition. The blocks are built with 2–3 layers where the final one establishes links (or escapes) between the inputs or the outputs. In Fig. 6, we describe the block model design for this network.

From these basic building blocks, a multi-block network model can be straightforwardly designed. In our case we have defined 10 blocks which configure a non-deep network which can be deployed in smart boards in an efficient way.

In this design, the inputs are 120×160 images. We designed two models (A,B) in the configuration of the residual blocks:

– 2 Conv-2D are applied in model (A) and 3 Conv-2D are applied in model (B).
– Stride is the number of pixels shifts over the input in Conv2D. It is set to stride $= 1$ in A) and stride $= 2$ in the block B). Stride $= 2$ provides a down-sampling of the original input size.
– Kernels determine the dimensions of the kernel in the convolution. They are set to size $= 3$.
– The number of filters define the number of output channels created after the kernel is convolved over the input. They are increased from 32 to double size progressively in blocks.

The creation of the 10 residual blocks are interleaved between models A,B in the shape $A, B, \cdot, A, B$. In Fig. 6, we describe the configuration of residual blocks A and B.

At the end, the output of the last layer, sized (8, 10, 512), is finally integrated into a normalization layer by an average mean layer (instead of applying the maximum, like in traditional neural networks). The unrolling of the blocks generates 17 layers for the creation of final network.

To relate the final abstract output of the last layer with the output, a neural network which is composed of 3 dense layers has been created. It reduces the abstract patterns using 2048, 512, 128 neurons up to 30 values of the regression estimation, which finally configures the values of the positions of the landmarks (x and y). The total model requires more than 40 million parameters to estimate.

The residual neural network performs learning in a iterative way using mean square error for rectification and the Adam method as an adaptive learning rate optimizer [13]. The final configuration of the network is shown in Fig. 6.
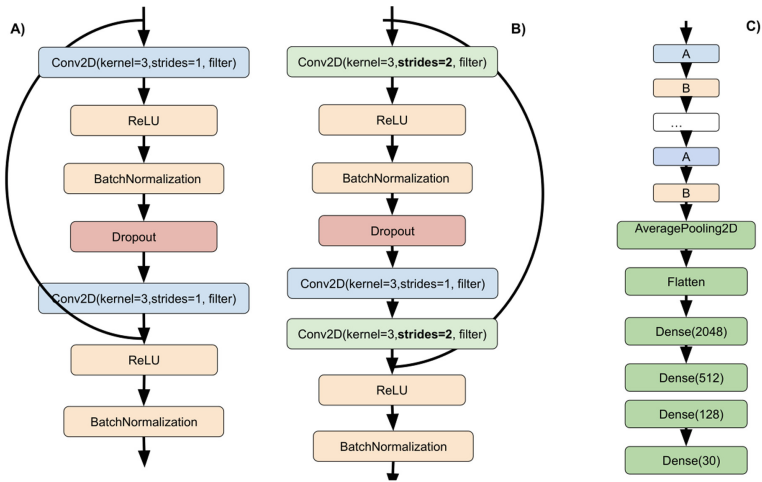

Fig. 6. Models (A) and (B) design of residual blocks. Model B develops a downsampling of input size. (C) Residual neural network based on configuration of blocks A and B with final optimization layers.

4   Case Study

In this section, we present the results obtained from the evaluation of keypoints of an inhabitant's body landmarks from thermal images. The case study involves 4 participants.

First of all, we have to highlight that a very rapid data collection has been carried out with the approach proposed in the work. 120 samples were collected for each participant (a total of 480) performing different frontal poses with thermal vision and visible-spectrum cameras. The participants performed tai chi exercises over 6 min while the IoT device collected the images at 3-second intervals.

For noise removal, normalization and body highlighting in the thermal images, a membership function, whose values are $l_1 = 122, L_2 = 255$ respectively, was applied on the values of the thermal matrix. The thermal data were augmented (K = 10 times) and processed with OpenPose to automatically label the thermal images using the MPI body landmarks format.

A leave-one-out cross-validation was applied to perform the evaluation using data not observed in the training set. So, the training dataset was collected from 3 participants (360 original frames), which was augmented (K = 10) to obtain 3600 synthetic training frames. The test dataset is composed by the left out participant (120 original frames).

The residual network model proposed for the keypoints regression has been compiled for learning in a batch of 64 images, which are loaded in this size of block and whose weights are optimized at the end of the batch. Learning was done for a total number of 50 epochs on a computer with a seventh-generation Intel i7 processor and 16 GB of RAM. It took 12 and a half hours.

The root mean square error (RMSE) measures the deviation of the landmark values obtained from the ground truth. In Fig. 7, we describe the evolution of the RMSE in training and testing regarding learning in the residual network epochs. We can see how the test evaluation error is significantly greater than the training error, being estimated at RMSE(test) = 2.46 and RMSE(train) = 9.80 in the last epoch.

As the RMSE value is not descriptive enough with respect to the quality of the visual results, in the Fig. 8 we include some images of the generated model and the model's validation of several thermal images to estimate the 15 landmark points. Classic poses have high accuracy; however, poses with foreshortening are not well estimated in all the parts of the body.

We note that the testing images were not integrated into the learning process and the results are very encouraging, especially considering the small number of images used in the data collection. In future works, data collection from more users will allow us to establish a more precise model for pose recognition.
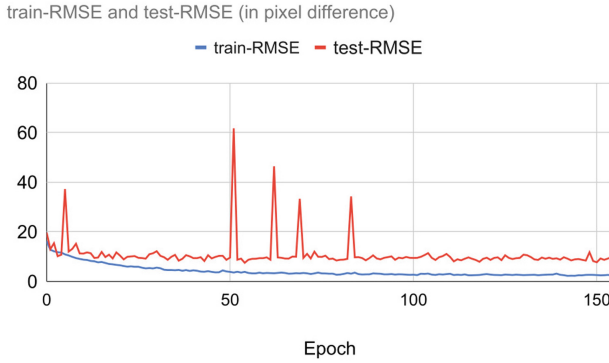
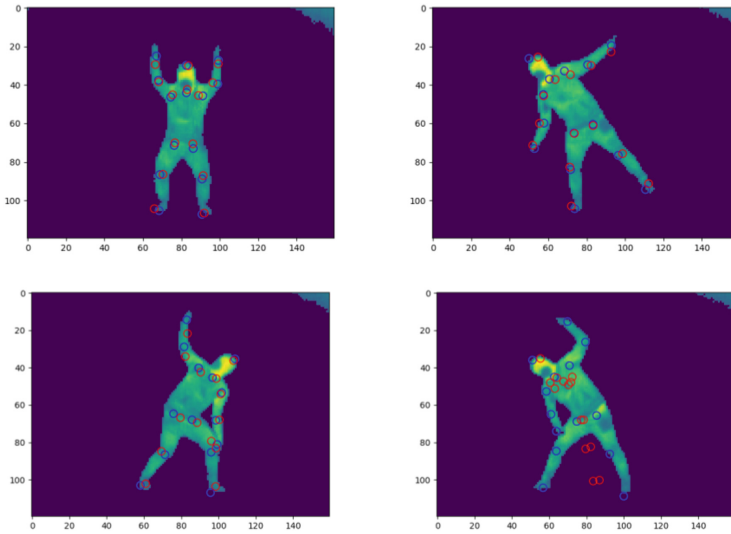**Fig. 7.** Evolution of RMSE in training and testing regarding learning in residual network epochs.

Fig. 8. Results

5 Conclusions, Limitations and Ongoing Work

In this work we have presented a residual neural network developed to compute the keypoints of body landmarks of inhabitants. In this approach, for auto labeling: i) an IoT device with dual-vision thermal and visible-spectrum sensors collect paired images, ii) OpenPose computes MPI landmarks to generate the ground truth from visible-spectrum images. So, the residual neural network learns in the new thermal vision domain from the knowledge of the trained visible-spectrum Open Pose neural network.

The results are encouraging, achieving high quality estimation; however, some poses with foreshortening require deep training with additional wider data, including balancing of poses. We mainly highlight the importance of including dual-vision sensors in an IoT board and a data augmentation method to collect a significant amount of high-quality data in a few minutes. This could be expanded further by collecting a larger dataset with different users and poses in heterogeneous contexts.

Finally, in order to obtain a model as robust as OpenPose for thermal vision, some limitations of the work have to be worked on in future works. First, poses are frontal, without being affected by occlusion or segmentation of the inhabitant's image. Second, multi-occupancy is not supported. These shortcomings will need to be addressed with several models developed over different stages: detection of users by bounding box or estimation of visible/non-visible landmarks. In addition, in pre-processing data, automatic estimation of homography between cameras and an automatic background remover would be necessary for the approach to be robust in different deployment and heat conditions.

References

1. Al-Sarawi, S., Anbar, M., Alieyan, K., Alzubaidi, M.: Internet of Things (IoT) communication protocols. In: 2017 8th International Conference on Information Technology (ICIT), pp. 685–690. IEEE (2017)
2. Ali Hamad, R., Järpe, E., Lundström, J.: Stability analysis of the t-SNE algorithm for human activity pattern data. In: The 2018 IEEE International Conference on Systems, Man, and Cybernetics (SMC 2018) (2018)
3. Badave, H., Kuber, M.: Evaluation of person recognition accuracy based on openpose parameters. In: 2021 5th International Conference on Intelligent Computing and Control Systems (ICICCS), pp. 635–640. IEEE (2021)
4. Cao, Z., Hidalgo, G., Simon, T., Wei, S.E., Sheikh, Y.: OpenPose: realtime multi-person 2D pose estimation using part affinity fields. IEEE Trans. Pattern Anal. Mach. Intell. **43**(1), 172–186 (2019)
5. Cao, Z., Simon, T., Wei, S.E., Sheikh, Y.: Realtime multi-person 2D pose estimation using part affinity fields. In: Proceedings of the IEEE Conference on Computer Vision and Pattern Recognition, pp. 7291–7299 (2017)
6. Csurka, G.: Domain adaptation for visual applications: a comprehensive survey. arXiv preprint arXiv:1702.05374 (2017)
7. Espinosa, Á.V., López, J.L.L., Mata, F.M., Estevez, M.E.E.: Application of IoT in healthcare: keys to implementation of the sustainable development goals. Sensors **21**(7), 2330 (2021)

8. Griffiths, E., Assana, S., Whitehouse, K.: Privacy-preserving image processing with binocular thermal cameras. Proc. ACM Interact. Mob. Wearab. Ubiquit. Technol. **1**(4), 1–25 (2018)

9. Han, J., Bhanu, B.: Human activity recognition in thermal infrared imagery. In: 2005 IEEE Computer Society Conference on Computer Vision and Pattern Recognition (CVPR 2005)-Workshops, pp. 17. IEEE (2005)

10. He, K., Zhang, X., Ren, S., Sun, J.: Deep residual learning for image recognition. In: Proceedings of the IEEE Conference on Computer Vision and Pattern Recognition, pp. 770–778 (2016)

11. Hidalgo, G., Raaj, Y., Idrees, H., Xiang, D., Joo, H., Simon, T., Sheikh, Y.: Single-network whole-body pose estimation. In: Proceedings of the IEEE/CVF International Conference on Computer Vision, pp. 6982–6991 (2019)

12. Hiriyannaiah, S., Akanksh, B.S., Koushik, A.S., Siddesh, G.M., Srinivasa, K.G.: Deep learning for multimedia data in IoT. In: Tanwar, S., Tyagi, S., Kumar, N. (eds.) Multimedia Big Data Computing for IoT Applications. ISRL, vol. 163, pp. 101–129. Springer, Singapore (2020). https://doi.org/10.1007/978-981-13-8759-3_4

13. Jais, I.K.M., Ismail, A.R., Nisa, S.Q.: Adam optimization algorithm for wide and deep neural network. Knowl. Eng. Data Sci. **2**(1), 41–46 (2019)

14. Jara-Quito, H.J., Guerrero-Vasquez, L.F., Parra-Luzuriaga, K.A., Ojeda-Sanchez, M.V., Bravo-Torres, J.F.: Avatar: human-computer interface for interaction with children using a live animation process based in facial and body landmarks recognition. In: 2021 International Conference on Computing, Communication, and Intelligent Systems (ICCCIS), pp. 715–720. IEEE (2021)

15. Jin, S., et al.: Whole-body human pose estimation in the wild. In: Vedaldi, A., Bischof, H., Brox, T., Frahm, J.-M. (eds.) ECCV 2020. LNCS, vol. 12354, pp. 196–214. Springer, Cham (2020). https://doi.org/10.1007/978-3-030-58545-7_12

16. Kong, X., Meng, Z., Meng, L., Tomiyama, H.: A privacy protected fall detection IoT system for elderly persons using depth camera. In: 2018 International Conference on Advanced Mechatronic Systems (ICAMechS), pp. 31–35. IEEE (2018)

17. Li, X., Liu, Y., Wang, Y., Yan, D.: Computing homography with RANSAC algorithm: a novel method of registration. In: Electronic Imaging and Multimedia Technology IV, vol. 5637, pp. 109–112. International Society for Optics and Photonics (2005)

18. López-Medina, M., Espinilla, M., Cleland, I., Nugent, C., Medina, J.: Fuzzy cloud-fog computing approach application for human activity recognition in smart homes. J. Intell. Fuzzy Syst. **38**(1), 709–721 (2020)

19. Martínez-González, A., Villamizar, M., Canévet, O., Odobez, J.M.: Efficient convolutional neural networks for depth-based multi-person pose estimation. IEEE Trans. Circuits Syst. Video Technol. **30**(11), 4207–4221 (2019)

20. Medina-Quero, J., Zhang, S., Nugent, C., Espinilla, M.: Ensemble classifier of long short-term memory with fuzzy temporal windows on binary sensors for activity recognition. Expert Syst. Appl. **114**, 441–453 (2018)

21. Mohammadmoradi, H., Munir, S., Gnawali, O., Shelton, C.: Measuring people-flow through doorways using easy-to-install IR array sensors. In: 2017 13th International Conference on Distributed Computing in Sensor Systems (DCOSS), pp. 35–43. IEEE (2017)

22. Ordóñez, F.J., Roggen, D.: Deep convolutional and LSTM recurrent neural networks for multimodal wearable activity recognition. Sensors **16**(1), 115 (2016)

23. Osokin, D.: Real-time 2D multi-person pose estimation on CPU: lightweight openpose. arXiv preprint arXiv:1811.11004 (2018)

24. Patricia, N., Caputo, B.: Learning to learn, from transfer learning to domain adaptation: a unifying perspective. In: Proceedings of the IEEE Conference on Computer Vision and Pattern Recognition, pp. 1442–1449 (2014)
25. Polo-Rodriguez, A., Cruciani, F., Nugent, C.D., Medina, J.: Domain adaptation of binary sensors in smart environments through activity alignment. IEEE Access **8**, 228804–228817 (2020)
26. Quero, J.M., Burns, M., Razzaq, M.A., Nugent, C., Espinilla, M.: Detection of falls from non-invasive thermal vision sensors using convolutional neural networks. In: Multidisciplinary Digital Publishing Institute Proceedings, vol. 2, p. 1236 (2018)
27. Shorten, C., Khoshgoftaar, T.M.: A survey on image data augmentation for deep learning. J. Big Data **6**(1), 1–48 (2019)
28. Sixsmith, A., Johnson, N.: A smart sensor to detect the falls of the elderly. IEEE Perv. Comput. **3**(2), 42–47 (2004)
29. Srivastava, N., Hinton, G., Krizhevsky, A., Sutskever, I., Salakhutdinov, R.: Dropout: a simple way to prevent neural networks from overfitting. J. Mach. Learn. Res. **15**(1), 1929–1958 (2014)
30. Voulodimos, A., Doulamis, N., Doulamis, A., Protopapadakis, E.: Deep learning for computer vision: a brief review. In: Computational Intelligence and Neuroscience 2018 (2018)
31. Wang, J., Chen, Y., Hao, S., Peng, X., Hu, L.: Deep learning for sensor-based activity recognition: a survey. Pattern Recogn. Lett. **119**, 3–11 (2019)
32. Xie, S., Girshick, R., Dollár, P., Tu, Z., He, K.: Aggregated residual transformations for deep neural networks. In: Proceedings of the IEEE Conference on Computer Vision and Pattern Recognition, pp. 1492–1500 (2017)
33. Zagoruyko, S., Komodakis, N.: Wide residual networks. arXiv preprint arXiv:1605.07146 (2016)
34. Zhang, S., Wei, Z., Nie, J., Huang, L., Wang, S., Li, Z.: A review on human activity recognition using vision-based method. J. Healthcare Eng. **2017** (2017)

NMF for Quality Control of Multi-modal Retinal Images for Diagnosis of Diabetes Mellitus and Diabetic Retinopathy

Anass Benali[1,2(✉)], Laura Carrera[1,2], Ann Christin[1,2], Ruben Martín[1,2,6], Anibal Alé[3], Marina Barraso[3], Carolina Bernal[3], Sara Marín[3], Silvia Feu[3], Josep Rosinés[3], Teresa Hernandez[3,6], Irene Vilá[3,6], Cristian Oliva[3,6], Irene Vinagre[4,5,6], Emilio Ortega[4,5,6], Marga Gimenez[4,5,6], Enric Esmatjes[4,5,6], Javier Zarranz-Ventura[3,4,6], Enrique Romero[1,2], and Alfredo Vellido[1,2]

[1] Intelligent Data Science and Artificial Intelligence Research Center (IDEAI-UPC), Barcelona, Spain
anass.benali@gmail.com
[2] Computer Science Department, Facultat d'Informàtica de Barcelona (FIB), Universitat Politècnica de Catalunya (UPC BarcelonaTech), Barcelona, Spain
[3] Institut Clínic d'Oftalmología (ICOF), Hospital Clínic de Barcelona, Barcelona, Spain
[4] Diabetes Unit, Hospital Clínic de Barcelona, Barcelona, Spain
[5] Institut Clínic de Malalties Digestives i Metaboliques (ICMDM), Hospital Clínic de Barcelona, Barcelona, Spain
[6] August Pi i Sunyer Biomedical Research Institute (IDIBAPS), Barcelona, Spain

Abstract. In current ophthalmology, images of the vascular system in the human retina are used as exploratory proxies for pathologies affecting different organs. In this brief paper, we use multi-modal retinal images for assisting diagnostic decision making in diabetes mellitus and diabetic retinopathy. We report the use of matrix factorization-based source extraction techniques to pre-process the images as a data quality control step prior to their classification. Through this quality control, we unveil some relevant sources of bias in the data. After correcting for them, promising pathology classification results are still obtained, which merit further exploration.

Keywords: Retinal imaging · Non-negative matrix factorization · Source extraction · Medical data quality control · Diabetes mellitus · Diabetic retinopathy

1 Introduction

Diabetic Retinopathy (DR) is the leading cause of human blindness in Type 1 Diabetes Mellitus (DM) patients. It is a serious and lifelong condition, estimated to constitute just between 5 to 10% of all diabetes cases [4] and characterized by
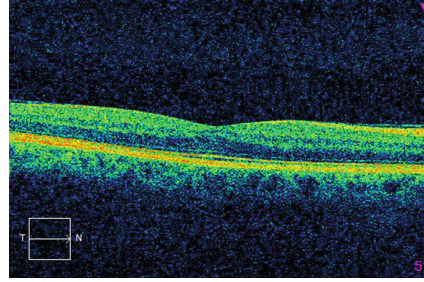
Fig. 1. Fundus retinography.

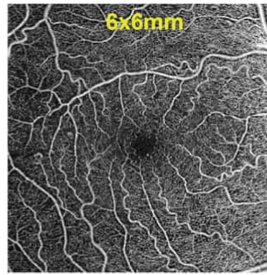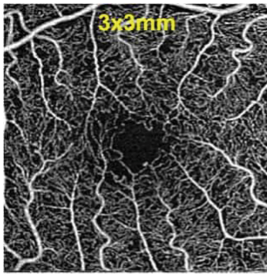**Fig. 2.** Optical coherence tomography.

Fig. 3. Optical coherence tomography angiography images at two resolution levels.

the pancreas inability to generate enough insulin. When related complications affect the blood vessels in the retina, it can develop in what its known as DR, which may cause several vision difficulties [12].

In its early stages, DR may cause no symptoms, making it hard to detect and diagnose, as the differences between a healthy eye and an eye with early-stage DR are not obvious. Consequently, detecting DR early on after onset is key to slow its advancement, or even prevent the vision complications which can lead to blindness if left untreated.

Different non-invasive imaging techniques can be applied to the study of retinal diseases in general, and DR in particular, such as fundus retinography (FR, Fig. 1), structural Optical Coherence Tomography (OCT, Fig. 2), or Optical Coherence Tomography Angiography (OCTA, Fig. 3).

Standard DR screening systems use FR [8] due to its widespread availability. For this reason, the vast majority of computational science applications in ophthalmology have been applied to FR images and, far more rarely, to OCT scans, which are not so readily available. Recently, the advent of the more advanced (and still scarcely used) OCTA technology allows for direct visualization of flow in the retinal vessels, easing the evaluation of these patients.

We analyze a high-quality multi-modal image dataset gathered in previous ophthalmology research projects [1–3,14]. The ultimate goal of its analysis is diagnostic classification to be provided to the expert for decision-making assis-

tance. In this study, though, we focus on image quality control prior to classification, using source extraction techniques, namely non-negative matrix factorization (NMF) and some of its variants. This quality control is a necessary step to guarantee the robustness of the diagnostic assistance tool.

2   Materials and Methods

There are three image modalities in the analyzed dataset, namely FR, OCT and OCTA. For the OCTA images there are, in turn, four sub-modalities: $3 \times 3mm$ *superficial*, $3 \times 3mm$ *deep*, $6 \times 6mm$ *superficial* and $6 \times 6mm$ *deep*. Here *superficial* and *deep* refer to the perifoveal superficial capillary plexus (SCP) and perifoveal deep capillary plexus (DSP), respectively.

This dataset is quite unique in that it only includes patients with Type 1 diabetes and that it also includes a subset of controls with no diabetes.

The DR scale is redefined to include such controls as *class 0* and, therefore, we have classes *0: Controls*, *1: No DR*, *2: Mild Non-proliferative DR*, *3: Moderate Non-proliferative DR*, *4: Severe Non-proliferative DR*, and *5: Proliferative DR*.

The original dataset includes 599 people in total. The retinal images acquired with the three imaging techniques (FR, OCT, OCTA) are available for both the left and right eye (whenever possible).

For a variety of reasons some of the images (and related clinical information) were missing in the original dataset. Therefore, the data needs some preliminary filtering. Also, some of the OCT, OCTA, FR scans are corrupted. Some examples of this can be seen in Fig. 4.
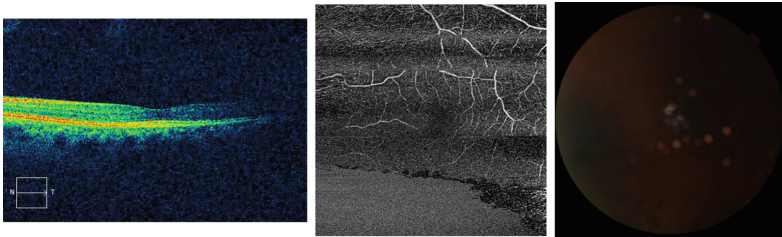

Fig. 4. Examples of corrupted OCT, OCTA and FR images.

Besides, some of the eyes on the dataset have other eye pathologies or previous treatments. To avoid biasing the models, only people with good enough quality OCT and OCTA were included. Also, patients that underwent treatment or surgery that can affect the captured features were filtered out.

The pre-filtering process for the OCT and OCTA was performed as specified in a previous study [2]. The FR images do not have any quality information and so they are all included in this filter.
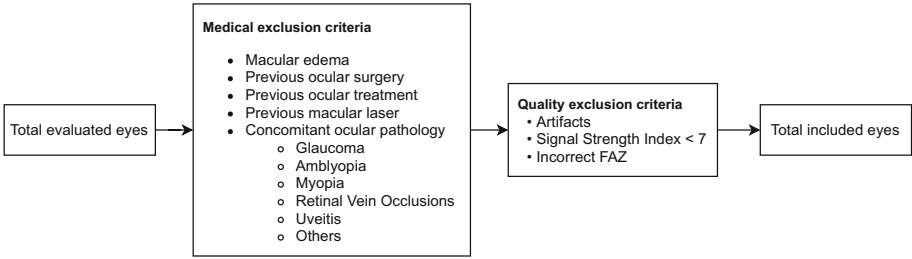
Fig. 5. Diagram showing the exclusion criteria [2].

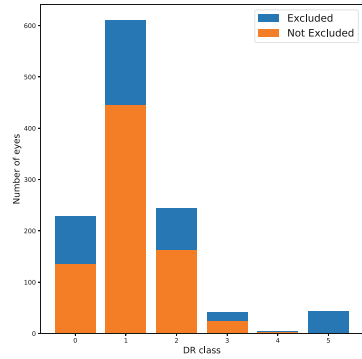| DR scale	No. eyes before filter	No. eyes after filter
0	228	136
1	610	445
2	245	162
3	42	25
4	5	2
5	44	1

Fig. 6. DR class counts.

Fig. 7. Distribution of exclusion by class labels.

After applying the exclusion criteria, as graphically described in Fig. 5, we are left with 771 eyes.

Inspecting the distribution of the instances in the dataset (See Fig. 6) and their distribution of exclusion (See Fig. 7), too few class 3, class 4 and class 5 eyes are found to remain after filtering. Thus, from a classification viewpoint, it makes more sense to aggregate them into three classes: class 0, class 1 and class {2,3,4,5}, representing Controls, Type 1 diabetic with no DR and Type 1 diabetic with DR, respectively.

The ultimate goal of this investigation is the assessment of the capabilities of discrimination in the following two binary classification problems:

– **classification task 0-15:** Discrimination between the eyes of non-diabetics (controls) and of Type 1 diabetics, which corresponds to class {0} *versus* class {1,2,3,4,5}.
– **classification task 1-25:** Discrimination between no DR eyes and clinical DR eyes, corresponding to class {1} *versus* class {2,3,4,5}.

We will start by building small standard NMF models for a first exploration of the quality of the extracted image sources, removing those which are artefactual and reconstructing the target image through a linear combination of the relevant

ones. In this setting, we prefer sources to capture sparse localized features so that the parts-based representation is easier to interpret for medical experts.

After this pre-processing, several models of the NMF family, namely standard NMF [10], Sparse NMF [9], Separable NMF [6] and Convex NMF [5] will be built for each of the six types of image. The rank r (number of extracted sources) will be estimated by inspecting the decay of the SVD eigenvalues. We will retain a relatively large number of components so as not to restrict too much the features the models can learn.

For each combination of image type, model and parametrization, the data matrix decomposition obtained consists of sources and weights (encoding). Following similar approaches [13] that used NMF as the basis for subsequent classification, the encoding matrices of all NMF variants will be used as input variables in preliminary feature selection and classification models.

3 Exploratory Pre-processing

The first exploratory step consists on experimenting with small standard NMF models for each type of image and inspecting the extracted sources. The result of this step reveal some issues that should be fixed before using the encoding matrices of NMF for classification.

3.1 Retinography

Some small standard NMF models were built from the FR photographs, where images were initially modeled in a RGB (Red, Green, Blue) colour space. From Fig. 8, we see that the extracted sources only separate the colour channels, the shades and illuminations, instead of intrinsic anatomical differences. Therefore, we will need to normalize the illumination in order to learn more effective features. This can be achieved with local adaptive filters. Here, we make use of the FR image pre-processing method made public by the winner of the Kaggle 2015 FR images competition [7].
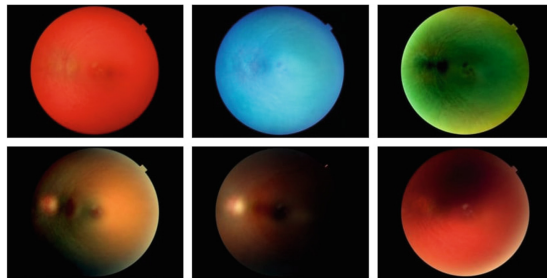

Fig. 8. Six sources of the FR exploratory model

3.2   OCT

Looking at the sorces reported in Fig. 9, it seems clear that the NMF model is actually learning different translations and rotations of the OCT scans, which, again, is not what we sought. Moreover, the strange-looking last source is actually the result of some OCT scans being in a grayscale colour space instead of RGB.

An expert ophthalmologist confirmed that OCT scans were originally grayscale and that the colour in the image is extraneous. Therefore, they were all transformed to grayscale.
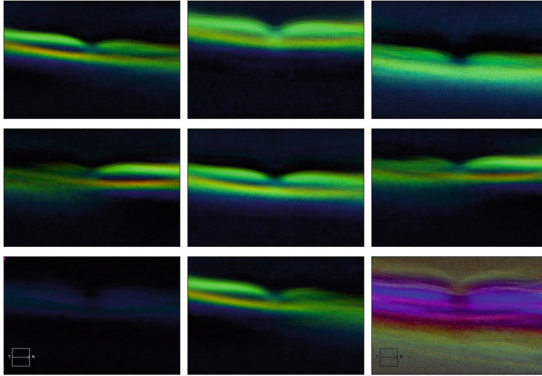

Fig. 9. Nine OCT sources of the exploratory model

To learn more intrinsic features instead, we developed a pre-processing step to isolate the regions of interest (ROI).

The existence of a legend and symbol on the bottom-left of the OCT scan was also noticed. This recurrent feature was being isolated in its own source by NMF. Interestingly, the artefactual patterns present in the OCT scans (a magenta bar and the legend) where not identified as completely individual sources until setting the models to extract 13 sources (rank $r = 13$).

3.3   OCTA

OCTA images were found to be mostly fine to be used as they are. In Fig. 10, some of the extracted sources are shown. Nevertheless, we still used noise reduction filters such as a median filter, bilateral filter and different types of image thresholding to improve the images.

The model still identified artefacts in some of the images. For example, one source helped identifying six images (see Fig. 11) containing the camera model watermark on the bottom right. It also identified the eye of a patient with a very unusual path of the eye nerve through the FAZ area, as seen in Fig. 12. All these edge cases were fixed or filtered out.
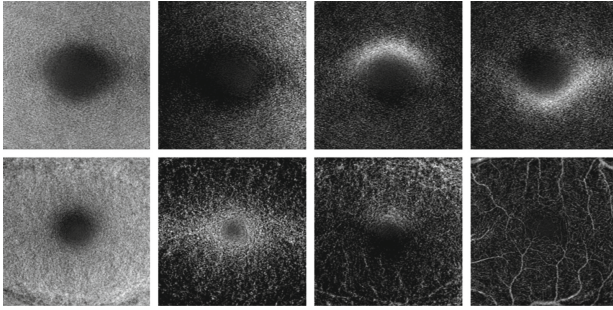
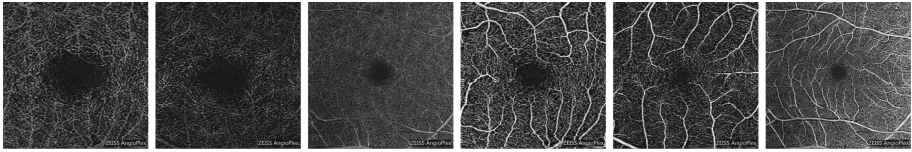**Fig. 10.** Top row: OCTA *deep* sources. Bottom row: OCTA *superficial* sources.

Fig. 11. OCTA images with a watermark on the bottom right corner.
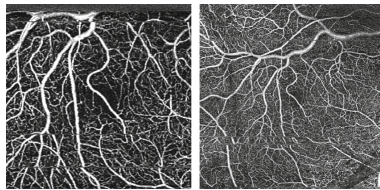
Fig. 12. Eye with unusual vessel pathing. Left: $3 \times 3\,\text{mm}$ Right: $6 \times 6\,\text{mm}$

4 Learning Unsupervised Part-Based Representations

Once the pre-processing of the images was carried out, a definitive extraction was implemented with all the models. Each NMF variant was run with different initializations (random, NNDSVD and NNDSVDa).

Regarding the number of components or sources to extract in the factorization models, since the ultimate goal is using the transformed data as the basis for a classification problem, a cross-validation (CV) scheme could be used for its choice. However, it would have to be tuned for each model and initialization. This is a rather cumbersome procedure and, therefore, we opted for a different strategy: a sensible range of values was found by inspecting the decay of the SVD eigenvalues (tantamount to looking at the retained variance of PCA) and was run for different numbers of sources. Supervised feature selection was then applied and used to decide which decomposition was best in terms of classification.

We tried to use the images at full resolution, but, for computational expediency, and given that preliminary results were not significantly different, image

sizes were reduced (for FR, to 256×256; for OCT, to 100×500; and for OCTA, to 256×256). With these, the SVD explained variance was calculated (see Fig. 13).
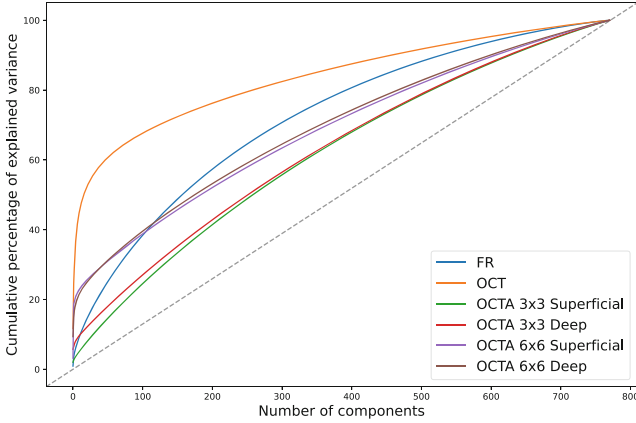

Fig. 13. SVD cumulative percentage of variance explained, for all image modalities.

It is noteworthy that OCT images show a "better" curve than the rest, as a low number of components already explain much variance. A possible reason for that could be that the factorization method does not agree well with the vessel variability present on the FR and OCTA images.

Based on the plot, we decided to run the models for $r \in \{64, 128, 256, 384\}$. Going beyond that for most models would result in learning specific cases, instead of features. For the sparse models though, it could make sense to have a larger number of features, but we do not expect to have a large amount of relevant sparse and localized features in the data.

The resulting encoding matrices were subsequently used as input features in classification designs. Then a feature selection and double CV scheme was performed to train and test the models.

4.1   Feature Selection and Classifier Training

A supervised feature selection approach based on mutual information (MI) was applied and a stratified double-cross CV scheme was used to robustly train and test the classification models.

Feature selection was carried for each of the classification tasks (diabetic or non-diabetic and presence of DR) and for each subset of features (FR, OCT, OCTA and all of them). The following ML/statistical classifiers were used: LR, LDA, Linear SVM and RBF-SVM.

Each selected subset of features was ordered from highest to lowest MI with the target class and the first 32 features were selected. This procedure uses a

10-fold CV; thus, the MI of each variable is computed for each CV split, resulting on 10 MI estimates for each variable that are then averaged.

Then, using a double CV scheme, the hyper-parameters of the classification models were optimized and the generalization error estimated. Specifically, the inner CV was used to select the best hyper-parameters according to the averaged validation AUC metric. Once the parameters of the models have been defined, a (optional) backward elimination wrapper method was applied to remove the irrelevant or less useful features for the model. In order to check if a feature can be safely removed, the hyper-parameters are re-optimized on the same corresponding inner CV to see if there is a decrease on the averaged AUC metric. Once the features and hyper-parameters are selected, a model is re-trained for each inner CV train split and are tested on the corresponding outer test CV fold.

The stratified double CV is defined with 5 splits on the outer CV and 4 splits of the inner CV (a total of 20 iterations). Using this scheme, 20 test estimates are obtained, which are displayed in the study as a boxplot.

The grid search for the classifier hyper-parameters is shown in Table 1.

Table 1. Grid search values for the hyper-parameters of the classification methods. The notation $x : y$ denotes all the integers in the range $[x, y]$.

Method	Hyper-parameters
Logistic regression	$C = 10^{-3:3}$
LDA	None
Linear SVM	$C = 10^{1:4}$
RBF-SVM	$C = 10^{1:4}$, $\gamma = 10^{-4:1}$

5 Results and Discussion

5.1 Useful Sources Learnt

After executing the models, we take a look at the learnt components. We show some of the relevant learnt standard NMF sources for each type of image when initialized with NNDSVD. Here, the NMF variants components are not shown because they are less intuitive to interpret and not always parts-based representations.

Some of the learnt NMF components for the FR images are represented in Fig. 14. The sources mostly seem to capture the thickest vessels. Like in the OCTA sources, there is variability on the positioning of the vessels which ends captured in different sources.

Figure 15 shows some of the sources learnt by NMF for OCT images. We can see that the sources are a localized parts-based representation.

Looking at the learnt NMF components for the *deep* OCTA images (Fig. 16) reveals that they capture the different patterns around the FAZ area.
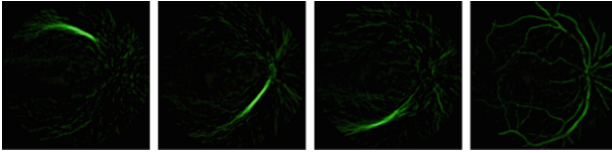
Fig. 14. Some NMF sources from FR images when initialized with NNDSVD
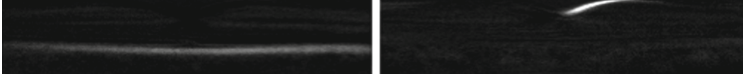
Fig. 15. Some NMF sources from OCT retinal images (initialized with NNDSVD)
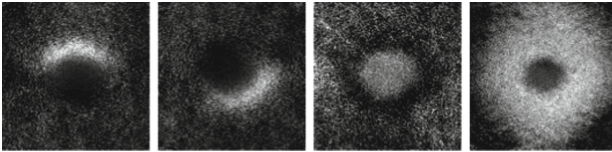
Fig. 16. Some NMF sources from OCTA *deep* images (initialized with NNDSVD)

The learnt NMF features for the *superficial* OCTA images can bee seen in Fig. 17. A sparse representation is learnt. We notice that the bottom vessel is being captured by different components depending of its position.
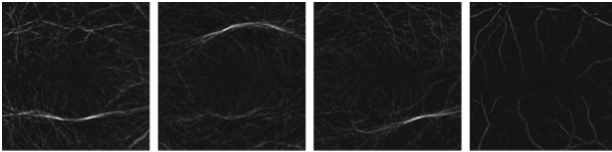
Fig. 17. Some NMF sources from OCTA *superficial* (initialized with NNDSVD)

5.2   Classification Results

For comparison, a *Dummy Classifier* that generates predictions by following the training set class distribution is included. It will have an average AUC of 0.5.

We note that if the pre-processing explained on Sect. 3 is not applied, the classification results are no better than random.

Discriminating DR. For classification task 1-25 (see Sect. 2), we obtain the results shown in Fig. 18. OCT features yield the best results. The FR and OCTA features produce more or less similar results. The best results are obtained for logistic regression and LDA. We hypothesize that the reason SVM classifiers

work worse is because the hyper-parameter search was not exhaustive enough, but this should be further investigated (Fig. 19).
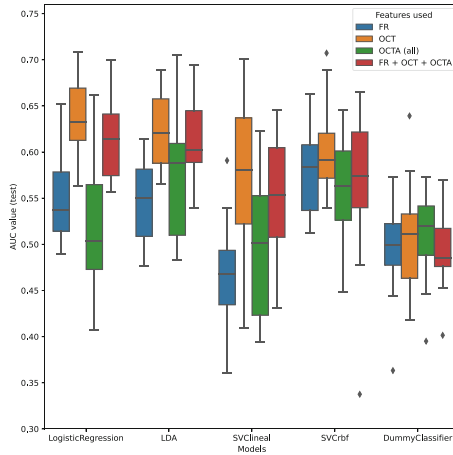
Fig. 18. Boxplot of AUC results for classification *task 1-25*.

Discriminating DM. For classification task 0-15, we obtain the results shown on Fig. 19(a). It can again be seen that the OCT features yield the best performance. The FR features work better than random, while the OCTA features are all over the place. At this point, we inspected the sources yielding the best results and found a bias in the data: that the range of images from 388 to 420 have OCT scans with an unexpected noise and level of gray. Some examples can be observed in Figs. 20 and 21.

This, in itself, would not be necessarily a problem if it was not because that range of images has more controls than the other classes. In the filtered data, those are 32 individuals of class 0, 4 of class 1 and 1 of class 2.

According to the ophthalmologist, a possible explanation for this could be that the lens of the camera equipment was dirty when those images were taken, or an artefact in the export from the camera equipment software. We decided to test how the model performs when removing those instances. This change means reducing the number of *class 0* eyes from 136 to 104. By doing so, the results shown in Fig. 19(b) are obtained. They worsen slightly for OCT and have higher variance. Oddly enough, the results for retinography marginally improved. Since there is no quality filter for the FR images, it could be that the removed instances were difficult ones where the models previously failed. Also, we notice that, although the OCTA results worsen slightly on average, they exhibit lower variance.
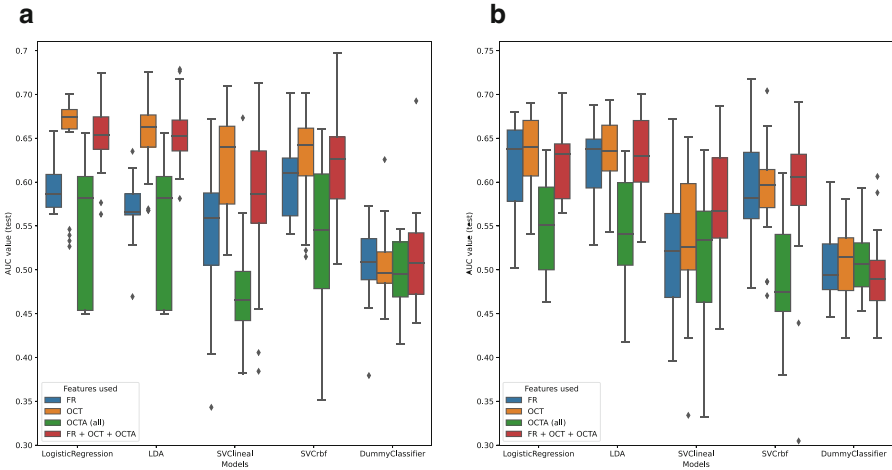
Fig. 19. Boxplots of the results when discriminating DM from controls. (a) Boxplot of *task 0-15*. (b) Boxplot of *task 0-15* (without bias)
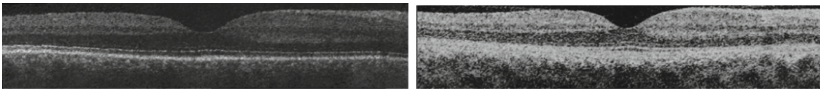
Fig. 20. Example of the found bias in the preprocessed data
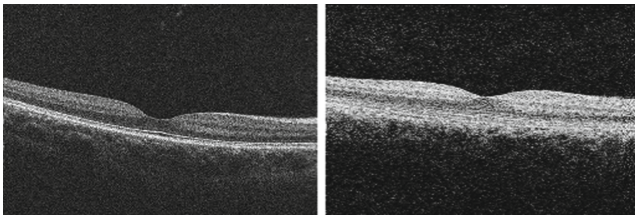
Fig. 21. Example of the found bias on the original images

Discriminating Controls from DR. For completeness, we perform the classification task class 0 versus {2,3,4,5}. Hence, we remove *class 1* (the majority class), emphasizing the importance of the detected bias of *class 0*. We call this classification *task 0-25*. Experiments were run with and without the biased data. The results are reported in Figs. 22(a) and (b), respectively.

The results are consistently better and with less variability when including the biased image range: all the models perform similarly (even SVM, which yielded worse results in the other tasks). Removing the biased range decreases the performance and increases the variability of the results, but it is still far better than the dummy classifier. Worth stressing that the use of all the features
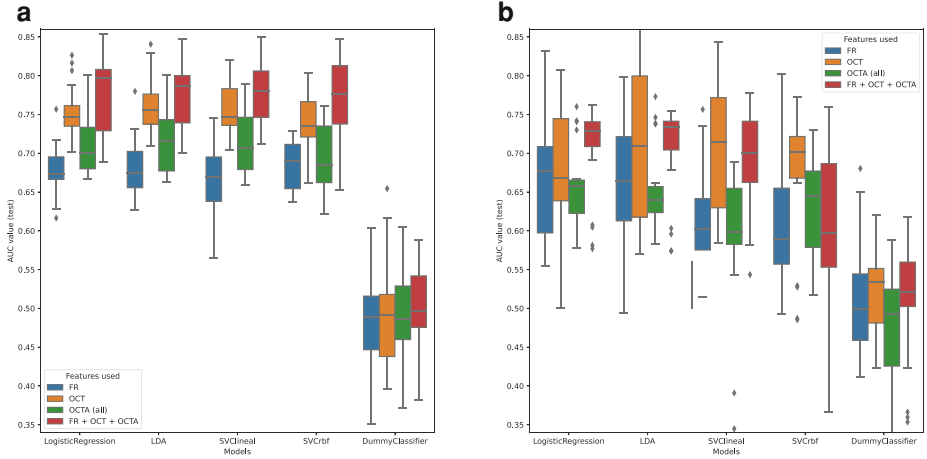
Fig. 22. (a) AUC boxplot for *task 0-25*. (b) AUC boxplot for *task 0-25* (without bias).

(FR, OCT, OCTA) gives consistently the best results, with and without bias. This task showcases the importance of having found the bias on the image data and exemplifies the potential of NMF as a quality control tool.

6   Summary and Conclusion

In this brief paper, we have shown how a matrix decomposition method for feature extraction, namely NMF, can successfully be used for quality control in a medical imaging problem, by detecting data artefacts and biases. These methods can also provide further insight into the images themselves, increasing the interpretability of the results, a requisite for the application of ML models to medical problems [11].

The results reported in the previous section indicate that the NMF description of the image data is capable of discriminating in the tasks posed, albeit with varied results. OCT with logistic regression yields the best results in task 0-15 (between 0.6 and 0.65 average AUC) and, most interestingly, for the more difficult problem of task 1-25 (between 0.65 and 0.70), which opens the door to early DR warnings for patients already with Type I DM. Encouragingly, the discrimination between controls and DR patients consistently reaches average AUC values over 0.70 with the use of all modalities. Logistic regression is a tried and trusted model in the medical domain, which could provide an extra push to the practical implementation of the NMF based analytical pipeline.

With the experiments for task 0-25 we have shown how a significant bias found using NMF-based feature extraction affects the results. This exemplifies how important is quality control and how NMF can help to identify data issues given the right settings. Overall, these promising results warrant further inves-

tigation and comparison with alternative feature extraction methods and data representations.

References

1. Alé-Chilet, A., Bernal-Morales, C., Barraso, M., et al.: Optical coherence tomography angiography in type 1 diabetes mellitus. Report 2: diabetic kidney disease. J. Clin. Med. **11**(1), 197 (2022)
2. Barraso, M., Alé-Chilet, A., Hernández, T., et al.: Optical coherence tomography angiography in type 1 diabetes mellitus. Report 1: diabetic retinopathy. Transl. Vis. Sci. Technol. **9**(10), 34 (2020)
3. Bernal-Morales, C., Alé-Chilet, A., Martín-Pinardel, R., et al.: Optical coherence tomography angiography in type 1 diabetes mellitus. Report 4: glycated haemoglobin. Diagnostics **11**(9), 1537 (2021)
4. Daneman, D.: Type 1 diabetes. Lancet **367**(9513), 847–858 (2006)
5. Ding, C.H., Li, T., Jordan, M.I.: Convex and semi-nonnegative matrix factorizations. IEEE Trans. Pattern Anal. Mach. Intell. **32**(1), 45–55 (2008)
6. Gillis, N., Vavasis, S.A.: Fast and robust recursive algorithms for separable nonnegative matrix factorization. IEEE Trans. Pattern Anal. Mach. Intell. **36**(4), 698–714 (2013)
7. Graham, B.: Kaggle diabetic retinopathy detection competition report (2015). https://www.kaggle.com/c/diabetic-retinopathy-detection/discussion/15801
8. Grzybowski, A., Brona, P., Lim, G., Ruamviboonsuk, P., Tan, G.S., Abramoff, M., Ting, D.S.: Artificial intelligence for diabetic retinopathy screening: a review. Eye **34**(3), 451–460 (2020)
9. Kim, H., Park, H.: Sparse non-negative matrix factorizations via alternating nonnegativity-constrained least squares for microarray data analysis. Bioinformatics **23**(12), 1495–1502 (2007)
10. Lee, D.D., Seung, H.S.: Learning the parts of objects by non-negative matrix factorization. Nature **401**(6755), 788–791 (1999)
11. Lisboa, P., Saralajew, S., Vellido, A., Villmann, T.: The coming of age of interpretable and explainable machine learning models. In: Proceedings of the 29th European Symposium on Artificial Neural Networks, Computational Intelligence and Machine Learning (ESANN 2021), pp. 547–556 (2021)
12. National Health Service UK: Diabetic retinopathy (2018). https://www.nhs.uk/conditions/diabetic-retinopathy/
13. Núñez, L.M., Romero, E., Julià-Sapé, M., Ledesma-Carbayo, M.J., Santos, A., Arús, C., Candiota, A.P., Vellido, A.: Unraveling response to temozolomide in preclinical gl261 glioblastoma with MRI/MRSI using radiomics and signal source extraction. Sci. Rep. **10**(1), 1–13 (2020)
14. Zarranz-Ventura, J., Barraso, M., Alé-Chilet, A., et al.: Evaluation of microvascular changes in the Perifoveal vascular network using optical coherence tomography angiography (octa) in type i diabetes mellitus: a large scale prospective trial. BMC Med. Imaging **19**(1), 1–6 (2019)

Radiomic-Based Lung Nodule Classification in Low-Dose Computed Tomography

Wojciech Prazuch[1(✉)] ⓘ, Malgorzata Jelitto-Gorska[2] ⓘ, Agata Durawa[2] ⓘ,
Katarzyna Dziadziuszko[2] ⓘ, and Joanna Polanska[1] ⓘ

[1] Department of Data Science and Engineering, Faculty of Automatic Control, Electronics
and Computer Science, Silesian University of Technology, Gliwice, Poland
{wojciech.prazuch,joanna.polanska}@polsl.pl
[2] 2nd Department of Radiology, Medical University of Gdansk, ul. Smoluchowskiego 17,
80-001 Gdansk, Poland
{Jelitto,agata.durawa,kado}@gumed.edu.pl

Abstract. Radiomics is a systematic approach to characterize objects in terms of their radiological appearance. We used radiomic features of 5027 objects of 6 classes and trained a binary classifier with 79% accuracy. Features were obtained by using our novel preprocessing pipeline for object segmentation from the lung tissue in a low-dose Computed Tomography (LDCT) imaging technique. Our results show that radiomic features prove effective in distinguishing between suspicious and benign objects located in the lung tissue. Our data shows that there is vast space for improvement from both model- as well as a data-centric approach to developing Computer-aided detection (CAD) systems based on radiomics for early lung cancer detection. We show our results in the paper.

Keywords: Lung cancer · Machine learning · Classification · CT

1 Introduction

Although the number of new cases is steadily declining in recent years [1], lung cancer is still one of the 4 leading cancers across the globe. [2] showed that the 5-year survival rate for patients between 2003–2009 was 54% for the localized stage of the disease and dropped to as low as 4% for the distant stage. On the other hand, recent data [1] shows that survival rate for lung cancer increased over the past years thanks to reductions in smoking and improvements in early detection and treatment. Data [3] shows that lung cancer mostly affects heavy smokers, or patients with a long history of smoking, aged 55 or more. For that group of patients, well-defined procedures [4] such as periodical low-dose Computed Tomography (LDCT) screenings increase chances of early diagnosis. Thanks to those programmes, lung cancer is now detected more frequently in the early stage of the disease.

Standard dose computed tomography technique provides significant radiation dose to the patient during screening. According to guidelines [4] annual screening for high risk groups is recommended, such frequency of screening puts patients at the risk of

over-radiation and radiation-related diseases, including cancer [5]. Therefore, screening programmes most often focus on low-dose computed tomography imaging technique, as it proved to reduce cancer mortality among patients [6]. In comparison with standard computed tomography, the radiation dose applied to the patient is much lower, but provides comparable diagnostic value to the standard dose [7] in case of lung lesion. This makes LDCT more suitable for frequent, annual screenings for high risk groups of patients.

During screening, the radiologist searches for any object present in the lung tissue. Besides lung nodules, there are more objects present in the lung tissue with their own radiological characteristics. The most common include fibrosis, lymph node, nodule, calcification, suspicious nodule, inflammation. The task of a radiologist is to assess each object found in the lung tissue in terms of its malignancy risk. If the object seems suspicious, the patient is either scheduled for another CT screening in a short period of time, or the biopsy is taken to validate the nodule's malignancy.

Lung screening programmes more often than not are adopted only partially [5]. Annual screening for a group of long-time smokers at the age of 55 or higher puts pressure on the current radiological staffing across the world. Time spent on one screening is approximately 5–15 min. Lack of radiologists causes extended waiting time for the results, and is often impossible due to short staffing among hospitals. In this case, performing such frequent screening trials is difficult or sometimes impossible.

For cost reduction and time optimization purposes, automatic or semi-automatic systems supporting radiologists are being developed. Detection and segmentation systems of the objects present in lung tissue are already being used [8]. Nodule classification systems built directly, or on top of such systems can further reduce the time spent on a single volume, which increases the throughput of the volumes validated by radiologists. [9] showed that the adoption of computed-aided detection (CAD) for chest CT can reduce reading time by 7%–44% with respect to standard approach. Moreover, AI classification systems may act as a secondary check for the radiologist and provide the valuable interpretation of the radiological features. [10] showed that using AI as a second reader increased sensitivity of lung cancer detection compared to the setup of double reading of two radiologists. Finally, thanks to explainability it may be used as a training programme for novice radiologists [11].

Currently, Machine Learning systems designed for medical imaging are criticized due to lack of explainability. Deep learning models being the most performant tools in Artificial Intelligence are often called black boxes due to their high complexity and lack of interpretability. If the deep neural network stands behind prediction, it is hard to explain the exact reason for the diagnosis. Many approaches were developed to enhance, or create a level of explainability, such as GradCAM [12]. However, the level of explainability and insight is insufficient for the purpose of medical diagnosis.

Radiomics is a potential approach to solving explainability issues in Machine Learning for medical imaging. Radiomics is designed to systematically transform object segmentations into a set of features used for diagnostic purposes [13]. Each radiomic feature is strictly defined and calculated using a given formula. Such an approach provides a sufficient explainability for the radiologist [14].

We created a radiomics pipeline based on the segmentation masks of objects, which transforms the input segmentation into a set of radiomic features, which are used for risk assessment of the object in terms of potential malignancy.

2   Materials and Methods

Data consists of 928 low-dose computed tomography screenings collected during a public screening programme in Medical University of Gdansk. Patients were aged 50–75 years old and had a smoking history of at least 20 pack-years.

For each object found in the lung tissue, a single point in 3D space constituting the part of the object was provided as an annotation by radiologists. For that point, a class of the whole object was also assigned. The 3D point will be used to create a segmentation map of the whole object in an unsupervised manner. By performing the following procedure, an annotated dataset of 5027 objects was created. Classes defined during the procedure were: fibrosis, lymph node, benign nodule, calcification, suspicious nodule, inflammation (Table 1).

Table 1. Object type counts in the dataset.

Object Type	Count	Percentage	Binary Class	Binary Class Count
Suspicious nodule	304	6.0	Suspicious Nodule	418
Inflammation	114	2.3		
Benign nodule	1011	20.1	Benign	4609
Lymph node	1124	22.4		
Fibrosis	1715	34.1		
Calcification	759	15.1		
Total	5 027			

The classes were additionally divided into two groups: benign and suspicious nodules. Inflammatory objects as well as suspicious nodules were merged together due to suspicious appearance of the inflammation without a global context of the lung tissue itself, which would indicate ongoing infection. This way we increased the count of the positive class, which is highly imbalanced in comparison with the negative class. Positivive class is called suspicious as malignancy of the nodule is only confirmed by performing biopsy on a suspicious object (Table 2).

Table 2. Training and validation set counts.

Class	Training Set Count	Validation Set Count
Suspicious	318	100
Benign	4509	100
Total	4 827	200

3 Methods

As a preliminary step for the radiomic approach, segmentation masks of objects present in lung tissue are required. The masks are used to extract voxels containing the object and based on those voxels, the radiomic feature values are calculated.

For each object found during screening, a segmentation map is usually created either manually by radiologist, or by using automatic, or semi-automatic CAD software [15]. We created a CT volume processing pipeline, which semi-automatically extracts masks of the marked object based on a single voxel coordinate of an object provided by the radiologist.

We first segment the lungs out of the entire CT volume. We use [16] to segment lung regions from each axial slice. The method is based on the U-Net convolutional network [17] trained on a diversified set of thoracic CT scans. The network is composed of contracting and expansive paths, used for extending the spatial information flow in the network. The network accepts a 2D axial slice of the CT volume, and returns a binary mask, with lung pixels set as a positive class, and background as negative class. Next, 2D segmentation maps are merged to create a 3D lung mask.

We then perform Gaussian Mixture Modelling on a segmented lung tissue extracted with the use of 3D lung mask as an approach to cluster voxels of similar intensity into masks. We model the voxel intensity distribution with the use of 3 components. The first component groups the low intensity voxels, constituting the airways in the lungs, whereas the second component contains the range of voxels spanning the lung tissue. The third component contains blood vessels, bronchovascular bundle as well as objects found in the lung tissue. We cluster the voxels into objects using connectivity criterion in the 3D space. We then find object segmentation maps by searching for the overlapped segmentation maps with provided 3D point annotations.

We run a radiomic pipeline on segmented objects using the PyRadiomics package presented in [18]. The method takes the input volume together with a binary mask of an object and calculates the radiomic features. Python implementation for feature calculation was presented in [19] and was used widely in many medical imaging applications. Calculated radiomic features are scalar values, with the computation formulas described and explained previously in [19]. The script produces 107 radiomic features.

We used Logistic Regression as the classification model for our system to be trained on resulting radiomic features. We first standardized each radiomic feature in the dataset

to unit variance and used them to train the model. Feature weights will be used for assessing the importance of each radiomic feature in the diagnostic decision in an Explainable AI (XAI) manner. Using a diagnostic description of the radiomic feature, the following setup provides a high explainability level for the radiological expert. We trained a Logistic Regression classifier in a binary setup explained earlier, with class weights set to mitigate the class imbalance of the training set.

4   Results

In order to explore the discriminative value of the radiomic features, we used Kruskal-Wallis test on each feature with classes assigned previously by radiologists. For Kruskal-Wallis test results, we computed effect size for the radiomic features and ranked them in terms of the strength of the effect. We observed that the majority of features provide strong discriminative value among classes (Fig. 1).
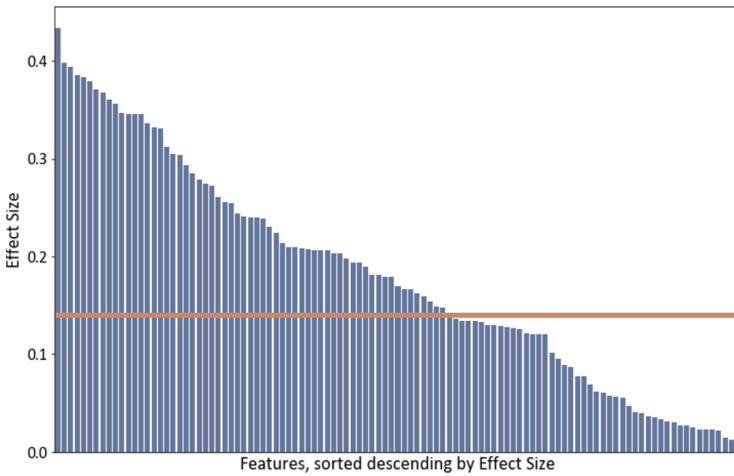
Fig. 1. Radiomic features were sorted in a descending order by their respective Effect Size values. Horizontal line marks the strong Effect Size threshold of 0.14. 61 features obtained a strong effect size for the gathered classes proving significant discriminative value of the radiomic features.

We obtained following results for the trained Logistic Regression classifier (Table 3).

Table 3. Classification metrics for the validation set for the trained Logistic Regression model.

Measure	Sensitivity	Specificity	PPV	NPV	Accuracy	F1 Score
Value	77.0%	81.0%	80.2%	77.9%	79.0%	78.6%

5   Conclusions

Our study shows that radiomics is a promising approach for systematic assessment of potential malignancy of objects found in the lung tissue in low-dose Computed Tomography.

We have created a classifier, which uses radiomic features obtained by using our novel CT volume preprocessing technique. The classifier contains feature importance weights, which can be used for XAI. Each diagnostic decision is explained by the set of ranked radiomic feature weights. This experiment proves the value of using radiomics as a reliable tool for assessing malignancy of lung cancer tumors. Presented results show promising opportunities for creating supporting malignancy assessment systems trained on larger datasets.

References

1. Siegel, R.L., Miller, K.D., Fuchs, H.E., Jemal, A.: Cancer statistics, 2021. CA. Cancer J. Clin. **71**(1), 7–33 (2021). https://doi.org/10.3322/caac.21654
2. Torre, L.A., Siegel, R.L., Jemal, A.: Lung cancer statistics. In: Ahmad, A., Gadgeel, S. (eds.) Lung Cancer and Personalized Medicine. AEMB, vol. 893, pp. 1–19. Springer, Cham (2016). https://doi.org/10.1007/978-3-319-24223-1_1
3. Dela Cruz, C.S., Tanoue, L.T., Matthay, R.A.: Lung cancer: epidemiology, etiology, and prevention. Clin. Chest Med. **32**(4), 605–644 (2011). https://doi.org/10.1016/j.ccm.2011.09.001
4. Jaklitsch, M.T., et al.: The American Association for Thoracic Surgery guidelines for lung cancer screening using low-dose computed tomography scans for lung cancer survivors and other high-risk groups. J. Thorac. Cardiovasc. Surg. **144**(1), 33–38 (2012). https://doi.org/10.1016/j.jtcvs.2012.05.060
5. Sands, J., et al.: Lung screening benefits and challenges: a review of the data and outline for implementation. J. Thorac. Oncol. **16**(1), 37–53 (2021). https://doi.org/10.1016/j.jtho.2020.10.127
6. Rampinelli, C., Origgi, D., Bellomi, M.: Low-dose CT: technique, reading methods and image interpretation. Cancer Imaging **12**(3), 548–556 (2012). https://doi.org/10.1102/1470-7330.2012.0049
7. Kubo, T., Ohno, Y., Takenaka, D., Nishino, M., Gautam, S.: Standard-dose vs. low-dose CT protocols in the evaluation of localized lung lesions: capability for lesion characterization—iLEAD study. Eur. J. Radiol. Open **3**, 67–73 (2016). https://doi.org/10.1016/j.ejro.2016.03.002
8. Shariaty, F., Mousavi, M.: Application of CAD systems for the automatic detection of lung nodules. Inf. Med. Unlocked **15**, 100173 (2019). https://doi.org/10.1016/j.imu.2019.100173
9. Brown, M., et al.: Integration of chest CT CAD into the clinical workflow and impact on radiologist efficiency. Acad. Radiol. **26**(5), 626–631 (2019). https://doi.org/10.1016/j.acra.2018.07.006

10. Schreuder, A., Scholten, E.T., van Ginneken, B., Jacobs, C.: Artificial intelligence for detection and characterization of pulmonary nodules in lung cancer CT screening: ready for practice? Transl. Lung Cancer Res. **10**(5), 2378–2388 (2021). https://doi.org/10.21037/tlcr-2020-lcs-06

11. Suarez-Ortega, C., Franco-Valiente, J.M.: Using CAD systems and e-Learning in radiologists training. In: 2013 IEEE 15th International Conference on e-Health Networking, Applications and Services, Healthcom 2013, pp. 172–176 (2013). https://doi.org/10.1109/HealthCom.2013.6720661

12. Selvaraju, R.R., Cogswell, M., Das, A., Vedantam, R., Parikh, D., Batra, D.: Grad-CAM: visual explanations from deep networks via gradient-based localization. Int. J. Comput. Vis. **128**(2), 336–359 (2019). https://doi.org/10.1007/s11263-019-01228-7

13. Gillies, R.J., Kinahan, P.E., Hricak, H.: Radiomics: images are more than pictures, they are data. Radiology **278**(2), 563–577 (2016). https://doi.org/10.1148/radiol.2015151169

14. van Timmeren, J.E., Cester, D., Tanadini-Lang, S., Alkadhi, H., Baessler, B.: Radiomics in medical imaging—"how-to" guide and critical reflection. Insights Imaging **11**(1), 91 (2020). https://doi.org/10.1186/s13244-020-00887-2

15. Shaukat, F., Raja, G., Frangi, A.F.: Computer-aided detection of lung nodules: a review. J. Med. Imaging **6**(02), 1 (2019). https://doi.org/10.1117/1.JMI.6.2.020901

16. Hofmanninger, J., Prayer, F., Pan, J., Röhrich, S., Prosch, H., Langs, G.: Automatic lung segmentation in routine imaging is primarily a data diversity problem, not a methodology problem. Eur. Radiol. Exp. **4**(1), 1–13 (2020). https://doi.org/10.1186/s41747-020-00173-2

17. Ronneberger, O., Fischer, P., Brox, T.: U-Net: convolutional networks for biomedical image segmentation. In: Navab, N., Hornegger, J., Wells, W.M., Frangi, A.F. (eds.) MICCAI 2015. LNCS, vol. 9351, pp. 234–241. Springer, Cham (2015). https://doi.org/10.1007/978-3-319-24574-4_28

18. Van Griethuysen, J.J.M., et al.: Computational radiomics system to decode the radiographic phenotype. Cancer Res. **77**(21), e104–e107 (2017). https://doi.org/10.1158/0008-5472.CAN-17-0339

19. Zwanenburg, A., et al.: The image biomarker standardization initiative: Standardized quantitative radiomics for high-throughput image-based phenotyping. Radiology **295**(2), 328–338 (2020). https://doi.org/10.1148/radiol.2020191145

Segmentation of Brain MR Images Using Quantum Inspired Firefly Algorithm with Mutation

Alokeparna Choudhury, Sourav Samanta, Sanjoy Pratihar[(✉)], and Oishila Bandyopadhyay

Computer Science and Engineering, Indian Institute of Information Technology, Kalyani 741235, India
sanjoy@iiitkalyani.ac.in

Abstract. Segmentation of brain images generated by magnetic resonance imaging (MRI) is an important part of clinical medicine as it enables three-dimensional reconstruction and downstream analysis of normal and pathological regions. Segmenting white matter (WM), grey matter (GM), and cerebrospinal fluid (CSF) automatically are challenging tasks. In this paper, a clustering-based segmentation of MR images is performed using a modified quantum-inspired firefly algorithm with mutation operation. In the proposed method, a mutation operation based on the X-gate has overcome the restriction on initial centroids trapped in local optima. The objective function is chosen to be the minimum intracluster distance. The suggested approach has been tested on several sections of human brain images with differing cluster numbers. Correlation, SSIM, entropy, and PSNR have been used to evaluate the outputs of the method. The evaluation metrics indicate that the proposed clustering-based algorithm successfully segmented the MR images.

Keywords: MR image clustering · Quantum inspired firefly algorithm · Quantum mutation

1 Introduction

MRI is considered an effective diagnostic tool for fast diagnosis of stroke cases among patients [1]. A stroke happens due to some significant abnormal changes in the brain, such as lack of blood flow, formation of a blood clot in the Middle Cerebral Artery (MCA), etc. Magnetic Resonance (MR) images show a clear view of brain tissues and the presence of any lesions or other abnormalities in the brain tissue [2–6]. These abnormalities can be easily detected by automated analysis of such images. MRI is one of the effective diagnosis methods for intracranial pathology, and it is used for the analysis of various diseases, including glioma, meningiomas and neurocytoma [3,4]. Automated segmentation of gray matter, white matter, and CSF from brain MRI can be used for abnormality detection and disease diagnosis. Image segmentation is applied to extract the anatomical regions of interest in the medical domain. Further, the segmented section

of the MR image is utilized to diagnose abnormalities in the brain like lesions, blockages, clots, etc. This work proposes a modified Quantum Inspired Firefly Algorithm (QIFA) with quantum mutation to segment the different components of brain MR images.

The overall contributions of this work can be summarized as follows:

1. The modified QIFA with the quantum mutation has been proposed for clustering.
2. The quantum mutation operation has been proposed using X-gate.
3. The proposed clustering has been applied to segment the various cross-sections of brain MRI.
4. The result proves that the proposed algorithm efficiently segments the different areas of the human brain.
5. The result has been analyzed using various metrics, e.g., correlation, SSIM, entropy, and PSNR.

The organization of the paper is as follows. Section 1 discusses the necessity of segmentation of MR images, i.e., the motivation of the work. Section 2 presents the state of the art. The fundamentals of quantum computing and the classical firefly algorithm are discussed in Sect. 3. In Sect. 4, a modified quantum-inspired firefly method with mutation operation is proposed for cluster generation. Section 5 discusses on data set, objective function and evaluation metrics. Finally, Sect. 6 analyzes the results and Sect. 7 presents concluding remarks.

2   Related Works

Different research groups have applied the firefly algorithm and other nature-inspired computing techniques for image segmentation in recent years. Masang-cap et al. [7] improved the notion of brightness and movement of fireflies. They have experimented on enhanced K-means and expectation-maximization algorithms based on various performance evaluation criteria. The results indicate that using a modified initialization strategy of the firefly algorithm prior to clustering increases intra-cluster similarity and decreases inter-cluster homogeneity. Xie et al. [8] introduced some variants of the firefly algorithm focusing on inward intensified exploration and compound intensified exploration. The main objectives of the modifications were to solve the initialization sensitivity problem and overcome the local optima traps found in K-means clustering. The statistical study demonstrates a considerable improvement over K-means clustering and other firefly method versions. Khrissi et al. [9] proposed image segmentation by combining cuckoo search with Fuzzy C-means (FCM). Here, the cuckoo search was used to establish the cluster centers randomly, and subsequently, the centers were adjusted according to cuckoo search criteria by minimizing the objective function. The results show good quality of segmentation. Pal et al. [10] utilized a genetic algorithm to implement a weighted clustering technique for wireless sensor networks with a modified objective function. The approach is incredibly efficient in terms of energy use. Zhao et al. [11] proposed a firefly algorithm

based on an improved density peaks clustering method. It combines the cut-off kernel with the Gaussian kernel defined by the density peaks clustering technique and then uses a weighting factor to balance the impacts of the two kernels. Dey et al. [12] implemented a group of quantum-inspired versions of known metaheuristic algorithms, e.g., particle swarm optimization and spider monkey optimization, where the objective was to find the optimal number of clusters. A comparison has been made between quantum-inspired algorithms and their classical counterparts. Quantum-inspired algorithms have been more efficient than their classical equivalents in terms of fitness, mean, standard deviation, standard errors of fitness, convergence curves, and computing time. Das et al. [13] developed brain MR image segmentation using quantum-inspired modified genetic algorithm based FRCM algorithm. Compared to the classic FRCM algorithm, the proposed technique segmented the brain image into distinct regions with high accuracy. Dhal et al. [14] presented a fuzzy clustering technique using firefly algorithm. Verma et al. [15] utilized particle swarm optimization to overcome the problem of being trapped into local minima when working with the fuzzy c-means clustering algorithm. Dey et al. [16] proposed two variations of quantum-inspired crow search optimization algorithm for automatic clustering of color images.

It has been observed that most of the recent works have adopted a hybrid approach for clustering. In particular, when compared to its classical form, quantum-inspired clustering algorithms show great promise. The research presented by Choudhury et al. [17] confirmed the relevance of a quantum-inspired firefly algorithm method in the segmentation of microscopic hippocampal images. The objective of this work is to judge the applicability of the quantum-inspired firefly algorithm presented by [17] in clustering-based image segmentation of human brain MR images. As the method focuses on the clustering problem, one mutation operator is introduced with the quantum-inspired firefly algorithm to accommodate the limitation of a traditional clustering algorithm.

3   Preliminaries of Quantum Computing and Firefly Algorithm

The quantum computer is regulated by the laws of quantum physics, which distinguishes it from the classical computer. In contrast to conventional computers, quantum computers operate on the smallest unit of information called qubits [18]. Researchers explored several quantum computing aspects that can be implemented in a classical computer to enhance the performance of classical algorithms. The *quantum inspired evolutionary algorithm*, proposed by Han and Kim [19], combined the features of quantum computing and evolutionary algorithm.

Qubit. The qubit is expressed using two basic states, *normal state* and *excited state*, and located in the 2-D Hilbert space. These two states, *normal state* and *excited state*, can be considered as 0 and 1 respectively. Equation 1 represents

the qubit. In Eq. 1, α_0 and α_1 represent probabilistic position of the state $|0\rangle$ and $|1\rangle$. This equation shows that the qubit is in the linear superposition form of the two basic states. The necessary and sufficient condition for every qubit to be in the linear superposition is shown in Eq. 2. The probabilistic amplitudes are defined as $\frac{1}{\sqrt{2}}$, which is consistent with Eq. 2 and Eq. 3.

$$|\psi\rangle = \alpha_0 |0\rangle + \alpha_1 |1\rangle \tag{1}$$

$$|\alpha_0|^2 + |\alpha_1|^2 = 1 \tag{2}$$

$$|\psi\rangle = \frac{1}{\sqrt{2}}|0\rangle + \frac{1}{\sqrt{2}}|1\rangle \tag{3}$$

Quantum Gate. In the literature on quantum computing, various quantum gates are used to operate on the qubit. The Hadamard gate, Rotation gate, and X-gates have been utilized in this work. The Hadamard gate (H) is represented by the Eq. 4. It prepares the superposition of qubit states.

$$H = \frac{1}{\sqrt{2}} \begin{bmatrix} 1 & 1 \\ 1 & -1 \end{bmatrix} \tag{4}$$

The Quantum rotation gate is widely used in the field of quantum-inspired meta-heuristic algorithms because of its role in the convergence of the algorithm. A qubit is updated by *rotation gate* as shown in Eq. 5. Qubit update is done by multiplying the original qubit by the rotation gate $U(\Delta\theta i)$. The rotation gate $U(\Delta\theta i)$ is shown in the Eq. 6. Here, $\Delta\theta i$ is the rotation angle. The Quantum *NOT* or *X-gate* is a single qubit gate that is a quantum version of the classical *NOT* gate. It flips the probability amplitudes of $|0\rangle$ and $|1\rangle$. The X-gate is represented in Eq. 7.

$$\begin{bmatrix} \alpha'_{0i} \\ \alpha'_{1i} \end{bmatrix} = \mathrm{U}(\Delta\theta_i) * \begin{bmatrix} \alpha_{0i} \\ \alpha_{1i} \end{bmatrix} \tag{5}$$

$$U(\Delta\theta i) = \begin{bmatrix} \cos(\Delta\theta_i) & -\sin(\Delta\theta_i) \\ \sin(\Delta\theta_i) & \cos(\Delta\theta_i) \end{bmatrix} \tag{6}$$

$$X = \begin{bmatrix} 0 & 1 \\ 1 & 0 \end{bmatrix} \tag{7}$$

3.1 The Firefly Algorithm (FA)

In 2008, Yang [20] proposed the firefly algorithm. Firefly algorithm works on the flashing behavior of firefly [20]. The algorithm was devolved by imposing the following rules on the flashing and movement pattern of firefly [21,22].

1. There is no concept of gender. So, a firefly F_i may be attracted to a firefly F_j, disregarding the gender of F_j.
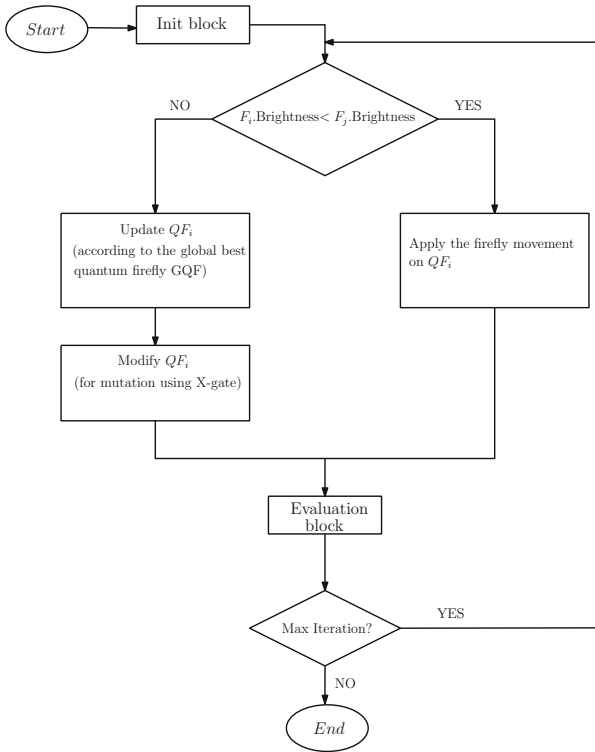
Fig. 1. Flow diagram of the proposed QIFAM.

2. The degree of attraction, i.e., *attractiveness* shown by the firefly F_i is in accordance with the *brightness* of firefly F_j. As a result, the firefly with lower brightness will move toward the firefly with higher brightness. When the distance between two fireflies increases, both the attractiveness and brightness of the fireflies decrease. Fireflies will move randomly in the absence of a brighter neighbor.
3. Brightness of the firefly will depend on the search surface of the objective function.

The firefly algorithm uses two key concepts: measuring the difference in brightness between two fireflies and defining attractiveness. The brightness intensity I of a firefly, is linked with the firefly's search landscape information x, and the connection is formulated as: $I(x) \propto f(x)$, where $f(x)$ is some fitness function. The attractiveness, β, is formulated in Eq. 8 and 9. Here, the light intensity $I(r)$ is inversely proportional to distance r. Here, I_0 signifies the light intensity at zero distance, and γr signifies the light absorption coefficient. Here, β_0 signifies the attractiveness at $r = 0$. Finally, the movement of a firefly with lower intensity towards a higher one is given by Eq. 10.

$$I = I_0 e^{-\gamma r} \tag{8}$$

$$\beta = \beta_0^{-\gamma r^2} \tag{9}$$

$$x_i = x_i + \beta_0 e^{-\gamma_{ij}^2} (x_j - x_i) + \alpha \epsilon_i \tag{10}$$

Algorithm 1: QUANTUM-MUTATION-USING-X-GATE.

---

1 i ⟵ Iteration;

2 c_k ⟵ Number of cluster;

3 ɭ ⟵ Length of binary value of centroid;

4 L ⟵ $c_k \times$ ɭ;

5 n_{mp} ⟵ $\left(\frac{1}{i} \times c_k \times$ ɭ$\right) + 1$; /* number of mutation points */

6 for $t \leftarrow 1$ **to** n_{mp} **do**

7 $\quad m_p = rand\,() \times L$; /* mutation point */

8 $\quad$ **if** $(QF_{bin}(m_p) \neq QF_{bin}^g(m_p))$ **then**

9 $\quad\quad \alpha = QF_{quantum}(1, m_p)$;

10 $\quad\quad \beta = QF_{quantum}(2, m_p)$;

11 $\quad\quad \begin{bmatrix} \alpha' \\ \beta' \end{bmatrix} = X \times \begin{bmatrix} \alpha \\ \beta \end{bmatrix}$

12 $\quad\quad QF_{quantum}(1, m_p) = \acute{\alpha}$;

13 $\quad\quad QF_{quantum}(2, m_p) = \acute{\beta}$;

14 $\quad$ **end**

15 $\quad t \leftarrow t + 1$;

16 end

---

4   Quantum Inspired Firefly Algorithm with Quantum Mutation (QIFAM)

This proposed method for the clustering-based segmentation of MR images utilizes the modified quantum-inspired firefly algorithm with mutation operation. The population of quantum fireflies is initialized using the Hadamard gate. By two successive operation measurements and decimal to binary conversion, the initial c cluster points are produced. Input images are segmented by the initial cluster points and segmentation quality by the objective function. Once each firefly's fitness is evaluated and ranked, the best firefly alone with binary and quantum firefly are preserved as per the previously modified quantum-inspired firefly algorithm. The movement of firefly is the primary update strategy for the next iteration. Here, two kinds of update strategies have been considered. When the fitness $F_i < F_j$, conventional firefly fly movement is applied; in other cases, the quantum update followed by quantum mutation operation will be applied to update the firefly for the next iteration. After completing one iteration, the exact measurement, binary to decimal conversion, fitness evaluation, and ranking is done. Subsequently, the global best quantum firefly (GQF) is updated in accordance with the ranked firefly population. This process executes up to the

maximum number of iterations. The mutation operation is introduced to avoid the problem of trapping initial cluster points in the local optimum. The concept of mutation is from the Genetic Algorithm, which makes small random changes in the chromosome to introduce diversity in the population. Here, the mutation on the quantum firefly has been implemented using X-gate. The number of mutation points is calculated based on the iteration, the number of clusters, and the length of the binary value of the centroid. Since our work focuses on grayscale images, the length of the binary value of the centroid is 8.

The flow diagram of the proposed *quantum inspired firefly algorithm with quantum mutation* (QIFAM) is shown in Fig. 1. The **Init block** does the following in order: initializes the initial cluster centers by quantum firefly using Hadamard gate, prepares binary firefly using quantum measurement, converts binary firefly to decimal firefly, clusters the image using decimal firefly, evaluates the rank of the fireflies using values of objective functions and stores the current global best quantum firefly.

The **Evaluation block** does the following in order as stated below: prepares binary firefly using quantum measurement, converts binary firefly to decimal firefly, clusters the image using decimal firefly, evaluates the rank of the fireflies using values of objective functions and updates the current global best quantum firefly.

The proposed mutation method has been shown in Algorithm 1. The current quantum firefly is denoted by $QF_{quantum}$ and the corresponding binary form is represented by QF_{bin}. The QF_{bin}^g is the best quantum firefly found so far. Though the total number of mutation points is n_{mp}, X-gate will not modify all mutation points. When the bit value of QF_{bin} and QF_{bin}^g are different at the mutation point, then only the values of the value of α and β of $QF_quantum$ will be flipped at the mutation point by the X-gate. The details of the mutation process are demonstrated in Fig. 2. The variation of the number of mutation points with the number of clusters is plotted in Fig. 3.

					mp_1						mp_2				
0	0	0	1	1	0	1	0	1	1	1	1	0	1	0	1

QF_{bin}^g

1	0	1	1	1	0	1	0	0	1	1	0	0	1	0	1

QF_{bin}

0.5262	0.2149	0.3117	0.9074	0.8336	0.5631	0.9748	0.1856	0.6624	0.6177	0.8749	0.8917	0.4323	0.6998	0.6675	0.8039
0.6883	0.8861	0.8297	0.3042	0.408	0.661	0.1588	0.9024	0.5811	0.6183	0.3536	0.3290	0.7535	0.5479	0.5766	0.4428

Before Mutation - $QF_{quantum}$

0.5262	0.2149	0.3117	0.9074	0.8336	0.5631	0.9748	0.1856	0.6624	0.6177	0.8749	0.3290	0.4323	0.6998	0.6675	0.8039
0.6883	0.8861	0.8297	0.3042	0.408	0.6610	0.1588	0.9024	0.5811	0.6183	0.3536	0.8917	0.7535	0.5479	0.5766	0.4428

After Mutation - $QF_{quantum}$
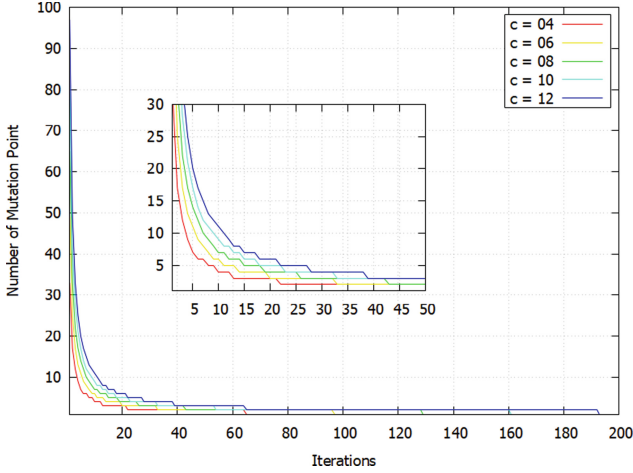
Fig. 2. Mutation using X-gate.

Fig. 3. Variation of number of mutation points with number of clusters.

5   Experimental Setup

All the human brain MR images used for this experiment have been taken from eHealth Lab, Department of Computer Science, University of Cyprus [23]. In this experiment, 24 cross-section images of two persons have been considered.

Objective Function. The sum of squares of distances within a cluster determines the clustering quality. It considers the Euclidean distance to measure the distance between two points in the clusters. A cluster with a small sum of squares value is considered more compact than one with a large sum of squares value. At this point, it is necessary to utilize the average distance from the centroid to compare the within-cluster variabilities of distinct clusters. Hence, we consider the objective function as given in Eq. 11.

$$\mathfrak{F} = \sum_{j=1}^{k} \sum_{i=1}^{n} \left|\left| x_i^j - c_j \right|\right|^2 \tag{11}$$

Evaluation Measures. Four parameters have been considered to measure the segmentation outcome: correlation, SSIM, entropy, and PSNR. Correlation is the measurement of conformity level between the original (A) and segmented image $\left(\hat{A}\right)$ and expressed by Eq. 12. The structural similarity between (A) and $\left(\hat{A}\right)$ by SSIM which is expressed by Eq. 13. Entropy implies the image information measure of $\left(\hat{A}\right)$ using Eq. 14. Peak signal to noise ratio of $\left(\hat{A}\right)$ is measured using
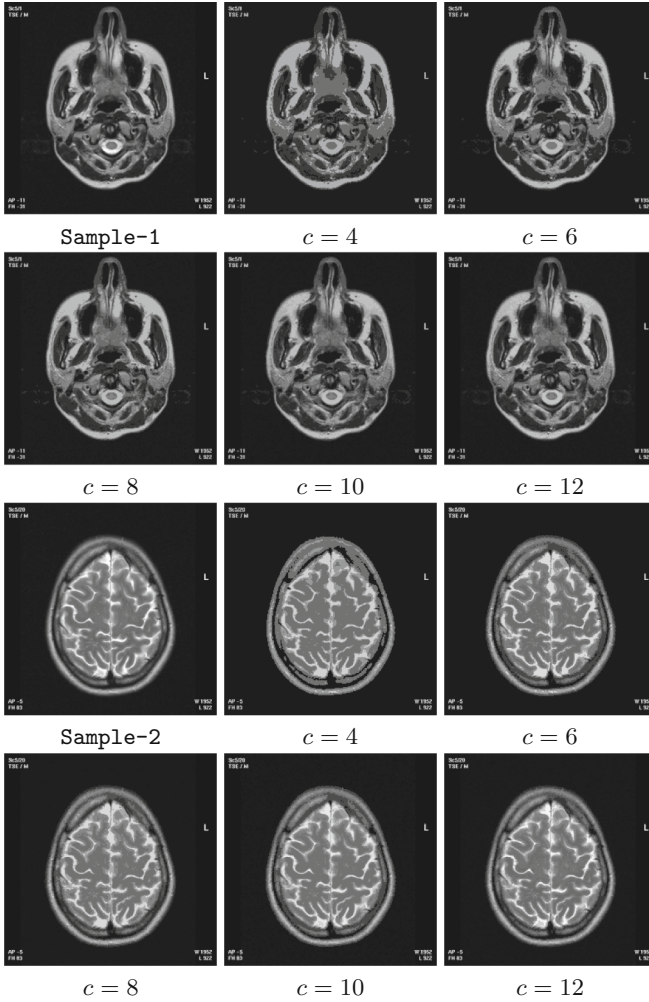
Fig. 4. Sample images and segmentation for various number of clusters; `Sample-1`: top two rows; `Sample-2`: bottom two rows.

Eq. 15. In addition, the convergence and the execution time have been utilized to assess the quality of the segmentation obtained.

$$Correlation\left(A, \hat{A}\right) = \frac{\sum_m \sum_n (A_{mn} - A_\iota)\left(\hat{A}_{mn} - \hat{A}_\iota\right)}{\sqrt{\left(\sum_m \sum_n (A_{mn} - A_\iota)^2\right)\left(\sum_m \sum_n \left(\hat{A}_{mn} - \hat{A}_\iota\right)^2\right)}} \qquad (12)$$

$$SSIM\left(A, \hat{A}\right) = \frac{\left(2\mu_A \mu_{\hat{A}} + c_1\right)\left(2\sigma_{A\hat{A}} + c_2\right)}{\left(\mu_A^2 + \mu_{\hat{A}}^2 + c_1\right)\left(\sigma_A^2 + \sigma_{\hat{A}}^2 + c_2\right)} \qquad (13)$$

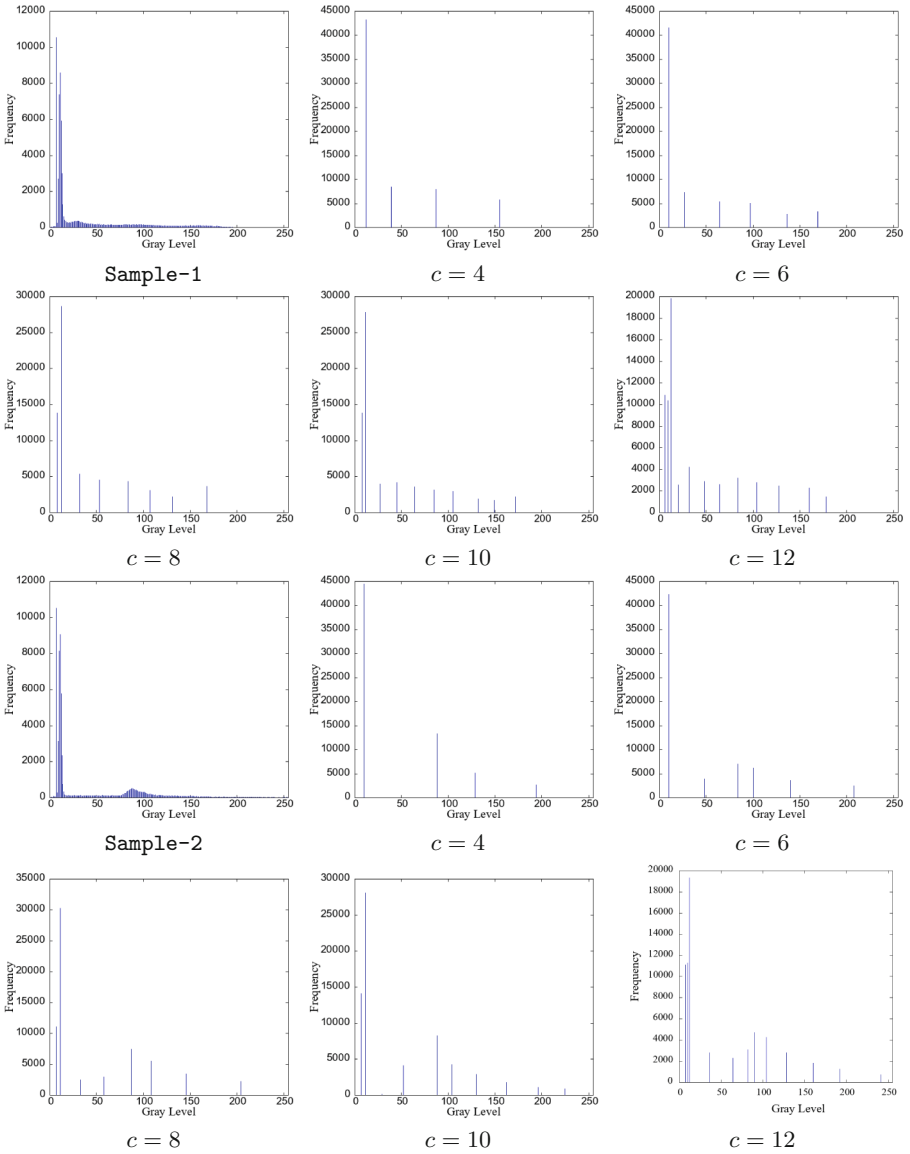**Fig. 5.** Histograms (Gray Level vs Frequency) of original samples and segmented images (shown in Fig. 4) for various number of clusters; Sample-1: top two rows; Sample-2: bottom two rows.

$$Entropy = -\sum_{i=1}^{n} p_i log_2 p_i \tag{14}$$

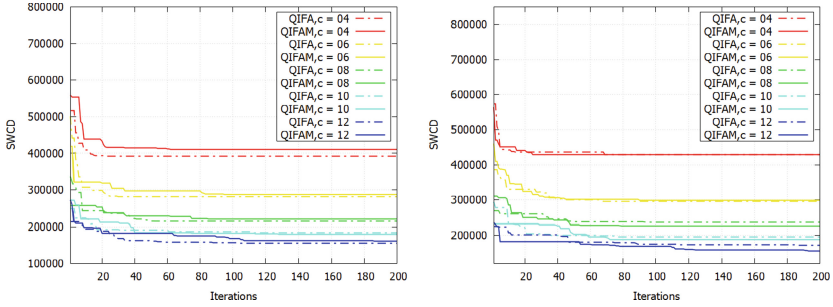$$PSNR = 20log_{10}\left(\frac{max_f}{\sqrt{MSE}}\right) \tag{15}$$

Fig. 6. Convergence curves for various cluster number c, corresponding to the samples shown in Fig. 4: left: `Sample-1`, right: `Sample-2`.
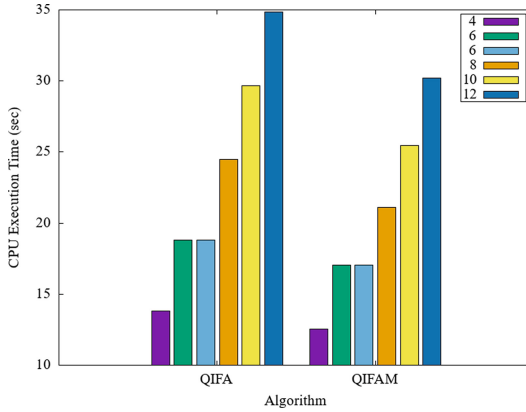
Fig. 7. Average execution time for various cluster number c: QIFA vs QIFAM.

6   Results and Analysis

This section will analyze the results obtained using the proposed QIFAM. The proposed algorithm segmented various cross-sectional MR images of the human brain. The algorithm is used to determine which cluster points are optimal for segmentation. Any conventional clustering approach has the disadvantage of confining the initial centroid in local optima. X-gate-based quantum mutation

Table 1. Segmentation evaluation metrics: QIFA vs QIFAM.

Sample	# Cluster	QIFA				QIFAM			
		Corr.	SSIM	Entropy	PSNR	Corr.	SSIM	Entropy	PSNR
Sample-1	4	0.9764	0.8901	1.4251	27.7166	0.9758	0.8921	1.4575	27.994
	6	0.9678	0.8981	1.6263	26.7359	0.9885	0.9323	1.7637	31.209
	8	0.9898	0.8997	2.4719	31.7035	0.9914	0.9536	2.4191	32.4774
	10	0.9657	0.9244	2.5091	26.3327	0.9937	0.9629	2.6002	33.8175
	12	0.9956	0.9733	2.8041	34.5215	0.9952	0.9736	3.0717	34.9959
Sample-2	4	0.9763	0.8896	1.3207	26.9984	0.9762	0.8903	1.3231	26.9783
	6	0.9887	0.9277	1.6628	29.3609	0.9887	0.9331	1.7277	30.2115
	8	0.9798	0.8608	2.4464	27.7073	0.9915	0.9531	2.3775	31.4568
	10	0.9896	0.9448	2.4735	30.3227	0.9938	0.9545	2.4248	32.809
	12	0.9964	0.9716	2.965	35.2232	0.9965	0.9758	3.0137	35.3281
Sample-3	4	0.9665	0.8776	1.3715	24.9338	0.9732	0.8851	1.4348	27.2574
	6	0.9387	0.8274	1.8455	23.6785	0.9862	0.9272	1.7966	29.7603
	8	0.9784	0.8876	2.5579	27.9504	0.9880	0.9495	2.5384	30.6500
	10	0.9236	0.8055	2.5164	22.7149	0.9905	0.9577	2.8902	31.6575
	12	0.995	0.9686	2.788	34.1547	0.995	0.9705	2.8097	34.4285
Sample-4	4	0.9729	0.8718	1.4006	27.3156	0.9752	0.8753	1.3948	27.7925
	6	0.9865	0.9139	1.8969	30.4205	0.9876	0.9193	1.7361	30.7293
	8	0.9921	0.9401	2.0068	32.7121	0.9901	0.9471	2.4944	31.6606
	10	0.9918	0.9545	2.7930	32.3861	0.9918	0.9578	2.8853	32.4443
	12	0.9858	0.9540	2.8835	30.2210	0.9946	0.9699	2.9015	34.2695
Sample-5	4	0.9689	0.8537	1.3861	25.1727	0.9697	0.8623	1.3880	25.7135
	6	0.9147	0.4427	2.1207	21.0374	0.9841	0.8871	1.8283	27.5708
	8	0.8750	0.6789	1.936	19.6386	0.9926	0.9279	2.4387	31.7476
	10	0.9905	0.8914	2.3516	30.5575	0.9951	0.9498	2.7041	33.5534
	12	0.9893	0.9377	2.8099	29.9451	0.9969	0.9578	2.8947	35.4906
Sample-6	4	0.9139	0.6927	1.4997	20.9961	0.9728	0.8485	1.4579	25.9062
	6	0.9873	0.8964	1.9028	29.1773	0.9849	0.8953	1.9083	28.5095
	8	0.9919	0.9229	2.5357	31.1398	0.9922	0.9223	2.4540	31.3274
	10	0.9948	0.9219	2.3725	32.4571	0.9942	0.9445	2.9412	32.5973
	12	0.9959	0.9556	3.0303	34.1690	0.9960	0.9564	3.0881	34.1137

has been used in this case to address this issue. This mutation rate was initially relatively high at the start of the iterations but has gradually decreased. The algorithm has been applied for a different number of clusters c. In the experiment, clustering of 12 cross-sections images with the different value of $c = 4, 6, 8, 10, 12$ have been carried out. Two sample images and their segmentation outputs for different c values have been shown in Fig. 4. Histograms of corresponding images are also shown in Fig. 5. Correlation, SSIM, entropy, and PSNR evaluated the segmentation quality. All the evaluation metrics are shown in Table 1 for some of the samples, including Sample-1 and Sample-2.

It is observed that the correlation value of the segmented output is close to 1 in case of $c = 8, 10, 12$. Similarly, the SSIM value of clustered images is close to 1 in most cross-section images with $c = 10$ and 12. The observation is that we obtained good entropy and PSNR value at a higher value of c than the lower value of c. Convergence graphs for two sample images of Fig. 4 are shown in Fig. 6 considering various values of c. The graphs in Fig. 6 signify the minimization of the sum of the within-cluster distances. It is clear from the graphs that the proposed algorithm has obtained convergence for all values of c. The algorithm executed 200 iterations and found the optimal value within 100 iterations in most cases. The average execution time, on twelve samples, for various cluster numbers ($c = 4, 6, 8, 10, 12$) is shown in Fig. 7. The plot shows a comparison between QIFA and QIFAM also. When the number of clusters is increased, the execution time of the algorithm does not change much, and this is observed from Fig. 7.

7   Conclusion

A novel quantum-inspired firefly algorithm with quantum mutation is presented in this paper with the objective of cluster finding based segmentation of human brain MR images. The presented work's contribution lies with the proposal that the inclusion of quantum mutation operation can avoid the local optima finding of cluster centroids. The effectiveness of the proposed algorithm has been checked using convergence tests. The work can be further extended to color images and auto-selection of optimal cluster points.

References

1. Jeena, R.S., Kumar, S.: A comparative analysis of MRI and CT brain images for stroke diagnosis. In: 2013 Annual International Conference on Emerging Research Areas and 2013 International Conference on Microelectronics, Communications and Renewable Energy, pp. 1–5 (2013)
2. Kloska, S.P., Wintermark, M., Engelhorn, T., Fiebach, J.B.: Acute stroke magnetic resonance imaging: current status and future perspective. Neuroradiology **52**(3), 189–201 (2009)
3. Mamelak, A.N., Jacoby, D.B.: Targeted delivery of antitumoral therapy to glioma and other malignancies with synthetic chlorotoxin (TM-601). Expert Opin. Drug Deliv. **4**(2), 175–186 (2007)
4. Ostrom, Q.T., et al.: The epidemiology of glioma in adults: a "state of the science" review. Neuro-Oncol. **16**(7), 896–913 (2014)
5. Olivero, W.C., Lister, J.R., Elwood, P.W.: The natural history and growth rate of asymptomatic meningiomas: a review of 60 patients. J. Neurosurg. **83**(2), 222–224 (1995)
6. Lee, W., et al.: MR imaging features of clear-cell meningioma with diffuse leptomeningeal seeding. AJNR Am. J. Neuroradiol. **21**(1), 130–132 (2000)
7. Masangcap, M.L.G., Sison, A.M., Medina, R.P.: An improved initialization method using firefly movement and light intensity for better clustering performance. In: Proceedings of the 2nd International Conference on Software Engineering and Information Management, pp. 30–34 (2019)

8. Xie, H., et al.: Improving k-means clustering with enhanced firefly algorithms. Appl. Soft Comput. **84**, 105763 (2019)

9. Khrissi, L., Akkad, N.E., Satori, H., Satori, K.: Simple and efficient clustering approach based on cuckoo search algorithm. In: 2020 Fourth International Conference on Intelligent Computing in Data Sciences (ICDS), pp. 1–6 (2020)

10. Pal, R., Yadav, S., Karnwal, R., Aarti: EEWC: energy-efficient weighted clustering method based on genetic algorithm for HWSNs. Complex Intell. Syst. **6**(2), 391–400 (2020). https://doi.org/10.1007/s40747-020-00137-4

11. Zhao, J., Tang, J., Shi, A., Fan, T., Xu, L.: Improved density peaks clustering based on firefly algorithm. Int. J. Bio-Inspir. Comput. **15**(1), 24 (2020)

12. Dey, A., Dey, S., Bhattacharyya, S., Platos, J., Snasel, V.: Novel quantum inspired approaches for automatic clustering of gray level images using particle swarm optimization, spider monkey optimization and ageist spider monkey optimization algorithms. Appl. Soft Comput. **88**, 106040 (2020)

13. Das, S., De, S., Dey, S., Bhattacharyya, S.: Magnetic resonance image segmentation using a quantum-inspired modified genetic algorithm (QIANA) based on FRCM (2020)

14. Dhal, K.G., Das, A., Ray, S., Gálvez, J.: Randomly attracted rough firefly algorithm for histogram based fuzzy image clustering. Knowl.-Based Syst. **216**, 106814 (2021)

15. Verma, H., Verma, D., Tiwari, P.K.: A population based hybrid FCM-PSO algorithm for clustering analysis and segmentation of brain image. Expert Syst. Appl. **167**, 114121 (2021)

16. Dey, A., Dey, S., Bhattacharyya, S., Platos, J., Snasel, V.: Quantum inspired metaheuristic approaches for automatic clustering of colour images. Int. J. Intell. Syst. **36**(9), 4852–4901 (2021)

17. Choudhury, A., Samanta, S., Pratihar, S., Bandyopadhyay, O.: Multilevel segmentation of Hippocampus images using global steered quantum inspired firefly algorithm. Appl. Intell. **52**, 7339–7372 (2021). https://doi.org/10.1007/s10489-021-02688-6

18. Deutsch, D.: Quantum theory, the church-turing principle and the universal quantum computer. Proc. R. Soc. London A Math. Phys. Sci. **400**(1818), 97–117 (1985)

19. Han, K.H., Kim, J.H.: Quantum-inspired evolutionary algorithm for a class of combinatorial optimization. IEEE Trans. Evol. Comput. **6**(6), 580–593 (2002)

20. Yang, X.-S.: Firefly algorithms for multimodal optimization. In: Watanabe, O., Zeugmann, T. (eds.) SAGA 2009. LNCS, vol. 5792, pp. 169–178. Springer, Heidelberg (2009). https://doi.org/10.1007/978-3-642-04944-6_14

21. Yang, X.S.: Nature-Inspired Metaheuristic Algorithms. Luniver Press (2010)

22. Dey, N. (ed.): Applications of Firefly Algorithm and its Variants. STNC, Springer, Singapore (2020). https://doi.org/10.1007/978-981-15-0306-1

23. eHealth Lab, Department of Computer Science, U.O.C.: Dataset: http://www.medinfo.cs.ucy.ac.cy/index.php/facilities/32-software/218-datasets. Accessed 10 Mar 2022

Computational Support for Clinical Decisions

Single-Channel EEG Detection of REM Sleep Behaviour Disorder: The Influence of REM and Slow Wave Sleep

Irene Rechichi[1][(✉)] , Federica Amato[1] , Alessandro Cicolin[2] ,
and Gabriella Olmo[1]

[1] Department of Control and Computer Engineering, Politecnico di Torino,
Turin, Italy
{irene.rechichi,federica.amato,gabriella.olmo}@polito.it
[2] Department of Neuroscience, Sleep Disorders Centre, University of Turin,
Turin, Italy
alessandro.cicolin@unito.it

Abstract. Sleep Disorders have received much attention in recent years, as they are related to the risk and pathogenesis of neurodegenerative diseases. Notably, REM Sleep Behaviour Disorder (RBD) is considered an early symptom of α-synucleinopathies, with a conversion rate to Parkinson's Disease (PD) up to 90%. Recent studies also highlighted the role of disturbed Non-REM Slow Wave Sleep (SWS) in neurodegenerative diseases pathogenesis and its link to cognitive outcomes in PD and Dementia. However, the diagnosis of sleep disorders is a long and cumbersome process. This study proposes a method for automatically detecting RBD from single-channel EEG data, by analysing segments recorded during both REM sleep and SWS. This paper inspects the underlying microstructure of the two stages and includes a comparison of their performance to discuss their potential as markers for RBD. Machine Learning models were employed in the binary classification between healthy and RBD subjects, with an 86% averaged accuracy on a 5-fold cross-validation when considering both stages. Besides, SWS features alone proved promising in detecting RBD, scoring a 91% sensitivity (RBD class). These findings suggest the applicability of an EEG-based, low-cost, automatic detection of RBD, leading to potential use in the early diagnosis of neurodegeneration, thus allowing for disease-modifying interventions.

Keywords: EEG · Machine learning · Sleep disorders · RBD · REM sleep behaviour disorder · Automatic classification

1 Introduction

Sleep is a transient state of altered consciousness opposed to wake, and provides a restorative function to the human organism. Given its complex nature, it is a reservoir of significant clinical data. Human sleep cyclically alternates between

two different states – which also entail two different kinds of brain activity: rapid-eye movement sleep (REM) and non-REM sleep (NREM). The latter, according to the American Academy of Sleep Medicine (AASM) guidelines, is further divided into three stages, from light to deep: N1, N2 and Slow Wave Sleep (SWS) [1]. REM Sleep, on the contrary, exhibits mixed features and is often referred to as *paradoxical sleep*; it supports memory consolidation and is characterised by skeletal muscle atonia, as well as electrical brain activity resembling wake [21].

It has been demonstrated that the quality of both REM and SWS contributes to neurological outcomes in older adults [20], and their disruption not only leads to sleep disorders, but plays a role in the pathogenesis of neurodegenerative diseases.

Recent studies highlighted the role of sleep in clearing toxic metabolites – such as Amyloid-β – from the brain [14]. This occurs primarily during SWS through the glymphatic system, which is instead inhibited throughout wakefulness [28]. Consequently, poor sleep is associated to a variety of Sleep Disorders, which, in turn, entail a lower Quality of Life (QoL) [15], as well as an increased risk for neurodegeneration.

Sleep disorders may manifest in different ways. Among these, REM Sleep Behaviour Disorder (RBD), a REM parasomnia characterised by lack of physiological muscle atonia during REM Sleep [18], features a prevalence of approximately 2% in the elderly population worldwide [9]. RBD in its isolated phenotype is considered an early prodrome of α-synucleinopathy – e.g., Parkinson's Disease (PD), Dementia with Lewy Bodies (DLB) and multiple system atrophy [10,23]; indeed, the phenoconversion rate to PD is around 90% [7].

Polysomnography (PSG) is the gold standard to diagnose sleep disorders. It consists in recording various biosignals during sleep; including the electroencephalogram (EEG), pivotal to assess sleep stages, the electromyogram (EMG), and the electrooculogram (EOG). However, a PSG exam is costly and cumbersome; besides, the recordings are manually scored by a sleep technologist, thus significantly hindering the diagnostic process. Different studies undertook the automatic classification of sleep disorders through Machine Learning (ML) algorithms, in an attempt to accelerate and support the diagnosis [12]. They either employed PSG features [27] – i.e., clinical variables descriptive of the quality of sleep – or PSG biosignals [26]. Automatic RBD detection has also been addressed, primarily through EMG features [4,5], but also relying on EEG data only [3]. This study aims at performing an automatic classification between healthy and RBD subjects, based on single-channel EEG. Features extracted from the REM and SWS segments are input to ML models, in order to explore their applicability and determine which of the two stages is more relevant to the application at hand. To this end, in this work the feature sets derived from the two stages are analysed both separately and collectively.

2   Materials and Methods

2.1   Subjects and Data

For the purpose of this work, both a public and a private datasets were employed. The public dataset is the CAP Sleep Database [25], available on PhysioNet [8]. It includes PSG recordings of 22 subjects affected by RBD (19 males, aged 70 ± 6 years) and 16 healthy subjects (9 males, aged 32 ± 5 years). The recordings were studied along with the provided manual annotations of sleep stages, scored according to the AASM standards [1]. The additional data for this study were taken from a private dataset – the Turin Sleep Disorders Database (TuSDi Database) – encompassing PSG recordings of 10 healthy subjects (6 males, aged 37 ± 16 years) and 10 RBD subjects (8 males, aged 62 ± 6 years). Data were collected at the Center for Sleep Disorders at Molinette Hospital (Turin, Italy); the procedure has been conducted in accordance with the Declaration of Helsinki and approved by the Ethics Committee of A.O.U. Città della Salute e della Scienza di Torino (approval No. 00384/2020). Informed consent for observational study was obtained from the participants. Inclusion criteria were suspected or diagnosed RBD, with polysomnographic evidence of REM Sleep Without Atonia; exclusion criteria included dementia or other psychiatric conditions that could affect the correct execution of the PSG exam. All participants received detailed information on the study purpose and execution, and informed consent was obtained.

PSG recordings in the TuSDi Database were manually scored and annotated by a sleep technologist, according to the AASM standards. To sum up, this work considered for the analysis 26 healthy and 32 RBD subjects.

Being a single-channel EEG classification, only the recordings from the central EEG channel have been employed. Therefore, the C3-A2 channel (or C4-A1, if the former was not available) was selected for the subsequent analysis. Given the aim of the study, only sleep segments related to the REM stage and SWS were taken into account for the feature extraction step, detailed in Sect. 2.3.

2.2   Data Pre-processing

First of all, the sleep segments' duration was inspected; all subjects presented with at least 5 min of REM episodes and SWS and were therefore included in the study. The majority of EEG signals were collected at a sampling frequency 512 Hz; signals presenting with a different sampling frequency were resampled 512 Hz. This work relies on raw EEG data, meaning that the analysis did not require additional processing such as artefact removal or spatial filtering. However, in order to decrease high-frequency noise, all recordings have been preprocessed through a low-pass, zero-phase Chebyschev Type 1 Filter (cut-off frequency: 40 Hz). To prevent the acquisition conditions from affecting the analysis, the signals amplitude was converted to μV.

2.3   Feature Extraction

In this work, a total of 367 features were extracted. The features comprised both polysomnographic features – i.e., clinical parameters that describe the overall sleep structure – and features extracted from the EEG during REM and SWS segments. The feature extraction procedure is detailed in the following paragraphs.

Polysomnographic Features. As previously introduced, a first set of polysomnographic variables was computationally extracted from the hypnogram – i.e., the sleep scoring array. This set consists of variables that are commonly employed by sleep experts to assess overall sleep structure and quality – e.g., Sleep Onset Latency (SOL), Sleep Efficiency (SE); other parameters that describe the architecture of sleep stages – e.g., the proportion of each stage per sleep time, Minutes of REM Sleep (MREM), Minutes of SWS (MSWS) – and, lastly, variables that describe the variability within sleep stages and the sleep fragmentation – e.g., Arousal Index (ARI), Sleep Transition Index (STI). The complete set of employed polysomnographic features is presented in Table 1, and a detailed definition is provided for each parameter.

Electroencephalographic Features. Electroencephalographic features were extracted from the available central EEG channel (C3-A2 or C4-A1) from both REM and SWS segments, respectively. The features were extracted in three domains: Time, Frequency and Non-Linear. Given the fact that the AASM criteria score sleep by inspecting the EEG signal in 30 s epochs, the data in this study were analysed accordingly. Therefore, each sleep segment (i.e., REM or SWS) was divided into 30 s epochs, and time-domain features were extracted from each epoch. Spectral (i.e., frequency-domain) and Non-Linear features were extracted on 2 s sub-epochs and then averaged across the corresponding 30 s macro-epoch, thus ensuring stationarity for the EEG signal as well as a reasonable spectral resolution. At the end of the feature extraction process, for each variable, the values corresponding to the 30 s epochs were assembled into one feature array, and three statistics were computed – i.e., mean value, standard deviation (STD) and 75$^{\text{th}}$ percentile. A list of the employed EEG features is provided in Table 2, grouped according to their domain – i.e., Time, Frequency or Non-Linear.

Temporal features mainly account for the information provided by the amplitude of the signal or its waveform. For the purpose of this work, the latter is evaluated through the Form (FF), Crest (CF) and Impact factors (IF), defined in Eqs. (1), (2), (3) – where x is the considered signal.

$$FF = \frac{x_{RMS}}{|x|_{mean}} \tag{1}$$

$$CF = \frac{x_{peak}}{x_{RMS}} \tag{2}$$

Table 1. Polysomnographic features employed in the study, along with their acronym and description.

Feature (Acronym)	Description
Sleep Onset Latency (SOL)	The amount of time required to fall asleep (min)
Wake After Sleep Onset (WASO)	The amount of time the subject is awake during the night (min)
Total Sleep Time (TST)	Total hours of sleep
Time in bed (TIB)	Lights-off to lights-on interval (h)
Sleep Efficiency (SE)	The percentage of time spent asleep while in bed (%)
Arousal Index (ARI)	Frequency of occurrence of arousals
Minutes of REM Sleep (MREM)	Total duration of REM Sleep (min)
Minutes of SWS Sleep (MSWS)	Total duration of SWS (min)
Proportion of N1 Sleep (PN1)	N1 Sleep per TST (%)
Proportion of N2 Sleep (PN2)	N2 Sleep per TST (%)
Proportion of SWS Sleep (PN3)	SWS Sleep per TST (%)
Proportion of REM Sleep (PNR)	REM Sleep per TST (%)
NREM Fragmentation Index (NFI)	A measure of the number of transitions from NREM to any other NREM stage per hour of NREM sleep
REM Fragmentation Index (RFI)	A measure of the number of transitions from REM to any other sleep stage per hour of REM
Wake Proportion (WP)	Awake time during the night (%)
Sleep Transition Index (STI)	A measure of the number of transitions from REM to NREM (and vice versa) per hours of sleep
Average Length N1 (ALN1)	Average length of N1 segments (min)
Average Length N2 (ALN2)	Average length of N2 segments (min)
Average Length SWS (ALN3)	Average length of SWS segments (min)
Average Length REM (ALREM)	Average length of REM segments (min)

$$IF = \frac{x_{peak}}{|x|_{mean}} \tag{3}$$

The Hjorth Parameters – i.e., Activity, Mobility, Complexity – were also computed on the EEG signal and its first- and second-order derivatives. They are defined in Eqs. (4), (5), (6).

$$Activity = var(x) \tag{4}$$

$$Mobility = \sqrt{\frac{var(\frac{dx}{dt})}{var(x)}} \qquad (5)$$

$$Complexity = \frac{Mobility(\frac{dx}{dt})}{Mobility(x)} \qquad (6)$$

As regards the spectral features, the Power Spectral Density (PSD) was estimated on each mini-epoch through the Welch Periodogram (50% overlap, 1 s Hamming Window). Then, statistics on the power spectrum density (PSD) were computed, the mean and median frequencies were retrieved, as well as the absolute and relative powers for each clinically relevant EEG band and entropy measures. The Teager-Kaiser Energy Operator was also computed on the mini-epochs, for the whole available spectrum (0–40 Hz), as previously introduced in [17].

Sleep Substructure Features. Though previously introduced as homogeneous states, both the REM Sleep and SWS stages are characterised by an underlying substructure. In particular, the REM stage features two micro-states: the tonic stage (TREM) and the phasic stage (FREM) [22]. In further detail, aside from the diversity regarding the morphology of the signal, the two aforesaid micro-states significantly differ from a spectral point of view. In fact, as also presented in [17], the FREM and TREM micro-states lie in the frequency ranges 2–8 Hz and 7–16 Hz, respectively; these two sub-bands are noteworthy for feature extraction purposes. Likewise, deep sleep – i.e., SWS – presents with an underlying substructure, with 1 Hz threshold being particularly significant. While commonly and clinically located in the δ-band (0.5–4 Hz), SWS is indeed further divided into two sub-bands: slow oscillations (SOs) and slow-wave activity (SWA). From a spectral point of view, SOs are the slowest waves of deep sleep (<1 Hz), whereas SWA lies in the 1–4 Hz range [2]. Recent works highlighted the significance of this dychotomy in relation to Amyloid-β aggregation [14]. In particular, the latter shows positive correlation with the SWA frequency range; thus proving its significance in the neurodegeneration process. In accordance with these statements, additional features regarding the spectral substructure of the REM and SWS stages were extracted, and are listed in Table 3.

Table 2. Employed features, along with the domain and proper reference. ⋄: adapted from the cited study, †: first proposed in this study.

Category	Feature (Name and description)	Reference
Time	Amplitude metrics: mean, standard deviation, skewness, kurtosis, range, maximum and minimum value	Various
	Zero Crossing Rate	[24]
	Hjorth Parameters	[13]
	Percentiles (25th, 75th, 95th)	Various
	Form, Crest and Impact Factors	Various
	Coastline	[29]
Frequency	Fast Fourier Transform: numerical and statistical measures (mean and median frequencies, total power, ...)	Various
	Spectral Edge Frequencies (SEF25, SEF75, SEF95)	⋄[17]
	Spectral Edge Frequencies differentials $(75-25, 95-25, 95-50)$	†
	Absolute Power for each clinically relevant band $(\delta, \theta, \alpha, \beta, \gamma)$	Various
	Relative Power for each clinically relevant band $(\delta, \theta, \alpha, \beta, \gamma)$	Various
	Entropy measures	⋄[17]
Non-Linear	Teager-Kaiser Energy Operator: numerical and statistical measures	⋄[11]

Table 3. Additional spectral features, extracted according to sleep sub-structure. ⋄: adapted from the cited study, †: first proposed in this study.

Sleep Stage	Feature	Reference
REM stage	Absolute and Relative Power in TREM, FREM	⋄[17]
	Mean, Median Frequencies and Spectral Percentiles (SEF_x) in TREM, FREM	⋄[17]
	Total Power Ratio TREM/FREM	⋄[17]
Slow Wave Sleep	Absolute and Relative Power in SOs, SWA	⋄[19]
	Mean, Median Frequencies, Spectral percentiles (SEF_x), statistical measures in SOs, SWA	†

2.4   Data Post-processing and Feature Sets

Section 2.3 described the steps employed in the feature extraction process. Owing to the fact that the extracted features belong to diverse domains – e.g., clinical scores and computational parameters – Z-score normalization was applied to the whole feature set (367 features), thus transforming the features to the continuous range [0, 1]. This procedure allowed the feature arrays to follow a normal distribution, easing the subsequent implementation of distance-based measures and classifiers.

At the end of the post-processing steps, three feature sets (FeatSet$_i$) are obtained:

– **FeatSet$_1$**: Polysomnographic + REM Sleep features;
– **FeatSet$_2$**: Polysomnographic + Slow Wave Sleep features;
– **FeatSet$_3$**: Polysomnographic + REM Sleep + Slow Wave Sleep features.

The three feature sets are then used for binary classification purposes, in an attempt to discriminate between healthy and RBD subjects.

2.5   Feature Selection

As regards Feature Selection, a minimal-optimal approach was adopted, which aims at selecting the set of features that, once grouped, have the highest predictive power. The employed feature selection method is the Minimum Redundancy Maximum Relevance (mRMR) [16], based on Pearson Correlation and F-test, which maximises the mutual information provided by the features in spite of their redundancy. This method ranks the features according to their relevance to the target variable. The resulting top-5 features for each subset are shown in Table 4. As appreciable, when considering FeatSet$_3$ (i.e., REM, SWS + PSG), three features out of five belong to SWS.

2.6   Classification

The aim of this work was to perform an automatic binary classification between healthy and RBD subjects. To this end, supervised Machine Learning methods were applied to the three feature sets presented in Sect. 2.4. Four different models were tested, namely: Support Vector Machine (SVM), K-Nearest Neighbour (KNN), Naive-Bayes (NB), Decision Tree (DT), along with an ensemble method, Bootstrap Aggregating (BAG). The latter is a meta-algorithm specifically designed to reduce variance within the dataset, thus preventing overfitting. The model randomly samples the original dataset, creating from such different sub-sets; it then parallel-trains the sub-sets separately and finally yields prediction scores based on majority voting. As regards the other models, a brief description follows:

– **SVM**: it aims at finding the hyperplane which best separates data of the two classes, while maximising the margin – i.e., the distance between the data points (support vectors) and the hyperplane.
– **KNN**: it is a non-parametric method that classifies observations based on their similarity to its closest data-points in the datasets (i.e., *neighbours*).
– **NB**: it is a probabilistic classifier based on the Naive-Bayes theorem.
– **DT**: this model is based on decision rules; it starts from a root-node and classifies observations by testing them at each decision node, eventually leading to the terminal node – i.e., the label.

Table 4. Top-5 ranked features with the mRMR feature selection method, in all three employed feature sets. For FeatSet$_3$: ⋆ REM features, ∘ SWS features

FeatSet	Top-5 Features
FeatSet$_1$ (PSG + REM)	Relative Power (α)
	Minutes in REM Sleep
	WASO
	Mobility (2nd order)
	SEF75
FeatSet$_2$ (PSG + SWS)	Relative Power SWA (75th pctl)
	Relative Power (θ), STD
	Relative Power (α), STD
	Minimum Amplitude
	Median (75th pctl)
FeatSet$_3$ (PSG + SWS + REM)	Relative Power SWA (75th pctl), ∘
	Relative Power (θ), STD, ∘
	Mobility (2nd order), ⋆
	Relative Power (α), ⋆
	Minimum Amplitude, ∘

Hyperparameters optimisation (Bayesian approach) was applied to each model. Finally, to prevent overfitting k-fold cross-validation (CV) ($k = 5$) was applied. This technique samples the dataset into k different sub-sets; it performs training on $k - 1$ subsets and tests the model on the remaining one. Considering the random sampling adopted by the CV, and to prevent the classification performance from being affected by weak generalization capability, this procedure was iterated 10 times.

3   Results

As introduced earlier, the models presented in Sect. 2.6 were employed in a binary classification task, with the aim of discriminating healthy from RBD subjects, (CAP Sleep Database and TuSDi Database). This Section presents the classification performance, for each considered Feature Set (*cf.* Sect. 2.4).

3.1   Classification Performance: REM Features

The first Feature Set considered for the analysis (FeatSet$_1$) comprised PSG features and features extracted from the REM segments. The classification performance of the five models tested is displayed in Table 5; the values refer to a 5-fold CV, averaged over 10 iterations. The macro-averaged accuracy (across all tested classifiers) is 80.29% ± 0.03. The best overall performance was attained through

the KNN classifier (Accuracy: 83.91% ± 0.81, Sensitivity: 86.46% ± 2.95). As regards the KNN model optimisation, the searched parameters were: K (number of neighbours, 1 to 29) and distance metrics, resulting in the optimised parameters K = 3 and Chebyshev Distance.

Table 5. Classification performance (%) of the employed classifiers as regards FeatSet$_1$ (PSG + REM features).

	SVM	KNN	NB	DT	BAG
Accuracy	81.03 ± 0.5	83.91 ± 0.81	74.14 ± 1.72	82.18 ± 0.81	80.17 ± 0.86
Sensitivity	84.38 ± 3.13	86.46 ± 2.95	73.44 ± 1.56	85.42 ± 5.31	82.81 ± 1.56
Specificity	76.92 ± 3.85	80.77 ± 3.14	75 ± 1.92	78.21 ± 7.2	76.92 ± 0.1
Precision	81.94 ± 1.94	84.78 ± 1.75	78.33 ± 1.67	83.28 ± 4.25	82.16 ± 0.91
F1	83.06 ± 0.52	85.55 ± 0.9	75.81 ± 1.61	84.07 ± 0.87	82.16 ± 0.91
AUC	0.87 ± 0.05	0.87 ± 0.01	0.76 ± 0.02	0.83 ± 0.03	0.89 ± 0.02

3.2 Classification Performance: REM + SWS Features

Secondly, the classifiers were tested on FeatSet$_3$, which adds to the previous one the features extracted from the SWS stage. The classification performance consistently increases for all classifiers (Table 6). This feature set, indeed, presents with an overall macro-averaged accuracy of 85.70% ± 0.04 (+6% with respect to FeatSet$_1$), and a 8.3% increase for the AUC metric. The best classification performance is achieved through the DT (Accuracy: 90.80% ± 0.8, Sensitivity: 95.83% ± 2.95). As for best model optimisation, the searched hyperparameters were Split Criterion (method) and N (maximum number of splits, range: 1–57); the resulting optimised parameters were cross entropy as Split Criterion and N = 4.

Table 6. Classification performance (%) of the employed classifiers as regards FeatSet$_3$ (PSG + REM + SWS features).

	SVM	KNN	NB	DT	BAG
Accuracy	89.08 ± 1.63	85.34 ± 2.59	79.31 ± 1.72	90.80 ± 0.8	83.62 ± 0.86
Sensitivity	92.71 ± 2.95	93.75 ± 0.4	82.81 ± 4.69	95.83 ± 2.95	85.94 ± 1.56
Specificity	86.42	75 ± 5.77	75 ± 1.92	84.62 ± 3.14	80.77
Precision	88.11 ± 0.33	82.33 ± 3.38	80.32 ± 0.32	88.54 ± 1.82	84.61 ± 0.24
F1	90.33 ± 1.56	87.63 ± 1.92	81.47 ± 2.11	91.99 ± 0.79	85.26 ± 0.89
AUC	0.98 ± 0.01	0.92 ± 0.03	0.82 ± 0.03	0.92 ± 0.02	0.93 ± 0.05

3.3   Classification Performance: SWS Features

Finally, given the final aim of the study – i.e., determine which stage (REM vs SWS) is more informative in the automatic detection of RBD – the classifiers were tested also on the remaining feature set (FeatSet$_2$), encompassing PSG features and variables extracted from the SWS stage alone. The performance metrics are displayed in Table 7. As appreciable, the classifiers achieved reasonably good results, with an overall macro-averaged accuracy of 81.10% $\pm$ 0.03. Though the average accuracy (across classifiers) only shows a slight overall increase with respect to the REM Subset, the SVM classifier clearly outperforms the performances of the classifiers on FeatSet$_1$. In fact, it achieved an Accuracy of 86.21% $\pm$ 2.11 and Sensitivity of 91.23% $\pm$ 5.24, as well as an AUC value of 0.94 $\pm$ 0.02. As regards SVM, the searched parameters were Kernel Function and Maximum Penalty; the optimised model featured a cubic Kernel Function and a Maximum Penalty of 2.56 (search range: 0.001–1000).

Table 7. Classification performance (%) of the employed classifiers as regards FeatSet$_2$ (PSG + SWS features only).

	SVM	KNN	NB	DT	BAG
Accuracy	86.21 $\pm$ 2.11	80.46 $\pm$ 4.94	78.74 $\pm$ 4.30	79.52 $\pm$ 7.21	80.60 $\pm$ 3.31
Sensitivity	91.23 $\pm$ 5.24	83.71 $\pm$ 12.26	76.67 $\pm$ 6.73	80.83 $\pm$ 9.78	79.13 $\pm$ 5.58
Specificity	83.36 $\pm$ 1.57	80.83 $\pm$ 2.94	81.16 $\pm$ 3.15	79.06 $\pm$ 6.25	82.19 $\pm$ 1.92
Precision	76.92 $\pm$ 2.72	74.36 $\pm$ 7.90	76.92 $\pm$ 5.44	74.04 $\pm$ 6.72	77.88 $\pm$ 3.19
F1	83.36 $\pm$ 2.38	77.58 $\pm$ 3.58	76.50 $\pm$ 4.14	77.04 $\pm$ 7.31	78.34 $\pm$ 2.98
AUC	0.94 $\pm$ 0.02	0.85 $\pm$ 0.02	0.81 $\pm$ 0.02	0.77 $\pm$ 0.09	0.9 $\pm$ 0.02

4   Discussion

As described above (*cf.* Sects. 3.1–3.3), the employed classifiers generally achieved a good global performance on all tested feature sets. Indeed, the best classifier for the REM subset scored an overall Accuracy of 84%, with 86.5% sensitivity to the RBD class. As appreciable from the data presented in Table 6, the classification performance significantly increases when including the SWS features into the analysis, yielding a 91% Accuracy and 96% Sensitivity (best score). Furthermore, the SWS features alone proved efficient in addressing the binary classification task, achieving an overall 86% Accuracy and 91% Sensitivity (SVM classifier).

As displayed in Fig. 1, that compares the best models on each tested feature set, FeatSet$_2$ (SWS features) outperforms the REM subset, suggesting its applicability and relevance in the automatic detection of RBD.

This consideration is in line with the results presented in [3], which performed a stage-agnostic feature extraction, and highlighted the δ-range – and in
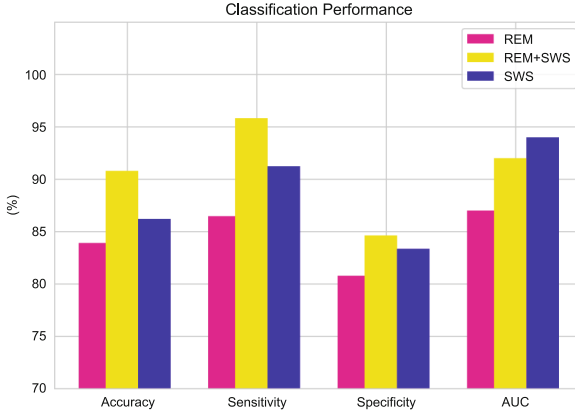
Fig. 1. Performance comparison of the best model for each analysed feature set.

particular the 1.5–2 Hz sub-band – as the most important in a healthy vs RBD classification approach. In addition, the classification performance was compared to the cited study, which addressed the task employing the same publicly available data (CAP Sleep Database) [3]. Therefore, the cited study analysed the EEG recordings across the whole spectrum (0.5–50 Hz), with no stage distinction; our results outperform their metrics when considering features from both SWS and EEG (FeatSet$_3$), with a balanced accuracy (averaged across all models) of 86% versus 83%, as well as a 26% improvement on Specificity, and +2% on Sensitivity. When considering the metrics on the SWS feature set only, the SVM classifier yielded comparable performances as regards Accuracy and Sensitivity, and achieved a 22% increase on Specificity with respect to [3].

5   Conclusion and Future Work

The clinical diagnosis of RBD involves a overnight full-PSG exam and additional anamnestic interviews. Though being the gold standard for the detection and monitoring of sleep disorders, PSG is invasive and impractical. Indeed, not only it entails a high number of recording electrodes, but the manual and visual scoring process is labourious, thus significantly hindering the diagnosis. Given that RBD itself foreruns the onset of α-synucleinopathy up to 14 years, there is the need to accelerate the detection process, providing accurate and lightweight alternatives to manual scoring.

This paper proposed a method for the automatic detection of RBD from single-channel EEG data. Data were extracted from the recordings during REM Sleep and SWS. The implemented ML methods achieved high performance, suggesting the applicability of single-channel electroencephalography in detecting RBD subjects.

Moreover, the performance attained by the SWS features alone is quite promising, therefore implying its applicability to the study of RBD and the

related neurodegenerative process. These findings indicate the feasibility of a lightweight screening tool, thus easing the scoring and diagnostic process. Furthermore, automatic classification would reasonably facilitate follow-up procedures, and allow for early detection and early disease-modifying interventions which would have beneficial impact on the QoL of patients [6].

Future work will address a larger dataset to further investigate the SWS dychotomy and its role in the development of RBD, and will combine the investigation of the breathing frequency patterns during both REM Sleep and SWS.

References

1. Berry, R.B., et al.: The AASM manual for the scoring of sleep and associated events. Rules,Terminology Tech. Specifications Darien Illinois Am. Acad. Sleep Med. **176**, 2012 (2012)
2. Björn, R., Jan, B.: About sleep's role in memory. Physiol. Rev. **93**, 681–766 (2013)
3. Buettner, R., Grimmeisen, A., Gotschlich, A.: High-performance diagnosis of sleep disorders: a novel, accurate and fast machine learning approach using electroencephalographic data. In: Proceedings of the 53rd Hawaii International Conference on System Sciences (2020)
4. Cooray, N., Andreotti, F., Lo, C., Symmonds, M., Hu, M.T., De Vos, M.: Detection of REM sleep behaviour disorder by automated polysomnography analysis. Clin. Neurophysiol. **130**(4), 505–514 (2019)
5. Cooray, N., Andreotti, F., Lo, C., Symmonds, M., Hu, M.T., De Vos, M.: Proof of concept: screening for REM sleep behaviour disorder with a minimal set of sensors. Clin. Neurophysiol. **132**(4), 904–913 (2021)
6. Fayyaz, M., Jaffery, S.S., Anwer, F., Zil-E-Ali, A., Anjum, I.: The effect of physical activity in Parkinson's disease: a mini-review. Cureus **10**(7), e2995 (2018)
7. Galbiati, A., Verga, L., Giora, E., Zucconi, M., Ferini-Strambi, L.: The risk of neurodegeneration in REM sleep behavior disorder: a systematic review and meta-analysis of longitudinal studies. Sleep Med. Rev. **43**, 37–46 (2019)
8. Goldberger, A.L., et al.: Physiobank, physiotoolkit, and physionet: components of a new research resource for complex physiologic signals. Circulation **101**(23), e215–e220 (2000)
9. Haba-Rubio, J., Frauscher, B., Marques-Vidal, P., et al.: Prevalence and determinants of rapid eye movement sleep behavior disorder in the general population. Sleep **41**(2), zsx197 (2018)
10. Hu, M.T.: Rem sleep behavior disorder (RBD). Neurobiol. Dis. **143**, 104996 (2020)
11. Lajnef, T., et al.: Learning machines and sleeping brains: automatic sleep stage classification using decision-tree multi-class support vector machines. J. Neurosci. Methods **250**, 94–105 (2015)
12. López-Garcıa, D., Ruz, M., Ramırez, J., Górriz, J.: Automatic detection of sleep disorders: multi-class automatic classification algorithms based on support vector machines. In: International Conference on Time Series and Forecasting, ITISE 2018, vol. 3, pp. 1270–1280 (2018)
13. Motamedi-Fakhr, S., Moshrefi-Torbati, M., Hill, M., Hill, C.M., White, P.R.: Signal processing techniques applied to human sleep EEG signals-a review. Biomed. Signal Process. Control **10**, 21–33 (2014)
14. Ngo, H.V.V., Claassen, J., Dresler, M.: Sleep: slow wave activity predicts amyloid-β accumulation. Curr. Biol. **30**(22), R1371–R1373 (2020)

15. Pavlova, M.K., Latreille, V.: Sleep disorders. Am. J. Med. **132**(3), 292–299 (2019)
16. Peng, H., Long, F., Ding, C.: Feature selection based on mutual information criteria of max-dependency, max-relevance, and min-redundancy. IEEE Trans. Pattern Anal. Mach. Intell. **27**(8), 1226–1238 (2005)
17. Rechichi, I., Zibetti, M., Borzì, L., Olmo, G., Lopiano, L.: Single-channel EEG classification of sleep stages based on rem microstructure. Healthc. Technol. Lett. **8**(3), 58 (2021)
18. Schenck, C.H., Bundlie, S.R., Ettinger, M.G., Mahowald, M.W.: Chronic behavioral disorders of human rem sleep: a new category of parasomnia. Sleep **9**(2), 293–308 (1986)
19. Schreiner, S.J., et al.: Reduced regional NREM sleep slow-wave activity is associated with cognitive impairment in Parkinson disease. Front. Neurol. **12**, 156 (2021)
20. Scullin, M.K., Gao, C.: Dynamic contributions of slow wave sleep and REM sleep to cognitive longevity. Curr Sleep Med. Rep. **4**(4), 284–293 (2018)
21. Siegel, J.M.: Rem sleep: a biological and psychological paradox. Sleep Med. Rev. **15**(3), 139 (2011)
22. Simor, P., van der Wijk, G., Nobili, L., Peigneux, P.: The microstructure of rem sleep: why phasic and tonic? Sleep Med. Rev. **52**, 101305 (2020)
23. Stefani, A., Högl, B.: Sleep in Parkinson's disease. Neuropsychopharmacology **45**(1), 121–128 (2020)
24. Šušmáková, K., Krakovská, A.: Discrimination ability of individual measures used in sleep stages classification. Artif. Intell. Med. **44**(3), 261–277 (2008)
25. Terzano, M.G., et al.: Atlas, rules, and recording techniques for the scoring of cyclic alternating pattern (cap) in human sleep. Sleep Med. **2**(6), 537–553 (2001)
26. Urtnasan, E., Joo, E.Y., Lee, K.H.: Ai-enabled algorithm for automatic classification of sleep disorders based on single-lead electrocardiogram. Diagnostics **11**(11), 2054 (2021)
27. Widasari, E.R., Tanno, K., Tamura, H.: Automatic sleep disorders classification using ensemble of bagged tree based on sleep quality features. Electronics **9**(3), 512 (2020)
28. Xie, L., et al.: Sleep drives metabolite clearance from the adult brain. Science **342**(6156), 373–377 (2013)
29. Yetton, B.D., Niknazar, M., Duggan, K.A., McDevitt, E.A., Whitehurst, L.N., Sattari, N., Mednick, S.C.: Automatic detection of rapid eye movements (REMS): a machine learning approach. J. Neurosci. Methods **259**, 72–82 (2016)

A Deep Learning Framework for the Prediction of Conversion to Alzheimer Disease

Sofia Ostellino$^{(\boxtimes)}$, Alfredo Benso , and Gianfranco Politano

Computer Science and Automation Department, Politecnico di Torino, Torino, Italy
{Sofia.Ostellino,Alfredo.Benso,Gianfranco.Politano}@polito.it

Abstract. Alzheimer disease (AD) is the most common form of senile brain disorder. AD is not reversible, but its neuropathology can be detected several years before severe clinical manifestations. AD diagnosis is carried out relying on several clinical data, such as MRI structural and functional data, PET and DTI imaging, neuropsychological tests' scores, genetic data, and others. Approaches that use complementary information and heterogeneous sources of data might have a decisive impact on the ability to early identify and consequently treat those subjects with a higher probability of conversion. We propose an on-going work on a Deep Learning framework that integrates different sources of data such as imaging data, clinical data, neuropsychological tests' scores, and the temporal information related to the last medical evaluation of the subject, with the aim of estimating the probability of conversion from mild-cognitive-impairment (MCI) to AD or from a stable clinical profile to MCI in a period of time that varies from 6 months to 18 months. The possibility of predicting disease conversion is an open problem in this field, and wants to answer to a specific need of clinicians. The ADNI public data-set represents the reference data-set: an extensive and detailed analysis of ADNI has been performed to assess the sample size available for the training and testing of the network, that is now under construction, and the first results will be soon available. The network will also be tested with clinical data of the Fondazione Santa Lucia, Rome (Italy), and results will be discussed with the neurologists, neuropsychologists, and physics that are actively working with us.

Keywords: Alzheimer disease · Deep Learning · Prediction · Biomarkers identification

1 Introduction

1.1 Alzheimer Disease

Alzheimer disease (AD) is the most common form of senile brain disorder which is caused by the β-amyloid peptide deposition [1]. AD is not reversible and there is no existing cure, but the neuropathology related to AD can be detected several years before severe AD clinical manifestations. The disease generally

starts with a light deterioration of cognitive reserves and gradually worsens into a more severe form of dementia. The initial phase of the disease is identified as Mild Cognitive Impairment (MCI) and has a wide spectrum that varies from cognitive difficulties that are challenging to detect to more evident cognitive deficits. Around the 10% and 15% of MCI patients per-year tend to convert to AD [2]. Given the nature of its long, progressive, and variable prodromal phase, early discrimination of those patients that develop Alzheimer disease from those who manifest a stable MCI is fundamental. Therefore, administering a treatment prior to AD conversion can efficiently decelerate AD evolution.

AD diagnosis is carried out relying on several clinical data, such as MRI structural and functional data, PET and DTI imaging, neuropsychological tests' scores, genetic data, and others. Recent literature proposes various methods for AD detection that rely on Deep Learning principles. Some of them are focused on the classification of AD, MCI and control subjects using fMRI or structural MRI data, others are based on multi-modality imaging data [3]. Not only AD detection is needed, but also the ability of algorithms to predict the probability of conversion from MCI to AD is required. Given the variegated nature of AD, approaches that use complementary information and heterogeneous sources of data might have a decisive impact on the ability to early identify and consequently treat those subjects with a higher probability of conversion to AD.

2   Materials and Methods

2.1   The ADNI Dataset

The ADNI dataset [4,5] was selected as it is, at present, the most used dataset which is public available and referred to an on-going initiative. ADNI was launched more than a decade ago, and participants are recruited across North America during each phase of the study and agree to complete a variety of imaging and clinical assessments: participants are followed and reassessed over time to track the pathology of the disease as it progresses. Results are shared by ADNI through the USC Laboratory of Neuro Imaging's Image and Data Archive (IDA) [6]. The goals of the ADNI study are:

– To detect AD at the earliest possible stage and identify AD's biomarkers;
– to support advances in AD intervention;
– to administer ADNI's data-access policy.

The ADNI data-set was analyzed so as to quantifying the amount and the typology of data that could be used for the purposes of our research, starting from the information summarized in the file *ADNI Merge*, which contains a sum-up of almost all the information available in ADNI. ADNI Merge contains 85 variables and a total of 15754 time-points when it was analysed for this study. At present, 2380 subjects are part of the ADNI data-set, and each subject has been screened for a variable number of time-points, depending on the ADNI phase he or she had been enrolled in. Figure 1 shows the distribution of the RIDs (Roster
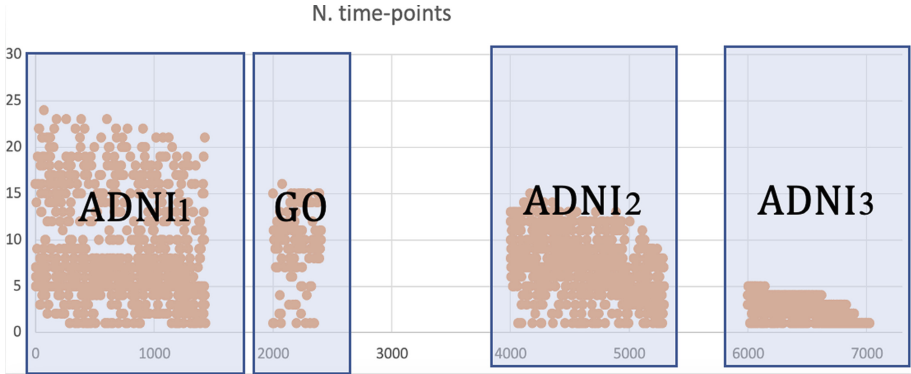
Fig. 1. Distribution of RIDs and the number of time-points per RID in each ADNI phase.

Ids) (horizontal axis), which uniquely identifies each subject, and the number of time-points per RID (vertical axis).

The following is the distribution of the RIDs with respect to the ADNI's phase:

– ADNI1: RID from 0 to 1999;
– ADNIGO: RID from 2000 to 3999;
– ADNI2: RID from 4000 to 5999;
– ADNI3: RID >= 6000.

The data-set is characterized by a high degree of variability in the information it contains, and this variability needs to be handled for the purposes of our analysis. To give an idea, Fig. 2 shows the numerosity of the several clinical variables summarised in ADNI Merge: we can notice that some are always present, some others are rarely acquired. This depends on the differences between the phases of ADNI (ADNI1, ADNIGO, ADNI2 and ADNI3).
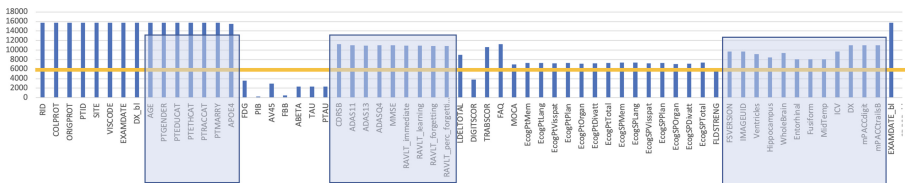
Fig. 2. Numerosity for clinical variables contained in ADNI Merge.

2.2 State-of-the-Art

Several works in the recent Literature focus on the problem of predicting conversion to AD. So far, most of the papers focus on the classification of AD, healthy

control, and MCI using imaging data [8–11]. However, there are few relevant papers (see of example Spasov et al. [7]) that combine the necessity of predicting the conversion to MCI or AD in time with the importance of using different sources of data, as we propose in this paper. In addition, we propose a method that predicts the conversion from CN to MCI and from MCI to AD in a time window that is not fixed, but varies between 6, 12 and 18 months (see Sect. 2.4).

2.3   ADNI Analysis

For each subject in *ADNI Merge* it is possible to obtain several details, for example the diagnosis that is made during the first visit (baseline visit) and the diagnosis carried out during the following monitoring visits. It is relevant to notice that, during the baseline visit, subjects are categorized as Controls (CN), AD (Alzheimer), LMCI and EMCI (Late Mild Cognitive Impairment and Early Mild Cognitive Impairment), and SMC (Significant Memory Concern): during the monitoring visits subject are classified as CN, AD or MCI (loosing the distinction between LMCI and EMCI). All the analyses that follow were performed with the Pandas Python library. The analyses proposed in this study are rare in literature, and we believe it was fundamental to share these results. Our choices have been driven by the numeracy of the ADNI data, that does not allow at this stage to extend the analysis to other phases of the pathology such as the SMC, or the LMCI and EMCI, but our approach does not exclude such extension in the future.

Table 1 summarises the number of time-points with the respective labels.

Table 1. Time-points and labels at baseline.

	Number of time-points
Total time-points	15754
Time-points classified at baseline as SMC	1246 (8%)
Time-points classified at baseline as LMCI	5158 (33%)
Time-points classified at baseline as EMCI	2881 (18%)
Time-points classified at baseline as AD	1713 (11%)
Time-points classified at baseline as CN	4728 (30%)

2.4   Selection Criteria and Data-Set Creation

The goal of the presented Deep Learning framework is to integrate different sources of data such as imaging data, clinical data, neuropsychological tests' scores, and the temporal information related to the last medical evaluation of the subject to estimate the probability of conversion from mild-cognitive-impairment (MCI) to AD or from a stable clinical profile to MCI in a period of time that varies from 6 months to 18 months.

Because of this, we are interested in those subject that happen to have more than one time-point, and that present a switch of the diagnosis in time: Table 2 exemplifies what we mean with the conversion of the diagnosis.

Table 2. Example of a subject that is diagnosed as MCI after 18 months.

Visit (months from baseline)	Diagnose
0 (baseline)	CN
06	CN
12	CN
18	MCI

Consequently, selection criteria were defined to create the data-set for the network, starting from ADNI:

– 253 single-time-points were not considered;
– those time-points for which no diagnosis is given were not considered, as none of them corresponded to a switch point;
– each time-point has been further labelled as shown in Table 3

We labelled all the time-points for which there had been a change in the diagnosis during the subsequent clinical examination, as we are interested in predicting the conversion during time, and clinical data referred to the exam previous to conversion are considered to be informative.

Table 3. Example of a subject that is diagnosed as MCI after 18 months.

Visit (months from baseline)	Diagnose	Switch
0 (baseline)	CN	CN-CN
06	CN	CN-MCI
12	MCI	MCI-MCI
18	MCI	Last time-point

It was further noticed that 151 time-points showed reversion, as exemplified in Table 4: this might be due to errors in the data-set or to the difficulty in detecting MCI, as the majority of reversions is a MCI-CN reversion. It will be decided how to treat those points later on: these will be excluded or included as a particular class of reversion.

Table 4. Example of a subject with a reversion in the diagnosis

Visit (months from baseline)	Diagnose	Reversion
0 (baseline)	CN	CN-CN
06	CN	CN-MCI
12	MCI	CN-CN
18	MCI	Last time-point

Table 5 reports the numerosity of the time-points for each switch, those that belong to the control group, MCI group or AD group, and those that revert the diagnosis.

Table 5. Number of time-points with a switch of the diagnosis.

	CN	MCI	AD
CN	2822	175	6
MCI	121	3531	411
AD	1	29	1567

2.5   Data for the Deep Learning Framework Training

As we are interested in giving as input to the network a time reference along with clinical data, we focused on computing the distribution of the time-points of each switch in time. In order to compute the interval of time between different points, we based on the *EXAMDATE* parameter, and not on the *VISCODE* variable present in *ADNI Merge*: the ADNI documentation[1] highlight that the *EXAMDATE* is more reliable. The *VISCODE* was used to match the time-point in *ADNI Merge* with the corresponding images to download them from the ADNI repository. As shown in Table 5, the size of the classes of interest (i.e. those time-points that show a switch in the diagnosis), is not so consistent as only 175 time-points switch from CN to MCI, and only 411 switch from MCI to AD. We will test the possibility of expanding the size of classes by considering not only the time-point that precede the switch of the diagnosis (see Table 4), but also all the previous time-points and labelling them by adding, for each time-point, the distance from the conversion (see Table 6).

As shown in Table 7, the majority of switches is condensed between 3 and 36 months. The time-points after the 100th month do not show switches. Moreover, the CN-AD conversion class is almost non-existing: this is why the Deep Learning architecture will be trained to predict the conversion in 12, 24, 36 months from CN to MCI and from MCI to AD.

---

[1] https://adni.loni.usc.edu/support/.

Table 6. Example of data selection that takes into consideration all the time-points before the switch.

Visit (months from baseline)	Diagnose	Reversion	Modified reversion
0 (baseline)	CN	CN-CN	CN-MCI - 12 m
06	CN	CN-CN	CN-MCI - 6 m
12	MCI	CN-MCI	CN-MCI - 0 m
18	MCI	Last time-point	–

This task has a particular importance from a clinical point of view, as no bio-marker exists for the prediction of the conversion from a stable clinical profile to a MCI profile, nor for the prediction of the conversion from the MCI profile to the AD profile. The possibility of predicting Alzheimer disease and its prodrome, mild-cognitive-impairment, can have a real impact on the readiness of administering the right treatment and assistance to the patient.

Table 7. Distribution of the interval of time (months).

Interval (months)	CN-MCI	CN-AD	MCI-AD
3–12	106	2	406
12–24	120	12	359
24–36	366	18	390
36–100	407	141	588
100–180	55	28	14

The data that will be used as input for the deep learning architecture are both clinical data, such as neuropsychological tests scores (MMSE, RAVLT, CDRSB, ADAS etc.), and imaging data (depending on the numerosity, sMRI or fMRI), along with the information about the time elapsed from the baseline visit, since the clinical profile of a patient that convert to MCI from CN after 6 months is different from the one of a patient that converts after 18 months.

Some patients show multiple conversions (see Table 8), and those patients are of particular interest, especially for testing the performances of the deep learning architecture.

Table 8. Example of multiple conversions.

Visit (months from baseline)	Rev. CN-MCI	Rev. MCI-AD
0 (baseline)	CN-MCI - 10 m	MCI-AD - 12 m
06	CN-MCI - 4 m	MCI-AD - 6 m
10	CN-MCI - 0 m	MCI-AD - 2 m
12	MCI-AD - 0 m	MCI-AD - 0 m
18	AD	AD

2.6 The Deep Learning Architecture

We propose a Deep Learning framework that integrates different sources of data, with the aim of estimating a probability index of conversion from CN to MCI and from MCI to AD in 12, 24, and 36 months. The Deep Learning framework is now under construction and the first results will be available soon.

The data-set that is public available and that is mostly used is the Alzheimer's Disease Neuroimaging Initiative (ADNI) database, and it was chosen as a starting point, but the system will also be tested with real clinical data of the Fondazione Santa Lucia (Rome, IT), and discussed with the neurologists and neurospychologists that work with us. The architecture will merge different type of data, giving as output the prediction of conversion to MCI or AD in a window of time that varies between 6 and 18 months. Beyond this, the results of the framework will be used to identify a subset of relevant clinical features that can serve as bio-markers for the AD disease.

3 Discussion and Conclusions

The Deep Learning framework proposed in this paper whose results will be available soon refers to a specific clinical need related to the importance of providing a tool which is capable of predicting the conversion to MCI and to AD, to guide clinicians in choosing the best treatment for a patient. Furthermore, ad extensive analysis has been performed on ADNI and its main results were presented in this paper: literature lacks of such analysis, and we believed it was relevant to share its main points, as well as devote the right amount of time to such analysis.

Results will be compared with state-of-the-art methods. Lin et al. [13] propose a prediction of conversion MCI-AD in 3 years that rely on MRI features, FDG-PET features, CSF biomarkers, and one gene feature of ADNI, giving the multi-modal data as input to an Extreme Learning Machine (ELM) algorithm. Platero et al. [12] propose as well to predict the conversion MCI-AD with MRI markers and neuropsychological tests in 3 years time. These two recent papers rely on machine learning approaches, and focus on the conversion from MCI to AD: our proposed method, on the contrary, is based on Deep Learning and focuses both on the conversion from CN-MCI, and MCI-AD, in a variable period of time.

The Deep Learning framework will be also tested with real clinical data provided by the Fondazione Santa Lucia, Rome (IT), and we will discuss along with clinicians to ensure the best performances and making the best adjustments, with the aim of creating a tool that can be used during the real clinical practice, identifying reliable bio-markers for monitoring the Alzheimer disease.

References

1. Murphy, M.P., LeVine III, H.: Alzheimer's disease and the Amyloid-β Peptide. J. Alzheimer's Dis. **19**(1), 311–323 (2010). content.iospress.comhttps://doi.org/10.3233/JAD-2010-1221

2. Barnes, D.E., Yaffe, K.: The projected effect of risk factor reduction on Alzheimer's disease prevalence. Lancet Neurol. **10**, 819–828 (2011). https://doi.org/10.1016/S1474-4422(11)70072-2

3. Ebrahimighahnavieh, M.A., et al.: Deep learning to detect Alzheimer's disease from neuroimaging: a systematic literature review. Comput. Methods Programs Biomed. **187**, 105242 (2020). https://doi.org/10.1016/j.cmpb.2019.105242

4. Petersen, R.C., et al.: Alzheimer's disease neuroimaging initiative (ADNI). Neurology **74**(3), 201–209 (2020). https://doi.org/10.1212/WNL.0b013e3181cb3e25

5. ADNI Homepage. https://adni.loni.usc.edu/

6. Learn more about the ADNI Initiative. http://adni.loni.usc.edu/about/

7. Simeon, S., et al.: A parameter-efficient deep learning approach to predict conversion from mild cognitive impairment to Alzheimer's disease. NeuroImage **189**, 276–287 (2019). https://doi.org/10.1016/j.neuroimage.2019.01.031

8. Sarraf, S., Tofighi, G.: Classification of Alzheimer's disease using fMRI data and deep learning convolutional neural networks. arXiv:1603.08631 [cs], March 2016

9. Li, W., et al.: Detecting Alzheimer's disease based on 4D fMRI: an exploration under deep learning framework. Neurocomputing **388**, 280–287 (2020). https://doi.org/10.1016/j.neucom.2020.01.053

10. Parmar, H., et al.: Spatiotemporal feature extraction and classification of Alzheimer's disease using deep learning 3D-CNN for fMRI data. J. Med. Imaging **7**(5), 056001 (2020). https://www.spiedigitallibrary.org, https://doi.org/10.1117/1.JMI.7.5.056001

11. Giulietti, G., et al.: Whole brain white matter histogram analysis of diffusion tensor imaging data detects microstructural damage in mild cognitive impairment and Alzheimer's disease patients: DTI histograms for staging AD. J. Magn. Reson. Imaging **48**(3), 767–769 (2018). https://doi.org/10.1002/jmri.25947

12. Platero, C., et al.: Predicting Alzheimer's conversion in mild cognitive impairment patients using longitudinal neuroimaging and clinical markers. Brain Imaging Behav. **15**(4), 1728–1738 (2021). https://doi.org/10.1007/s11682-020-00366-8

13. Lin, W., et al.: Predicting Alzheimer's disease conversion from mild cognitive impairment using an extreme learning machine-based grading method with multimodal data. Front. Aging Neurosci. **12**, 77 (2020). https://www.frontiersin.org/article/10.3389/fnagi.2020.00077

Gene Expression Tools from a Technical Perspective: Current Approaches and Alternative Solutions for the KnowSeq Suite

Daniel Castillo-Secilla[1]($\boxtimes$), Daniel Redondo-Sánchez[2], Luis Javier Herrera[3],
Ignacio Rojas[3], and Alberto Guillén[3]

[1] CoE Data Intelligence, Fujitsu Technology Solutions S.A., Camino del Cerro de los
Gamos, 1, Pozuelo de Alarcón, 28224 Madrid, Spain
cased@ugr.es

[2] Instituto de Investigación Biosanitaria ibs.GRANADA, CIBER de Epidemiología
y Salud Pública (CIBERESP), Escuela Andaluza de Salud Pública, Avda. de Madrid,
15. Pabellón de Consultas Externas 2, 2ª Planta, 18012 Granada, Spain

[3] Department of Computer Architecture and Technology, University of Granada.
C.I.T.I.C., Periodista Rafael Gómez Montero, 2, 18014 Granada, Spain

Abstract. The precision and personalized medicine is declared as the next revolutionary paradigm in the current health outlook. With this assumption, many challenges must be faced to achieve that paradigm shift. One of these important challenges is the creation and development of tools with the capability of exploiting biological data to infer or extract new and relevant knowledge. In this sense, these tools must fulfill a set of requirements such as scalability, security and a user-friendly design. That is the way to change the users scope from technicians to all type of researchers, physicians and other non-technical users. Along this article, a review of several gene expression analysis tools has been addressed, with the aim of studying their pros and cons. Then, two different implementations are proposed taking into account the current state of KnowSeq R/Bioc package, with the purpose of showing different use cases to migrate one concrete tool to a web application.

Keywords: RNA-Seq · Gene Expression Tools · Web platform

1 Introduction

Since the last decade, omics-data have suffered an exponential growth due to the technological advances and the decrease of the data extraction costs as well. Thanks to this fact, the number of researchers and physicians who have access to that type of data has grown too, provoking a paradigm shift from the current stratified medicine to the precision and personalized medicine. One of the main purposes of this new paradigm relies on the creation and design of Clinical-Decision Support Systems (CDSS) and tools as a service, which could help to treat each patient in a

personalized way, taking into account biological information from different omics, e.g. genomics, transcriptomics, proteomics or radiomics [3,12].

In this sense, and in order to successfully achieve this paradigm transition, it is important to develop tools which may serve the research community in the discovery of novel and relevant biological knowledge and interrelations. Moreover, it is also crucial to offer user-friendly tools, specially when there in an important number of heterogeneous steps involved in biological analyses needed. With the previous ideas in mind, KnowSeq was developed to solve complex gene expression analyses by covering all the essential steps. KnowSeq was one of the first tools that integrate under the same programming language (R), the required functionalities to carry out gene expression analysis from RAW data up to machine learning assessment and functional enrichment. In addition, KnowSeq counts with an intelligent HTML report for those scientists and researchers far from a technical background [4].

The current state of KnowSeq package includes a Docker container which deploys in a web browser an R studio server to work with our tool (https://hub.docker.com/r/casedugr/knowseq). However, from a wider perspective, KnowSeq could be more useful for the community if the current technical constraints are completely removed by implementing a web service, in an open manner and deployed using a web framework. This paper performs a comparative of the different software tools providing omics-data processing features and focuses on those which provide the service on-line. Afterwards, it proposes an architecture for adapting the KnowSeq software to be deployed in this web environment, facilitating the use from the scientific community.

Along this manuscript, many tools have been studied in-depth, keeping only those that cover a wide range of RNA-seq analysis steps. Nevertheless, it is important to mention other tools which are focused on specific steps and that operate in a powerful and useful manner, and that might be integrated in new pipelines:

– HTSeq by Anders, S et al. [2].
– Sparta by Johnson, B. K. et al. [15].
– MeV by Howe, E. A. et al. [13].
– BioWDL by Vorderman, R. [24].
– MyRNA by Lagmead, B.et al. [19].
– RSeqFlow by Wang, Y. et al. [29].
– RNA123 by Law, C. W. [20].

2   RNA-Seq Workflow Tools for Different Languages and Platforms

2.1   Non Web Platform Based Pipelines

GEO2RNAseq is an RNA-seq pipeline codified in R language mainly focused on RAW data pre-processing [26]. This pipeline allows the NCBI/GEO RNA-seq series automatic download. Then, it uses the FASTQ files to align them by

using TopHat2 or Hisat2 aligners [16,17]. Once the aligned files are obtained, GEO2RNAseq implements a feature count and a Differential Expressed Genes (DEGs) extraction step, choosing among 8 differential expression analysis tools. Moreover, the package counts with visualization module to plot the results.

Although GEO2RNAseq does not count with further steps beyond DEGs selection, it allows integrating its functionality with other pipelines thanks to its modular design.

GEO2RNAseq R package is available at Anaconda repository [1], but only for UNIX systems and Mac OS.

SARTools is a RNA-seq pipeline codified in R which has the aim of providing an automatized way of extracting DEGs [27]. For that, SARTools allows for choosing between two well-known DEGs extraction methods, by offering the users different templates depending on the selected tool. In addition, SARTools relies on HTML reports to check and validate in a more user-friendly manner the quality of the DEGs extraction process.

SARTools R package is available at the Bioconductor repository and at Anaconda [11]. In addition, it is offered under Windows, Mac OS and UNIX systems.

RobiNA is a gene expression tool codified in Java which allows the users to perform Microarray and RNA-seq DEGs extraction under a Graphic User Interface (GUI) [21]. In the background, this tool makes use of R and Bioconductor packages to get away the users from any technical difficulties. It is available under Windows, Mac OS and UNIX systems, and comprehends the steps of Quality analysis, DEGs extraction and visualization.

At this moment, RobiNA seems to be under no support from the original developers as there are no updates since 2012 or 2013. However, the installation file can be found at http://mapman.gabipd.org/web/guest/robin.

RNAseqR is a RNA-seq pipeline in R with a total of 6 steps which include quality assessment, read alignment and transcript quantification, differential expression analysis, and functional analysis [6]. This tool proposes a pipeline with only 6 functions, one per step, in order to try to minimizes the user interaction. The package counts with an important number of plot types to assess the study quality. The pipeline can be launched from different points and not only from the fastq files.

RNAseqR R package is available at Bioconductor repository, but only for UNIX systems and Mac OS.

DEWE counts with a containerized Java GUI, containing also the most important tools and R packages to perform RNA-seq analysis [22]. Concretely, this pipeline comprehends all the steps between the RAW data pre-processing and DEGs extraction, plus a posterior pathway analysis step. This tool is very attractive for users as it is easy to install thanks to its containerization.

DEWE installers are freely available at the website of their own creators: https://www.sing-group.org/dewe. Moreover, DEWE is available for Windows, Mac OS and UNIX systems.

RNA-Seq Pipe is a very complete RNA-seq pipeline codified in Python which implements the following steps: raw pre-processing, visualization, DEGs extraction, GOs enrichment, KEGG pathways and related diseases [30]. Although RNA-Seq Pipe is more like a general tutorial instead of a tool, we consider that it covers all the necessary steps to be considered as a pipeline.

RNA-Seq Pipe is publicly available at https://github.com/MaayanLab/Zika-RNAseq-Pipeline. Furthermore, this pipeline was encapsulated into a container with the aim of providing a way of launching it no matter the OS. The container can be found at https://hub.docker.com/r/maayanlab/zika/.

TCGAbiolinks allows the users to automatically retrieve TCGA data or to load their own data as well. Furthermore, this pipeline implements methods for pre-processing, analysing and visualizing not only RNA-seq data but also other omics data such as CNV, miRNA methylation, i.e. [7]. Although TCGAbiolinks is a R package, there is also a GUI version named TCGAbiolinksGUI. The GUI version is available as Docker image https://hub.docker.com/r/tiagochst/tcgabiolinksgui/.

TCGAbiolinks is available at Bioconductor. Both TCGAbiolinks and TCGAbiolinksGUI are available under Windows, Mac OS and UNIX systems.

HppRNA is written in a variety of programming languages such as Perl, R and Python, and it cover the steps from RAW pre-processing up to DEGs extraction and visualization [28]. Moreover, this pipeline proposes processes to analyze mRNAs, lncRNAs and circRNAs, dealing with the detection of sequence variations such as fusion genes and SNPs from RNA-seq data. To connect all the functionalities, HppRNA uses Snakemake framework [18] which is a workflow engine.

HppRNA is publicly available following the next link: https://sourceforge.net/projects/hpprna/. Some of the alignment tools are not available to be run in Windows, but all of them can run in Mac OS and UNIX systems.

VIPER is based on Snakemake framework, and implements a complete RNA-seq pipeline with alignment, quality control, differential gene expression and pathway analyses steps [8]. Thanks to the workflow engine, VIPER uses tools from different languages and technology.

Viper can be found at https://bitbucket.org/cfce/viper/src/master/ and it is available for Mac OS and UNIX systems.

2.2   Web Platform Based Pipelines

DEAR-O. The DEAR-O platform [31] *was* a web platform for performance evaluation of differential expression analysis based on high-throughput RNA sequencing data.

No technical aspects about implementation are provided in the paper. The authors indicate one URL for the software and another one for a discussion group. However, up to the date, it is not possible to reach any of the links.

Although this fact could lead to a null analysis, it is possible to think about the causes of this unavailability: technical debt and cybersecurity incident could be the easiest answers. Therefore, valuable information can be extracted from this fact in order to propose a new software architecture.

Degust D. Powell developed Degust (https://degust.erc.monash.edu/) [23] which allows researchers to upload RNA-seq files to explore, analyse and visualise them.

The implementation is available at Github so the results should be easily replicated. The welcome page is clear with for main sections or attention elements: citation, video showing functionality, demo to try the software and the possibility to upload a dataset and start working.

It also has the possibility to sign in using several platforms.

From the technical point of view, by looking at the source code, it is clear that the design pattern chosen is model, view, controller.

Other element is that the institution provides support by signing the certificate providing a secure connection using TLS 1.2 with 128 bits keys.

Analysing the headers from the petition it is possible to see that the server is based on Linux (Ubuntu) and that it runs the Apache software.

The demo page performs one request to the backend and the rest of interactions are made in the client by means of javascript.

The source files use the coffee syntax for javascript generation as well as the vue.js library. Everything packed with webpack.

ARMT. This tool is a recent RNA-seq analysis pipeline codified in R language which implements the needed steps to process RNA-seq data from count files up to differential expression analysis and functional enrichment [14]. In addition, ARMT add some extra steps which are very interesting: survival analysis, differential analysis for mutation and GSVA score and mutant mapping. This package also has a GUI designed in Shiny with the aim of helping the user to use it in an easy and comfortable manner.

ARMT is available at https://github.com/Dulab2020/ARMT and for all the OS which support R (Windows, Mac OS and UNIX systems).

RAP. As stated by D'Antonio in [9] *"...RAP (RNA-Seq Analysis Pipeline) is a web application implementing a fully automated analysis workflow, designed*

to integrate in-house developed scripts as well as open source analysis tools into one pipeline...".

The software is available at: https://bioinformatics.cineca.it/rap/. However, by the time of writing this paper the following statement is on the top header:

"Analysis service closed. We would like to inform all users that due to the obsolescence of the analysis workflow, this service is now officially discontinued and no longer available for new analyses. Previous analyses will be kept available in read-only mode for already registered users, but new registrations will not be accepted. We apologise for any inconvenience this may cause." Therefore, far from the hypothesis thrown in the DEAR-O case, here, we have the certain of the cause for the service to be stopped: technical debt.

The source code is not available, but from a superficial analysis it is possible to deduce that there is a backend running in PHP and the front-end is based on HTML and Javascript using the charts provided by the tool https://nvd3.org/, probably, in combination with the Foundation5 front-end framework which has been usually used in combination with the WordPress content management system.

As with the previous tool, the service is running in a Linux (Ubuntu) machine with the Apache server.

The communication is authenticated using a Let's encrypt certificate using TLS 1.3.

3 Proposed Architecture Web KnowSeq

From previous developments it is possible to devise several paths to design a possible architecture. Besides the fate of previous developments, there are several technologies that could drive the deployment toward several directions. In the following sections we will describe two possibilities.

3.1 Using the Shiny Package

This first approach is thought from considering the lessons learnt from having a complex software that could incur into a high technical debt during development and reach a point where it is not feasible to be maintained. Starting from an R development, to keep all the code with the same technology, there is the chance to use the Shiny package https://shiny.rstudio.com/. This tool allows developers to provide a web deployment with a few lines of code, in a simple way [5].

The development must include a server file and a user interface both written in R as well as a CSS file. Then the main application file contains the ShinyApp, which, in this case, is the previously developed KnowSeq.

Once the interface is loaded, it is possible to have the following actions from the menu:

– Data loading: presents two input fields to upload csv files, one for the labels (i.e.x. "solid tissue" vs "tumor") and another for the DEGs matrix. In addition, it is possible to choose the training and test partition percentages for the posterior Machine Learning process.

– Genes selection: Selects the number of genes to be used afterwards.
– Model training: Allows to choose between several algorithms for feature selection as well as among several classification paradigms. Beside, it allows to select the number of folds performed during cross-validation.
– Model validation: The previously trained model is validated against test data set.
– Gene ontologies: the GO terms for the final selected DEGs are retrieved.
– KEGG pathways: the KEGG pathways terms for the final selected DEGs are acquired.
– Related diseases: the related diseases for each of the final selected DEGs are obtained.

A prototype implementation is available at https://github.com/CasedUgr/KnowSeq-ShiVer and the deployed version can be accessed following the next link: https://knowseqshiver.shinyapps.io/KnowSeq-ShiVer/. The app could be accessed as soon as possible through the following link: https://bioapp.ugr.es/knowseq-shiver.

App Deployment Discussion. When deploying the app programmed using the shiny tool, there are three possibilities regarding its deployment:

– On premises with Shiny Server
– On premises with Rstudio Connect
– Through Shinyapps.io

There is a table comparing each of the previous approaches although it might be biased by the fact that RStudio is the commercial alternative to the open source solution Shiny Server.

There would be other possibilities which would require third party elements like cloud providers: set up a container or a virtual machine. Moreover, this discussion is presented in https://aws.amazon.com/es/blogs/architecture/scaling-rstudio-shiny-using-serverless-architecture-and-aws-fargate/ which allows applications to easy escalate and to keep a small budget when no use is done. This fact could be very interesting for a service with low demand or few users.

3.2   Using a Framework Stack

Although this approach is very simple and effective, it lacks from useful aspects that could be tackled using an alternative approach.

By using frameworks, the software bill of materials increases significantly but so it does the features available. Another advantage is that the maintenance cost is distributed through the community.

One of the main benefits is the integration for user authentication so an user or a group of them can access to their uploaded datasets and models trained.

Thinking on getting reproducibility and more control over the models, which also has the benefit of saving re-training constantly and could help saving cloud

costs, it is worth mention SnapperML https://github.com/SnapperML [10]. By using this tools we have at once the integration of ml-flow[1], Optuna[2] and Ray [3].

In the case of using a cloud deployment, instead of configuring these stacks (which is possible) we could think of using some of the tools the cloud providers already offer. The main drawback of using these tools is that it makes really hard, if not impossible, to change the provider afterwards.

On the Use of Microservices and App Deployment. The R web framework ecosystem is increasing in number of alternatives, but these are mostly focused in minimal functionality (see plumber [25], beakr [4], fiery [5], ambiorix [6] and the already commented Shiny). While this approach makes sense for certain contexts, it might not support enough features. To solve this issue and to adequate the integration between other web-frameworks and languages like Python, Node.js, PHP, the most advisable approach would be the microservices solution. Figure 1 shows a diagram of the architecture.

In this scenario, we would have different services running in containers and communicating each other using efficient messaging software like Redis [7] or RabbitMQ [8].

A possible list of services could be:

– Data storage: data base for the gene data and users information. The choice of NoSQL vs classic SQL approaches should be done in terms of efficiency and RAM requirements. However, if no clear solution is available, it would be possible to define a schema for user data and other app requirements in NoSQL and user the classical approach for the Gene dataset. Other alternatives could go through configuring an storage service like an S3 AWS bucket or Azure Blobs to read and upload the Gene datasets.
– Backend service: running the framework for the user administration, API implementation and other features. The choices available are quite numerous but the most popular technologies nowadays are between python (with Django, Fast API, Flask as possible frameworks) and node.js (with express.js or meteor.js as the most popular frameworks). Any of these tools could provide a Restful API to communicate the web front-end with the other services.
– App service: which would run the R application encapsulated and digesting data through the Data storage service and the messaging services that could run in the same service than the backend.

---

[1] https://mlflow.org/.
[2] https://optuna.org/.
[3] https://www.ray.io/.
[4] https://mazamascience.github.io/beakr/.
[5] https://rdocumentation.org/packages/fiery/versions/0.2.3.
[6] https://cran.r-project.org/web/packages/ambiorix/readme/README.html.
[7] https://redis.io/.
[8] https://www.rabbitmq.com/.
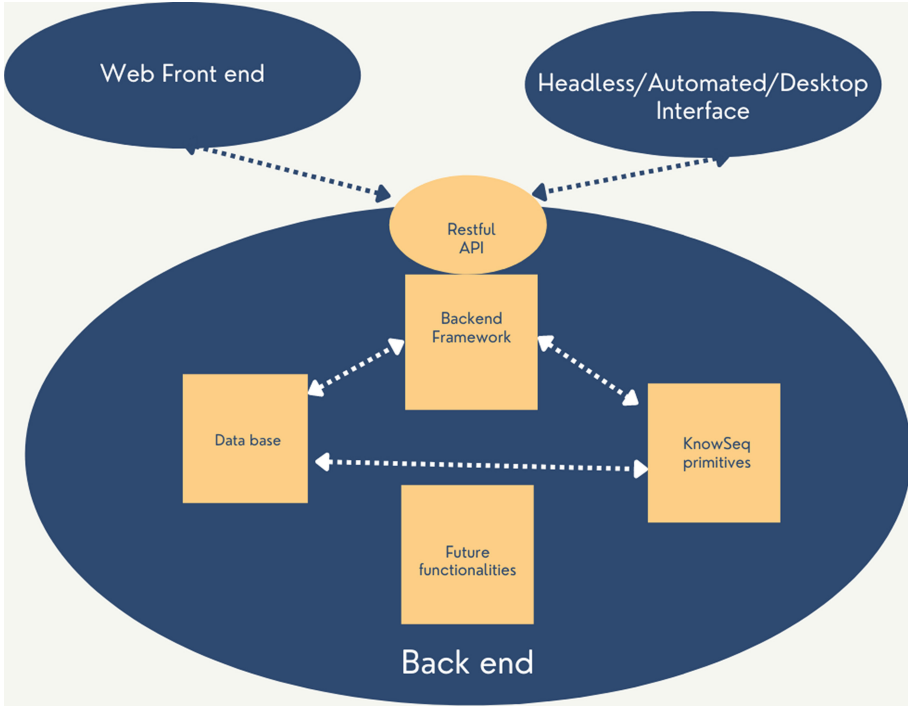
Fig. 1. Diagram for the framework stack implementation. Communication between users is made through the web front end or using a specific application that invoques the Restful API. Microservices communicate between each other using queue systems/ through libraries or even using the Restful API.

4   Conclusions

In this paper we have reviewed the current solutions to carry out DEGs analysis, comparing those which provide an online service. From this review, and considering the elements that have led to service discontinuation from some providers, two approaches for the deployment of the KnowSeq ecosystem have been presented. The first one relies on a keep-it-simple solution to provide basic functionality avoiding maintenance overhead. The other one proposes a solution stack where microservices allow to have a compromise between functionality and complexity. Both approaches are compatible and, as long as possible, both are recommended. The simple one allows for quick disemination and feature testing meanwhile the second is more recommended for providing a commercial service due to deploy scalability and security.

References

1. Anaconda: The world's most popular data science platform. https://www.anaconda.com/

2. Anders, S., Pyl, P.T., Huber, W.: HTSeq-a python framework to work with high-throughput sequencing data. Bioinformatics **31**(2), 166–169 (2015)

3. Beauchemin, M., Murray, M.T., Sung, L., Hershman, D.L., Weng, C., Schnall, R.: Clinical decision support for therapeutic decision-making in cancer: a systematic review. Int. J. Med. Inform. **130**, 103940 (2019)

4. Castillo-Secilla, D., et al.: KnowSeq R-Bioc package: the automatic smart gene expression tool for retrieving relevant biological knowledge. Comput. Biol. Med. **133**, 104387 (2021)

5. Chang, W., et al.: Shiny: Web Application Framework for R (2021). https://CRAN.R-project.org/package=shiny, R package version 1.7.1

6. Chao, K.H., et al.: RNASeqR: an R package for automated two-group RNA-Seq analysis workflow. IEEE/ACM Trans. Comput. Biol. Bioinform. **18**, 2023–2031 (2019)

7. Colaprico, A., et al.: TCGAbiolinks: an R/Bioconductor package for integrative analysis of TCGA data. Nucl. Acids Res. **44**(8), e71–e71 (2016)

8. Cornwell, M., et al.: VIPER: visualization pipeline for RNA-Seq, a snakemake workflow for efficient and complete RNA-Seq analysis. BMC Bioinform. **19**(1), 1–14 (2018)

9. D'Antonio, M., et al.: RAP: RNA-Seq analysis pipeline, a new cloud-based NGS web application. BMC Genom. **16**(6), 1–11 (2015)

10. Domenech, A.M., Guillén, A.: ml-experiment: a python framework for reproducible data science. J. Phys. Conf. Ser. **1603**(1), 012025 (2020). https://doi.org/10.1088/1742-6596/1603/1/012025

11. Gentleman, R.C., et al.: Bioconductor: open software development for computational biology and bioinformatics. Genome Biol. **5**(10), 1–16 (2004)

12. Gómez-López, G., Dopazo, J., Cigudosa, J.C., Valencia, A., Al-Shahrour, F.: Precision medicine needs pioneering clinical bioinformaticians. Brief. Bioinform. **20**(3), 752–766 (2019)

13. Howe, E.A., Sinha, R., Schlauch, D., Quackenbush, J.: RNA-Seq analysis in MeV. Bioinformatics **27**(22), 3209–3210 (2011)

14. Huang, G., et al.: ARMT: an automatic RNA-Seq data mining tool based on comprehensive and integrative analysis in cancer research. Comput. Struct. Biotechnol. J. **19**, 4426–4434 (2021)

15. Johnson, B.K., Scholz, M.B., Teal, T.K., Abramovitch, R.B.: Sparta: simple program for automated reference-based bacterial RNA-Seq transcriptome analysis. BMC Bioinform. **17**(1), 1–4 (2016)

16. Kim, D., Langmead, B., Salzberg, S.L.: HiSAT: a fast spliced aligner with low memory requirements. Nat. Methods **12**(4), 357–360 (2015)

17. Kim, D., Pertea, G., Trapnell, C., Pimentel, H., Kelley, R., Salzberg, S.L.: TopHat2: accurate alignment of transcriptomes in the presence of insertions, deletions and gene fusions. Genome Biol. **14**(4), 1–13 (2013)
18. Köster, J., Rahmann, S.: Snakemake-a scalable bioinformatics workflow engine. Bioinformatics **28**(19), 2520–2522 (2012)
19. Langmead, B., Hansen, K.D., Leek, J.T.: Cloud-scale RNA-sequencing differential expression analysis with Myrna. Genome Biol. **11**(8), 1–11 (2010)
20. Law, C.W., et al.: RNA-Seq analysis is easy as 1-2-3 with limma, Glimma and edgeR. F1000Research, vol. 5 (2016)
21. Lohse, M., et al.: Robina: a user-friendly, integrated software solution for RNA-Seq-based transcriptomics. Nucl. Acids Res. **40**(W1), W622–W627 (2012)
22. López-Fernández, H., Blanco-Míguez, A., Fdez-Riverola, F., Sánchez, B., Lourenço, A.: DEWE: a novel tool for executing differential expression RNA-Seq workflows in biomedical research. Comput. Biol. Med. **107**, 197–205 (2019)
23. Powell., D.R.: Degust: interactive RNA-Seq analysis. https://doi.org/10.5281/zenodo.3258932
24. SASC Team, L.U.M.C.: BioWDL: a collection of WDL pipelines for sequencing analyses. https://biowdl.github.io/
25. Schloerke, B., Allen, J.: Plumber: an API Generator for R (2022). https://www.rplumber.io, https://github.com/rstudio/plumber
26. Seelbinder, B., et al.: Geo2RNASeq: an easy-to-use r pipeline for complete preprocessing of RNA-Seq data. BioRxiv, p. 771063 (2019)
27. Varet, H., Brillet-Guéguen, L., Coppée, J.Y., Dillies, M.A.: SARTools: a DESeq2- and edgeR-based R pipeline for comprehensive differential analysis of RNA-Seq data. PloS ONE **11**(6), e0157022 (2016)
28. Wang, D.: hppRNA-a snakemake-based handy parameter-free pipeline for RNA-Seq analysis of numerous samples. Brief. Bioinform. **19**(4), 622–626 (2018)
29. Wang, Y., et al.: Rseqflow: workflows for RNA-Seq data analysis. Bioinformatics **27**(18), 2598–2600 (2011)
30. Wang, Z., Ma'ayan, A.: An open RNA-Seq data analysis pipeline tutorial with an example of reprocessing data from a recent zika virus study. F1000Research **5**, 1574 (2016)
31. Zhang, Z.H., Wray, N.R., Zhao, Q.Y.: Dear-O: differential expression analysis based on RNA-Seq data-online. BioRxiv, p. 069807 (2016)

COVID-19. Bioinformatics and Biomedicine

Optimal Chair Location Through a Maximum Diversity Problem Genetic Algorithm Optimization

Rubén Ferrero-Guillén(✉) , Javier Díez-González(✉) , Paula Verde(✉) ,
Alberto Martínez-Gutiérrez(✉) , José-Manuel Alija-Pérez(✉) ,
and Rubén Álvarez(✉)

Department of Mechanical, Computer, and Aerospace Engineering, Universidad de León, 24071 León, Spain
rferrg00@estudiantes.unileon.es, {jdieg,pverg,amartg,jmalip, ralvf}@unileon.es

Abstract. The coronavirus disease (COVID-19) pandemic has challenged multiple aspects of our lives. Social distancing among other preventive measures for reducing the contagion probability have supposed a significant challenge for many establishments. Restaurants, schools, conferences are establishments founded by the congregation of participants, distributed in tables or chairs over a certain scenario. These enterprises now face an optimization problem in their daily routine, where they seek to maximize the interpersonal distance while also allocating the maximum number of assistants. The optimization of these distribution paradigms, such as the CLP (Chair Location Problem), has been defined as NP-Hard, therefore, the use of metaheuristic techniques, such as Genetic Algorithms is recommended for obtaining an optimal solution within a polynomial time. In this paper, a GA is proposed for solving the CLP, attaining an optimal solution that maximizes the interpersonal distance among assistants while also guaranteeing a minimum distance separation for reducing the contagion probability. Results of the proposed methodology and multiple fitness evaluation strategies prove its viability for attaining a valid distribution for these establishments, thus satisfying the main objectives of this research.

Keywords: CLP · COVID-19 · Genetic algorithm · Maximum diversity problem

1 Introduction

COVID-19 pandemic is supposing a major challenge for society. The appearance of an airborne-transmitted virus with great infection capacity and the possibility of causing potential severe effects in infected patients has forced the different governments around the world to act looking for a reduction of the propagation of the disease among their citizens.

Initially, the lack of knowledge about the transmission of the virus and the unpredictable effects of letting the virus propagate without limitations, promoted the declaration of strict lockdowns forcing people to stay at home in order to reduce the contagion

probability of the disease. These methods were effective to contain the virus after several weeks of promoting telework and the closure of non-essential facilities.

Meanwhile, studies of the disease were conducted by the scientific community around the world for better understanding this novel virus. These studies proved the infection capacity of the virus [1], the primary airborne transmission [2], the differences between outdoor and indoor environments for the contagion probability [3] or the weather conditions that promote the propagation [4].

This knowledge acquired through experimentation allowed the definition of a series of rules for progressively reducing the strict measures for controlling the disease such as interpersonal distance [5], wearing facemasks [6], ventilation [7], the use of hydroalcoholic gels [8], the isolation of closed contacts [9] or the reduction of the capacity in public places [10]. All these rules started a new period looking for living with the virus reducing the economic impact of strict measures.

This period has been extended until now, where limitations are starting to be reduced due to the rollout of vaccines for reducing the severe effects of the disease. However, although the vaccines are proving their effectiveness, still, the appearance of novel virus variants with more propagation capabilities are supposing a concern [11].

In this sense, maintaining some of the restrictions, especially those that apply to conditions where the risk of contagion is greatest, is critical to reducing the impact of the COVID-19 pandemic. Among these high-risk conditions, keeping the interpersonal distance in indoor environments represent one of the most affordable measures in determined activities. This fact has proven an effective effect in reducing the contagion probability while wearing facemasks in indoor spaces [12].

However, maintaining the social distancing has been demonstrated to be especially harsh in dynamic dense environments where people is moving around [13]. This is not the case for environments in which people remain seated or localized in a particular location such as schools, cinemas, weddings or conferences.

In these cases, the use of space to place separate tables or chairs, contributes to increase the capacity or reduce the contagion probability in those conditions. For addressing the table arrangement, some methods following regular patterns (e.g. rectangular o triangular) have been proposed in the literature [14]. These methods attain competitive results in geometric rooms without obstacles. However, rough spaces with obstacles and furniture represent a considerable challenge for achieving optimal table distributions.

In these cases, we previously proposed a methodology for optimally locating student tables in a primary school through the employment of Genetic Algorithms (GA) [15]. This entailed the definition of the Table Location Problem (TLP) which consists of finding the optimal subset of Cartesian coordinates for each of the tables displayed among every potential table location in the room in such a way that allows the maximal distance among the tables.

We later improved this technique for hostelry applications through the finding of the optimal deployment of the tables addressing particular hostelry conditions such as keeping enough space for the waiters to complete an affordable service to the client or enabling the location of all the potential clients around the tables [16, 17].

In this paper, we continue this research line by locating seats in conference rooms enough spaced to reduce the contagion probability during the pandemic. This requires

the definition of a novel problem, the Chair Location Problem (CLP), which is a novel definition of the well-known Maximum Diversity Problem (MDP) [18] particularized for this problem context. The MDP looks for finding the optimal subset of elements which maximizes the differences among their individuals. This means in this context that, the maximum distance among the seats in the conference room can be achieved through the application of this problem.

The NP-Hard definition of this problem [19] suggests the implementation in this paper of a GA to address it and attain competitive results in acceptable time. For these reasons, we present in this paper, the binary codification of the individuals, the mating, selection, mutation and elitism techniques to perform the evolutionary process to find an optimal chair allocation to reduce the contagion probability in conference rooms.

The remainder of the paper is organized as follows: we define and particularized the MDP to the chair allocation optimization presented defining the novel CLP in Sect. 2; the GA implementation to address the CLP is presented in Sect. 3; the characterization of a conference room scenario, the hyperparameters of the optimization and the results obtained are introduced in Sect. 4 while Sect. 5 concludes and presents the benefits of the proposal of this paper.

2 Problem Definition

The CLP seeks to find the optimal coordinates of each chair position for maximizing the interpersonal distance for a given scenario, thus reducing the contagion probability of the COVID-19 pandemic. Consequently, the decision variables of the proposed optimization are the Cartesian coordinates of each chair ($\langle t_i \rangle = \langle x_i, y_i \rangle$).

Furthermore, the optimal distribution of chairs (i.e., the chair distribution that achieves the interpersonal distance among other criteria) is constituted of the optimal Cartesian coordinates of each chair, being represented as the subset (T_i). This subset is contained within the set of possible solutions (T), where each solution represents a certain chair distribution. The number of possible solutions within the set (T) can be derived from the following expression:

$$P = \prod_{i=0}^{n_c-1} (n_{CLE} - i) \tag{1}$$

where P is the number of potential distributions of n_c chairs and n_{CLE} is the number of points that are possible locations for each chair over the given scenario.

The presented optimization can be described through the following mathematical model:

$$Maximize\ Z = ff\,(ff_k(T_i), ff_{obs}(T_i)) \tag{2}$$

Subject to:

$$x_{lim_1} \leq x_i \leq x_{lim_2}\ \forall x_i \in t_i;\ t_i \in T_i;\ t_i \notin U \tag{3}$$

$$y_{lim_1} \leq y_i \leq y_{lim_2}\ \forall y_i \in t_i;\ t_i \in T_i;\ t_i \notin U \tag{4}$$

$$d_{min} \geq d_{sd} \; \forall i, j \in 1, \ldots, n_c; \; i \neq j \qquad (5)$$

where ff_k and ff_{obs} are the main fitness estimators of the proposed methodology, evaluating the distancing among chairs and the presence of obstacles respectively; x_{lim1}, x_{lim2} and y_{lim1}, y_{lim2} are the lower and upper bounds for the location of chairs within the proposed scenario; U represents the subset that contains each forbidden region for the location of any chair due to the presence of obstacles or irregularities; d_{min} is the minimum interpersonal distance of the resulting distribution, which must superior to the standard distance d_{sd}, fixed as 1.5 m, following the Spanish legislation.

However, the interpersonal distance evaluation that constitutes the fitness function ff_k may undergo different optimization strategies. MDP such as the CLP commonly employ two different optimization strategies. The first strategy entails the maximization of the minimum distance (i.e., min-max), while the second strategy relies on the maximization of the sum of all values (i.e., max-sum). The implementation of both strategies is discussed and described in the following Section.

3   GA Implementation

Genetic Algorithms (GA) are a field of evolutionary algorithms that apply the Darwinian theory for attaining the optimal solution. These optimization algorithms define a set of individuals, encoded with the main decision variables, as well as an environment, also dependent of those variables. Through multiple genetic operators, such as elitism, mutation and selection, the most fitted individuals to the proposed environment prevail, passing their genetic information (i.e., the adopted solution) to the following generations. Over the course of multiple iterations of fitness evaluation and individual crossover, the algorithm may converge to the optimal solution, an individual who carries the values of the decision variables that optimize the fitness function and fulfills all given constraints.

GA are widely used throughout the literature, especially for multimodal problems (i.e., problems with several valid solutions) with a search space of considerable magnitude or even unlimited [20]. GA are also commonly implemented for optimizations problems of elevated complexity, such is the case of the (Maximum Diversity Problem) MDP, or problems where the cost function in non-derivable [21]. These algorithms have been implemented into multiple fields, mainly for static optimizations, including wing design [22], charging times of electric vehicle routing [23], and node location optimizations [24, 25].

The CLP (Chair Location Problem) is characterized by the number of possible solutions derived from its combinatorial nature. The resulting complexity along the dependency among chair locations compromises the implementation of exact methodologies. Therefore, an evolutionary optimization approach proves favorable for obtaining a valid solution in a polynomial time.

The GA implementation for the CLP starts by defining the codification of the individuals, the environment, and the interaction among them. Each individual must carry all the required information for defining a certain solution, in our case a given chair distribution. Following the MDP definition of the optimal solution (i.e., the subset of elements

inside a greater set that maximize the diversity among elements), each individual could carry the subset of the selected chair locations that results in a valid solution.

As shown in Fig. 1, the genetic information of each individual contains the complete set of possible chair locations. Each location is represented as a binary variable, where a value of 0 represents a non-selected position while a value of 1 is a selected chair location. We can also define a correlation between each binary variable and its corresponding cartesian coordinates, which result vital for the individual evaluation. Furthermore, in order to preserve the viability of this codification we must ensure that the number of ones contained in each individual genetic information is preserved throughout the multiple genetic operators. This supposes a significant transition from previous works.
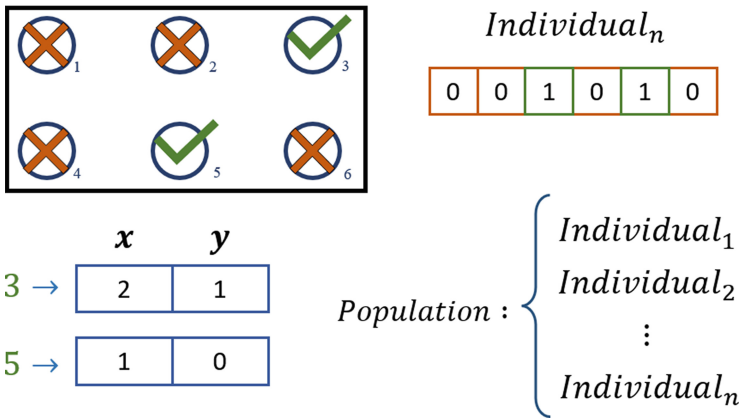
Fig. 1. Codification of the population and its interaction with the selected scenario.

Once defined the genetic information of each individual, the GA implementation requires the definition of a fitness function for evaluating the suitability of each chair distribution. This function is the main guidance of the optimization, therefore, the definition of this function and its dependency of the individuals encoded variables results critical for the optimization.

MDP optimization methodologies are commonly based on two different cost functions. The first optimization function, usually referred as max-sum, seeks to find the optimal solution to the MDP by maximizing the sum or mean of the distances among elements. On the other hand, a second approach, referred as min-max, pursue the optimal solution by imposing that the minimum distance of each distribution is to be maximized.

Both methodologies result valid for the proposed problem, where a set of chairs are to be located inside certain limits in a way that maximizes both the interpersonal distance and the minimum distance separation of each chair.

Consequently, the fitness function of our proposed GA optimization can be described as:

$$ff_{\min|\max} = \lambda + ff_{obs} + \min\left(\sqrt{(x_i - x_j)^2 + (y_i - y_j)^2}\right)^a \tag{6}$$

$$ff_{\max|\text{sum}} = \lambda + ff_{obs} + \frac{1}{l}\left[\sum_{i=1}^{n}\left(\sum_{j=1}^{n}\sqrt{(x_i - x_j)^2 + (y_i - y_j)^2}\right)\right]^b \tag{7}$$

$$ff_{obs} = -J\kappa \tag{8}$$

$$\forall\, i,j : \sqrt{(x_i - x_j)^2 + (y_i - y_j)^2} \leq \rho; i \neq j, \tag{9}$$

where J is the number of chairs located inside obstacles; x_i, y_i are the cartesian coordinates of the chair i; n is the number of chairs; l represents the number of computed distances (i.e., $n^2 - n$); ρ is the maximum distance calculation delimiter and λ, κ, a, b are weight hyperparameters for the fitness function evaluation.

Once defined the individual codification and the fitness function evaluation, the GA optimization takes place. This optimization, described in Fig. 2, starts by randomly generating the population while also guaranteeing that the number of disposed chairs is valid.

Algorithm 1: GA for the CLP (π, π_{limits}, $\pi_{obstacles}$, n, N, *Convergence Criteria*, Z, *Elitism Percentage*, *Mutation Percentages*)

1   *Population* ← Random Distribution of *N* Individuals with a subset of *n* chair locations over the scenario π, respecting π_{limits} and $\pi_{obstacles}$;
2   **while** *Convergence criteria is not fulfilled* **do**
3   **for** *Individual in Population* **do**
4   *Distance Matrix* ← Calculate all distances between the selected chair positions (*Individual*, π);
5   ff_{obs} ← Determine how many chairs are located inside the scnenario obstacles (*Individual*, $\pi_{obstacles}$);
6   ff ← Evaluation of the suitability of the chair distribution, through the selected fitness function strategy (*Distance Matrix*, ff_{obs}, Z);
7   **end**
8   *Elitist Inidividuals, Population* ← Elitism operator (*Population*, *Elitism Percentage*);
9   *Population* ← Selection operator (*Population*);
10   *Population* ← Crossover operator (*Population*);
11   *Population* ← Mutation operator (*Population*, *Mutation Percentages*);
12   *Population* ← Join Population and preserved elitist individuals (*Population*, *ElititstIndividuals*);
13 **end**

Fig. 2. Pseudocode for the GA optimization of the CLP.

The algorithm then evaluates the initial population, assigning a fitness value to all individuals according to the fitness function expression previously discussed. This fitness value is later on utilized for the elitism and selection operators. Through elitism, a certain percentage of the individuals of the optimization is preserved for the following generations, replacing those worst fitted.

Once the elitism operator takes place, all individuals are arranged by the selection operator. The resulting order of this arrangement is crucial for the following step of the algorithm, the crossover, which produces the offspring and thus the individuals of the next generation. This arrangement is based on the fitness value, and selection methodologies (e.g., roulette, tournament) usually favor the most suited individuals, nevertheless, these arrangements always carry some stochastic component.

GA optimizations are based on two principle evolutionary principles. Selection pressure results vital for enforcing an adaptation to a given scenario, a higher percentage of elitism and selection methodologies which further reward the fitness of each individual result in an increase of the selection pressure, which favors a faster convergence to a solution. However, an excessively accelerated convergence may induce the optimization into a local maximum. In order to compensate this selection pressure, GA introduce entropy into the optimization for enhancing the exploration of the space of solutions, avoiding local maximums.

This entropy can be introduced by applying selection methodologies that introduce a random component into the population arrangement as well as the mutation operator. In this step of the optimization, certain individuals endure a random mutation of their genetic information, this introduces entropy into the optimization which avoids a premature stagnation of the optimization. Nevertheless, introducing an excessive degree of entropy into the optimization may lead to an unstable convergence to any solution, rendering the optimization unproductive. Therefore, the balance between exploration and intensification of the final solution is critical for ensuring an acceptable optimization performance.

4   Results

In order to test the performance of the proposed methodology, a common conference room scenario have been designed, shown in Fig. 3. This scenario includes varying obstacles where no chair should be located. Figure 3 also displays a square pattern distribution of chairs over the proposed scenario, which is one of the most applied techniques to real distributions [14].

Due to the high obstacle density of the proposed scenario, its resulting irregularity and the form factor of the room, the displayed regular pattern is not capable of exploiting all the available space for properly distancing the chairs.

On the other hand, the proposed GA is capable of exploring the complete space of solutions, obtaining optimal chair distributions for each possible scenario of application.

All simulations of the GA were coded and executed in the Python software environment and performed with an Intel® i7 2.4 GHz of CPU and 16 Gb of RAM. Moreover, the selected hyperparameters for the GA optimization are presented in Table 1.

In order to evaluate the performance of the min-max and max-sum fitness functions, multiple GA optimizations were performed with both methodologies for a varying number of chairs to be allocated. A comparison of the obtained results of both GA techniques as well as the regular pattern approach are presented in Table 2.

The obtained results indicate an increase in performance for the 19 chairs GA min-max strategy optimization from the regular pattern distribution. This strategy optimized
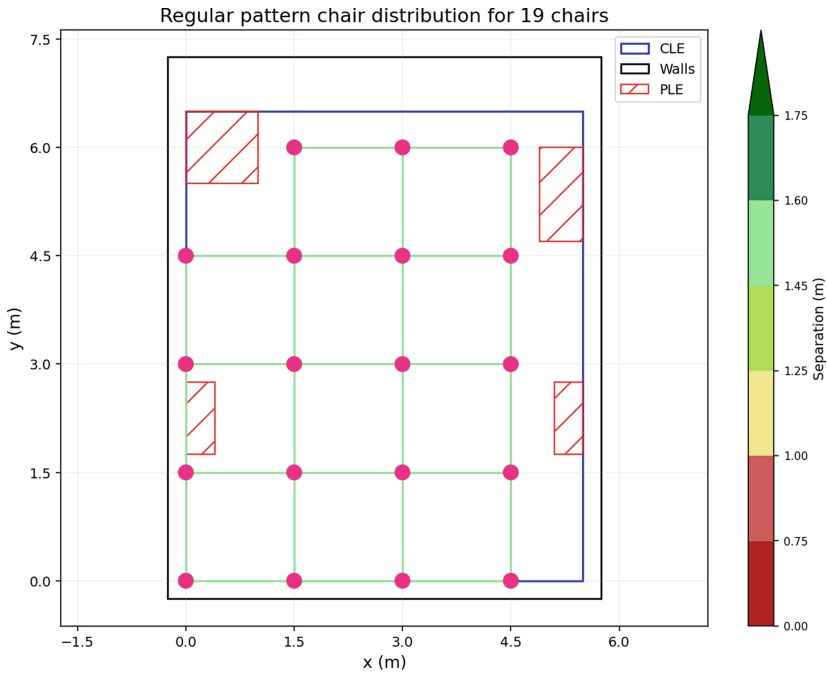
Fig. 3. Chair distribution obtained from a regular square pattern distribution for 19 chairs over the CLE (Chair Location Environment). Obstacles are denoted as red rectangles, representing the PLE (Prohibited Location Environment)

Table 1. Values of all hyperparameters implemented into the GA optimization. The parameter adjustment was based on the methodology presented in [15, 16, 26].

Parameter	Value
Number of individuals	200
Selection methodology	Tournament 2
Elitism percentage	15%
Mutation percentage	10% Population 10% Mutation Rate
Stop criteria	300 Generations or 90% Population Equal
a	5
b	2
λ	1
κ	100 m
ρ	2.0 m
Number of points	12100
Number of possible solutions for 19/20 chair distributions	$3.68 \cdot 10^{77} / 4.45 \cdot 10^{81}$

Table 2. Comparison of the obtained chair distributions of the regular pattern and the implemented GA for 19 and 20 chairs.

Optimization	Min distance	Mean distance	Standard deviation
19 Chairs - Pattern	1.5 m	1.5 m	0 m
19 Chairs - MaxSum	0.14 m	1.72 m	0.81 m
19 Chairs - MinMax	1.51 m	1.68 m	0.15 m
20 Chairs - MinMax	1.41 m	1.61 m	1.69 m

the available space obtaining a chair distribution that allocated the same number of chairs yet with a greater distancing among them. However, the max-sum strategy although it achieved a superior mean distancing, the resulting minimum distance is unacceptable, failing the optimization restriction of 1.5 m of minimum separation. This strategy has proven unfeasible as it does not represent the need of a minimum separation in its fitness evaluation, which proves the importance of this step.

Furthermore, the min-max GA optimization is capable of allocating a greater number of chairs than the regular pattern distributions, sacrificing both mean and minimum distance in the process. Nevertheless, the obtained solution achieved an acceptable minimum distancing, proving the flexibility of this methodology.
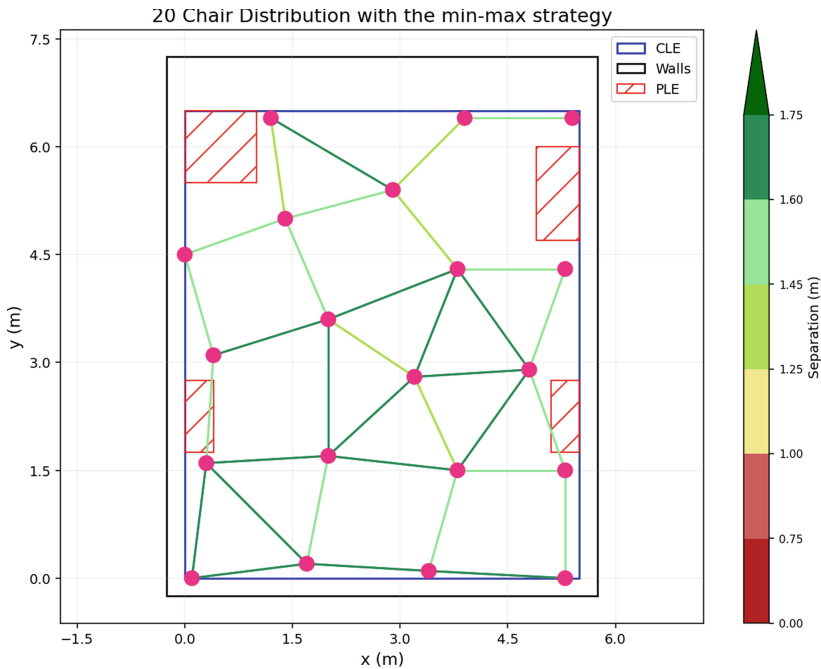
Fig. 4. Achieved chair distribution from the GA min-max strategy for 20 chairs. No other tested methodology attained a viable distribution for this number of chairs.

Finally, Fig. 4 shows the attained distributions for 20 chairs from the min-max strategy, the only tested methodology that achieved a viable solution for this number of chairs.

5   Conclusions

The arrival of the COVID-19 pandemic has reshaped in multiple ways our way of life. The spread capability of this disease has challenged the continuity of social interaction events. Multiple measures have been deployed with a common objective, reducing the contagion probability, including facemasks, active ventilation and guaranteeing a certain interpersonal distance.

In static environments, such as schools, hostelry establishments and conference meetings, the chair distribution is directly correlated with the resulting interpersonal distance, and consequently, the contagion probability.

The distribution of a given number of chairs over a scenario in a way that optimizes the distancing among assistants without severely impacting the event capacity is a combinatorial NP-Hard problem, thus a direct resolution remains unfeasible. Consequently, the event managers usually tend for distributing the chair following a regular pattern that guarantees the minimum distance, however, the performance of this solution is dependent of the scenario geometry and the presence of obstacles, as it may not exploit all the available space in certain scenarios.

Therefore, in this paper a GA optimization is proposed for solving the chair location problem. The CLP definition have been attained accordingly to the maximum diversity problem, implementing multiple strategies common in these optimization paradigms (i.e., min-max, and max-sum strategies). Results show that the min-max proposal outperforms both the regular pattern and the max-sum approaches, proving as a valuable alternative for irregular scenarios with a high obstacle density and for applications with a high flexibility requirement, thus fulfilling the main objectives of this paper.

References

1. Bullard, J., et al.: Predicting infectious severe acute respiratory syndrome Coronavirus 2 from diagnostic samples. Clin. Infect. Dis. **71**(10), 2663–2666 (2020)
2. Borak, J.: Airborne transmission of COVID-19. Occup. Med. **70**(5), 297–299 (2020)
3. Rowe, B.R., Canosa, J.A., Drouffe, J.M., Mitchell, J.B.: Simple quantitative assessment of the outdoor versus indoor airborne transmission of viruses and COVID-19. Environ. Res. **198**, 111189 (2021)
4. Ujiie, M., Tsuzuki, S., Ohmagari, N.: Effect of temperature on the infectivity of COVID-19. Int. J. Infect. Dis. **95**, 301–303 (2020)
5. Welsch, R., Hecht, H., Chuang, L., Von Castell, C.: Interpersonal distance in the SARS-CoV-2 crisis. Human Factors J. Human Factors Ergonomics Soc. **62**(7), 1095–1101 (2020)
6. Lisi, M.P., Scattolin, M., Fusaro, M., Aglioti, S.M.: A Bayesian approach to reveal the key role of mask wearing in modulating projected interpersonal distance during the first COVID-19 outbreak. Plos One **16**(8), e0255598 (2021)

7. Bhagat, R.K., Wykes, M.D., Dalziel, S.B., Linden, P.F.: Effects of ventilation on the indoor spread of COVID-19. J. Fluid Mech. **903**, F1 (2020). https://doi.org/10.1017/jfm.2020.720

8. Berardi, A., et al.: Hand sanitisers amid CoViD-19: a critical review of alcohol-based products on the market and formulation approaches to respond to increasing demand. Int. J. Pharm. **584**, 119431 (2020)

9. Kretzschmar, M.E., Rozhnova, G., Van Boven, M.: Isolation and contact tracing can tip the scale to containment of COVID-19 in populations with social distancing. Front. Phys. **8**, 677 (2021)

10. Mandel, A., Veetil, V.: The economic cost of COVID lockdowns: an out-of-equilibrium analysis. Econ. Disasters Climate Change **4**, 431–451 (2020)

11. Del Rio, C., Omer, S.B., Malani, P.N.: Winter of Omicron—the evolving COVID-19 pandemic. JAMA **327**(4), 319–320 (2022)

12. Lelieveld, J., et al.: Model calculations of aerosol transmission and infection risk of COVID-19 in indoor environments. Int. J. Environ. Res. Public Health **17**(21), 8114 (2020)

13. Echevarría-Huarte, I., Garcimartín, A., Hidalgo, R.C., Martín-Gómez, C., Zuriguel, I.: Estimating density limits for walking pedestrians keeping a safe interpersonal distancing. Sci. Rep. **11**, 534 (2021)

14. Bañón, L., Bañón, C.: Improving room carrying capacity within built environments in the context of COVID-19. Symmetry **12**(10), 1683 (2020)

15. Ferrero-Guillén, R., Díez-González, J., Verde, P., Álvarez, R., Perez, H.: Table organization optimization in schools for preserving the social distance during the COVID-19 pandemic. Appl. Sci. **10**(23), 8392 (2020)

16. Ferrero-Guillén, R., Díez-González, J., Martínez-Guitiérrez, A., Álvarez, R.: Optimal COVID-19 adapted table disposition in hostelry for guaranteeing the social distance through memetic algorithms. Appl. Sci. **11**(11), 4957 (2021)

17. Ferrero-Guillén, R., Díez-González, J., Verde, P., Martínez-Gutiérrez, A., Alija-Pérez, J.-M., Perez, H.: Memory chains for optimizing the table disposition during the COVID-19 pandemic. In: Rojas, I., Castillo-Secilla, D., Herrera, L.J., Pomares, H. (eds.) BIOMESIP 2021. LNCS, vol. 12940, pp. 472–483. Springer, Cham (2021). https://doi.org/10.1007/978-3-030-88163-4_40

18. Ghosh, J.B.: Computational aspects of the maximum diversity problem. Oper. Res. Lett. **19**(4), 175–181 (1996)

19. Kuo, C.-C., Glover, F., Dhir, K.S.: Analyzing and modeling the maximum diversity problem by zero-one programming. Decis. Sci. **24**(6), 1171–1185 (1993)

20. Li, Y., Ng, K.C., Murray-Smith, D.J., Gray, G.J., Sharman, K.C.: Genetic algorithm automated approach to the design of sliding mode control systems. Int. J. Control **63**(4), 721–739 (1996)

21. Díez-González, J., Álvarez, R., González-Bárcena, D., Sánchez-González, L., Castejón-Limas, M., Perez, H.: Genetic algorithm approach to the 3D node localization in TDOA systems. Sensors **19**(18), 3880 (2019)

22. Ferrero-Guillén, R., Álvarez, R., Díez-González, J., Sánchez-Fernández, Á., Pérez, H.: Genetic algorithm optimization of lift distribution in subsonic low-range designs. In: Herrero, Á., Cambra, C., Urda, D., Sedano, J., Quintián, H., Corchado, E. (eds.) SOCO 2020. AISC, vol. 1268, pp. 520–529. Springer, Cham (2021). https://doi.org/10.1007/978-3-030-57802-2_50

23. Karakatič, S.: Optimizing nonlinear charging times of electric vehicle routing with genetic algorithm. Expert Syst. Appl. **164**, 114039 (2021)

24. Kim, Y.-H., Yoon, Y.: An efficient GA for maximum coverage deployment in WSN's. IEEE Trans. Cybern. **43** (2013)

25. Verde, P., Díez-González, J., Ferrero-Guillén, R., Martínez-Gutiérrez, A., Perez, H.: Memetic chains for improving the local wireless sensor networks localization in urban scenarios. Sensors **21**(7), 2458 (2021)
26. Ferrero-Guillén, R., Díez-González, J., Álvarez, R., Pérez, H.: Analysis of the genetic algorithm operators for the node location problem in local positioning systems. In: de la Cal, E.A., Villar Flecha, J.R., Quintián, H., Corchado, E. (eds.) HAIS 2020. LNCS (LNAI), vol. 12344, pp. 273–283. Springer, Cham (2020). https://doi.org/10.1007/978-3-030-61705-9_23

Collecting SARS-CoV-2 Encoded miRNAs via Text Mining

Alexandra Schubö, Armin Hadziahmetovic(✉), Markus Joppich, and Ralf Zimmer

Department of Informatics, Ludwig-Maximilians-Universität München, Amalienstr. 17, 80333 Munich, Germany
hadziahmetovic@bio.ifi.lmu.de

Abstract. Established text mining approaches can be used to identify miRNAs mentioned in published papers and preprints. Here, we apply such a targeted approach to the LitCovid literature collection in order to find viral miRNAs published in connection to SARS-CoV-2. As LitCovid aims at being a comprehensive collection of literature on new findings on SARS-CoV-2 and the COVID-19 pandemic, it is perfectly suited for our goal of finding all reported SARS-CoV-2 miRNAs. The identified miRNAs provide an up-to-date and quite comprehensive collection of potential viral miRNAs, which is a useful resource for further research to fight the current pandemic.

We identified 564 putative SARS-CoV-2 miRNAs together with the respective evidences, i.e. the original publications, and collect them for critical review. The text mining method and the corresponding synonym list are optimized for finding viral miRNAs and the results are manually curated. Since not all miRNAs were experimentally verified, the collection might contain false positives, but it is highly sensitive. Moreover, the text mining approach and resulting collection of miRNA candidates can be useful resources for further SARS-CoV-2 research and for experimental validation.

Keywords: SARS-CoV-2 · COVID-19 · svRNAs · Viral miRNAs · miRNAs · Text-mining · Literature search

1 Introduction

The Severe Acute Respiratory Syndrome Coronavirus 2 (SARS-CoV-2) is the causative agent behind the ongoing novel coronavirus disease (COVID-19) pandemic. As of March 17, 2022, SARS-CoV-2 has infected over 460 million people worldwide [5], and has heavily impacted our health, our social lives and the economy. While COVID-19 is a systemic disease, targeting various organs, it is known that a successful containment of SARS-CoV-2 infection is characterized by a strong interferon stimulated gene signature [23]. Indeed, the severe COVID-19 disease progression is driven by a derailment of both adaptive and innate immunity [10,14,21,32]. But as the pathological mechanisms are still not fully

understood, it is important to gain more insights into the interactions between SARS-CoV-2 and the infected host cell. It has been shown that both human and viral miRNAs target the gene expression, possibly also contributing to immune evasion [18]. While this has mostly been observed for DNA viruses, there is accumulating evidence that also RNA viruses are capable of utilizing miRNAs: Morales et al. [19] discovered three SARS-encoded svRNAs and showed that their expression was dependent on the level of viral replication, indicating that they contribute to pathogenesis. They concluded, that antagonizing those svR-NAs could be a promising therapeutic approach. Therefore, information about SARS-CoV-2 encoded miRNAs and RNA-RNA interactions between virus and the host cell could not only lead to further understanding of pathogenesis, but also aid in finding novel therapeutic approaches.

2   The Need for a SARS-CoV-2 miRNA Collection

Human miRNAs have been intensively studied, many are characterized and experimentally validated, and many more are predicted and annotated with high confidence levels [13]. There are online databases for both miRNAs and their targets. Additional tools can be used for target prediction or finding homologs of miRNA sequences.

One of the most popular databases for human miRNAs, miRBase, contains a comprehensive and authoritative collection of the names, sequences, targets and annotation of published miRNAs [13]. In addition, the miRBase database is not limited to human miRNAs, but also contains miRNAs from several other organisms, including viruses. Another database, VIRmiRNA [24], specializes in viral miRNAs, but unfortunately, both databases still lack entries of SARS-CoV-2 encoded miRNAs at the time of writing. Thus, there is a need for a systematic collection of SARS-CoV-2 miRNA candidates.

The most recent source for gathering information on SARS-CoV-2 miRNAs are the scientific publications and preprints, which describe recent coronavirus miRNA candidates, sometimes also their potential targets and miRNA-RNA interactions. Chen et al. reports that almost 10.000 new articles related to SARS-CoV-2 were published each month in 2021 [3]. Therefore, a lot of information on viral miRNAs might be available, which can be extracted from relevant articles. Automated text mining of literature hubs with curated articles about COVID-19 like LitCovid [2] provide more or less complete and comprehensive collections on SARS-CoV-2 publications. Since the metadata is available from the LitCovid FTP page, LitCovid serves as an excellent source for a systematic text mining approach to extract recent miRNA information. Thus, an up-to-date and complete collection of SARS-CoV-2 miRNAs can be made available including references to the supporting (literature) evidence. The comprehensive, but manageable size of the collection allows to assess the sensitivity and specificity and the overall usefulness of a text mining approach for information extraction and the identification of useful evidence for viral miRNAs. This might also extend FAIR principles to recent findings on miRNAs relevant to the ongoing pandemic.

3 Text Mining on Literature Servers

In July 2021, we downloaded the LitCovid database in BioC format containing full-texts and abstracts of COVID-19-related articles. Since LitCovid is a collection of COVID-19 related articles from PubMed, preprint articles are not included. First, sentences for both abstracts and full-texts were extracted. Sentence splitting was done using the spaCy [7] and scispaCy [20] model "en_core_sci_lg" model version 0.4.0. The model recognizes the structure of sentences and can be used to classify the kind of relation the terms have with each other in the text.

Table 1. miRNA "ontology" for our text mining run. The first column shows the categories, the following columns show an example of synonyms we searched for. We looked for the co-occurrences of synonyms taken from either category state or state_vir and mir_form. The initial run was done using only the categories in row 1–3. After finding our first hits, we added the third category, which includes the names given to the miRNAs by the authors. This table only shows an excerpt of the names, for the mir_form category, all terms were also added in their plural form.

MIR_STATE:	Predicted	Putative	Potential	In-silico	Computed		
MIR_STATE_VIR:	viral	SC2V	SARS-CoV-2-encoded	COV2	Virus-encoded	SARS	
MIR_FORM:	miR	mature miRNA	mature Transcript	vmiRNA	mature micro-RNA	pre-miR	...
MIR_NAME:	SC2V-mir-M	MD19	SCoV-2-miR	SARS-CoV-2-pre-miR	COV2_MR	SARS-CoV-2-miR	...

The sentences are extracted from the XML file into an output file where each sentence is written into a new line and marked with an identifier. The identifier (for instance 7754930.3.85) includes information about the source article and position in the text: the first digits represent the article ID (e.g. PMC or PMID), the digit in the middle is a paragraph ID (title = 1, abstract = 2, text = 3, table = figure = supplement = 4) and the last digits show the position in the paragraph.

We created an "ontology" and resulting synonym list of terms we wanted to scan the literature for, splitting the terms into three categories: *miRNA state* (putative, potential, predicted,...), *viral miRNA state* (virus encoded, viral, ...) and *miRNA form* (miR, mature miRNA, pre-miR, ...). This list is shown in Table 1. Since this was done to ensure all different combinations of terms from the mentioned categories are considered during the search process. Text mining is performed using a named-entity recognition (NER) approach. The named-entities are supplied as synonym lists and searched in the input sentences using an Aho-Corasick trie (see [8] for detailed description of miRExplore text mining system). We scanned each document to identify sentences in which the synonyms were mentioned in a combination of one of both "states" and the "form" category. Matches in sentences were only eligible if the terms are found at most

50 characters apart, e.g. "viral" and "miRNA" have to be in the 50 character proximity in order to be recognized as a valid co-occurrence. We then checked the content of every identified sentence manually to evaluate the relevance of the detected occurrence. To increase the pool of publications to search from, we performed a second text mining run on the articles from EuropePMC which also covers preprints. Including preprints might include articles that have not yet been peer-reviewed, but increases the sensitivity of the overall search. We follow the same protocol described above, with the difference that we now included the names of viral miRNAs, which we manually retrieved from the articles we have previously found in literature from LitCovid. Since both text mining runs were done in July 2021, we repeated our text mining search in April 2022 to update our miRNA and miRNA paper collection. An overview of the text mining process can also be seen in Fig. 1. The source code required for the text mining is available online, please see Sect. 6 for details.

Table 2. Example rows from the miRNA synonym list, the whole list contains 564 entries. The entries start with the miRNA name, given by the authors, and are then followed by synonym names. When adding a new miRNA to the list, it is checked for similarities with previously collected miRNAs and if they have the same sequence, the names are treated as synonyms. The amount of columns, i.e. synonyms is variable, but the last two entries for each miRNA are the sequence, in both U and T version, since both versions are found in the literature. For clarity, the sequences are shown on top of instead of next to each other. The full miRNA synonym list can be found online, for details see Sect. 6.

SARS-CoV-2-pre-miR-R6	SARS-CoV-2-MR304 3P	COV2_MR304	UUUAUAUAGCCCAUCUGCCUUG TTTATATAGCCCATCTGCCTTG
SARS-CoV-2-pre-miR-R5	AGAUGAAACAUCUGUUGUCACU AGATGAAACATCTGTTGTCACT		
SARS-CoV-2-pre-miR-R5	UCUGUUGUCACUUACUGUACAA TCTGTTGTCACTTACTGTACAA		
SARS-CoV-2-pre-miR-R4	SARS-CoV-2-miR-079	AUCAACAAUUUUAUUGUAGAUG ATCAACAATTTTATTGTAGATG	
SarsCov2-mir1_1	AACAAAAGCUAGCUCUUGGAGGU AACAAAAGCTAGCTCTTGGAGGT		
SarsCov2-mir1_2	AGCUAGCUCUUGGAGGUUCCGUG AGCTAGCTCTTGGAGGTTCCGTG		
SarsCov2-mir1_3	UCCGUGGCUAUAAAGAUAACAGA TCCGTGGCTATAAAGATAACAGA		
SCoV-2-miR-3	SCoV-2-miR-4	CGCGACGUGCUCGUACGUGGCU CGCGACGTGCTCGTACGTGGCT	
SCoV-2-miR-5	3'stem-miRNA 41	GGCUACUAACAAUCUAGUUGUA GGCTACTAACAATCTAGTTGTA	
SCoV-2-miR-6	AAACUCAAACCCGUCCUUGAUU AAACTCAAACCCGTCCTTGATT		

4 Results of the Text Mining Runs

In the first text mining run in July 2021 on the LitCovid text corpus, we found a total of 111 articles matching our search terms. As mentioned before, LitCovid is growing fast. Therefore, we performed a new repeat text mining run in April 2022, resulting in additional 130 articles. We will indicate the additional results from April 2022 in parentheses. In Fig. 1 the differences between the two runs are shown: in red July 2021 and in yellow the new additions between July 2021 and April 2022.

The LitCovid articles include a range of publication types, such as reviews or conference proceedings, but no preprints. After checking the hits manually, we found that for 30 (2022: 52) articles, the text mining approach found sentences which roughly matched the topic of the role of miRNAs in SARS-CoV-2 infection. 13 (2022: 31) of them, while generally matching our topic (human miRNAs, miRNA binding sites, therapeutic approaches with miRNAs) did not deal with novel viral miRNAs. The remaining 17 (2022: 21) articles actually included very relevant information for the field of viral miRNAs, e.g. literature reviews, and 12 (2022: 6) of them published predicted viral miRNAs. We did a manual search on the LitCovid website after both (July 2021 and April 2022) text mining runs to check whether we missed relevant articles. This did not yield any further results. However, we found a preprint about predicted viral miRNAs on bioRxiv which we included in our selection, resulting in a total of 19 (in 2021: 12 + 1, 2022: 6) articles about SARS-CoV-2 encoded miRNAs. An overview of all articles and information about the protocols used to find or predict the miRNAs is given in Table 3 and Table 4.

For the 111 relevant LitCovid articles we also checked the accessibility and comprehensiveness of the downloaded data. Every article was listed with metadata like authors, journal, publication date and PubMed or PMC ID. For 24 (2022: 21) articles, however, only the abstracts, but no full-texts were available (for details see Fig. 1). Since those articles were sourced from PubMed, the metadata included the PubMed-IDs (PMID). 20 (2022: 20) of those 24 (2022: 21) articles with PMIDs did have a link (PMCID) to a PubMedCentral full-text, which was not directly linked in the LitCovid metadata, but could be retrieved through the PubMed website. For those 20 (2022: 20) articles, full-texts are available, but may only be retrieved manually. Such cases will always appear, as the synchronization between the literature hubs has delays. Moreover, for 4 (2022: 1) articles, there was no link to PMC at the time the text mining run was performed, and the full-text was not available without subscribing to a publishers content. Since then, at least two of those articles were added to PMC, making it possible to view the full-text without subscription.

In the follow up text mining run, which was done on EuropePMC, we found two articles with predicted viral miRNAs, which we also found before in our LitCovid search. Moreover, comprehensive SARS-CoV-2 infected cell RNA-seq datasets became available (e.g. by Wyler [33]) as well as 9 other articles with topics that are relevant for human and viral miRNA interactions.
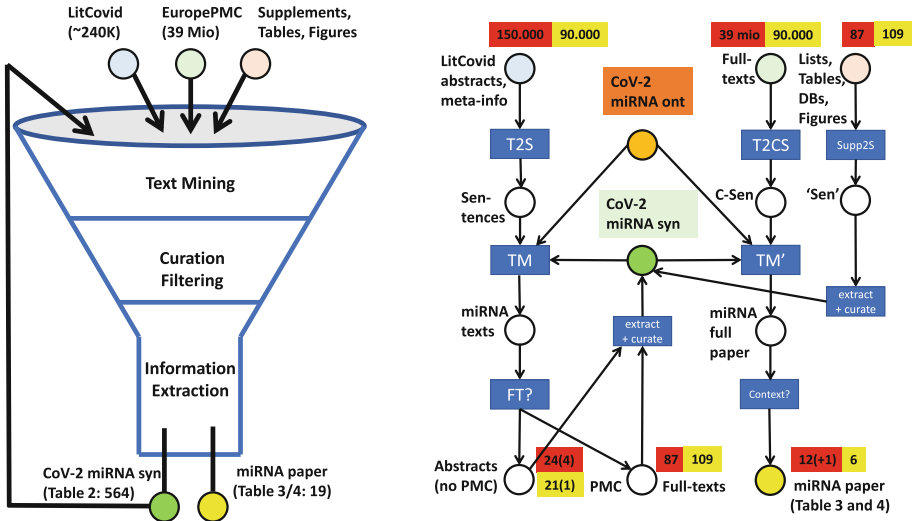
Fig. 1. Overview of the CoV2Collect approach (left) and its implementation (right). The goal of the CoV2Collect approach is to collect relevant information about putative miRNAs in the SARS Coronavirus 2 (SARS-CoV-2). The CoV-2 miRNA syn (synonym list) collects identifiers, common names and the putative mature miRNA sequences. Currently CoV-2 miRNA syn contains 564 entries. The approach also collects the available evidence for those miRNAs by the list of papers describing the evidence for the respective miRNAs ("miRNA paper", currently 19 entries). CoV2Collect uses the comprehensive LitCovid literature collection of the NIH/NCBI to both collect and refine the synonym list and then uses the list for comprehensive text mining on LitCovid and EuropePMC abstracts and full-texts. Moreover, the supplementary material (lists, tables and figures) are used in a semi-automated approach to collect more information and miRNA annotation into the synonym list CoV-2 miRNA syn (e.g. complement the names or add the sequences of identified miRNA candidates). The numbers depicted are the numbers of articles at each place, red representing the text mining run done in July 2021 and yellow the additions until April 2022. For the miRNA paper, the (+1) indicates the paper found in bioRxiv by text mining the EuropePMC articles. (Color figure online)

Furthermore, Fig. 1 exemplifies the structure of our workflow and how it may be applied iteratively: On the right a Petri net sketches the implementation of the CoV2Collect pipeline including the used input data and the resulting collections (miRNA paper and CoV-2 miRNA syn, see Table 3 and 4, and Table 2 respectively). Central is a sensitive text mining approach (TM), which uses the synonym list and a concise miRNA "ontology" (CoV-2 miRNA ont, see Table 1) to identify articles, miRNA occurrences, and miRNA sequences in supplements and tables. The red and yellow boxes indicate the number of respective entries identified in the first (July 2021 run, red) and second (April 2022 version, yellow) text mining run. Essentially, TM and TM' use an Aho-Corasick keyword tree approach to identify all co-occurrences of miRNA synonyms, and miRNA

names or sequences in extracted sentences. This is described in more detail in Sect. 3. The ontology (CoV-2 miRNA ont, overview in Table 1) is used to classify the type of the miRNA mentioning (evidence: predicted/experimental/..., and form: mature/pri-/pre-miRNA) if possible. The input data, as available from the respective sources, is converted (text to sentences: T2S, text to chapter sentences: T2CS) into collections of sentences with unique sentence identifiers, if available in full-texts also with chapter information (C-sentences). Supplemental material (e.g. excel tables) is also extracted into sentences ('Sen') typically from table rows containing sequence information. Abstracts pointing to papers with relevant information on miRNAs are manually curated and associated full-text papers are identified (FT?). Information on synonym names and sequences are collected (extract+curate) and extend the synonym list. The full-texts and supplements for the identified abstracts are retrieved from EuropePMC. The full papers are manually checked (Context?) to collect the final list (miRNA paper) of papers containing the evidence for all identified (putative) miRNAs in CoV-2 miRNA syn. Supplements come in even more diverse formats, Supp2S tries to extract sentences ('Sen') from this material in order to extend, in particular, sequence information in the final CoV-2 miRNA syn.

5   Limitations and Outlook on Text Mining in Research Questions

In our analysis of SARS-CoV-2 miRNAs in LitCovid we could assess some options and limitations of using text mining tools on published articles with respect of extracting relevant evidence. Since research about SARS-CoV-2 only started in late 2019, the literature about SARS-CoV-2 is a set of manageable size. Therefore, it seems that if scientists are interested in a certain aspect of SARS-CoV-2 research, one would be able to use text mining to go through every published paper. Similar to an approach that was done on atherosclerosis [9], it should be possible to collect all available information on miRNAs, interactions and targets related to COVID-19. This could then be used to build a database of viral miRNAs relevant in SARS-CoV-2 infection, which again can be a foundation for any integrative database building upon viral miRNAs, e.g. for human target-gene detection. Collecting this kind of information could help understand the pathology of infection and also lead to quicker exploration of therapeutic possibilities.

Via text mining, we were able to collect a set of relevant, viral miRNA related articles, but the approach still required manual screening of the hits, especially since a lot of the nomenclature used in those articles is not consistent across articles. Manual intervention is also still needed for the correct extraction of information on the viral miRNAs, since some articles present names, sequences and other details in figures or non-machine-readable tables. One problem are missing full-texts: while many preprint and literature servers allow to download the whole corpus and the respective metadata, the availability of full-texts and

Table 3. Overview over the articles found regarding viral miRNAs, either via text-mining or manual search. Due to limited space only short summaries are given, which are intended to serve as a gross overview of the methods used. For more detail please review the articles. The number of miRNAs given in column 2 might vary from the number of sequences in the synonym list since some authors listed both 3′ and 5′ sequences for one miRNA.

Title, Author and Year	# miRNAs	Genome source	Pre-miRNA prediction tool	Mature miRNA prediction tool	Target prediction	Experimental validation	Additional steps
Novel SARS-CoV-2 encoded small RNAs in the passage to humans, Merino et al. 2021[17]	6	SARS-CoV-2 isolate Wuhan-Hu-1 (NC_045512.2)	deep convolutional neural network, deeSOM model and one-class support vector machine	MatureBayes and smallRNA-seq read profiles	Diana MR-microT	Checked for coverage in smallRNA-seq data	miRNA sequence alignment with other CoV-genomes
Predicted SARS-CoV-2 miRNAs Associated with Epigenetic Viral Pathogenesis and the Detection of New Possible Drugs for Covid-19 by Cetin et al. 2021[36]	4	SARS-CoV-2 isolate Wuhan-Hu-1 (NC_045512)	VMir, additional validation with miRBoost	FOMiR and mirDup	MirTarget via mirDB website		Mutational examination of precursors and structure evaluation with RNAfold
An in-silico approach to study the possible interactions of miRNA between human and SARS-CoV2 by Sarma et al. 2020[28]	46	SARS-CoV-2 isolates from China, India, USA, Italy and Jamaica (NC_045512.2, MT435086, MT339041, MT066156 and MT507794.1)	VMir	MatureBayes	Human miRNAs as "targets", checked by RNAhybrid		Sequence similarity and hybridization pattern between precursor candidates and human miRNAs was checked using miRBase's SSEARCH and RNA hybrid. Also, secondary structure prediction with RNAfold was done
Genome-wide computational prediction of miRNAs in severe acute respiratory syndrome coronavirus 2 (SARS-CoV-2) revealed target genes involved in pulmonary vasculature and antiviral innate immunity by Saini et al. 2020[27]	25	SARS-CoV-2 isolate Wuhan-Hu-1 (GenBank MN908947, same as NC_045512)	VMir to predict, ViralMir to select candidate precursors	Mature Bayes	mirDB target prediction		Mfold to predict secondary structure
Computational analysis of microRNA-mediated interactions in SARS-CoV-2 infection by Demirci, Adan 2020[4]	30	SARS-CoV-2 isolate Wuhan-Hu-1 (GenBank MN908947, same as NC_045512)	RNAfold to produce hairpins, izMiR (with decision tree, naive Bayes and random forest classifiers) to select candidates	Fragmented hairpins were filtered by size and position	psRNATarget		
SARS-CoV-2 encoded microRNAs are involved in the process of virus infection and host immune response by Liu et al. 2021[15]	88	SARS-CoV-2 isolate Wuhan-Hu-1 (GenBank MN908947, same as NC_045512)	VMir to predict, RNAfold and HuntMi to select candidates	MatureBayes	TargetFinder and miRanda	qPCR in SARS-CoV-2 infected Vero-Cells, showing further evidence for 4 miRNAs	Checked target gene expression for the 4 validated miRNAs and transfected human cells with one miRNA
Epigenetic Regulator miRNA Pattern Differences Among SARS-CoV, SARS-CoV-2, and SARS-CoV-2 World-Wide Isolates Delineated the Mystery Behind the Epic Pathogenicity and Distinct Clinical Characteristics of Pandemic COVID-19 by Khan et al. 2020[12]	170	SARS-CoV-2 isolate Wuhan-Hu-1 (NC_045512.2)	miRNAFold, then consensus of RNAfold, FOMmir and iMiRNA-SSF to select candidates	MatureBayes	RNA-RNA interactions with IntaRNA 2.0, microRNA.org and psRNATarget		
miRNAs in SARS-CoV 2: A Spoke in the Wheel of Pathogenesis by Satyam et al. 2020[29]	85	SARS-CoV-2 isolate Wuhan-Hu-1 (NC_045512.2)	VMir and miRNAFold to predict, miRNA-dis and miRBoost to select candidates	miRduplexSVM	miRanda and miRDB		Structure prediction with RNAfold, homology with human miRs using BLASTN and miRBase SSEARCH
Interplay between SARS-CoV-2-derived miRNAs, immune system, vitamin D pathway and respiratory system by Karimi et al. 2021[11]	39	SARS-CoV-2 isolate Wuhan-Hu-1 (NC_045512.2.26)	miRNAFold and SSMB, miREval 2.0 for additional validation	SSMB and MiRdup 1.2	miRDB and RNAhybrid		Secondary structure prediction with RNAfold,
Identification and host response interaction study of SARS-CoV-2 encoded miRNA-like sequences: an in silico approach by Roy et al. 2021[26]	85	SARS-CoV-2 genome (no further specifications)	VMir to predict, ViralMir for further validation	MatureBayes	MirTarget via mirDB website		Phylogeny of miRNAs with PhyML, secondary structure prediction with Mfold

Table 4. Continued: Overview over the articles found regarding viral miRNAs, either via text-mining or manual search. Due to limited space only short summaries are given, which are intended to serve as a gross overview of the methods used. For more detail please review the articles. The number of miRNAs given in column 2 might vary from the number of sequences in the synonym list since some authors listed both 3' and 5' sequences for one miRNA. *The authors mostly focused on the N-gene coded miRNAs, but listed 21 unique sequences in their supplementary data, which we all added to the miRNA list.

Title, Author and Year	# miRNAs	Genome source	Pre-miRNA prediction tool	Mature miRNA prediction tool	Target prediction	Experimental validation	Additional steps
Computationally predicted SARS-COV-2 encoded microRNAs target NFKB, JAK/STAT and TGFB signaling pathways by Aydemir et al. 2021[1]	40	SARS-CoV-2 isolate Wuhan-Hu-1 (NC_045512)	VMir to predict, MiPred to remove pseudo-miRs	MatureBayes	TargetScanHuman 7.2 custom, miRDB custom and miRanda 3.0		Structure prediction with RNAfold, homology with human miRs using BLASTN and miRBase
Computational prediction of SARS-CoV-2 encoded miRNAs and their putative host targets by Verma et al. 2020[31]	8	SARS-CoV-2 isolate Wuhan-Hu-1 (NC_045512.2)	VMir to predict, filtering by MFE calculated with MFold	MatureBayes	MiRTarget via mirDB website	Alignment against reads from RNA seq data (GSE147507)	
Annotation of miRNAs in COVID-19 coronavirus by Yu, Chen & Wang 2021[34]	3	16 SARS-CoV-2 sequences from NGDC/CNCB, mature viral miRNA sequences from miRBase	BLAST of previously described viral miR sequences against SCV2 genome, RNAfold to predict hairpins around aligned areas. Verification by using overlap with precursors predicted with MiPred, iMIRNA-PseDPC, iMCRNA-ExPseSSC and miRNA-dis				
SARS-CoV-2-Encoded MiRNAs Inhibit Host Type I Interferon Pathway and Mediate Allelic Differential Expression of Susceptible Gene by Zhu et al. 2021[35]	8	SARS-CoV-2 isolate Wuhan-Hu-1 (GenBank MN908947, same as NC_045512)	Preselection via small-RNA-seq read data, then miRCat and miRMat to determine and confirm mature miRNAs	miRCat	RNAhybrid and miRanda	qRT-PCR of mature miRNAs after transfection of pre-miRNAs in cell culture	Check for similarity with human and other viral miRNA using miRBases, conservation analysis with other coronaviruses
A virus-derived microRNA-like small RNA serves as a serum biomarker to prioritize the COVID-19 patients at high risk of developing severe disease by Fu et al. 2021[6]	1	SARS-CoV-2 isolate Wuhan-Hu-1 (NC_045512)	Serum small-RNA-seq reads aligned to SCV2 genome, area around it was selected as precursors. Candidate selection via secondary structure using Mfold	Read sequence		qRT-PCR in Covid-19 patient's serum samples	Checked for link with disease severity and suitability as biomarker
Decrypting the role of predicted SARS-CoV-2 miRNAs in COVID-19 pathogenesis: A bioinformatics approach by Rahaman et al. 2021[25]	34	SARS-CoV-2 isolate Wuhan-Hu-1 (NC_045512.2)	VMir to predict, filtered by MFE (RNAfold), ImiRNA-PseDPC to eliminate pseudo-miRs	MiRduplexSVM	Diana MIRmicroT and miRDB	Secondary structure prediction with RNAfold, functional synyergistic network generation and check for hybridization with relevant human transcripts via RNAhybrid	
A virus-derived microRNA targets immune responsegenes during SARS-CoV-2infection by Singh et al. 2021[30]	2	SARS-CoV-2 isolate Wuhan-Hu-1 (NC_045512.2)	Two predominant small-RNA-seq reads from SCV2 infected cells, matching several miRNA criteria and, precursor predicted with Vienna RNA Package	Read sequence	Identification of complementary sites on 3'UTR of genes "computationally" (no further details given)	RT-qPCR of stem loop, checked DICER dependency and AGO binding via RIP	Conservation analysis with other coronaviruses
SARS-CoV-2 expresses a microRNA-like small RNA able to selectively repress host genes by Pawlica et al. [22]	1	No information given	In IGV visible peak in small-RNA-seq reads from SCV-2 infected cells, strong hairpin (prediction tool not specified)	Read sequence	Custom script using RNAduplex from Vienna RNA Package	Northern blot detection of precursor and RT-qPCR in patient samples, checked AGO binding via RIP	Checked for sequence similarity with other coronaviruses
Viral MicroRNAs Encoded by Nucleocapsid Gene of SARS-CoV-2 Are Detected during Infection, and Targeting Metabolic Pathways in Host Cells by Meng et al. 2021[16]	21*	Samples SARS-CoV-2 isolate HK-95 (MT835143) and HK 405 (MW856793)	Top 10 highest expressed reads of both cell lines and isolates calculated via SAMtools, confirmed with IGV	Summit of peak in IGV	Target search combining miRDB and DIANA tools	Partly validated with RT-ddPCR	Secondary structure predicted with RNAfold and forna

supplemental material is not guaranteed. For the set of 111 articles from Lit-Covid with text mining hits, only 87 articles were available with full-texts. This was the state for the text mining run performed during July 2021. Repeating the text mining in April 2022, the number of identified articles increased to 241 (containing all 111 previously identified articles). Six of the newly found 130 articles contained viral miRNAs. The ratio of full-texts to only abstracts remained similar: From those 130 new articles, 109 were available with full-text, i.e. 84% in April 2022, compared to 78% in July 2021.

Additionally, the extraction of the information about the predicted miRNAs, like sequences or interactions was difficult: relevant miRNAs and their sequences are often found in figures, tables or supplementary data. For information in this form, retrieving the miRNAs or targets from literature without manual intervention is very challenging. On EuropePMC, we were able to automatically extract tables from the supplementary data from the full-text articles. For a small set of articles, this yielded miRNA related information, e.g. names and sequences, but the structure of the information was not sufficient to fully automate the extraction without human intervention. Therefore, for the time being, manual search and curation by human experts still outperforms text mining based approaches for miRNA (sequence) extraction. At the time of our search, three articles with predicted viral miRNAs were not open access and therefore might not be available to everyone. Nonetheless, at the time of submission, all articles were available on PMC.

The text mining based literature search is a useful resource for future research. The scientific community can be able to get an overview of the current literature and ongoing research and it would be possible to summarize the available data about SARS-CoV-2 encoded miRNAs in one collection. This would also allow for frequent updates. But as stated before, there are some obstacles for our approach: inconsistent nomenclature of miRNAs and the limited availability of full-texts. Moreover, accessing information in figures, tables and supplemental material, e.g. in various table formats and Excel sheets, is difficult. Some current publishing servers do not provide efficient means to access articles, their full texts, including tables, figures, and supplemental data for large scale analyses. Non open access journals pose another difficulty for this approach, therefore making all information available for the public quickly would be another important step to take. Making information more easily accessible and machine readable could aid the scientific community to build their research on each other's findings and save time and resources, especially in situations where time is an important factor, like the ongoing pandemic. Our search yielded 564 viral miRNA candidates and the collection of miRNAs and the related publications can be a promising source for further review of the field and could serve as the base for experimental validation. As the result of this project we provide the identified articles (miRNA paper, see Table 3 and 4) and the collected putative miRNAs (CoV-2 miRNA syn). For availability see Sect. 6.

6   Availability

The CoV-2 miRNA syn (synonym list), as well as all miRNAs in FASTA format can be downloaded from our website https://www.bio.ifi.lmu.de/software/cov2_mirna/index.html.

Source code and scripts for performing the text mining are available on GitHub: https://github.com/mjoppich/sarscov2_mirna_tm.

References
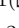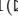
1. Aydemir, M.N., Aydemir, H.B., Korkmaz, E.M., Budak, M., Cekin, N., Pinarbasi, E.: Computationally predicted SARS-CoV-2 encoded microRNAs target NFKB, JAK/STAT and TGFB signaling pathways. Gene Reports 22 (2021)
2. Chen, Q., Allot, A., Lu, Z.: Keep up with the latest coronavirus research. Nature **579**, 193–194 (2020)
3. Chen, Q., Allot, A., Lu, Z.: LitCovid: an open database of COVID-19 literature. Nucl. Acids Res. **49**, D1534–D1540 (2021)
4. Demirci, M.D.S., Adan, A.: Computational analysis of microRNA-mediated interactions in SARS-CoV-2 infection. PeerJ **8**, e9369 (2020)
5. Dong, E., Du, H., Gardner, L.: An interactive web-based dashboard to track COVID-19 in real time. Lancet. Infect. Dis **20**, 533–534 (2020)
6. Fu, Z., et al.: A virus-derived microRNA-like small RNA serves as a serum biomarker to prioritize the COVID-19 patients at high risk of developing severe disease. Cell Discov. **7**, 1–4 (2021)
7. Honnibal, M., et al.: explosion/spaCy: v2.1.7: improved evaluation, better language factories and bug fixes, August 2019
8. Joppich, M.: Integrative bioinformatics applications for complex human disease contexts, November 2021
9. Joppich, M., Weber, C., Zimmer, R.: Using context-sensitive text mining to identify miRNAs in different stages of atherosclerosis. Thromb. Haemost. **119**, 1247–1264 (2019)
10. Kaiser, R., et al.: Self-sustaining IL-8 loops drive a prothrombotic neutrophil phenotype in severe COVID-19. JCI Insight **6** (2021)
11. Karimi, E., Azari, H., Yari, M., Tahmasebi, A., Azad, M.H., Mousavi, P.: Interplay between SARS-CoV-2-derived miRNAs, immune system, vitamin D pathway and respiratory system. J. Cell Mol. Med. **25**, 7825–7839 (2021)
12. Khan, M.A.A.K., Sany, M.R.U., Islam, M.S., Islam, A.B.M.M.K.: Epigenetic regulator miRNA pattern differences among SARS-CoV, SARS-CoV-2, and SARS-CoV-2 world-wide isolates delineated the mystery behind the epic pathogenicity and distinct clinical characteristics of pandemic COVID-19. Front. Genet. **11** (2020)
13. Kozomara, A., Birgaoanu, M., Griffiths-Jones, S.: MiRBase: from microRNA sequences to function. Nucl. Acids Res. **47**, D155–D162 (2019)
14. Liao, M., et al.: Single-cell landscape of bronchoalveolar immune cells in patients with COVID-19. Nat. Med. **26**, 842–844 (2020)

15. Liu, Z., et al.: SARS-CoV-2 encoded microRNAs are involved in the process of virus infection and host immune response. J. Biomed. Res. **35**, 216 (2021)
16. Meng, F., et al.: Viral MicroRNAs encoded by nucleocapsid gene of SARS-CoV-2 are detected during infection, and targeting metabolic pathways in host cells. Cells **10**(7), 1762 (2021)
17. Merino, G.A., et al.: Novel SARS-CoV-2 encoded small RNAs in the passage to humans. Bioinformatics **36**, 5571–5581 (2020)
18. Mishra, R., Kumar, A., Ingle, H., Kumar, H.: The interplay between viral-derived miRNAs and host immunity during infection. Front. Immunol. **10**, 3079 (2020)
19. Morales, L., Oliveros, J.C., Fernandez-Delgado, R., tenOever, B.R., Enjuanes, L., Sola, I.: SARS-CoV-encoded small RNAs contribute to infection-associated lung pathology. Cell Host Microbe **21**, 344–355 (2017)
20. Neumann, M., King, D., Beltagy, I., Ammar, W.: ScispaCy: fast and robust models for biomedical natural language processing. In: BioNLP 2019 - SIGBioMed Workshop on Biomedical Natural Language Processing, Proceedings of the 18th BioNLP Workshop and Shared Task (2019)
21. Nicolai, L., et al.: Vascular neutrophilic inflammation and immunothrombosis distinguish severe COVID-19 from influenza pneumonia. J. Thromb. Haemost. **19**, 574–581 (2021)
22. Pawlica, P., et al.: SARS-CoV-2 expresses a microRNA-like small RNA able to selectively repress host genes. Proc. Natl. Acad. Sci. **118**, e2116668118 (2021)
23. Pekayvaz, K., et al.: Protective immune trajectories in early viral containment of non-pneumonic SARS-CoV-2 infection. Nat. Commun. **13**, 1018 (2022)
24. Qureshi, A., Thakur, N., Monga, I., Thakur, A., Kumar, M.: VIRmiRNA: a comprehensive resource for experimentally validated viral miRNAs and their targets. Database J. Biol. Databases Curation **2014** (2014)
25. Rahaman, M., Komanapalli, J., Mukherjee, M., Byram, P.K., Sahoo, S., Chakravorty, N.: Decrypting the role of predicted SARS-CoV-2 miRNAs in COVID-19 pathogenesis: a bioinformatics approach. Comput. Biol. Med. **136**, 104669 (2021)
26. Roy, S., et al.: Identification and host response interaction study of SARS-CoV-2 encoded miRNA-like sequences: an in silico approach. Comput. Biol. Med. **134**, 104451 (2021)
27. Saini, S., Saini, A., Thakur, C.J., Kumar, V., Gupta, R.D., Sharma, J.K.: Genome-wide computational prediction of miRNAs in severe acute respiratory syndrome coronavirus 2 (SARS-CoV-2) revealed target genes involved in pulmonary vasculature and antiviral innate immunity. Mol. Biol. Res. Commun. **9**, 83 (2020)
28. Sarma, A., Phukan, H., Halder, N., Madanan, M.G.: An in-silico approach to study the possible interactions of miRNA between human and SARS-CoV-2. Comput. Biol. Chem. **88**, 107352 (2020)
29. Satyam, R., et al.: miRNAs in SARS-CoV 2: a spoke in the wheel of pathogenesis. Curr. Pharm. Des. **27**, 1628–1641 (2020)
30. Singh, M., et al.: A virus-derived microRNA targets immune response genes during SARS-CoV-2 infection. EMBO Rep. **23**, e54341 (2022)
31. Verma, S., Dwivedy, A., Kumar, N., Biswal, B.K.: Computational prediction of SARS-CoV-2 encoded miRNAs and their 2 putative host targets. bioRxiv (2020)
32. Wilk, A.J., et al.: A single-cell atlas of the peripheral immune response in patients with severe COVID-19. Nat. Med. **26**, 1070–1076 (2020)
33. Wyler, E., et al.: Transcriptomic profiling of SARS-CoV-2 infected human cell lines identifies HSP90 as target for COVID-19 therapy. iScience **24**, 102151 (2021)
34. Yu, T.Y., Chen, M., Wang, C.D.: Annotation of miRNAs in the COVID-19 Novel Coronavirus. J. Electron. Sci. Technol. **19**, 100060 (2021)

35. Zhu, Y., et al.: SARS-CoV-2-encoded MiRNAs inhibit host type i interferon pathway and mediate allelic differential expression of susceptible gene. Front. Immunol. **12** (2021)
36. Çetin, Z., Bayrak, T., Oğul, H., İlker Saygılı, E., Akkol, E.K.: Predicted SARS-CoV-2 miRNAs associated with epigenetic viral pathogenesis and the detection of new possible drugs for Covid-19. Curr. Drug Deliv. **18**, 1595–1610 (2021)

COVID-19 Severity Classification Using a Hierarchical Classification Deep Learning Model

Sergio Ortiz[1]([✉]) [iD], Juan Carlos Morales[1], Fernando Rojas[1] [iD],
Olga Valenzuela[2] [iD], Luis Javier Herrera[1] [iD], and Ignacio Rojas[1]([✉]) [iD]

[1] School of Information Technology and Telecommunications Engineering,
Department of Computer Architecture and Technology, University of Granada,
Granada, Spain
sergioortiz1@correo.ugr.es, irojas@ugr.es
[2] Faculty of Science, Department of Applied Mathematics, University of Granada,
Granada, Spain

Abstract. One of the most important situations in recent years has been originated by the 2019 Coronavirus disease (COVID-19). Nowadays this disease continues to cause a large number of deaths and remains one of the main diseases in the world. In this disease is very important the early detection to avoid the spread, as well as to monitor the progress of the disease in patients, and techniques of artificial intelligence (AI) is very useful for this. This is where this work comes from, trying to contribute in the study to detect infected patients. Drawing inspiration from previous work, we studied the use of deep learning models to detect COVID-19 and classify the patients with this disease. The work was divided into three phases to detect, evaluate the percentage of infection and classify patients of COVID-19. The initial stage use CNN Densenet-161 models pre-trained to detects the COVID-19 using multi-class X-Ray images (COVID-19 vs. No-Findings vs. Pneumonia), obtaining 88.00% in accuracy, 91.3% in precision, 87.33% in recall, and 89.00% in F1-score. The next stage also use CNN Densenet-161 models pre-trained to evidenced the percentage of infection COVID-19 in the different CT-scans slices belonging to a patient, obtaining in the evaluation metrics a result of 0.95 in PC, 5.14 in MAE and 8.47 in RMSE. The last stage creates a database of histograms of different patients using their lung infections and classifies them into different degrees of severity using K-Means unsupervised learning algorithms with PCA.

Keywords: Deep learning · COVID-19 · Predicting severity · X-Ray and CT-scans

1 Introduction

The appearance of coronavirus disease 2019 (COVID-19) has been one of the most important points in recent years in the world. The coronavirus appeared

in the city of Wuhan, Hubei province, China in late 2019. This disease is causing millions of deaths since it spread throughout the world. This pneumonia causes significant damage to people's lungs and respiratory system [1]. The mainly symptoms in the patients are essentially fever, cough or shortness of breath. One of the most critical points is the easy transmission, spreading from person to person quickly, and therefore early detection is essential to avoid accelerated contagion.

This is one of the points where thousands of people from different fields work against the rapid detection of this disease. The main method for detect COVID-19 is reverse transcription polymerase chain reaction (RT-PCR) [2], but it reported false negative rates, this being his major problem in detecting the disease [3]. For this reason, and as it is done to detect other respiratory diseases, the images of the lungs of the patients can be used as a complement for the specialists.

The medical imaging and deep Learning (DL) is a excellent option to study and detect the COVID-19, giving the experts a great potential to improve the diagnosis [4]. Two types of medical images are used for this task, X-rays and computed tomography (CT) images [5]. Chest X-ray images have a short acquisition time and low cost, which is why they are used more frequently. [6] This imaging have a lot of pros but have high limitation in detection the infection COVID-19. For these reasons, CT-scans are used as an alternative of chest x-rays to study the patients infection and to evaluate cases of COVID-19 with more sensibility. Nevertheless, the CT-scans acquisition is more difficult and more complex, resulting in higher costs and acquisition times [7].

Deep learning have the ability to perform automatic feature extraction from raw data, also called feature learning. Its structure is made up of artificial neurons and multiple data processing layers in a deep architecture called the Deep Neural Network. Convolutional neural networks (CNN) are a peculiarity of this networks and it have demonstrated to be favourable in image processing [3]. Artificial Intelligence (AI) can have the solution to make this process automatic and restrict the need of the radiology specialist to detect the COVID-19 infection in patients.

2   Process Description

The work realized can be divided in three stages, where from the detection of COVID-19 in a patient, the severity of this is determined and classified. The first stage detects COVID-19 in chest X-ray images, using a CNN Densenet-161. The detection is carried out by multi-class images (COVID vs. Pneumonia vs. No-Findings). The second stage resolved the percentage of infection in the lungs of the patients, by using their CT-scans slices through another Densenet-161. Finally the last stage classify patients according to their percentage infection histograms. For this phase is used unsupervised learning algorithms KNN with PCA (Figs. 1 and 2).
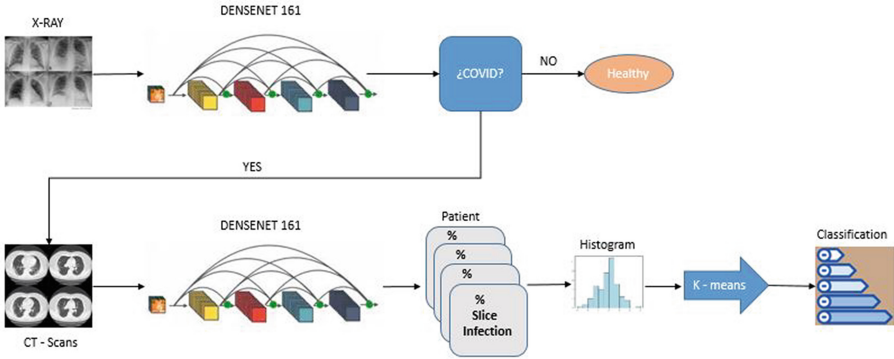
Fig. 1. Process description

3   Material and Methods

3.1   Dataset

Two different datasets is used to detect COVID-19 and predict the infection percentage. The first data set is made up of X-ray images and the second is made up of CT scans lungs.

– Dataset 1: This first database that is raised for this study was collected [8] and is composed by X-ray images. Three types of images make up this database, images of patients with COVID-19, images of patients with pneumonia and images of people without findings. We use 127 X-ray images with COVID-19, 43 belong to female and 82 to male with positive diagnosis, 500 no-findings and 500 pneumonia.
– Dataset 2: The second dataset is composed by CT scans with positive COVID-19 diagnosis. In this dataset each slice of CT scans have associated its COVID-19 infection percentage, percentage that was fixed by two experienced thoracic radiologists. This dataset has been collected by [7].

3.2   Methods

1) CNN's Densenet

   In order to realized the process above-mentioned, Convolutional Neural Network architectures are used. The convolutional neural network has an important aspect due to the reduction the number of parameters in Artificial Neural Networks. These structures convolve the input with filters or kernels to extract functionalities and for this reason they are known by this name [11]. The CNN chosen for this study is Densenet-161. Traditional CNNs, give the output of the l_{th} layer using a nonlinear transformation H to the previous layer's output x_{l-1},

$$x_l = H_l(x_{l-1}) \tag{1}$$
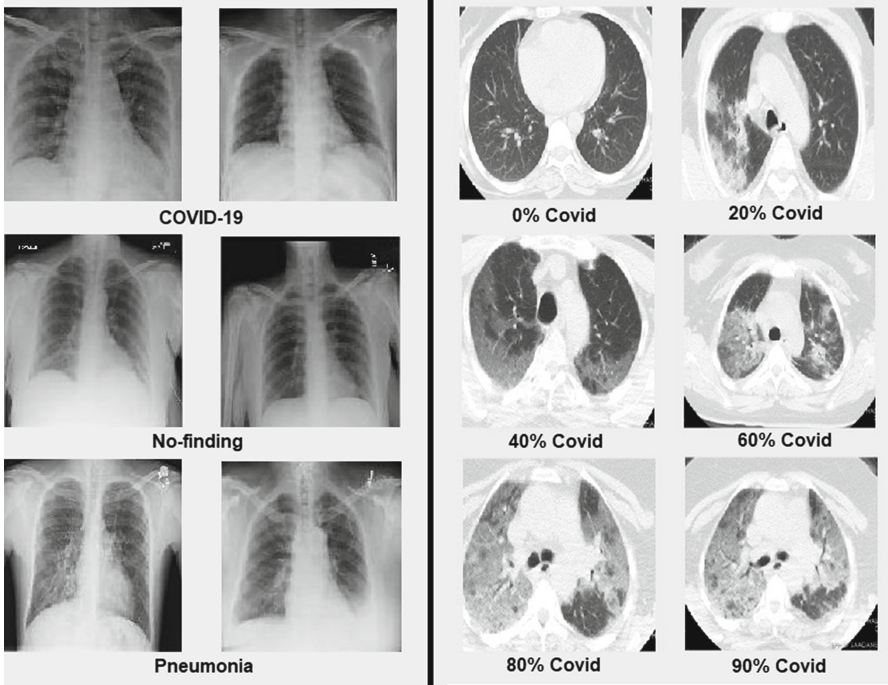
Fig. 2. Sample X-ray images from dataset1 and CT scan images from dataset2

However DenseNet (Dense Convolutional Network) layers are densely connected to each other

$$x_l = H_l(x_0, x_1, ..., x_{l-1}) \tag{2}$$

where $[x_0, x_1, ..., x_{l-1}]$ is a tensor constructed by concatenation of the previous layers' output feature maps. For this reason, this structure allows one layer to receive all inputs from previous layers, and in the same way transmit your feature maps to all subsequent layers [9].

2) K-Means

K-Means is an unsupervised clustering algorithm for data classification, without labeling. The M-clustering aim is partitioning a data set $X = X_1, ...X_N$ into M disjoint subsets, $C_1, C_2...C_M$ named clusters and defined by one point called centroid, such as the data set are divided depending on similar characteristics. Initially, the k centroids (k-number of clusters), are randomly selected. The most used clustering criterion is the sum of the squared Euclidean distances between each observation of data base x_i and the centroid m_k [12]. The process can be defined in two step. The first step is called 'Data Mapping Step', where each observation is assigned to the closest centroid based in squared Euclidean distances.

$$\arg \min_C ||x_i - m_k||^2 \tag{3}$$

The second step is called 'Centroid update step', where the centroids of each group are recalculated. This is done by taking the average of all the points assigned to this cluster in the previous step.

3) PCA

PCA is a mathematical procedure that allows to rotate the axes of the data space on the lines of maximum variation, thus allowing to minimize the complexity of spaces with high dimensional vectors without deleting much information. The axes of greatest variation are called principal components [13]. Having the characteristics of each subject, normalized and stored in the following way $X = [X_1, X_2, ..., X_N]$ where N is the total number of subjects, the co-variance matrix of matrix X is calculated:

$$C = cov(X, X) = \frac{1}{N} * XX^t \tag{4}$$

Once this co-variance matrix is calculated, we will obtain the eigenvalues λ and the associated eigenvectors γ. The next step is performed on the eigenvectors, on all or on the most important. The eigenvectors are unitary and perpendicular to each other and they provide us with information about the patterns in the data.

4) Loss function

the Loss function is used in the CNN to calculate the gradients, these being the ones in charge of updating the weights of the Neural [10].

Mean squared error (MSE): estimates the mean of the squared differences between true and predicted values. The equation is:

$$L_{MSE} = \frac{1}{N} \sum_{i=1}^{N} (x_i - \hat{x}_i) \tag{5}$$

where x_i is the ground-truth percentages and $\hat{x}_i$ is the predicted percentages for each input.

Cross-entropy: the purpose is minimize the distance between the predicted probability scores and the label truth probabilities:

$$L_{CE} = -\sum_{i=1}^{N} p_i log q_i \tag{6}$$

where p_i is the ground-truth percentages, and q_i is the predicted percentages for each images. Stochastic gradient descent is used to minimized this loss function.

5) Evaluation metrics

We use the overall classification Accuracy, precision, recall, f1-score, mean absolute error (MAE), root mean squared error (RMSE) and Pearson correlation coefficient (PC) .

$$Accuracy = \frac{TP + TN}{TP + FP + FN + TN} \tag{7}$$

$$Precision = \frac{TP}{TP + FP} \tag{8}$$

$$Recall = \frac{TP}{TP + FN} \tag{9}$$

$$F1Score = \frac{2 * (Recall * Precision)}{(Recall + Precision)} \tag{10}$$

F1 is very useful especially when the dataset have an uneven class distribution.

$$MAE = \frac{1}{n} \sum_{i=1}^{N} |y_i - \hat{y}_i| \tag{11}$$

$$RMSE = \sqrt{\frac{1}{n} \sum_{i=1}^{N} (y_i - \hat{y}_i)^2} \tag{12}$$

where y_i is the ground-truth percentages and $\hat{y}_i$ is the predicted percentages for each input. Pearson

$$PC = \frac{\sum_{i=1}^{N}(y_i - \overline{y}_i)(\hat{y}_i - \overline{\hat{y}}_i)}{\sqrt{\sum_{i=1}^{N}(Y_i - \overline{Y}_i)^2}\sqrt{\sum_{i=1}^{N}(\hat{y}_i - \overline{\hat{y}}_i)^2}} \tag{13}$$

4   Results

Densenet-161 is the CNN used in the first two stage. In model training, the parameter settings are 20 in batch and 50 in the number of epochs. The learning rate varies from 1e−3 to 1e−6 in the first 3 decades and continuing with 1e−6 until the end. In addition, to improve performance, cross-validation (K-fold) is used. This consists of dividing the original dataset into k equal subsets, where $k - 1$ sets will be used for training and 1 set for evaluating performance. Images are pre-rendered, resized to 224 × 224, and have two data augmentation techniques applied to them: random cropping and rotation. This procedure is applied to them before they are sent to the neural network.

4.1   COVID-19 Prediction Results

The Densenet-161 model is trained with the X-ray images in dataset 1. The optimizer used is RMSprop with momentum equal to 0.9 and the loss function is Cross-entropy.

The confusion matrixes (CM) about the result of Densenet-161 with RMSprop optimizer to detect COVID-19 through X-Ray are shown in Fig. 3. The figures shows 5-fold confusion matrix validation and the summary confusion matrix, obtaining an average precision of 86.7%.
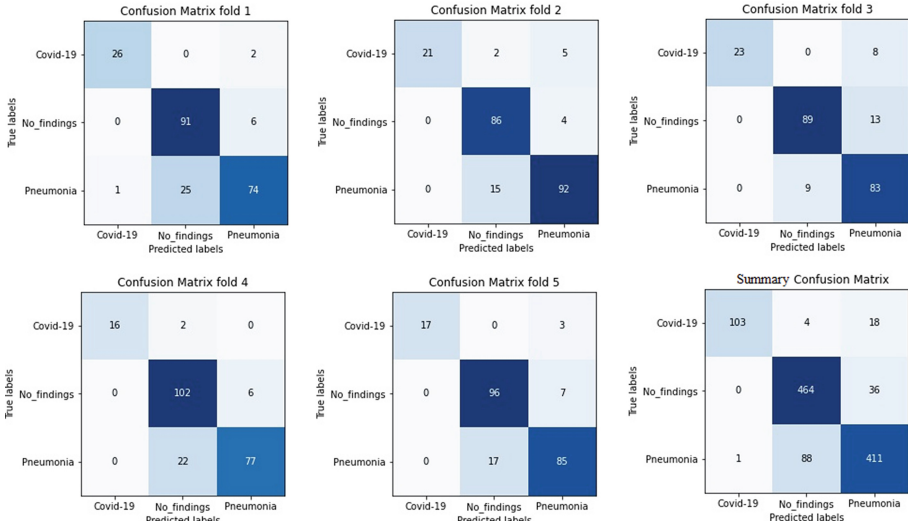
Fig. 3. 5-fold confusion matrixes validation and the summary confusion matrix, from Densenet-161 trained with X-ray imaging and RMSprop optimizer.

Besides this it is important other parameters to evaluated the results and for this more detailed analysis of the model with the RMSprop optimizer. The Table 1 collect the results, being these 88.00% in accuracy, 91.3% in precision, 87.33% in recall, and 89.00% in F1-score.

Table 1. Results of 5 folds in the stage 1 with Densenet-161 and RMSprop optimizer.

Fold-1	Precision	Recall	F1-score	Images	Fold-2	Precision	Recall	F1-score	Images
COVID-19	96	93	95	28	COVID-19	100	75	86	28
No-findings	78	94	85	97	No-findings	83	96	89	90
Pneumonia	90	74	81	100	Pneumonia	91	86	88	107
Accuracy			85	225	Accuracy			88	225
Fold-3	Precision	Recall	F1-score	Images	Fold-4	Precision	Recall	F1-score	Images
COVID-19	100	74	85	31	COVID-19	100	89	94	18
No-findings	91	87	89	102	No-findings	81	94	87	108
Pneumonia	80	90	85	92	Pneumonia	93	78	85	99
Accuracy			87	225	Accuracy			87	225
Fold-5	Precision	Recall	F1-score	Images	Summary	Precision	Recall	F1-score	Images
COVID-19	100	85	92	20	COVID-19	99	83	90	125
No-findings	85	93	89	103	No-findings	84	93	88	500
Pneumonia	89	83	86	102	Pneumonia	87	82	85	500
Accuracy			88	225	Accuracy			87	1125

4.2 Results of the Estimation of the Percentage of Infection in the Lungs

Another Densenet-161 is used to estimate the percentage of infection in the lungs. This CNN is training by CT-Scans images and the loss functions used is Mean squared error. For this stage, RMSprop optimizer is used with momentum equal to 0.9 as in the previous stage.

The RMSprop optimizer results are 0.95 PC, 4.87 MAE and 8.10 RMSE. The Fig. 4 represent the summary of the 5 folds results of the three evaluation metrics, where we can highlight the best results in the Folds 4 and the worst result respectively in the Fold 3. This aspect can probably be produced by the variability and imbalance of the data in the different folds.

4.3 Results of Classify a Patient Within Different Degrees of Severity

This stage classifies a patient into different degrees of severity based on the histogram of infection of the different slices of the lungs. For this, it was made up a gravity histogram database of using the CT-scans. Due to the number of slices on each patient it not the same, a normalization by the number of slices must be performed to prevent this parameter from influencing the comparison of the histograms

The distributions of each histogram is defined by 100 characteristics, one for each possible degree of COVID-19 infection. To visualize some patients in depending on others it is necessary reduced data dimensions and PCA is used for this.

After the creation of the histogram's dataset, the K-Means clustering algorithm divide it in different classes. To know which is the number of the cluster that divided the most convenient dataset, using the elbow curve that explains the variation of the data as a function of the number of clusters.
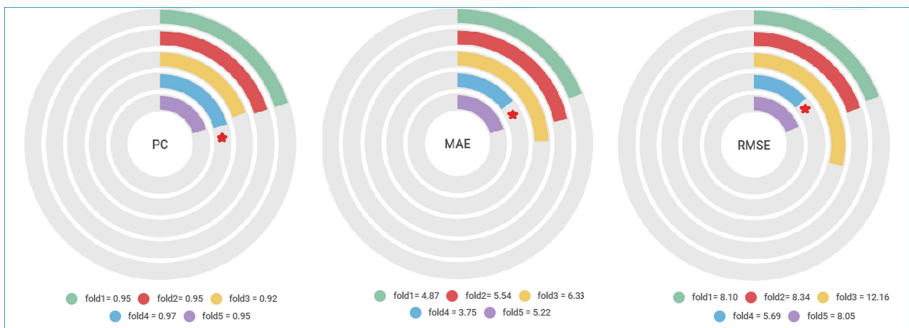
Fig. 4. Summary of evaluation metrics in the stage2. Results of Densenet-161 with optimizer RMSprop in the different 5 folds (testing phase). The best performing fold is the market with the red star. (Color figure online)

The histogram dataset are not labeled in depending on COVID-19 gravity and for this it is utilized K-Means as an unsupervised clustering algorithm for data classification. This algorithm first self-discovers any naturally occurring patterns in that training dataset and then assigns a labels to an input data in the stage of test.
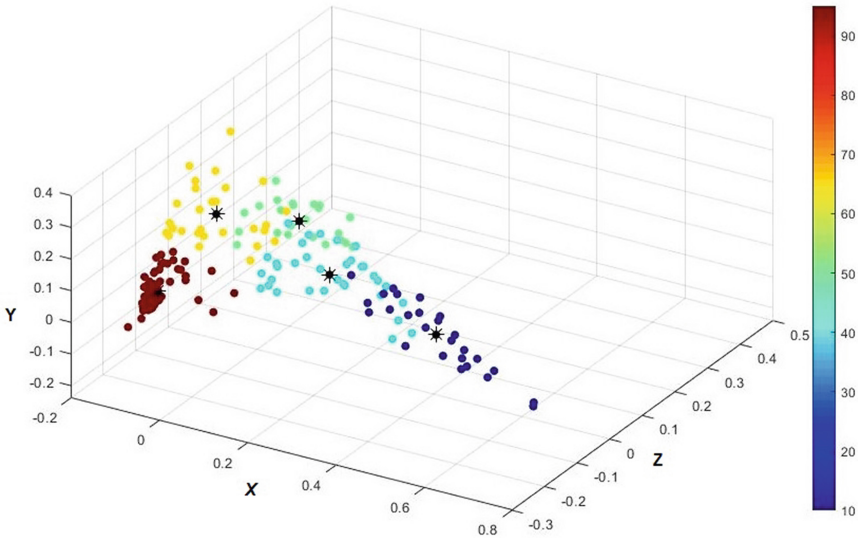
Fig. 5. Representation of the different clusters of the severity COVID-19 degree. (Color figure online)

The Fig. 5 shows the five clusters where have been split our dataset. Every single different colour refers to a COVID-19 degree of severity, and as the colour bar indicates, the colour blue refers to the lowest degree and the red to the highest degree. The grades are labeled from the very mild stage to the severe stage. The black points in the representation are the position of centroids calculated for K-Means and the points that define the clusters. The four first cluster indicates mild or mild-moderate degrees of the disease, and the last group represented in red refers to moderate or severe degree where the patients have more infection in the lungs. In order to ensure that the classification provided by K-Means is correct and the patients are labeled with a good diagnosis, the histograms of the labeled classes are checked. In the Fig. 6, we can see the representation of different histograms of the data set.
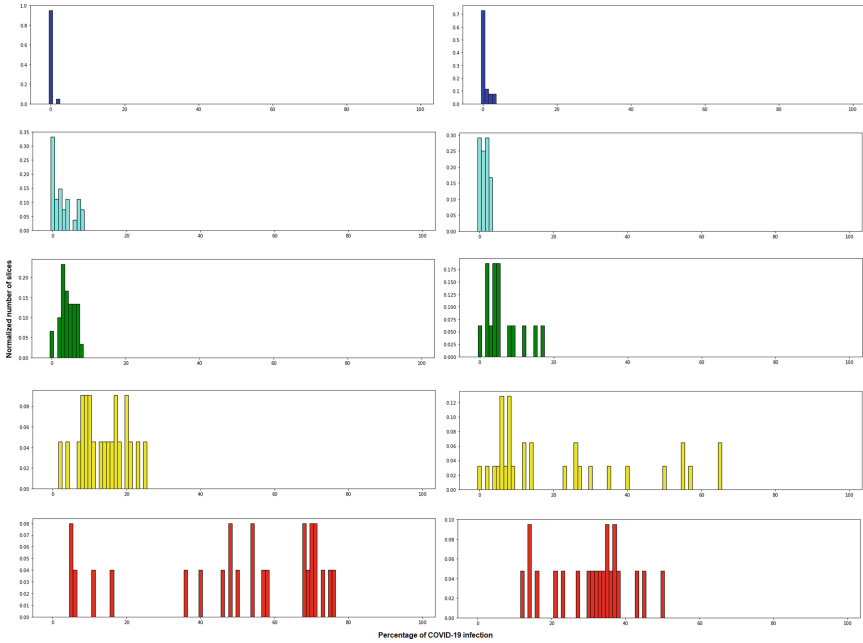
Fig. 6. Representation of the histograms belonging to the different groups obtained.

5   Conclusion

The purpose of this study is to detect and classify COVID patients based on the infection of their lungs. For this two database with imaging X-ray images and CT-scans is used. For the detection of COVID and percentage of infection, pre-trained CNN Densenet-161 models are used with RMSprop optimizers. In the last stage of patient classification, unsupervised techniques are used that detect characteristics of the infection histograms. For the detection of COVID-19 the results achieved has been 91.3% in precision, 87.33% in recall, 89.00% in F1-score and 88.00% in accuracy. In the other hand the COVID-19 infection by computed tomography give a results 0.95 in PC, 5.14 in MAE and 8.47 in RMSE. Giving these results an encouraging proposal both in the detection of COVID and in the detection of the percentage of infection. Finally, the infection histograms allow us to evaluate and classify patients through unsupervised methods, in addition to observing the contribution of infection in a very visual way. In short, through this research it is intended to contribute as much as possible in the study, detection and support against COVID-19.

References

1. Lei, Z., Haixia, L., Junli, Z., Kang, L.: Different methods of COVID-19 detection. Health Sci. J. **15**, 1–6 (2021)
2. Udugama, B., et al.: Diagnosing COVID-19: the disease and tools for detection. ACS Nano **14**, 3822–3835 (2020)
3. Desai, S.B., Pareek, A., Lungren, M.P.: Deep learning and its role in COVID-19 medical imaging. Intell. Based Med. **3**, 100013 (2020)
4. Fan, D.P., et al.: INF-Net: automatic COVID-19 lung infection segmentation from CT images. IEEE Trans. Med. Imaging **39**, 2626–2637 (2020)
5. Bharati, S., Podder, P., Mondal, M., Prasath, V.: Medical imaging with deep learning for COVID-19 diagnosis: a comprehensive review. arXiv preprint (2021). arXiv:2107.09602
6. Farias, L.D.P.G.D., et al.: Imaging findings in COVID-19 pneumonia. Clinics **75**, 1–8 (2020)
7. Bougourzi, F., Distante, C., Ouafi, A., Dornaika, F., Hadid, A., Taleb-Ahmed, A.: Per-COVID-19: a benchmark dataset for COVID-19 percentage estimation from CT-scans. J. Imaging **7**, 189 (2021)
8. Ozturk, T., Talo, M., Yildirim, E.A., Baloglu, U.B., Yildirim, O., Acharya, U.R.: Automated detection of COVID-19 cases using deep neural networks with X-ray images. Comput. Biol. Med. **121**, 103792 (2020)
9. Zhu, Y., Newsam, S.: DenseNet for dense flow. In: Proceedings of the 2017 IEEE International Conference on Image Processing (ICIP), Beijing, pp. 790–794, 17–20 September 2017
10. Ruby, U., Yendapalli, V.: Binary cross entropy with deep learning technique for image classification. Int. J. Adv. Trends Comput. Sci. Eng. **9**, 5393–5397 (2020)
11. Chauhan, R., Ghanshala, K.K., Joshi, R.C.: Convolutional neural network (CNN) for image detection and recognition. In: 2018 First International Conference on Secure Cyber Computing and Communication (ICSCCC) (2018)
12. Likas, A., Vlassis, N., Verbeek, J.J.: COVID-19 recognition using ensemble-CNNs in two new chest X-ray databases. Pattern Recogn. **36**, 1742 (2003)
13. Roweis, S.: EM algorithms for PCA and SPCA. Adv. Neural Inf. Process. Syst. (1998)

The Role of Information Sources, Trust in Information Sources, and COVID-19 Conspiracy Theory in the Compliance with COVID-19 Related Measures

Ana Jovančević[1]([✉]) [ID], Izabel Cvetković[2], and Nebojša Milićević[1]

[1] Faculty of Philosophy, Department of Psychology, University of Niš, Niš, Serbia
ana.jovancevic@filfak.ni.ac.rs
[2] Faculty of Mathematics, Informatics and Natural Sciences (MIN), Department of Informatics,
University of Hamburg, Hamburg, Germany
izabel.cvetkovic@uni-hamburg.de

Abstract. The aim of this study was to check the role of information sources, trust in information sources and COVID-19 related conspiracy in the compliance with COVID-19 related measures at the beginning of the pandemics and at the moment in which study was conducted, on Serbian and German sample. Previous studies have found that information and conspiracy theories are important variables in predicting compliance with COVID-19 related measures, and that Serbian and German culture differ in these behaviors. Instruments used were questions regarding Information sources, questions regarding Trust in information sources (both separated into Formal and Informal), question measuring belief that COVID-19 was created in the laboratory, and two question measuring self-assessed compliance with COVID-19 related measures. Data was analyzed with moderated path analysis through structural equation modeling. The results of this study show that Trust in formal sources negatively predicted belief that COVID-19 was created in the laboratory and positively compliance with COVID-19 related measures, on both samples. On Serbian sample Informal sources also negatively predicted belief that COVID-19 was created in the laboratory, while this belief predicted (negatively) compliance with COVID-19 measures at the beginning of pandemics. We can conclude that there are some cultural differences, and that COVID-19 related conspiracy is more important on Serbian than on the German sample.

Keywords: Information sources · Trust in Information sources · COVID-19 conspiracies · Compliance with anti-covid measures · Germany and Serbia

1 Introduction

Previous studies regarding compliance with COVID-19 related measures explored various roles of COVID-19 related information. One study shows that feeling distressed by information can lead to better compliance with COVID-19 preventive measures [1],

but only if individual does not recur to information avoidance [1]. Further, feeling disinformed lowers compliance with COVID-19 preventive measures [2]. Previous studies also suggest that information sources are important in predicting compliance with COVID-19 related measured [3]. Trust is also an important variable in predicting compliance with COVID-19 related measures. Namely, one study showed that trust in science can predict compliance with the above-mentioned measures [4]. In this study Trust in information sources was a form of trust which was studies separately from information sources [5]. Further, previous studies also suggest that Information sources and Trust in information sources can be separated into Formal and Informal ones [6]. Formal sources include sources like government, doctors giving interviews on TV, whereas Informal sources include forums, friends, web pages and similar. Formal sources are the ones which can increase the adaptation of protective health behavior [7]. Proper information is also relevant in terms of willingness to get vaccinated [8]. With regards to Trust in information sources, previous studies suggest that it is an important variable in vaccination intention [9]. Conspiracy theories have also proven to be important variable when it comes to compliance with anti-covid measures [3]. Connection between information and conspiracy has also been found in previous studies. Namely, Informal sources, like social networks are the field where conspiracy theories arise [10].

Previous studies have also found cultural differences in COVID-19 related psychological reactions [11] including mental health outcomes [12]. Among others, differences were found between Serbian and Latin-American [3] and between Serbian and German culture [13].

These findings lead to conclusion that there are studies suggesting that information awareness is important for both vaccination intention and compliance with anti-covid measures; that trust in information sources is important for vaccination intention; that conspiracy theories are important variable when predicting compliance with anti-covid measures, and that Serbian and German culture differ in COVID-19 related behaviors. However, there is a lack of studies examining both Information sources and Trust in these sources, separating them into dimensions, while taking into consideration conspiracy that hinder compliance with COVID-19 related measures. Also, there is a lack of research examining differences between compliance with measures at the beginning of pandemics and later on. The afore-mentioned findings motivate this study to examine differences between Serbian and German culture in regards to the role of Information sources, Trust in information sources and conspiracy theories in compliance with anti-covid measures at the beginning of the pandemic and later on during the pandemic.

2   Method

Sample

We used convenience sample, from Serbia ($N = 115$; Females $= 88.6\%$; Age: $M = 31.37$; $SD = 11.33$), and Germany ($N = 101$; Females $= 65.3\%$; Age: $M = 28.74$; $SD = 8.52$). In Serbian sample there were .9% respondents with elementary school, 38.6% with high school, 4.4% with college, 37.7% with university degree, 13.2% with master's degree, and 5.3% with Ph.D. or specialization. In German sample there were 17.8%

without vocational training qualification, 7.9% with a recognized vocational training, 5% with technical college degree, 41.6% with a bachelor's degree, 24.8% with a master's degree, and 3% with Ph.D.

We used these two samples due to large differences between these cultures (according to Hofstede's dimensions[1]). We aimed to examine the relation between these variables on two different cultures. Both from experience and from previous studies [1], it is well known that different countries reacted differently on the COVID-19 threat.

Instruments

Instruments used in this study were:

1. Questions regarding Information sources [3] Internal consistency reliability was adequate ($\alpha = .832$, $\alpha = .647$, for formal and informal sources, respectively).
2. Questions regarding Trust in information sources [3]. Internal consistency reliability was adequate ($\alpha = .912$, $\alpha = .640$, for formal and informal sources, respectively).
3. One question measuring belief that COVID-19 was created in laboratory [3].
4. Two questions measuring self-assessed compliance with COVID-19 measures. Question for compliance with measures during the examination [13] and question for compliance at the beginning of pandemics created for the purposes of this study. For scales containing three questions or less previous authors recommend using average inter-item correlation as a method of assessing reliability [14, 15]. Due to this we calculated inter-item correlation for these two items (.22). Previous authors [15] suggest that we can consider that the instrument has adequate reliability if the intercorrelations of items are between .15 and 50. According to this, we consider our items regarding compliance with COVID-19 measures to be reliable.

All questions were rated on Likert-type 5-point scale

Data Analysis

The data was analyzed using JASP and AMOS.

Nationality was a moderator variable, informal and formal sources of information as well as trust in these sources were predictor variables, conspiracy about COVID-19 was a mediator and compliance with COVID-19 related measures was the dependent variable. Moderation path SEM analysis was used.

Full model is presented in the Fig. 1. Nationality was a moderator between all paths in the model.

3   Results

First, we have conducted measurement invariance testing in JASP in order to examine whether we can compare Serbian and German sample on the selected variables.

For information sources the results show that two groups are comparable. Fit indices were relatively adequate (CFI = .960, TLI = .944, NNFI = .944, RMSEA = .065, SRMR

---

[1] Retrieved from https://www.hofstede-insights.com/product/compare-countries/.
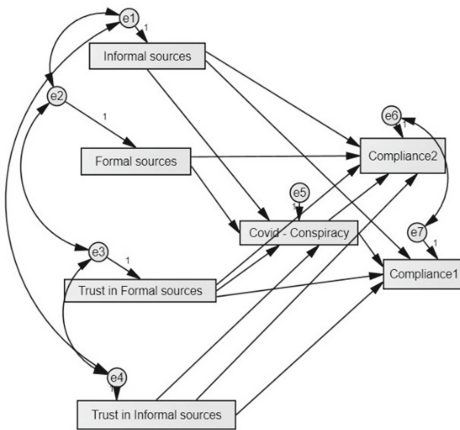
Note. Compliance1 - Compliance with anti-covid measures at the beginning of pandemics; Compliance2 – Compliance with anti-covid measures at the moment in which the research was conducted;

Fig. 1. Model of the relation between information sources, covid-conspiracy and compliance with anti-covid measures. *Note.* Compliance1 – Compliance with anti-covid measures at the beginning of pandemics; Compliance2 – Compliance with anti-covid measures at the moment in which the research was conducted;

= .087, GFI = .927). Metric invariance is achieved. When it comes to comparison of trust in information sources in these two countries, configural measurement invariance is fully achieved, but metric is partially achieved when trust in health web pages is excluded from the analysis (CFI = .964, TLI = .949, NNFI = .949, RMSEA = .079, SRMR = .081, GFI = .930). Metric invariance could not be checked for the other variables since they are comprised of only one question. Previous authors suggest that partial metric invariance is sufficient for group comparison [16, 17], so we can proceed to further analyses.

After this, moderated mediation was conducted in AMOS. Model showed adequate fit indices (CFI = .997, TLI = .965, NFI = .986, RMSEA = .035, SRMR = .029, GFI = .993).

On the Serbian sample Informal sources (Estimate = −.247) and Trust in Formal sources (Estimate = −.460) predicted belief that COVID-19 was created in laboratory, both negatively. Trust in formal sources further predicts compliance with COVID-19 measured at the moment of research (Estimate = .269) and at the beginning of pandemics (Estimate = .484) positively. Finally, belief that COVID-19 was created in the laboratory predicted only compliance with measures at the beginning of pandemics (Estimate = − .18).

On the German sample Trust in Formal sources (Estimate = −.358) predicted belief that COVID-19 was created in laboratory negatively, and compliance with COVID-19 measured at the moment of research (Estimate = .3) and at the beginning of pandemics (Estimate = .256) positively.

4   Conclusions

The results are in accordance with previous studies since they show that information awareness is important for compliance with anti-covid measures [3, 6]. They are also in accordance with results regarding the important role of Formal information sources [7]. They are partially in accordance with previous studies regarding the role of conspiracy theories [3], since this was only confirmed on Serbian sample. Also, the results are partially in accordance with the studies suggesting connection between Informal sources and conspiracy [10], since this was only confirmed on Serbian sample. With this study we demonstrate that Trust in information sources is more important than the Information sources themselves. Further, Trust in Formal sources leads to more adequate COVID-19 related behavior in both samples. Trust in formal sources is the only significant predictor in the German sample. This can be understood through previous studies which show that German sample shows more adaptive mechanisms in COVID-19 situation [9] since the Formal sources are the sources which share most appropriate information regarding COVID-19. Conspiracy was shown to be significant for compliance with measures only at the beginning of pandemics on Serbian sample. These results also confirm cross-cultural differences between Serbia and Germany in the context of the current pandemics. Differences can be accounted by Hofstede's cultural dimension Individualism. Namely, previous studies have linked low Individualism (meaning Collectivistic cultures) with higher belief in conspiracy theories [18]. Serbia has low score on Individuals as dimension, meaning it represents a collectivistic culture [18]. Previous studies also show that on Serbian sample obtaining COVID-19 related information from Informal sources can have an impact on conspiracy theories [3], which was confirmed in this study here. So, when it comes to Informal sources and conspiracy theories there are some cross-cultural differences. On the other hand, Trust in formal sources was found to be a variable leading to adaptive behavior in both cultures.

Practical implication of this finding could be that Trust in formal sources of information is something that should be further addressed to in the attempts to contain the spread of COVID-19. Theoretical implication of these results are a deeper understanding of the role sources of information and trust in those sources have in the compliance with COVID-19 related measures, by taking into account conspiracy theories about COVID-19.

Limitations

Limitations of this study include a sample size. For the future studies we suggest using a larger and more representative sample. Second limitation is the usage of only two cultures – for the future studies we suggest including other cultures also. Finally, for the future studies we suggest adding more questions regarding conspiracy theories – so that we could examine in a more profound way cultural differences of COVID-19 related conspiracy and their effect on compliance with COVID-19 related measures.

References

1. Siebenhaar, K.U., Köther, A.K., Alpers, G.W.: Dealing with the COVID-19 infodemic: distress by information, information avoidance, and compliance with preventive measures. Front. Psychol. **11**, 2981 (2020)

2. Hameleers, M., van der Meer, T.G.L.A., Brosius, A.: Feeling "disinformed" lowers compliance with COVID-19 guidelines: evidence from the US, UK, Netherlands and Germany. Harvard Kennedy School Misinf. Rev. (2020). https://doi.org/10.37016/mr-2020-023

3. Jovančević, A., Milićević, N.: Optimism-pessimism, conspiracy theories and general trust as factors contributing to COVID-19 related behavior–a cross-cultural study. Personality Individ. Differ. **167**, 110216 (2020)

4. Plohl, N., Musil, B.: Modeling compliance with COVID-19 prevention guidelines: the critical role of trust in science. Psychol. Health Med. **26**(1), 1–12 (2021)

5. Maykrantz, S.A., Gong, T., Petrolino, A.V., Nobiling, B.D., Houghton, J.D.: How trust in information sources influences preventative measures compliance during the COVID-19 pandemic. Int. J. Environ. Res. Publ. Health **18**(11), 5867 (2021)

6. Jovančević, A., Milićević, N., Đorić, S.: What is stopping us to get vaccinated? The role of optimism-pessimism, information sources, trust, conspiracy theories and fear in the willingness to get vaccinated (2022). [Unpublished manuscript]

7. Qazi, A., et al.: Analyzing situational awareness through public opinion to predict adoption of social distancing amid pandemic COVID-19. J. Med. Virol. **92**(7), 849–855 (2020)

8. Jovančević, A., Milićević, N., Đorić, S.: Information sources and conspiracy theories as predictors of vaccination intention. Presented at the International Conference on Bioengineering, Biomedical Signal and Image Processing (BIOMESIP), 19–21 July 2021 (2021)

9. Qiao, S., Friedman, D.B., Tam, C.C., Zeng, C., Li, X.: Vaccine acceptance among college students in South Carolina: do information sources and trust in information make a difference? MedRxiv (2020). https://www.medrxiv.org/content/medrxiv/early/2020/12/04/2020.12.02.20242982.full.pdf

10. Bessi, A., Coletto, M., Davidescu, G.A., Scala, A., Caldarelli, G., Quattrociocchi, W.: Science vs conspiracy: collective narratives in the age of misinformation. PLoS ONE **10**(2), e0118093 (2015)

11. Yap, S., Lee, A., Ji, L.-J., Li, Y., Dong, Y.: Cultural differences in people's psychological response to COVID-19. Front. Psychol. (2021). https://doi.org/10.3389/fpsyg.2021.636062

12. Dean, D.J., et al.: Cross-cultural comparisons of psychosocial distress in the USA, South Korea, France, and Hong Kong during the initial phase of COVID-19. Psychiatry Res. **295**, 113593 (2021)

13. Jovančević, A., Cvetković, I., Milićević, N.: Information sources and conspiracy theories as predictors of vaccination intention [Conference Poster Presentation]. In: 49th Meeting of the European Brain and Behaviour Society (EBBS), 3–8 September 2021 (2021). https://www.ebbs2021.org

14. Briggs, S.R., Cheek, J.M.: The role of factor analysis in the development and evaluation of personality scales. J. Pers. **54**(1), 106–148 (1986)

15. Clark, L.A., Watson, D.: Constructing validity: basic issues in objective scale development. Psychol. Assess. **7**(3), 309–319 (1995)

16. Steenkamp, J.-B.E.M., Baumgartner, H.: Assessing measurement invariance in crossnational consumer research. J. Consum. Res. **25**, 78–90 (1998)

17. Sinkovics, R.R., Henseler, J., Ringle, C.M., Sarstedt, M.: Testing measurement invariance of composites using partial least squares. Int. Market. Rev. (2016). https://www.researchgate.net/profile/Marko_Sarstedt/publication/274196136_Testing_Measurement_Invariance_of_Composites_Using_Partial_Least_Squares/links/59fd8381a6fdcca1f29962d1/Testing-Measurement-Invariance-of-Composites-Using-Partial-Least-Squares.pdf

18. Adam-Troian, J., et al.: Investigating the links between cultural values and belief in conspiracy theories: the key roles of collectivism and masculinity. Polit. Psychol. **42**(4), 597–618 (2021)

Author Index